ornl

NUREG/CR-4888
ORNL-6377

OAK RIDGE NATIONAL LABORATORY

MARTIN MARIETTA

Pressurized-Thermal-Shock Test of 6-in.-Thick Pressure Vessels. PTSE-2: Investigation of Low Tearing Resistance and Warm Prestressing

R. H. Bryan
B. R. Bass
S. E. Bolt
J. W. Bryson
W. R. Corwin
J. G. Merkle
R. K. Nanstad
G. C. Robinson

Prepared for the U.S. Nuclear Regulatory Commission
Office of Nuclear Regulatory Research
Under Interagency Agreements DOE 0551-0551-A1 and 0552-0552-A1

OPERATED BY
MARTIN MARIETTA ENERGY SYSTEMS, INC.
FOR THE UNITED STATES
DEPARTMENT OF ENERGY

Available from

Superintendent of Documents
U.S. Government Printing Office
Post Office Box 37082
Washington, D.C. 20013-7982

and

National Technical Information Service
Springfield, VA 22161

NUREG/CR-4888
ORNL-6377
Dist. Category RF

Engineering Technology Division

PRESSURIZED-THERMAL-SHOCK TEST OF 6-IN.-THICK PRESSURE VESSELS. PTSE-2: INVESTIGATION OF LOW TEARING RESISTANCE AND WARM PRESTRESSING

R. H. Bryan
B. R. Bass*
S. E. Bolt
J. W. Bryson
W. R. Corwin
J. G. Merkle
R. K. Nanstad†
G. C. Robinson

*Computing and Telecommunications Division
†Metals and Ceramics Division

Manuscript Completed — December 1987
Date Published — December 1987

Prepared for the
U.S. Nuclear Regulatory Commission
Office of Nuclear Regulatory Research
under Interagency Agreements DOE 0551-0551-A1 and 0552-0552-A1

NRC FIN No. B0119

Prepared by the
OAK RIDGE NATIONAL LABORATORY
Oak Ridge, Tennessee 37831
operated by
MARTIN MARIETTA ENERGY SYSTEMS, INC.
for the
U.S. DEPARTMENT OF ENERGY
under Contract No. DE-AC05-84OR21400

CONTENTS

LIST OF FIGURES

LIST OF TABLES

FOREWORD

The work reported here was performed at Oak Ridge National Laboratory (ORNL) under the Heavy-Section Steel Technology (HSST) Program, under the direction of C. E. Pugh and W. R. Corwin, prior and current program managers, respectively. The program is sponsored by the Office of Nuclear Regulatory Research of the U.S. Nuclear Regulatory Commission (NRC). The technical monitor for the NRC is M. E. Mayfield, who succeeded Milton Vagins, the monitor during the performance of most of this work.

This report is designated HSST Report 93. Prior reports in this series are listed below:

1. S. Yukawa, *Evaluation of Periodic Proof Testing and Warm Prestressing Procedures for Nuclear Reactor Vessels*, HSSTP-TR-1, General Electric Company, Schenectady, N.Y. (July 1, 1969).
2. L. W. Loechel, *The Effect of Testing Variables on the Transition Temperature in Steel*, MCR-69-189, Martin Marietta Corporation, Denver, Colo. (November 20, 1969).
3. P. N. Randall, *Gross Strain Measure of Fracture Toughness of Steels*, HSSTP-TR-3, TRW Systems Group, Redondo Beach, Calif. (November 1, 1969).
4. C. Visser, S. E. Gabrielse, and W. VanBuren, *A Two-Dimensional Elastic-Plastic Analysis of Fracture Test Specimens*, WCAP-7368, Westinghouse Electric Corporation, PWR Systems Division, Pittsburgh, Pa. (October 1969).
5. T. R. Mager and F. O. Thomas, *Evaluation by Linear Elastic Fracture Mechanics of Radiation Damage to Pressure Vessel Steels*, WCAP-7328 (Rev.), Westinghouse Electric Corporation, PWR Systems Division, Pittsburgh, Pa. (October 1969).
6. W. O. Shabbits, W. H. Pryle, and E. T. Wessel, *Heavy-Section Fracture Toughness Properties of A533 Grade B Class 1 Steel Plate and Submerged Arc Weldment*, WCAP-7414, Westinghouse Electric Corporation, PWR Systems Divison, Pittsburgh, Pa. (December 1969).
7. F. J. Loss, *Dynamic Tear Test Investigations of the Fracture Toughness of Thick-Section Steel*, NRL-7056, Naval Research Laboratory, Washington, D.C. (May 14, 1970).
8. P. B. Crosley and E. J. Ripling, *Crack Arrest Fracture Toughness of A533 Grade B Class 1 Pressure Vessel Steel*, HSSTP-TR-8, Materials Research Laboratory, Inc., Glenwood, Ill. (March 1970).
9. T. R. Mager, *Post-Irradiation Testing of 2T Compact Tension Specimens*, WCAP-7561, Westinghouse Electric Corporation, PWR Systems Division, Pittsburgh, Pa. (August 1970).
10. T. R. Mager, *Fracture Toughness Characterization Study of A533, Grade B, Class 1 Steel*, WCAP-7578, Westinghouse Electric Corporation, PWR Systems Division, Pittsburgh, Pa. (October 1970).

11. T. R. Mager, *Notch Preparation in Compact Tension Specimens*, WCAP-7579, Westinghouse Electric Corporation, PWR Systems Division, Pittsburgh, Pa. (November 1970).

12. N. Levy and P. V. Marcal, *Three-Dimensional Elastic-Plastic Stress and Strain Analysis for Fracture Mechanics, Phase I: Simple Flawed Specimens*, HSSTP-TR-12, Brown University, Providence, R.I. (December 1970).

13. W. O. Shabbits, *Dynamic Fracture Toughness Properties of Heavy Section A533 Grade B Class 1 Steel Plate*, WCAP-7623, Westinghouse Electric Corporation, PWR Systems Division, Pittsburgh, Pa. (December 1970).

14. P. N. Randall, *Gross Strain Crack Tolerance of A 533-B Steel*, HSSTP-TR-14, TRW Systems Group, Redondo Beach, Calif. (May 1, 1971).

15. H. T. Corten and R. H. Sailors, *Relationship Between Material Fracture Toughness Using Fracture Mechanics and Transition Temperature Tests*, T&AM Report 346, University of Illinois, Urbana, Ill. (August 1, 1971).

16. T. R. Mager and V. J. McLaughlin, *The Effect of an Environment of High Temperature Primary Grade Nuclear Reactor Water on the Fatigue Crack Growth Characteristics of A533 Grade B Class 1 Plate and Weldment Material*, WCAP-7776, Westinghouse Electric Corporation, PWR Systems Division, Pittsburgh, Pa. (October 1971).

17. N. Levy and P. V. Marcal, *Three-Dimensional Elastic-Plastic Stress and Strain Analysis for Fracture Mechanics, Phase II: Improved Modelling*, HSSTP-TR-17, Brown University, Providence, R.I. (November 1971).

18. S. C. Grigory, *Tests of 6-in.-Thick Flawed Tensile Specimens, First Technical Summary Report, Longitudinal Specimens Numbers 1 through 7*, HSSTP-TR-18, Southwest Research Institute, San Antonio, Tex. (June 1972).

19. P. N. Randall, *Effects of Strain Gradients on the Gross Strain Crack Tolerance of A533-B Steel*, HSSTP-TR-19, TRW Systems Group, Redondo Beach, Calif. (June 15, 1972).

20. S. C. Grigory, *Tests of 6-Inch-Thick Flawed Tensile Specimens, Second Technical Summary Report, Transverse Specimens Numbers 8 through 10, Welded Specimens Numbers 11 through 13*, HSSTP-TR-20, Southwest Research Institute, San Antonio, Tex. (June 1972).

21. L. A. James and J. A. Williams, *Heavy Section Steel Technology Program Technical Report No. 21, The Effect of Temperature and Neutron Irradiation Upon the Fatigue-Crack Propagation Behavior of ASTM A533 Grade B, Class 1 Steel*, HEDL-TME 72-132, Hanford Engineering Development Laboratory, Richland, Wash. (September 1972).

22. S. C. Grigory, *Tests of 6-Inch-Thick Flawed Tensile Specimens, Third Technical Summary Report, Longitudinal Specimens Numbers 14 through 16, Unflawed Specimen Number 17*, HSSTP-TR-22, Southwest Research Institute, San Antonio, Tex. (October 1972).

23. S. C. Grigory, *Tests of 6-Inch-Thick Tensile Specimens, Fourth Technical Summary Report, Tests of 1-Inch-Thick Flawed Tensile Specimens for Size Effect Evaluation*, HSSTP-TR-23, Southwest Research Institute, San Antonio, Tex. (June 1973).

24. S. P. Ying and S. C. Grigory, *Tests of 6-Inch-Thick Tensile Specimens, Fifth Technical Summary Report, Acoustic Emission Monitoring of One-Inch and Six-Inch-Thick Tensile Specimens*, HSSTP-TR-24, Southwest Research Institute, San Antonio, Tex. (November 1972).

25. R. W. Derby, J. G. Merkle, G. C. Robinson, G. D. Whitman, and F. J. Witt, *Test of 6-Inch-Thick Pressure Vessels. Series 1: Intermediate Test Vessels V-1 and V-2*, ORNL-4895, Oak Ridge Natl. Lab., Oak Ridge, Tenn. (February 1974).

26. W. J. Stelzman and R. G. Berggren, *Radiation Strengthening and Embrittlement in Heavy Section Steel Plates and Welds*, ORNL-4871, Oak Ridge Natl. Lab., Oak Ridge, Tenn. (June 1973).

27. P. B. Crosley and E. J. Ripling, *Crack Arrest in an Increasing K-Field*, HSSTP-TR-27, Materials Research Laboratory, Inc., Glenwood, Ill. (January 1973).

28. P. V. Marcal, P. M. Stuart, and R. S. Bettes, *Elastic-Plastic Behavior of a Longitudinal Semi-Elliptic Crack in a Thick Pressure Vessel*, HSSTP-TR-28, Brown University, Providence, R.I. (June 1973).

29. W. J. Stelzman, R. G. Berggren, and T. N. Jones, *ORNL Characterization of Heavy-Section Steel Technology Program Plates 01, 02 and 03*, NUREG/CR-4092 (ORNL/TM-9491), Oak Ridge Natl. Lab., Oak Ridge, Tenn. (April 1985).

30. Canceled.

31. J. A. Williams, *The Irradiation and Temperature Dependence of Tensile and Fracture Properties of ASTM A533, Grade B, Class 1 Steel Plate and Weldment*, HEDL-TME 73-75, Hanford Engineering Development Laboratory, Richland, Wash. (August 1973).

32. J. M. Steichen and J. A. Williams, *High Strain Rate Tensile Properties of Irradiated ASTM A533 Grade B Class 1 Pressure Vessel Steel*, Hanford Engineering Development Laboratory, Richland, Wash. (July 1973).

33. P. C. Riccardella and J. L. Swedlow, *A Combined Analytical-Experimental Fracture Study of the Two Leading Theories of Elastic-Plastic Fracture (J-Integral and Equivalent Energy)*, WCAP-8224, Westinghouse Electric Corporation, Pittsburgh, Pa. (October 1973).

34. R. J. Podlasek and R. J. Eiber, *Final Report on Investigation of Mode III Crack Extension in Reactor Piping*, Battelle Columbus Laboratories, Columbus, Ohio (December 14, 1973).

35. T. R. Mager, J. D. Landes, D. M. Moon, and V. J. McLaughlin, *Interim Report on the Effect of Low Frequencies on the Fatigue Crack Growth Characteristics of A533 Grade B Class 1 Plate in an Environment of High-Temperature Primary Grade Nuclear Reactor Water*, WCAP-8256, Westinghouse Electric Corporation, Pittsburgh, Pa. (December 1973).

36. J. A. Williams, *The Irradiated Fracture Toughness of ASTM A533, Grade B, Class 1 Steel Measured with a Four-Inch-Thick Compact Tension Specimen*, HEDL-TME 75-10, Hanford Engineering Development Laboratory, Richland, Wash. (January 1975).

37. R. H. Bryan, J. G. Merkle, M. N. Raftenberg, G. C. Robinson, and J. E. Smith, *Test of 6-Inch-Thick Pressure Vessels. Series 2: Intermediate Test Vessels V-3, V-4, and V-6*, ORNL-5059, Oak Ridge Natl. Lab., Oak Ridge, Tenn. (November 1975).

38. T. R. Mager, S. E. Yanichko, and L. R. Singer, *Fracture Toughness Characterization of HSST Intermediate Pressure Vessel Material*, WCAP-8456, Westinghouse Electric Corporation, Pittsburgh, Pa. (December 1974).

39. J. G. Merkle, G. D. Whitman, and R. H. Bryan, *An Evaluation of the HSST Program Intermediate Pressure Vessel Tests in Terms of Light-Water-Reactor Pressure Vessel Safety*, ORNL/TM-5090, Oak Ridge Natl. Lab., Oak Ridge, Tenn. (November 1975).

40. J. G. Merkle, G. C. Robinson, P. P. Holz, J. E. Smith, and R. H. Bryan, *Test of 6-In.-Thick Pressure Vessels. Series 3: Intermediate Test Vessel V-7*, ORNL/NUREG-1, Oak Ridge Natl. Lab., Oak Ridge, Tenn. (August 1976).

41. J. A. Davidson, L. J. Ceschini, R. P. Shogan, and G. V. Rao, *The Irradiated Dynamic Fracture Toughness of ASTM A533, Grade B, Class 1 Steel Plate and Submerged Arc Weldment*, WCAP-8775, Westinghouse Electric Corporation, Pittsburgh, Pa. (October 1976).

42. R. D. Cheverton, *Pressure Vessel Fracture Studies Pertaining to a PWR LOCA-ECC Thermal Shock: Experiments TSE-1 and TSE-2*, ORNL/NUREG/TM-31, Oak Ridge Natl. Lab., Oak Ridge, Tenn. (September 1976).

43. J. G. Merkle, G. C. Robinson, P. P. Holz, and J. E. Smith, *Test of 6-In.-Thick Pressure Vessels. Series 4: Intermediate Test Vessels V-5 and V-9 with Inside Nozzle Corner Cracks*, ORNL/NUREG-7, Oak Ridge Natl. Lab., Oak Ridge, Tenn. (August 1977).

44. J. A. Williams, *The Ductile Fracture Toughness of Heavy Section Steel Plate*, NUREG/CR-0859, Hanford Engineering Development Laboratory, Richland, Wash. (September 1979).

45. R. H. Bryan, T. M. Cate, P. P. Holz, T. A. King, J. G. Merkle, G. C. Robinson, G. C. Smith, J. E. Smith, and G. D. Whitman, *Test of 6-in.-Thick Pressure Vessels. Series 3: Intermediate Test Vessel V-7A Under Sustained Loading*, ORNL/NUREG-9, Oak Ridge Natl. Lab., Oak Ridge, Tenn. (February 1978).

46. R. D. Cheverton and S. E. Bolt, *Pressure Vessel Fracture Studies Pertaining to a PWR LOCA-ECC Thermal Shock: Experiments TSE-3 and TSE-4 and Update of TSE-1 and TSE-2 Analysis*, ORNL/NUREG-22, Oak Ridge Natl. Lab., Oak Ridge, Tenn. (December 1977).

47. D. A. Canonico, *Significance of Reheat Cracks to the Integrity of Pressure Vessels for Light-Water Reactors*, ORNL/NUREG-15, Oak Ridge Natl. Lab., Oak Ridge, Tenn. (July 1977).

48. G. C. Smith and P. P. Holz, *Repair Weld Induced Residual Stresses in Thick-Walled Steel Pressure Vessels*, NUREG/CR-0093 (ORNL/NUREG/TM-153), Oak Ridge Natl. Lab., Oak Ridge, Tenn. (June 1978).

49. P. P. Holz and S. W. Wismer, *Half-Bead (Temper) Repair Welding for HSST Vessels*, NUREG/CR-0113 (ORNL/NUREG/TM-177), Oak Ridge Natl. Lab., Oak Ridge, Tenn. (June 1978).

50. G. C. Smith, P. P. Holz, and W. J. Stelzman, *Crack Extension and Arrest Tests of Axially Flawed Steel Model Pressure Vessels*, NUREG/CR-0126 (ORNL/NUREG/TM-196), Oak Ridge Natl. Lab., Oak Ridge, Tenn. (October 1978).

51. R. H. Bryan, P. P. Holz, J. G. Merkle, G. C. Smith, J. E. Smith, and W. J. Stelzman, *Test of 6-in.-Thick Pressure Vessels. Series 3: Intermediate Test Vessel V-7B*, NUREG/CR-0309 (ORNL/NUREG-38), Oak Ridge Natl. Lab., Oak Ridge, Tenn. (October 1978).

52. R. D. Cheverton, S. K. Iskander, and S. E. Bolt, *Applicability of LEFM to the Analysis of PWR Vessels Under LOCA-ECC Thermal Shock Conditions*, NUREG/CR-0107 (ORNL/NUREG-40), Oak Ridge Natl. Lab., Oak Ridge, Tenn. (October 1978).

53. R. H. Bryan, D. A. Canonico, P. P. Holz, S. K. Iskander, J. G. Merkle, J. E. Smith, and W. J. Stelzman, *Test of 6-in.-Thick Pressure Vessels, Series 3: Intermediate Test Vessel V-8*, NUREG/CR-0675 (ORNL/NUREG-58), Oak Ridge Natl. Lab., Oak Ridge, Tenn. (December 1979).

54. R. D. Cheverton and S. K. Iskander, *Application of Static and Dynamic Crack Arrest Theory to TSE-4*, NUREG/CR-0767 (ORNL/NUREG-57), Oak Ridge Natl. Lab., Oak Ridge, Tenn. (June 1979).

55. J. A. Williams, *Tensile Properties of Irradiated and Unirradiated Welds of A533 Steel Plate and A508 Forgings*, NUREG/CR-1158 (ORNL/Sub-79/50917/2), Hanford Engineering Development Laboratory, Richland, Wash. (July 1979).

56. K. W. Carlson and J. A. Williams, *The Effect of Crack Length and Side Grooves on the Ductile Fracture Toughness Properties of ASTM A533 Steel*, NUREG/CR-1171 (ORNL/Sub-79/50917/3), Hanford Engineering Development Laboratory, Richland, Wash. (October 1979).

57. P. P. Holz, *Flaw Preparations for HSST Program Vessel Fracture Mechanics Testing; Mechanical-Cyclic Pumping and Electron-Beam Weld-Hydrogen Charge Cracking Schemes*, NUREG/CR-1274 (ORNL/NUREG/TM-369), Oak Ridge Natl. Lab., Oak Ridge, Tenn. (May 1980).

58. S. K. Iskander, *Two Finite Element Techniques for Computing Mode I Stress Intensity Factors in Two- or Three-Dimensional Problems*, NUREG/CR-1499 (ORNL/NUREG/CSD/TM-14), Computer Sciences Div., Union Carbide Corp. Nuclear Div., Oak Ridge, Tenn. (February 1981).

59. P. B. Crosley and E. J. Ripling, *Development of a Standard Test for Measuring K_{Ia} with a Modified Compact Specimen*, NUREG/CR-2294 (ORNL/Sub-81/7755/1), Materials Research Laboratory, Glenwood, Ill. (August 1981).

60. S. N. Atluri, B. R. Bass, J. W. Bryson, and K. Kathiresan, *NOZ-FLAW: A Finite Element Program for Direct Evaluation of Stress Intensity Factors for Pressure Vessel Nozzle-Corner Flaws*, NUREG/CR-1843 (ORNL/NUREG/CSD/TM-18), Computer Sciences Div., Oak Ridge Gaseous Diffusion Plant, Oak Ridge, Tenn. (March 1981).

61. A. Shukla, W. L. Fourney, and G. R. Irwin, *Study of Energy Loss and Its Mechanisms in Homalite 100 During Crack Propagation and Arrest*, NUREG/CR-2150 (ORNL/Sub-7778/1), University of Maryland, College Park, Md. (August 1981).

62. S. K. Iskander, R. D. Cheverton, and D. G. Ball, *OCA-I, A Code for Calculating the Behavior of Flaws on the Inner Surface of a Pressure Vessel Subjected to Temperature and Pressure Transients*, NUREG/CR-2113 (ORNL/NUREG-84), Oak Ridge Natl. Lab., Oak Ridge, Tenn. (August 1981).

63. R. J. Sanford, R. Chona, W. L. Fourney, and G. R. Irwin, *A Photoelastic Study of the Influence of Non-Singular Stresses in Fracture Test Specimens*, NUREG/CR-2179 (ORNL/Sub-7778/2), University of Maryland, College Park, Md. (August 1981).

64. B. R. Bass, S. N. Atluri, J. W. Bryson, and K. Kathiresan, *OR-FLAW: A Finite Element Program for Direct Evaluation of K-Factors for User-Defined Flaws in Plate, Cylinders, and Pressure-Vessel Nozzle Corners*, NUREG/CR-2494 (ORNL/CSD/TM-165), Oak Ridge Natl. Lab., Oak Ridge, Tenn. (April 1982).

65. B. R. Bass and J. W. Bryson, *ORMGEN-3D: A Finite Element Mesh Generator for 3-Dimensional Crack Geometries*, NUREG/CR-2997, Vol. 1 (ORNL/TM-8527/V1), Oak Ridge Natl. Lab., Oak Ridge, Tenn. (December 1982).

66. B. R. Bass and J. W. Bryson, *ORVIRT: A Finite Element Program for Energy Release Rate Calculations for 2-Dimensional and 3-Dimensional Crack Models*, NUREG/CR-2997, Vol. 2 (ORNL/TM-8527/V2), Oak Ridge Natl. Lab., Oak Ridge, Tenn. (February 1983).

67. R. D. Cheverton, S. K. Iskander, and D. G. Ball, *PWR Pressure Vessel Integrity During Overcooling Accidents: A Parametric Analysis*, NUREG/CR-2895 (ORNL/TM-7931), Oak Ridge Natl. Lab., Oak Ridge, Tenn. (February 1983).

68. D. G. Ball, R. D. Cheverton, J. B. Drake, and S. K. Iskander, *OCA-II, A Code for Calculating Behavior of 2-D and 3-D Surface Flaws in a Pressure Vessel Subjected to Temperature and Pressure Transients*, NUREG/CR-3491 (ORNL-5934), Oak Ridge Natl. Lab., Oak Ridge, Tenn. (February 1984).

69. A. Sauter, R. D. Cheverton, and S. K. Iskander, *Modification of OCA-I for Application to a Reactor Pressure Vessel with Cladding on the Inner Surface*, NUREG/CR-3155 (ORNL/TM-8649), Oak Ridge Natl. Lab., Oak Ridge, Tenn. (May 1983).

70. R. D. Cheverton and D. G. Ball, *OCA-P, A Deterministic and Probabilistic Fracture-Mechanics Code for Application to Pressure Vessels*, NUREG/CR-3618 (ORNL-5991), Oak Ridge Natl. Lab., Oak Ridge, Tenn. (May 1984).

71. J. G. Merkle, *An Examination of the Size Effects and Data Scatter Observed in Small Specimen Cleavage Fracture Toughness Testing*, NUREG/CR-3672 (ORNL/TM-9088), Oak Ridge Natl. Lab., Oak Ridge, Tenn. (April 1984).

72. C. E. Pugh et al., *Heavy-Section Steel Technology Program — Five-Year Plan FY 1983–1987*, NUREG/CR-3595 (ORNL/TM-9008), Oak Ridge Natl. Lab., Oak Ridge, Tenn. (April 1984).

73. D. G. Ball, B. R. Bass, J. W. Bryson, R. D. Cheverton, and J. B. Drake, *Stress Intensity Factor Influence Coefficients for Surface Flaws in Pressure Vessels*, NUREG/CR-3723 (ORNL/CSD/TM-216), Oak Ridge Natl. Lab., Oak Ridge, Tenn. (February 1985).

74. W. R. Corwin, R. G. Berggren, and R. K. Nanstad, *Charpy Toughness and Tensile Properties of Neutron Irradiated Stainless Steel Submerged-Arc Weld Cladding Overlay*, NUREG/CR-3927 (ORNL/TM-9309), Oak Ridge Natl. Lab., Oak Ridge, Tenn. (September 1984).

75. C. W. Schwartz, R. Chona, W. L. Fourney, and G. R. Irwin, *SAMCR: A Two-Dimensional Dynamic Finite Element Code for the Stress Analysis of Moving CRacks*, NUREG/CR-3891 (ORNL/Sub/79-7778/3), University of Maryland, College Park, Md. (November 1984).

76. W. R. Corwin, G. C. Robinson, R. K. Nanstad, J. G. Merkle, R. G. Berggren, G. M. Goodwin, R. L. Swain, and T. D. Owings, *Effects of Stainless Steel Weld Overlay Cladding on the Structural Integrity of Flawed Steel Plates in Bending, Series 1*, NUREG/CR-4015 (ORNL/TM-9390), Oak Ridge Natl. Lab., Oak Ridge, Tenn. (April 1985).

77. R. H. Bryan, B. R. Bass, S. E. Bolt, J. W. Bryson, D. P. Edmonds, R. W. McCulloch, J. G. Merkle, R. K. Nanstad, G. C. Robinson, K. R. Thoms, and G. D. Whitman, *Pressurized-Thermal-Shock Test of 6-in.-Thick Pressure Vessels. PTSE-1: Investigation of Warm Prestressing and Upper-Shelf Arrest*, NUREG/CR-4105 (ORNL-6135), Oak Ridge Natl. Lab., Oak Ridge, Tenn. (April 1985).

78. R. D. Cheverton, D. G. Ball, S. E. Bolt, S. K. Iskander, and R. K. Nanstad, *Pressure Vessel Fracture Studies Pertaining to the PWR Thermal-Shock Issue: Experiments TSE-5, TSE-5A, and TSE-6*, NUREG/CR-4249 (ORNL-6163), Martin Marietta Energy Systems, Inc., Oak Ridge Natl. Lab., Oak Ridge, Tenn. (June 1985).

79. R. D. Cheverton, D. G. Ball, S. E. Bolt, S. K. Iskander, and R. K. Nanstad, *Pressure Vessel Fracture Studies Pertaining to the PWR Thermal-Shock Issue: Experiment TSE-7*, NUREG/CR-4304 (ORNL-6177), Martin Marietta Energy Systems, Inc., Oak Ridge Natl. Lab., Oak Ridge, Tenn. (August 1985).

80. R. H. Bryan, B. R. Bass, S. E. Bolt, J. W. Bryson, J. G. Merkle, R. K. Nanstad, and G. C. Robinson, *Test of 6-in.-Thick Pressure Vessels. Series 3: Intermediate Test Vessel V-8A — Tearing Behavior of Low Upper-Shelf Material*, NUREG/CR-4760 (ORNL-6187), Martin Marietta Energy Systems, Inc., Oak Ridge Natl. Lab., Oak Ridge, Tenn. (May 1987).

81. R. D. Cheverton and D. G. Ball, *A Parametric Study of PWR Pressure Vessel Integrity During Overcooling Accidents, Considering Both 2-D and 3-D Flaws*, NUREG/CR-4325 (ORNL/TM-9682), Martin Marietta Energy Systems, Inc., Oak Ridge Natl. Lab., Oak Ridge, Tenn. (August 1985).

82. E. C. Rodabaugh, *Comments on the Leak-Before-Break Concept for Nuclear Power Plant Piping Systems*, NUREG/CR-4305 (ORNL/Sub/82-22252/3), E. C. Rodabaugh Associates, Inc., Hilliard, Ohio (August 1985).

83. J. W. Bryson, *ORVIRT.PC: A 2-D Finite Element Fracture Analysis Program for a Microcomputer*, NUREG/CR-4367 (ORNL-6208), Martin Marietta Energy Systems, Inc., Oak Ridge Natl. Lab., Oak Ridge, Tenn. (October 1985).

84. D. G. Ball and R. D. Cheverton, *Adaptation of OCA-P, A Probabilistic Fracture-Mechanics Code, to a Personal Computer*, NUREG/CR-4468 (ORNL/CSD/TM-233), Martin Marietta Energy Systems, Inc., Oak Ridge Natl. Lab., Oak Ridge, Tenn. (January 1986).

85. J. W. Bryson and B. R. Bass, *ORMGEN.PC: A Microcomputer Program for Automatic Mesh Generation of 2-D Crack Geometries*, NUREG/CR-4475 (ORNL-6250), Martin Marietta Energy Systems, Inc., Oak Ridge Natl. Lab., Oak Ridge, Tenn. (March 1986).

86. G. D. Whitman, *Historical Summary of the Heavy-Section Steel Technology Program and Some Related Activities in Light-Water Reactor Pressure Vessel Safety Research*, NUREG/CR-4489 (ORNL-6259), Martin Marietta Energy Systems, Inc., Oak Ridge Natl. Lab., Oak Ridge, Tenn. (March 1986).

87. C. Inversini and J. W. Bryson, *[illegible]T.PC: A Graphic Utility for ORMGEN.PC and ORVIRT.PC*, NUREG/CR-[illegible]3 (ORNL-6291), Martin Marietta Energy Systems, Inc., Oak Ridge Natl. Lab., Oak Ridge, Tenn. (June 1986).

88. J. J. McGowan, R. K. Nanstad, and K. R. Thomas, *Characterization of Irradiated Current-Practice Welds and A533 Grade B Class 1 Plate for Nuclear Pressure Vessel Service*, NUREG/CR-4880 (ORNL/TM-10387), Martin Marietta Energy Systems, Inc., Oak Ridge Natl. Lab., Oak Ridge Tenn. (to be published).

89. K. V. Cook and R. W. McClung, *Flaw Density Examinations of a Clad Boiling Water Reactor Pressure Vessel Segment*, NUREG/CR-4860 (ORNL/TM-10364), Martin Marietta Energy Systems, Inc., Oak Ridge Natl. Lab., Oak Ridge, Tenn. (April 1987).

90. D. J. Naus et al., *Crack-Arrest Behavior in SEN Wide Plates of Quenched and Tempered A 533 Grade B Steel Tested Under Nonisothermal Conditions*, NUREG/CR-4930 (ORNL-6388), Martin Marietta Energy Systems, Inc., Oak Ridge Natl. Lab., Oak Ridge, Tenn. (August 1987).

91. D. B. Barker et al., *A Report on the Round Robin Program Conducted to Evaluate the Proposed ASTM Standard Test Method for Determining the Plane Strain Crack Arrest Fracture Toughness K_{Ia} of Ferritic Materials*, NUREG/CR-4966 (ORNL/Sub/79-7778/4), University of Maryland, College Park, Md. (to be published).

92. W. H. Bamford, *A Summary of Environmentally Assisted Crack-Growth Studies Performed at Westinghouse Electric Corporation Under Funding from the Heavy-Section Steel Technology Program*, NUREG/CR-5020 (ORNL/Sub/82-21598/1), Westinghouse Electric Corp., Pittsburgh, Pa. (to be published).

EXECUTIVE SUMMARY

The second pressurized-thermal-shock experiment (PTSE-2) in the Heavy-Section Steel Technology Program is the most recent of a long succession of fracture-mechanics experiments on a scale that allows important aspects of fracture behavior of reactor pressure vessels to be simulated. Such experiments are the means by which theoretical models of fracture behavior can be evaluated for possible application to fracture analysis of vessels in nuclear plants. The principal issues of concern in the pressurized-thermal-shock experiments are (1) warm-prestressing phenomena, (2) crack propagation from brittle to ductile regions, (3) transient crack stabilization in ductile regions, and (4) crack shape changes in bimetallic zones of clad vessels.

Three experiments have been planned to help resolve the four principal issues:

PTSE-1 — to demonstrate effectiveness of warm prestressing and to investigate rapid crack propagation into the ductile upper shelf and subsequent tearing stability,

PTSE-2 — to study additional aspects of warm prestressing and to investigate the transition from cleavage fracture to unstable ductile tearing, and

PTSE-3 — to investigate the influence of stainless steel cladding in restricting the growth of short flaws.

The PTSE-2 experiment was concerned, primarily, with the behavior of a crack in material with low tearing resistance, and, secondarily, with warm prestressing. Vulnerability of existing reactor pressure vessels to damage in overcooling accidents is a potential problem mainly in instances of vessel steels that have high copper contents and, consequently, high susceptibility to fast-neutron embrittlement. Coincidentally, the irradiated high-copper steels have low ductile-tearing resistance at temperatures on the Charpy upper shelf. In the past, overcooling accident evaluations have characterized the high-copper irradiated low-upper-shelf steels solely by their effective reference temperature for the nil ductility transition, RT_{NDT}. Ductile tearing has generally been ignored.

The PTSE-1 experiment had explored, with high toughness material (i.e., resistart to ductile tearing), warm prestressing and the nature of crack propagation and arrest as the crack approached the ductile zone within the wall of the test vessel. The PTSE-2 experiment employed a steel that had low toughness in the ductile fracture regime, so that fracture behavior representative of that of irradiated low-upper-shelf steel could be observed under transient conditions relevant to a flawed nuclear reactor pressure vessel.

The vessel used for PTSE-1 and two earlier fracture tests was repaired for the PTSE-2 experiment. A 1-m-long sharp flaw was implanted in a welded-in insert of low-upper-shelf material in the 148-mm-thick test

vessel. The vessel was instrumented to give measurements of crack-mouth-opening displacement, temperature profiles through the vessel wall, and internal pressure during the experiment. With this instrumentation scheme, posttest fracture analyses could be conducted on the basis of actual loads experienced during the pressurized-thermal-shock transients. This procedure facilitated the interpretation of the fracture phenomena that transpired by eliminating, in the final analyses, the considerable uncertainties of heat transfer calculations.

Extensive experimental and analytical studies preceded the transient experiment. Mechanical and physical properties of the special material in which the flaw resided were determined by extensive characterization tests. Numerous prospective transients were analyzed to define experimental procedures with good expectations for success in spite of uncertainties. Two transients were defined and conducted.

The first transient generated the conditions necessary for the warm-prestressing investigation. In this transient, the temperature dropped from ~300°C throughout the vessel to ~8°C on the outside surface. The transient included a warm-prestressing phase, in which the pressure was reduced from ~63 to 10 MPa, followed by repressurization until the flaw propagated in a brittle mode of fracture (at ~46 MPa). In the course of this transient, stable ductile tearing occurred before and after the brittle fracture. The second transient generated the conditions for a deep brittle crack propagation terminated by an arrest or conversion of the brittle fracture to ductile tearing under conditions conducive to a tearing instability. The initial temperature was ~275°C, and the outside surface cooled to ~4°C while the pressure increased monotonically from 3 to 67.3 MPa. The desired conditions were attained in both transients. In the final transient the test vessel ruptured, as had been expected but not especially desired, but without damage to the test facility or loss of information.

This experiment produced, for the first time with stress and toughness states representative of reactor pressure vessels, (1) the arrest of a brittle fracture with an immediate tearing instability and (2) brittle fracture following warm prestressing. Principal conclusions are that (1) low-upper-shelf material can exhibit very high arrest toughness, (2) ductile tearing promotes more severe fractures in low-upper-shelf material, (3) warm prestressing inhibits brittle fracture to some degree even when crack driving forces are increasing with time, (4) benefits of warm prestressing are diminished by ductile tearing, (5) a simple theoretical analysis of warm prestressing represented fracture conditions reasonably well, and (6) calculations of ductile tearing based on resistance curve test data did not consistently predict the observed tearing.

PRESSURIZED-THERMAL-SHOCK TEST OF 6-IN.-THICK PRESSURE VESSELS. PTSE-2: INVESTIGATION OF LOW TEARING RESISTANCE AND WARM PRESTRESSING

R. H. Bryan
B. R. Bass*
S. E. Bolt
J. W. Bryson
W. R. Corwin
J. G. Merkle
R. K. Nanstad†
G. C. Robinson

ABSTRACT

The second pressurized-thermal-shock test of a 148-mm-thick steel pressure vessel with a 1-m-long flaw was performed to investigate fracture behavior of a vessel under conditions relevant to a flawed nuclear reactor pressure vessel during an overcooling accident. The objectives were to observe transitional crack behavior in a steel with low tearing resistance and the effects of warm prestressing on crack initiation. Two combinations of pressure and thermal transient conditions were imposed on the vessel with initial vessel temperatures of ~300 and 275°C. The first transient, designed for studying warm prestressing, required a depressurization from ~63 MPa and repressurization to ~52 MPa. After being warm prestressed while $K_I > K_{Ic}$, the crack propagated during repressurization. Warm prestressing elevated the load at fracture significantly above K_{Ic}. The second transient produced a cleavage crack propagation and arrest followed immediately by unstable tearing. Stable ductile tearing preceded both brittle fractures and also followed the first crack arrest. The final cleavage propagation arrested at high K_I levels (~420 MPa$\cdot\sqrt{m}$) in spite of the low ductile-tearing resistance.

---

1. INTRODUCTION

A major activity in the Heavy-Section Steel Technology (HSST) Program at Oak Ridge National Laboratory (ORNL) has been the testing of thick-section vessels to determine the capability of analytical methods to predict flaw behavior under known conditions of flaw geometry, materials properties, and loading. These vessels were termed intermediate by virtue of their size relative to a full-scale light-water reactor pressure vessel and a small model vessel. They have served to provide a considerable body of experimental data over a wide range of fracture behavior for isothermal conditions when subjected to internal pressure

---

*Computing and Telecommunications Division.

†Metals and Ceramics Division.

loadings.[1-7] Also, eight thermal-shock experiments have been performed on unpressurized thick-wall cylindrical sections to study flaw behavior during a loss-of-coolant accident.[8-11] As a result of nuclear plant operating experience, it is recognized that transients can occur in pressurized-water reactors that involve pressure loadings concurrent with overcooling, that is, pressurized-thermal-shock transients.[12,13] Such transients produce potential fracture behavior that needs further investigation to determine whether existing methods used to assess vessel integrity are valid and to establish new methods. The results of a pressurized-thermal-shock experiment, designed to contribute significantly to this need, are contained in this report.

An accidental pressurized-thermal-shock transient, when imposed on a thick-wall vessel, may produce high tensile stresses on the cooled surface of the vessel. In cases in which irradiation embrittlement is significant, as is the case in some pressurized-water-reactor vessels, preexisting shallow flaws on the cooled surface may propagate in a fast fracture mode. If pressure is present, stresses are produced that become more dominant as the crack advances through the wall, and vessel integrity may be threatened in the absence of crack arrest or an action to reduce the load. The positive gradient in temperature and the diminution of damage through the thickness from neutron attenuation provide mechanisms to enhance crack arrest and terminate an incident without breaching the vessel wall. The primary objective of the series of experiments, of which PTSE-2 is a part, is to provide an experimental basis for the confirmation of current theoretical methods of fracture analysis or for the development of new methods.

Fracture phenomena that need investigation or confirmation and are tractable in pressurized-thermal-shock experiments are

1. fracture mode transition as the crack propagates into ductile regions;
2. propensity for ductile tearing, prior to initial propagation of a crack by cleavage;
3. inhibiting effects of warm prestressing on initiation of cleavage fracture; and
4. evolution of crack shape changes in clad vessels.

To realize the primary objective of the series of experiments it was necessary to use a flawed test vessel with which it was feasible to generate stress states and toughness conditions that are realistic relative to full-scale reactor pressure vessels. Furthermore, properties of the material in the vicinity of the flaw had to be appropriate to the experiments and be reasonably well defined. The HSST intermediate test vessel offered many advantages over other test configurations. In particular, the desired stress states in a requisite thick section were attainable, and a test section could be fabricated from materials with the desired properties. Several methods for pressurizing and thermally shocking a vessel were studied, and it was determined that an external flaw in the cylindrical section of the vessel resulted in a very practical configuration for achieving the desired loadings. In this geometry, the vessel would be cooled on the external surface from an initial isothermal condition and be pressurized internally to achieve predetermined loads at the

crack tip. This method simplified the coolant system by permitting an optimization of heat transfer performance at lower pressures, thus eliminating the high operating pressure requirement for a pump and other components, which were determined to be inordinately expensive but would have been necessary if the inside surface were shocked. Also, the vessel pressure boundary did not have to be penetrated by coolant lines; most importantly, thermal and pressure loadings could be uncoupled and thus controlled independently to produce the desired transients more easily.

The first pressurized-thermal-shock test of a flawed test vessel (PTSE-1) was performed in 1984 to investigate the effects of warm prestressing and the nature of arrest of a rapidly propagating crack at temperatures that correspond to the Charpy (ductile) upper shelf.[14] PTSE-1 clearly demonstrated that crack propagation was strongly inhibited during phases of warm prestressing in which the stress intensity factor K_I was decreasing with time ($\dot{K}_I < 0$) or when K_I was much lower than an earlier maximum. PTSE-1 also demonstrated that crack arrest could occur at high K_I values, exceeding the implied limit of 220 MPa$\cdot\sqrt{m}$ of Sect. XI of the *ASME Boiler and Pressure Vessel Code*,[15] and that arrest could occur in a positive K_I gradient. Both these results have salutary implications in evaluations of pressure vessel integrity by current rules.

The second pressurized-thermal-shock experiment (PTSE-2) was concerned, primarily, with the behavior of a crack in material with low tearing resistance and, secondarily, with warm prestressing. Vulnerability of existing reactor pressure vessels to damage in overcooling accidents is a potential problem mainly in instances of vessel steels that have high copper contents and, consequently, high susceptibility to fast-neutron embrittlement. Coincidentally, these high-copper steels have low ductile tearing resistance at temperatures on the Charpy upper shelf.[16] While conclusions from overcooling accident analyses are principally determined by transition temperature and its effect on crack initiation, in some hypothetical transients crack arrest is the controlling phenomenon. Crack-arrest toughness in low-upper-shelf steels has been presumed to have the same dependence on temperature T and the reference temperature for the nil ductility transition RT_{NDT} as do steels with higher upper-shelf toughness, but this has not been established experimentally. Furthermore, irrespective of cleavage arrest toughness, an arrested crack may be unstable relative to ductile tearing, particularly if the tearing resistance J_R is low.

The test vessel for PTSE-2 (Fig. 1.1) was fabricated from the HSST Program intermediate test vessel V-8 and had previously been tested three times, as V-8, V-8A, and PTSE-1. A 2 1/4 Cr-1 Mo steel insert welded into the cylindrical test section of the vessel was the site of the initial 1-m-long flaw. The insert was heat treated to obtain low Charpy impact energy (~50 to 70 J) on the ductile upper shelf, which ensured low ductile-tearing resistance.

During the experiment, the vessel was enclosed in a stainless steel shroud (Fig. 1.2) that served (1) as an oven for heating the test vessel to the desired initial temperature and (2) as a means for directing chilled coolant at proper velocity along the cylindrical external surface of the test vessel.

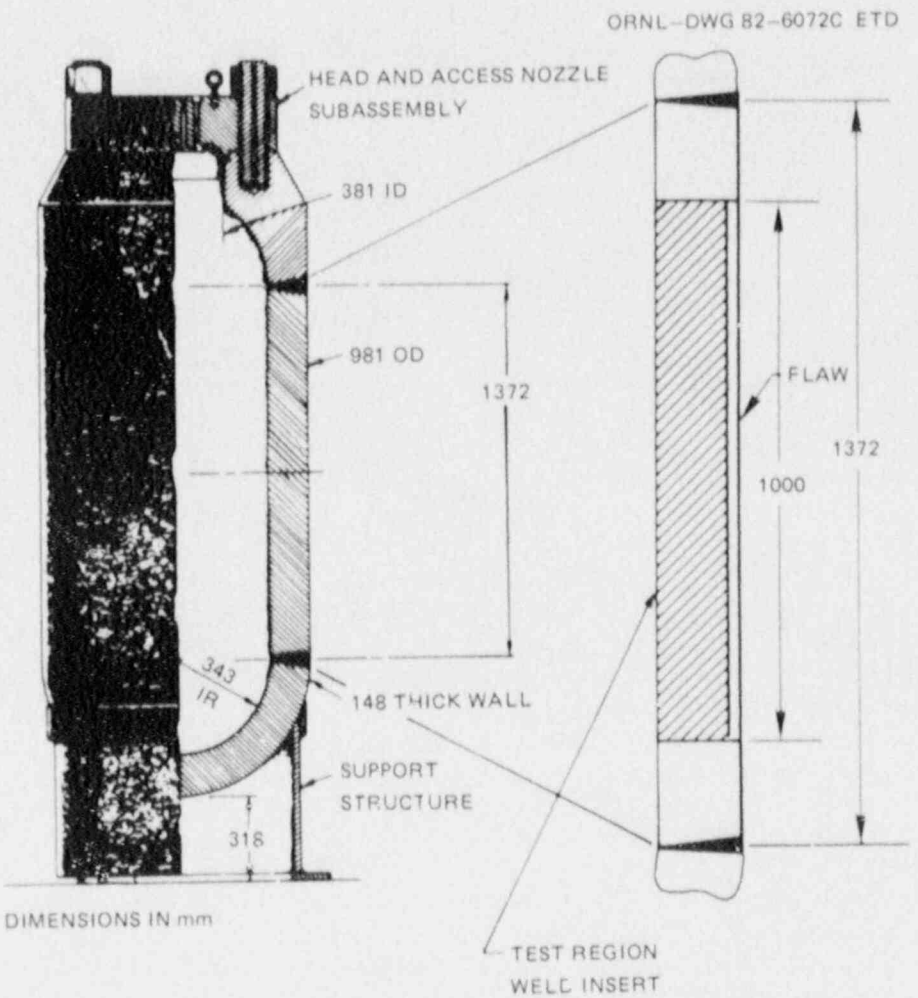

Fig. 1.1. PTSE-2 test vessel geometry.

The experiment was planned and conducted in two separate pressurized-thermal-shock transients. The first transient generated the conditions necessary for the warm-prestressing investigation. The transient included a warm-prestressing phase ($\dot{K}_I < 0$), followed by repressurizing to produce $\dot{K}_I > 0$ until the flaw propagated in cleavage. During the first transient, ductile tearing occurred before and after the cleavage event. The second transient generated the conditions for a deep propagation of the flaw by cleavage with a cleavage arrest or conversion to ductile tearing under conditions conducive to a tearing instability. The desired conditions were attained in both transients. In the final transient the test vessel ruptured, as had been expected but not especially desired.

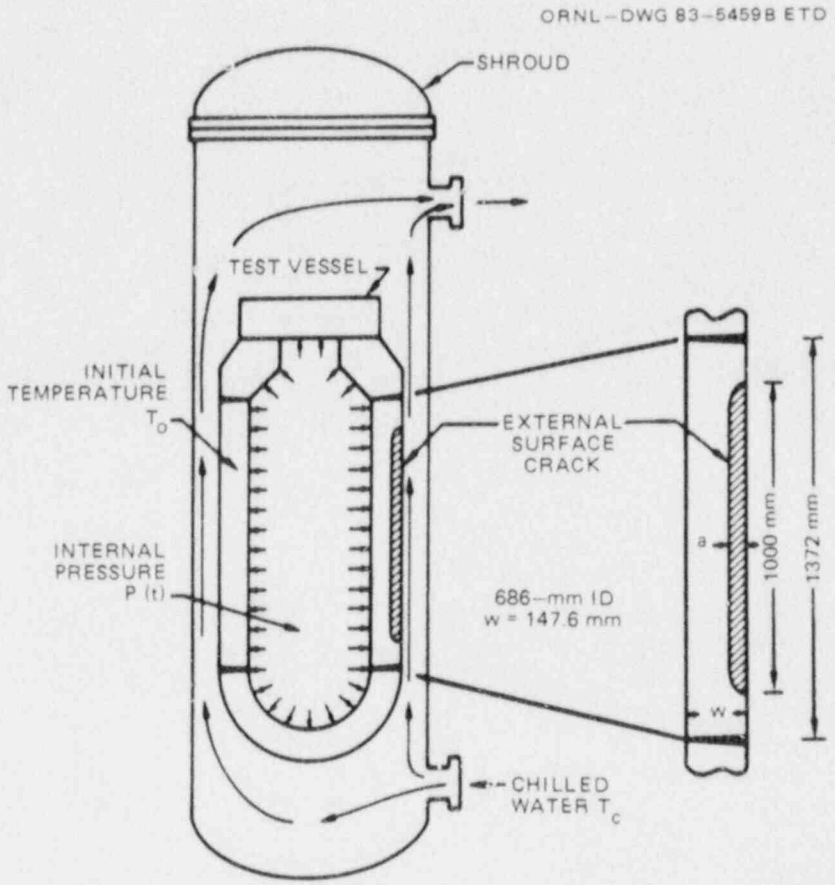

Fig. 1.2. Schematic view of pressurized-thermal-shock vessel inside shroud. Dimensions shown are for the PTSE-2 vessel.

References

1. R. W. Derby et al., *Test of 6-Inch-Thick Pressure Vessels. Series 1: Intermediate Test Vessels V-1 and V-2*, ORNL-4895, Union Carbide Corp. Nuclear Div., Oak Ridge Natl. Lab., February 1974.

2. R. H. Bryan et al., *Test of 6-Inch-Thick Pressure Vessels. Series 2: Intermediate Test Vessels V-3, V-4, and V-6*, ORNL-5059, Union Carbide Corp. Nuclear Div., Oak Ridge Natl. Lab., November 1975.

3. J. G. Merkle et al., *Test of 6-In.-Thick Pressure Vessels. Series 3: Intermediate Test Vessel V-7*, ORNL/NUREG-1, Union Carbide Corp. Nuclear Div., Oak Ridge Natl. Lab., August 1976.

4. J. G. Merkle et al., *Test of 6-In.-Thick Pressure Vessels. Series 4: Intermediate Test Vessels V-5 and V-9 with Inside Nozzle Corner Cracks*, ORNL/NUREG-7, Union Carbide Corp. Nuclear Div., Oak Ridge Natl. Lab., August 1977.

5. R. H. Bryan et al., *Test of 6-in.-Thick Pressure Vessels. Series 3: Intermediate Test Vessel V-7A Under Sustained Loading*, ORNL/NUREG-9, Union Carbide Corp. Nuclear Div., Oak Ridge Natl. Lab., February 1978.

6. R. H. Bryan et al., *Test of 6-in.-Thick Pressure Vessels. Series 3: Intermediate Test Vessel V-7B*, NUREG/CR-0309 (ORNL/NUREG-38), Union Carbide Corp. Nuclear Div., Oak Ridge Natl. Lab., October 1978.

7. R. H. Bryan et al., *Test of 6-in.-Thick Pressure Vessels. Series 3 Intermediate Test Vessel V-8*, NUREG/CR-0675 (ORNL/NUREG-58), Union Carbide Corp. Nuclear Div., Oak Ridge Natl. Lab., December 1979.

8. R. D. Cheverton, *Pressure Vessel Fracture Studies Pertaining to a PWR LOCA-ECC Thermal Shock: Experiments TSE-1 and TSE-2*, ORNL/NUREG/TM-31, Union Carbide Corp. Nuclear Div., Oak Ridge Natl. Lab., September 1976.

9. R. D. Cheverton and S. E. Bolt, *Pressure Vessel Fracture Studies Pertaining to a PWR LOCA-ECC Thermal Shock: Experiments TSE-3 and TSE-4 and Update of TSE-1 and TSE-2 Analysis*, ORNL/NUREG-22, Union Carbide Corp. Nuclear Div., Oak Ridge Natl. Lab., December 1977.

10. R. D. Cheverton et al., "Fracture Mechanics Data Deduced from Thermal-Shock and Related Experiments with LWR Pressure Vessel Material," *J. Pressure Vessel Technology, Trans. ASME*, 105 (May 1983).

11. R. D. Cheverton, "Thermal-Shock Investigations," pp. 55–60 in *Heavy-Section Steel Technology Program Quart. Prog. Rep. July–September 1983*, NUREG/CR-3334, Vol. 3 (ORNL/TM-8787/V3), Union Carbide Corp. Nuclear Div., Oak Ridge Natl. Lab.

12. Doan L. Phung, *Pressure Vessel Thermal Shock at U.S. Pressurized Water Reactors: Events and Precursors, 1963–1981*, NUREG/CR-2789 (ORNL/NSIC-210), Union Carbide Corp. Nuclear Div., Oak Ridge Natl. Lab., April 1983.

13. D. L. Selby et al., *Pressurized Thermal Shock Evaluation of the H. B. Robinson Unit 2 Nuclear Power Plant*, NUREG/CR-4183, Vols. 1 and 2 (ORNL/TM-9567/V1 and V2), Martin Marietta Energy Systems, Inc., Oak Ridge Natl. Lab., September 1985.

14. R. H. Bryan et al., *Pressurized-Thermal-Shock Test of 6-in.-Thick Pressure Vessels. PTSE-1: Investigations of Warm Prestressing and Upper-Shelf Arrest*, NUREG/CR-4106 (ORNL-6135), Martin Marietta Energy Systems, Inc., Oak Ridge Natl. Lab., April 1985.

15. "Rules for In-Service Inspection of Nuclear Power Plant Components," *ASME Boiler and Pressure Vessel Code, Section XI*, American Society of Mechanical Engineers, New York, 1983.

16. R. Johnson, *Resolution of the Task A-11 Reactor Vessel Materials Toughness Safety Issue*, NUREG-0744, Vols. 1 and 2, Rev. 1, U.S. Nuclear Regulatory Commission, Washington, D.C., October 1982.

2. TEST VESSEL

2.1 Prior History

The vessel used in the PTSE-2 experiment was originally procured for the HSST Program as intermediate test vessel V-8. Prior to its preparation for PTSE-2, vessel V-8 was tested twice in the HSST simulated service test series [tests V-8 (Ref. 1) and V-8A (Ref. 2)] and once in the three-step test series identified as the pressurized-thermal-shock test PTSE-1 (Ref. 3).

2.1.1 Original fabrication

The cylindrical test section of vessel V-8 was fabricated of 152-mm-thick steel plate meeting American Society for Testing and Materials (ASTM) A 533 grade B class 1 specifications. The configuration of the vessel is shown in Fig. 2.1. The vessel was fabricated under contract with the Taylor Forge Division of Gulf and Western Products Company, with V-8 being one of four intermediate test vessels using steel plate for the

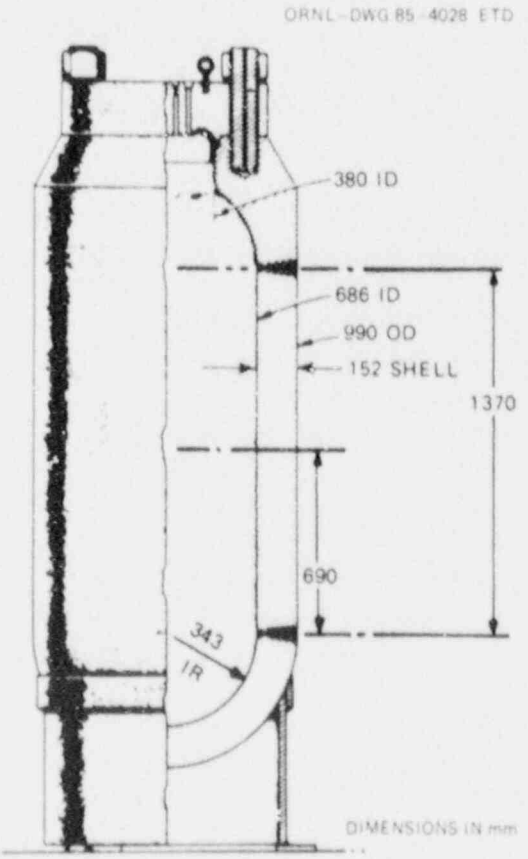

Fig. 2.1. Intermediate test vessel V-8.

cylindrical courses. Design and procurement of the vessels are described in detail in Ref. 4; principal features pertaining to vessel V-8 are summarized here.

The cylindrical shell courses and prolongations for vessels V-7 through V-10 were fabricated from plate produced by Lukens Steel Company from a single heat identified as B5233-2. Chemical analysis reported by the Lukens Mill Certification for this heat follows.

Ladle analysis

Material	Quantity (wt %)
C	0.20
Mn	1.23
P	0.015
S	0.017
Si	0.26
Ni	0.49
Mo	0.52

The mechanical test results from specimens representing the shell material are presented in Table 2.1.

Table 2.1. Mechanical test results from Data Trac specimens representing heat B5233-2 of ASTM A 533 grade B class 1 material for the cylindrical course of the test vessel[a]

Yield strength (MPa)	Tensile strength (MPa)	Elongation in 51 mm (2 in.) (%)	Longitudinal CVN at −12°C	Lateral expansion (mm)	Fracture appearance (% shear)
450	586	26			
432	563	29	125-96-106	1.55-1.93-1.52	70-70-70

[a]Nil-ductility transition temperature as determined by drop-weight tests: −51°C.

2.1.2 Test V-8

To meet the objectives of the V-8 test, a large repair weld was deliberately performed by the half-bead technique prescribed by Sect. XI of the *ASME Boiler and Pressure Vessel Code*.[5] In such a weldment, one expects locally high residual stresses and material properties within heat-affected zones not typical of weldments that have undergone the normal high-temperature postweld heat treatment. Details of the repair cavity are shown in Fig. 2.2.

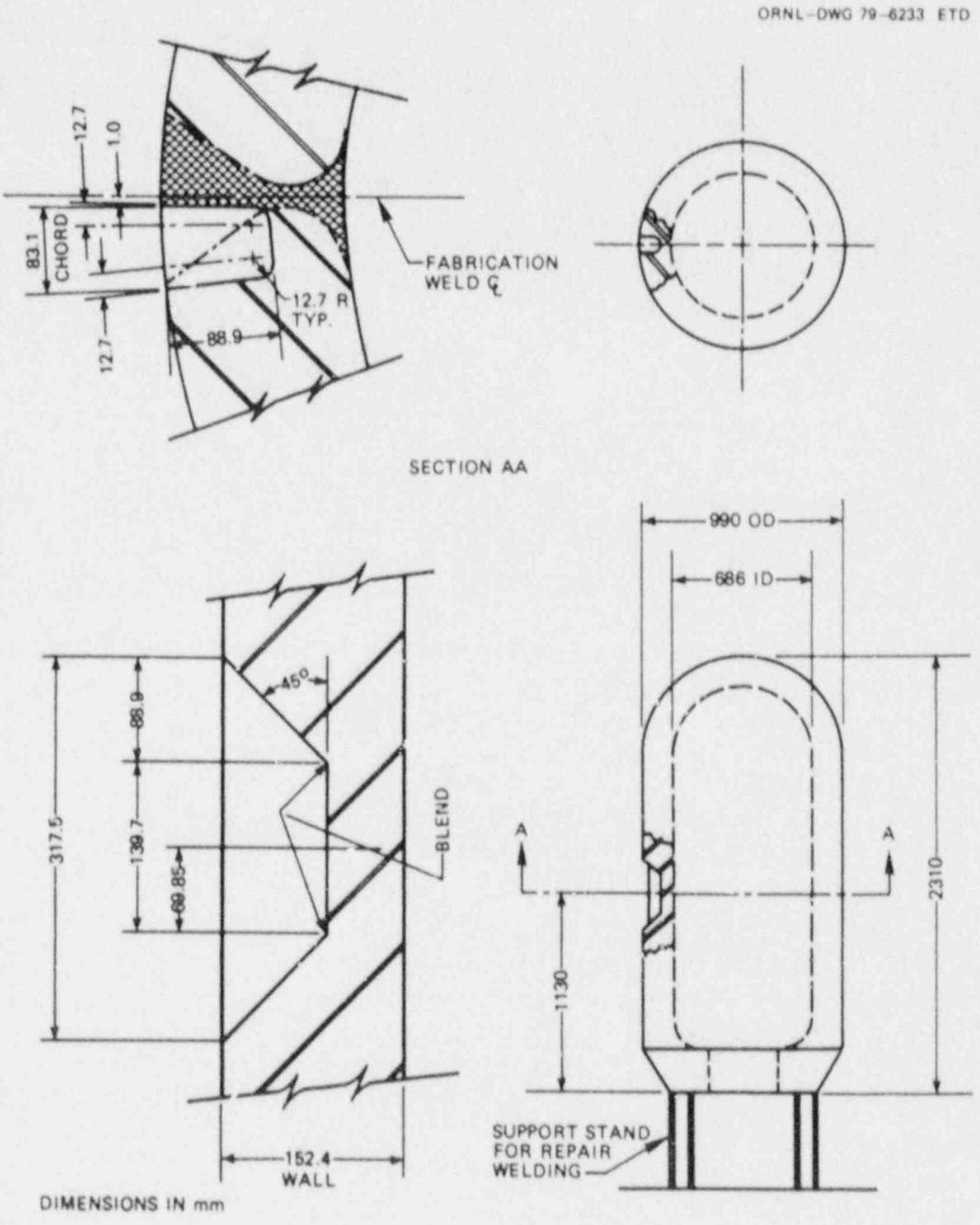

Fig. 2.2. Details of cavity prepared in vessel V-8 for Sect. XI repair welding.

A fatigue-sharpened flaw was implanted in a radial-axial plane of the vessel adjacent to the repair weld in the longitudinal seam weld. In the test, the vessel was cooled to ~24°C and hydrostatically pressurized to 65.3 MPa. The flaw propagated by cleavage and arrested, as predicted. Maximum strains in the cylindrical test section outside the flawed region were well within the elastic limits of the material.

2.1.3 Test V-8A

In preparation for the V-8A test, the flawed region of the vessel was removed, the cavity was plug welded, and a special seam weld with low-upper-shelf toughness was placed in the vessel[6] (Fig. 2.3). The test vessel was stress relieved, and a fatigue-sharpened flaw was implanted in the special seam weld. The vessel was heated to 150°C for the fracture test to ensure that ductile fracture conditions would prevail. The vessel was pressurized until unstable tearing was induced; then the pressure was reduced to prevent bursting. The maximum pressure was 143 MPa, at which the inside surface strains in the cylindrical section remote from the flaw exceeded the yield point, leaving the vessel with moderate residual stresses.

2.1.4 Repair for PTSE-1

The V-8A flaw was flame cut from the vessel, which was then repaired and machined under subcontract with the Babcock & Wilcox Company. Details of the repair are presented in Ref. 7.

The test material in which the PTSE-1 flaw would reside was a plug of material cut from a forged cylinder, designated TSC-6, procured to meet the specifications of SA-508 class 2 steel, and delivered in the quenched but not tempered condition. The plug of test material and the characterization material from the forging were subjected to tempering heat treatments designed to produce the toughness desired for the pressurized-thermal-shock experiment. The plug for the PTSE-1 vessel was cut from TSC-6, machined as shown in Fig. 2.4, and welded into the PTSE-1 vessel as shown in Fig. 2.5. The final tempering heat treatment, shown in Fig. 2.6, for the plug also served to stress relieve the vessel.

The vessel was machined after the final heat treatment to a nominal outside diameter of 981.08 mm (specified as 38.625 in. ± 0.010 in.). Final dimensions of the vessel are shown in Fig. 2.7 as reported by the Babcock & Wilcox Company. The geometry of the completed PTSE-1 test vessel is shown in Fig. 2.8.

The transient test was performed in three phases; in each phase the vessel was initially in an isothermal state (~290°C). Each phase consisted of a pressure transient and a thermal transient, which were coordinated to produce an evolution of stress and toughness states that would fulfill the objectives of the plan. The experiment was performed successfully, and all objectives were attained. Test data and posttest examination of the fracture surfaces revealed that the flaw propagated in a fast brittle mode (predominantly cleavage) and arrested in each of two transients.

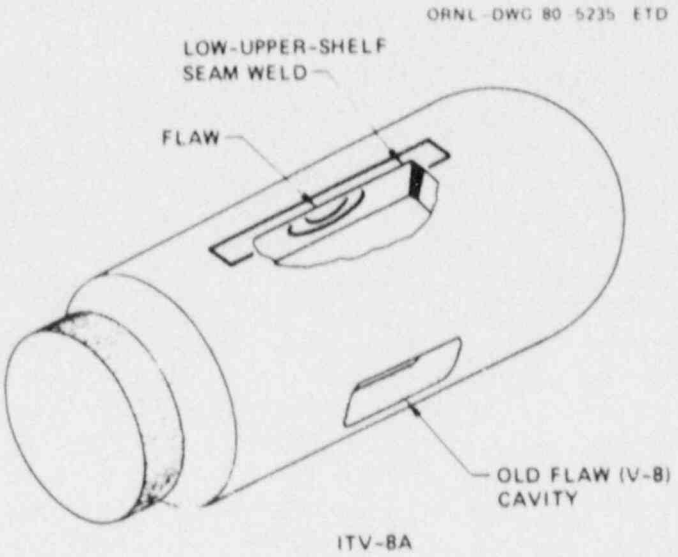

Fig. 2.3. Schematic of vessel V-8A showing location of flaw relative to special seam weld.

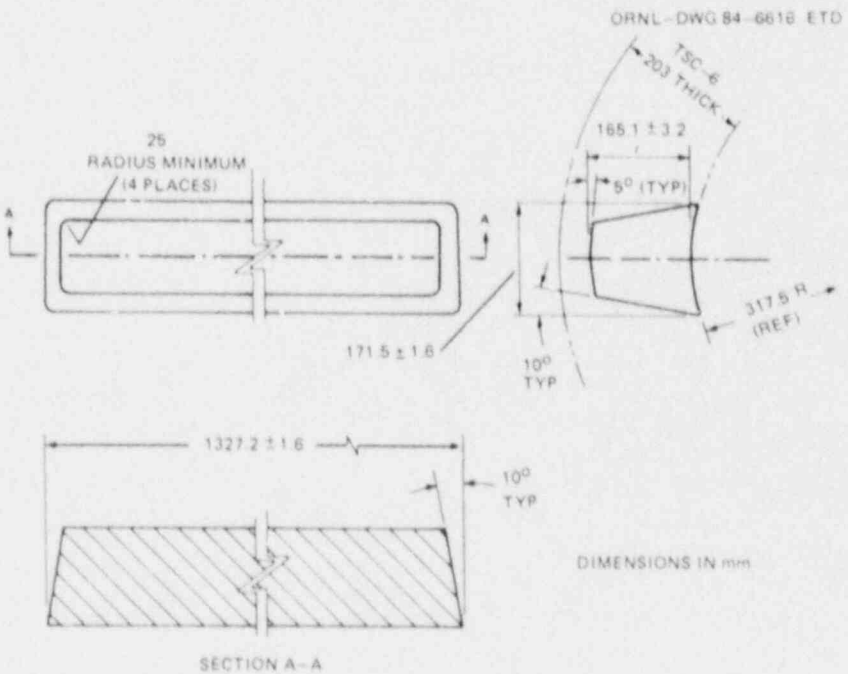

Fig. 2.4. Nominal dimensions of plug inserts made from TSC-6 for vessel V-8.

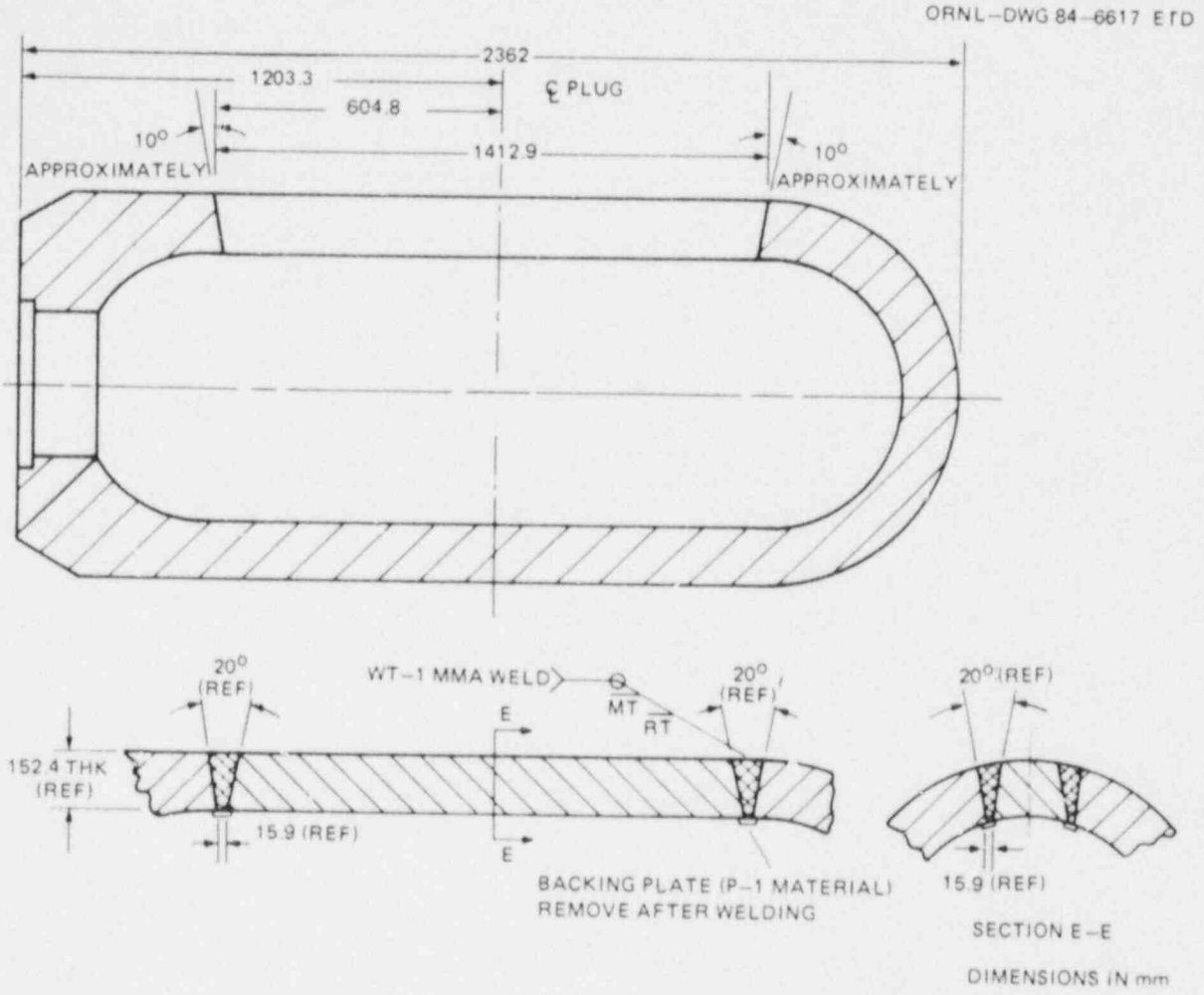

Fig. 2.5. Plug insert welds in vessel V-8.

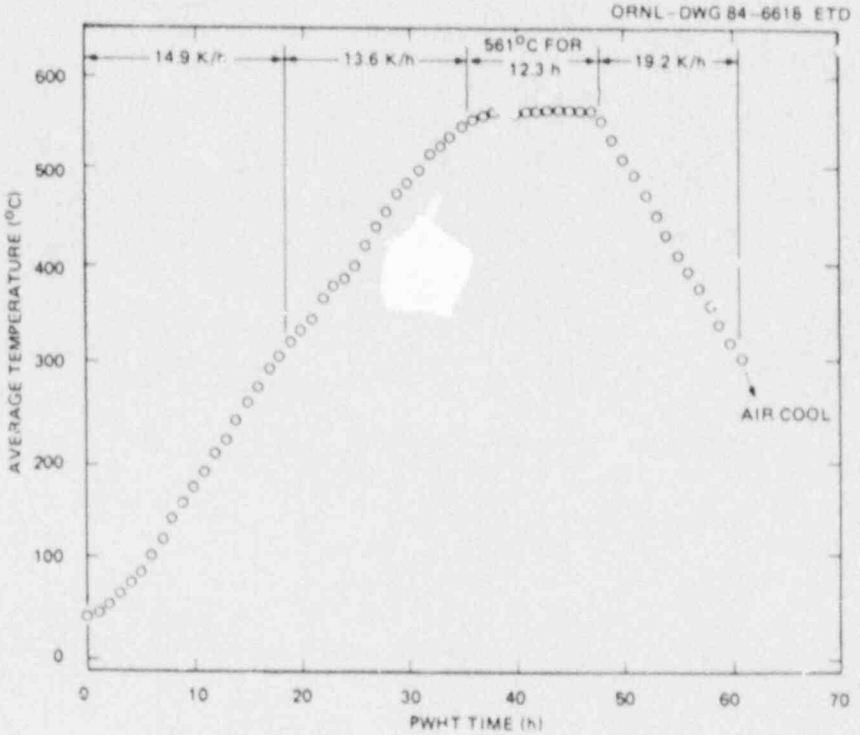

Fig. 2.6. Average postweld heat treatment temperature of vessel V-8 and TSC-6 as function of time.

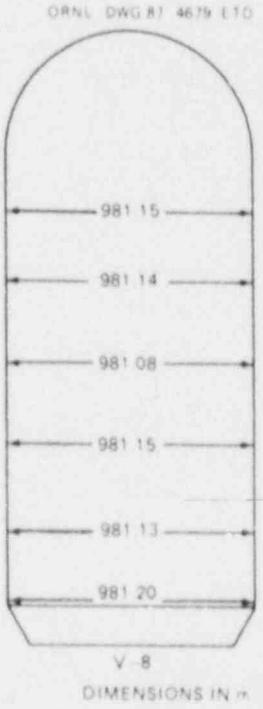

Fig. 2.7. Outside dimension of machined vessel.

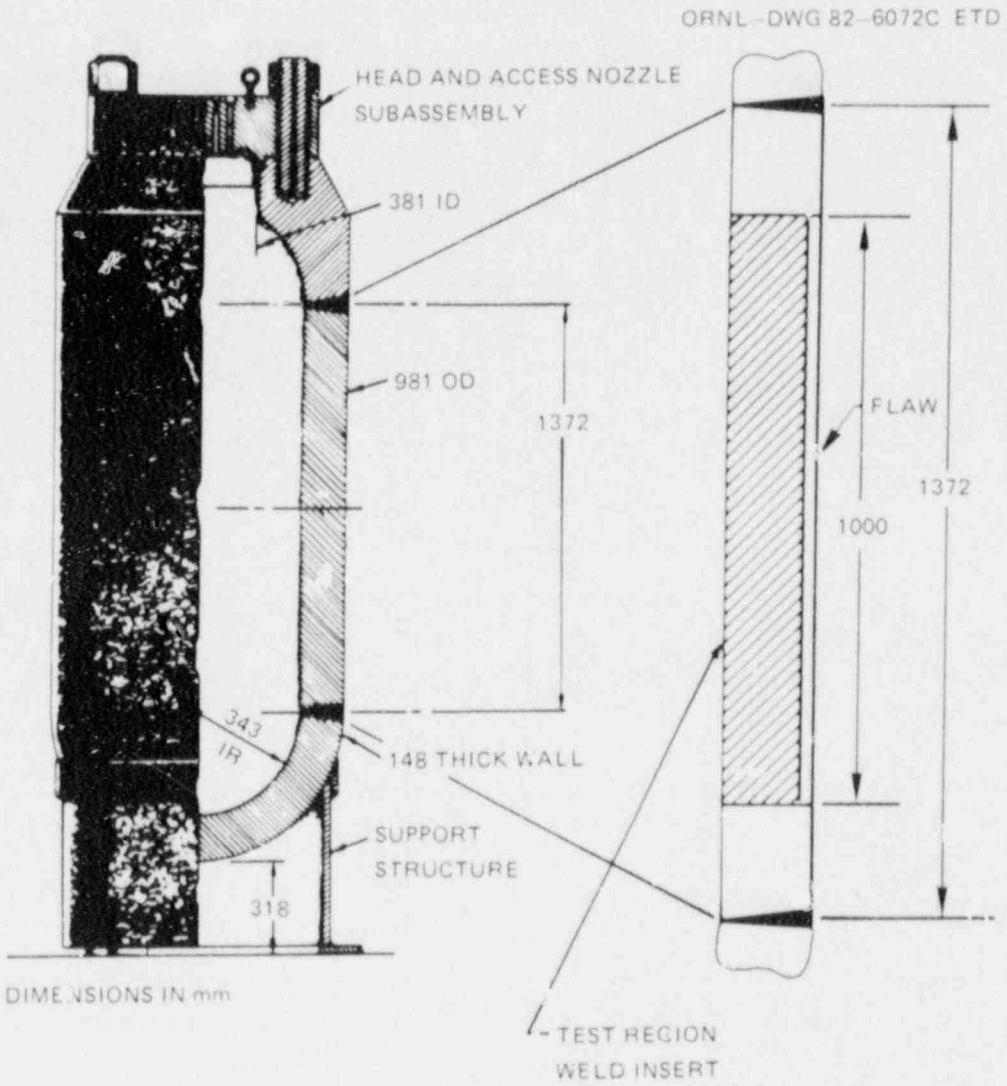

Fig. 2.8. Geometry of PTSE-1 test vessel.

2.2 Repair for PTSE-2

Following completion of the PTSE-1 test series, the TSC-6 insert material was flame-cut from the V-8 vessel leaving cavity dimensions as shown on Fig. 2.9. Then, after two rounds of competitive bidding with extensive specification modifications on the second round, a subcontract (Martin Marietta Energy Systems, Inc., purchase order 25Y-34128V) was let on March 21, 1985, to the Babcock & Wilcox Company to repair the V-8 vessel. The provisions of the subcontract incorporated two phases of work. The first phase consisted of (1) the development of a high-transition-temperature, low-upper-shelf material with closely specified mechanical, Charpy V-notch (CVN) and tearing resistance properties and (2) the validation of a welding procedure for welding the insert material

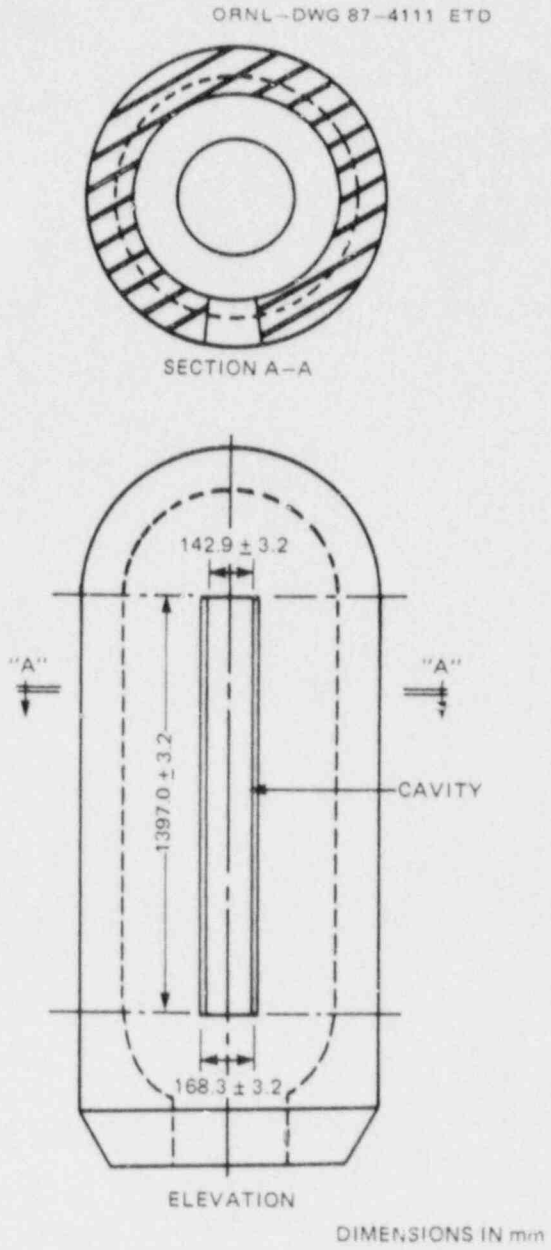

Fig. 2.9. Intermediate test vessel V-8 cavity dimensions.

into vessel V-8. Second-phase work, conditioned upon successful completion of the first phase, consisted of the implementation of the procedures under phase 1 to produce (1) a stress-relieved vessel with an insert of the requisite material, (2) accompanying characterization material, and (3) wide-plate specimens for crack-arrest studies.

In the first phase, the subcontractor procured a 159-mm-thick plate of A 387, grade 22 class 2 steel (a 2 1/4 Cr-1 Mo steel) to provide the material for the PTSE-2 insert, for characterization and qualification test specimens, and for six wide-plate specimens to be tested as part of

the HSST Program. The plate was eventually apportioned and cut as shown in Fig. 2.10 (which varies slightly from the subcontractor's plan[3]). The chemical composition of the plate is given in Table 2.2 (from Ref. 8).

Phase 1 work of the subcontract met all preliminary objectives except for the attainment of the specified yield strength, which was waived. However, early in the Phase 2 activity it was discovered that the properties of the plate were unusually sensitive to the heat treatment procedures. This situation necessitated an extension to the qualification efforts to produce satisfactory wide-plate specimens, a PTSE-2 vessel insert, and a PTSE-2 characterization material. These efforts by the subcontractor are documented by Ref. 8.

Based on the phase 1 heat treatment studies, the Babcock & Wilcox Company heat treated the left-hand portion (wide-plate specimens) of the plate, consisting of parts WP1 to WP6, WPC1, WPQ1, and WPQ2 (Fig. 2.10), at 552 ± 14°C for 7 h. In the subsequent characterization studies, it was discovered that part of this material had nonconforming properties, requiring that more extensive qualification studies be conducted to ensure that the material designated for the PTSE-2 vessel insert and characterization material would conform to the requisite properties.

With successful completion of these studies, the vessel insert (part I1 on Fig. 2.10) was machined as shown on Fig. 2.11. The vessel V-8 cavity was machined, and the machined insert was then positioned and welded as shown on Fig. 2.12. Following inspection, the vessel and its characterization material, parts PTC1 and PTQ1 on Fig. 2.10, were subjected to the postweld-heat-treatment (PWHT) cycle as shown on Fig. 2.13.

It was anticipated that welding of the insert would cause local out-of-roundness and that machining to restore circularity would appreciably increase the annulus dimension between the PTSE-2 vessel and the test shroud, leading to a potential degradation in the thermal transient that could be imposed during the PTSE-2 test. Consequently, it was decided to limit machining to the plug area to remove only the material that would interfere with the insertion of the vessel into the test shroud. Figure 2.14 provides the final machined dimensions of the PTSE-2 vessel. The geometry of the completed PTSE-2 test vessel, following flaw placement in the low-upper-shelf insert by electron-beam welding and hydrogen-charging, is shown by Fig. 2.15.

Table 2.2. Chemical composition of 2 1/4 Cr-1 Mo steel plate (heat C6384/slab 7) used for PTSE-2

	Composition (wt %)								
	C	Mn	P	S	Si	Cr	Ni	Mo	Cu
Heat analysis	0.012	0.42	0.009	0.017	0.18	2.21		0.95	
Product analysis	0.13	0.41	0.011	0.016	0.18	2.24		0.96	
B&W check analysis	0.13	0.40	0.009	0.018	0.19	2.25	0.11	0.94	0.08

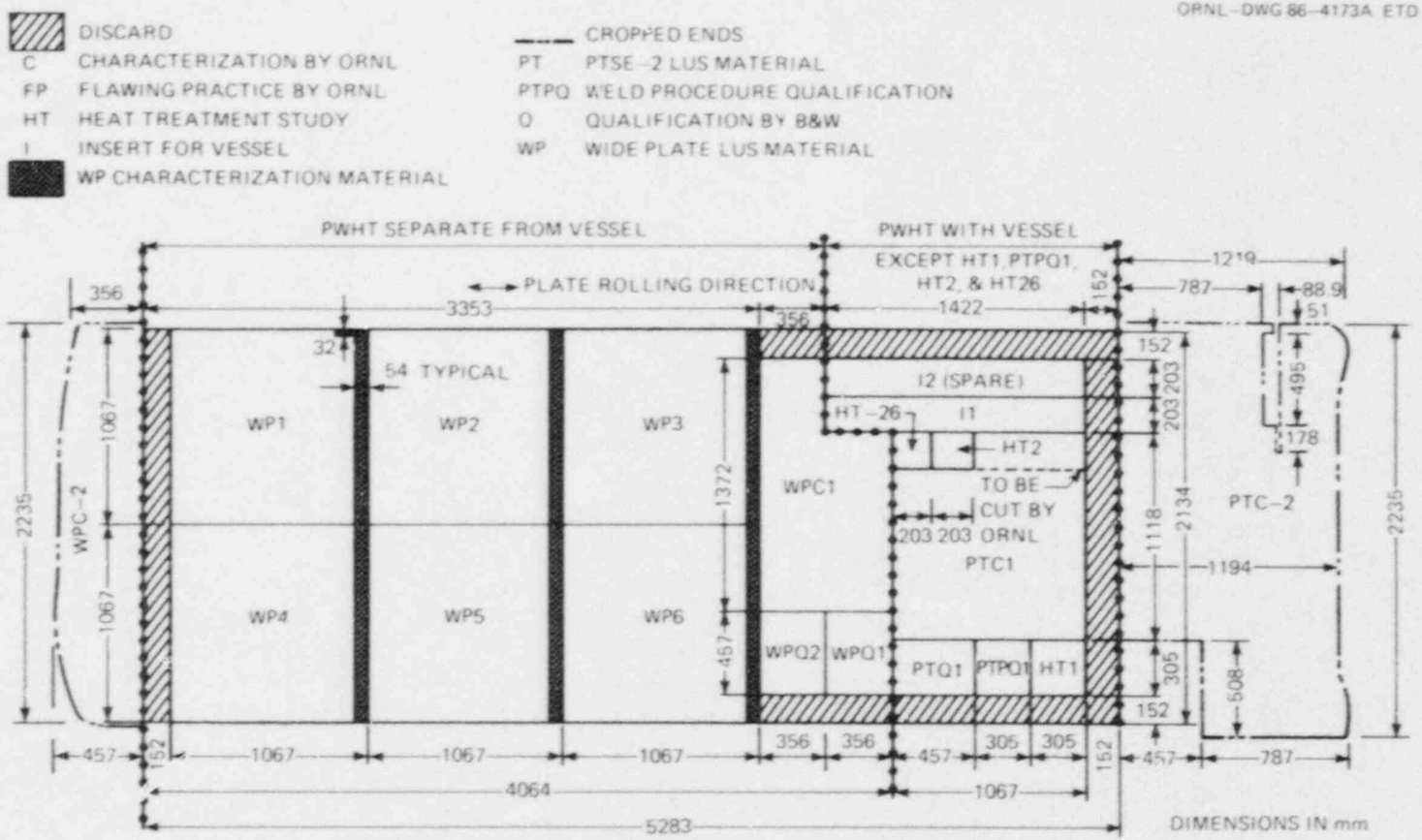

Fig. 2.10. Cutting diagram of 159-mm-thick A 387-22 (2 1/4 Cr-1 Mo) steel plate.

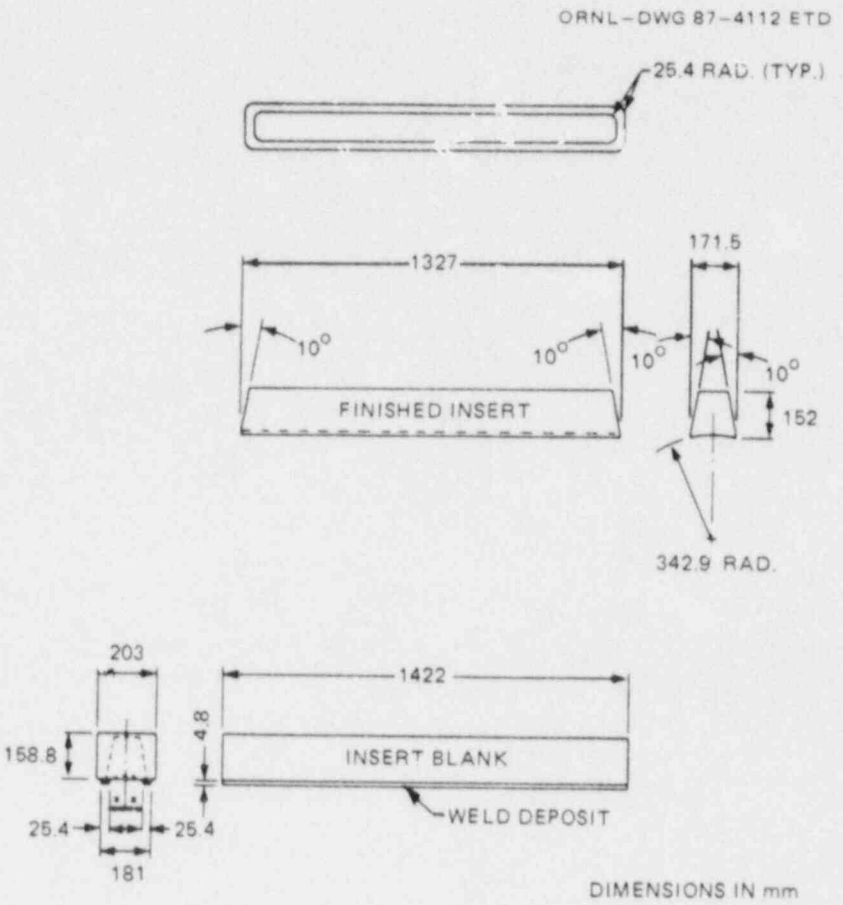

Fig. 2.11. Insert with weld buildup on vessel ID surface.

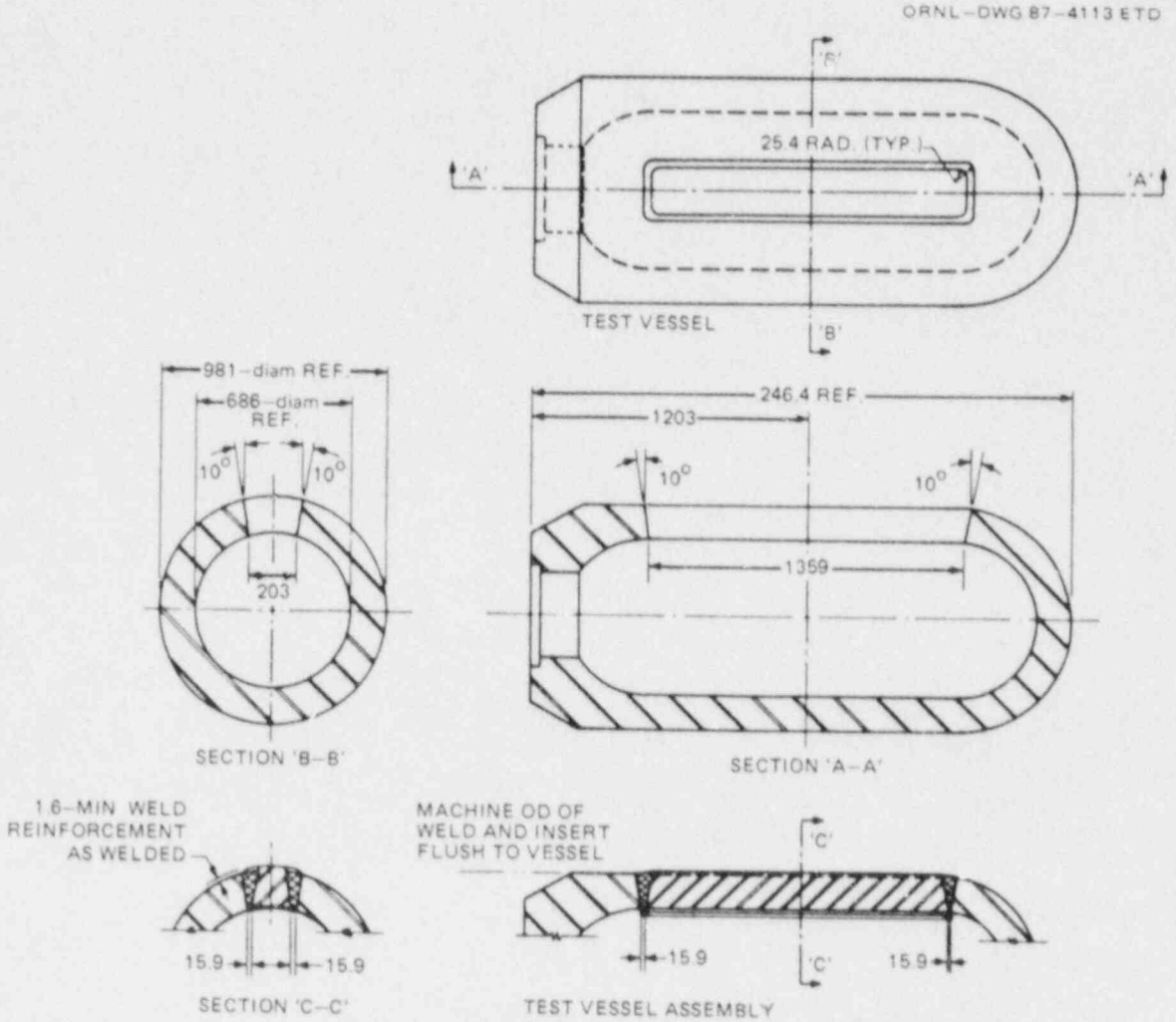

Fig. 2.12. Vessel cavity and insert assembly.

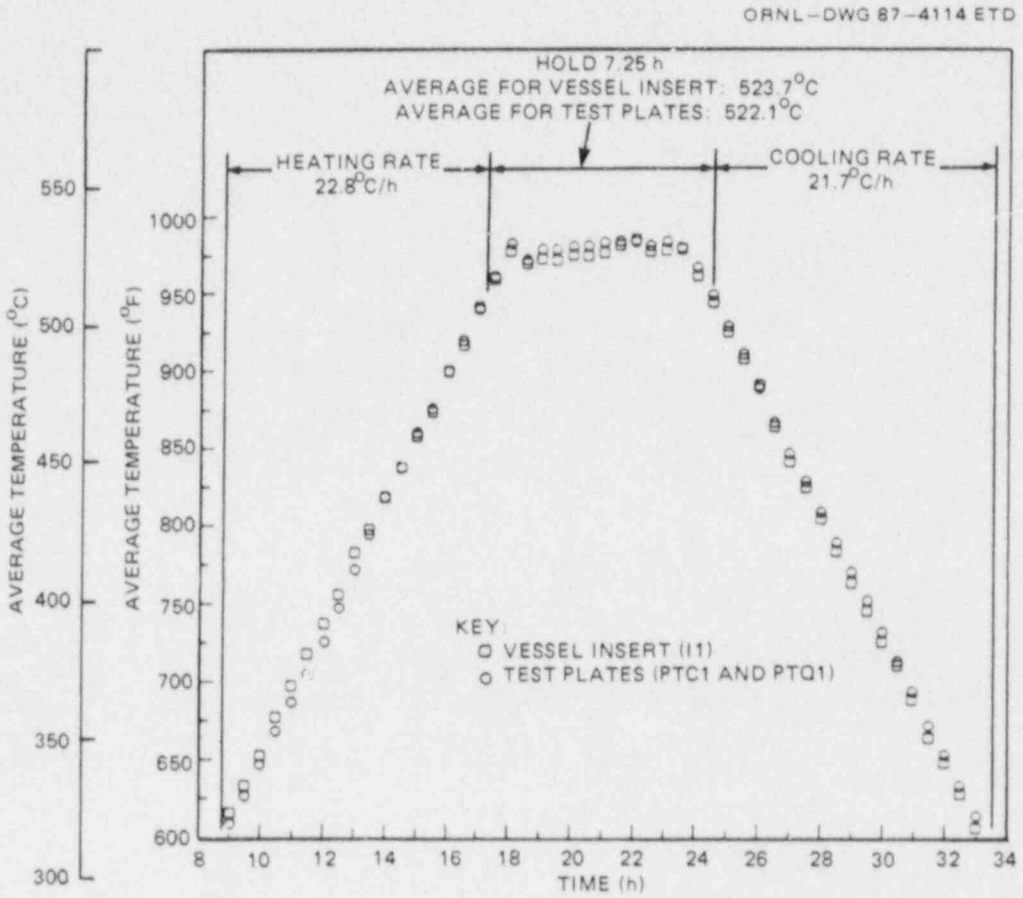

Fig. 2.13. Postweld heat treatment cycle for vessel insert and test plates.

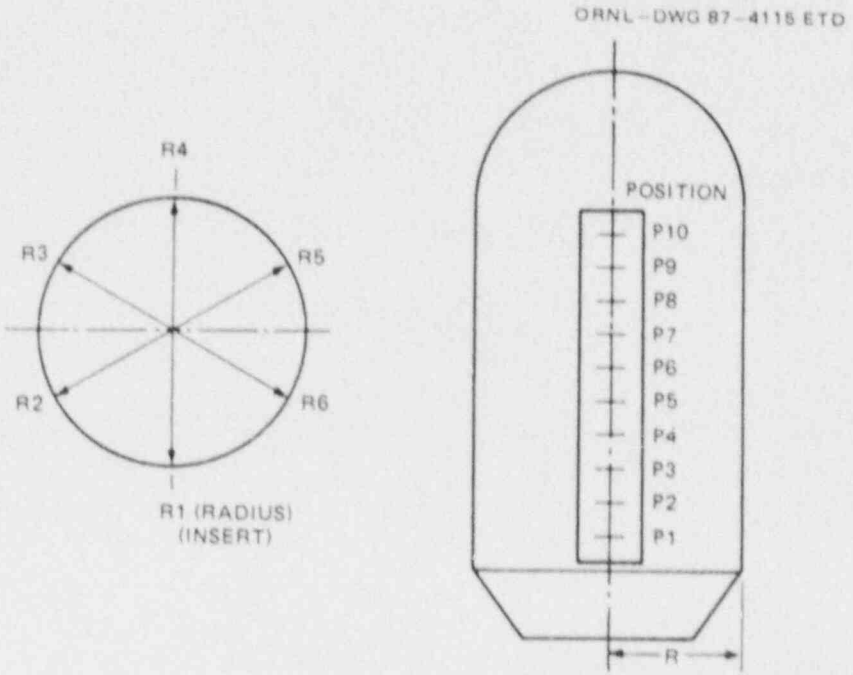

POSITION	RADIUS (mm)						
	R1	R2	R3	R4	R5	R6	AVERAGE
1	490.50	490.58	490.65	490.40	490.83	490.68	490.60
2	490.40	490.35	490.50	490.58	490.70	490.58	490.52
3	490.11	490.11	490.40	490.47	490.68	490.55	490.40
4	490.14	489.89	490.25	490.35	490.65	490.47	490.30
5	490.17	489.73	490.19	490.17	490.68	490.45	490.25
6	490.17	489.66	489.97	490.17	490.63	490.58	490.12
7	490.17	489.66	489.86	489.97	490.50	490.58	490.58
8	490.17	489.74	489.66	489.66	490.40	490.70	490.07
9	490.65	489.92	489.48	489.51	490.35	490.96	490.14
10	490.73	490.07	489.33	489.31	490.30	491.16	490.14
AVERAGE	490.32	489.97	490.04	490.07	490.58	490.65	490.27

Fig. 2.14. Outside radius dimensions of vessel after machining of insert.

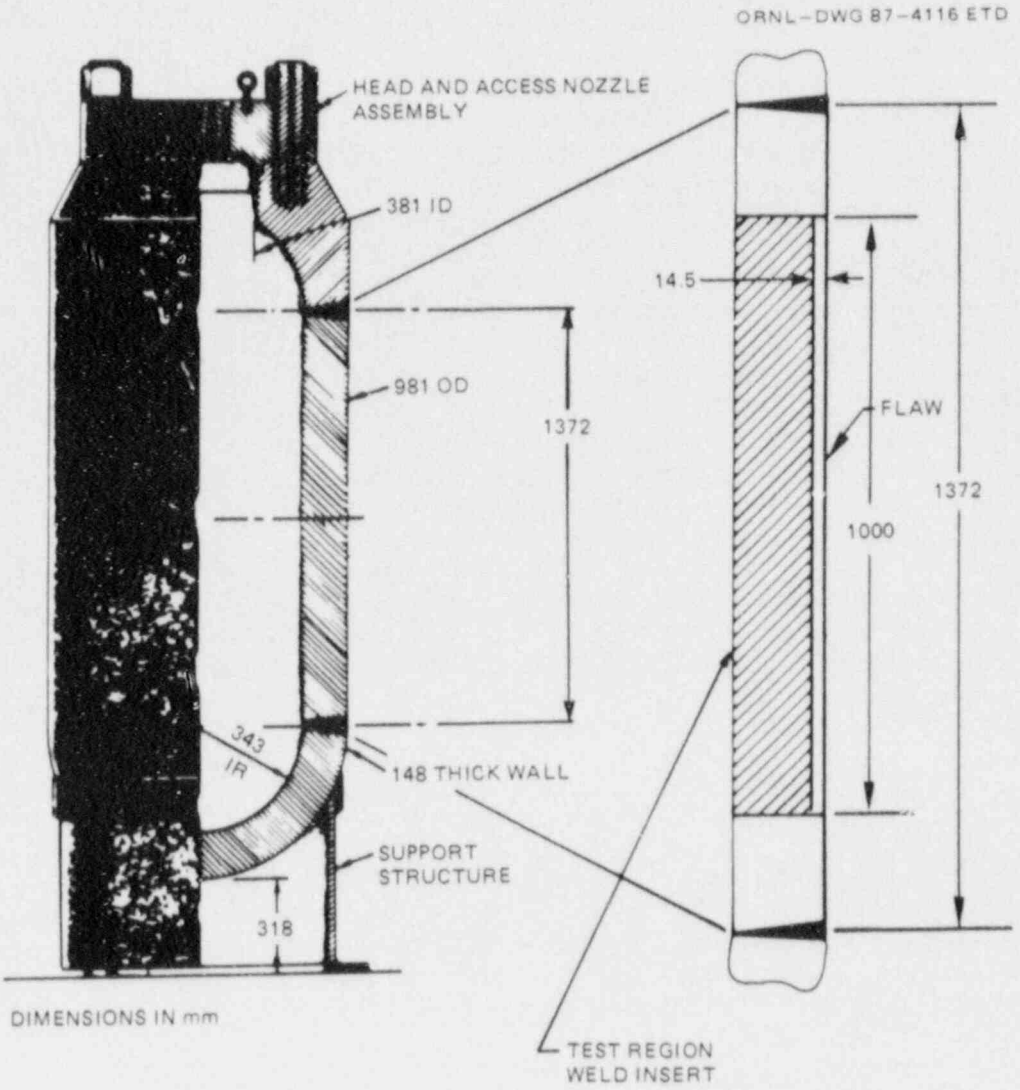

Fig. 2.15. Geometry of PTSE-2 test vessel.

2.3 Materials Investigations

Material characterization studies were conducted prior to the PTSE-2 experiment to provide data for experiment design. Those studies were performed principally with material removed from a characterization block designated PTC1 located in the original plate as shown in Fig. 2.10. Block PTC1 was given a stress-relief heat treatment in the furnace simultaneously with the test vessel. The stress-relief treatment was 524°C for 7.25 h, followed by cooling at a rate of about 22°C/h (Fig. 2.13). Prior to use of PTC1, other pieces of the plate, heat treated separately, were identified for the characterization studies, but CVN impact testing revealed that they did not satisfy the material toughness specifications because the CVN upper-shelf energies were too high and the transition

temperatures were too low. The reasons for such differences in the plate are not understood because detailed fabrication and heat treatment schedules are not available. Even the characterization block PTC1, which did satisfy the toughness specification and was given a stress-relief heat treatment with the vessel insert after it was welded in the vessel, has properties somewhat different than those of the actual vessel insert; these differences were revealed by postexperiment testing with material removed from the test vessel. Both the pretest and posttest characterization results are discussed in this chapter.

Mechanical tests were conducted to obtain tensile properties, hardness, CVN toughness, drop-weight nil-ductility transition (NDT) temperature, fracture toughness, and tearing resistance. Physical property determinations included bulk density, coefficient of thermal expansion, and electrical resistivity. Additionally, metallography was used to reveal microstructural features. Fractographic investigations of the vessel fracture surfaces are discussed in Sect. 9.3. Specimen orientations of greatest relevance to the pressurized-thermal-shock experiment were TS for Charpy, drop-weight, and toughness specimens and T for tensile specimens. Specimens with the TL orientation were tested primarily to provide characterization data relevant to the wide-plate specimens (Fig. 2.10), although the latter specimens were heat-treated at a higher temperature than PTC1.

2.3.1 Pretest metallographic evaluation and hardness testing of vessel insert and PTC1

Because properties of the original 2 1/4 Cr-1 Mo steel plate varied unexpectedly with location, metallographic and hardness evaluations were made at ORNL of the vessel insert and PTC1. Six locations on the welded-in insert were chosen, equally spaced across a 1.1-m length of the insert, and ground and polished using standard field techniques. Each polished section (~50 by 50 mm) was etched with a 2% nital solution followed by replication with RTV. Replicas were photographed in a metallograph to reveal the microstructures, as shown in Figs. 2.16 through 2.21. Location 1 is closest to the vessel closure. The figures show microstructures with ferrite contents from about 50 to 70%, with pearlite comprising the remainder.

Hardness tests were conducted in the same locations by using an Equotip portable hardness tester. The converted hardness values are given with the micrographs. The hardness results (HRB 93 to 96) show some differences across the insert, but they are not very significant in view of an observed measurement variation (four readings at each location) of about ±1 HRB. Location 6 apparently is harder than the others, but the microstructure does not reveal any obvious explanation.

The metallographic and hardness tests were performed on the outside surface of the vessel. Hardness testing with the portable tester was performed on the characterization block PTC1 for comparison. Hardness values for PTC1 varied from HRB 83 to 87 through the 159-mm thickness, with HRB 84 at one surface and HRB 87 at the other. The portable hardness tester was compared to a laboratory Rockwell hardness tester. On a calibrated test block with a hardness of HRB 96.6 ± 1, the laboratory machine measured HRB 96.5; the portable tester measured HRB 94. Similar

M&C PHOTO Y205607

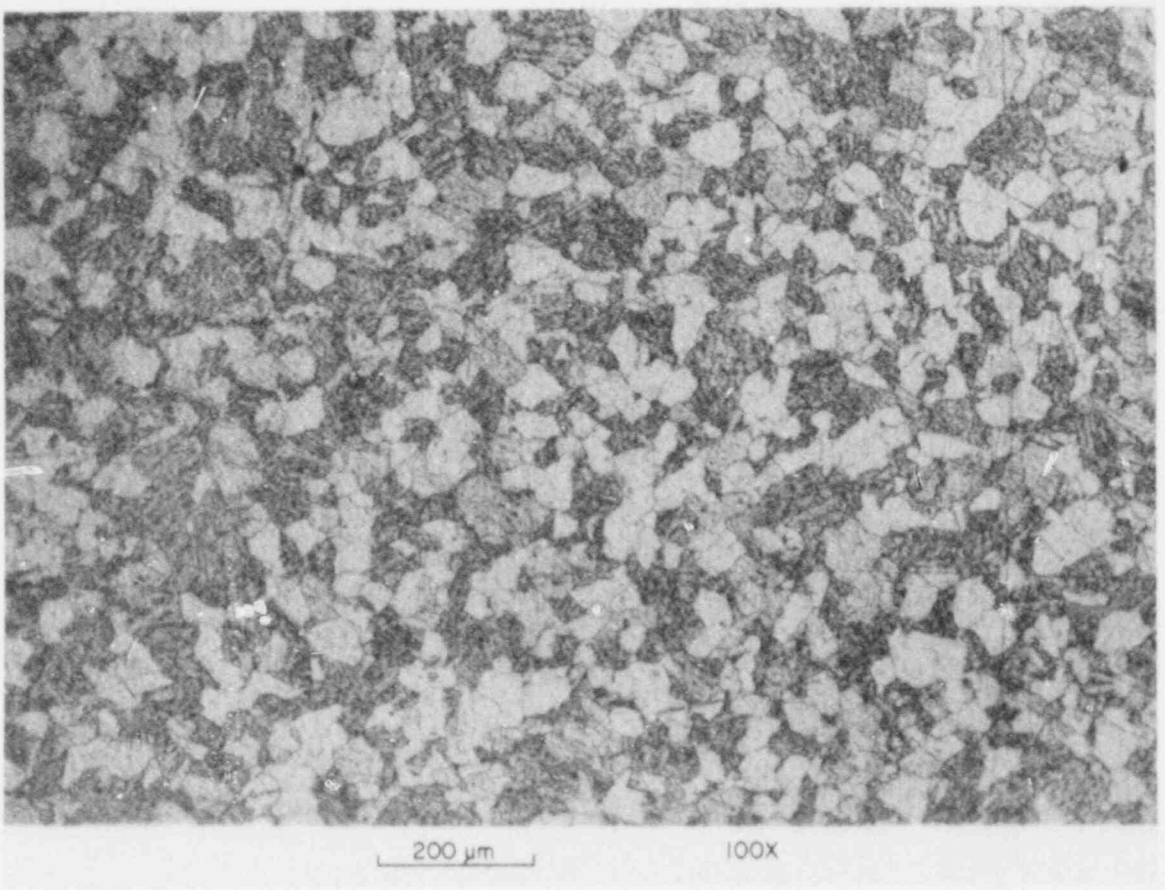

Fig. 2.16. Microstructure of PTSE-2 insert from field replication, location 1 (closest to vessel head), HRB 93.

M&C PHOTO Y205608

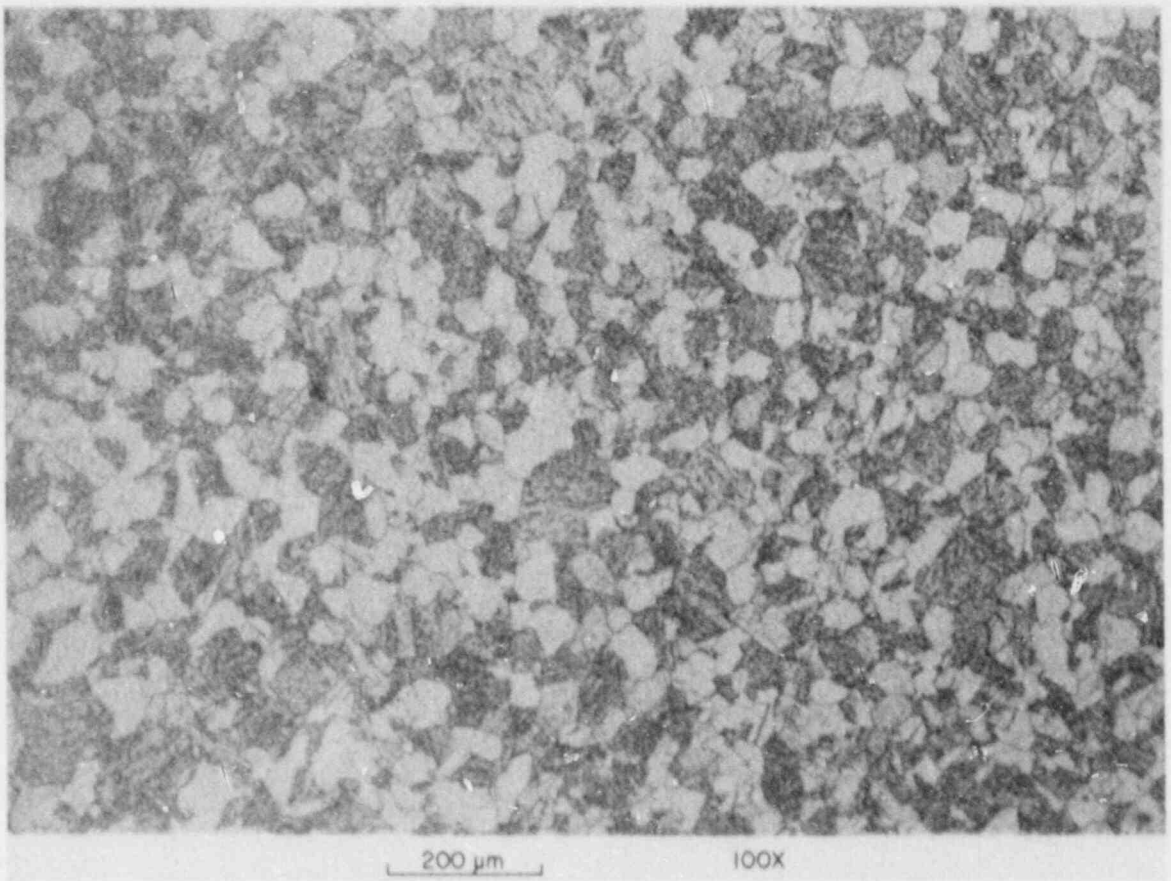

Fig. 2.17. Microstructure of PTSE-2 insert from field replication, location 2, HRB 94.

M&C PHOTO Y205609

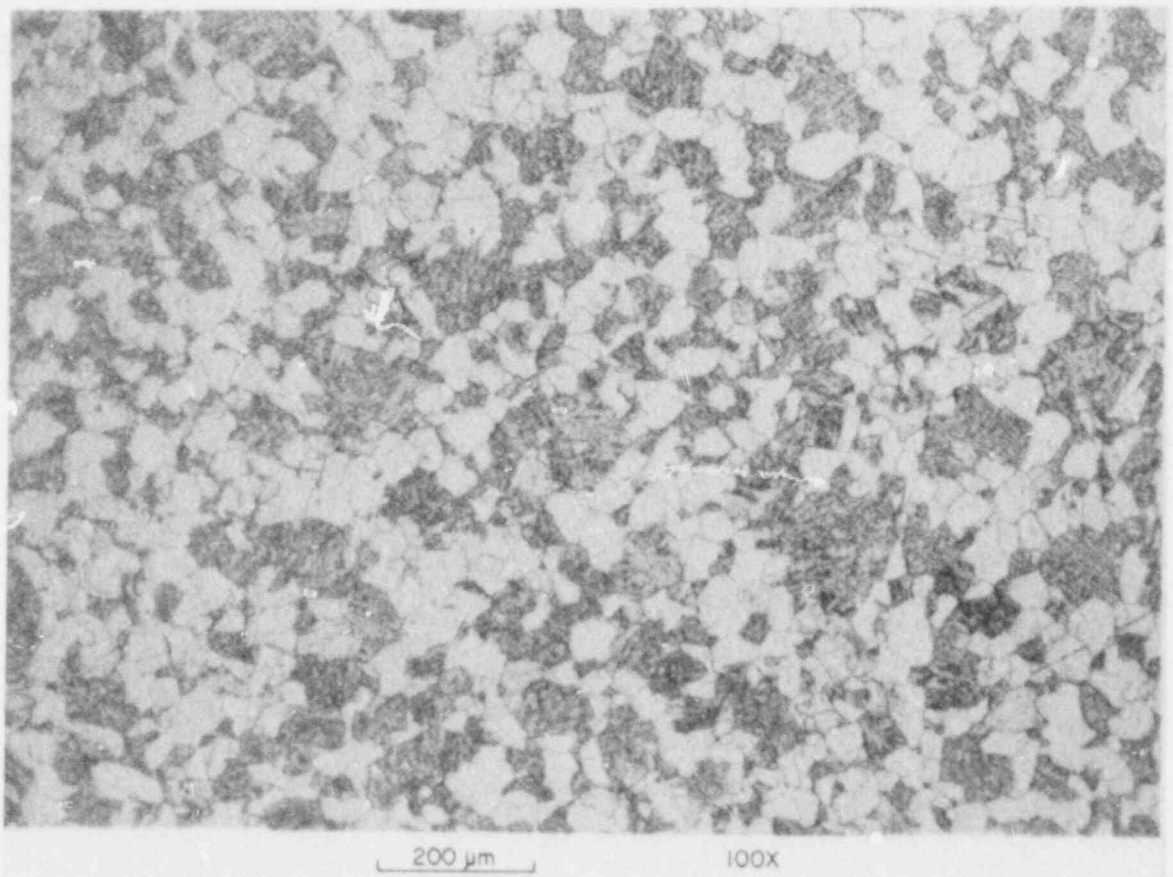

Fig. 2.18. Microstructure of PTSE-2 insert from field replication, location 3, HRB 94.

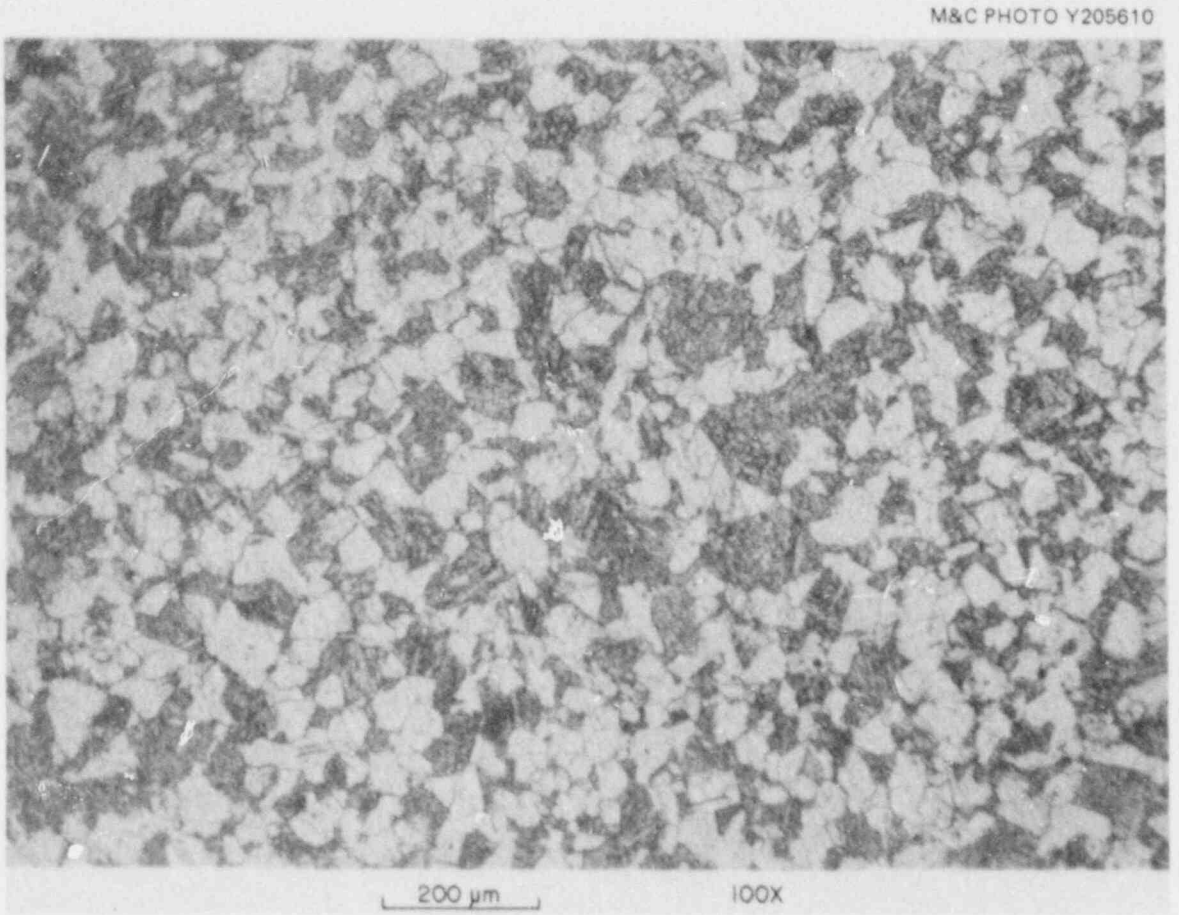

Fig. 2.19. Microstructure of PTSE-2 insert from field replication, location 4, HRB 93.

M&C PHOTO Y205611

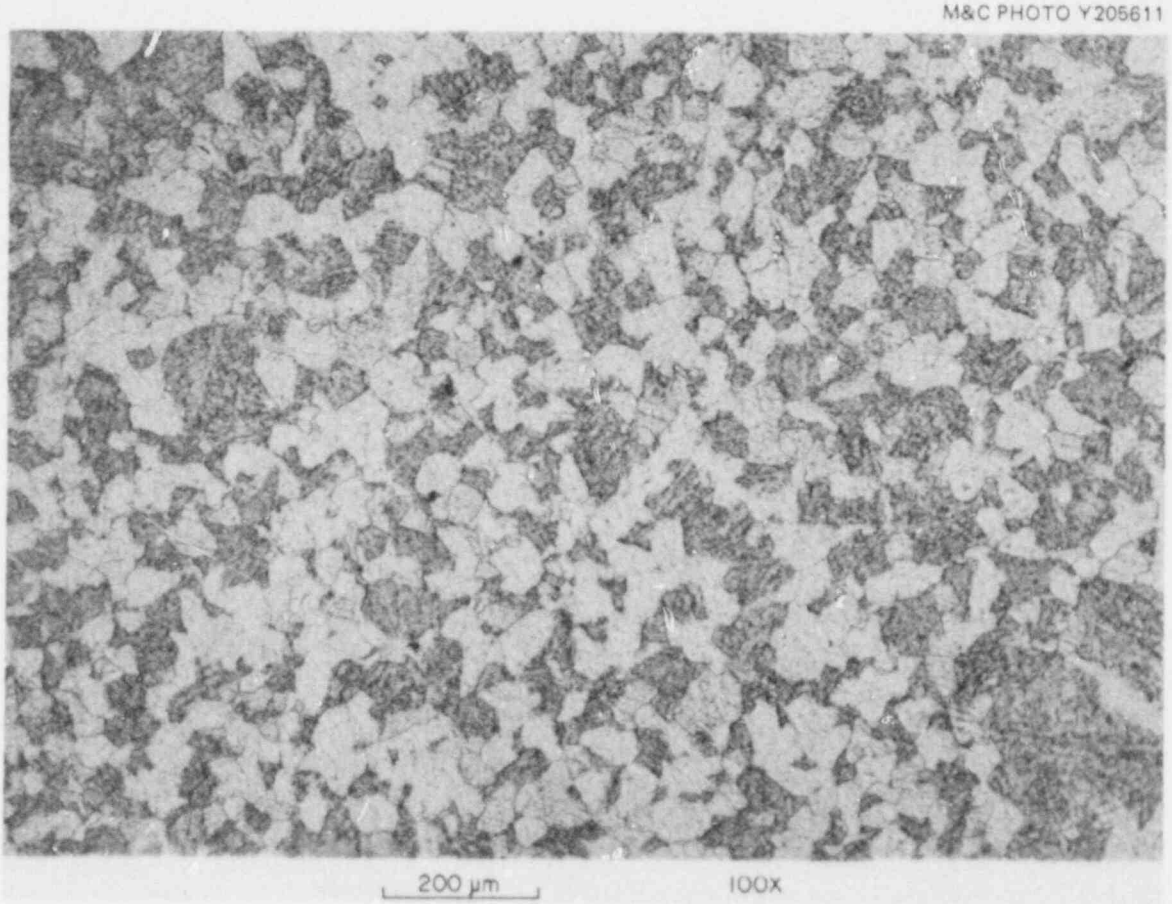

Fig. 2.20. Microstructure of PTSE-2 insert from field replication, location 5, HRB 94.

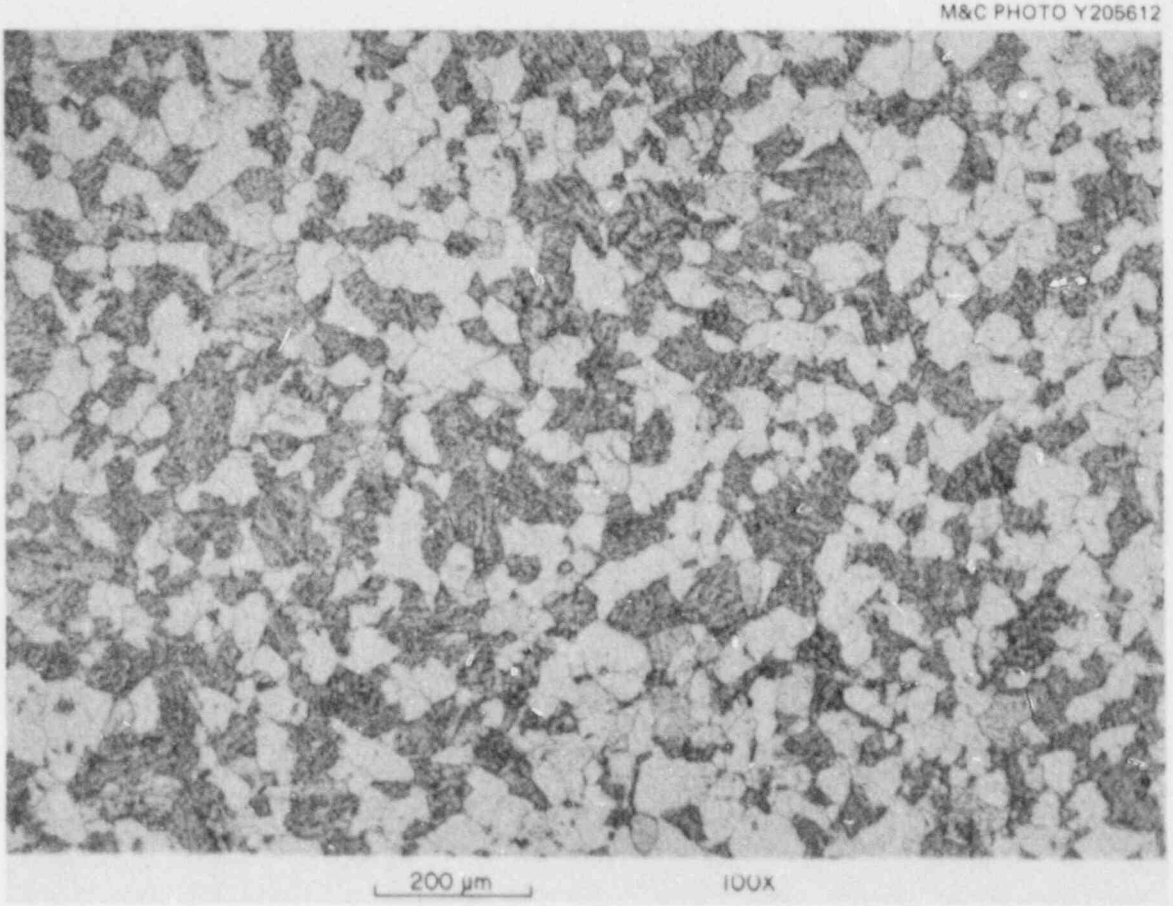

Fig. 2.21. Microstructure of PTSE-2 insert from field replication, location 6, HRB 96.

comparisons on PTC1 revealed even better agreement, within 1 HRB point. Therefore, the significant differences in hardness results between the PTSE-2 insert surface and PTC1 did not appear to be a result of errors from use of a portable hardness tester.

Thus, the PTSE-2 vessel insert had an average pretest surface hardness of about HRB 94 compared with HRB 86 for PTC1. Using the standard American Society for Testing and Materials (ASTM) correlation of hardness with tensile strength gives 675 MPa for the vessel and 558 MPa for PTC1. This difference is substantial in terms of strength and implies a higher yield strength and transition temperature for the insert. Mechanical testing of specimens removed from the vessel insert following the PTSE-2 test show somewhat higher tensile strength for the insert; as explained later, yielding during the experiment could have caused part of this difference.

Figures 2.22 and 2.23 show representative micrographs of PTC1 and the PTSE-2 insert, respectively, near the quarter-thickness depth. As shown, the two materials have similar amounts of pearlite. That observation is not consistent with posttest hardness testing, which showed the

M&C PHOTO Y209275

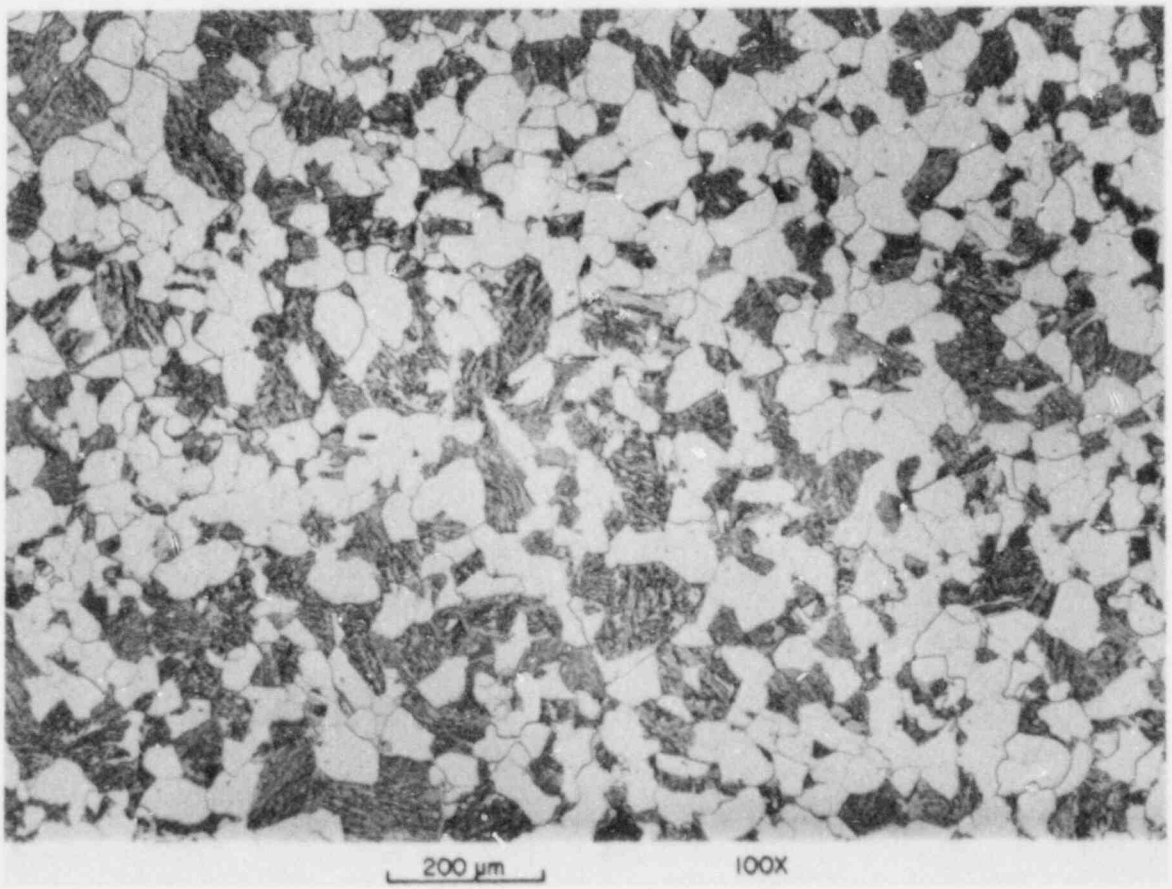

Fig. 2.22. Microstructure of characterization block PTC1 near quarter-thickness depth, longitudinal orientation.

M&C PHOTO Y209118

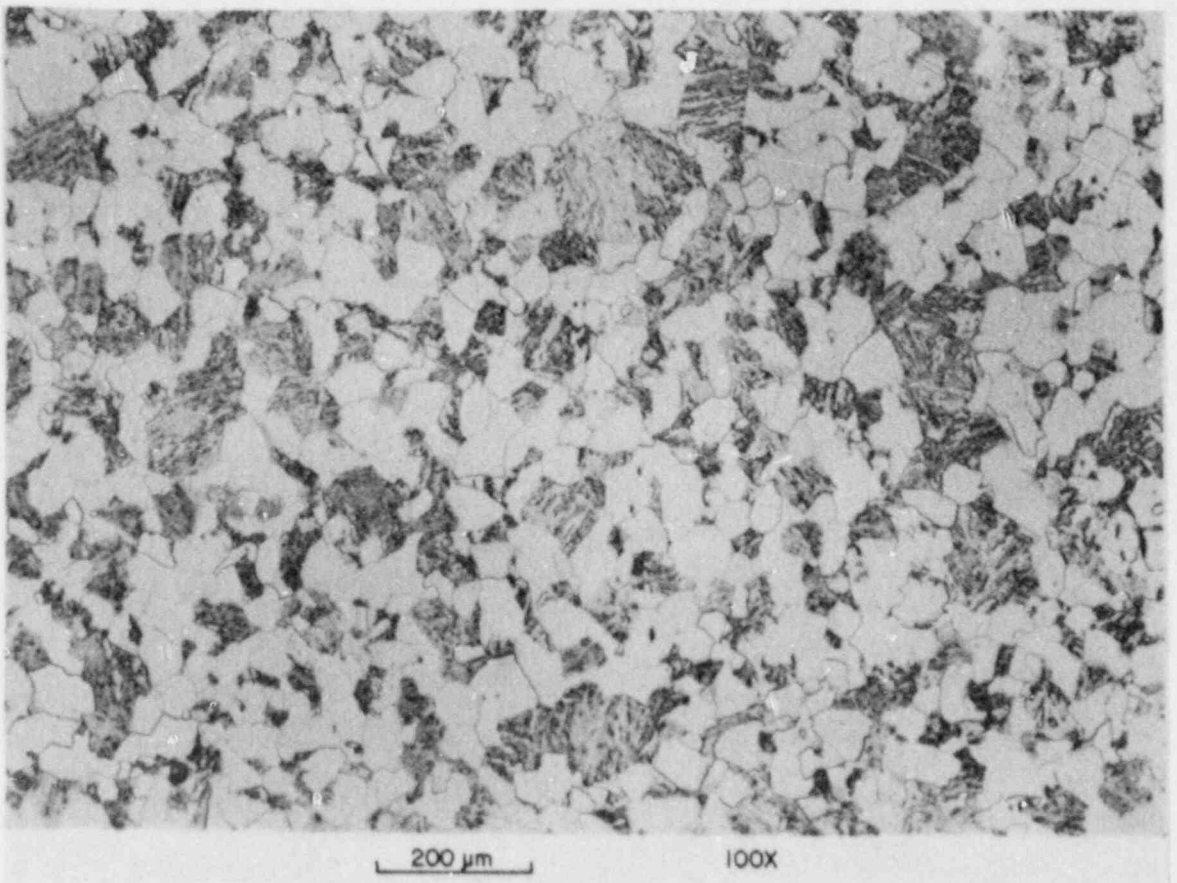

Fig. 2.23. Posttest microstructure of PTSE-2 insert near quarter-thickness depth, longitudinal orientation.

insert to be harder than PTC1. At the quarter-thickness (1/4t) depth, the insert has a hardness of HRB 90, while that of PTC1 is HRB 86, corresponding to tensile strengths (by correlation) of 620 and 558 MPa, respectively. The measured tensile strengths agree very well with the correlative predictions from hardness, as discussed in Sect. 2.3.4. The hardness variations through the thickness of PTC1 are summarized in Table 2.3 and do not show significant variation in hardness as a function of depth in the plate.

2.3.2 Physical properties

Physical properties of PTC1 were determined[9] for consideration in determining the contribution of the insert to thermal stresses during the PTSE-2 experiment and for documentation of the properties. This is discussed in Chap. 10. Properties determined include bulk density, electrical resistivity, and coefficient of thermal expansion.

Table 2.3. Hardness variation through thickness of characterization block PTC1, 2 1/4 Cr-1 Mo steel

Depth location (mm)	Portable tester[a]		Laboratory Rockwell tester[b] (HRB)
	Raw No.	Converted to HRB	
Near surface	444	87	84
12.7	440	86	85.5
25.4	437	85	85
38.1	445	87	87.5
50.8	447	88	87.5
63.5	450	88	89
76.2	451	88	87.5
88.9	437	85	85.5
101.6	438	86	85
114.3	431	84	86
127.0	433	85	85.5
139.7	428	83	84
Near surface	431	84	85

[a]Equotip portable hardness tester measured average value (five readings) of HRB 94 on calibration block calibrated to HRB 96.6 ± 1.0.

[b]Laboratory Rockwell hardness tester measured average (five readings) of HRB 96.5 on calibration block calibrated to HRB 96.6 ± 1.0.

Bulk density measurements (diameter, length, and weight) were determined at 27°C for 12 specimens, with an average result of 7.847 g/cm^3 ± 0.1%. The density of pure iron is 7.873 g/cm^3 at 20°C.

Electrical resistivity was also determined at 27°C for the 12 specimens, with an average value of 28.744 μΩ-cm ± 0.5%.

Thermal expansions were determined using a modification of a technique described by Kollie et al.[10] The technique uses a fused quartz push-rod dilatometer, which is considered to provide expansion measurements accurate within 2% of expected values. Within the range 0 to 350°C, the thermal expansion data can be described by the equation:

$$\alpha \cdot 10^6 = 10.20 + 12.496 \cdot 10^{-3} \cdot T \pm 0.93\% \ , \qquad (1)$$

where α is per Kelvin and T is degrees Celsius.

The results compare favorably with other measurements on similar materials and are about 10% lower than those for pure iron.

2.3.3 Drop-weight testing

Drop-weight testing was conducted with standard P-3 specimens per ASTM Method E208-84a. A single welding pass was used for application of the brittle weld bead. Pretest specimens were removed from PTC1 at the 1/4t depth in the plate. Posttest specimens were removed from portions of the vessel insert at the 1/4t and 3/4t depths. Table 2.4 shows the drop-weight results for each specimen. The NDT temperatures were determined by the procedures of E208 to be 49°C for PTC1 and 75°C for the vessel insert. Thus a substantial difference exists between the two materials. The specific test results reveal a fairly high degree of scatter, however, and further examination of the drop-weight specimens will be conducted to provide an explanation for such differences. A comparison between drop-weight NDT temperatures and CVN results is presented in a later section. It is interesting to note that the PTSE-2

Table 2.4. Results of drop-weight testing on 2 1/4 Cr-1 Mo material[a]

Specimen	Test temperature (°C)	Test results	
		Break	No break
PTC1 characterization block (TS)[b]			
PI261	66		✓
PI262	54		✓
PI263	38	✓	
PI264	49	✓	
PI265	54		✓
PI266	49	✓	
Flaw insert material segments (LS)[b]			
PE94	65		✓
PE95	45	✓	
PE96	55	✓	
PE97	60	✓	
PE98	65	✓	
PE99	70	✓	
PE100	75	✓	
PE101	85		✓
PE102	80		✓
PE103	80		✓
PE104	60	✓	
PE105	70		✓

[a]Results are listed in the order of testing.

[b]The drop-weight test is insensitive to specimen orientation per ASTM E208.

characterization material studied earlier (PTC2B from part PTC2 in Fig. 2.10), which was unacceptable because of a high CVN upper shelf and low CVN transition temperature, revealed a drop-weight NDT of 32°C.

2.3.4 Tensile testing

2.3.4.1 Pretest tensile tests. Results of tensile tests performed with three different specimen sizes made from characterization block PTC1 are shown in Table 2.5. Standard specimens 6.35 and 12.7 mm in diameter were tested to obtain stress-strain curves from 24 to 300°C. The load-displacement recording for specimen PI372, one of the six 12.7-mm-diam specimens of PTC1 material, was chosen as the basis for the stress-strain relationship (shown in Fig. 2.24) to use in pretest and posttest elastic-plastic finite-element analysis. This particular specimen was selected because it was tested at a temperature (100°C) that was appropriate for the thermal transients to be analyzed and because its load-displacement record exhibited a behavior that approximated an average for the set.

As seen in Table 2.5, the ultimate strengths, fracture strengths, and measures of ductility are in reasonable agreement among the various

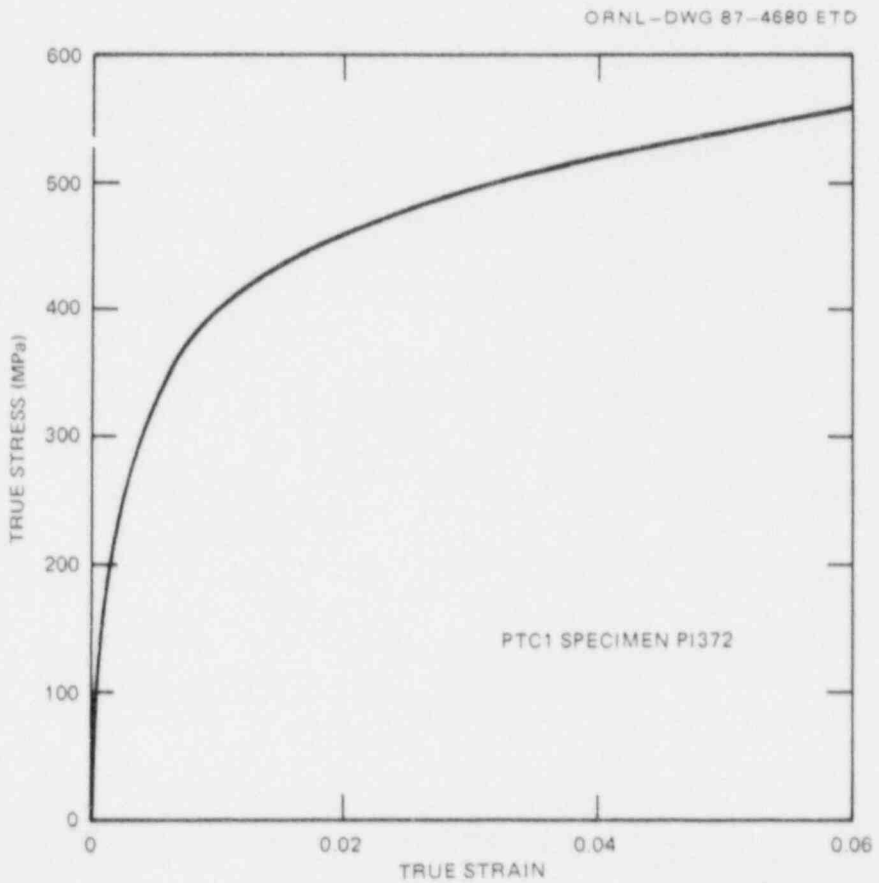

Fig. 2.24. True stress vs true strain from tensile test of specimen PI372 from PTC1 tested at 100°C.

Table 2.5. Pretest tensile results for PTC1, 2 1/4 Cr-1 Mo steel for transverse (T) orientation

Specimen[a]	Temperature (°C)	Strength (MPa)			Fracture stress (MPa)	Elongation[d] (%)	Reduction of area (%)
		Yield		Ultimate			
		[b]	[c]				
4.52-mm-diam (0.18-in.) specimens							
PI97	−100		512	715	573	35	50
PI93	−100		503	719	572	41	51
PI94	−50		348	664	470	28	51
PI127	0		321	603	466	26	53
PI118	0		346	599	468	25	56
PI123	100		320	537	441	21	48
PI98	200		269	493	411	20	50
PI114	300		327	533	478	15	38
6.35-mm-diam (0.25-in.) specimens							
PI283	24	266	348	574	467	26	51
PI291	24	314	314	586	501	25	44
PI285	100	265	359	530	446	22	47
PI286	100	266	337	523	432	24	50
PI292	100	259	340	530	449	26	47
PI287	200	241	315	511	447	20	46
PI288	200	248	315	509	434	19	46
PI293	200	234	330	513	442	20	45
PI289	300	290	344	520	454	16	41
PI290	300	244	325	513	454	17	43
PI294	300	248	335	515	461	16	41
12.7-mm-diam (0.5-in.) specimens							
PI369	24	275	336	578		26	47
PI370	25	295		603		27	50
PI371	100	256		536		23	46
PI372	100	276		554		24	46
PI374	200	263		534		23	47
PI373	300	254		524		21	42

[a]All specimens machined from 1/4t depth in plate with transverse orientation.

[b]Yield strength obtained from x-y plot of load vs strain extensometer (25.4-mm gage length).

[c]Yield strength obtained from strip-chart recording of load vs cross-head speed.

[d]Computed from strip-chart readings of elongation of specimen, corrected to a gage length of four diameters when necessary. The elongations for the 12.7-mm-diam specimens were computed from gage marks on the specimens.

tests. Comparison of results in this table revealed that yield strengths (at 0.2% offset) determined from the load-displacement curves from extensometer data were significantly lower than those obtained from load-displacement curves inferred from crosshead motion. Previous experience with tensile testing of 2 1/4 Cr-1 Mo and most other steels had resulted in good agreement between the two methods. Instrument calibrations were verified, and Batteile Columbus Division tested eight specimens as an independent check.[11] The results of the Battelle tests are shown in Table 2.6. The Battelle tests, which were instrumented with an extensometer, supported the conclusion that the yield strengths based on extensometer data were the more reliable. Accordingly, yield and flow stresses as a function of temperature were fit to the extensometer-based data in Table 2.5 by a least-squares procedure for use in the analysis of warm prestressing associated with transient PTSE-2A.

Table 2.6. Pretest tensile test results from Battelle Columbus Division for PTC1

Temperature (°C)	Strength (MPa)		Reduction of area (%)
	Yield	Ultimate	
26	262	551	54.8
27	275	553	53.3
100	245	503	54.5
100	208	449	60.4
200	205	443	55.8
200	193	425	56.8
288	212	450	52.0
288	200	429	52.5

The most likely cause for the observed discrepancies in yield strength determinations is the apparent absence of a proportional limit for this material. A discussion of the analysis and evaluation of this problem is outside the scope of this report and will be reported separately.

2.3.4.2 Posttest tensile testing. It was expected that material close to the flaw would experience large plastic strains in the two PTSE-2 transients and therefore be in a strain-hardened state after each transient. Nevertheless, since pretest hardness testing of the insert and PTC1 implied, before an opportunity for strain hardening, that the two pieces had different tensile properties, a series of posttest tensile tests with insert material were performed in an attempt to define more clearly the respective tensile properties relevant to the two transients. The posttest evaluation of tensile properties included the testing of both circumferentially and axially oriented specimens from the vessel

insert. These tests showed the expected effect of strain hardening, but the results were inconclusive with regard to the representativeness of the PTC1 tensile data.

The most important tensile property of the vessel insert was the stress-strain relationship, because this was the essential basis of all posttest fracture mechanics interpretations of the PTSE-2 experiment. All of the load-displacement records for the insert material were compared, and the record of one specimen, PE08, was chosen as representative of an average for the set of transversely oriented insert specimens. The specimens in this set are listed in Table 2.7. The true stress vs true strain for specimen PE08 is shown in Fig. 2.25. A comparison of the PTC1 and insert stress-strain properties is discussed in Chap. 10 (see Fig. 10.3).

Results of posttest tensile testing performed at different temperatures on vessel insert material are summarized in Tables 2.7 and 2.8. The specimens listed in Table 2.7 were transversely (T) oriented and from different depth locations. Material from the 1/4t and the 3/4t depths are reported together as 1/4t. Figure 2.26 compares the tensile strengths of 1/4t material from the PTC1 characterization block to that

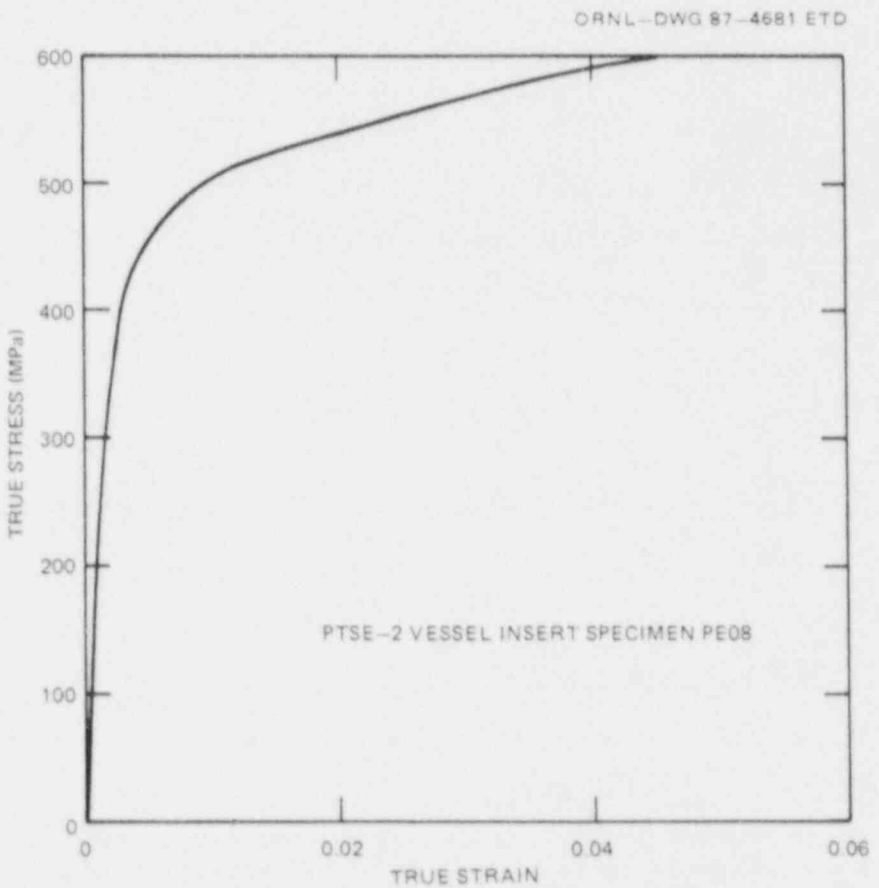

Fig. 2.25. True stress vs true strain from tensile test of specimen PE08 from vessel insert tested at 100°C.

Table 2.7. Posttest tensile results from PTSE-2 insert material, T-oriented, 6.35-mm-diam specimens

Specimen	Location (t)	Test Temperature (°C)	Strength (MPa)		Elongation[a] (%)	Reduction of area (%)
			0.2% yield[a]	Ultimate		
PE01	0	25	461	620	18	52
PE04	0	25	478	623	18	52
PE02	1/4	25	462	620	21	52
PE05	1/4	25	488	627	19	50
PE03	1/2	25	460	627	20	51
PE06	1/2	25	452	620	22	49
PE07[b]	0	100	455	564	19	73
PE10	0	100	443	578	16	49
PE08	1/4	100	442	585	17	49
PE11	1/4	100	440	579	16	46
PE09	1/2	100	422	580	19	48
PE12	1/2	100	423	577	20	47
PE13	0	200	436	545	13	45
PE16	0	200	449	550	14	47
PE14	1/4	200	415	534	17	46
PE17	1/4	200	414	541	17	48
PE15	1/2	200	403	548	19	46
PE18	1/2	200	403	549	20	42

[a]Determined from extensometer, x-y chart.

[b]This specimen broke in weld metal.

Table 2.8. Results of tensile tests performed on L-orientation, 6.35-mm-diam, 2 1/4 Cr-1 Mo material

Specimen	Location (t)	Test temperature (°C)	Strength (MPa)		Elongation[b] (%)	Reduction of area (%)
			0.2% yield[a]	Ultimate		
PTC1 characterization block material						
PC1	1/4	100	288	541	24	51
PC2	1/4	100	280	542	26	51
Flaw insert material						
PE109	1/2	26	365	617	29	48
PE115	1/2	26	377	621	23	47
PE111	1/4	100	389	538	22	49
PE117	1/4	100	374	567	22	52

[a]Extensometer, x-y chart.

[b]Measured from gage marks on specimens.

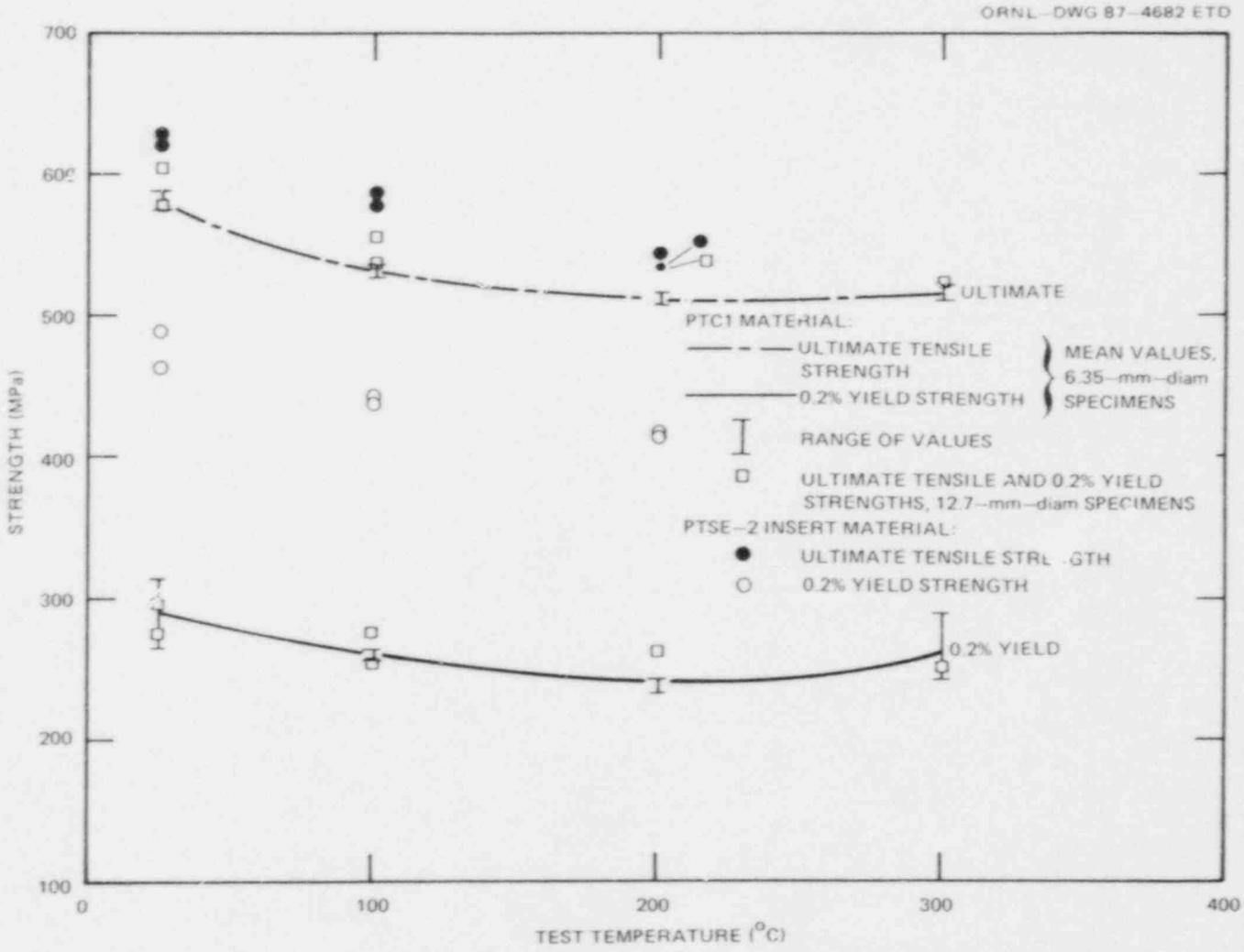

Fig. 2.26. Comparison of tensile strengths of PTC1 characterization block to flaw insert material, all from 1/4t depth and T orientation. The values for the yield strength are from extensometer data.

from the insert. The yield strength of the insert material is ~60 to 70% higher than the yield strengths obtained for characterization block material. All the tensile specimens had some weld metal that extended into the uniform section of the specimen, because the insert was not wide enough for T-oriented, 6.35-mm-diam tensile specimens from 2 1/4 Cr-1 Mo material alone. Except for specimen PE07, the fractures were in base metal, and most of the necking occurred in the base metal, as determined by etching of the specimens after testing. The effect of weld metal on the ultimate tensile strength of the flaw insert material is therefore presumed to be small. In any event, the specimens are representative of the actual structure.

The tensile test results for the L-oriented specimens are shown in Table 2.8. Comparison of the ultimate strengths for the 1/4t location material tested at 100°C shows that the averages for both these materials agree within 2%. The yield strength (average of two specimens) for the insert is 35% higher compared to the 60 to 70% observed for the T-orientated specimens. If the difference in yield strength of the insert relative to that of PTC1 was caused by strain-hardening, one would expect the effect to be greater for the T-oriented specimens.

The L-orientated PTC1 tensile specimens were subjected during the tensile tests to three cycles of loading and unloading. The purpose was to verify the actual extent of strain hardening for this particular material. In each cycle, unloading was initiated when the total strain was approximately 1, 2, and 3%, respectively, as shown in Fig. 2.27(*a*) for specimen PC1. The uniaxial strain hardening observed in specimen PC1 produced a stiffer material at incremental strains less than ~0.5% than is typical of insert material. Figure 2.27(*b*), which shows stress-strain curves for representative specimens from both PTC1 and the vessel insert, graphically illustrates differences in tensile behavior of the two materials. As discussed earlier, some uncertainties exist concerning the exact representation of the vessel insert material by the characterization material. Although the cyclic tests described above do not mitigate all those uncertainties, they show that the differences in tensile properties of the insert and the characterization material are likely due largely to strain hardening that occurred during the PTSE-2 experiments.

2.3.4.3 Determination of Young's modulus. Before the PTSE-2 experiment, the tensile tests of PTC1 specimens identified in Table 2.5 were the source of data on Young's modulus (E) for the vessel insert. Values inferred from extensometer data for 12.7-mm-diam specimens are presented in Table 2.9. The extensometer instrumentation used was designed to give data at high strains and, therefore, was not ideal for precise E measurements.

After the PTSE-2 experiment, Young's modulus was measured again with instrumentation capable of better resolution at low strains. Two L-orientated 1/4t specimens 6.35 mm in diameter from each of the vessel insert and characterization piece PTC1 were instrumented with strain gages to measure Young's modulus E and Poisson's ratio ν. On each specimen two axial and two circumferential gages were placed diametrically opposite each other and connected in series to average out bending strains due to misalignment. Measurements were made at two temperatures, 25 and 150°C. At each temperature the specimens were first subjected to

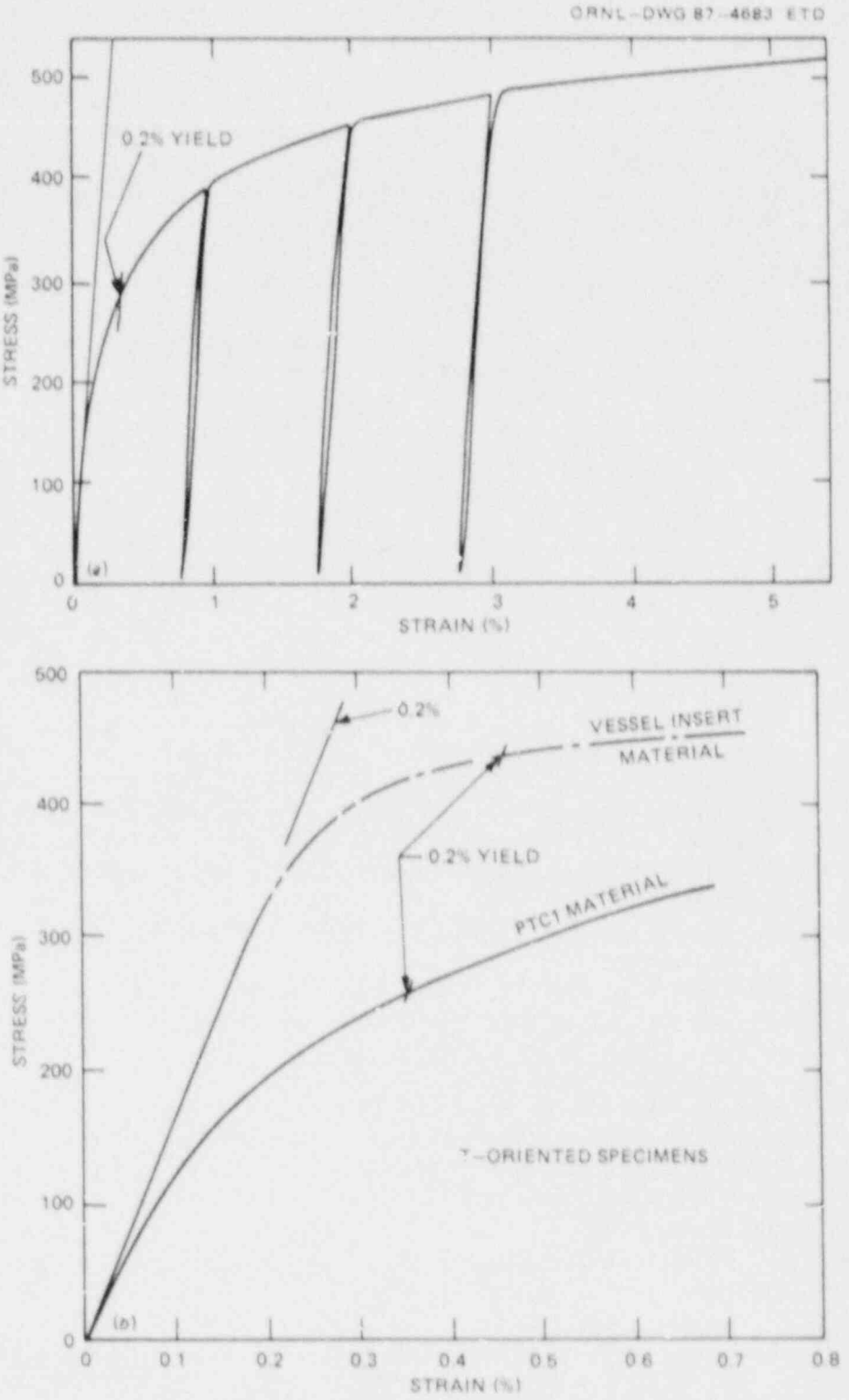

Fig. 2.27. (*a*) Cyclic stress-strain behavior of L-oriented specimen PC1 of PTC1 material and (*b*) comparison of stress vs strain curves of PTC1 and vessel insert.

Table 2.9. Pretest and posttest determination of Young's modulus E and Poisson's ratio ν

Specimen	Temperature (°C)	E (GPa)	ν
	PTC1, T orientation[a]		
PI369	24	211	
PI370	25	211	
PI371	100	216	
PI372	100	211	
PI374	200	216	
PI373	300	206	
	PTC1, L orientation[b]		
PC5	25	212	0.259
	150	205	0.267
PC6	25	206	0.258
	150	203	0.256
	Vessel insert, L orientation[b]		
PE107	25	206	0.257
	150	210	0.260
PE113	25	204	0.260
	150	194	0.263

[a]From extensometer data and 12.7-mm-diam specimens.

[b]From strain-gaged 6.35-mm-diam specimens.

three loading and unloading cycles between 0 and 55 MPa prior to recording data for determining E. The 0.2% yield for this material is about 280 MPa, but, because of the apparent lack of a proportional limit, the maximum stress was restricted to ~20% of this value. Measurements of the strain from the strain gages were recorded at stresses of 7 and 57 MPa, and E was calculated as the secant modulus between the two stresses. The E and ν values presented in Table 2.9 for the strain-gaged specimens are the averages of four measurements at each temperature: two each during loading and unloading. The accuracy of these E and ν values is estimated to be about 5 and 10%, respectively.

The Young's modulus values shown in Table 2.9 are plotted vs temperature in Fig. 2.28, with average values inferred from the extensometer data for the vessel insert specimens PE01 to PE18. This figure illustrates the scatter obtained in the E measurements.

Ultrasonic wave velocity measurements were made at room temperature on a 6.35-mm-thick coupon of PTC1 material to give a dynamic Young's modulus of 213 ± 1 GPa and a dynamic Poisson's ratio of 0.286 ± 0.003.

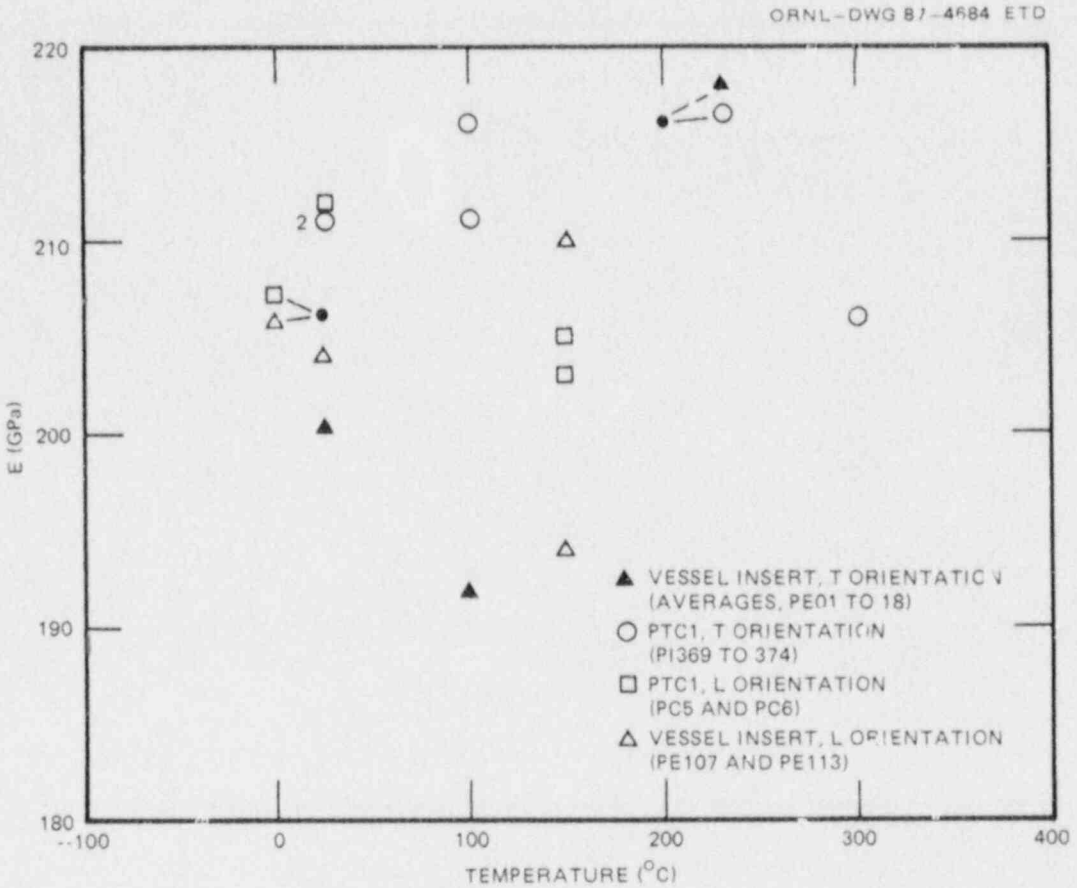

Fig. 2.28. Young's modulus vs T inferred from tensile tests of PTC1 and vessel insert.

Within the limits of the accuracy of these measurements, Young's modulus can be taken to be ~205 GPa and Poisson's ratio to be 0.26 with no temperature dependence detected in the range 25 to 1[illegible] °C.

2.3.5 Charpy V-notch testing

Pretest CVN impact testing was performed with PTC1 specimens taken from varying depths in the plate and in both the TS (crack propagation in thickness direction) and TL (crack propagation in rolling direction) orientations. A total of 192 CVN specimens from PTC1 were tested to examine variations of CVN toughness with temperature, location, and orientation. Absorbed energy, lateral expansion, and percent of ductile fracture were determined from brittle to fully ductile behavior, with −25°C the lowest and 250°C the highest test temperatures. Because the material was heat treated to obtain a low CVN upper-shelf energy, the variation in fully ductile CVN energy is of interest and was examined for the TS orientation by testing at 175°C eight specimens from each of five depths in the plate.

Figures 2.29 and 2.30 show the CVN data and hyperbolic tangent curve fits for the TS orientation for two depths in the plate, near-surface

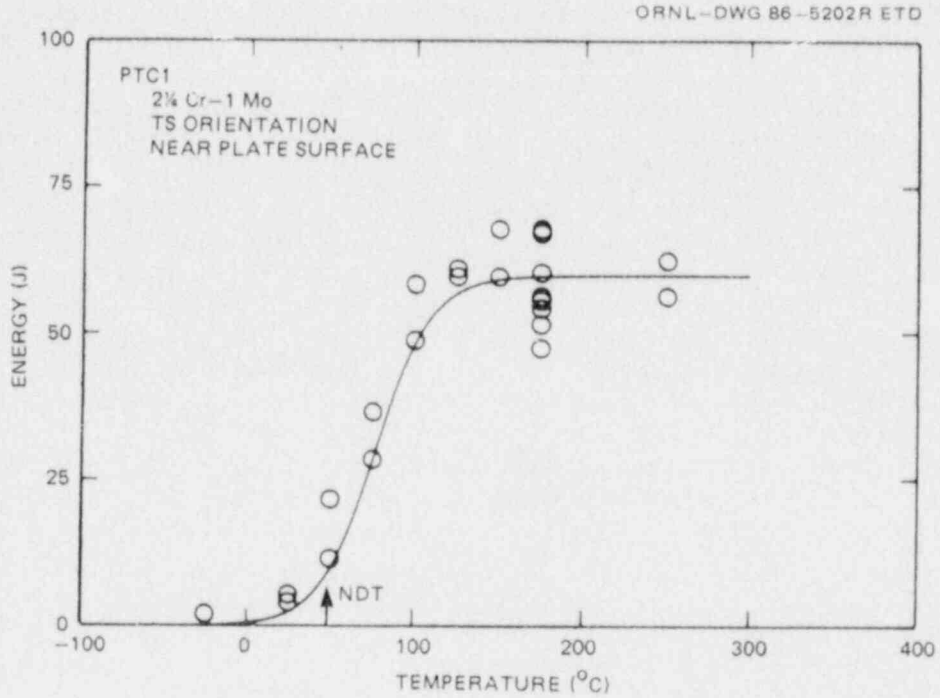

Fig. 2.29. Charpy V-notch impact energy vs temperature for characterization block PTC1 for TS orientation near plate surface.

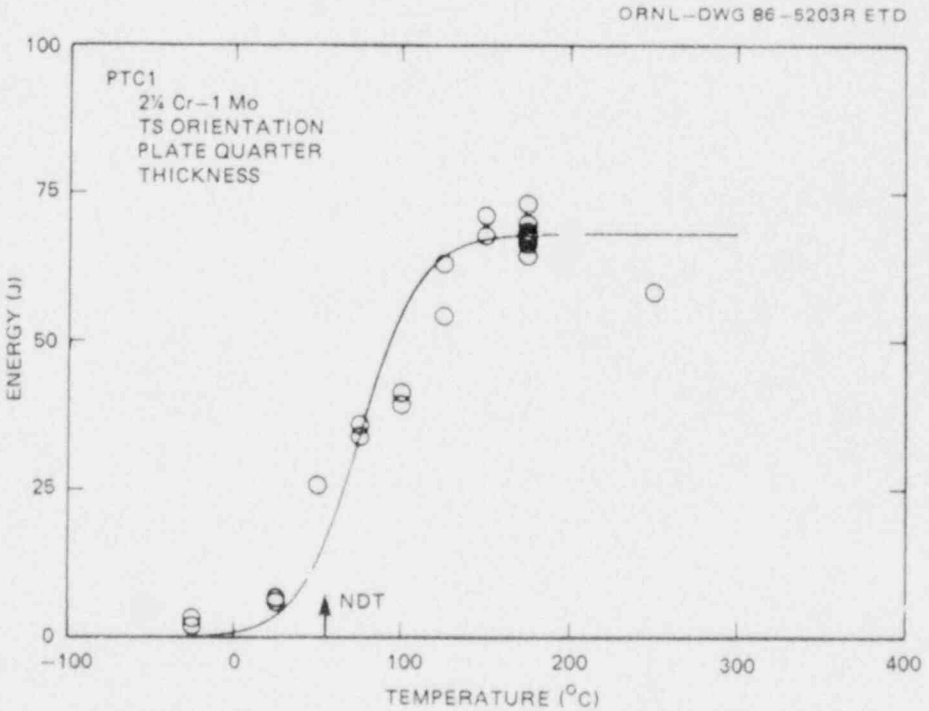

Fig. 2.30. Charpy V-notch impact energy vs temperature for characterization block PTC1 for TS orientation at quarter-thickness depth in plate.

(0t) and quarter-thickness (1/4t), respectively. The curves are similarly shaped, but the average upper-shelf energy is higher at the 1/4t. The variation in energies at 175°C is much greater at 0t than 1/4t. Furthermore, a large variation was seen at 1/2t but not at 3/4t. The variations of CVN energy at 175°C were about ±10 J at 0t and 1/2t but only ±3 to 4 J at 1/4t, 3/4t, and 1t. The reasons for such differences are not clear at this time.

Figure 2.31 provides a comparison of CVN curves for each plate depth in the TS orientation; Table 2.10 gives the curve fit parameters for each curve. The midcurve temperatures vary from about 73 to 77°C, exclusive of that for the 1/2t curve, which is 86°C. Upper-shelf energies based on the curve fits vary from about 60 to 73 J. The observed variations are not considered significant regarding potential effects on the behavior of the PTSE-2 experiments.

Charpy data and curve fits for the TL orientation are shown in Figs. 2.32 to 2.34. The applicable curve fit parameters are also shown in Table 2.10. The transition temperatures are very similar to those for

Table 2.10. Curve-fit parameters of Charpy energy for PTC1, 2 1/4 Cr-1 Mo steel

Depth (t)	$E_{CVN} = (A/2)\{1 + \tanh[B(T - C)]\}^a$			E_{CVN} at NDT, 49°C (J)	Temperature at 41 J (°C)
	A (J)	B ($°C^{-1}$)	( )		
			TS orientation		
0	59.85	0.03046	76.8	*b*	89.6
1/4	[illegible]15	0.01755	75.03	19.5	86.8
1/2	.34	0.01913	85.98	*b*	104.3
3/4	3.90	0.02214	73.16	*b*	81.8
1	2.81	0.01959	74.26	*b*	80.7
			TL orientation		
0	59.89	0.02062	80.6	*b*	99.4
1/4	59.43	0.01998	74.4	15.5	94.4
1/2	50.42	0.01675	75.8	*b*	119.7
3/4	63.63	0.02255	73.32	*b*	86.5
1	63.33	0.02112	77.74	*b*	92.1

[a] E_{CVN} = CVN energy at temperature T
A = upper-shelf energy
B = related to slope of curve in transition region
C = temperature corresponding to energy equal to one-half upper-shelf energy.

[b] Not calculated, drop-weight NDT was determined with specimens from 1/4t.

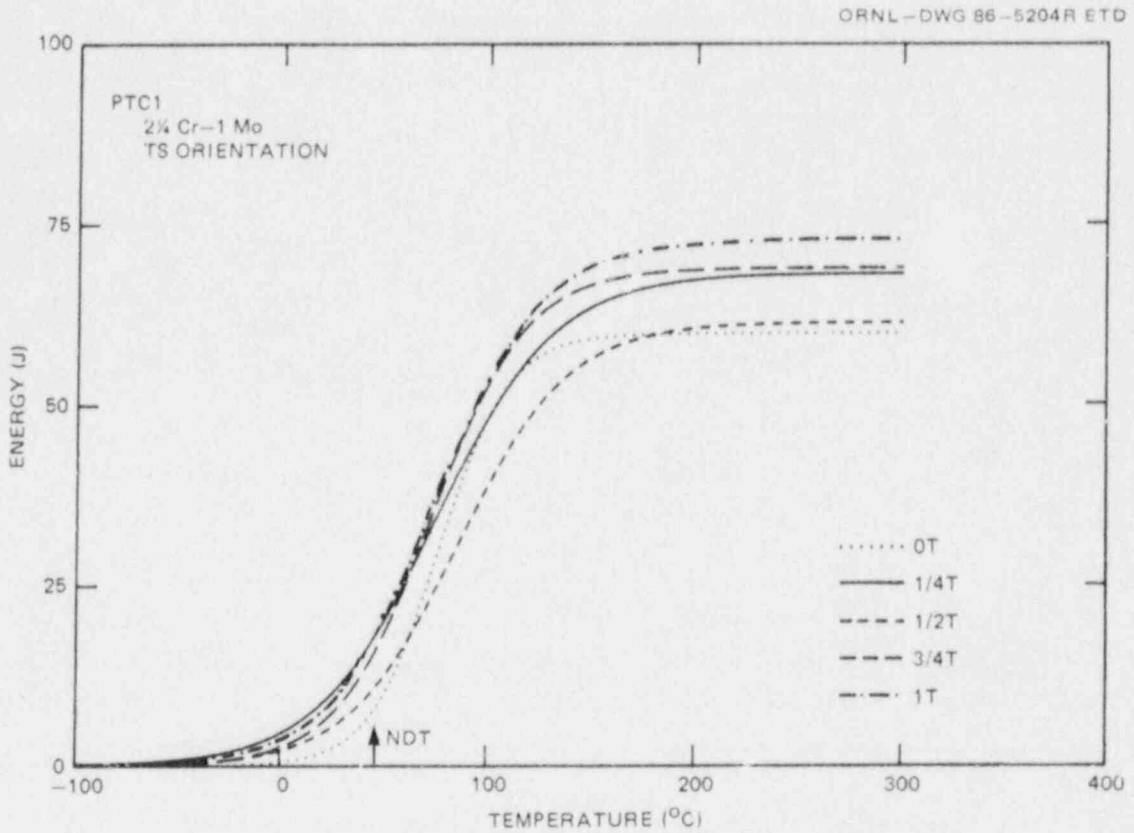

Fig. 2.31. Curve fits of Charpy V-notch impact energy vs temperature for characterization block PTC1 for TS orientation and various depths in plate.

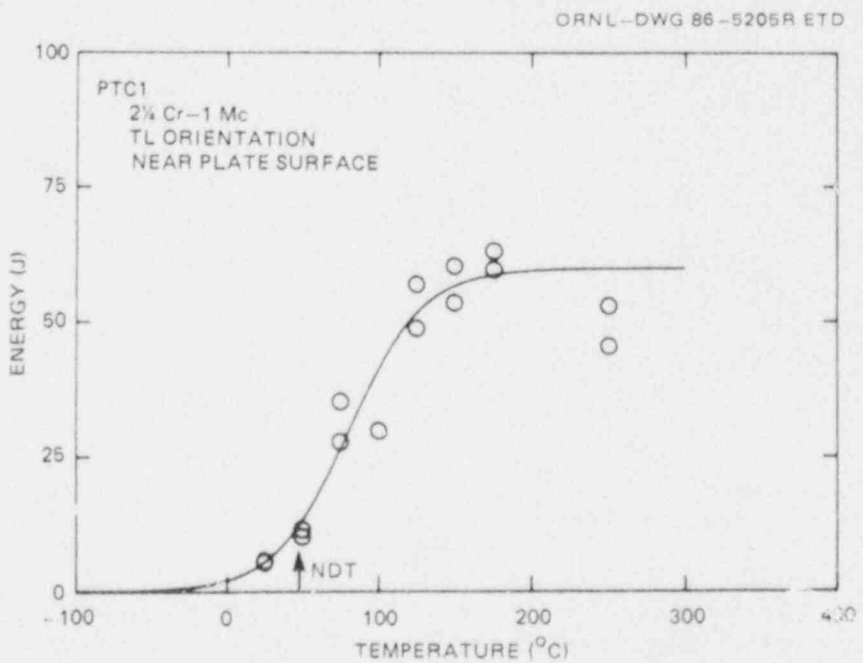

Fig. 2.32. Charpy V-notch impact energy vs temperature for characterization block PTC1 for TL orientation near plate surface.

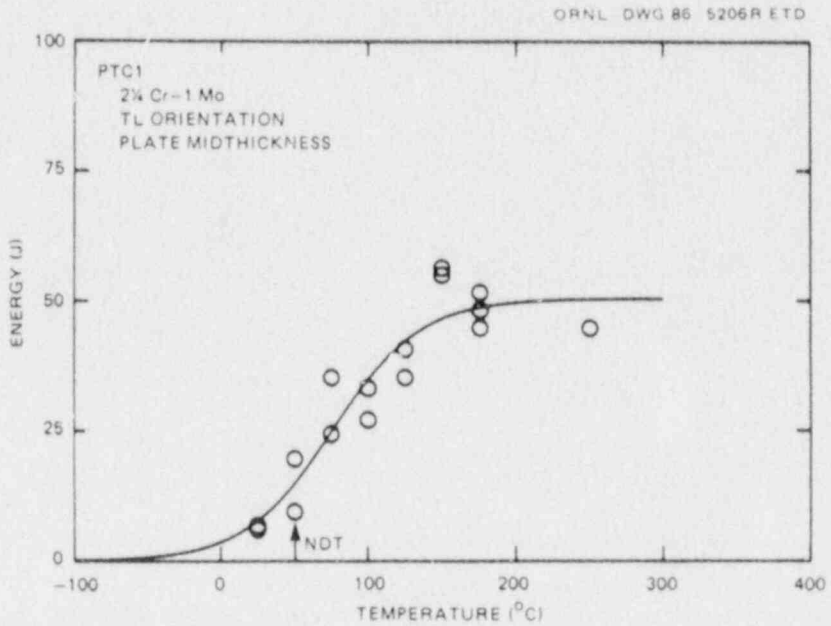

Fig. 2.33. Charpy V-notch impact energy vs temperature for characterization block PTC1 for TL orientation at midthickness depth in plate.

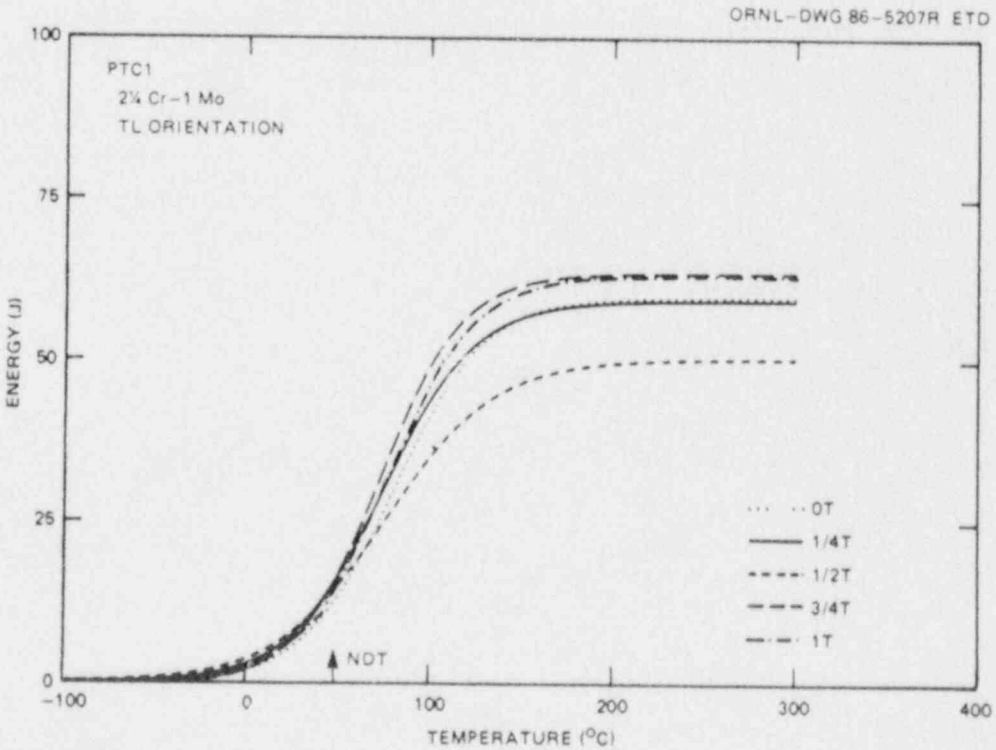

Fig. 2.34. Curve fits of Charpy V-notch impact energy vs temperature for characterization block PTC1 for TL orientation and various depths in plate.

the TS orientation, but the average upper-shelf energies for the TL orientation vary from about 50 to 64 J, somewhat lower than those for the TS orientation. Figures 2.35 and 2.36 are comparisons of CVN curves for both orientations at two different plate depths, near-surface and 1/4t, respectively. Those comparisons show only small differences between the CVN curves as a result of orientation.

Table 2.10 also shows, based on the curve fits, the energy corresponding to the drop-weight NDT and the 41-J transition temperature for each data set. The NDT corresponds to an average CVN energy of 19.5 J for the TS orientation and 15.5 J for the TL orientation. It is interesting to note that specimens from 1/2t depth showed the highest 41-J temperature in both orientations.

Posttest CVN specimens in the TS orientation were removed from the vessel insert at the surface, 1/4t, and 1/2t depths. The CVN data and curve fits are shown in Figs. 2.37 to 2.39. The curve fit parameters are given in Table 2.11. Figure 2.40 is a comparison of the pretest and posttest CVN results for specimens removed from the 1/4t depth in the plate. Comparison of the midenergy transition temperatures (parameter C) and the 41-J temperatures from Tables 2.10 and 2.11 reveals that the PTSE-2 vessel insert transition is about 20 K higher than that for the pretest characterization block PTC1 in the TS orientation at the 1/4t depth. The tables also show that the CVN upper-shelf energies of the insert are, on the average, slightly lower than those for PTC1 in the TS orientation.

These results are consistent with the implications mentioned earlier relative to the higher surface hardness of the insert and, especially, the posttest drop-weight NDT and tensile results. The difference in the

Table 2.11. Curve-fit parameters of Charpy energy for PTSE-2 posttest vessel insert, 2 1/4 Cr-1 Mo steel, TS orientation

Depth (t)	$E_{CVN} = (A/2)\{1 + \tanh[B(T - C)]\}^a$			E_{CVN} at NDT, 75°C (J)	Temperature at 41 J (°C)
	A (J)	B ($°C^{-1}$)	C (°C)		
0	60.57	0.01966	94.16	*b*	113.0
1/4	63.16	0.02293	93.92	18.6	107.3
1/2	56.03	0.01988	90.69	*b*	116.0

[a] E_{CVN} = CVN energy at temperature T
A = upper-shelf energy
B = related to slope of curve in transition region
C = temperature corresponding to energy equal to one-half upper-shelf energy.

[b] Not calculated, drop-weight NDT was determined with specimens from 1/4t.

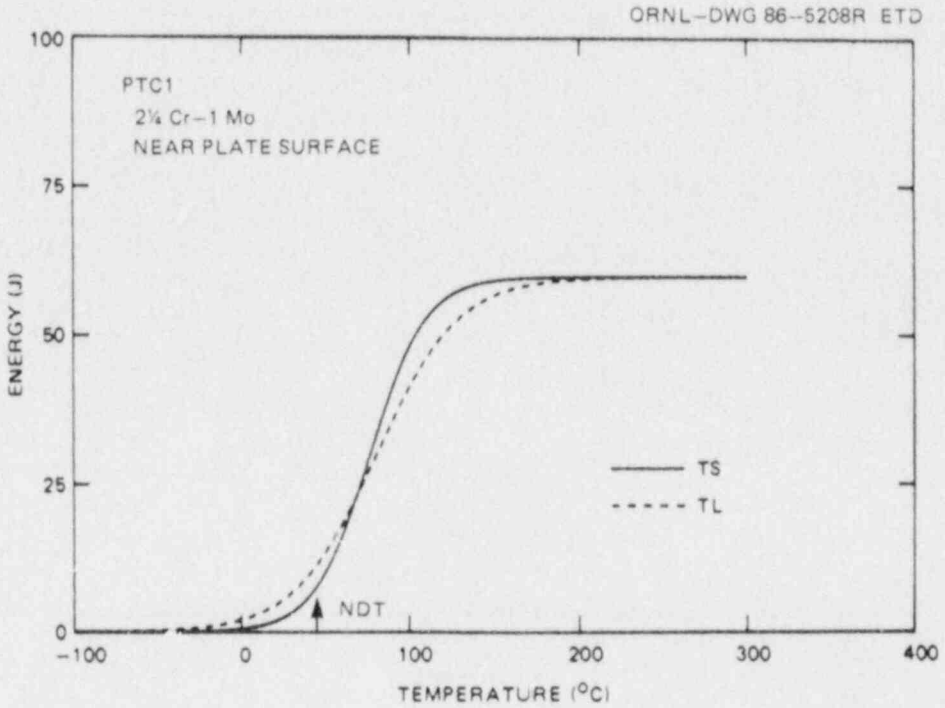

Fig. 2.35. Curve fits of Charpy V-notch impact energy vs temperature for characterization block PTC1 for TS and TL orientations near plate surface.

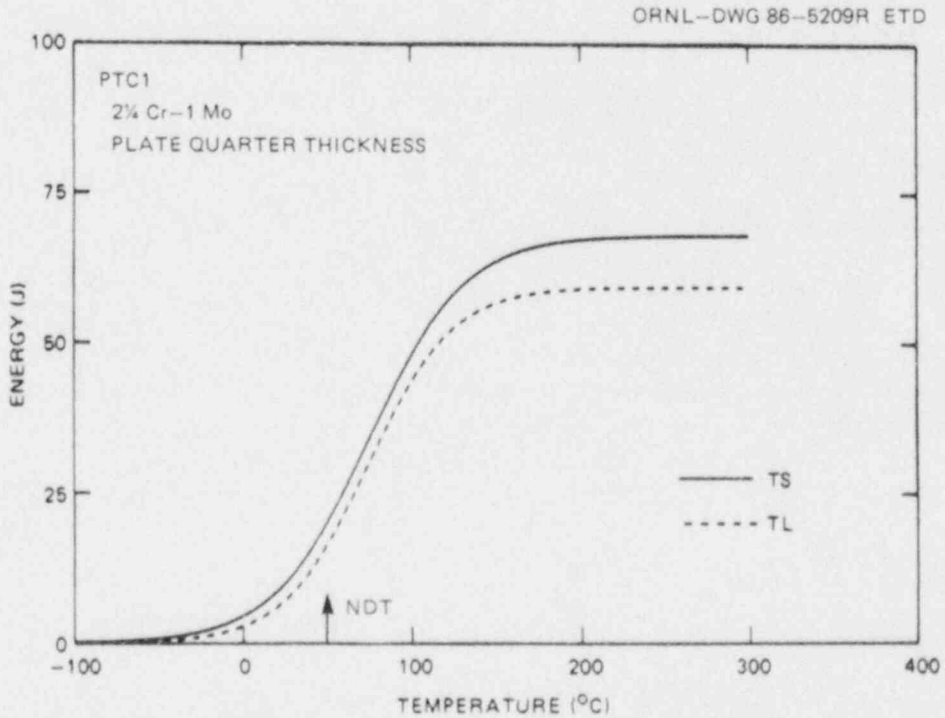

Fig. 2.36. Curve fits of Charpy V-notch impact energy vs temperature for characterization block PTC1 for TS and TL orientations at quarter-thickness depth in plate.

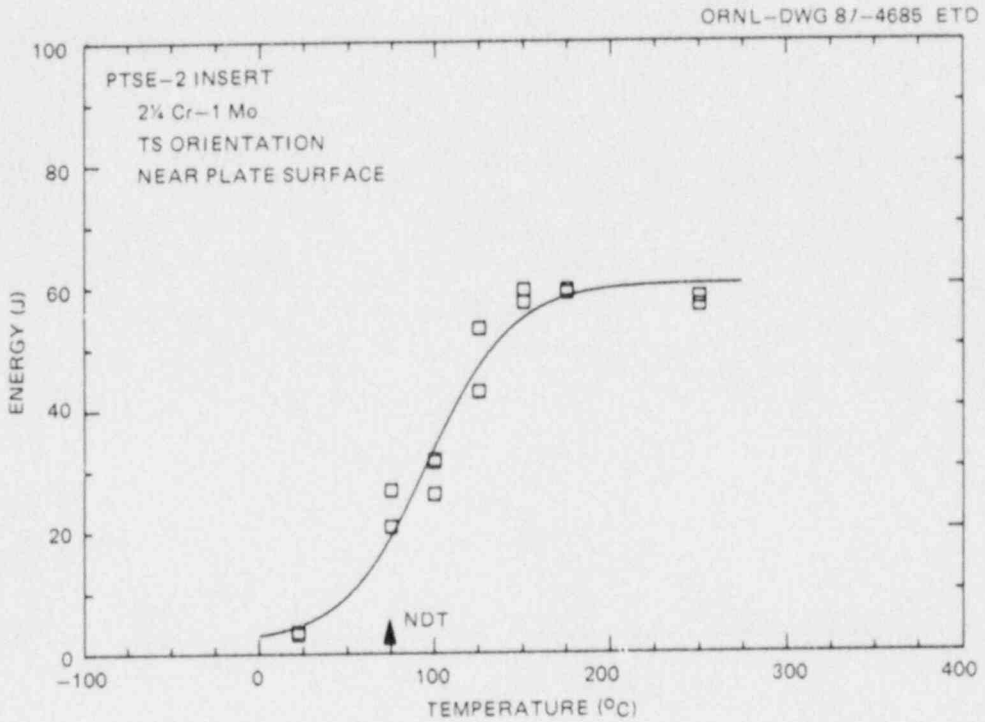

Fig. 2.37. Posttest Charpy V-notch impact energy vs temperature for PTSE-2 vessel insert for TS orientation near plate surface.

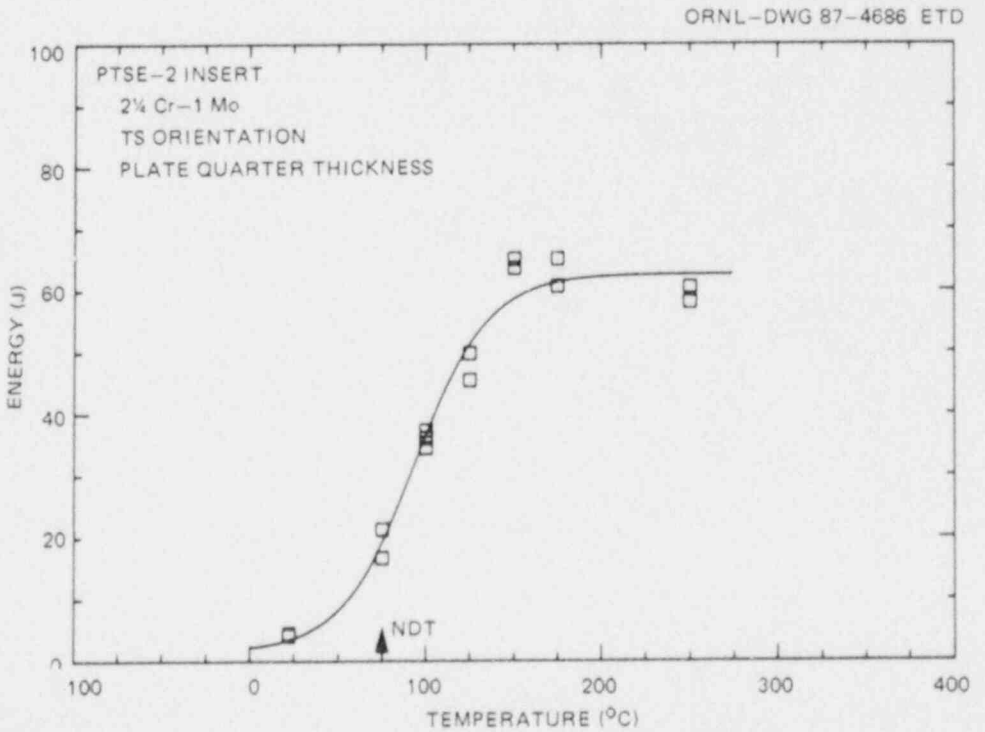

Fig. 2.38. Posttest Charpy V-notch impact energy vs temperature for PTSE-2 vessel insert for TS orientation at quarter-thickness depth.

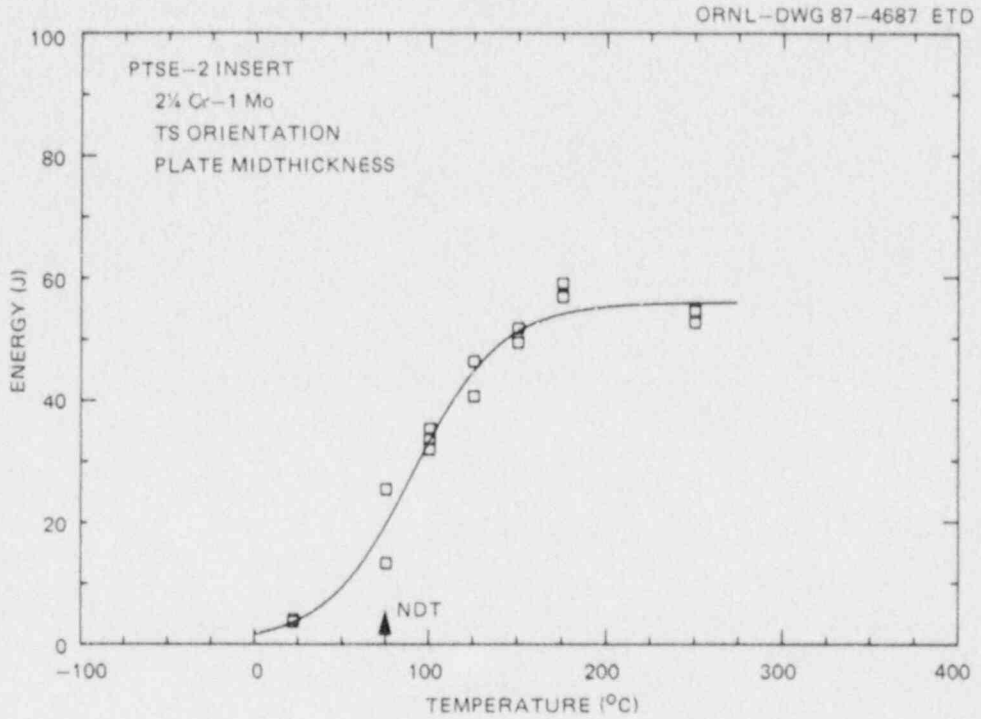

Fig. 2.39. Posttest Charpy V-notch impact energy vs temperature for PTSE-2 vessel insert for TS orientation at midthickness depth.

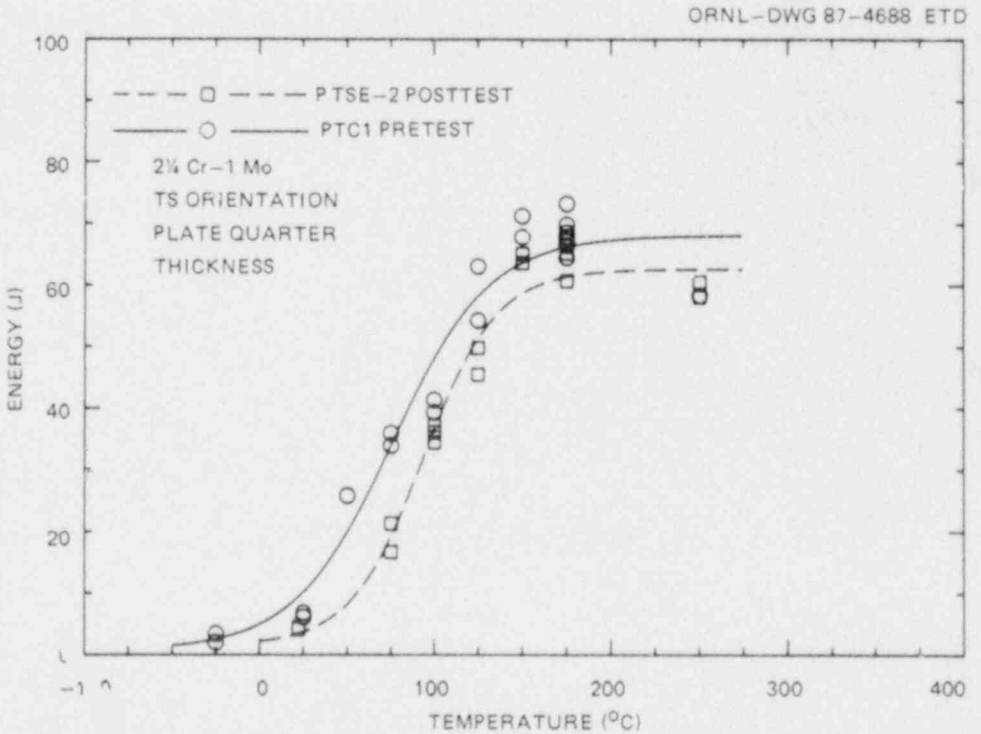

Fig. 2.40. Comparison of CVN results for pretest characterization block PTC1 and PTSE-2 posttest vessel insert for TS orientation at quarter-thickness depths.

1/4t Charpy transition temperatures is about 20 K, compared to a difference in the NDT temperatures of 26 K, a reasonably similar result. Inspection of Tables 2.10 and 2.11 shows that the CVN energy determined from the curve fit at the NDT temperature is about the same for the insert (18.6 J) as for PTC1 (19.5 J). As discussed earlier, the drop-weight tests for the vessel insert showed relatively high scatter. In spite of that, however, the CVN and drop-weight NDT results reflect similar differences between the pretest characterization of PTC1 and the posttest characterization of the PTSE-2 vessel insert. These observations are discussed further in Sect. 2.3.8.

Regarding determinations of a reference NDT temperature, RT_{NDT}, according to the *ASME Boiler and Pressure Vessel Code*, Sect. III (Ref. 12), none of the CVN data sets would result in an RT_{NDT} equal to the NDT because all sets have CVN energies, at NDT + 33 K, less than 68 J. From the curve fit, the pretest material at the 1/4t achieves 68 J at about 132°C (T_{68}), which, by defining RT^*_{NDT} as $T_{68} - 33$ K, gives an RT^*_{NDT} of 99°C. The vessel insert did not achieve 68 J even on the upper shelf; therefore an RT_{NDT} cannot be defined.

2.3.6 Fracture-toughness testing

2.3.6.1 Pretest fracture toughness. Pretest fracture-toughness testing was conducted from −75 to 250°C with 25.4-mm-thick compact specimens machined from near the surface of PTC1. Specimens were fatigue precracked and tested with both TS and TL orientations. In the transition region, where cleavage failure was expected, specimens were not side-grooved; at higher temperatures, however, where stable tearing occurs with no cleavage intervention, side-grooves were machined, after precracking, on each side to depths equal to 10% of the specimen thickness. In the transition region, a K_{Jc} value was calculated by determining the modified J-integral[13] at the point of cleavage (J_c) and using the relationship

$$K^2_{Jc} = EJ_c \ , \qquad (2)$$

where E is Young's modulus.

For the few smooth-sided specimens that experienced significant stable ductile tearing without final cleavage failure, J_c was determined at the point of maximum load reached during the test. It must be realized, however, that those values could be less than those for specimens that fail in cleavage after maximum load.

For the side-grooved specimens, J-integral versus crack extension values were determined using both the single-specimen compliance (SSC) and dc-potential drop (dc-PD) techniques. Only data beyond the 0.15-mm offset line were fit to a power law curve, and J_{Ic} was determined by the intersection of the curve with the 0.15-mm offset line. Values of $K_{J_{Ic}}$ were calculated as described previously for Eq. (2).

All tests were performed with a computer-interactive test system using the SSC technique. The dc-PD measurements were made during the

hold period before each unloading. To ensure that valid K_{Ic} values could be obtained according to ASTM E399, unloadings were not performed until the load-displacement curve passed the 95% secant line.

Tables 2.12 and 2.13 show the results of pretest fracture-toughness testing with smooth-sided specimens from PTC1 in the TS and TL orientations, respectively. The transition region data for the TS and TL orientations are shown graphically in Figs. 2.41 and 2.42, respectively. Ten specimens with TS orientation were tested at each of the three temperatures, 25, 50, and 75°C, to examine the variability in K_{Jc}. As can be seen in Fig. 2.41, the scatter is typical of the transition range with the upper value at each temperature being about twice the lowest value. At 75°C one specimen did not cleave, and five specimens failed in cleavage after reaching maximum load. For the 1L orientation at 75°C, all eight specimens cleaved, but four cleaved beyond maximum load. The

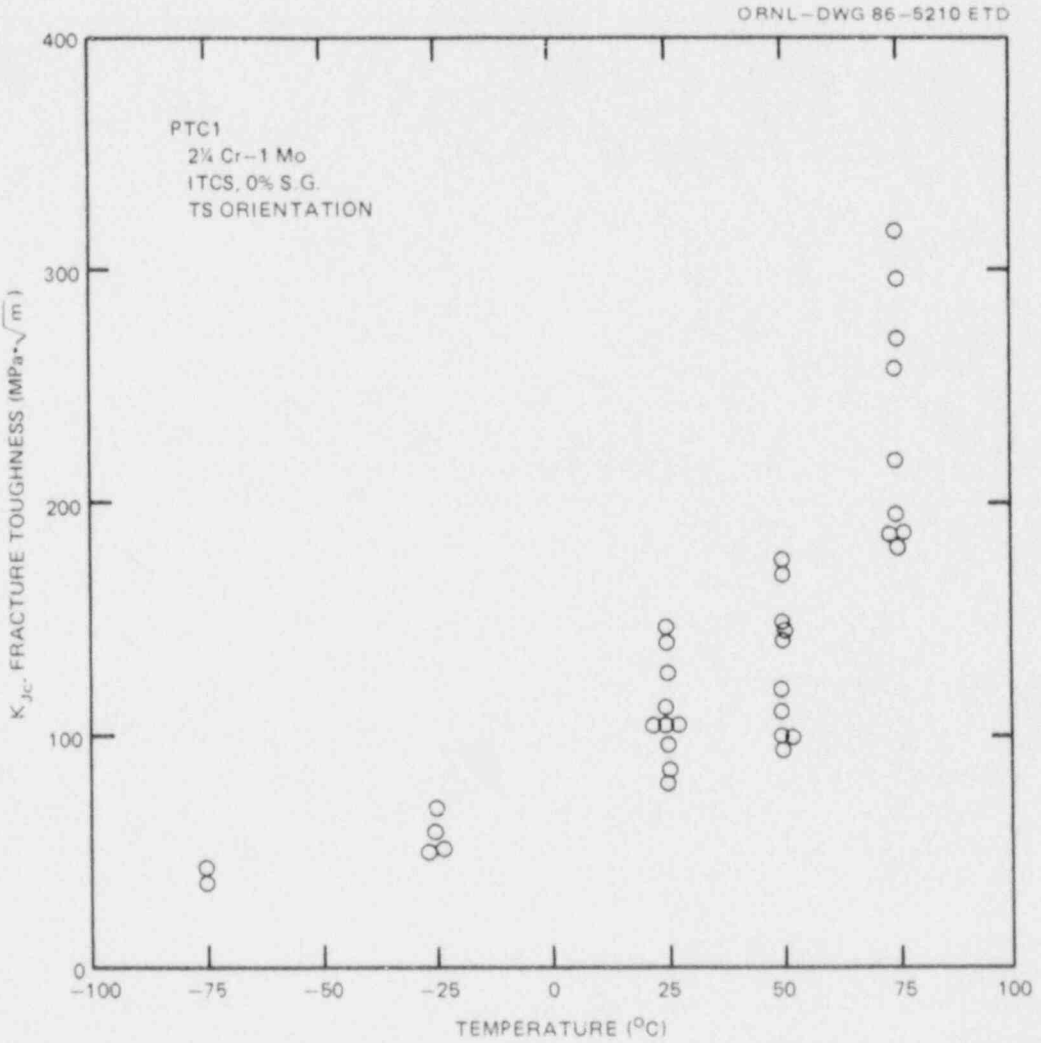

Fig. 2.41. Fracture toughness K_{Jc} vs temperature for characterization block PTC1 for TS orientation near plate surface. At 75°C, one specimen did not cleave, and five specimens cleaved after maximum load.

Table 2.12. Transition region fracture-toughness results for PTC1, 2 1/4 Cr-1 Mo steel, TS orientation, near plate surface

Specimen identification[a]	Test temperature (°C)	K_{Jc} (MPa·√m)	$K_{\beta c}$ (MPa·√m)	Stable crack extension (mm)
PI212	−75	41.2[b]	37.1	0
PI216	−75	36.4[b]	33.8	0
PI220	−25	49.7	39.6	0.061
PI217	−25	68.5	46.9	0.0432
PI204	−25	51.3	40.3	0
PI219	−25	57.7	43.0	0
PI208	25	97.5	51.8	0.127
PI215	25	128.2[c]	57.8	0.368
PI202	25	146.2	60.7	0.340
PI210	25	80.6	47.8	0.218
PI201	25	91.3	50.4	0.079
PI203	25	105.4	53.5	0.104
PI206	25	106.3	53.7	0.097
PI207	25	105.5	53.5	0.135
PI244	25	140.4	59.8	0.381
PI259	25	113.4	51.1	0.152
PI214	50	111.2	53.4	0.137
PI209	50	171.8	63.0	0.795
PI213	50	144.0	59.0	0.411
PI218	50	147.8	59.6	0.472
PI221	50	100.2	51.3	0.178
PI223	50	96.1	50.4	0.132
PI224	50	152.5	60.3	0.536
PI227	50	122.4	55.5	0.272
PI260	50	177.6	63.8	0.998
PI241	50	101.3	51.5	0.122
PI211[d]	75	272.6	73.4	3.335
PI222	75	196.7	65.4	1.222
PI245	75	[e]	[e]	5.202
PI258	75	181.1	63.5	1.148
PI251[d]	75	318.2	77.5	5.908
PI254[d]	75	298.5	75.8	4.412
PI239	75	189.0	64.5	1.267
PI226[d]	75	219.8	68.0	1.91
PI252[d]	75	259.9	72.2	3.401
PI240	75	188.8	64.4	1.140
PI232	100	[e]	[e]	11.285
PI233	100	[e]	[e]	8.311

[a] 25.4-mm-thick compact specimens.

[b] Valid K_{Ic} value.

[c] Pop-in at 69.7 MPa·√m.

[d] Cleavage after maximum load.

[e] Did not cleave.

Table 2.13. Transition region fracture-toughness results for PTC1, 2 1/4 Cr-1 Mo steel, TL orientation

Specimen identification[a]	Test temperature (°C)	K_{Jc} (MPa•$\sqrt{m}$)	$K_{\beta c}$ (MPa•$\sqrt{m}$)	Stable crack extension (mm)
TL orientation, near plate surface				
PI315	25	103.2	54.1	0.061
PI313	25	96.5	52.6	0.056
PI317	25	83.8	49.6	0.056
PI332	25	90.4	51.2	0.056
PI356	25	97.4	52.8	0.091
PI306	50	123.0	55.6	0.37
PI318	50	107.6	52.7	0.24
PI309	50	137.2	58.0	0.63
PI314	50	134.7	57.5	0.55
PI308	50	108.2	52.9	0.18
PI321[b]	75	191.2	64.7	1.94
PI307	75	152.1	59.5	0.87
PI320[b]	75	194.4	65.1	2.01
PI319[b]	75	264.9	72.7	5.00
PI334	100	[c]	[c]	7.358
PI340	100	[c]	[c]	7.224
PI354	100	[c]	[c]	5.895
TL orientation, near midthickness				
PI329	50	134.9	59.3	0.480
PI342	50	147.2	61.2	0.538
PI349	50	141.1	60.3	0.391
PI347	50	159.9	63.2	0.589
PI344	50	105.0	53.7	0.132
PI343[b]	75	225.6	70.5	3.205
PI350	75	210.7	68.8	2.337
PI331[d]	75	120.9	55.1	0.234
		(189.8)	(66.2)	(2.530)
PI346	75	171.0	63.8	1.346

[a] 25.4-mm-thick compact specimens.

[b] Cleavage after maximum load.

[c] Did not cleave.

[d] Pop-in at 120.9 MPa•$\sqrt{m}$, cleaved after reloading at 189.8 MPa•$\sqrt{m}$.

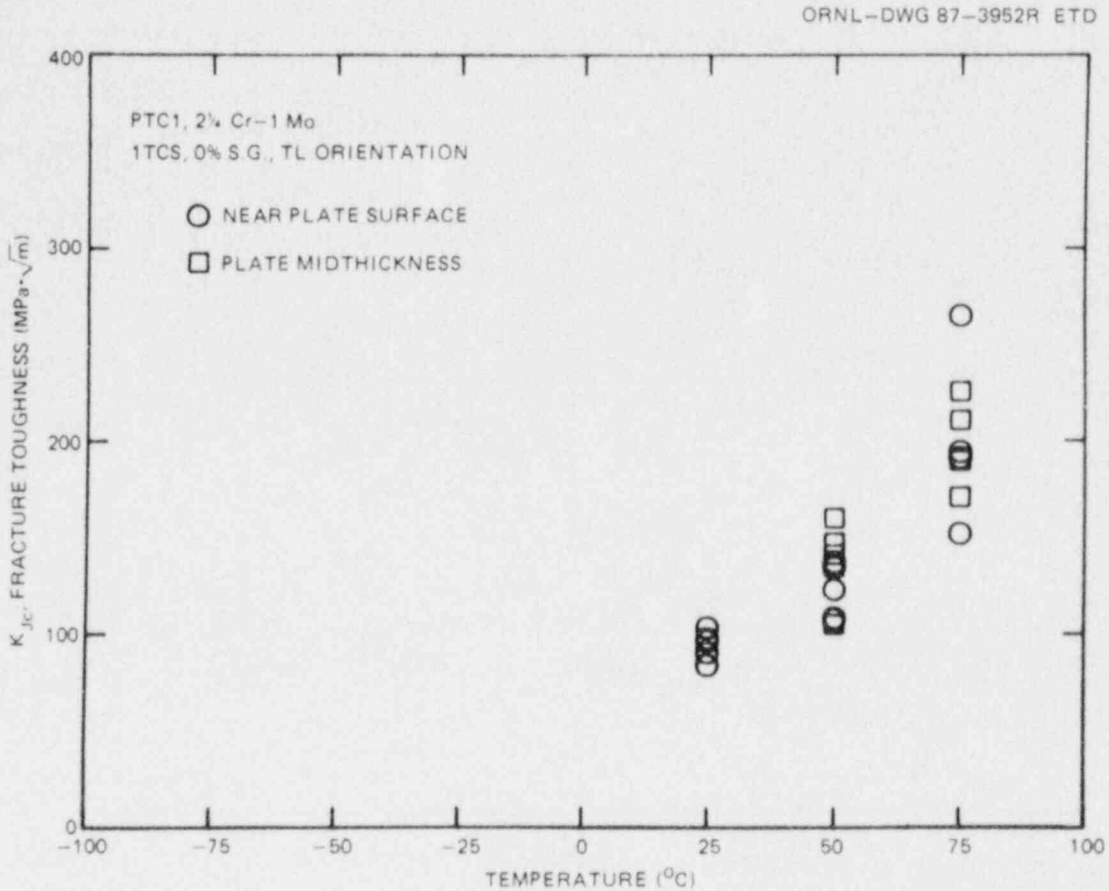

Fig. 2.42. Fracture toughness K_{Jc} vs temperature for characterization block PTC1 for TL orientation near plate surface and at midthickness. At 75°C, all eight specimens cleaved and four cleaved beyond maximum load.

tables also give the measured stable ductile crack extension (including blunting). At values of around 0.15 mm and greater, in-plane growth is taking place, and the tables show that stable in-plane growth begins to occur at about 100 MPa·√m. Because the yield strength of this material is relative y low, valid K_{Ic} values were not obtained except at the lowest test temperature (−75°C). The K_{Jc} results for midthickness and near-surface specimens in the TL orientation do not exhibit significant dependency on depth in the plate. At 100°C, none of the specimens cleaved, and further testing at 100°C and higher was performed with side-grooved specimens. Figure 2.43 provides a comparison of curve fits for K_{Jc} vs temperature for the TS and TL orientations and shows the TL orientation has only slightly lower fracture toughness.

The fracture toughness at the onset of cleavage, relative to prior stable crack growth can be presented in the form of a resistance curve. The values of J-integral at cleavage onset, J_c, for all specimens are shown vs crack extension in Fig. 2.44. The figure includes, of course, specimens tested at 25, 50, and 75°C; thus, the blunting and exclusion lines were constructed using flow strength at 50°C. Because the specimens were smooth-sided, crack front tunneling was prominent in specimens

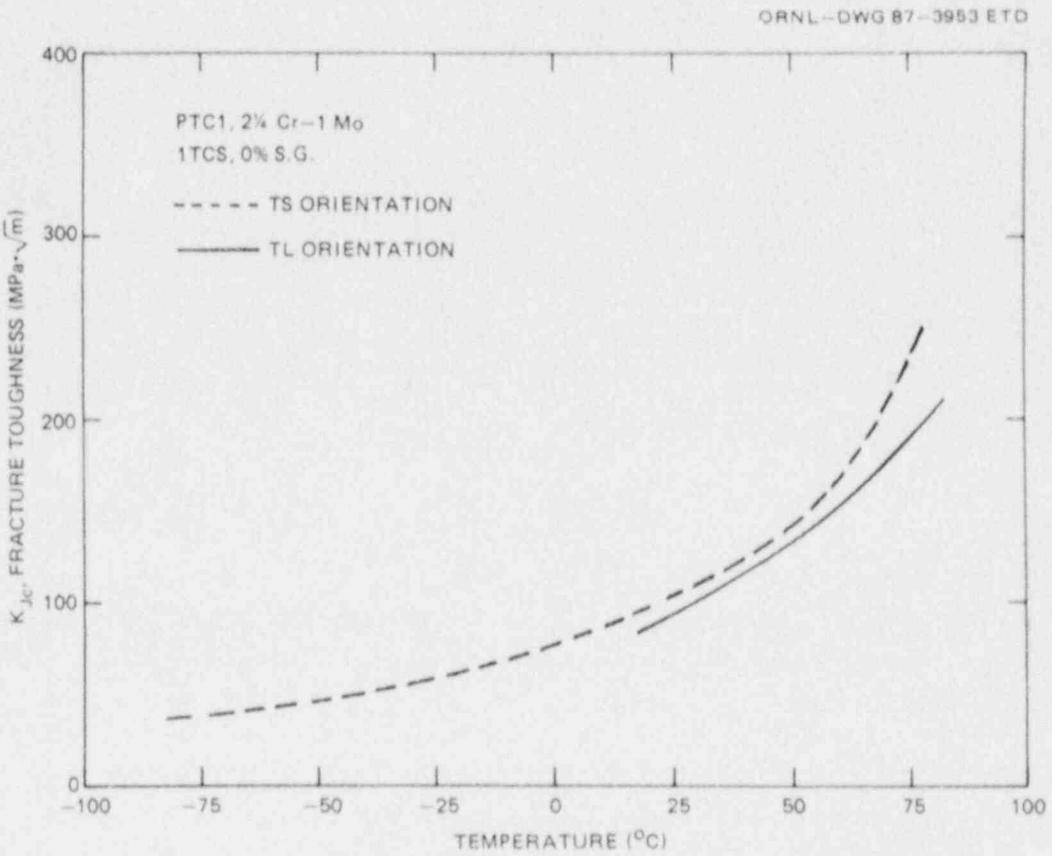

Fig. 2.43. Comparison of best-fit mean curves of K_{Jc} vs temperature for TS and TL orientations of characterization block PTC1.

that exhibited much stable crack extension. Crack extension measurements were determined using the nine-point averaging technique.

Power-law curve fits were determined for all three sets of data and are compared graphically in Fig. 2.45. As shown, the TS orientation has a much steeper resistance curve than that for the TL orientation. Table 2.14 provides the coefficients for the power-law curve fits as well as the values of J_{Qc} based on intersection of the power-law curve with the 0.15-mm offset line, the same method used to determine J_{Ic} for fully ductile specimens. As shown in the table, the TL orientation has lower tearing resistance than that for the TS orientation, but the J_{Qc} results show a mixed comparison.

Also shown in Tables 2.12 and 2.13 are $K_{\beta c}$ values calculated using the method described by Merkle.[14] The corrections are relatively large due to the low yield strength of the material.

Table 2.15 shows the results of testing side-grooved specimens from PTC1 at three different temperatures. The table shows J-integral results determined by two methods: (1) deformation theory J (J_D) as recommended in ASTM E813, and (2) the modified J (J_M) as formulated by Ernst.[13] The tearing modulus values were determined by linear regression fits to the

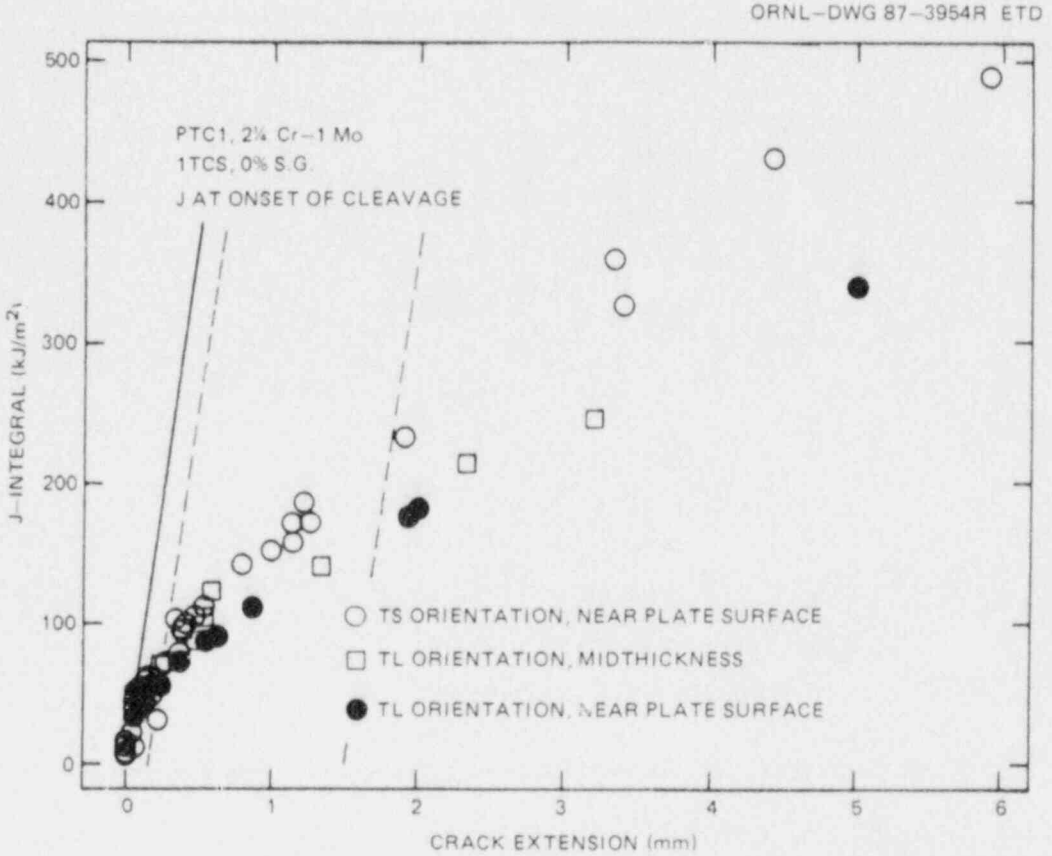

Fig. 2.44. J-integral (J_M) vs stable crack extension prior to cleavage for TL and TS orientations of characterization block PTC1.

Table 2.14. Power-law curve fit results for transition region fracture toughness, PTC1, 2 1/4 Cr-1 Mo steel

Orientation	Location in plate	C[a]	n[a]	J_{Qc}[b] (kJ/m²)	Tearing modulus[c]
TL	Near surface	131.1	0.559	57	102
TL	Midthickness	141.2	0.465	72	94
TS	Near surface	161.5	0.626	65	136

[a] $J = C\Delta a^n$, where Δa is crack extension, mm; J is value of modified J-integral at onset of cleavage.

[b] Intersection of power-law curve with the 0.15-mm offset line; not valid J_{Ic} values because the specimens cleaved.

[c] Average value of the tearing modulus between the 0.15- and 1.5-mm offset lines.

Table 2.15. Ductile-shelf fracture-toughness results for PTC1, 2 1/4 Cr-1 Mo steel, TS orientation

Specimen[a]	Test temperature (°C)	J_{Ic}[b] (kJ/m²)		$K_{J_{Ic}}$ (MPa·√m)		Final crack extension (mm)	Tearing modulus[c]	Power-law curve fit parameters[d]			
		J_D	J_M	J_D	J_M			A	B	C	D
PI230	100	64.0	41.5	113.6	91.5	11.58	120	109	0.338	0.565	−16.0
PI250	100	55.6	58.6	105.9	108.7	7.95	145	113	0.226	0.527	−18.4
PI228	175	58.3	51.5	107.2	100.7	8.17	106	214	0.167	0.240	−113
PI256	175	68.4	40.2	116.2	89.0	9.62	105	203	0.330	0.263	−108
PI238	250	52.8	41.5	100.1	89.5	9.47	67	245	0.259	0.158	−166
PI235	250	52.2	51.4	100.3	99.6	9.89	61	1482	0.398	0.029	−1410

[a] 25.4-mm-thick compact specimens.

[b] J_{Ic} determined by power-law curve intersection with 0.15-mm offset line; J_D is deformation theory J per ASTM E813; J_M is modified J after Ernst.

[c] Calculated using linear fit to data between offset lines.

[d] $J = A(\Delta a + B)^C + D$, where Δa = crack extension in millimeters.

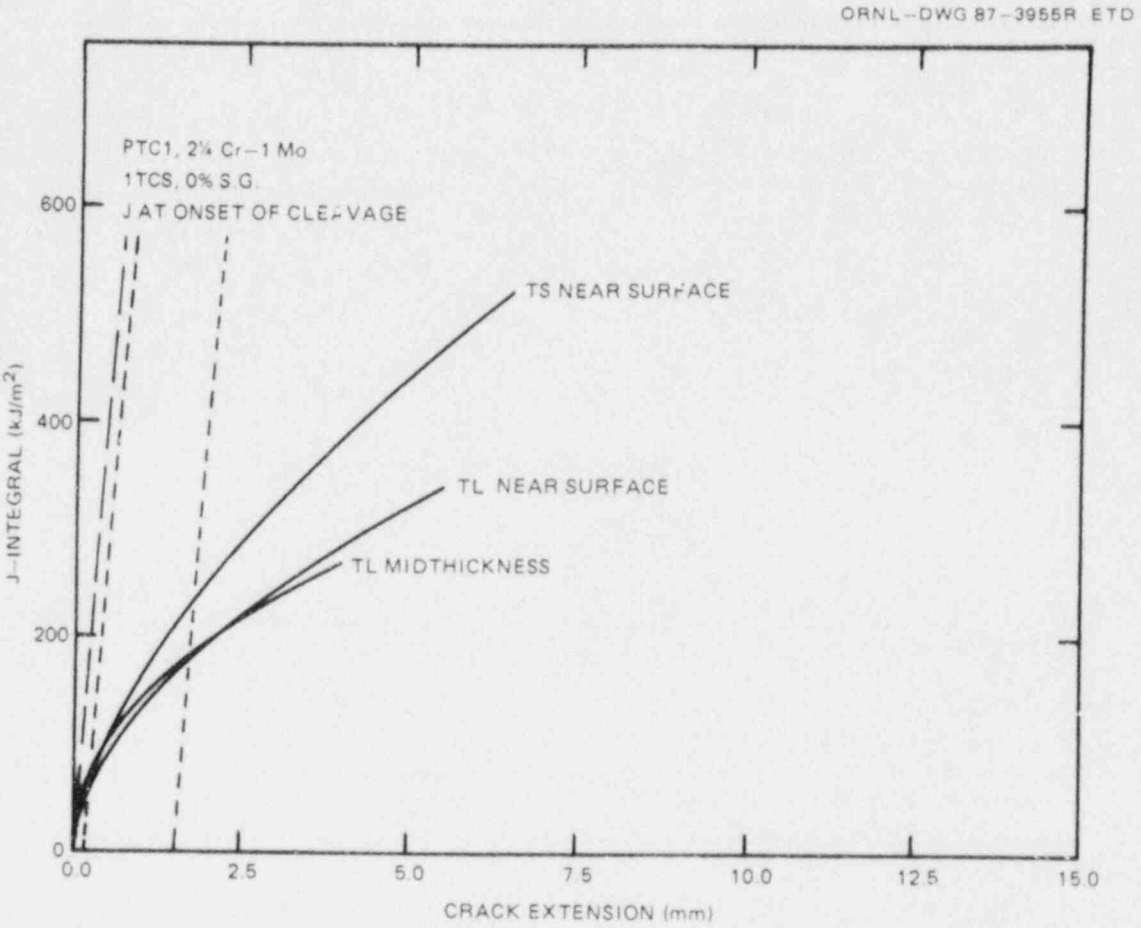

Fig. 2.45. Comparison of power-law curve fits of data shown in Fig. 2.44.

data between the exclusion lines using the J_M data. Up to the second exclusion line, values of J_D and J_M are very similar. This is discussed later in greater detail. Figures 2.46 to 2.48 show representative J_M vs crack extension results for each test temperature. The values of J_{Ic} determined by J_D and J_M are, in three cases, quite different, but that is considered to be strongly affected by the curve fitting operation, which includes data beyond the second exclusion line. The values of $K_{J_{Ic}}$ are very low compared with the K_{Jc} values determined at 75°C. The K_{Jc} values at 75°C were determined at the point of cleavage, which, for all specimens at 75°C, occurred after substantial amounts of stable tearing; the $K_{J_{Ic}}$ values, however, are calculated essentially at the onset of stable tearing. As shown in Table 2.15 and demonstrated graphically in Fig. 2.49, the tearing modulus decreased with increasing test temperature.

Similar tests were conducted with 25.4-mm-thick compact specimens from PTC1 in the TL orientation. For those tests, crack extension was

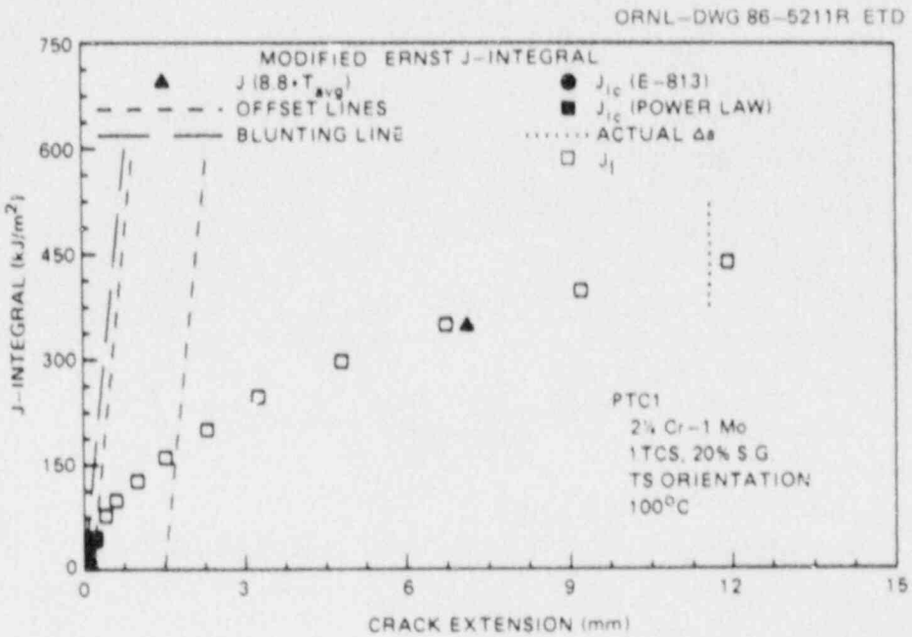

Fig. 2.46. J-integral (J_M) vs crack extension results at 100°C for TS orientation near plate surface of characterization block PTC1.

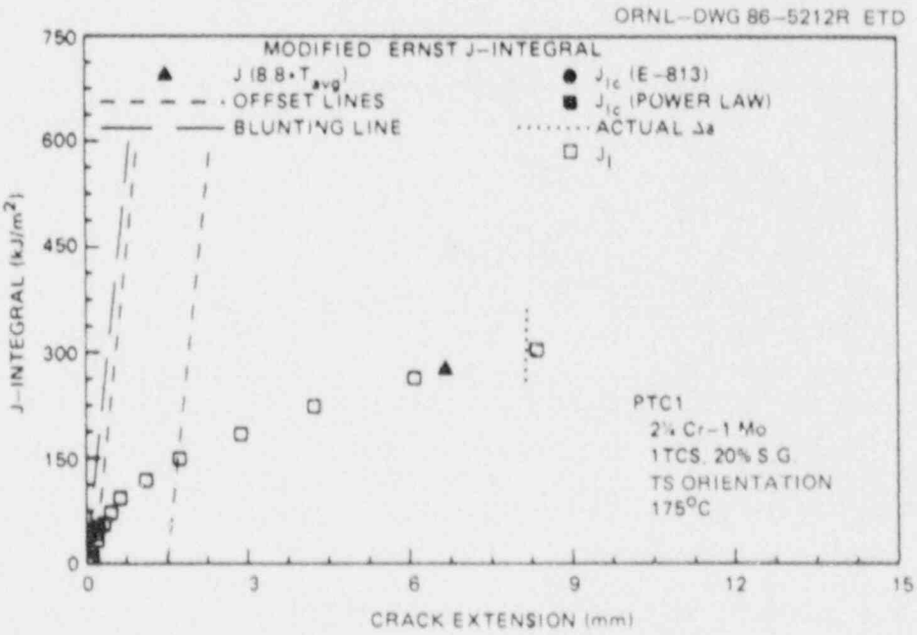

Fig. 2.47. J-integral (J_M) vs crack extension results at 175°C for TS orientation near plate surface of characterization block PTC1.

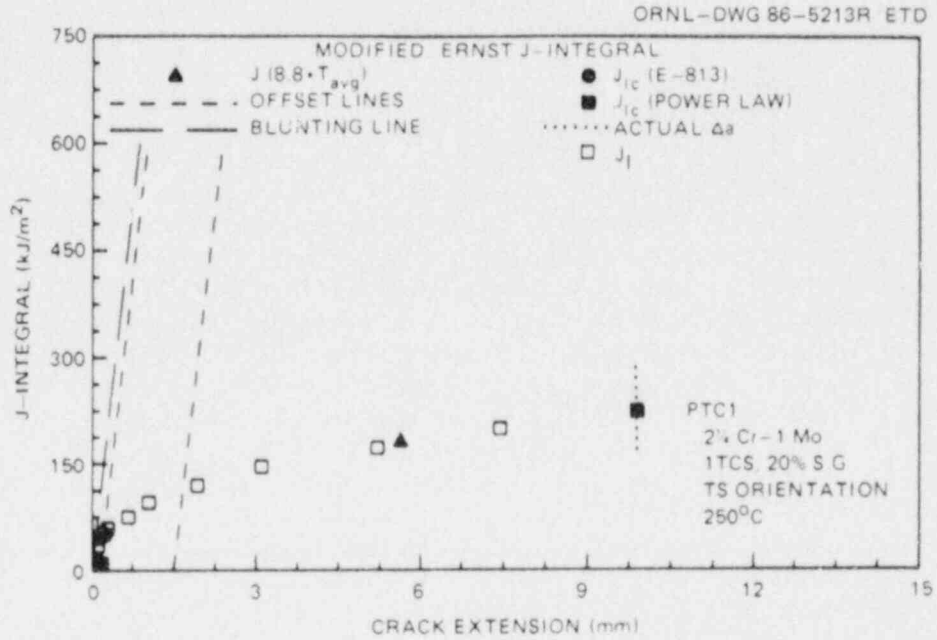

Fig. 2.48. J-integral (J_M) vs crack extension results at 250°C for TS orientation near plate surface of characterization block PTC1.

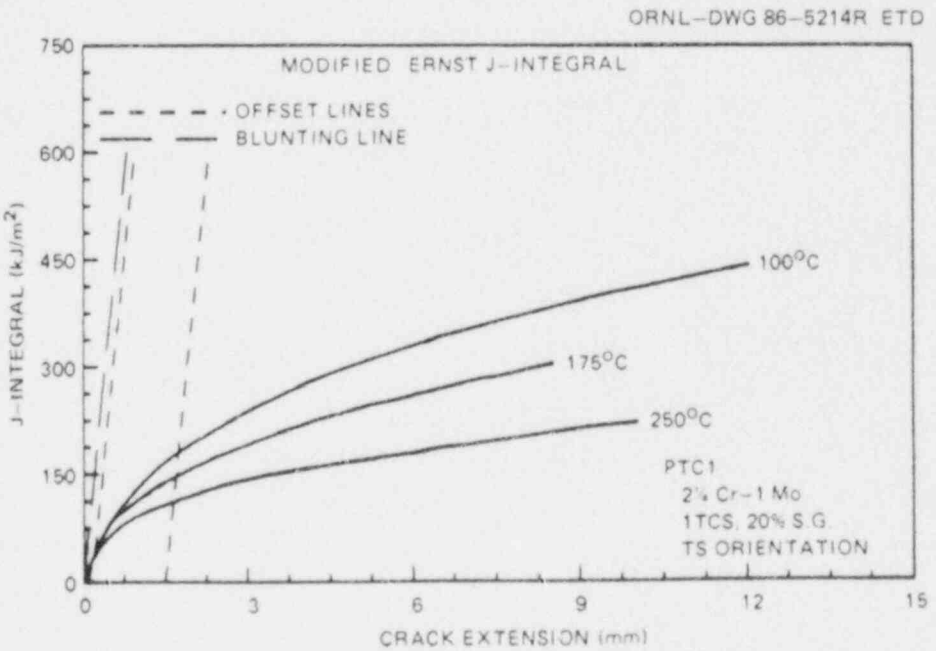

Fig. 2.49. Comparison of J-integral (J_M) resistance curves at three test temperatures for TS orientation near plate surface of characterization block PTC1.

monitored both with the compliance and dc-potential drop (dc-PD) techniques. Table 2.16 gives the results for both techniques using J_M and shows that the J_{Ic} values determined by dc-PD are consistently lower than those from the compliance technique. The dc-PD tends to give larger crack extension values in the early part of the test that will tend to result in lower J_{Ic} values. A typical J_M vs crack extension curve is shown in Fig. 2.50.

The predicted final crack extensions for the dc-PD curve do, however, compare much more favorably with the measured values than those predicted by the compliance technique. The tearing modulus values are in very good agreement between the two techniques. The TL-oriented specimens exhibited significant nonuniform crack growth through the thickness during both the fatigue precracking and the J-R test. Asymmetric and nonuniform crack extension can affect the measurement of crack extension, especially in the beginning of the test when accuracy of measurements is crucial. As shown in Table 2.16, the tearing modulus decreased with increasing test temperature. This result is demonstrated graphically by the comparison of the dc-PD power-law curve fits shown in Fig. 2.51 and is similar to that observed for the TS orientation. Comparison of tearing modulus values between the two orientations show the TL orientation

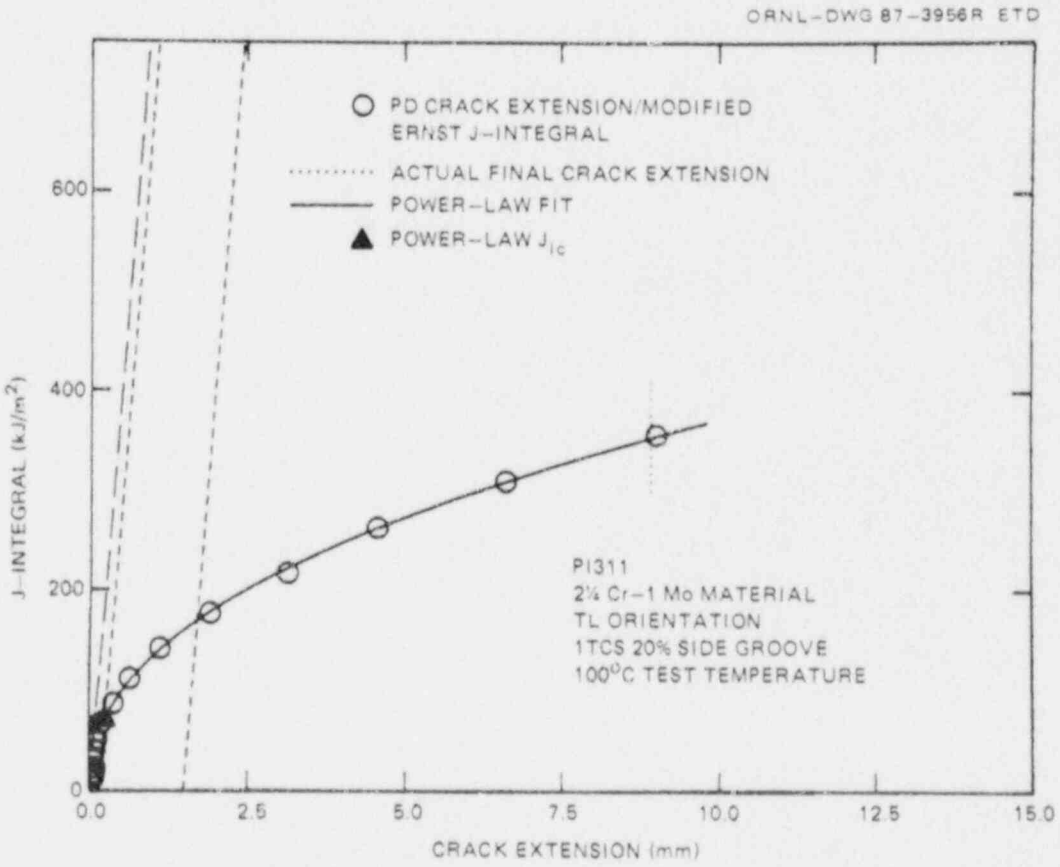

Fig. 2.50. J-integral (J_M) vs crack extension results at 100°C for TL orientation near plate surface of characterization block PTC1.

Table 2.16. Ductile-shelf fracture-toughness results for PTC1, 2 1/4 Cr-1 Mo steel, TL orientation, near plate surface

Specimen identification[a]	Test temperature (°C)	J_{Ic} (kJ/m^2)	$K_{J_{Ic}}$ (MPa·$\sqrt{m}$)	Tearing modulus	Crack extension (mm)		A[b]	B[b]
					Predicted	Measured		
PI357-PD	100	78.0	125.4	100	8.552	8.608	148.0	0.460
-UC	100	92.1	136.2	98	8.090	8.608	160.4	0.419
PI311-PD	100	69.7	118.5	95	9.009	8.920	132.5	0.447
-UC	100	84.5	130.5	87	8.705	8.920	145.8	0.401
PI325-PD	175	29.8	76.7	72	7.206	7.275	78.0	0.577
-UC	175	55.9	105.0	70	6.971	7.275	103.5	0.410
PI337-PD	175	50.0	99.3	80	9.678	9.604	103.6	0.474
-UC	175	63.6	112.0	79	9.244	9.604	116.6	0.416
PI335-PD	250	34.0	81.0	48	9.242	9.431	67.2	0.417
-UC	250	35.2	82.4	48	9.032	9.431	68.1	0.405
PI324-PD	250	28.2	73.7	54	9.832	9.853	65.0	0.499
-UC	250	44.2	92.4	54	9.272	9.853	80.9	0.385

[a] PD = dc-potential drop method; UC = unloading compliance method.

[b] $J = A\Delta a^B$, where Δa is crack extension, mm; $J = J_M$.

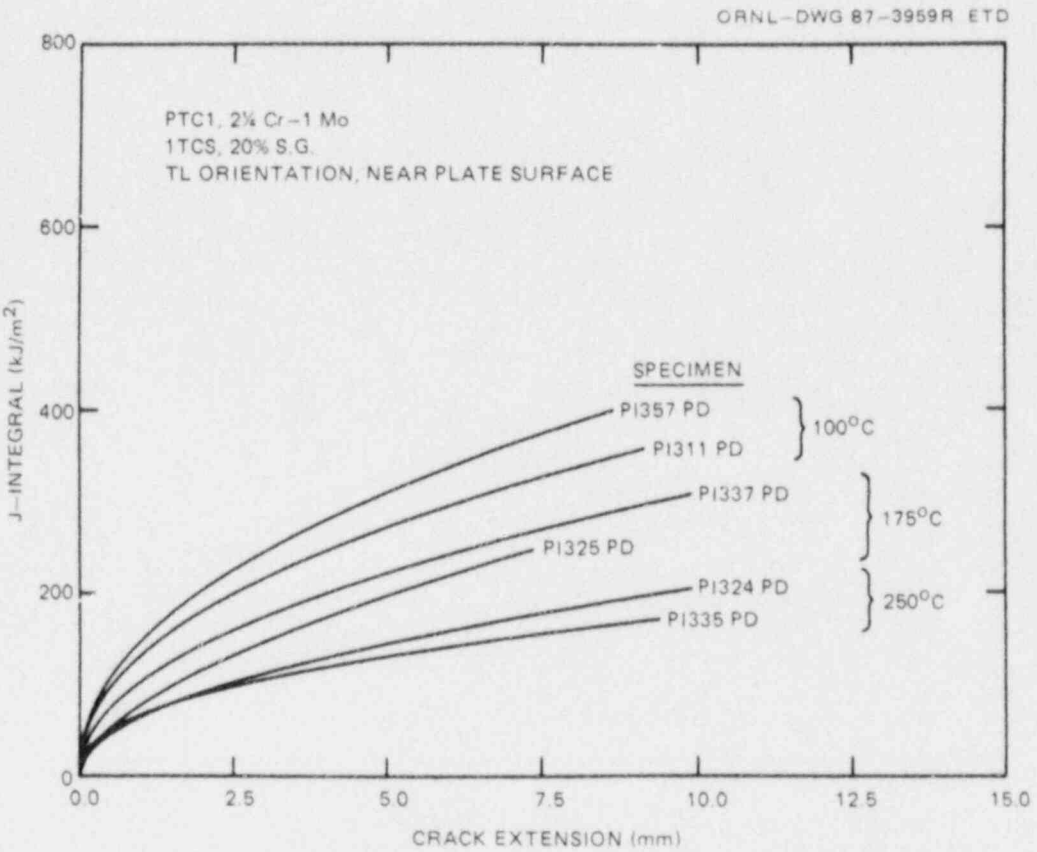

Fig. 2.51. Comparison of J-integral (J_M) resistance curves at three test temperatures for TL orientation near plate surface of characterization block PTC1.

has lower tearing resistance than that for the TS orientation. That observation is consistent with that shown by the results of stable tearing prior to cleavage shown in Fig. 2.45.

2.3.6.2 Posttest fracture toughness. Posttest fracture-toughness testing was performed from 50 to 250°C with fatigue precracked 25.4-mm-thick compact specimens machined from near the 1/4t depth in the PTSE-2 vessel insert. All specimens were tested in the TS orientation. All specimens except those tested at 50°C were side-grooved to 10% of the specimen thickness on each side. Values of K_{Jc}, $K_{\beta c}$, J_{Ic}, and T were determined as described earlier for the pretest characterization tests.

Table 2.17 shows the results of a posttest fracture-toughness test with specimens that experienced cleavage. Only the specimens tested at 50°C were smooth sided. Five specimens with TS orientation were tested at each of three temperatures, 50, 75, and 100°C. Figure 2.52 shows the data graphically in comparison with the pretest data shown in Fig. 2.41. The results indicated an upward temperature shift in fracture toughness for the posttest material compared to pretest material from characterization block PTC1. This observation is substantiated by the fact that no pretest specimens tested at 100°C experienced cleavage, while all five

Table 2.17. Transition region fracture-toughness results for PTSE-2 vessel insert, 2 1/4 Cr-1 Mo steel, TS orientation

Specimen	Test temperature (°C)	Side-groove (%)	K_{Jc} (MPa·$\sqrt{m}$)	$K_{\beta c}$ (MPa·$\sqrt{m}$)	Stable crack extension (mm)
PE64	50	0	122.3	75.4	0.226
PE66	50	0	124.2	75.9	0.249
PE68	50	0	122.6	75.5	0.274
PE70	50	0	125.3	76.2	0.371
PE72	50	0	100.4	68.8	0.071
PE74	75	20	139.0	74.0	0.947
PE76	75	20	104.4	65.5	0.300
PE78	75	20	105.7	65.8	0.297
PE80	75	20	128.7	71.7	0.752
PE82	75	20	124.4	70.7	0.627
PE85	100	20	139.2	73.0	1.209
PE67	100	20	179.9	80.9	3.726
PE69	100	20	220.2	87.3	7.000
PE71	100	20	187.0	82.1	4.050
PE73	100	20	185.6	81.8	3.655

posttest specimens cleaved at 100°C. Additionally, a comparison of Tables 2.12 and 2.17 reveals that the stable crack extensions at a given K_{Jc} level are less for the posttest material than for the pretest material. That is an indication of an increase in yield strength, which is reflected in the discussion in Sect. 2.3.4 on tensile testing. At an arbitrarily chosen K_{Jc} of 150 MPa·$\sqrt{m}$ the posttest material achieves that level of toughness at a temperature 30 K higher than the pretest material. As discussed in Sect. 2.3.8 that upward shift is slightly greater than that shown by the Charpy impact results and the drop-weight NDT results.

Table 2.18 shows the results of testing side-grooved specimens from the vessel insert at 175 and 250°C to obtain full J-R curves without cleavage intervention. Comparison with Table 2.15 shows that the posttest material exhibited slightly lower J_{Ic} values but significantly lower tearing modulus values than did the pretest material. Typical J_M vs crack extension data and curves are shown in Fig. 2.53. Comparison with those from the pretest material shown in Figs. 2.46 through 2.49 shows the effect graphically. The effect of plastic deformation during the vessel experiment increased the flow strength significantly and, because the flow strength occurs in the denominator of the equation for tearing modulus, will cause a 40 to 50% decrease in the tearing modulus even if the J-R curves are the same. In this case, however, the J-R curve slopes

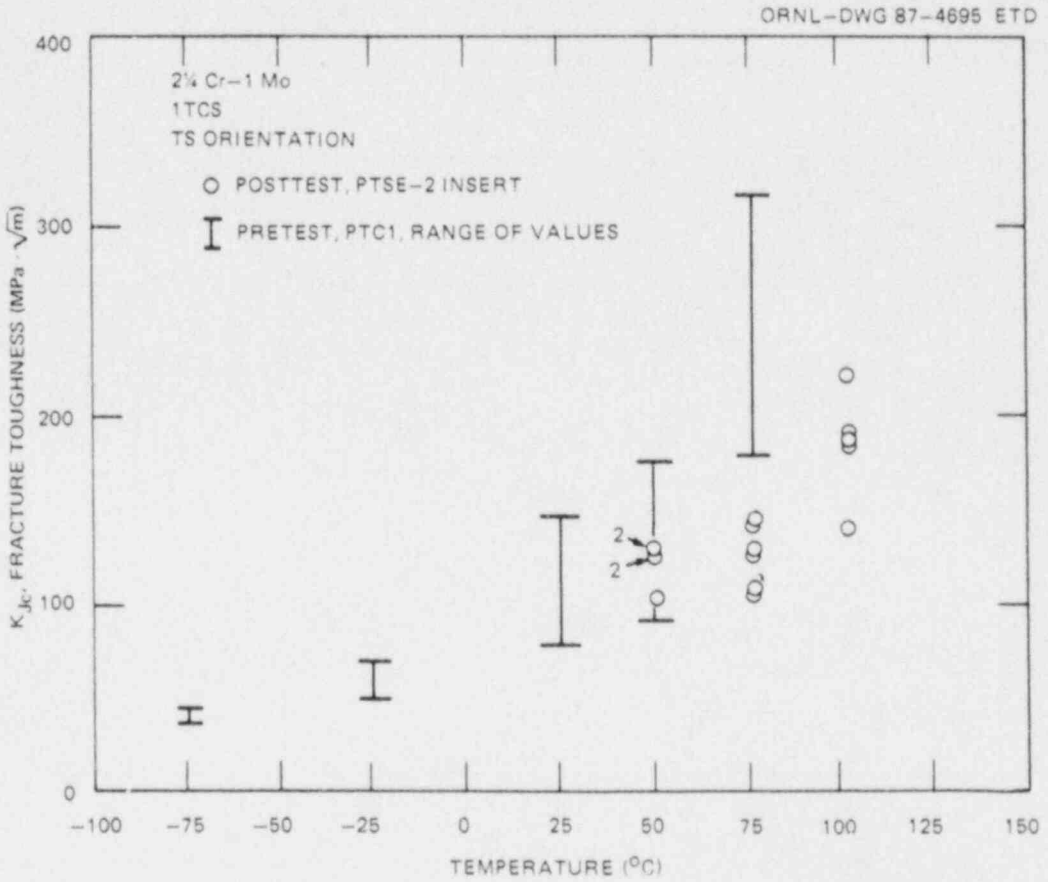

Fig. 2.52. Posttest fracture toughness K_{Jc} vs temperature for PTSE-2 vessel insert for TS orientation compared with similar specimens from pretest characterization block PTC1. All posttest specimens cleaved.

for the posttest material are much less than those for the pretest material. Thus, both the flow strength increase and a real degradation in the material tearing resistance has resulted in the lower tearing modulus results for the posttest material.

It is not clear whether the lower slopes of the J-R curves are a consequence of the experiment or a reflection of inherent differences in the vessel insert and PTC1.

2.3.7 Crack-arrest toughness testing

Crack-arrest toughness data obtained from the PTC1 characterization block for TS and TL specimens are listed in Tables 2.19 and 2.20 and are plotted in Fig. 2.54. The TS orientation is relevant to the PTSE-2 crack propagating radially in the cylinder, whereas the TL specimens are relevant to the crack propagating axially. The testing and evaluation were performed in accordance with Draft 86-04 of the ASTM Standard Test Method for Determining the Plane Strain Crack-Arrest Toughness of Ferritic

Table 2.18. Ductile-shelf fracture-toughness results for PTSE-2 vessel insert, 2 1/4 Cr-1 Mo steel, TS orientation

Specimen[a]	Test temperature (°C)	J_{Ic}[b] (kJ/m^2)	$K_{J_{Ic}}$ ($MPa\cdot\sqrt{m}$)	Final crack extension (mm)	Tearing modulus[c]	Power-law curve fit parameters[d]			
						A	B	C	D
PE75	175	46.3	95.5	8.49	28	70.7	0.075	0.373	2.76
PE77	175	52.7	102	8.87	28	67.9	0.195	0.379	4.75
PE79	175	45.3	94.6	9.09	31	71.3	0.110	0.407	1.26
PE81	250	49.8	98.0	9.42	19	43.9	0.195	0.371	18.58
PE83	250	35.9	83.3	8.70	20	56.1	0	0.296	1.70

[a] 25.4-mm-thick compact specimens.

[b] J_{Ic} determined by power-law curve intersection with 0.15-mm offset line; J is deformation theory J per ASTM E813.

[c] Calculated using linear fit to data between offset lines.

[d] $J = A(\Delta a + B)^C + D$, where Δa = crack extension in millimeters.

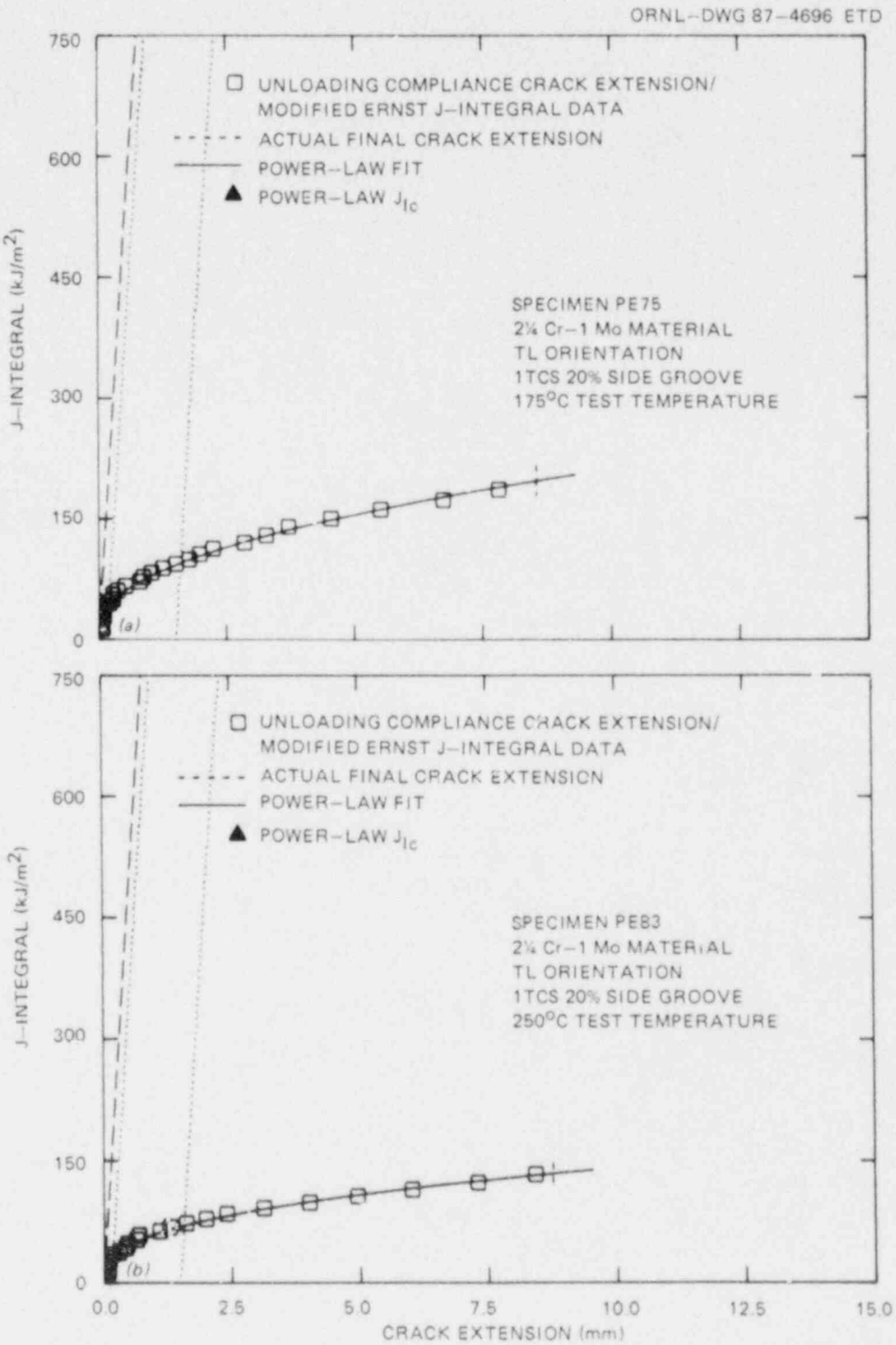

Fig. 2.53. Posttest J-integral (J_M) resistance curves at (*a*) 175°C and (*b*) 250°C for TS orientation of PTSE-2 vessel insert.

Table 2.19. Crack-arrest K_a data for PTCl material, TS orientation

Specimen	Test temperature (°C)	K_a (MPa·$\sqrt{m}$)
Weld-embrittled, 33 × 152 × 152 mm		
PI278	−75	28
PI279	0	60
PI280	0	56
PI277	22	58
PI275	49	96
PI281	49	92
PI276	69	87
PI282	69	99
Duplex, 33 × 152 × 152 mm		
PI359	80	130
PI364	90	148
PI362	90	101
PI360	90	168
PI365	100	174
PI361	100	218
PI363	100	163
PI367	110	194
PI368	110	178
PI366	110	183
Duplex, 51 × 203 × 203 mm		
PI300	110	180
PI301	110	158
PI302	110	144
Weld-embrittled, 34.9 mm thick[a]		
P2-3	53	76
P2-4	65	103
Duplex, 50.8 mm thick[a]		
P2-8	82	127
P2-9	100	109

[a]Data provided by Battelle Columbus Division.

Table 2.20. Crack-arrest K_a data for PTC1 material, TL orientation

Specimen	Test temperature (°C)	K_a (MPa·√m)
Weld-embrittled, 33 × 152 × 152 mm		
PI320	0	44
PI321	0	37
PI313	49	73
PI318	49	129
PI314	68	81
PI316	69	97
PI317	79	106
PI319	79	97
PI315	89	149
PI322	89	141
Duplex, 33 × 152 × 152 mm		
PI308	90	144
PI310	100	145
PI311	110	140
PI312	120	191
Precracked, 33 × 152 × 152 mm		
PTC1A	−75	38
PTC1C	−75	38
PTC1B	0	64

Steels, December 1986. Full details of these results, in particular, whether they meet the validity criteria of the Draft Standard, have been published previously.[15] Results of four tests performed by Battelle Columbus Division[16] have also been included in Table 2.19 and Fig. 2.54.

As Fig. 2.54 shows, no significant differences were observed in the data for the two orientations. The ASME Section XI K_{Ia} curve is included and has been adjusted with respect to the drop-weight NDT (49°C) rather than RT_{NDT}, since the latter is ill defined for this material (see Sect. 2.3.5).

Material from the vessel insert was used to fabricate TS-orientation "nugget" type specimens.[17] The test results are given in Table 2.21 and plotted in Fig. 2.55 together with the TS data for PTC1 material. The crack-arrest toughness of the vessel insert is less than that of the PTC1 material. At a toughness level of 150 MPa·√m for comparison, the arrest toughness of the flaw insert is shifted about 15 K toward a higher temperature than that of PTC1 material. This shift to a higher temperature

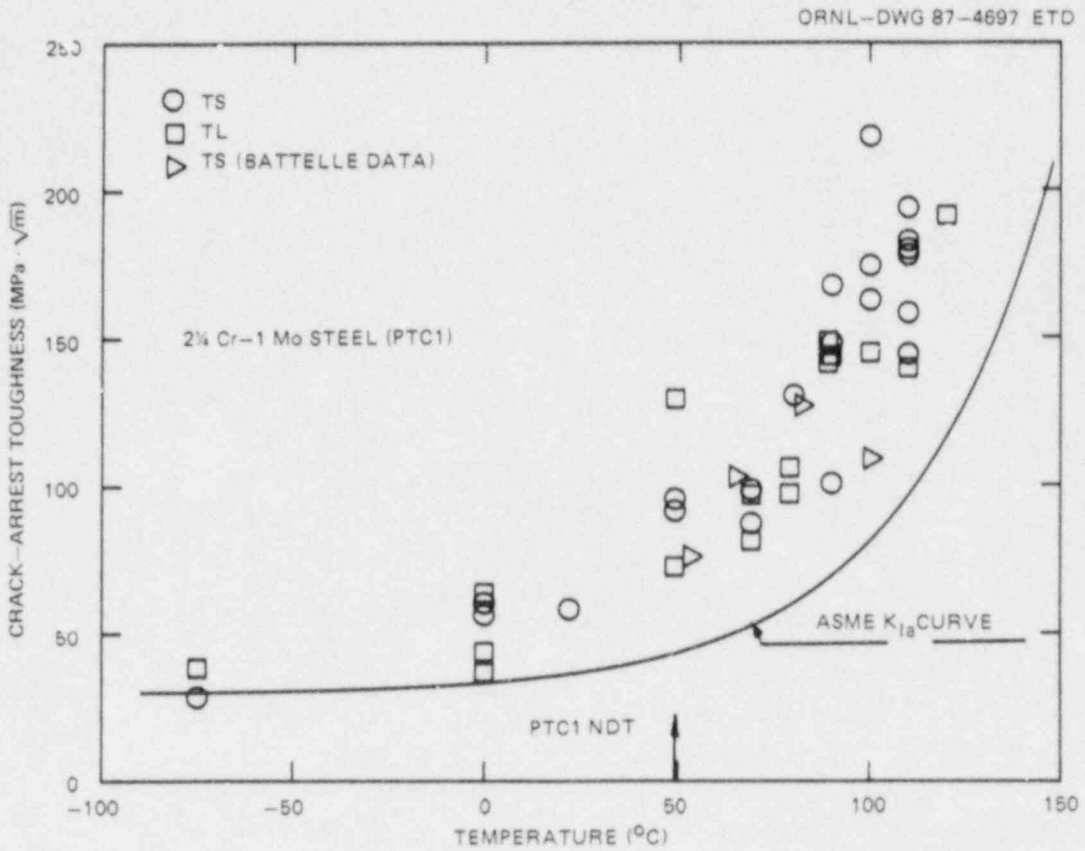

Fig. 2.54. Crack-arrest test results for TS and TL orientations of characterization block PTC1.

Table 2.21. Crack-arrest K_a data for flaw insert material, TS orientation

Specimen	Test temperature (°C)	K_a (MPa·√m)
Weld-embrittled, 32 × 152 × 152 mm		
PE86	50	58
PE87	50	58
PE88	50	62
PE84	80	64
PE85	80	76
Duplex, 33 × 152 × 152 mm		
PE89	110	139
PE90	110	179
PE91	110	119
PE92	110	136
PE93	110	148

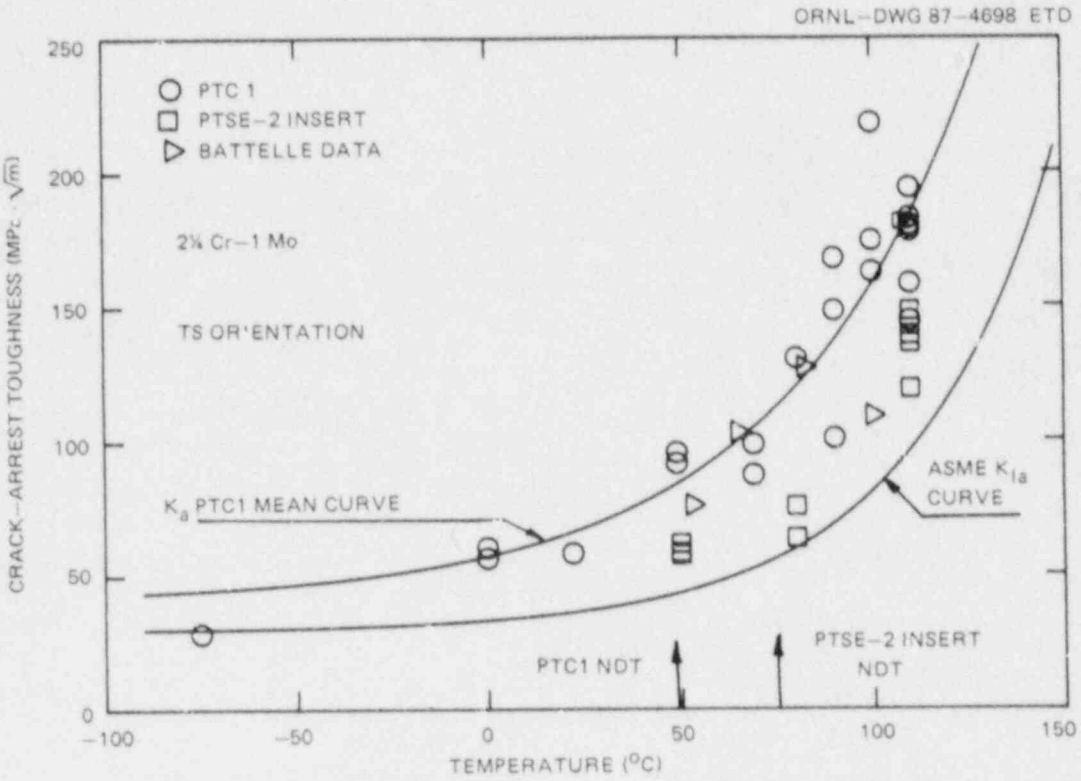

Fig. 2.55. Crack-arrest test results for TS orientation of vessel insert material compared to the characterization block PTC1.

is consistent with shifts noticed for other toughness measures, as discussed in Sect. 2.3.8.

2.3.8 Summary of comparisons of PTC1 and vessel insert

In Sect. 2.3.1, it was pointed out that preexperiment hardness testing performed on the vessel insert outer surface and PTC1 characterization material indicated, by correlation with hardness, a substantially higher strength for the vessel insert. It was expected that strains that developed in the vessel wall during the experiment would be large enough to cause significant strain hardening, with a consequential increase in yield strength and, possibly, increases in toughness transition temperatures. As discussed in Sect. 2.3.4, the posttest yield strength of the vessel insert is about 70% higher than that of PTC1, while the ultimate strength is about 8% higher. Of particular importance to the analysis and interpretation of the PTSE-2 experiment is the elevation of stresses at various strains for the insert relative to PTC1 (Figs. 2.24 and 2.25). This elevation decreases from 51% at 0.2% strain to 12% at 5% strain and significantly affects the fracture analysis of the experiment, as discussed in Chap. 10.

All the posttest vessel insert material tests showed higher transition temperatures than did those for PTC1. The increases were 26 K for

the drop-weight NDT temperature, 20 K for the CVN 41-J temperature, 30 K for the K_{Jc} 150-MPa$\cdot\sqrt{m}$ temperature, and 15 K for the K_a 150-MPa$\cdot\sqrt{m}$ temperature. Thus, the various measures of toughness transition temperature are from 15 to 30 K higher for the posttest vessel insert.

The cyclic tests described in Sect. 2.3.4.2 demonstrated that the differences in tensile properties are likely due largely to strain hardening that occurred during vessel experiments, and, therefore, it is likely that the effects of strain hardening were also manifested by the increases in toughness transition temperatures. A definitive experiment would be desirable but is outside the scope of this report.

It is believed that the material properties of the vessel insert prior to the PTSE-2 experiments is reasonably well represented by the PTC1 pretest characterization block, because the vessel insert and PTC were heat treated simultaneously, the tensile results are reasonably consistent with strain-hardening predictions of yield strength increases, and the four different measures of toughness transition temperatures show consistent differences.

References

1. R. H. Bryan et al., *Test of 6-in.-Thick Pressure Vessels. Series 3: Intermediate Test Vessel V-8*, NUREG/CR-0675 (ORNL/NUREG-58), Union Carbide Corp. Nuclear Div., Oak Ridge Natl. Lab., December 1979.

2. R. H. Bryan et al., *Test of 6-in.-Thick Pressure Vessels. Series 3: Intermediate Test Vessel V-8A — Tearing Behavior of Low Upper-Shelf Material*, NUREG/CR-4760 (ORNL-6187), Martin Marietta Energy Systems, Inc., Oak Ridge Natl. Lab., May 1987.

3. R. H. Bryan et al., *Pressurized-Thermal-Shock Test of 6-in.-Thick Pressure Vessels. PTSE-1: Investigation of Warm Prestressing and Upper-Shelf Arrest*, NUREG/CR-4106 (ORNL-6135), Martin Marietta Energy Systems, Inc., Oak Ridge Natl. Lab., April 1985.

4. C. E. Childress, *Fabrication and Mechanical Test Data for the Four 6-inch-Thick Intermediate Test Vessels Made from Steel Plate for the Heavy-Section Steel Technology Program*, Documentary Report 5, ORNL/TM-5074, Union Carbide Corp. Nuclear Div., Oak Ridge Natl. Lab., January 1976.

5. "Rules for In-Service Inspection of Nuclear Power Plant Components," *ASME Boiler and Pressure Vessel Code, Section XI, Subsubarticle IWB-4420*, 1974 Edition with Summer and Winter 1975 Addenda, American Society of Mechanical Engineers, New York.

6. H. A. Domian, *Vessel V-8 Repair and Preparation of Low Upper Shelf Weldment*, NUREG/CR-2676 (ORNL/Sub/81-85813/1), Babcock & Wilcox Company, Alliance, Ohio, June 1982.

7. H. A. Domian, *Vessel V-7 and V-8 Repair and Characterization of Insert Material*, NUREG/CR-3771 (ORNL/Sub/82-52845/1), Babcock & Wilcox Company, Alliance, Ohio, May 1984.

8. H. A. Domian, *Low Upper-Shelf Toughness, High Transition Temperature Test Insert in HSST PTSE-2 Vessel and Wide Plate Test Specimens*, ORNL/Sub/85-34128/1, Babcock & Wilcox Co., Alliance, Ohio, February 1987.

9. R. L. Graves, F. J. Weaver, and D. L. McElroy, internal memorandum to J. P. Strizak, Oak Ridge National Laboratory, September 15, 1986.

10. T. G. Kollie et al., "A Computer Operated Fused Quartz Differential Dilatometer," pp. 12–146 in *Thermal Expansion — 1973 AIP Conference Proceedings No. 17*, American Institute of Physics, New York, 1974.

11. Private communication from A. R. Rosenfield, Battelle Columbus Division, to R. H. Bryan, Oak Ridge National Laboratory, October 14, 1986.

12. *ASME Boiler and Pressure Vessel Code. An American National Standard*, ANSI/ASME BPV-III-1-NB, American Society of Mechanical Engineers, New York, 1986.

13. H. A. Ernst, "Material Resistance and Instability Beyond J-Controlled Crack Growth," *Second Symposium, Volume I — Inelastic Crack Analysis*, ASTM STP 803, American Society for Testing and Materials, Philadelphia, 1983, pp. I-191–213.

14. J. G. Merkle, *An Examination of the Size Effects and Data Scatter Observed in Small Specimen Cleavage Fracture Toughness Testing*, NUREG/CR-3672 (ORNL/TM-9088), Martin Marietta Energy Systems, Inc., Oak Ridge Natl. Lab., April 1984.

15. R. K. Nanstad et al., "Crack-Arrest Toughness Testing," pp. 51–55 in *Heavy-Section Steel Technology Program Semiann. Prog. Rep. October 1986–March 1987*, NUREG/CR-4219, Vol. 4, No. 1 (ORNL/TM-9593/V4&N1), Martin Marietta Energy Systems, Inc., Oak Ridge Natl. Lab.

16. A. R. Rosenfeld and P. N. Mincer, "Battelle HSST Support Program," pp. 166–68 in *Heavy-Section Steel Technology Program Semiann. Prog. Rep. April–September 1986*, NUREG/CR-4219, Vol. 3, No. 2 (ORNL/TM-9593/V3&N2), Martin Marietta Energy Systems, Inc., Oak Ridge Natl. Lab.

17. W. R. Corwin et al., "Nugget Specimen," p. 58 in *Heavy-Section Steel Technology Program Semiann. Prog. Rep. October 1986–March 1987*, NUREG/CR-4219, Vol. 4, No. 1 (ORNL/TM-9593/V4&N1), Martin Marietta Energy Systems, Inc., Oak Ridge Natl. Lab.

3. FLAW PREPARATION

3.1 Trial Flaw

Before the introduction of a flaw in the PTSE-2 test vessel, 30 trial flaws were produced in pieces of the 2 1/4 Cr-1 Mo material used as a plug in the test vessel. These flaws were generated by the electron-beam welding, hydrogen-charging technique used in flawing many previous heavy-section steel test cylinders and vessels.[1] The large number of samples was necessary to cover a range of welding parameters from which one set would be selected for the vessel flaw and also because of difficulties associated with the electron-beam welder. The welds were hydrogen-charged until a crack was observed and then fractured and visually examined. The sample exhibiting the type of fracture surface and geometry desired for the PTSE-2 flaw was selected. The welding parameters used for that sample were then used to produce a flaw in the PTSE-2 vessel. The sample flaw selected as a prototype is shown in Fig. 3.1 in three segments. The flaw (darkened area) is of a very uniform depth and texture.

3.2 Test Vessel Flaw

The test vessel was installed in the vacuum chamber of the Sciaky electron-beam welder in the Assembly Division of the Y-12 Plant. Figure 3.2 shows PTSE-1 in this welding chamber in a setup essentially identical to that used for PTSE-2. The electron-beam gun, directly above the test vessel, is capable of lateral and vertical motion. The insert of 2 1/4 Cr-1 Mo material is located directly under the gun in a radial-axial plane of the vessel. An electron-beam weld 1000 mm long and penetrating 14.5 mm deep from the vessel outside surface was made in that plane. The electron-beam gun-to-vessel surface distance was 152.4 mm, the vacuum in the chamber was 4.0 mPa, and the gun travel speed was 2286 mm/min. For this weld, the accelerating voltage of the beam was 54.6 kV, the beam current was 275 mA, and the beam focus current was 433 mA.

The vessel was removed from the welding chamber for hydrogen-charging of the weld. Hydrogen was released at the surface of the weld, which was covered by an aqueous solution of 5% sulfuric acid and 2×10^{-4} N sodium arsenite, by passing a 10-A current through the electrolyte. Continuous ultrasonic inspection of the weld during charging with the transducer located on the inside surface of the vessel indicated the presence of a crack after 18.5 h of hydrogen-charging. Ultrasonic scanning along the axis of the crack indicated it to be 1000 mm long with an average depth of 14.1 mm.

ORNL PHOTO 7807-86

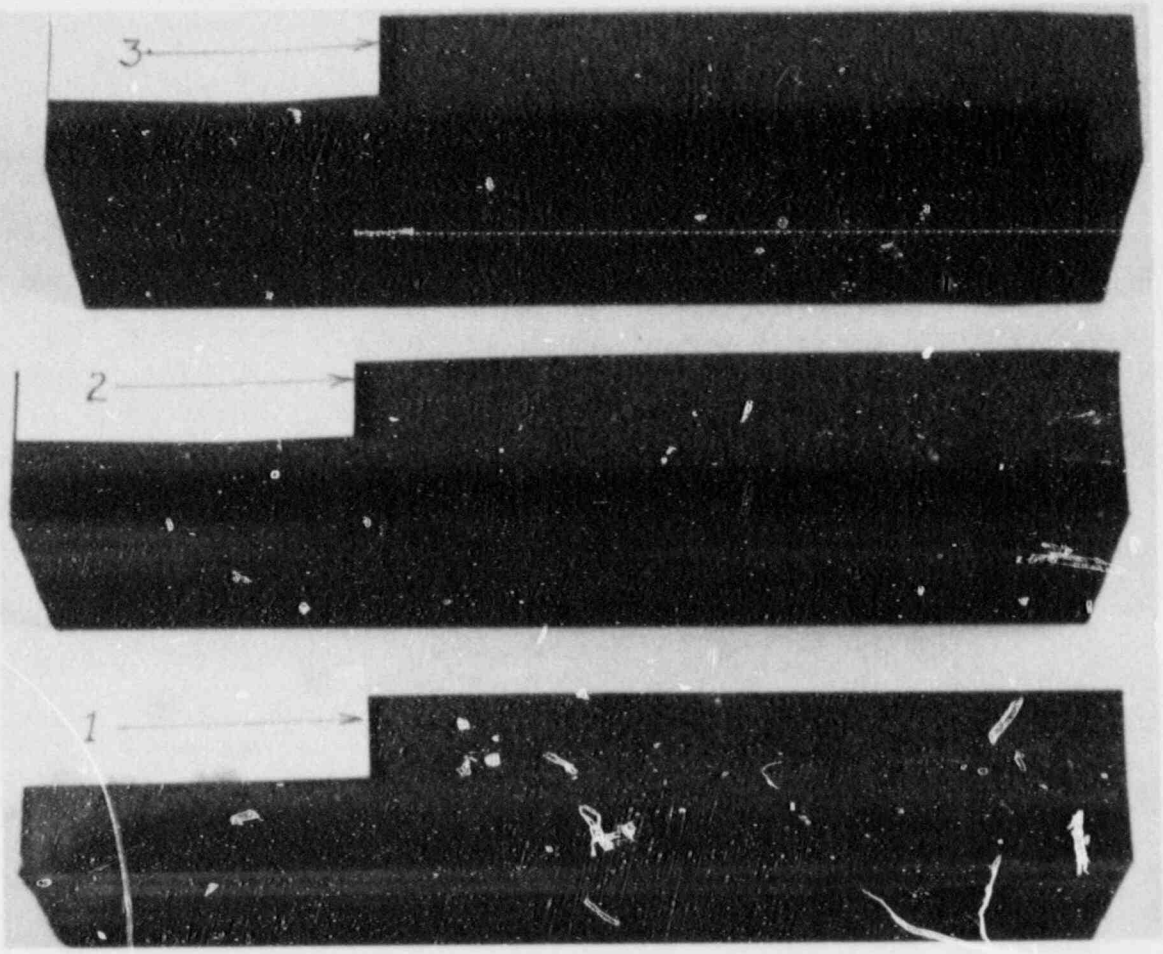

Fig. 3.1. PTSE-2 prototypic flaw.

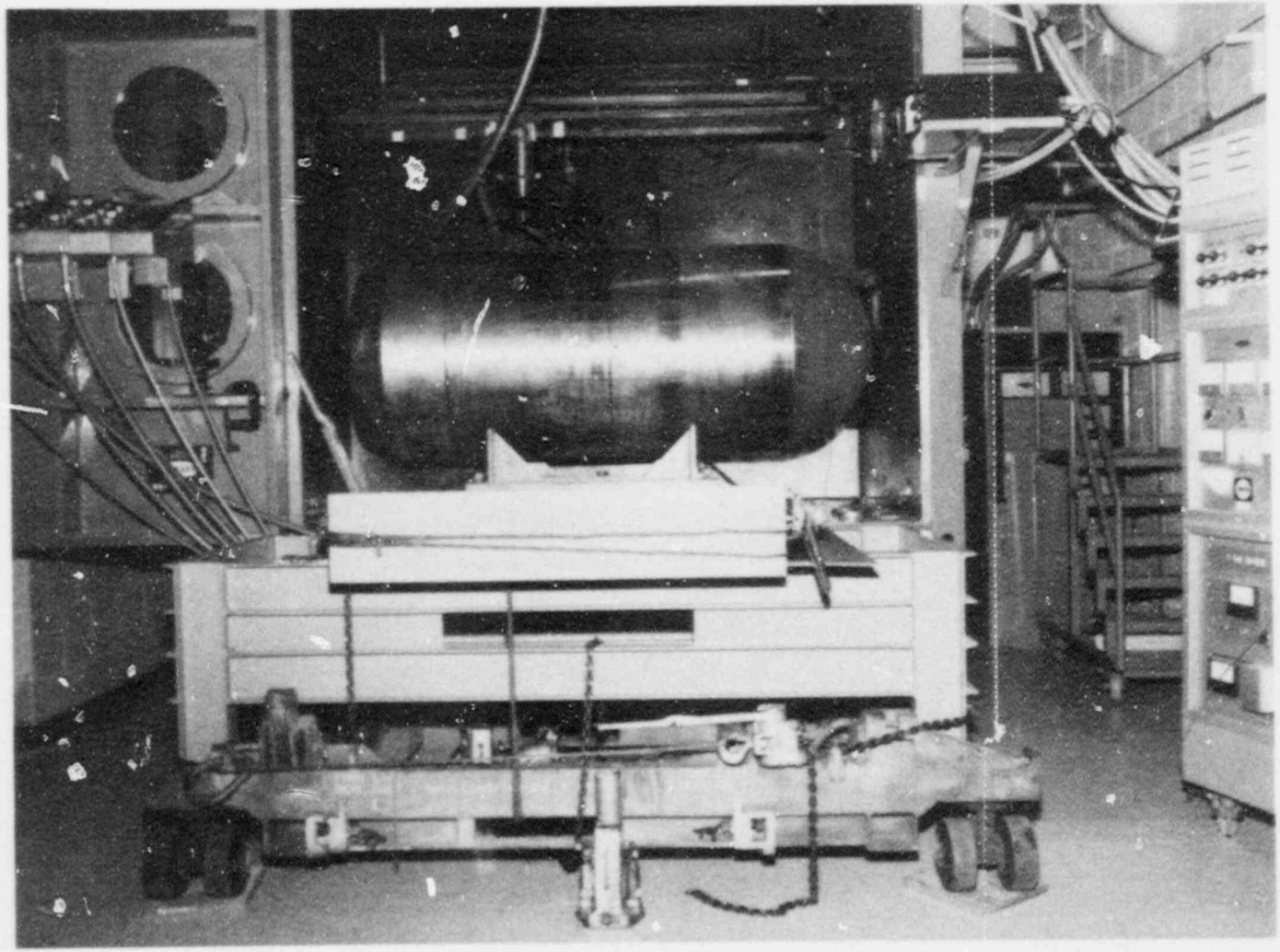

Fig. 3.2. PTSE-1 test vessel in chamber of electron-beam welder. The PTSE-2 setup was identical.

Reference

1. P. P. Holz, *Flaw Preparations for HSST Program Vessel Fracture Mechanics Testing: Mechanical Cyclic Pumping and Electron Beam Weld-Hydrogen-Charge Cracking Schemes*, NUREG/CR-1274 (ORNL/NUREG/ TM-369), Union Carbide Corp. Nuclear Div., Oak Ridge Natl. Lab., May 1980.

4. TEST FACILITY

4.1 Design Basis

The design of the facility for the pressurized-thermal-shock tests was adapted from the designs of the separate facilities previously used for the intermediate vessel tests[1] and for the first four thermal-shock cylinder tests.[2,3] The thermal-hydraulic design rationale incorporated the following basic considerations.[4]

1. The coolant composed of 40% by weight methanol and 60% by weight water was selected and demonstrated to provide adequate heat sink, heat transport, and heat transfer properties and to have acceptable fire and health characteristics.
2. The coolant storage capacity was determined to provide sufficient passive heat-sink capacity, so the change in physical properties of the coolant supplied to the specimen did not result in unacceptable heat transfer characteristics over a cooling period of 1/2 h.
3. The use of a backpressure orifice to limit the tendency for film boiling, and thereby ensure a short-boiling phase transient period, was shown to result in the rapid establishment of a readily controlled forced-convection heat-transfer mode.
4. A modified form of the Sieder-Tate turbulent flow heat transfer correlation[5] was shown to provide a reasonable basis for thermal-hydraulic design and for preliminary predictions of performance.

The facilities that existed for intermediate test vessel pressurization at the outset of design of the pressurized-thermal-shock facility consisted of two coupled intensifier units each capable of delivering $\sim 1.3 \times 10^{-3}$ m^3/min at 344.7 MPa. After considerable analyses of potential test conditions, it became clear that existing facilities could not provide the required flow conditions for pressurizing a test vessel. In addition, the cost of modifications required to achieve reasonably good control of the pressurizing and depressurizing rates was excessive. The method chosen to solve these difficulties was to use the existing intensifiers to precharge intermediate test vessel V-10 as an accumulator and to manually control the flow rates to and from the vessel being tested to achieve the desired pressurizing and depressurizing rates.

Existing cells for confining test vessels had been constructed to test the HSST intermediate test vessels[1] and prestressed concrete reactor vessel models.[6] These cell structures were modified to accommodate the pressurized-thermal-shock facility. In particular, the HSST cell was modified to accept intermediate test vessel V-10 as an accumulator, and the prestressed concrete reactor vessel cell was modified to accept intermediate test vessels as test specimens.

These facilities had been previously assessed for potential hazards and, in particular, had been determined to have the capability of resisting missile impact from destructive vessel testing with kinetic energies as high as 7.81×10^6 J. A review of the potential hazards associated with the pressurized-thermal-shock facility, based on a 50% by weight ethylene glycol and water mixture for the pressurizing medium and

assuming ballasting of the pressurized-thermal-shock intermediate test vessel with graphite to reduce the contained energy, showed that the cells had ample safety margin for the projected pressurized-thermal-shock tests.[7] After the performance of this analysis, it was discovered that ethylene glycol suffered a chemical breakdown at the projected pressurized-thermal-shock test conditions. A dimethyl polysiloxane fluid, Dow Corning 210 H, was then considered and confirmed by testing to be an acceptable alternative pressurizing medium.[8] This change in pressurizing media eliminated the primary source of kinetic energy for missiles, that is, latent heat that controlled the results of the previously conducted safety analysis.[7] Although the compressibility of dimethyl polysiloxane at pressurized-thermal-shock conditions is unknown (only room temperature data are available), based upon a comparison with water compressibility data, a net decrease in potential energy for missile production was expected.[8]

Figure 4.1 shows a plan view of the modified cells and principal items of the main coolant system; Fig. 4.2 shows a section elevation through the cells, again including principal items of the main coolant system.

4.2 Main Coolant System

Figure 4.3 shows a simplified flow diagram of the equipment used to achieve the temperature transients required for the pressurized-thermal-shock tests. The test shroud, surrounding the test vessel as shown in Fig. 4.3, serves dual purposes: (1) as an oven using electrical heaters to preheat the test specimen at a controlled rate to any designated temperature between room temperature and 300°C and (2) as a means to direct coolant flow through an annulus to achieve the desired temperature gradient in the intermediate test vessel wall. The mechanical refrigeration unit shown, with a specified minimum capacity of 26.4 kW at 4.4°C and 5.3 kW at −23°C, prechills the coolant in the storage tank (15.1-m^3 capacity) to the desired temperature level. As initially designed, the valves FCV 1 and FCV 2 were intended to be manipulated to accomplish two purposes: (1) to establish circulation in a bypass mode to verify that the recirculation pump is running at a steady state condition prior to diverting flow through the test tank to initiate the thermal shock and (2) to provide flow control to vary the transient temperature gradient imposed on the test vessel. After installation, valve FCV 1 was found to be incapable of withstanding the full pump design head with the valve fully closed. Valve FCV 2 had a similar, although less severe, deficiency. Because of these problems, flow through the shroud was initiated by presetting valves HCV 6, FCV 1, and FCV 2 to the proper position and then in a timed sequence opening the coolant storage tank isolation valve (HCV 4) and activating the recirculation pump to achieve flows up to 0.15 m^3/s. Measuring orifices in the shroud inlet and exit lines and in the bypass line permitted correlation of flow with valve position for both transient and steady state conditions of flow in preliminary flow tests discussed in Chap. 7. The jacket coolant storage tank provides a passive heat sink to permit precooling the shroud prior to activating the

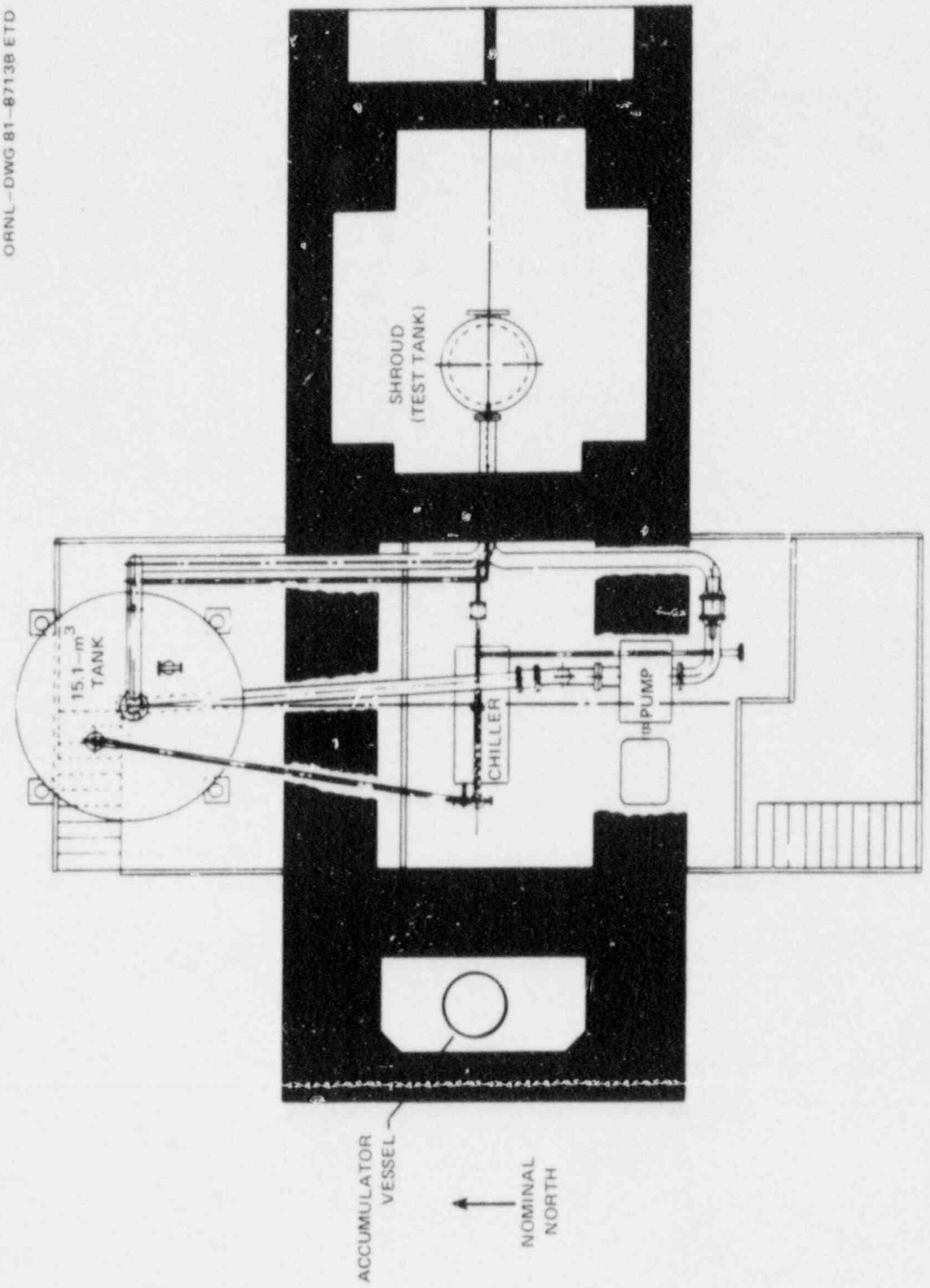

Fig. 4.1. Plan view of pressurized-thermal-shock test facility located in Bldg. K-702.

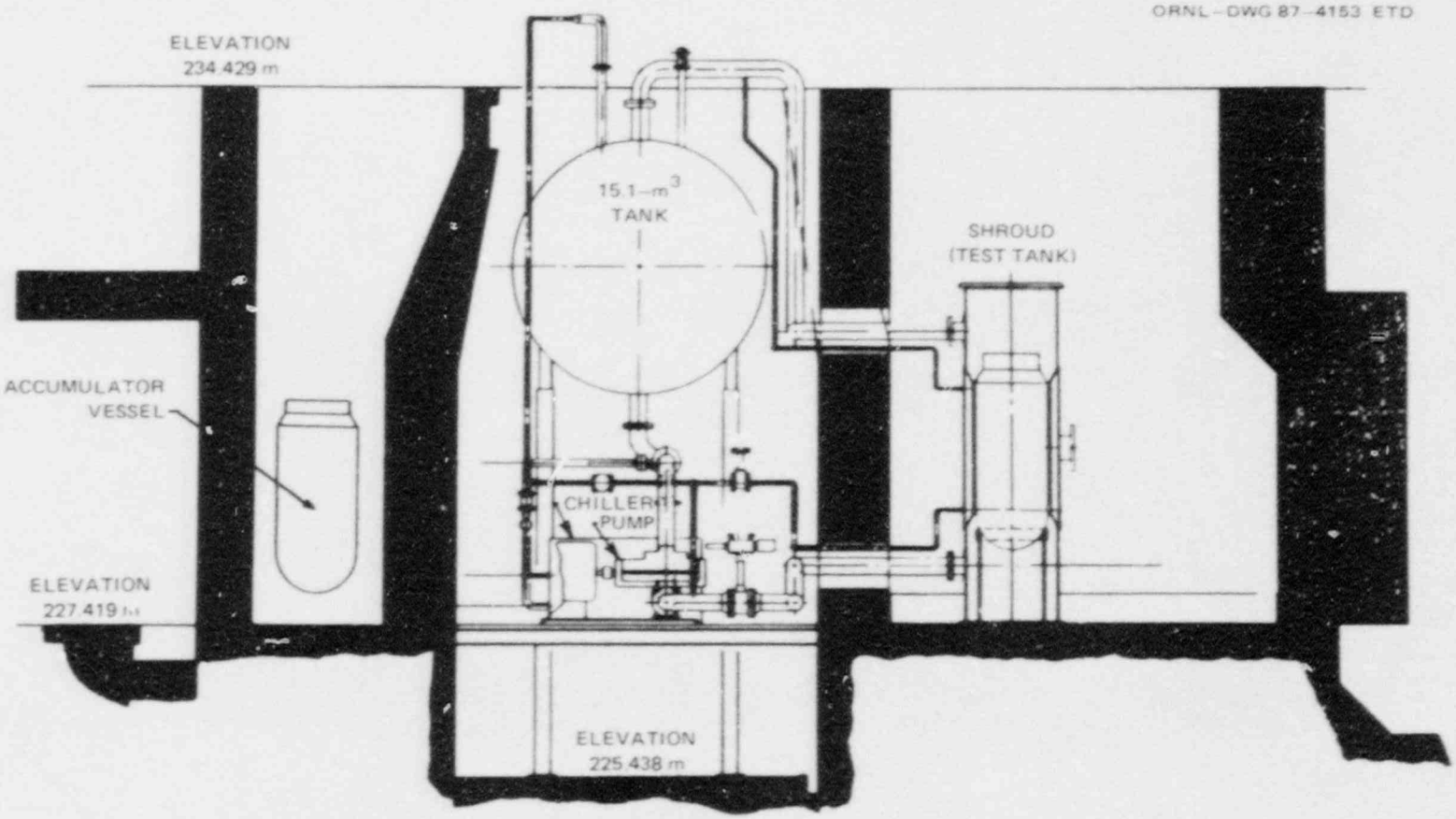

Fig. 4.2. Section elevation of pressurized-thermal-shock test facility.

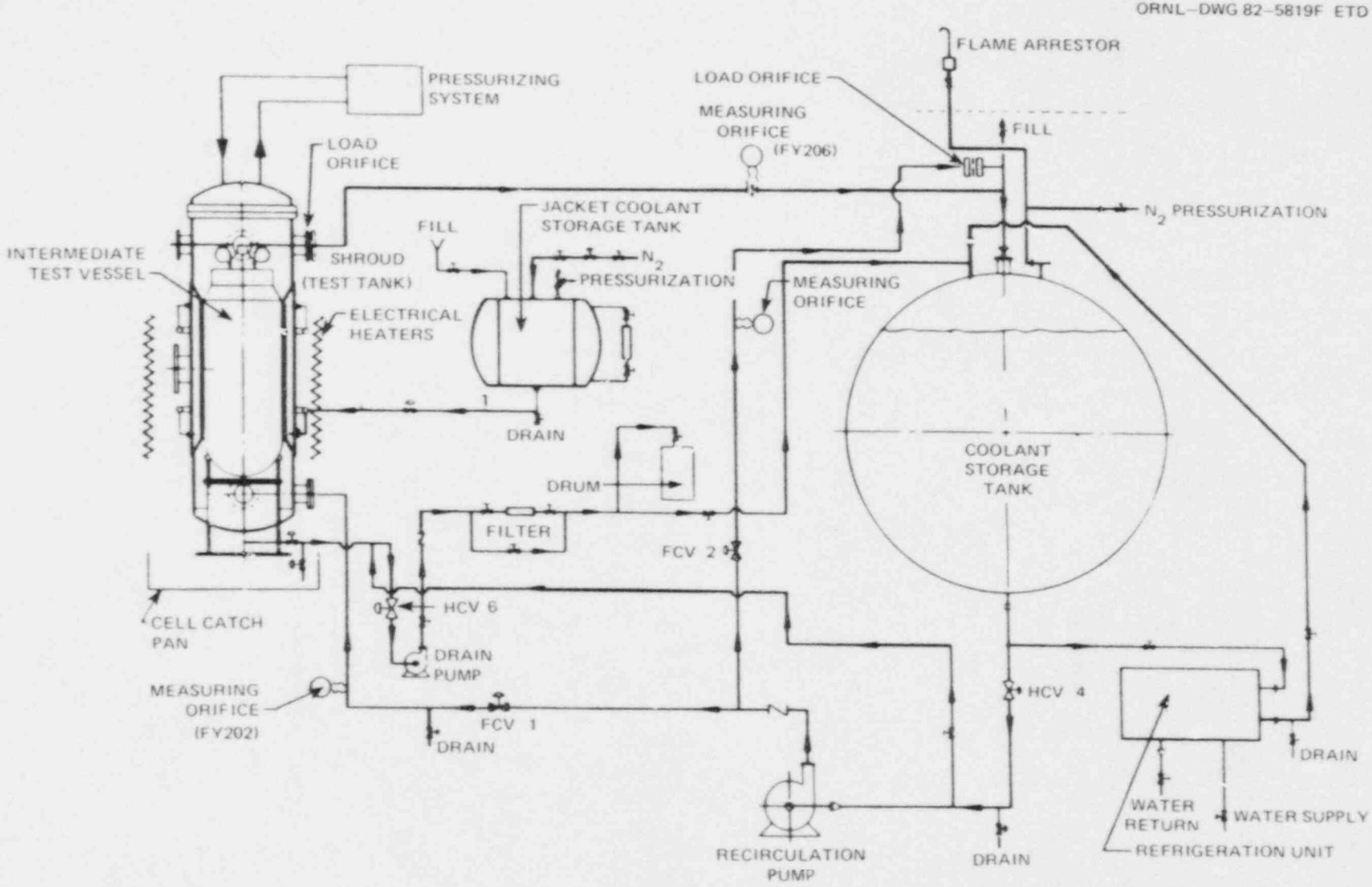

Fig. 4.3. Flow diagram for main coolant system for pressurized-thermal-shock test facility.

recirculation pump. The load orifice in the shroud exit provides sufficient pressure drop to maintain a head of at least 896.3 kPa to suppress film boiling in the early part of a pressurized-thermal-shock transient. This orifice and the load orifice in the bypass line supplement the flow control provided by the control valves, FCV 1 and FCV 2, to establish the required flow to the shroud. The drain system shown in Fig. 4.3 provides the capability for returning fluid remaining in the shroud to the coolant storage tank following a normal pressurized-thermal-shock test and, in the event of test vessel leakage, provides for transfer of coolant to drums for disposal. Although not initially anticipated, subsequent safety analysis revealed that under some flow conditions the test vessel would be subjected to levitation. To prevent this condition from occurring, the volume within the test vessel support structure in the bottom plenum of the shroud must always have a flow path to the suction side of the recirculation pump through existing interconnected drain lines whenever the recirculation pump is running.

Figure 4.4 shows a view of the coolant storage tank and associated piping. The isolation valve controlling fluid delivery to the recirculation pump is visible on the bottom line. Figure 4.5 shows a view of the recirculation pump and chiller. Figure 4.6 shows a view of the shroud installed in the pressurized-thermal-shock cell. Particularly prominent in this view are electrical heaters protruding radially outward from the shroud, nozzles in the shroud for the instrument penetrations, and steel-plate missile shielding around the coolant pipe penetrating the west concrete shield wall.

4.3 Pressurization System

Figure 4.7 shows a simplified flow diagram for the pressurized-thermal-shock pressurization system. Either of the existing intensifier systems can be used to pressurize the accumulator vessel V-10 to pressures up to 137.9 MPa. As shown in Fig. 4.7, the normal flow path to the test vessel was chosen to be from the prestressed concrete reactor vessel intensifier system because that intensifier had been used less. Valves FV 367 and FCV 368 provide a means of remote manual control of the pressurizing rate of the pressurized-thermal-shock test vessel. Valve FV 367 provides tight shut-off capability, and valve FCV 368 provides flow modulation. Similarly, valves FV 361, FV 362, and FCV 363 provide a means of remote manual control of the depressurizing rate of the pressurized-thermal-shock test vessel. Valves FV 361 and FV 362 provide tight shut-off capability and valve FCV 363 provides flow modulation. Valve FV 372 provides for the normal remote manual actuation for letdown of V-10; valves HV 309 and HV 310 provide local manual letdown of V-10 for off-normal conditions. Similarly, valves HV 365 and HV 366 provide local manual letdown of the pressurized-thermal-shock test vessel for off-normal conditions.

The system as shown in Fig. 4.7 was used for the PTSE-2A test, but as discussed in Chapter 7 it was necessary to change the configuration of the system to permit an adequate venting rate for the PTSE-2B test.

ORGDP PHOTO 83-1307B

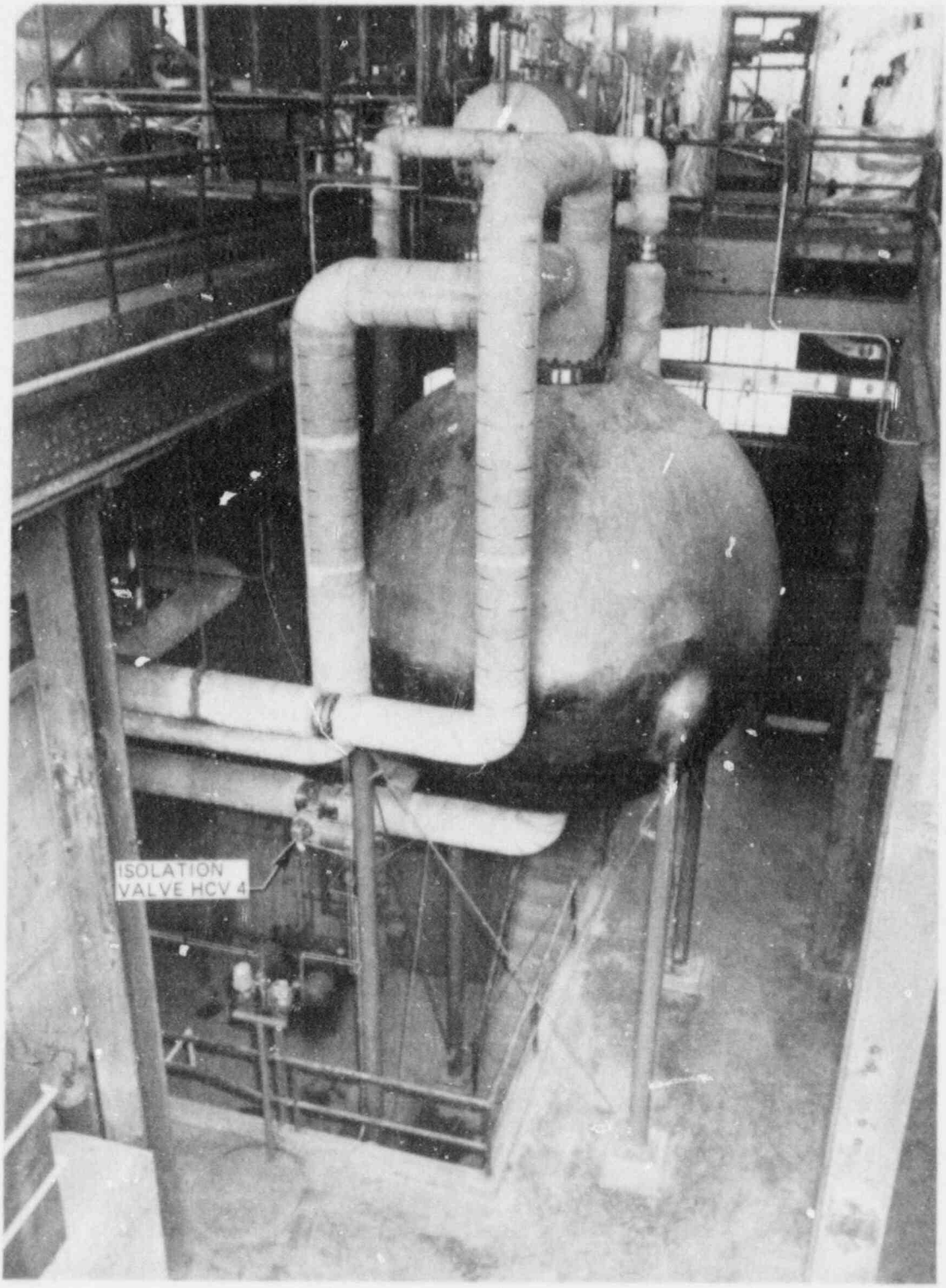

Fig. 4.4. View (toward west) of coolant storage tank and associated piping.

ORGDP PHOTO 83-1299

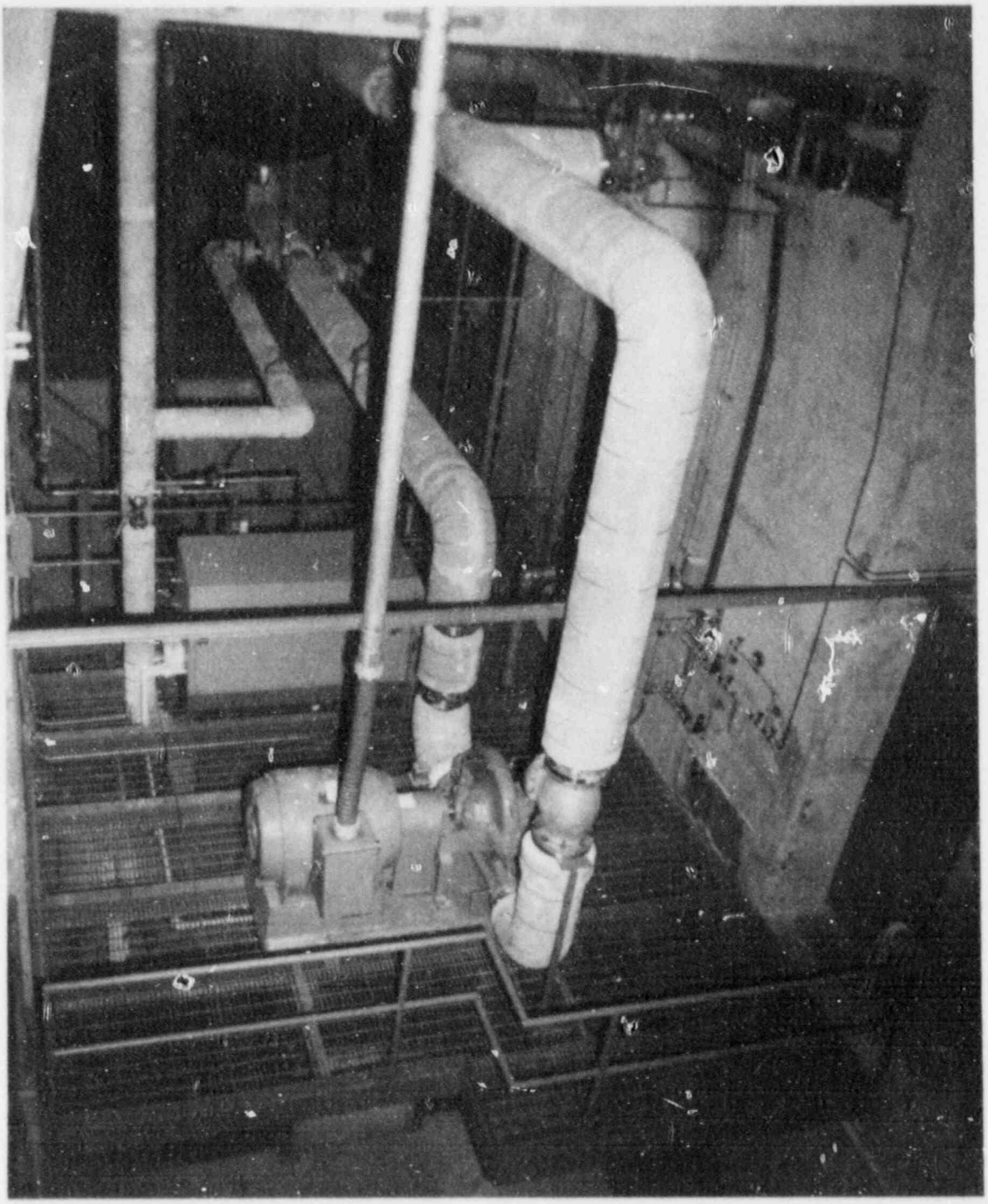

Fig. 4.5. View (toward north) of recirculation pump, chiller, and piping.

ORGDP PHOTO 83-1148

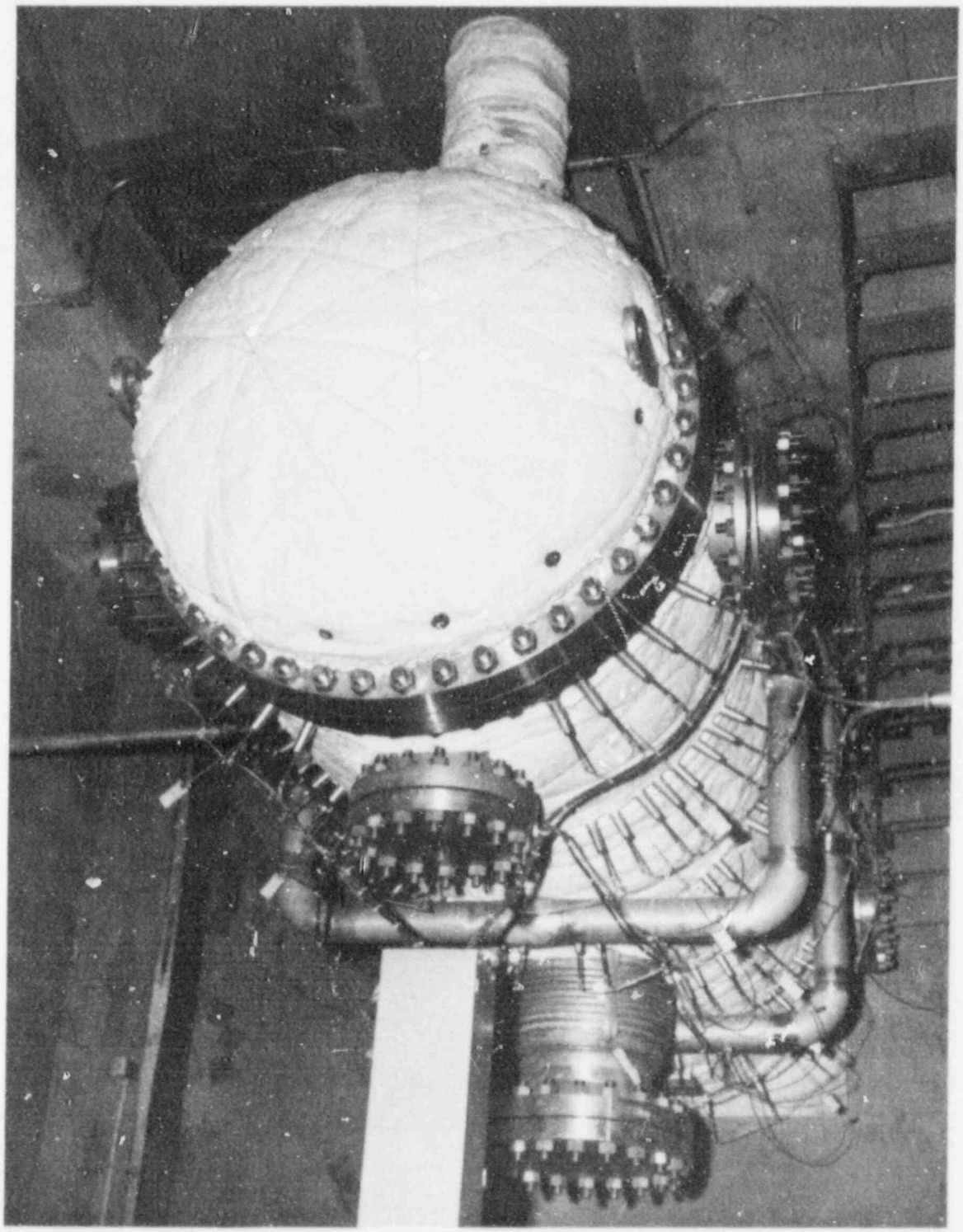

Fig. 4.6. View (toward west) of shroud from top of test cell.

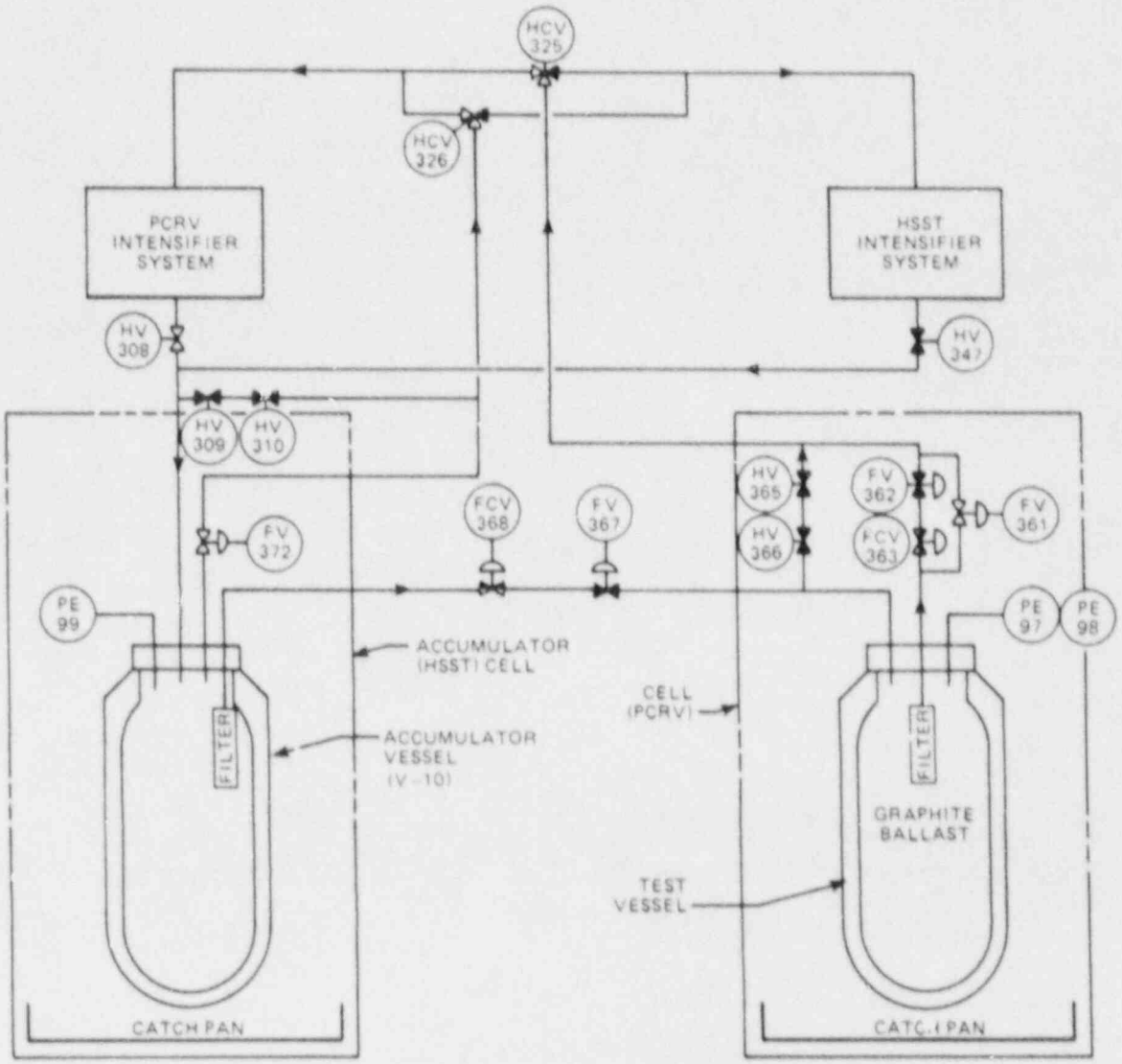

Fig. 4.7. Flow diagram for pressurizing system. [Prestressed-concrete reactor vessel (PCRV), Heavy-Section Steel Technology (HSST).]

4.4 Data Acquisition Systems

Three data acquisition systems are available in the facility for use in conducting a pressurized-thermal-shock experiment. The primary one is a computer-controlled data acquisition system, which is backed up by a data logger. In addition, there are various analog and digital displays and recorders in the control room. The three systems are essentially independent of each other although some primary sensors supply information to more than one system.

4.4.1 Computer-controlled data acquisition system

Figure 4.8 is a simplified block diagram of the computer-controlled data acquisition system. A PDP 11/34 computer is the central processing unit and is arranged to receive up to 195 thermocouples, 136 strain gages and crack-opening displacement gages, and 30 miscellaneous inputs from facility and test vessel sensors. Data are stored, manipulated, and made available through three separate terminals. One terminal is dedicated to operating instructions and calibration; the other two provide plotting or display of selected test data. A graphics copier is available for hard-copy printout. Real-time display of the data is available during the

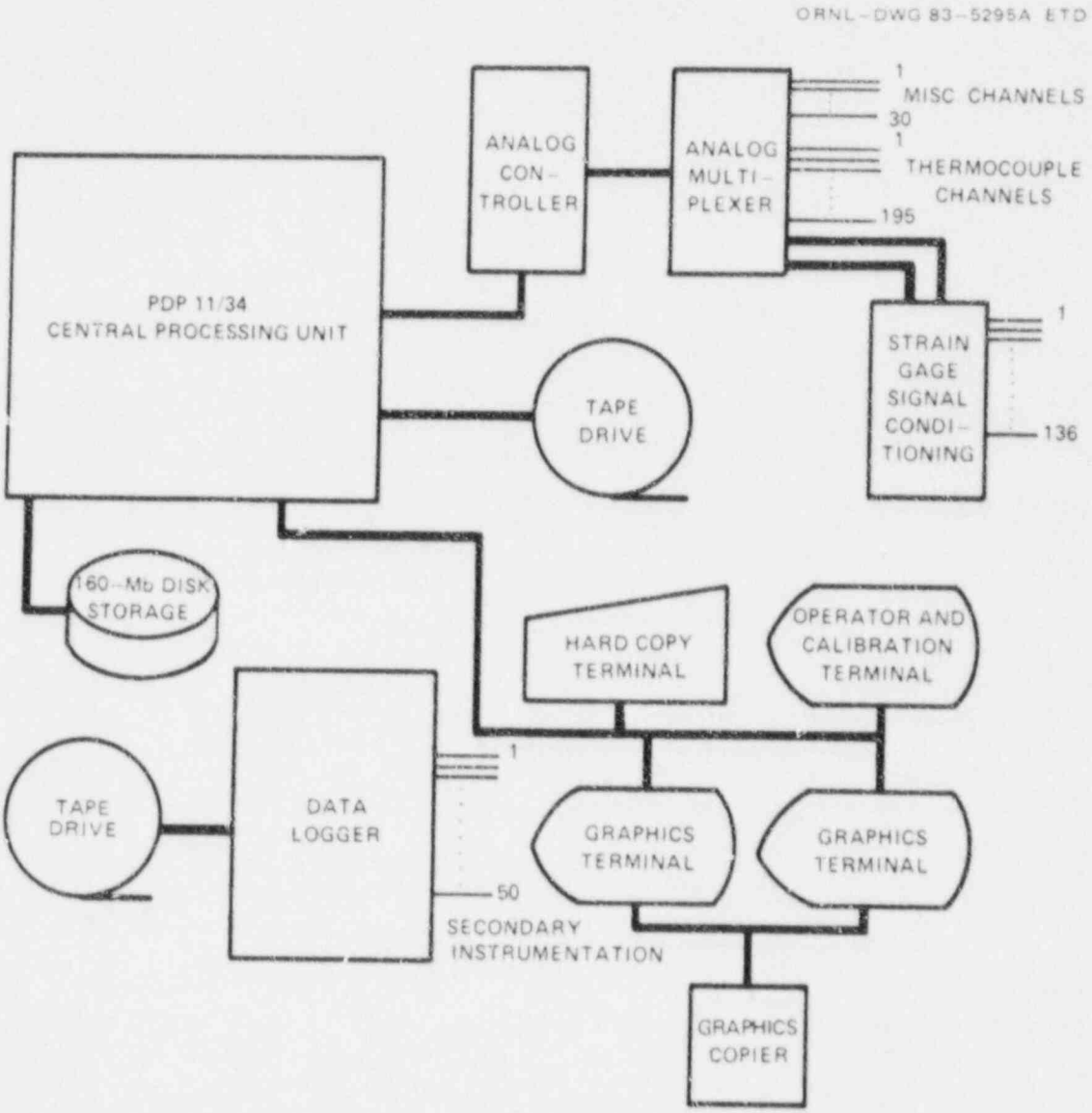

Fig. 4.8. Data acquisition system schematic.

test, and all of the data are stored on disks and/or tapes for later retrieval. The computer-controlled data acquisition system is capable of sampling and recording the output of the sensors at the rate of 10,000 points/s.

4.4.2 Data logger

The data logger is an independent system that records selected critical data from the test and facility instrumentation as a safeguard against loss of the computer-controlled data acquisition system records. In the configuration for PTSE-2, the logger scanned 40 channels and stored the data on magnetic tape at a rate of 1 complete scan every 5 s.

4.4.3 Control room instrumentation

Values of temperature, pressure, strain, and crack-mouth-opening displacement were displayed in the control room by digital and graphic displays. Some of this information was also recorded on strip-chart recorders to preserve the information. Most of these instruments were used in the operation of the various systems to permit proper coordination of the pressure and thermal transients necessary for a successful experiment.

References

1. C. L. Segaser, *System Design Description of the Intermediate Vessel Tests for the Heavy-Section Steel Technology Program*, ORNL/TM-2849, Union Carbide Corp. Nuclear Div., Oak Ridge Natl. Lab., June 1970; revised July 1973.

2. R. D. Cheverton, *Pressure Vessel Fracture Studies Pertaining to a PWR LOCA-ECC Thermal Shock: Experiments TSE-1 and TSE-2*, ORNL/NUREG/TM-31, Union Carbide Corp. Nuclear Div., Oak Ridge Natl. Lab., September 1976.

3. R. D. Cheverton and S. E. Bolt, *Pressure Vessel Fracture Studies Pertaining to a PWR LOCA-ECC Thermal Shock: Experiments TSE-3 and TSE-4 and Update of TSE-1 and TSE-2 Analysis*, ORNL/NUREG-22, Union Carbide Corp. Nuclear Div., Oak Ridge Natl. Lab., December 1977.

4. G. C. Robinson, "Pressurized Thermal Shock," in *Heavy-Section Steel Technology Program Quart. Prog. Rep. April–June 1981*, NUREG/CR-2141/V2 (ORNL/TM-7955/V2), Union Carbide Corp. Nuclear Div., Oak Ridge Natl. Lab.

5. W. H. McAdams, *Heat Transmission*, 2d ed., McGraw Hill Book Co., New York, 1942, p. 168.

6. J. P. Callahan, J. R. Dougan, and G. C. Robinson, "GCFR Pressure Vessel and Closure Studies," pp. 224–26 in *Gas-Cooled Reactor Programs*

Ann. Prog. Rep. December 31, 1978, ORNL-5560, Union Carbide Corp. Nuclear Div., Oak Ridge Natl. Lab.

7. G. C. Robinson and R. W. McCulloch, "Pressurized Thermal-Shock Studies," in *Heavy-Section Steel Technology Program Quart. Prog. Rep. January–March 1982*, NUREG/CR-2751/V1 (ORNL/TM-8369/V1), Union Carbide Corp. Nuclear Div., Oak Ridge Natl. Lab.

8. R. W. McCulloch and G. C. Robinson, "PTS Test Facility," in *Heavy-Section Steel Technology Program Quart. Prog. Rep. January–March 1983*, NUREG/CR-3384/V1 (ORNL/TM-8787/V1), Union Carbide Corp. Nuclear Div., Oak Ridge Natl. Lab.

5. SPECIAL FEATURES

5.1 Thermocouple Thimbles

The rationale for the development of special thermocouple thimbles to obtain accurate measurements of transient radial temperature profiles in the walls of the pressurized-thermal-shock test vessels has been covered in Ref. 1. These types of devices have been successfully used in several thermal-shock test cylinders and more recently in the PTSE-1 pressurized-thermal-shock test.[1] The thimbles for the PTSE-1 test were developed and fabricated with Martin Marietta Energy Systems, Inc., facilities and personnel. For PTSE-2, thimbles of a slightly modified design were procured by competitive bidding. A full complement of thermocouple thimbles was ordered from each of two companies: Groth Mazur Industries, Inc., on P.O. 67Y-33725V and Technology Corridor Instrumentation, Inc., on P.O. 67Y-33726V. Details of the thermocouple thimble assemblies procured through these purchase orders are given by Fig. 5.1.

During a preliminary test (PTSE-0) prior to PTSE-1, the sheath enclosing the leads of one thermocouple thimble failed by buckling with an attendant leakage of pressurizing fluid. The failure made it necessary to sever the leads and cap the sheath, which resulted in a loss of data. In the procurement of thermocouple thimbles for PTSE-2, a significant design change was made in the stainless-steel-sheathed lead configuration in an attempt to prevent a reoccurrence of sheath failure by buckling. In the PTSE-0 and PTSE-1 thimble design, the 12 leads were housed within the sheath with no attempt to establish a definite configuration. A considerable void volume within the sheath resulted. With this configuration the pressure of the pressurizing fluid, acting externally on an inadvertent kink introduced during installation, provided a scenario for the type of failure that occurred during the PTSE-0 test. As a remedy the 12 PTSE-2 thermocouple thimble leads were satellite arrayed around a central filler wire and tightly housed within the sheath by swaging. Although the redesigned sheathed assemblies were more resistant to failure, they were also stiffer and more difficult to install in the instrument penetration assemblies. This characteristic required design changes to the seals of the penetration assemblies described in Sect. 5.2.

5.2. High-Pressure Seals

An extensive description of the basis for development of special high-pressure, high-temperature seals for the pressurized-thermal-shock test series is given in Ref. 1. As described therein, commercial sources for several of the seal devices required were nonexistent, requiring the application of an ORNL development effort. Extensive efforts were expended in developing seals for the various instrument leads required to penetrate both the top head and the cylindrical shell of the test vessels. Figure 5.2 illustrates the use of a conical metal-to-metal seal feature to seal an instrument lead penetration assembly to the test-vessel cover

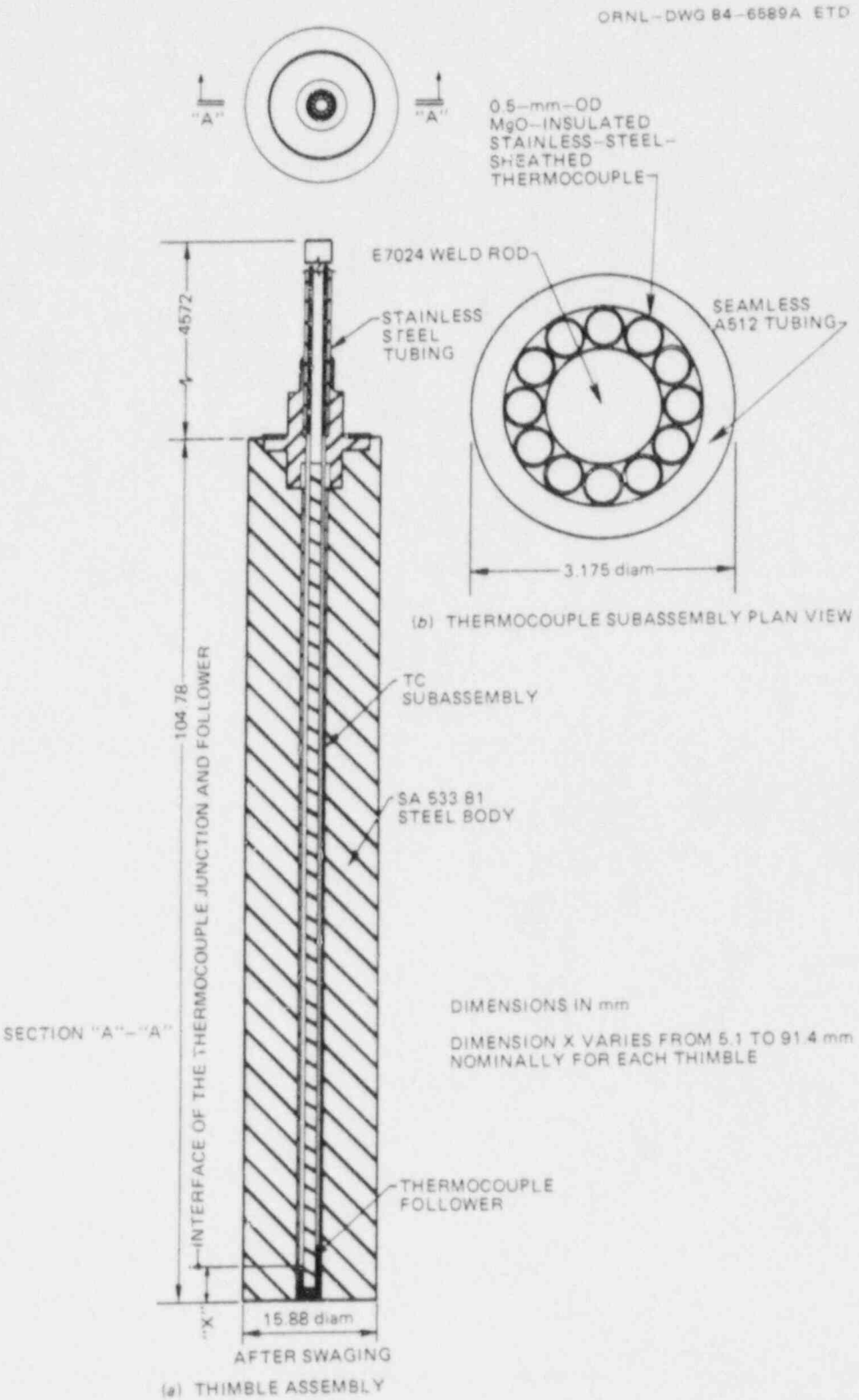

Fig. 5.1. Details of PTSE-2 therrocouple thimble assembly.

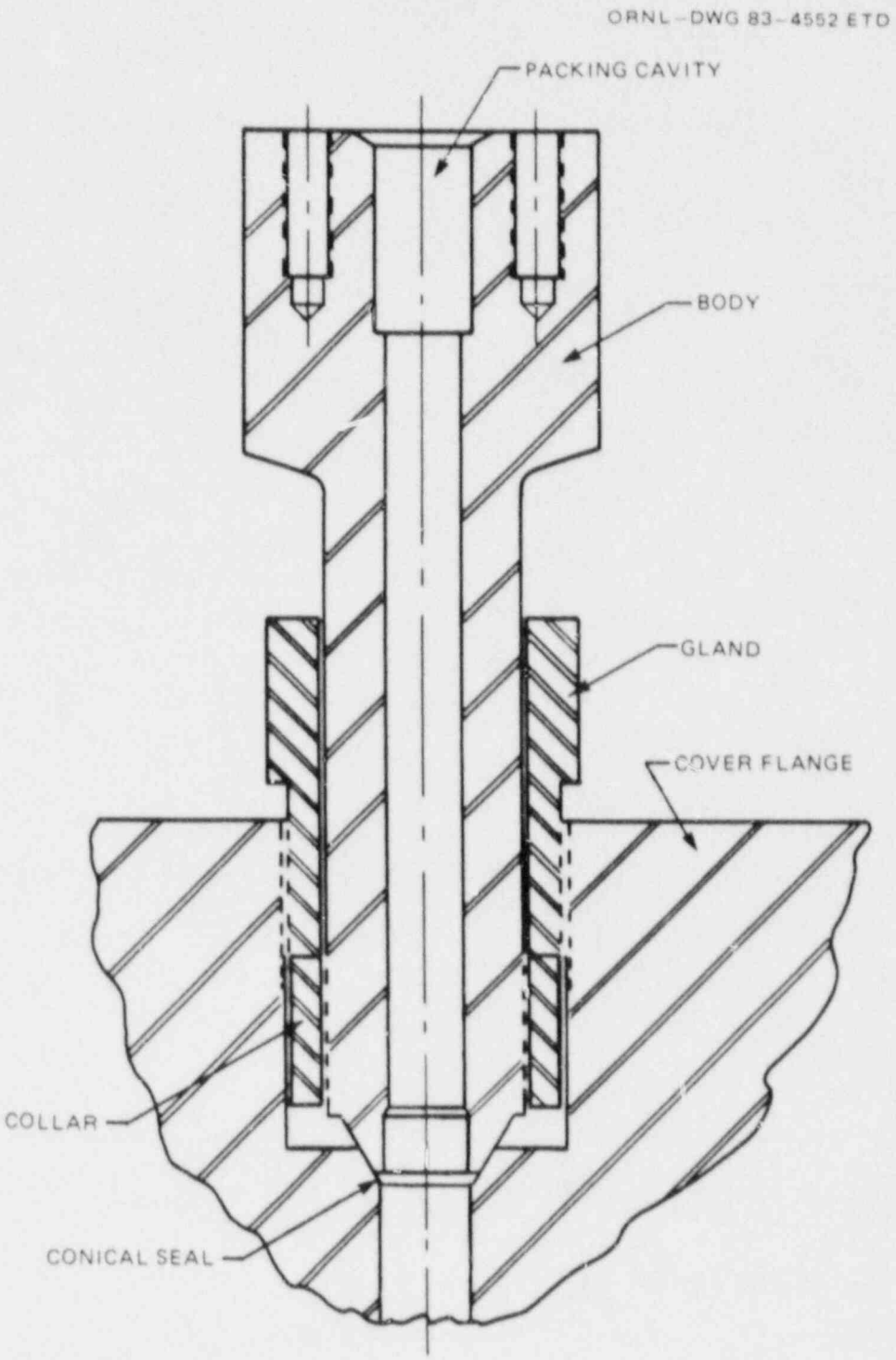

Fig. 5.2. Cross section of conical seal in instrument lead penetration assembly in cover flange.

flange and also identifies the packing cavity within which the packing assembly, shown on Fig. 5.3, resides. Packing assemblies such as that shown in Fig. 5.3 were developed to accept three different configurations, the first to accommodate six 1.5-mm-diam leads, the second to accommodate three 3.2-mm-diam leads, and the third to accommodate a single 3.2-mm-diam lead. In all the configurations, the soapstone packing shown in Fig. 5.3 was designed and fabricated as a single piece.

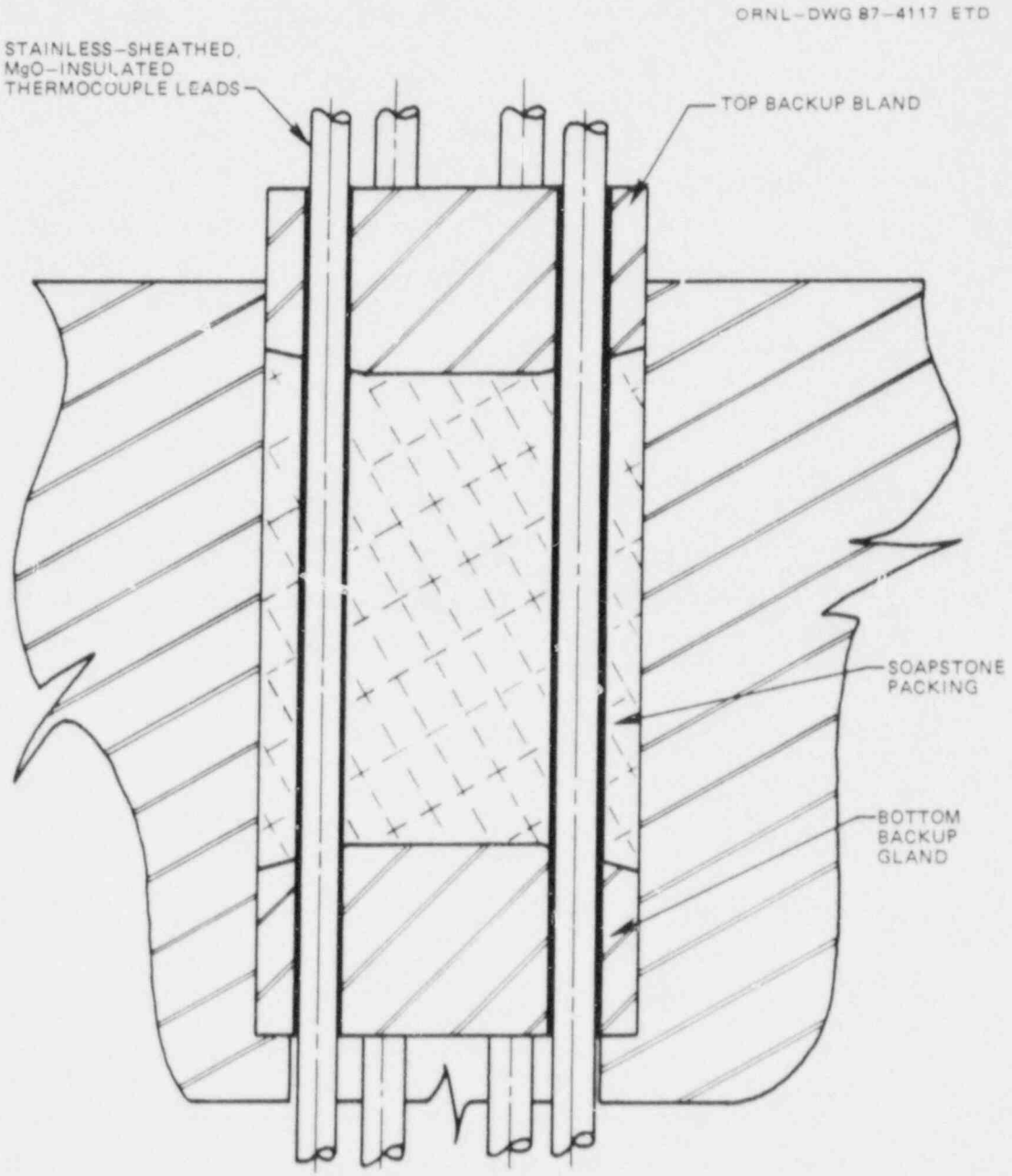

Fig. 5.3. Cross section of packing concept for instrument lead penetration.

The thermocouple thimble assemblies discussed in Sect. 5.1 are installed in the cylindrical shell of the test vessel in an orientation requiring a similar packing configuration as that used in the cover flange. However, as shown in Fig. 5.4, at the thimble a single 3.2-mm-diam lead is directed through the packing. The change in the design of the 3.2-mm-diam leads of the thimble assemblies, as discussed in Sect. 5.1, increased significantly the stiffness of the lead. This increased stiffness stimulated concern about the feasibility of assembly of the leads through the fragile soapstone packing, not only in the configuration illustrated in Fig. 5.4 but also in the three-hole version of the packing shown in Fig. 5.3. For prudence it was decided to design and proof test split configurations of the single-hole and three-hole packing for the 3.2-mm-diam leads. Exploded views of these configurations are shown in Figs. 5.5 and 5.6. Leak tests with cyclic load, prolonged hold periods, and pressures and temperatures at the most severe anticipated conditions were successfully conducted on the modified seal designs with two sources of native soapstone. Again for prudence sake, full complements of both the solid and the split configurations were fabricated in readiness for the PTSE-2 vessel assembly. Upon assembly of the PTSE-2 it was found

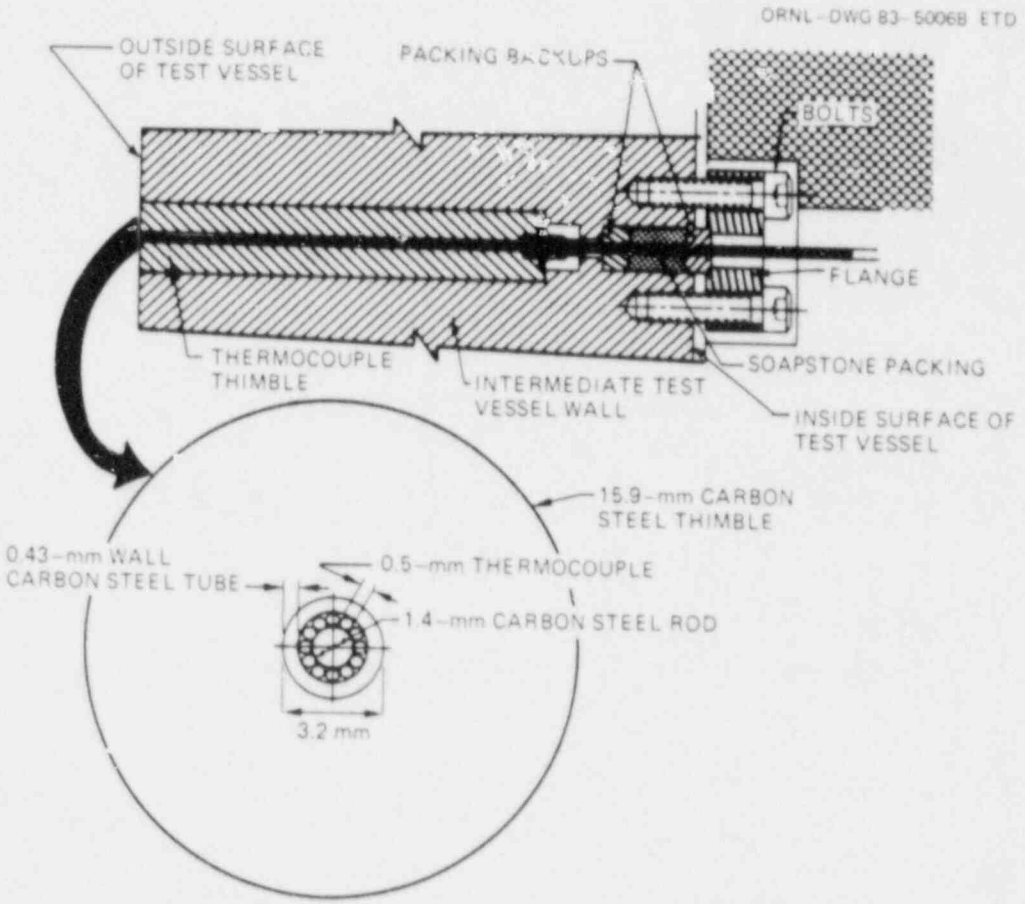

Fig. 5.4. Assembly of thermocouple thimble in wall of test vessel.

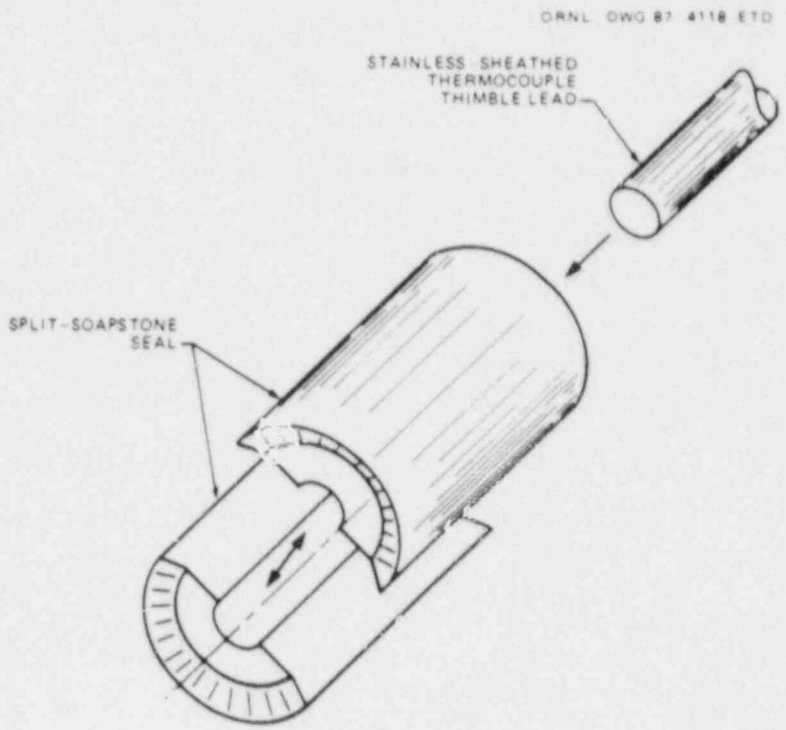

Fig. 5.5. Configuration of split-soapstone seals for PTSE thermocouple thimble single-lead penetration.

that this prudence was justified; only the split configuration packing designs could be satisfactorily installed.

As a consequence of utilization in several intermediate vessel and pressurized-thermal-shock tests, the PTSE-2 vessel was subjected to considerable inadvertent abuse. In spite of provisions made to protect seal surfaces during dismantling and repair operations these surfaces were badly scarred and required remedial treatment to be serviceable. The surface of the vessel closure flange in contact with the vessel head O-ring seal shown on Fig. 5.7 was especially severely damaged in several locations. Two proprietary Devcon filled epoxy compounds were selected for a screening test, one steel-filled and the other ceramic-filled. As a screening test, several plane-surfaced coupons having scar marks comparable to those in the PTSE-2 vessel were filled, cured, and polished to a smooth in-plane surface with both types of compounds and then subjected to a 24-h heat soak at 300°C. After removal from the furnace, the filled surfaces of the coupons were inspected under a microscope. The surfaces using the steel-filled compound had numerous pits, but the ceramic-filled surfaces remained smooth. Consequently, the head seal and the thermocouple lead-through seal surfaces were treated with the ceramic-filled epoxy compound. Several layers were required in some areas of the head seal in order to achieve circularity. Preoperational leak tests at 20 MPa and 290°C verified that the repair work was successful.

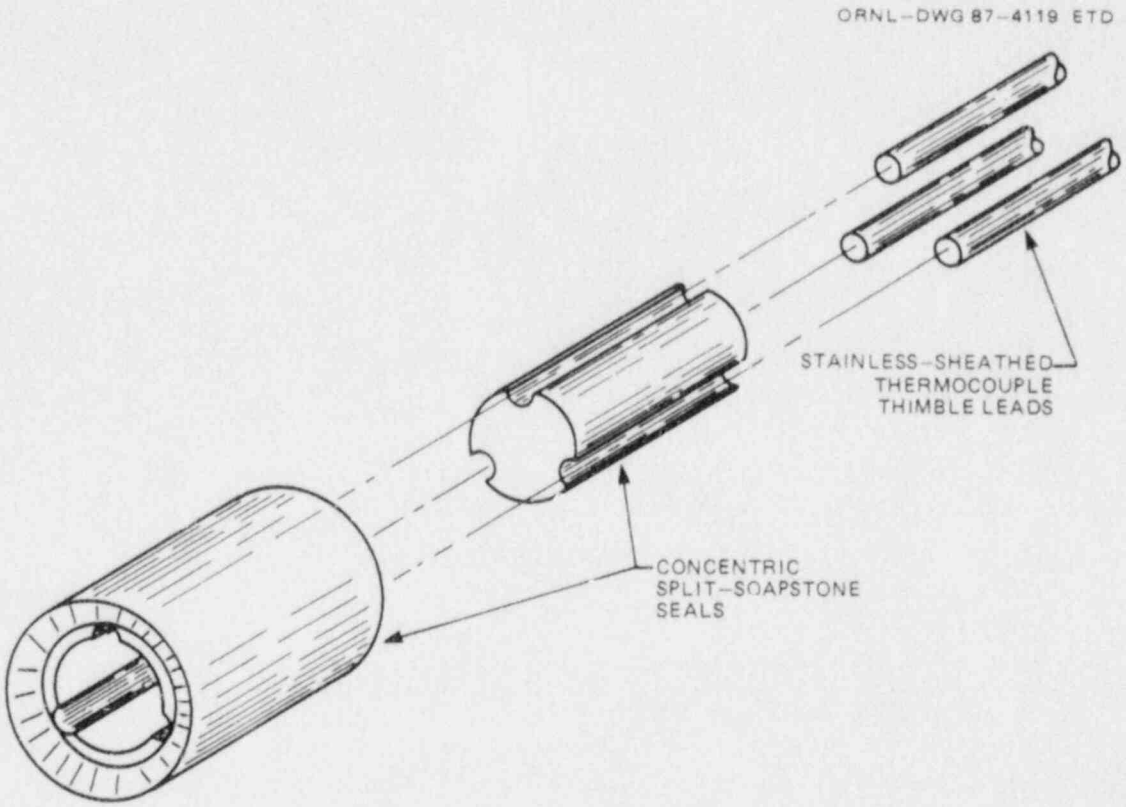

Fig. 5.6. Configuration of concentric split-soapstone seals for PTSE thermocouple thimble three-lead penetration.

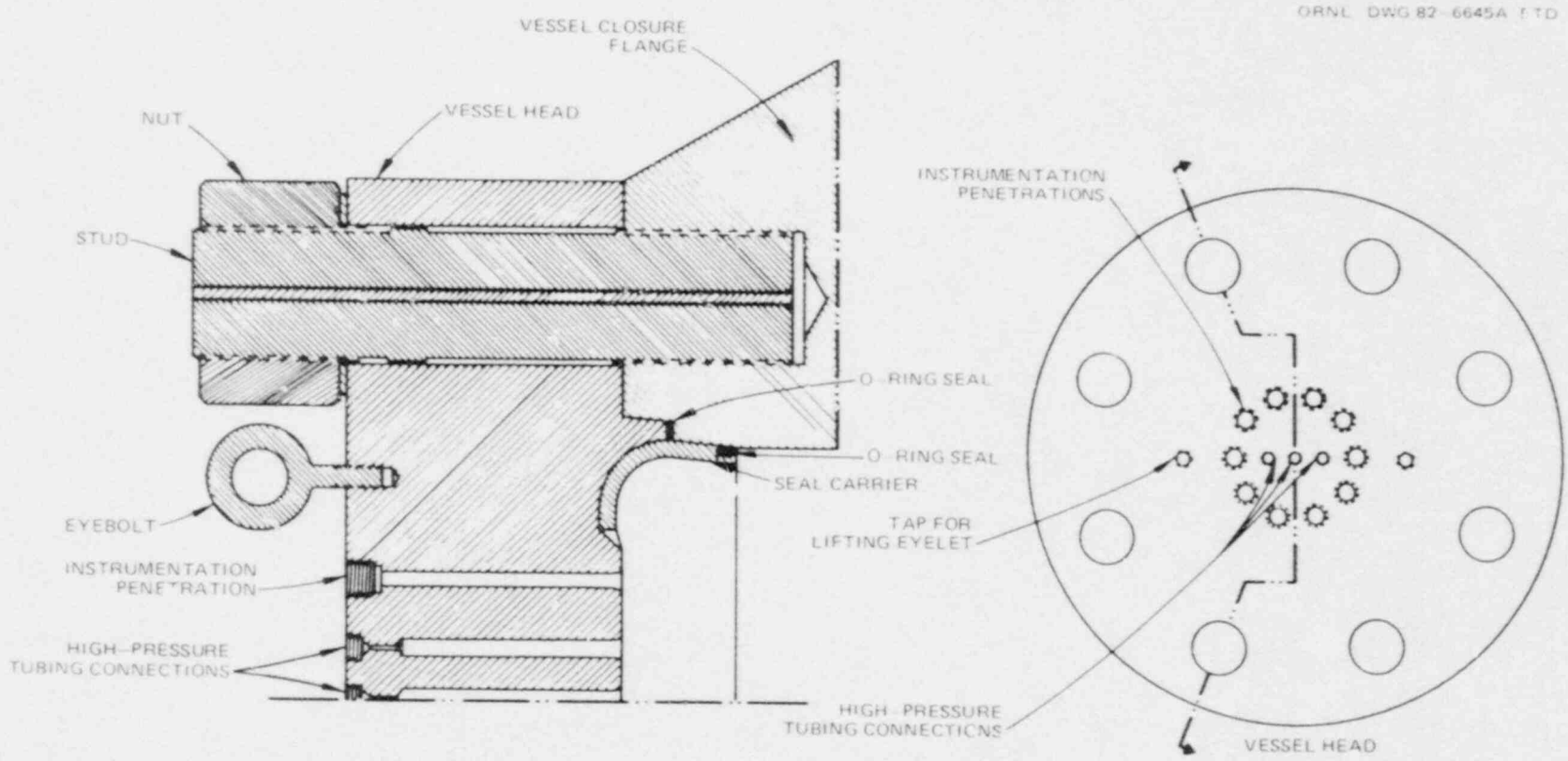

Fig. 5.7. Intermediate test vessel head and access nozzle assembly diagram showing locations of seals for closure and instrumentation penetration.

Reference

1. R. H. Bryan et al., *Pressurized-Thermal-Shock Test of 6-in.-Thick Pressure Vessels. PTSE-1: Investigation of Warm Prestressing and Upper Shelf Arrest*, NUREG/CR-4106 (ORNL-6135), Martin Marietta Energy Systems, Inc., Oak Ridge Natl. Lab., April 1985.

6. VESSEL INSTRUMENTATION

6.1 Measurement Plan

The important measurements to make and record during a pressurized-thermal-shock transient are the temperatures that control the thermal stress states; the temperatures that define the fracture-toughness conditions along the tip of the crack; the internal pressure, which defines the stress states from mechanical loading; and the displacements along and near the crack, which can be used to estimate crack depth and length. The systems for making and recording the measurements were almost identical to those used in the PTSE-1 experiment.[1] Instrumentation for these measurements was designed to transmit data to two systems that were isolated from one another to reduce the risk that a data system failure would disrupt the recovery of essential data on a transient. As described in Chap. 4, the essential variables were recorded by a primary computer-controlled data acquisition system and a secondary data logger. The sources of data and the modes of output and recording are summarized in Table 6.1. The data logger received signals from some of the sensors that transmitted information to the computer-controlled data acquisition system; pressure and CMOD are in this category. In these circuits, the signals are split by a buffer-amplifier to preclude interference between the separate recording systems. From sensor to recording device, circuits for temperature measurements were completely separate.

No serious attempt was made to make measurements from which precise heat-transfer characteristics could be deduced. However, to facilitate the planning and execution of transients, sufficient measurements were made of coolant flows, temperatures, and pressures to permit reasonable estimates of thermal performance.

6.2 Description of Sensors

6.2.1 Thermocouple thimbles

Temperature measurements within the cylindrical wall of the vessel were made with 9 thermocouple thimbles, each containing 12 type-K thermocouples. Details of the design are described in Chap. 5. The 12 junctions of the thermocouples were arranged at various depths, nominally given in Table 6.2 (see Fig. 5.1). The actual location of each junction was measured during the manufacture of the thimbles. Each thermocouple was calibrated by the manufacturer after thimble assembly by comparison with a laboratory standard type-S thermocouple at three temperatures between 0 and 289°C. In addition, two thimbles from each of the two manufacturers were subjected to thermal transient tests at ORNL.

Seven thermocouple thimbles fabricated by Groth-Mazur Industries, Inc., were installed in the PTSE-2 vessel and connected to the computer-controlled data acquisition system. Two thimbles fabricated by Technology Corridor Instrumentation, Inc., were connected to the data logger. Calibration data from Groth-Mazur Industries showed that temperatures

Table 6.1. Instrumentation output assignments for test vessel data sensors

Variable	Output[a,b]	Sensor location	Number of sensors	Sensor No.
Temperature profile in vessel wall	CCDAS[c]	See Fig. 6.1	84	TE1-1 to TE7-12
	DL		24	TE8-1 to TE9-12
Surface temperature	CCDAS	See Fig. 6.2	25	TE17,[d] 18, 21[d] to 29, 31 to 35, 37 to 39, 43, 61 to 65
	DL		7	TE19,[d] 20,[d] 30, 36, 40 to 42
Near-surface temperature[e]	CCDAS	See Fig. 6.1	7	TE66 to 72
CMOD	CCDAS	See Fig. 6.3	10	YE51, 54, 79 to 88
	DL		7	YE79, 80, 82 to 84, 86, 87
	SC		6	YE79, 82, 83, 84, 86, 88
	DO		2	YE79, 82
Dummy CMOD	CCDAS	See Fig. 6.3	2	YE50, 56
Strain	CCDAS	See Fig. 6.3	9	XE48, 52, 53, 55
	SC		2	XE52, 53
Pressure	CCDAS	Static line in test cell[f]	2	PE97, 98
	DL		1	PE98
	SC[g]		1	PE97
	DD[g]		1	PE97
Crack depth	PC		4	

[a]CCDAS - Computer-controlled data acquisition system
DL - Data logger
SC - Strip-chart recorder (in control room)
DD - Digital display (in control room)
DO - Digital oscilloscope (in control room)
MC - Microcomputer (in control room)

[b]Any datum collected by CCDAS could be listed on CRT display in control room.

[c]Selected near-surface temperature was plotted on CRT display in control room.

[d]TE17, 20, and 21 were damaged before the test. TE19 was consequently connected to the CCDAS rather than the DL.

[e]Intrinsic thermocouples welded to the bottom of 25-mm-deep holes drilled from the outside surface of the vessel.

[f]Pressurizing requirements made modifications to the system necessary. As a result, PE97 and 98 were on a vent line and a pressurizing line, respectively, so that in most phases of the test, one transducer was on a static line. See Fig. 7.4.

[g]Output located at pressurization system control station.

[h]Two channels of output processed from pressure (PY97) and CMOD (YE84 and 88).

Table 6.2. Nominal location of thermocouple junctions in a PTSE-2 thimble[a]

Thermocouple No.	Depth from cooled surface (mm)
1	5.1
2	7.6
3	11.4
4	15.2
5	22.9
6	30.5
7	38.1
8	45.7
9	61.0
10	76.2
11	91.4
12	101.6

[a]Actual locations determined after the test for some thimbles generally varied from the nominal locations.

indicated by the thimble thermocouples differed, at most, by 0.8 K from temperatures measured by a laboratory standard. Data from the ORNL Metrology Laboratory found even less maximum deviation (0.3 K) from a laboratory standard.

Each thimble was inserted in a radial hole drilled completely through the wall of the vessel. As shown in Fig. 6.1, three thimbles were situated in each of three axial locations: in the midplane of the flaw, 400 mm above the midplane, and 400 mm below the midplane. In each plane, the thimbles were separated by 120°.

6.2.2 Surface and near-surface thermocouples

Type-K thermocouples were attached to the outside and inside surfaces of the cylindrical section of the vessel. The inside thermocouples were MgO insulated and sheathed in stainless steel. The sheath at the position of the junction was fastened in position by shim-stock straps spot welded to the surface of the vessel. The outside thermocouples were identical to the inside thermocouples except that the outside junctions were bare and intrinsic, welded directly to the surface of the vessel. The intrinsic junctions were covered with room-temperature-curing Dow Corning 3145 Silicone rubber to protect the wires against physical damage. Seven near-surface intrinsic thermocouples were welded to the bottom of 25-mm-deep holes drilled from the outside surface at locations shown in Fig. 6.1. The junctions were covered with Silicone rubber, and the holes were filled with steel plugs. The inside-surface thermocouples were calibrated by the ORNL Metrology Laboratory by comparison with a

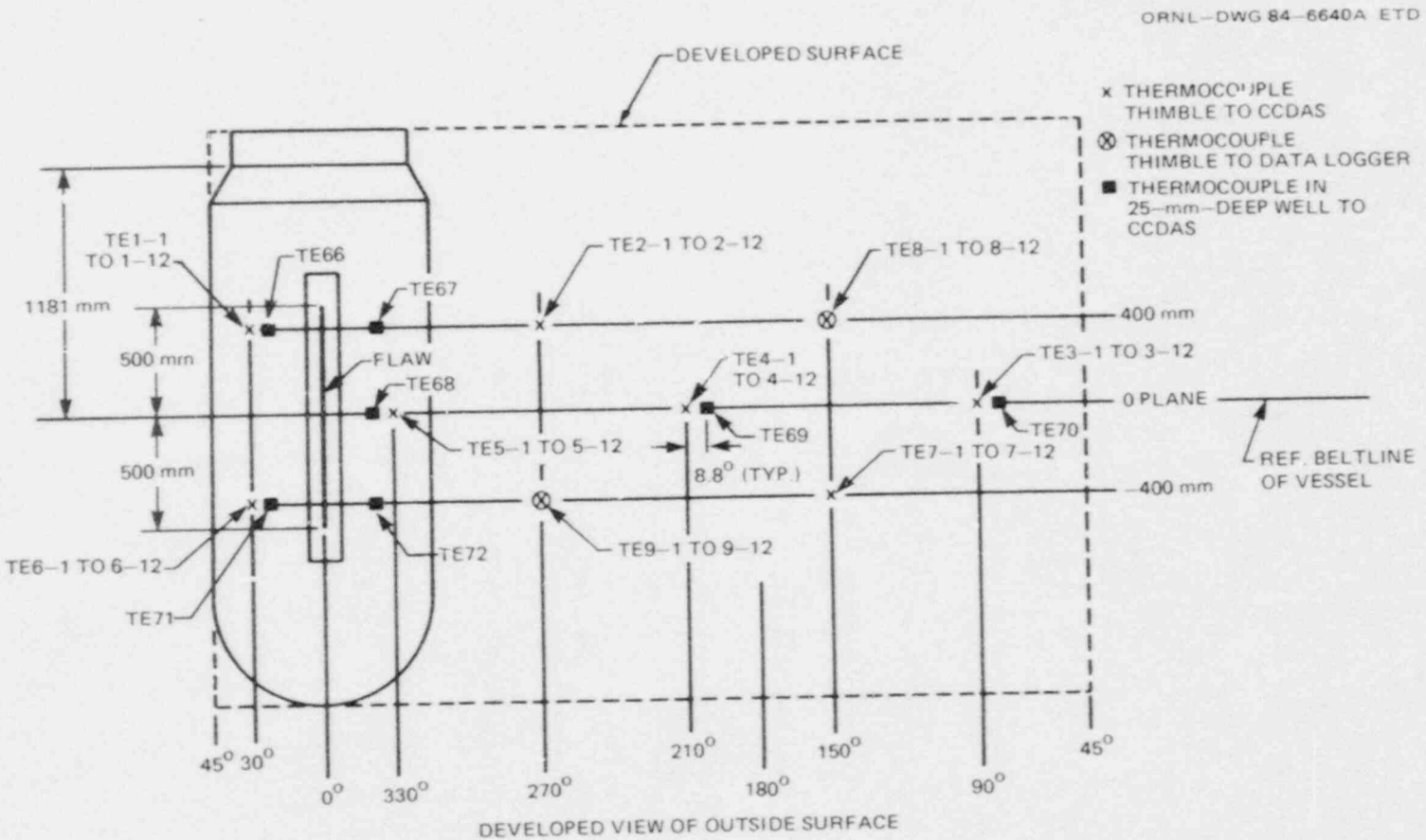

Fig. 6.1. Thermocouple thimble and near-surface thermocouple locations in PTSE-2 vessel. [Computer-controlled data acquisition system (CCDAS).]

laboratory standard type-S thermocouple at five temperatures between 93 and 292°C.

The locations of the surface thermocouples are shown in Fig. 6.2. Included on this diagram are the locations of thermocouples connected to the heater controller. All temperatures were monitored during the heating phase to evaluate the approach to isothermal conditions.

6.2.3 CMOD gages

CMOD gages were placed across the opening of the flaw at 100-mm intervals, as shown in Fig. 6.3. Special types of weldable strain gages,

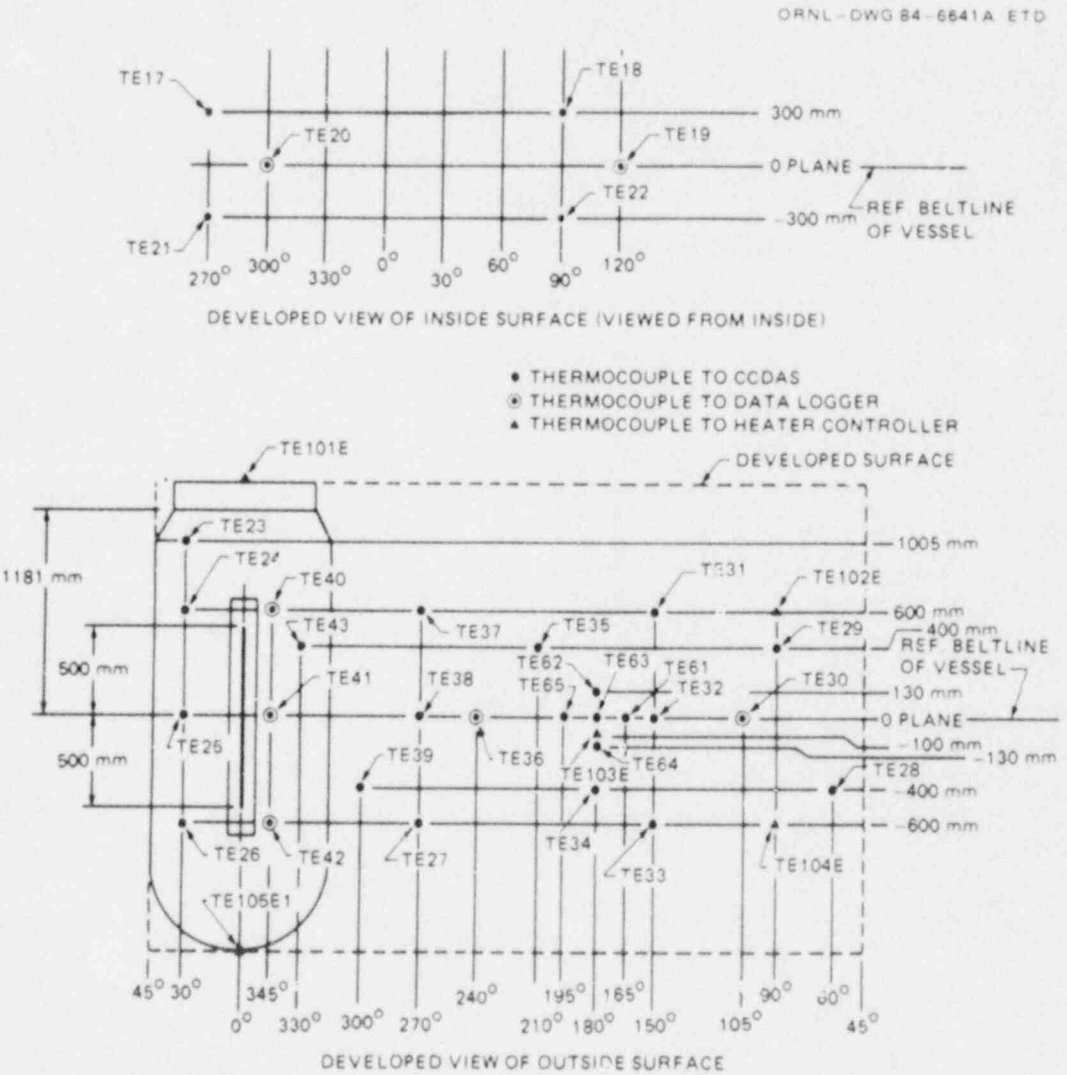

Fig. 6.2. Surface thermocouple locations on PTSE-2 vessel. [Computer-controlled data acquisition system (CCDAS).] As indicated in Table 6.1, TE19 was reconnected to the CCDAS because TE17, 20, and 21 were damaged before the test.

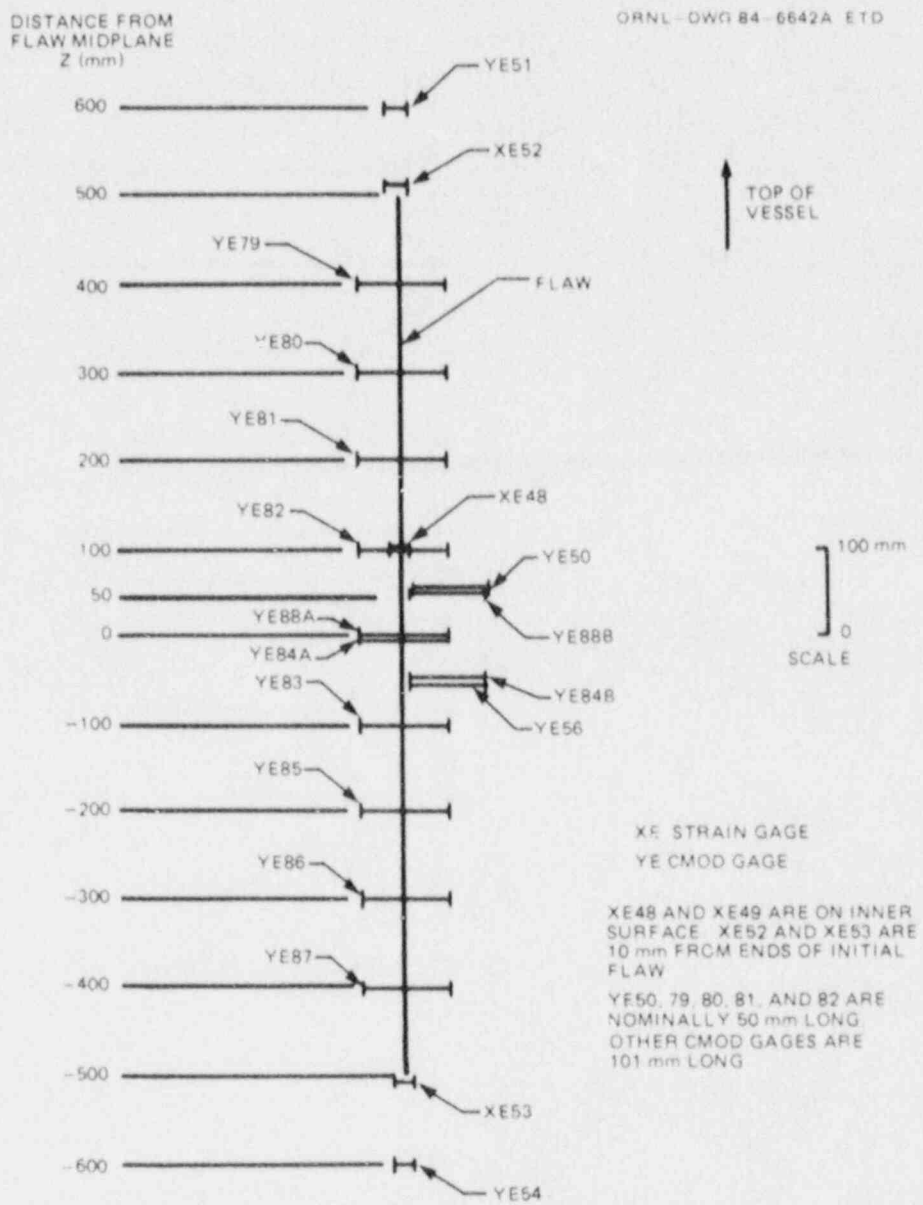

Fig. 6.3. Locations of CMOD gages and strain gages near flaw on PTSE-2 vessel.

50 and 101 mm long, manufactured by the Instrumentation Division of the Eaton Corporation, were used. Fifty-millimeter gages were type DG 125/1-06-15-6S; 101-mm gages were types DG 125/2-06H-26-6S and DG 125/2-06H-15-6. Gages were attached by a pair of short flanges spot welded to the vessel. The CMOD gage installation on the PTSE-2 vessel is shown in Figs. 6.4 and 6.5.

Dummy CMOD gages (YE50, 56, 84B, and 88B) did not cross the flaw. The dummy gages YE84B and 88B were connected in bridge circuits with gages YE84A and 88A, respectively, so that the output of each bridge would be biased to eliminate purely thermal effects. The outputs of the

ORNL PHOTO 7924-86A

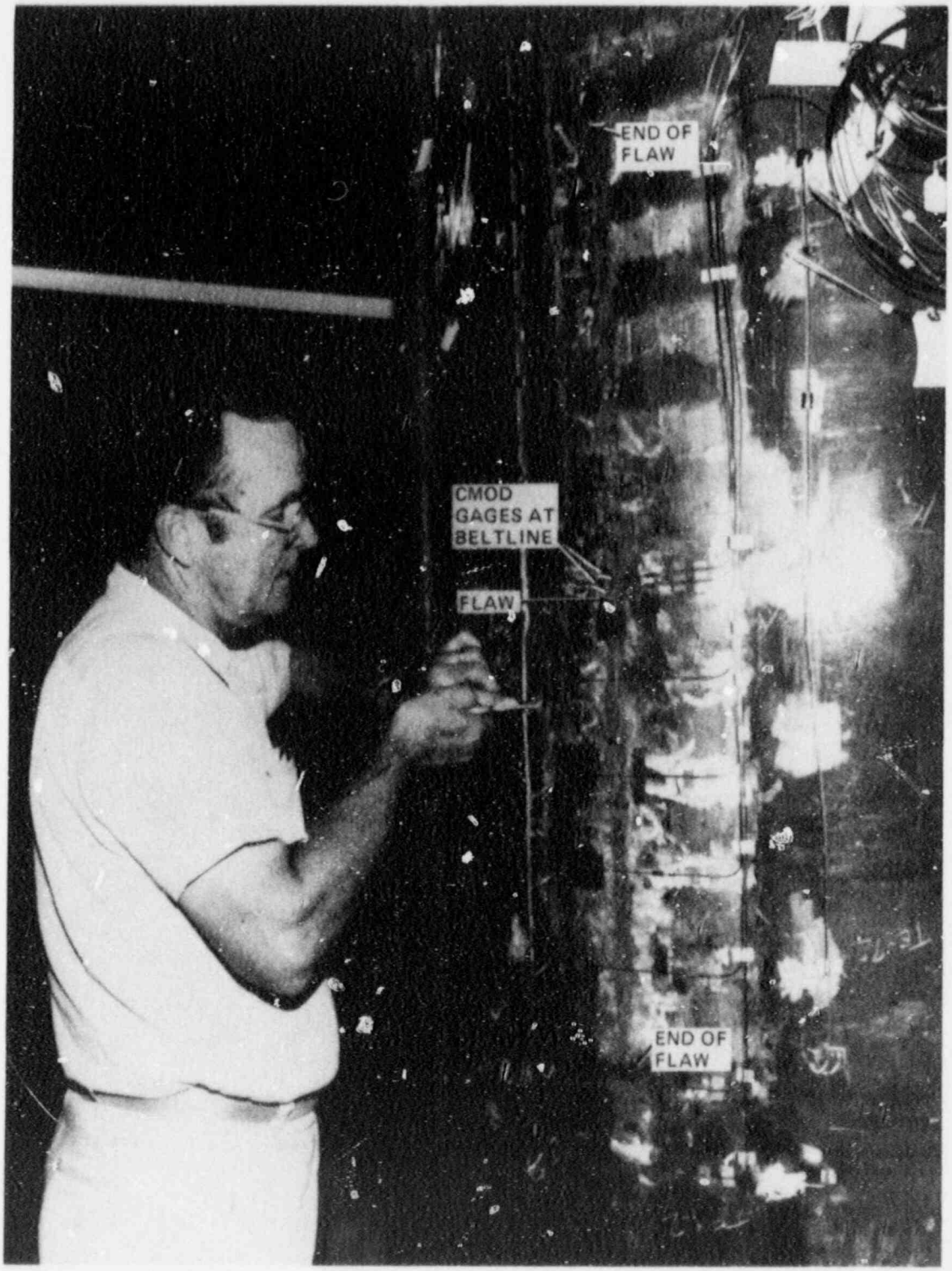

Fig. 6.4. Photograph of PTSE-2 vessel showing CMOD gage installation.

ORNL PHOTO 7921-86A

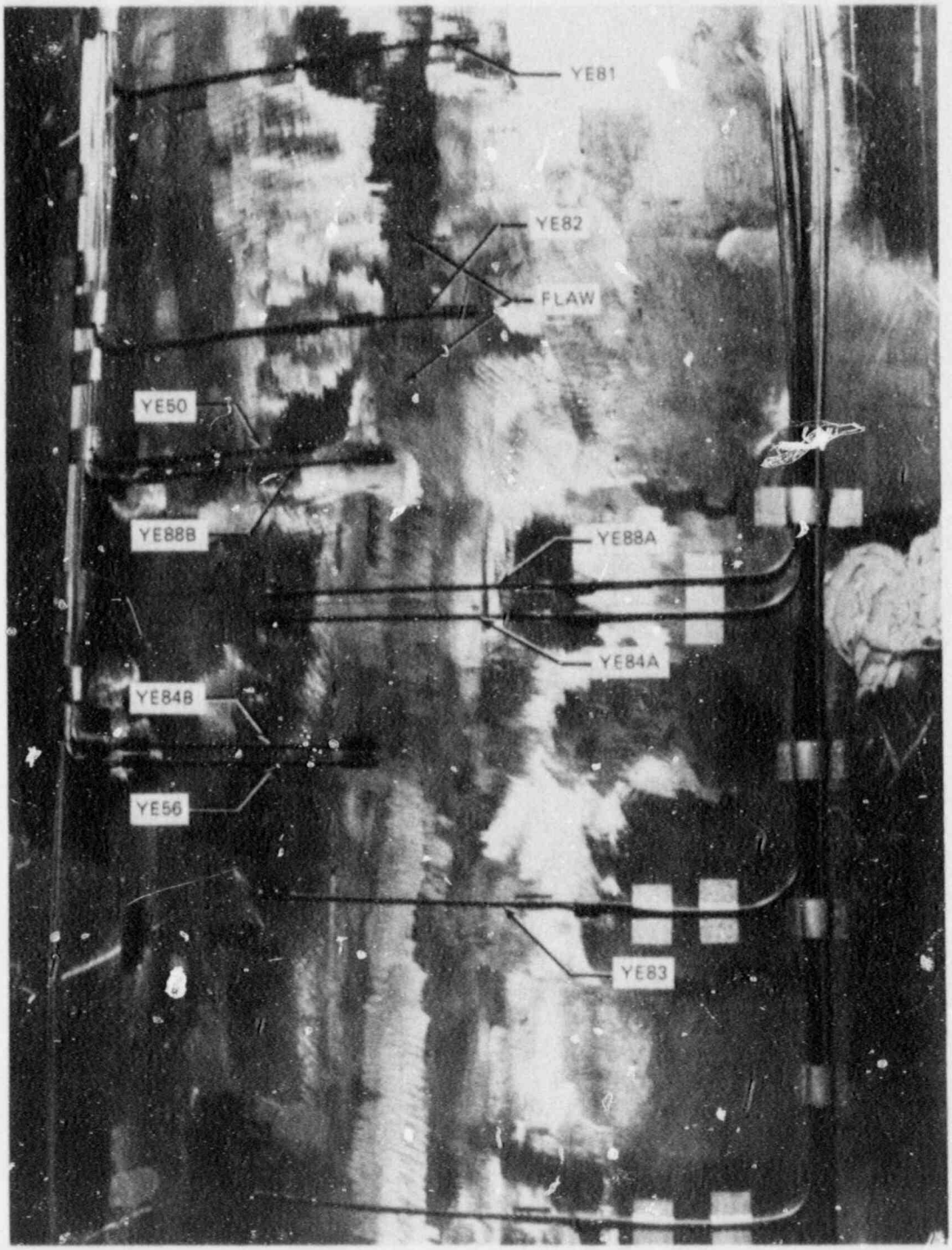

Fig. 6.5. Close-up view of CMOD gages near center of PTSE-2 flaw.

other two dummy gages, YE50 and 56, were recorded so that the magnitude of the thermal effect could be observed directly and adjustments of other CMOD records could be made.

6.2.4 Strain gages

Strain gages were installed on the vessel to evaluate both unexpected events and flaw growth. Gages remote from the flaw provided information that would be useful in evaluating the state of stress in the vessel if some unexpected or unplanned loading should occur. Gages on the inside surface in the plane of the flaw responded to changes in flaw depth. Gages on the outside surface in the plane of the flaw but beyond the two ends responded to changes in flaw length. The gages used were Eaton type SG 125-09F-15-6S with a gage length of 25 mm and a gage factor of 1.85. Locations are shown in Fig. 6.3.

Reference

1. R. H. Bryan et al., *Pressurized-Thermal-Shock Test of 6-in.-Thick Pressure Vessels. PTSE-1: Investigations of Warm Prestressing and Upper-Shelf Arrest*, NUREG/CR-4106 (ORNL-6135), Martin Marietta Energy Systems, Inc., Oak Ridge Natl. Lab., April 1985.

7. PRELIMINARY TESTS

7.1 Objectives

Two broad categories of preliminary tests were conducted on the pressurized-thermal-shock test facility in preparation for the PTSE-2 test series: (1) operational tests accompanied by maintenance and instrument calibration to establish that the test facility was in operational readiness and (2) specific tests designed to verify that the facility had the capability of performing the PTSE-2 test series as configured following the PTSE-1 test series or to establish the modifications necessary and then to verify that the reconfigured system would perform satisfactorily.

7.2 Results

7.2.1 Operational readiness tests

Because of the prolonged period of shutdown conditions for the test facility since the PTSE-1 tests were conducted, each of the subsystems was started and operated for the duration of a typical test to establish that the subsystem was mechanically ready for operation. As expected, some instrumentation and some mechanical systems did not function properly because of the long inactivity. Following resolution of mechanical problems, all instrumentation crucial either to subsystems operation or to PTSE-2 data acquisition was removed, calibrated, and reinstalled as required.

7.2.2 System modification tests

The previously performed PTSE-0 and PTSE-1 tests revealed that the pressurizing system performance was degraded from that anticipated because of three significant factors:

1. greater pressure drop from the accumulator vessel to the PTSE vessel than anticipated,
2. graphite ballast in the test vessels less effective than anticipated, and
3. limited venting capability.

An attempt was made to construct an improved analytical model of the behavior of the pressurizing system shown schematically in Fig. 7.1 with the following assumptions.

1. Although no high-temperature data were available, the compressibility of the silicone oil pressurizing fluid was estimated by adding a thermal expansion term to the existing room temperature compressibility data by the methods of Ref. 1.
2. The compressibility of the graphite was estimated by using the mean of the orthogonally different Young's moduli.

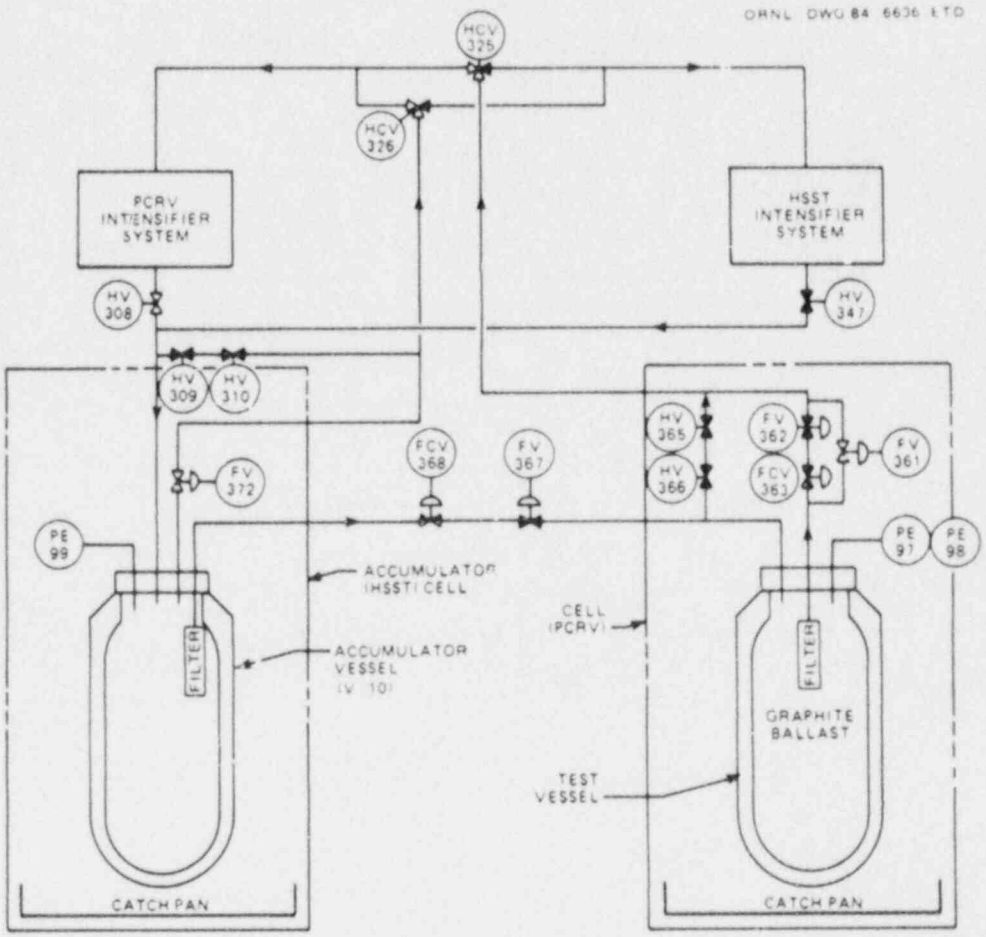

Fig. 7.1. Flow diagram for pressurizing system. [Prestressed-concrete reactor vessel (PCRV), Heavy-Section Steel Technology (HSST).]

3. The graphite pore volume was assumed to be unconnected to the pressurizing medium.
4. The dilation effect as a result of pressure was considered for both the V-10 accumulator vessel and the PTSE-2 vessel.
5. Because of the anticipated pressurizing rate requirement of the PTSE-2A test, 1.0 MPa/s, the transfer valve, FCV 368 on Fig. 7.1, was replaced with one having a flow coefficient C_V of 0.5.

The resulting model behavior calculation, for which results are shown on Fig. 7.2, indicates the peak attainable pressure for pressurizing PTSE-2 from zero pressure to be ~80 MPa and the maximum achievable pressurizing rate to be ~1.90 MPa/s. Valve FCV 368 rangeability was anticipated to permit the achievement of the pressurizing rate of 1.0 MPa/s required for PTSE-2A. After heating the PTSE-2 vessel to 290°C, pressurizing and venting rate tests were conducted for upper and lower pressure levels of 20 and 0 MPa, respectively. Pressurizing rates, varying from 1.66 to 2.14 MPa/s for valve openings varying from 20 to 100%, were observed and agreed roughly with the calculated behavior shown on Fig. 7.2.

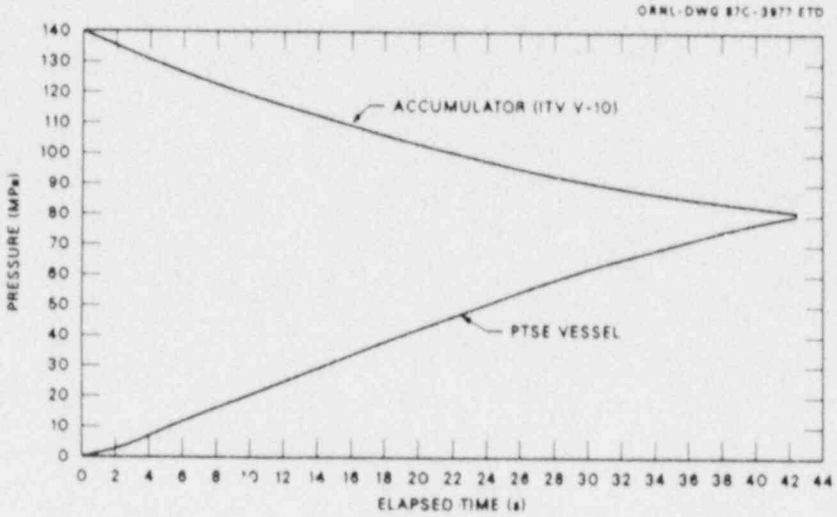

Fig. 7.2. Predicted pressurizing system behavior with flow control valve FCV 368 having flow coefficient, C_V = 0.5.

In connection with the pressurizing rate tests, venting rate tests were also conducted. Results of these tests are shown on Fig. 7.3 in which venting rate is displayed as a function of pressure and which valve or valves are fully open. The PTSE-2A experiment was planned to utilize

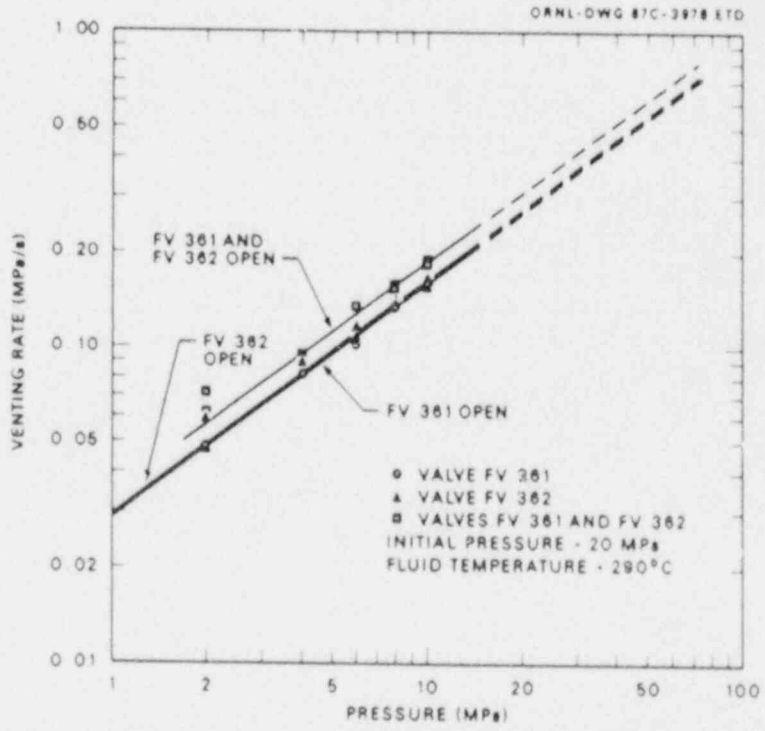

Fig. 7.3. Venting rate characteristics with original vent valve arrangement (Fig. 7.1). Flow control valve FCV 363 was fully open in all cases.

a maximum venting rate of 1.0 MPa/s venting from 60 to 20 MPa. If both venting paths (Fig. 7.1) are used, that is, FV 362 and FCV 363 in one path and FV 361 in the other, the maximum projected venting rate at 60 MPa is 0.7 MPa/s, a clearly deficient condition.

The pressurizing system was repiped as shown on Fig. 7.4 to provide independent flow paths from the PTSE-2 vessel to the control valves FV 361 and FV 362. In addition, valve FCV 363 was eliminated because its small flow coefficient indicated that flow would be too severely constricted through this path. Venting rate tests were again conducted with results as shown on Fig. 7.5. These results indicated that the required

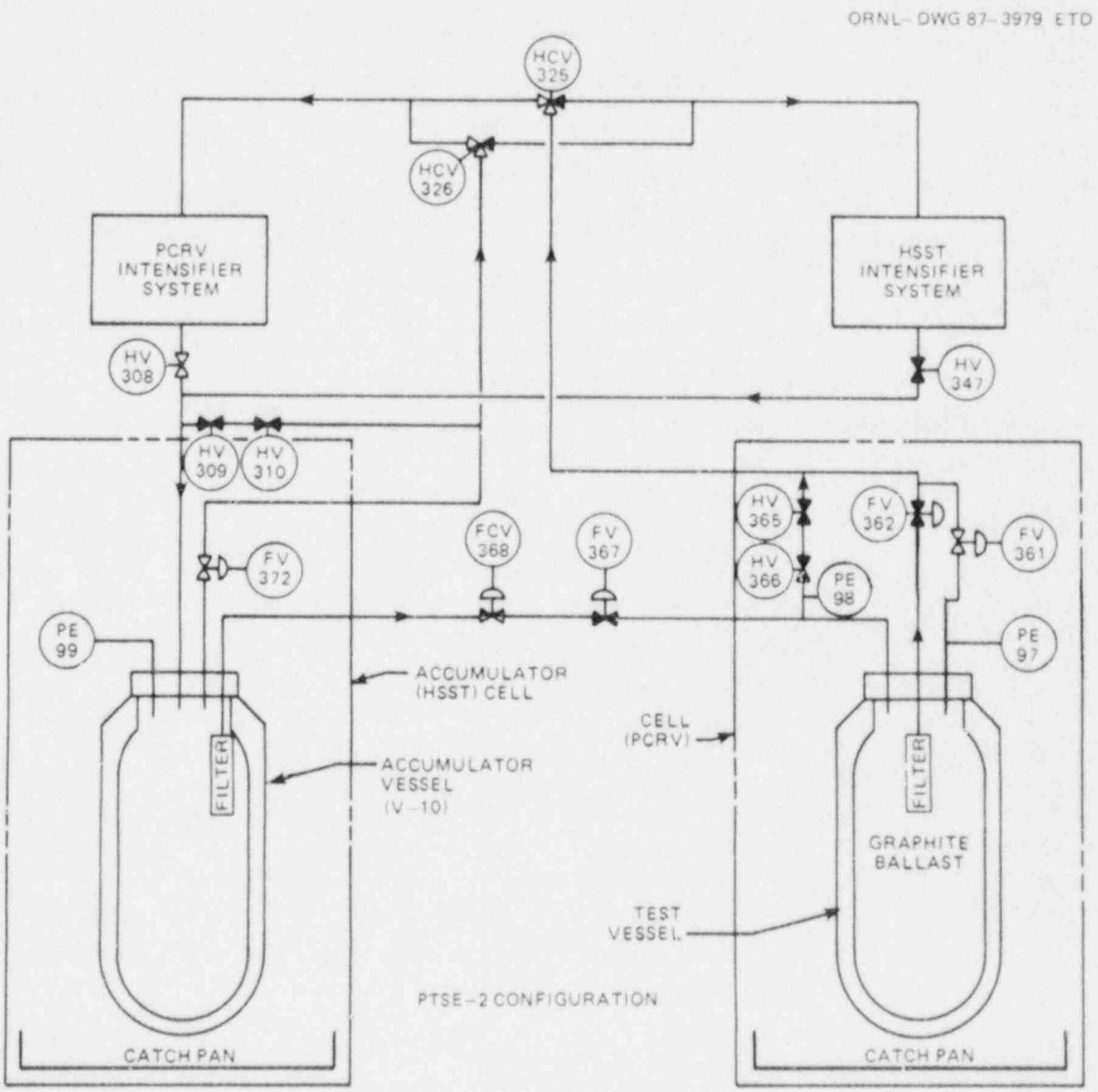

Fig. 7.4. Flow diagram for pressurizing system with modified venting arrangement. [Prestressed-concrete reactor vessel (PCRV), Heavy-Section Steel Technology (HSST).]

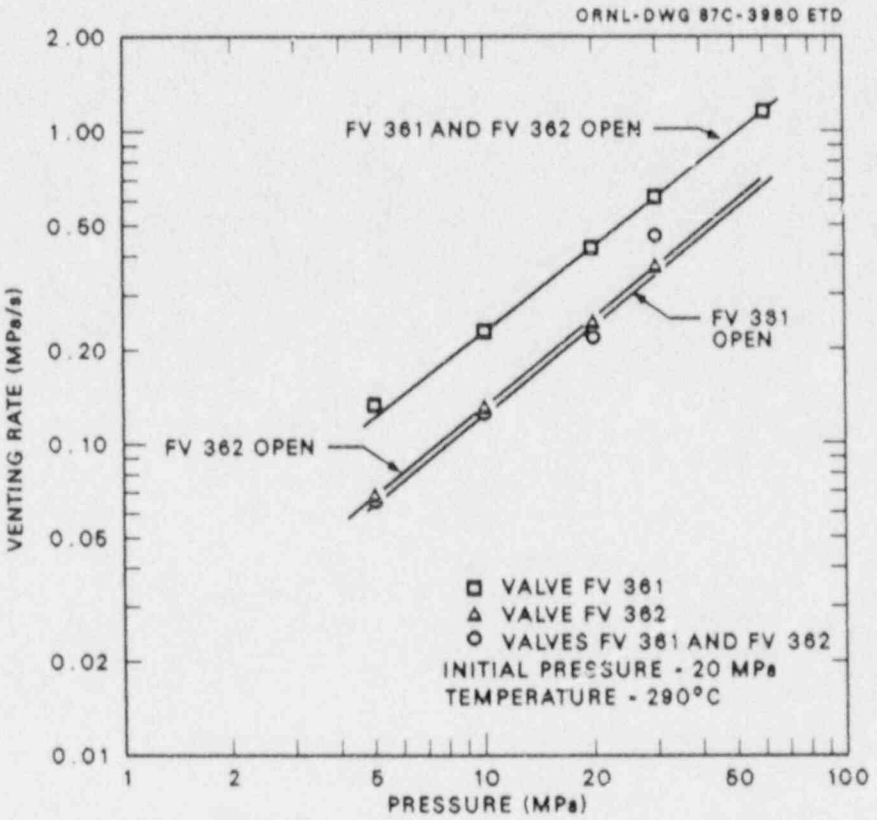

Fig. 7.5. Vent rate characteristics with modified arrangement (Fig. 7.4).

PTSE-2A depressurization rate could be attained with a slight modification in the plan, that is, an exponential depressurization curve replacing the originally planned bilinear depressurization curve. Both vent paths would be required in this case.

The valve with a flow coefficient C_V = 0.5, used satisfactorily for FCV 368 in the PTSE-2A transient, was incapable of regulating flow to obtain the lower pressurizing rates, ranging from 0.11 to 0.33 MPa/s, as required for the PTSE-2B transient. Consequently, between the PTSE-2A and PTSE-2B tests a valve having a flow coefficient C_V = 0.08 was substituted into the FCV 368 position shown in Fig. 7.4 and pretested. Results of the pretest shown in Fig. 7.6 indicated that the substituted valve could provide adequate regulating control for the PTSE-2B test.

7.2.3 Flow verification tests

The heat transfer conditions for the PTSE-2 tests were planned to be a duplication of the PTSE-1C test. Consequently, a 7.94-cm-ID load orifice, as used in the PTSE-1C test, was placed at the outflow flange position on the shroud (Fig. 7.7). Other physical conditions (e.g., temperature, fluid composition, and PTSE-2 vessel/shroud annulus size) were considered to be virtually identical so that a virtually identical response

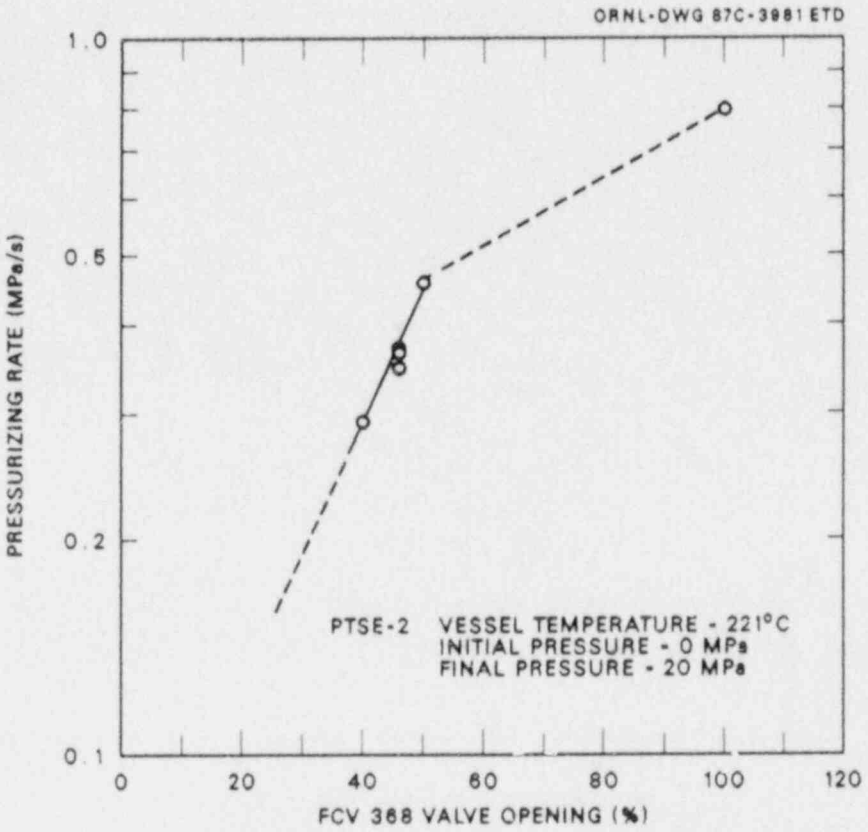

Fig. 7.6. Pressurizing characteristics for PTSE-2B test with flow control valve FCV 368 modified to have flow coefficient, C_V = 0.08.

was expected in flow pretests. Two surprises that occurred during flow pretests of the system shown in Fig. 7.7 are illustrated in Figs. 7.8 and 7.9.

As shown in Fig. 7.8, a delay of 17 s occurred between the time of energizing the pump motor and the initiation of flow to the shroud, as indicated by the pump control signal JY101 and flow orifice reading FY202 in Fig. 7.8. In Fig. 7.9 flow to the shroud (FY202) and flow from the shroud (FY206) are plotted as a function of the time elapsed from the start of data scanning. Flow from the shroud FY206 responded at the same time as that to the shroud FY202 but did not reach full flow conditions for an additional 260 s. Such delays were unprecedented in all previous operations of the coolant system. Furthermore, when achieved, full flow exceeded that achieved in the PTSE-1C by ~25%.

A hypothesis consistent with these observations and previous tests was that some type of construction debris had partially choked flow from the pump during PTSE-1C and had subsequently migrated around the loop and partially choked to the pump. With regard to the anomaly of Fig. 7.8, in all previous operations of the systems, to initiate flow, valve HCV4 was opened, and then after a lapse of 5 s, the recirculation pump was started. To determine whether 5 s was adequate with the assumed partial blockage, a test was made to determine the time required after opening

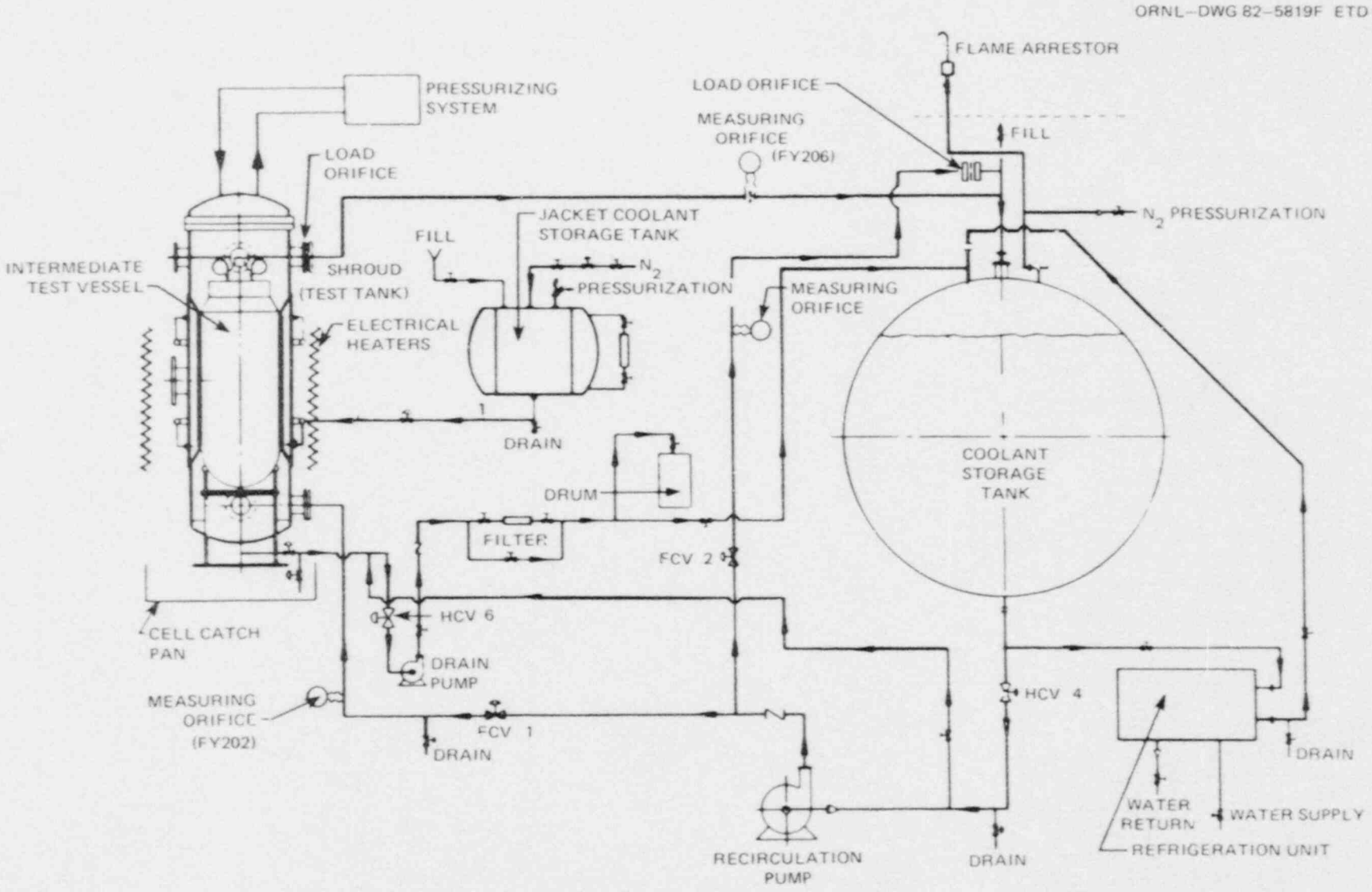

Fig. 7.7. Simplified flow diagram of main coolant system of pressurized-thermal-shock test facility.

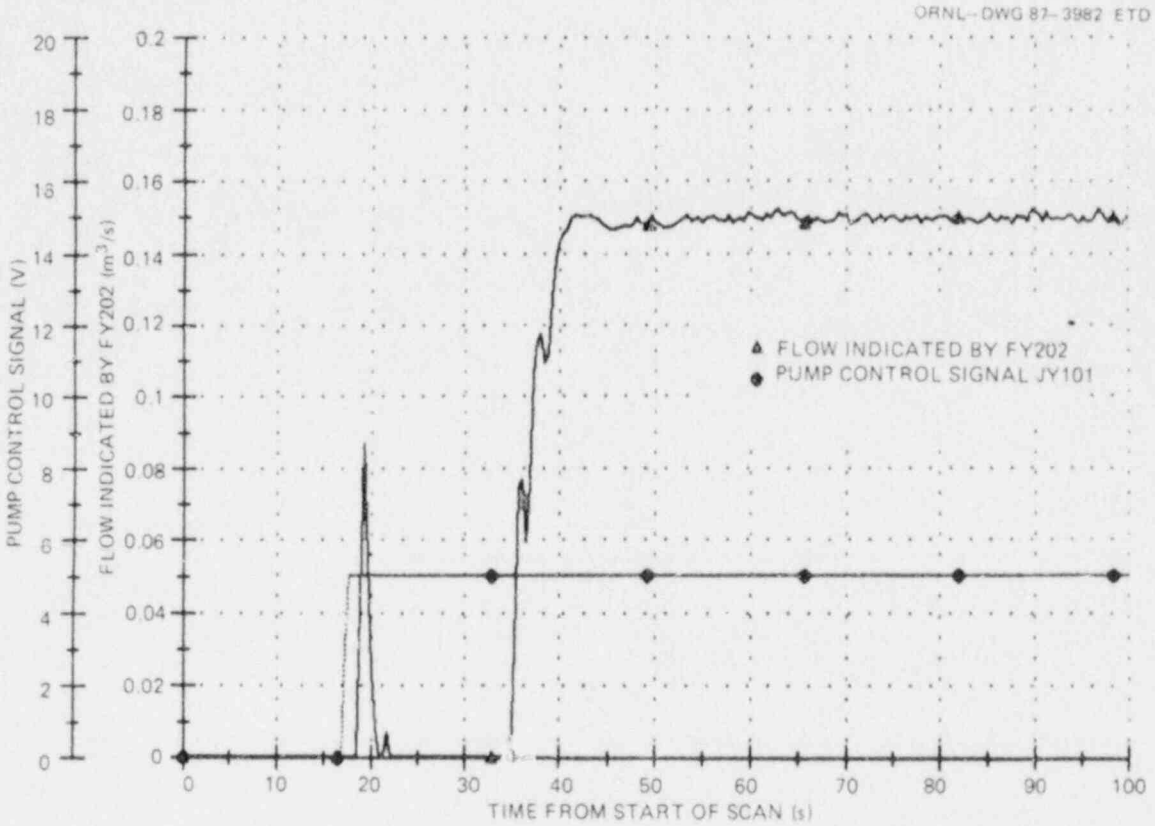

Fig. 7.8. Unsatisfactory recirculation pump flow-time response. In this trial the flow was not established until 17 s after the start of the pump.

HCV4 to provide coolant to the pump. A result of 10 s seemed to confirm the hypothesis of flow blockage. The operating procedure for the coolant system was revised to incorporate a 12-s delay between HCV4 opening and pump starting. All subsequent coolant system operations and the flow responses were normal.

To assess the potential effect of the higher flow conditions, calculations were made using the standard Sieder-Tate heat-transfer correlations[2] and a modified (12 1/2% lower values) Sieder-Tate correlation both with and without an assumed fouling factor. For simplicity the transient temperatures for the shroud, PTSE-2 vessel, and bulk coolant were assumed to be about the same as the PTSE-1C conditions. Physical values used in the heat-transfer correlations were, therefore, premised on the PTSE-1C temperature conditions; flow rates, however, were premised on the PTSE-2 pretest values. These heat-transfer rates were then used in the analysis to finalize the PTSE-2A test transient.

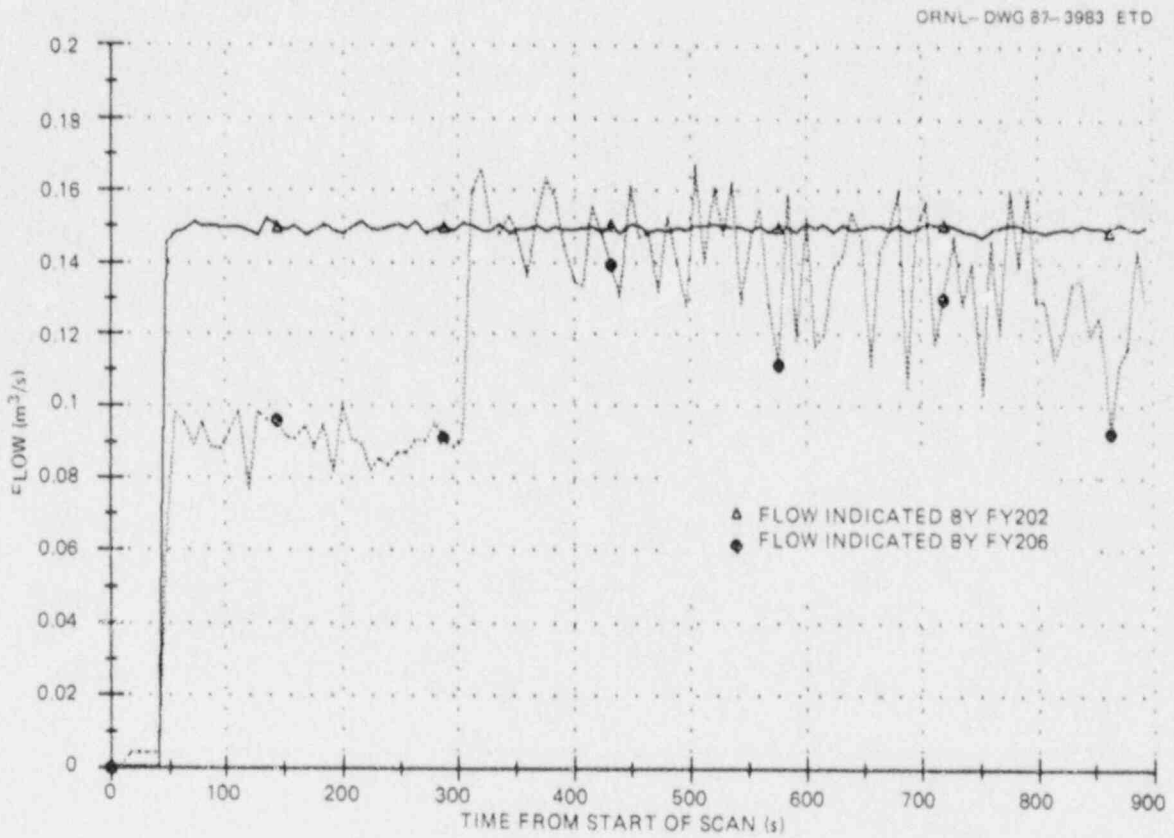

Fig. 7.9. Unsatisfactory recirculation pump flow-time response. This shows an anomalous mismatch of flows into and from the shroud.

References

1. R. S. Bradley and D. C. Munro, *High Pressure Chemistry*, Pergamon Press, Oxford, England, 1965, p. 42.

2. W. H. McAdams, *Heat Transmission*, 2d ed., McGraw Hill Book Co., New York, 1942, p. 168.

8. PTSE-2 EXPERIMENT

The PTSE-2 experiment was performed in two transients, the first on November 25 and the second on December 10, 1986. The experiment consisted of an installation phase, test-facility operations, and postoperational activities. In the installation phase, the PTSE-2 test vessel was placed in the test shroud, instrumentation circuits were completed, the main coolant and pressurization systems were closed, and all operating systems were made ready for operation. The test-facility operation for each transient started with a pretransient phase of a few days duration, followed by a pressure and thermal transient lasting a few minutes. The operation terminated by placing the testing system in a standby condition. Data records were secured in the terminal phase of operations. Postoperational activities included processing of data, removal of the test vessel, and examination of the vessel and flaw. This chapter describes these activities up to the point of vessel and flaw examinations, which are discussed in Chap. 9.

Both transients in the experiment were conducted successfully and generated the fracture conditions and modes that had been planned. During the first transient (PTSE-2A) the flaw first tore depthwise in a ductile mode, then propagated rapidly by cleavage, arrested, and finally tore again until the pressure was reduced. The cleavage fracture propagated both depthwise and lengthwise. During the second transient (PTSE-2B) the flaw first tore depthwise, propagated rapidly by cleavage, arrested, and immediately tore rapidly until the vessel ruptured.

8.1 Pretest Activities

The test vessel was fully instrumented, sealed, filled with the pressurizing fluid, and leak-tested at low pressure before being transported to the test site. The instrumented PTSE-2 vessel is shown in Fig. 8.1. In preparation for inserting the test vessel in the shroud, capacitance gap gages were attached to the cylindrical surface of the test vessel and calibrated in place. After the vessel was set into the shroud, the concentricity of the test vessel and shroud surfaces was measured by the gap gages and adjusted by means of a centralizing assembly attached to the closure flange of the test vessel (Fig. 8.2). The gap gages were removed before the shroud was closed.

8.2 Experimental Sequences

Test facility operation for each transient consisted of three phases:

1. pretransient phase, during which all system and equipment checks were made, the stored coolant was refrigerated to the desired temperature, the data acquisition system was set up to process and store data, the

ORNL PHOTO 7923-86

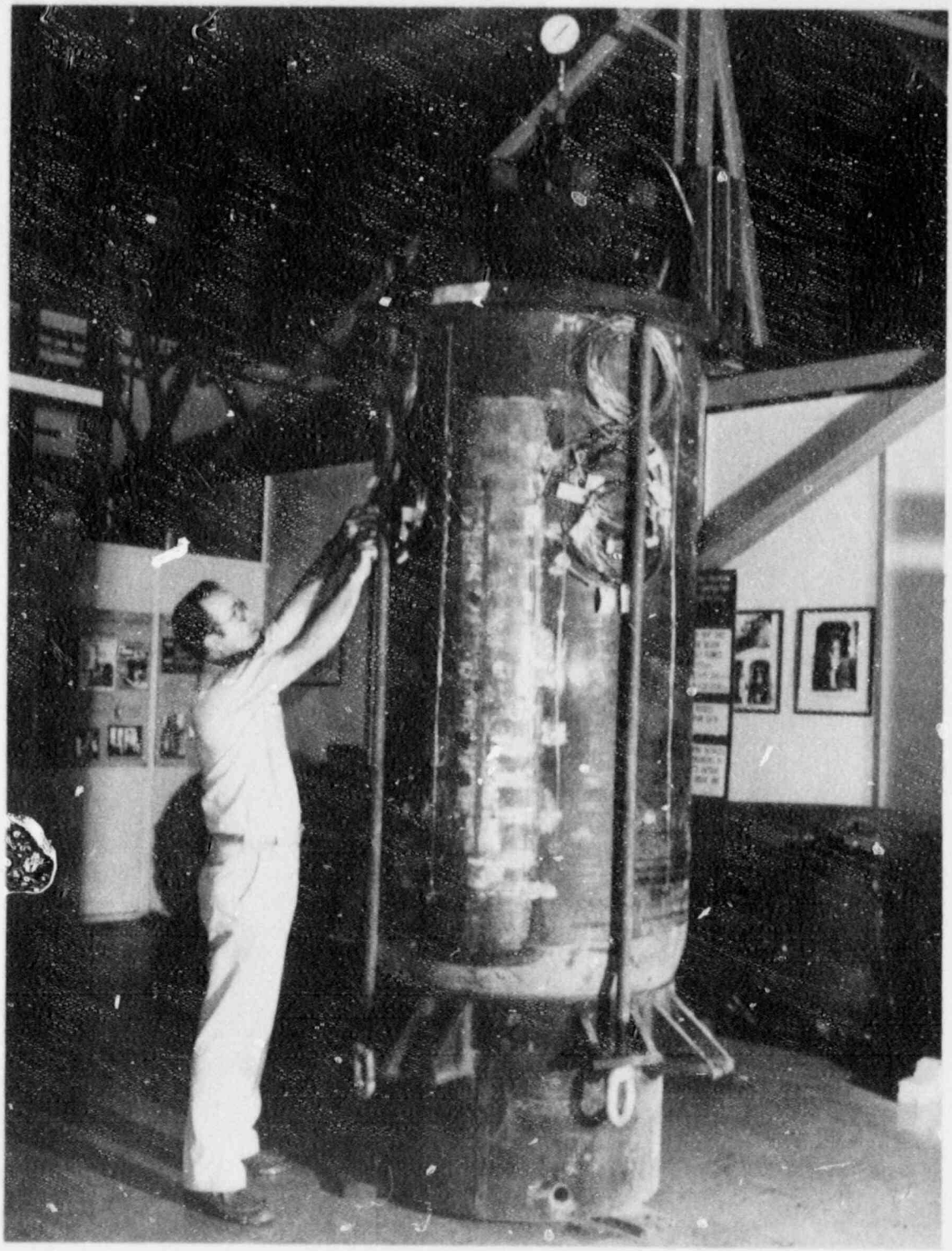

Fig. 8.1. Photograph of fully instrumented PTSE-2 vessel.

ORGDP PHOTO 86-3250A

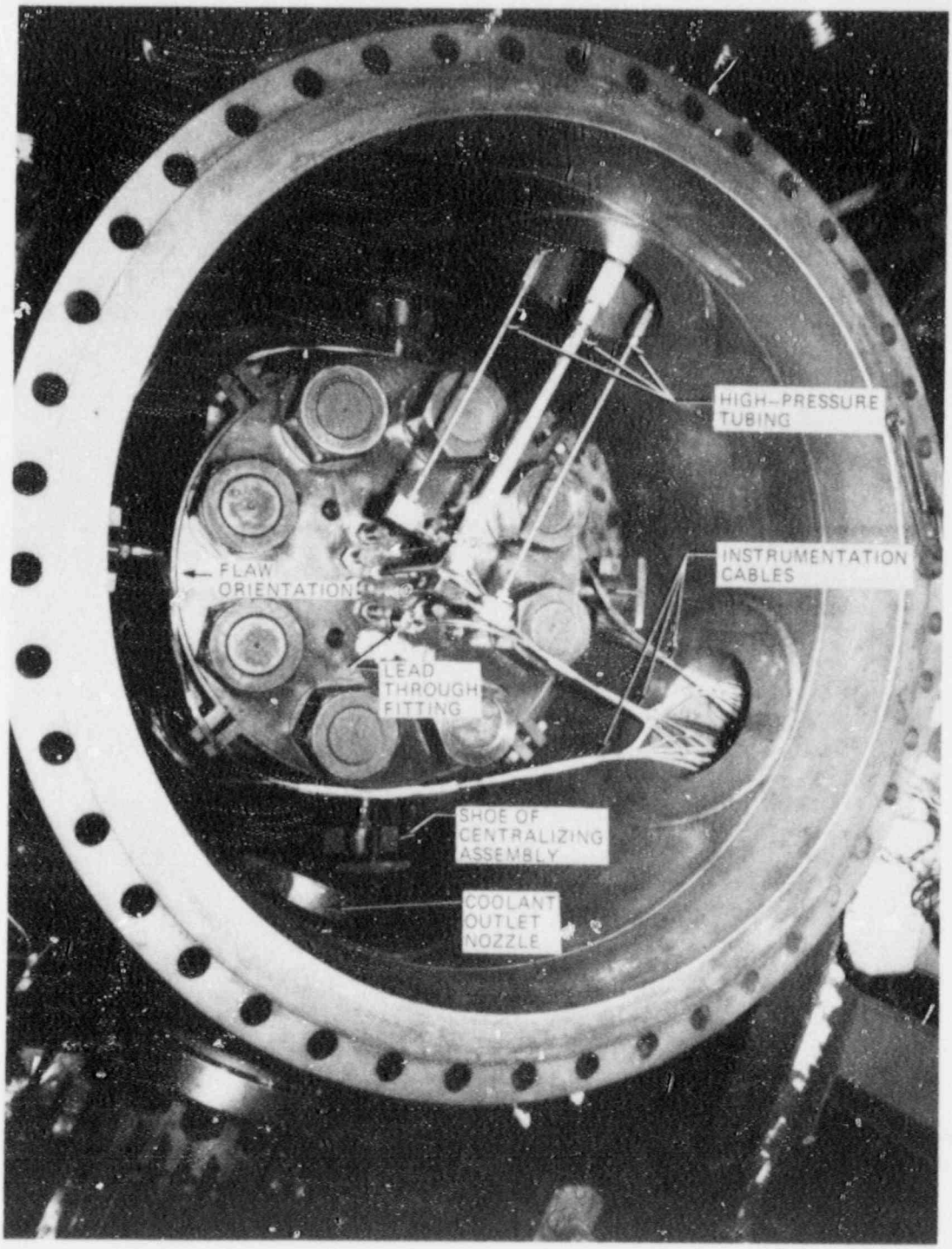

Fig. 8.2. Photograph of PTSE-2 vessel in test tank. The head centering fixture, high-pressure tubing connections, and sheathed instrumentation cables are visible. The arrow marked on the vessel head indicates the azimuthal location of the 1-m-long flaw.

heat-up of the test vessel was accomplished, the pressurization system was activated, final sensor calibrations were made, and readiness of all systems for the transient was confirmed;

2. transient phase, during which, sequentially, coolant was admitted to the shroud, steady flow was established along the cylindrical surface of the test vessel, the test vessel was pressurized in coordination with the thermal transient, crack behavior was monitored by observing CMOD gage readings, and the transient was terminated by depressurizing the test vessel and stopping coolant flow; and
3. posttransient phase, during which the coolant was pumped from the shroud to the storage tank, the test facility was put into a standby condition, and recorded data were copied and secured.

The control room of the test facility was equipped to present graphical and digital displays of information needed in conducting the operation. Pretransient conditions were monitored by strip-chart recordings of shroud and test vessel temperatures. All other system and test vessel sensors were displayed continuously or on demand by monitors in the main data acquisition system or the data logger.

The transients lasted ~270 and 430 s. The thermal transient was initiated by manual activation of controls with a delay of ~12 s. After initiation the thermal transient required no further planned action until a termination command was issued. The pressure transient was initiated and continuously controlled by manual manipulation of flow control valves. The operator followed a predetermined pressure history drawn on a strip-chart record of pressure. The strip chart was started automatically by a signal from the main coolant pump switch.

Plans were made to alter transient operation under some contingencies. Almost all decisions to alter a transient would have to be made within the first 60 s. The conditions that required monitoring for making operational decisions were coolant flow, nominal heat transfer coefficient, crack depth (estimated from changes in CMOD), and test vessel pressure.

Initial temperatures. The prescribed initial temperature of the test vessel was established by the shroud heaters, which were adjusted during the last few hours before a transient to produce nearly isothermal conditions in the cylindrical section of the vessel. Heater power was turned off during transients. The required initial temperature of the stored coolant was established by the operation of the refrigeration system, usually for a few days prior to each transient.

Coolant flow. Essentially steady state flow was normally established between 5 and 10 s after starting the main coolant pump. If the flow were too low, the transient would be terminated immediately. Valve positions and flows indicated on the control panel determined whether satisfactory flow conditions were obtained.

Heat transfer. Two transients, designated PTSE-2A and -2B, were conducted in the PTSE-2 experiment. The first transient (PTSE-2A) was preceded by flow tests with the entire system at ambient temperature (see Chap. 7). Although coolant flow rates were higher than in the PTSE-1 experiment, it was concluded that PTSE-1C heat-transfer rates were reasonably close to the rates expected in PTSE-2. The two transients were performed satisfactorily, confirming the validity of this conclusion.

Crack depth. For each transient, pretest analysis permitted estimates of expected crack growth. Decisions to terminate the transients at the proper time had to be made quickly and reliably to avoid conditions that might prevent attainment of test objectives.

Crack depth can be related to CMOD at any particular time in a well-defined transient. Test data were converted to crack depth by a microcomputer, and the results were plotted several times per second on a monitor. Also, CMOD values were displayed on strip-chart recorders in the control room. At any time that a sudden change in CMOD was observed, the change was graphically converted within ~10 s to crack depth by the test crew. The pretest computations that permitted this conversion are discussed in Chap. 10.

Pressure. Prior to each transient, the accumulator in the pressurization system was pressurized to 138 MPa, and the pressure of the test vessel was adjusted to the prescribed initial level. Actual pressure was monitored by the operator of the pressurization system and independently by another crew member. Pressure transients were permitted to follow the courses predetermined for the transients. The PTSE-2A transient was terminated by manual action when the crack depth observations indicated a sudden jump. In the PTSE-2B transient, the rapid crack jump ruptured the vessel, which rapidly reduced the pressure to ~5 MPa.

8.3 Processing Recorded Data

The highest priority task after the completion of a test was to secure the data recorded on magnetic tape by the primary data acquisition system. All data tapes were immediately copied to produce a working copy and duplicate tapes for filing separately in secure archives. Recorded data could also be printed or plotted immediately by the data acquisition system as needed for evaluating system performance.

The computer programs developed for PTSE-1 for processing the primary tapes were used for the PTSE-2 experiment. The purpose of these programs was to present data for convenient evaluation of sensor performance and the data themselves, to condition data for input to the OCA/USA (described in Chap. 10) and other computer programs, to generate on-line data sets representing raw and adjusted data, and to plot data from the on-line data sets.

8.3.1 Evaluation of performance

Every variable was plotted vs time from the raw data. Sensors that gave inconsistent or anomalous values and particular data records that were outside a reasonable range of values were identified. Very few sensors were unsatisfactory. All CMOD, thermocouple thimble, and inside-surface temperature data were useful. Both pressure transducers on the test vessel were satisfactory, but essential high-pressure tubing modifications made immediately before the test resulted in one transducer (PE97) being on the vent line and the other (PE98) on the fill line. Because the measured pressure is representative of the vessel pressure only when flow in the line between the point of measurement and the

vessel is approximately zero, the data from the transducers had to be interpreted with the operating status taken into account.

The operation of the computer-controlled data acquisition system was entirely satisfactory. Consequently, the data recorded by the data logger, including temperatures from thimbles 8 and 9, were not processed for posttest analysis.

8.3.2 Conditioning of temperature data for input to OCA/USA and ADINA

Thermocouple signals were converted into temperature values by the data acquisition system by means of standard conversions published by the National Bureau of Standards.[1] The thimble and inside-surface thermocouples were individually calibrated in the laboratory against a standard thermocouple. One function of posttest processing was to adjust the raw temperature data from each thermocouple by its individual calibration expression

$$T_x - T = a_0 + a_1 T + a_2 T^2 \ , \qquad (1)$$

where T_x is the temperature inferred from the experimental thermocouple (or the raw temperature); T is the temperature inferred from the standard thermocouple (or the true temperature); and a_0, a_1, and a_2 are coefficients determined by least-squares fit of the calibration data. For thimbles 1 to 7, the coefficients were small, as discussed in Chap. 6, and were consequently set to zero in posttest data processing.

PTSE-2 and calibration laboratory data from each thermocouple were reviewed for inconsistencies with physical reality. In cases in which an error was evident, the thermocouple was omitted from the list of those to be processed by OCA/USA unless a rational correction could be justified. Of the 84 thermocouples in thimbles 1 to 7, 15 were omitted, and 15 thermocouples had their positions transposed. Errors of location transposition were easily evident because they produced a reversed gradient. They were caused by errors in labeling of cables or connecting thermocouple wires to terminal strips. Locations of individual junctions within thimbles were stated by the manufacturers to be within 0.13 mm of the nominal depth. After the test, the thimbles were disassembled and locations of individual junctions were determined by radiography. Discrepancies in precise locations were taken into account in generating profiles for final posttest OCA/USA and finite-element analyses.

Temperatures for thermal stress computations by OCA/USA or ADINA must be defined over the domain of the entire thickness of the test vessel wall (147.6 mm); thimble measurements, however, extend only to a depth of ~100 mm from the outside surface. Furthermore, thimble and wall temperatures at the same depth are slightly different. The type of temperature profile generated for OCA/USA and ADINA input is illustrated by the dashed curve in Fig. 8.3. This profile was obtained by a nonlinear mapping of the temperature-depth coordinates of the thimble (T, x) to the temperature-depth coordinates of the vessel wall (T′, x′), as described in detail in Ref. 2. This mapping leaves the position and temperature at

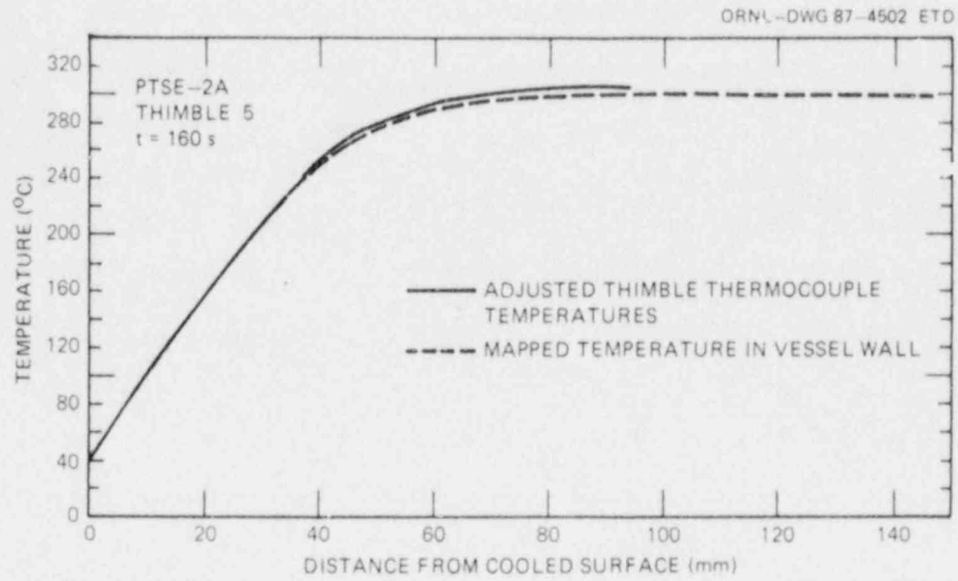

Fig. 8.3. Typical temperature profiles in thermocouple thimble and vessel wall. The effect of the mapping procedure is illustrated.

the cooled surface unchanged, and the position and temperature at the deepest thermocouple are mapped to coincide with the depth and temperature at the inside surface where there is a measured temperature. The mapping functions have the effect of changing temperature and position relatively little near the cooled surface. The results of calibration and coordinate adjustments are shown in Figs. 8.4 and 8.5 for thermocouple thimble 5, which is the thimble closest to the centerline of the flaw in the test vessel.

8.4 Transient Data

Pressure and temperature data characterize the loading history of each transient in the experiment; strain and CMOD data characterize the resulting response of the vessel and flaw. Examples of these data are presented here to identify important events in each transient. A complete set of graphical representations of temperature, pressure, CMOD, and strain data for the two PTSE-2 transients is presented in Appendix B.

The initiation of the thermal transient is marked by a sudden drop in the temperatures measured by outside-surface thermocouples. This drop is illustrated in Fig. 8.6 for the two transients. The PTSE-2A transient started at nominally 112 s from the start of the data scan and was terminated by depressurization and by stopping the main coolant pump at ~370 to 380 s. The pressure transient superimposed on the temperature plot in Fig. 8.6(*a*) shows the effect of thermal contraction of the vessel on the hydrostatic pressure of the vessel while valves in the pressurization system were closed so that no fluid could escape. The pressure transient imposed by the external pressurization system started at 185 s. The

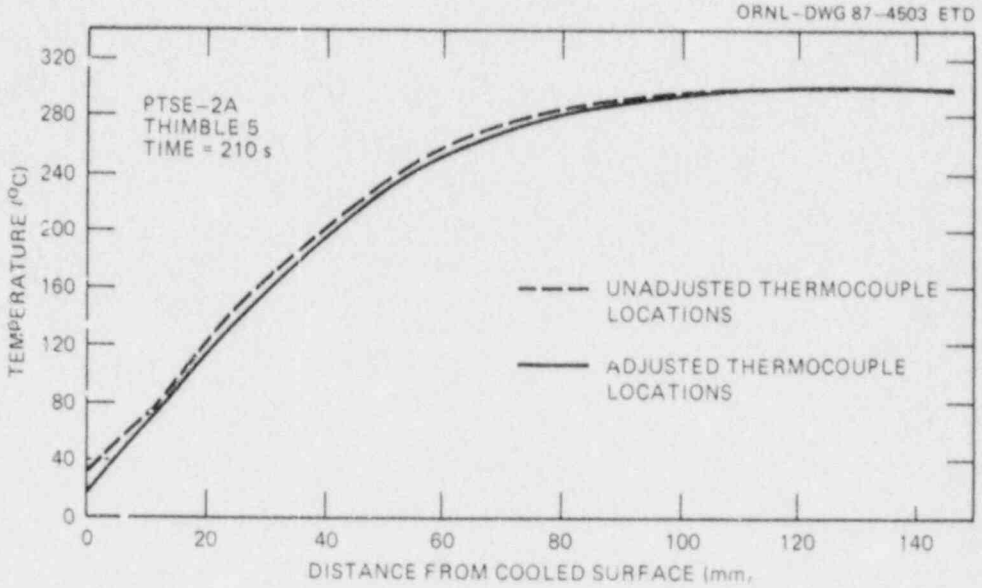

Fig. 8.4. Temperature profiles generated from data from thermocouple thimble 5 at 210 s in transient PTSE-2A. The effect of correcting junction locations is shown.

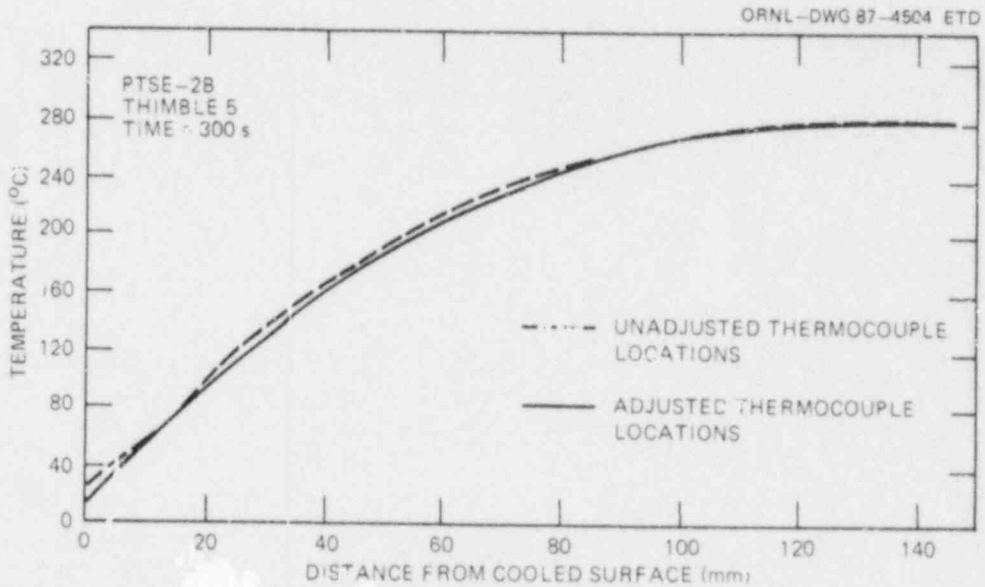

Fig. 8.5. Temperature profiles generated from data from thermocouple thimble at 300 s in PTSE-2B transient. The effect of correcting [illegible] shown.

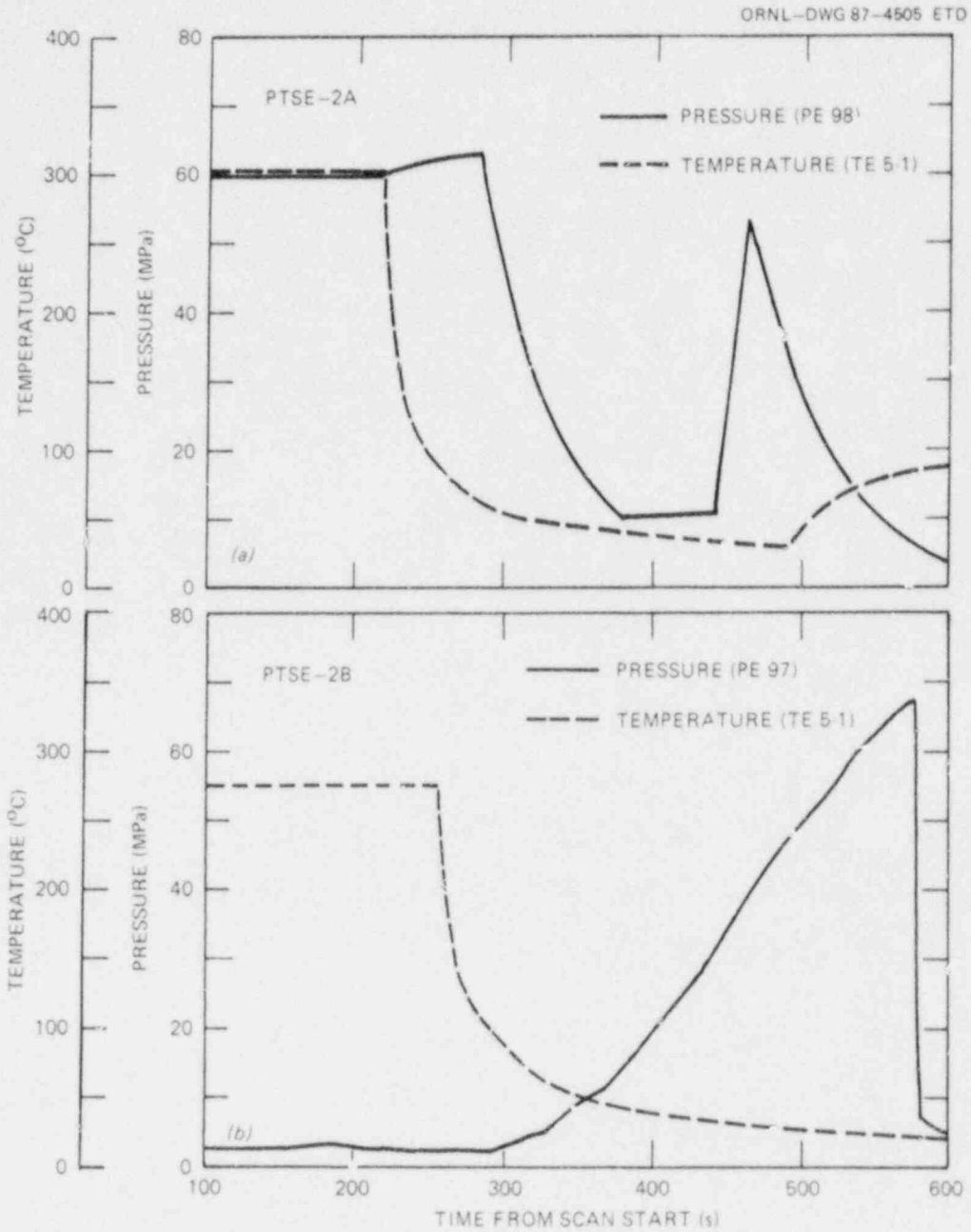

Fig. 8.6. Temperature and pressure data vs time recorded for PTSE-2 transients. (*a*) PTSE-2A and (*b*) PTSE-2B.

PTSE-2B transient started at ~155 s from the start of the scan and was terminated by depressurization at ~577 s.

The pressure transients near the times of the fast crack jumps in the A and B transients are shown in Fig. 8.7. The plot for PTSE-2A [Fig. 8.7(*a*)] is a composite of values measured by the two pressure transducers. The composite takes account of the recorded positions of

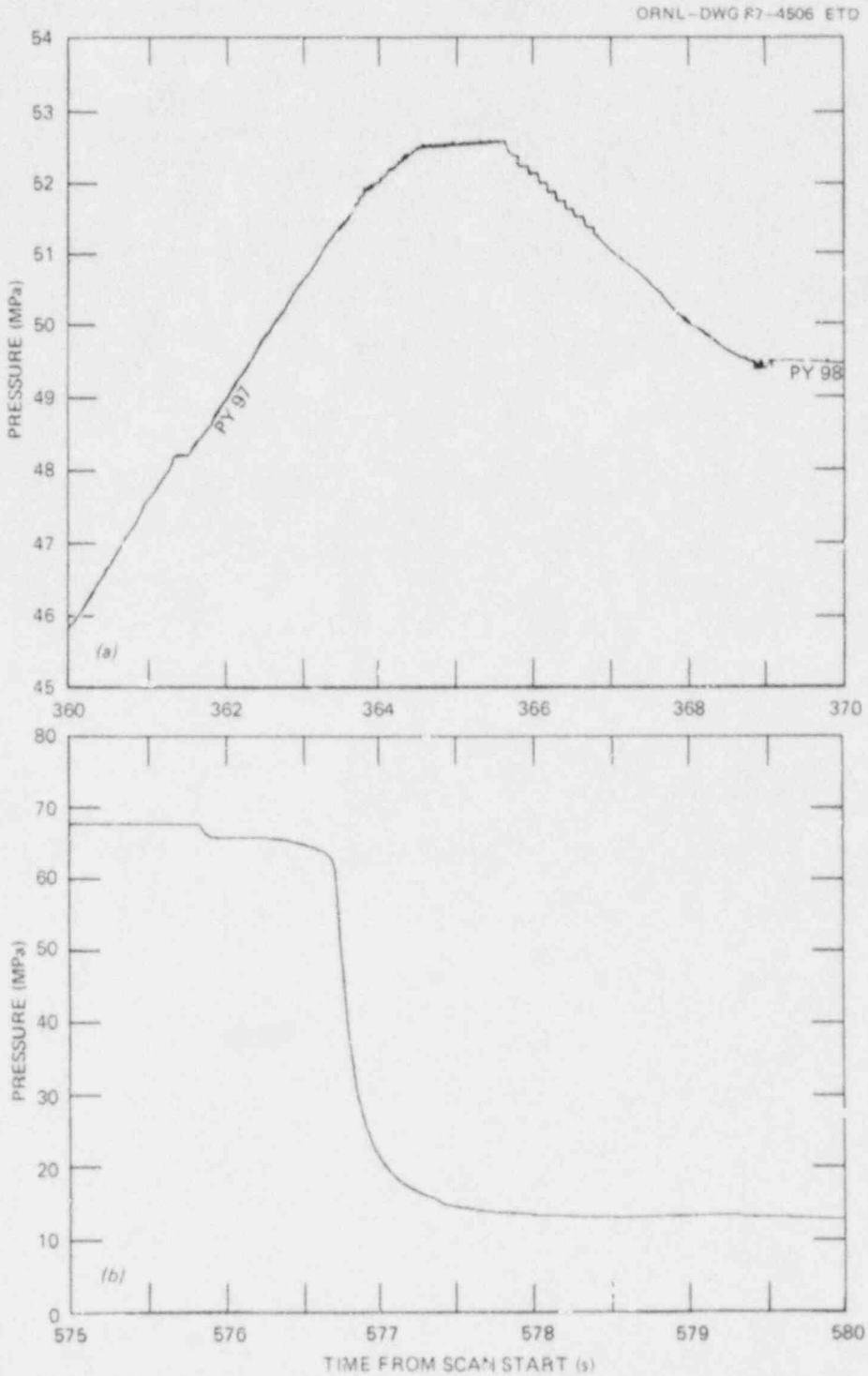

Fig. 8.7. Pressure transients near the times of cleavage crack propagation in PTSE-2. (*a*) PTSE-2A from 360 to 370 s and (*b*) PTSE-2B from 575 to 580 s.

flow valves to eliminate errors introduced by flow of the pressurizing fluid. When pressurizing fluid flows were low, the pressures indicated by the two transducers differed by 0.2 MPa or less.

The output of a CMOD gage mounted on the cooled surface was the sum of the effects of real displacement and temperature changes in the gage. Dummy CMOD gages (i.e., gages that did not cross the crack opening) were included in the vessel instrumentation so that purely thermal effects could be excluded from the displacement measurements (see Chap. 6). Two displacement-gage circuits (YE84 and YE88) each included both active and dummy elements so that the output of these two circuits represented net displacement, that is, the dummy output was subtracted from the active output. The output of all other displacement gages was unbiased, and data from two dummy gages were recorded to provide a basis for adjusting the unbiased displacement measurements. Typical responses of an unbiased and a biased gage are compared in Fig. 8.8 for the A and B transients.

Two CMOD gages, YE79 and YE82, were connected to a Nicolet digital oscilloscope that was set to record the output of the gages during the 1 ms before and after the device received a transient change in the signal. The recording of the cleavage event in PTSE-2B is shown in Fig. 8.9. The amplitude of the recorded signal was limited to ~0.4 mm. Figure 8.9(*b*) shows both an acceleration and deceleration of the crack mouth.

Most of the sensors on PTSE-2 produced useful information. However, some sensors or their cable connections were damaged during test preparations or in one of the transients. The sensors that gave dubious output are identified in Table 8.1.

Table 8.1. Sensors with dubious output

Variable	Sensor No.	Problem	Phase
Temperature	TE17, 20, 21	Damaged before test	A and B
	TE1-2, 2-2, 2-4, 2-5, 2-6, 2-7, 3-1, 3-5, 3-6, 4-6, 5-4, 5-6, 6-3, 6-4, 6-5	Inconsistent with other thermocouples	A and B
Strain (end-of-crack marker)	XE52	Normal except zero response to crack jump	A and B
	XE53	Broken[a]	B
CMOD	YE54	Slight or erratic response[b]	A and B
	XE79, 82	Anomalous response[c]	B
	YE86, 87	Low amplitude[d]	A, B

[a]Occurred during crack jump in PTSE-2A.

[b]Some response to the PTSE-2B crack jump was evident.

[c]CCDAS records were anomalous. Strip-chart and digital oscilloscope records were normal.

[d]The absence of normal response in PTSE-2B until the vessel ruptured may indicate that the gages were not properly pretensioned.

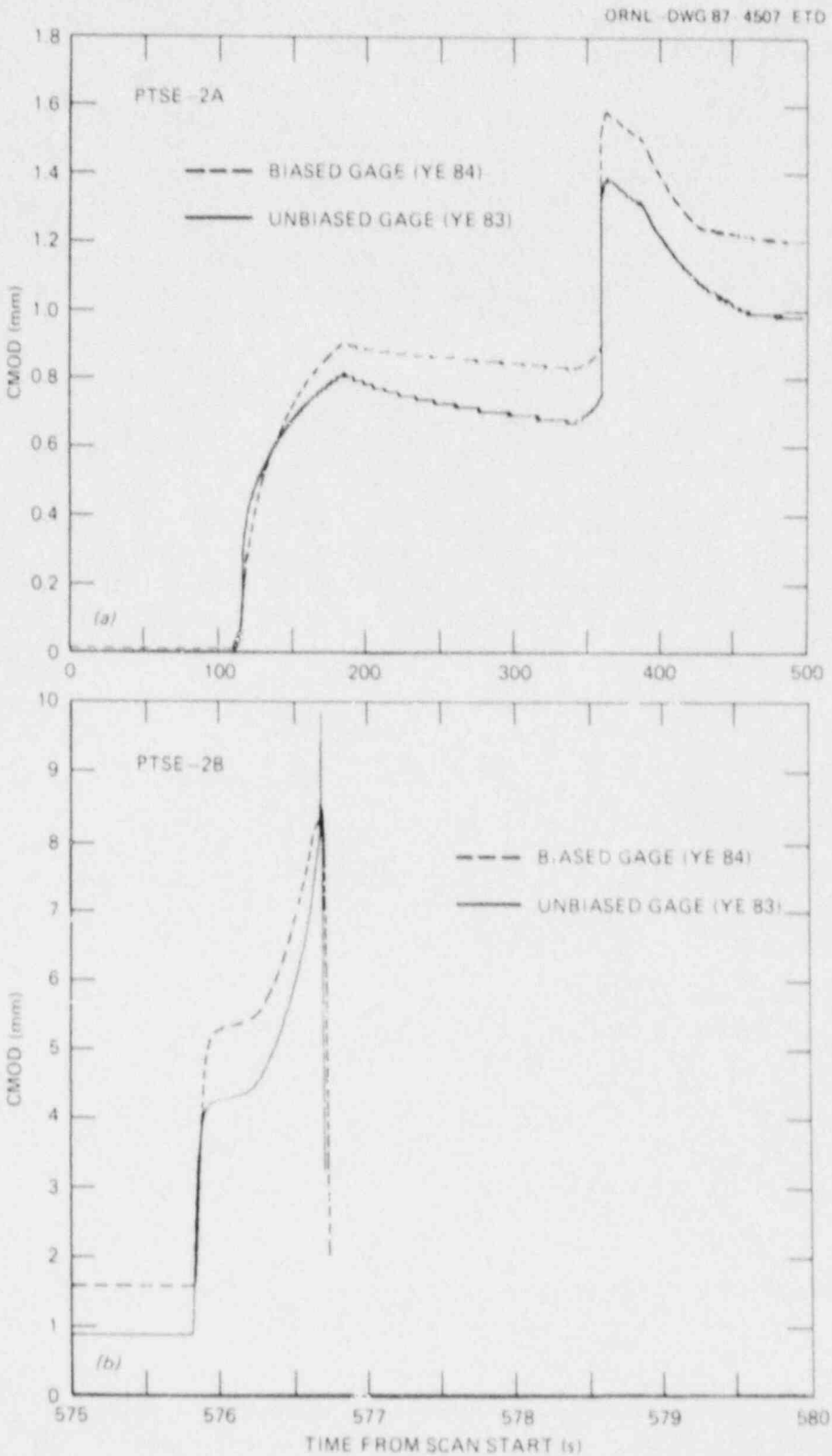

Fig. 8.8. Comparison of typical responses of unbiased and biased CMOD gages. (*a*) PTSE-2A and (*b*) PTSE-2B.

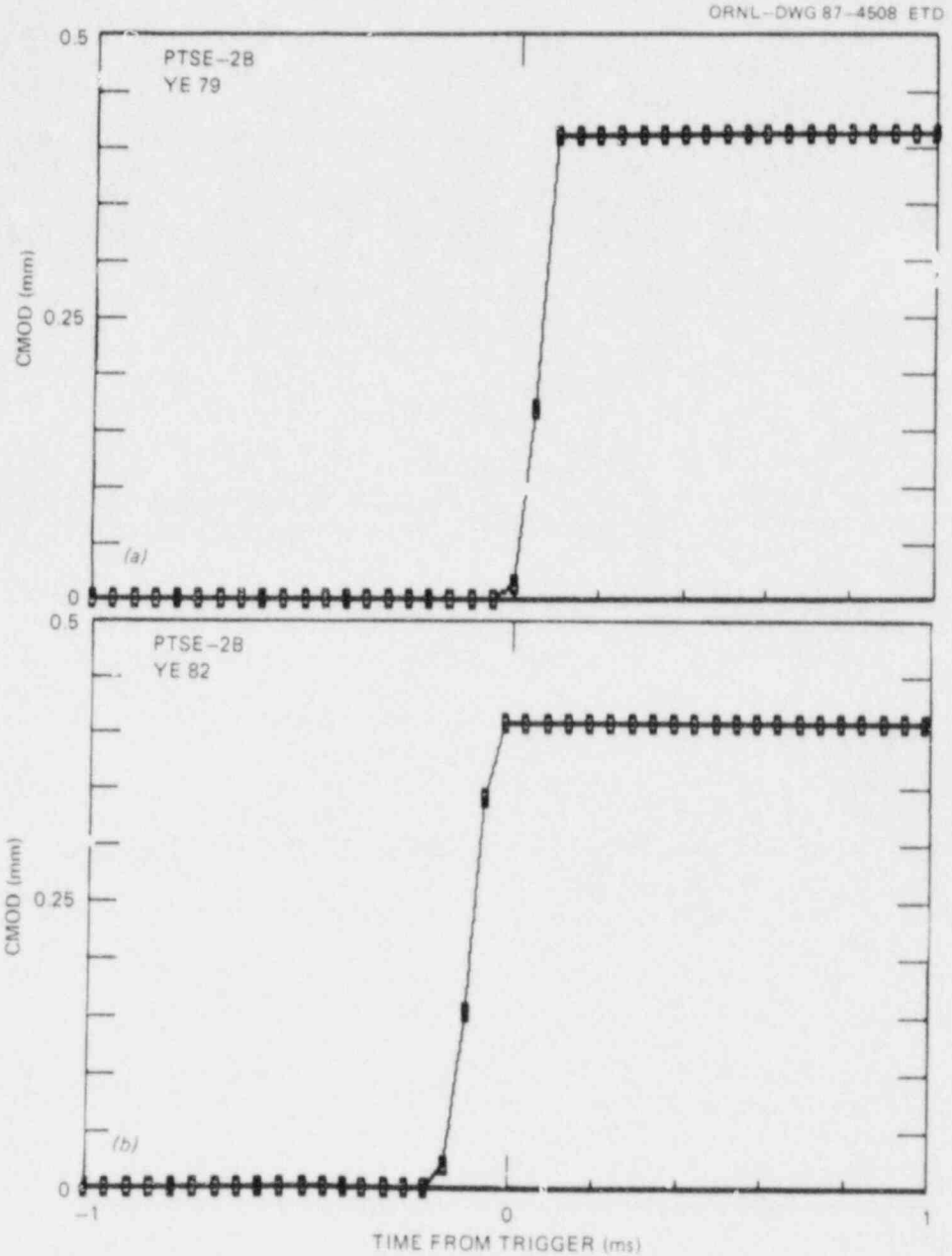

Fig. 8.9. CMOD change recorded on digital oscilloscope (Nicolet) from gages (*a*) YE79 and (*b*) YE82 at time of cleavage crack propagation in PTSE-2B.

8.5 Interpretation of Events

The experimental records of CMOD vs time in conjunction with finite-element calculations of displacements for a range of crack depths and times were the basis for identifying fracture events. The times of maximum and minimum K_I corresponded to abrupt changes in the slope of pressure as a function of time. The time of the vessel rupture is marked by a sharp drop in pressure and by abrupt changes in CMOD and strain gage outputs. The time of initiation of each thermal transient, which need not be precisely known, is marked by changes in outside surface temperatures.

Times of all events are given relative to the time of initiation of the computer-controlled data scans.

8.5.1 PTSE-2A

The thermal shock in the PTSE-2A transient started about 112 s after the initiation of the data scan. Subsequently and sequentially, the flaw tore ductilely while K_I was increasing; tearing ceased, presumably when K_I first decreased; tearing resumed at about the time K_I increased again; cleavage crack propagation and arrest occurred; and, finally, ductile tearing resumed after crack arrest until pressure was reduced. The succession of events identifiable from recorded transient data is summarized in Table 8.2. The behavior of the variables associated with events is illustrated graphically; the most probable times of events were determined by detailed evaluation of all relevant data.

CMOD behavior for the entire PTSE-2A transient is typified by the plot of data shown in Fig. 8.10. More detail for the period of initial tearing that preceded the initial maximum K_I is represented by two typical CMOD measurements vs time shown in Fig. 8.11. The first maximum K_I was reached at point A, when CMOD reached a maximum. The extent of ductile tearing that occurred during this period was deduced by analysis from the CMOD data, as discussed in Chap. 10. Examination of the fracture surface, discussed in Chap. 9, showed that ductile tearing enlarged the flaw depthwise with no significant axial tearing.

The second episode of ductile tearing transpired when CMOD again increased (from point B to C in Figs. 8.10 and 8.12). The crack propagated by cleavage, causing the rapid change in CMOD from C to C′. The final ductile tearing in PTSE-2A occurred while pressure and CMOD were increasing (from point C′ to D in Figs. 8.10 and 8.12).

The time of axial propagation and arrest is clearly demonstrated by the output shown in Fig. 8.13 of two gages located beyond the ends of the initial flaw. Displacement gage YE51, which was 100 mm above the upper end of the flaw, and strain gage XE53, which was 10 mm below the lower end, indicated abrupt changes simultaneously at the time of the cleavage crack propagation shown in Figs. 8.10 and 8.12. The fracture surfaces, discussed in Chap. 9, show that the axial propagation in the PTSE-2A transient was a cleavage mode fracture. There were no indications from any gages that another axial propagation occurred in either transient.

Table 8.2. Events identified by transient data in PTSE-2A and -2B

Event	Time[a] (s)	Evidence of event
	PTSE-2A	
Initiation of thermal shock	~112	Outside surface temperature
Initial tearing	112–184.6	Analysis and CMOD
First maximum K_I	184.6	Calculated K_I; CMOD, pressure
Minimum K_I	341.8	Calculated K_I; CMOD, pressure
Precleavage tearing	341.8–361.4	Analysis and CMOD
Initial cleavage propagation	361.4	CMOD
Crack arrest	361.4[b]	CMOD
Axial crack propagation	361.4	Strain and CMOD gages beyond ends of initial flaw
Postcleavage tearing	361.4–365.6	Analysis and CMOD
Final maximum K_I	365.6	Calculated K_I, CMOD, pressure
	PTSE-2B	
Initiation of thermal shock	~155	Outside surface temperature
Precleavage tearing	155–575.8	Analysis and CMOD
Cleavage propagation	575.82	CMOD
Crack arrest	575.82[b]	CMOD
Postcleavage tearing	576.2–576.7	Analysis and CMOD
Rupture of vessel wall	576.7	Pressure, CMOD, strain

[a]Time after start of scanning by the data acquisition system.

[b]Time intervals <10 ms cannot be resolved by the data acquisition system.

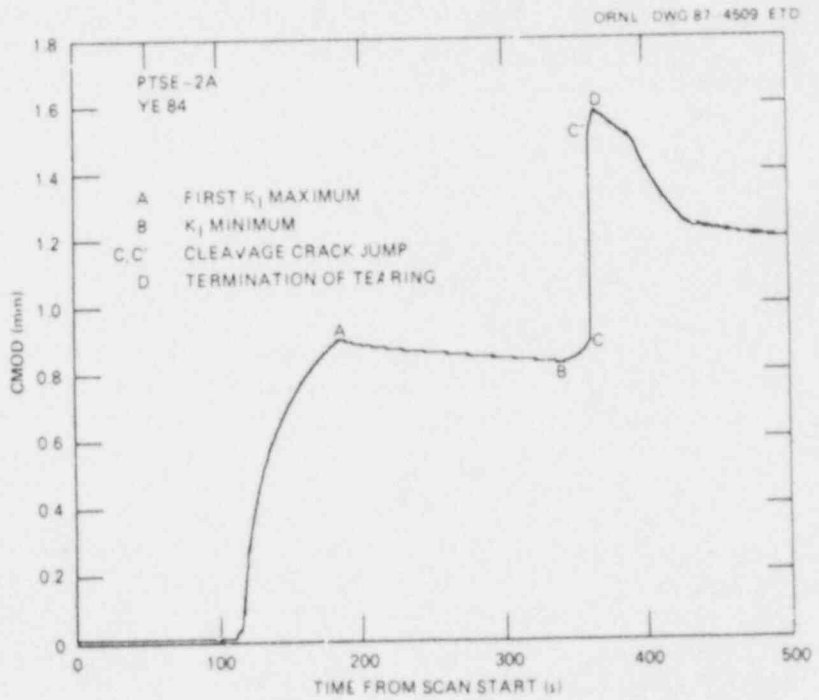

Fig. 8.10. CMOD vs time at center of flaw for PTSE-2A transient.

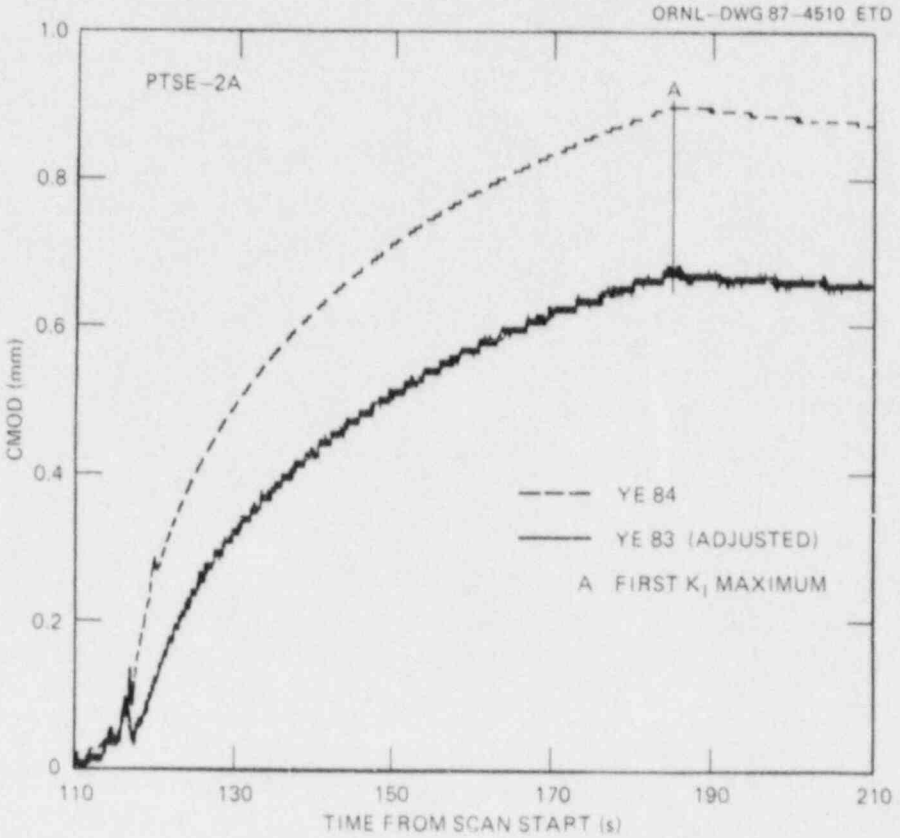

Fig. 8.11. CMOD vs time during early phase of PTSE-2A measured at center of flaw (z = 0) and 100 mm below center (z = −100 mm) by gages YE84 and YE83, respectively. The YE84 output was naturally biased by incorporation of a dummy gage in the bridge circuit. The YE83 output has been adjusted by subtraction of the output of a dummy gage (YE56).

8.5.2 PTSE-2B

The thermal shock in the PTSE-2B transient started at about 155 s after initiation of the data scan. In this transient, K_I increased monotonically until about the time of the rapid cleavage crack propagation. The extended crack that had developed during the PTSE-2A transient first tore depthwide and then converted to cleavage. The propagating cleavage fracture arrested and proceeded to propagate by ductile tearing until the vessel ruptured. The events in this transient are summarized in Table 8.2.

The CMOD behavior typical of the time before cleavage is shown by the CMOD at the center of the flaw in Fig. 8.14. The time of the start of the cleavage event is reasonably well defined by all of the active CMOD and strain gages. The separation of subsequent events is more complicated because it must be assumed *a priori* that postcleavage tearing progressed with nonuniform velocity. Plots of several variables reflecting the status of the fracture during the 1-s period, including the

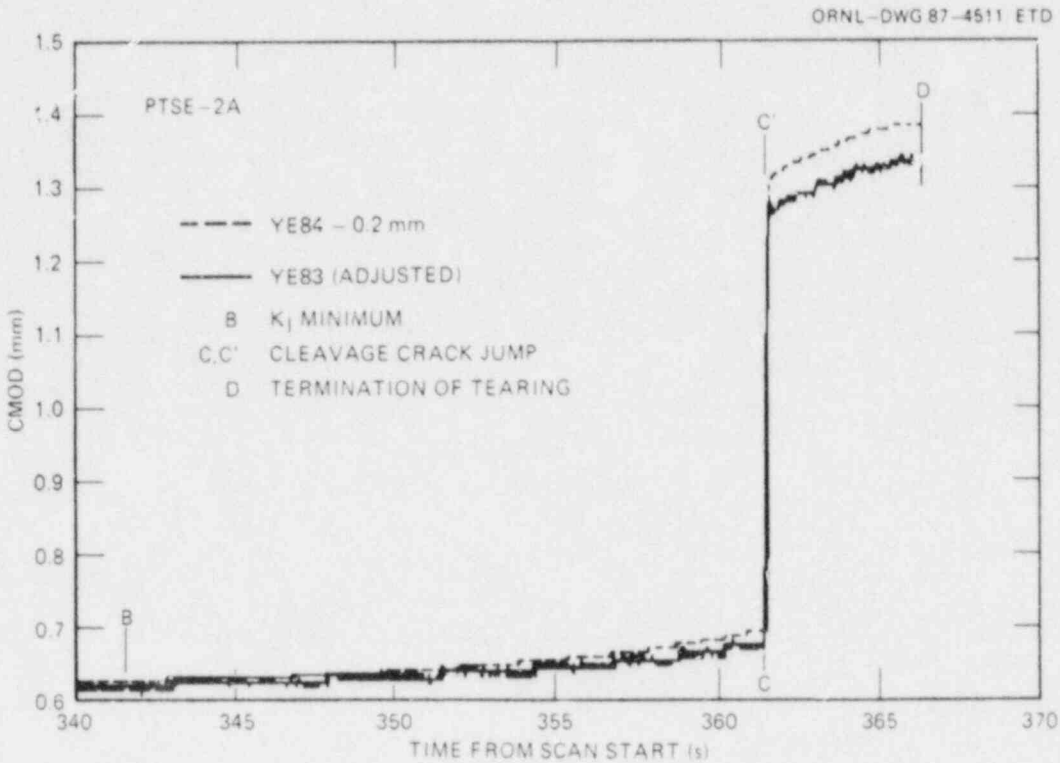

Fig. 8.12. CMOD vs time for final phase of PTSE-2A. The effects of precleavage tearing, cleavage crack propagation, and postcleavage tearing are shown. The output of gage YE84 has been shifted arbitrarily by 0.2 mm to facilitate comparison of the changes in CMOD at two proximal points while the crack was growing.

cleavage, tearing, and rupture, are shown in Fig. 8.15. Cleavage occurred at the time marked A in this figure. The data show that postcleavage unstable tearing possibly started immediately after crack arrest but was definitely proceeding from B to C. The rapid decrease of pressure at 576.72 s (point C) clearly indicates that the vessel had ruptured by that time; the more gradual pressure drops during the preceding second were the consequence of the vessel bulging as the crack advanced. All of the active CMOD gages indicated a rapid crack advance at about 575.82 s, as shown in Fig. 8.16. Sudden off-scale increases in CMOD exhibited by gages YE80, 81, and 85 at about 576.35, 576.12, and 575.83, respectively, were coincident with gage failure and, therefore, may only be indicative of idiosyncrasies of the gages. Figure 8.17 shows the changes in CMOD relative to the precleavage values. This figure shows that the change in CMOD resulting from the rapid crack advance is a maximum at the center of the crack ($z = 0$) and diminishes toward the ends of the crack. The rate of change in CMOD was never constant in this time interval, initially as a consequence of plastic flow with the crack stationary and subsequently as a consequence of plastic flow or of slow tearing or of both. The acceleration of the CMOD change after 576.1 s is an indication that tearing was proceeding at that time.

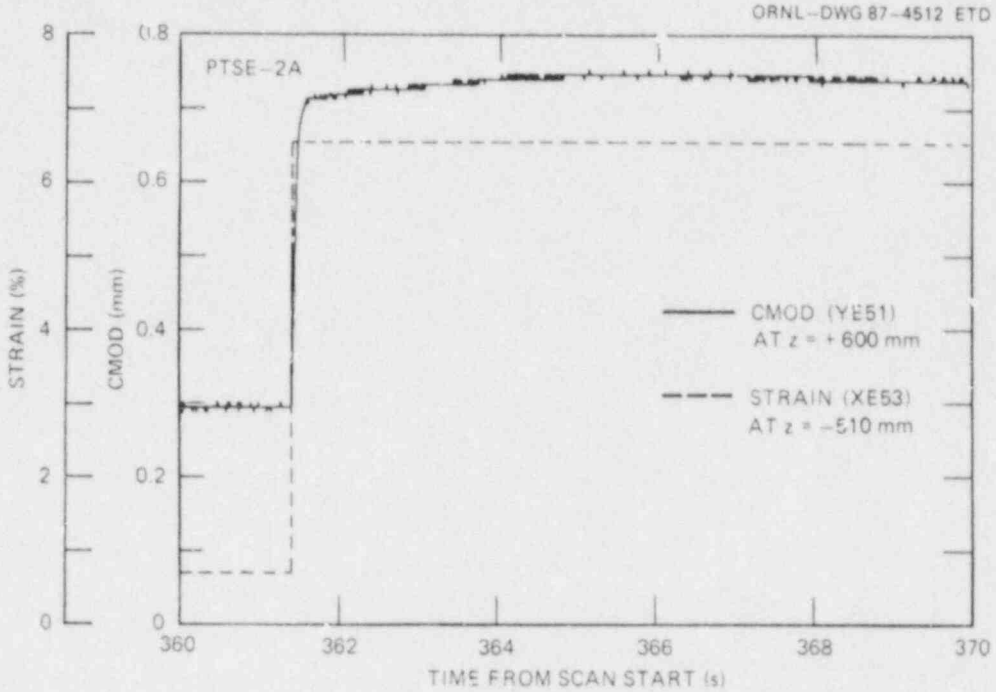

Fig. 8.13. Response of gages indicating rapid axial crack propagation in PTSE-2A. YE51 is a CMOD gage 100 mm above the top end of the initial flaw (z = 600 mm). XE53 is a strain gage 10 mm below the bottom end of the initial flaw (z = −510 mm).

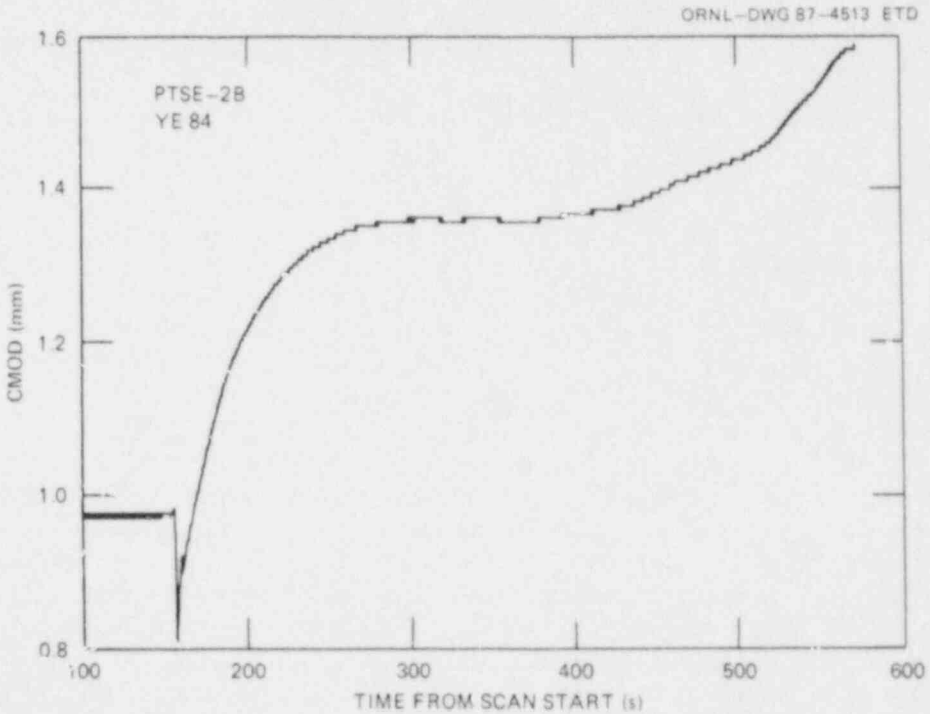

Fig. 8.14. Typical CMOD behavior during the PTSE-2B transient. CMOD gage YE84 is at the center of the flaw.

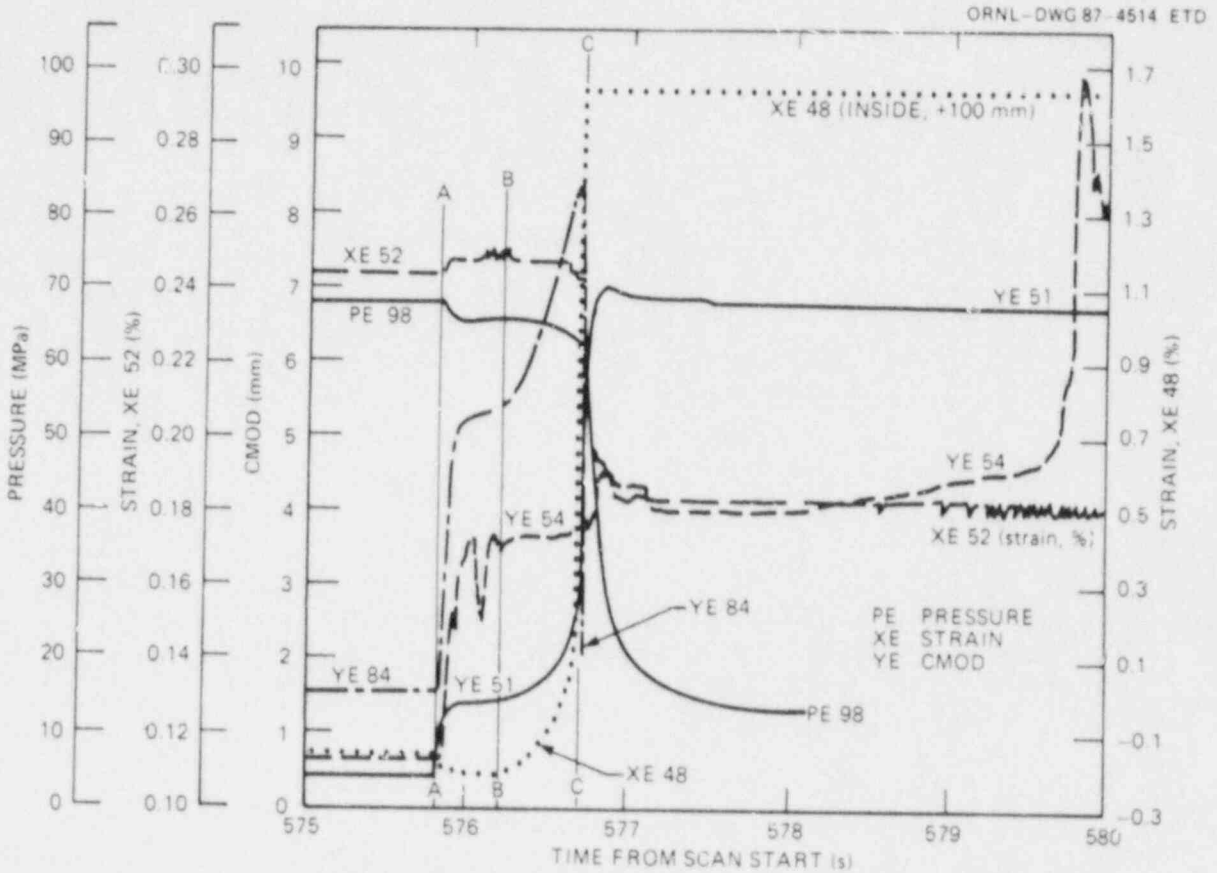

Fig. 8.15. Response of variables during final phase of PTSE-2B, including cleavage, tearing, and vessel rupture. Pressure, strain, and CMOD vs time are shown for the period from 575 to 580 s. See Fig. 6.3 for locations of gages.

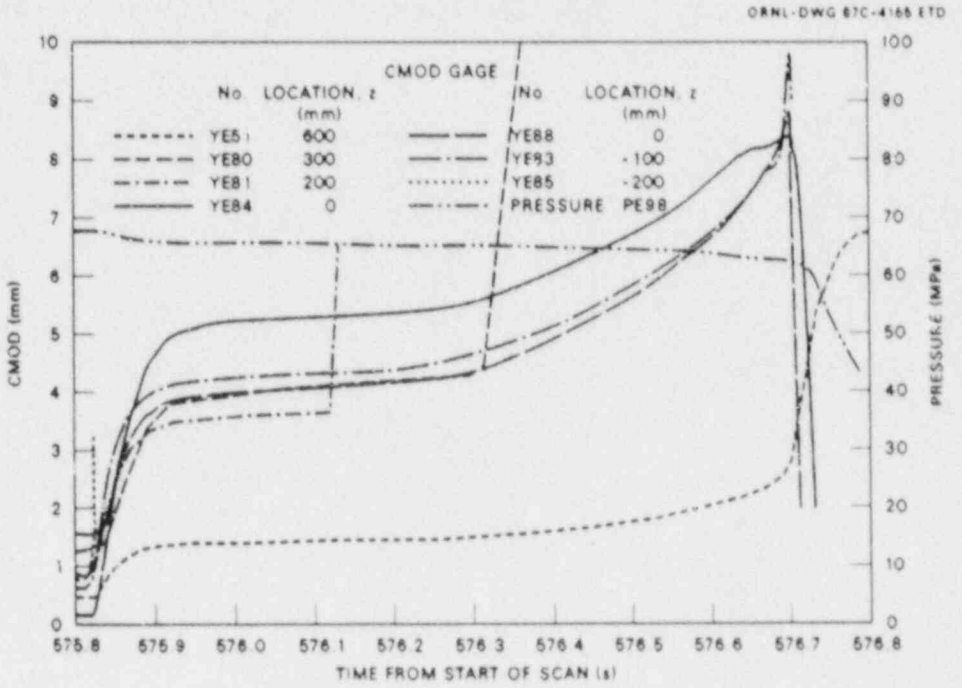

Fig. 8.16. Pressure and CMOD vs time for the cleavage, tearing, and rupture phase of the PTSE-2B transient.

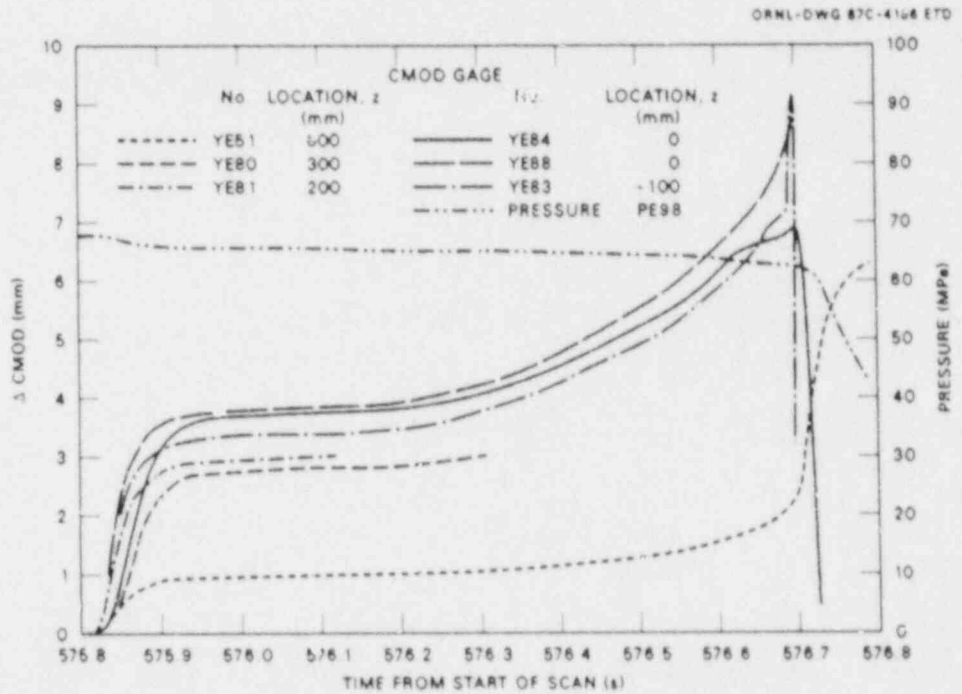

Fig. 8.17. Pressure and ΔCMOD vs time for the cleavage, tearing, and rupture phase of the PTSE-2B transient.

References

1. R. L. Powell et al., *Thermocouple Reference Tables Based on the IPTS-68*, Monograph 125, U.S. National Bureau of Standards, Washington, 1974.

2. R. H. Bryan et al., *Pressurized-Thermal-Shock Test of 6-in.-Thick Pressure Vessels. PTSE-1: Investigations of Warm Prestressing and Upper-Shelf Arrest*, NUREG/CR-4106 (ORNL-6135), Martin Marietta Energy Systems, Inc., Oak Ridge Natl. Lab., April 1985.

9. POSTTEST EXAMINATION OF FLAW

9.1 Surface Features of Flaw

The PTSE-2 experiment produced two fast crack jumps during the two transients. The final crack propagation led to rapid ductile tearing that penetrated the wall of the vessel. An outside view of the vessel after the test is shown in Fig. 9.1, which shows the entire length of the flaw. During the first cleavage crack propagation the crack ran radially to a depth of 42.4 mm (at the center) and axially from both ends of the original flaw to the ends of the low-upper-shelf insert, a total length of 1340 mm. The inner surface was ruptured over an axial distance of 729 mm. The residual opening of the flaw at the outside surface (~8 mm) is evident in Fig. 9.1. While the vessel was intact the trace of the flaw at the inside surface was indistinct. After the block containing the insert and the entire flaw was cut from the vessel, the flaw was easily visible at the inside surface. Deformation of the inside surface is shown in Fig. 9.2 at the two ends of the flaw block.

9.2 Flaw Geometry

A block of material 1372 mm long by 178 mm wide was flame-cut from the vessel and sawed into six 240-mm-long segments (Fig. 9.3). Segments 3 and 4 were already fractured completely; the small ligaments in segments 2 and 5 were broken by bending the segments at room temperature. The unbroken ends of segments 1 and 6 were trimmed off, and the remaining portions were chilled in liquid nitrogen and broken apart. Prominent features of the flaw are identified in Figs. 9.4–9.6 and Table 9.1. Photographs of all segments of the fracture surfaces are included in Appendix C.

The B side of the flaw was examined under a low-power microscope to map the profiles of the crack at the stages described in Table 9.1. The coordinates of several points in each segment were measured with a scale graduated in millimeters. The measurements are presented graphically in Fig. 9.7. Figure 9.8 shows a photograph of one fracture surface with the cut segments reassembled in order. See Fig. 9.4 for the definition of the coordinate system. The average depth of the flaw at several stages is given in Table 9.2.

9.3 Fractographic and Metallographic Evaluation of Fracture Surface

The fractographic and metallographic evaluations of PTSE-2 generally confirm the fracture modes that were observed macroscopically. Fractographic examination with the scanning electron microscope (SEM) confirmed that initial ductile tearing and crack propagation in a cleavage mode occurred in the first transient with arrest at a depth of about

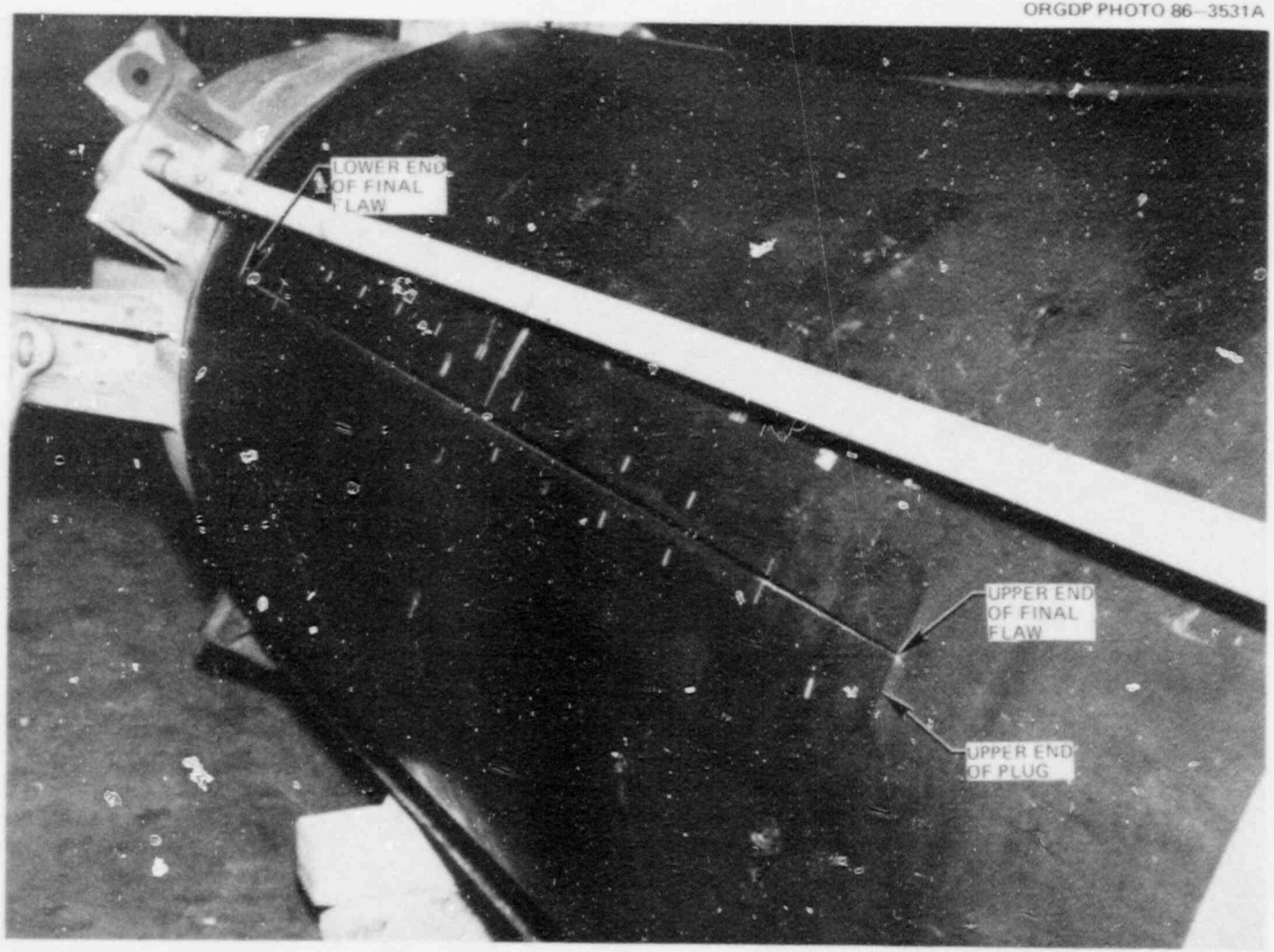

Fig. 9.1. Photograph of PTSE-2 vessel after the test. The entire length of the flaw is visible on the outside surface.

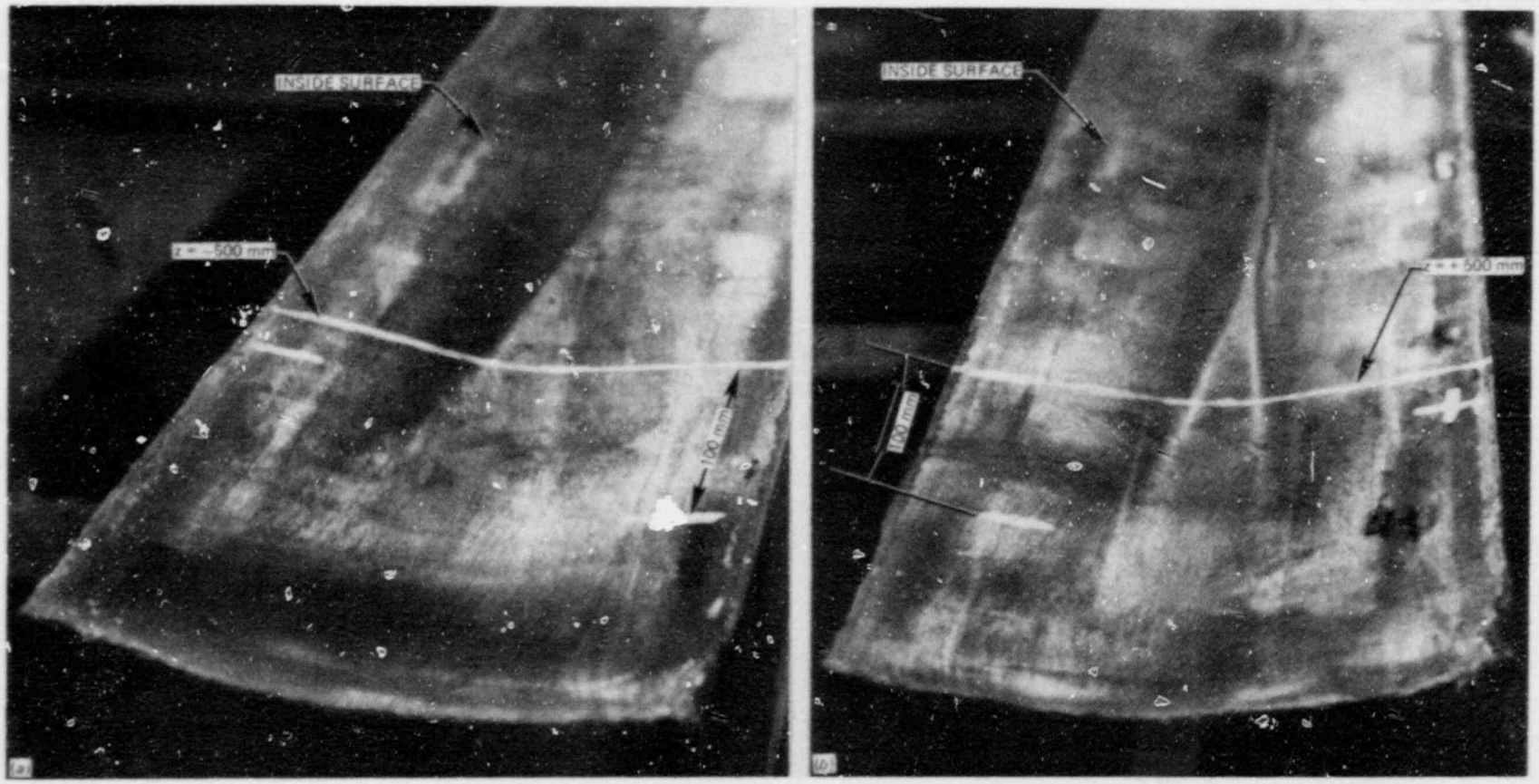

Fig. 9.2. Photographs of inside surface of the block containing PTSE-2 flaw. These views of the (*a*) lower and (*b*) upper ends of the block show the residual plastic deformation at the ends of the flaw.

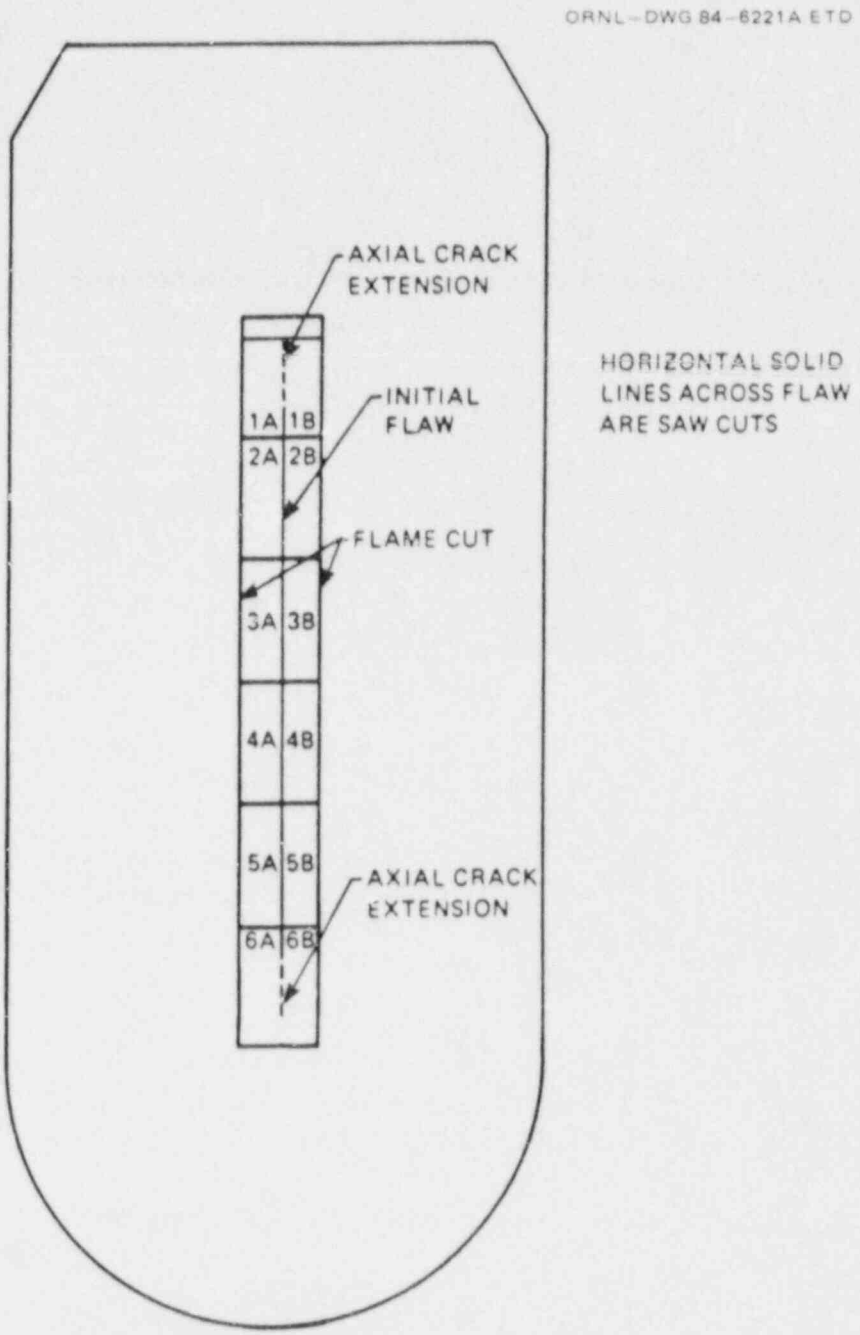

Fig. 9.3. Scheme for cutting and labeling segments of the block containing PTSE-2 fracture surfaces. Surfaces labeled A are viewed toward left, and B, toward right.

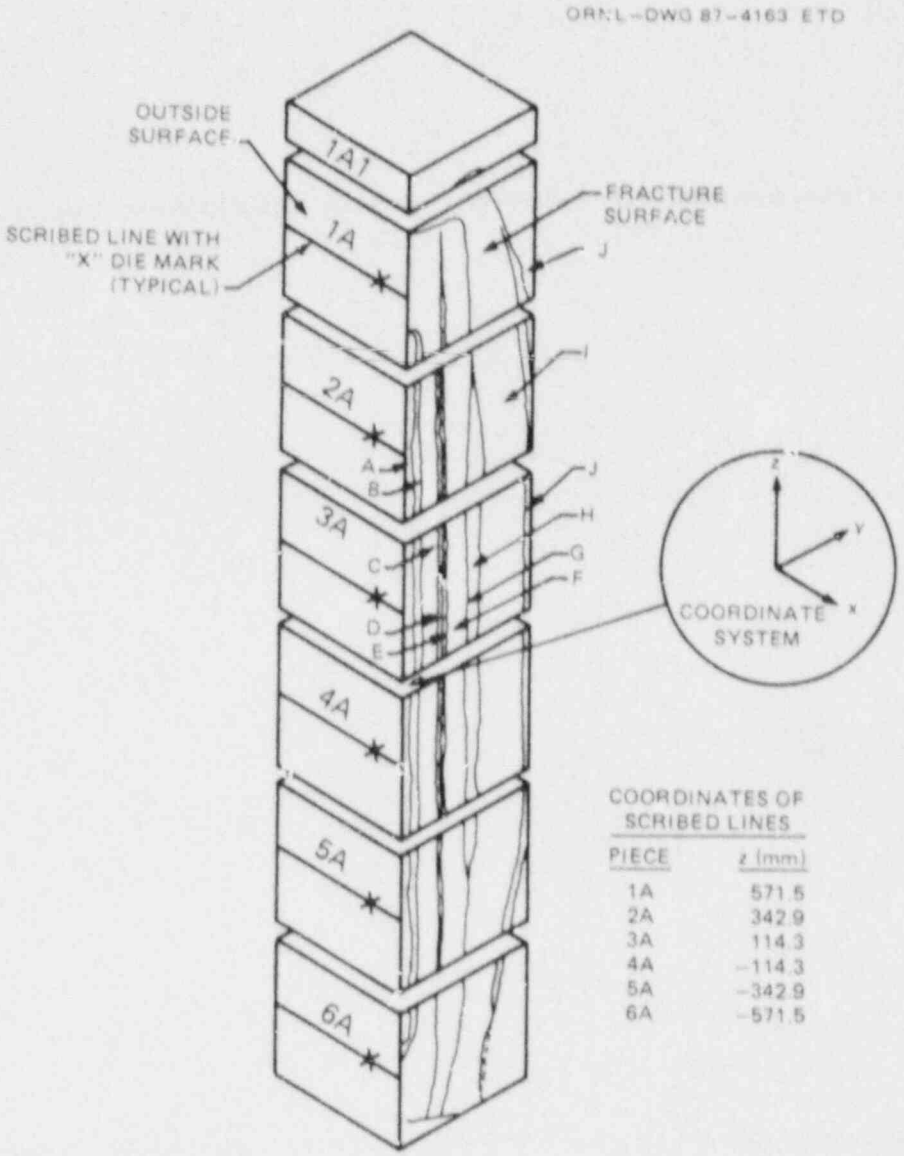

Fig. 9.4. Geometry of PTSE-2 flaw segments. Features labeled A to J are described in Table 9.1 and shown in photographs in Figs. 9.5 and 9.6 and in Appendix C.

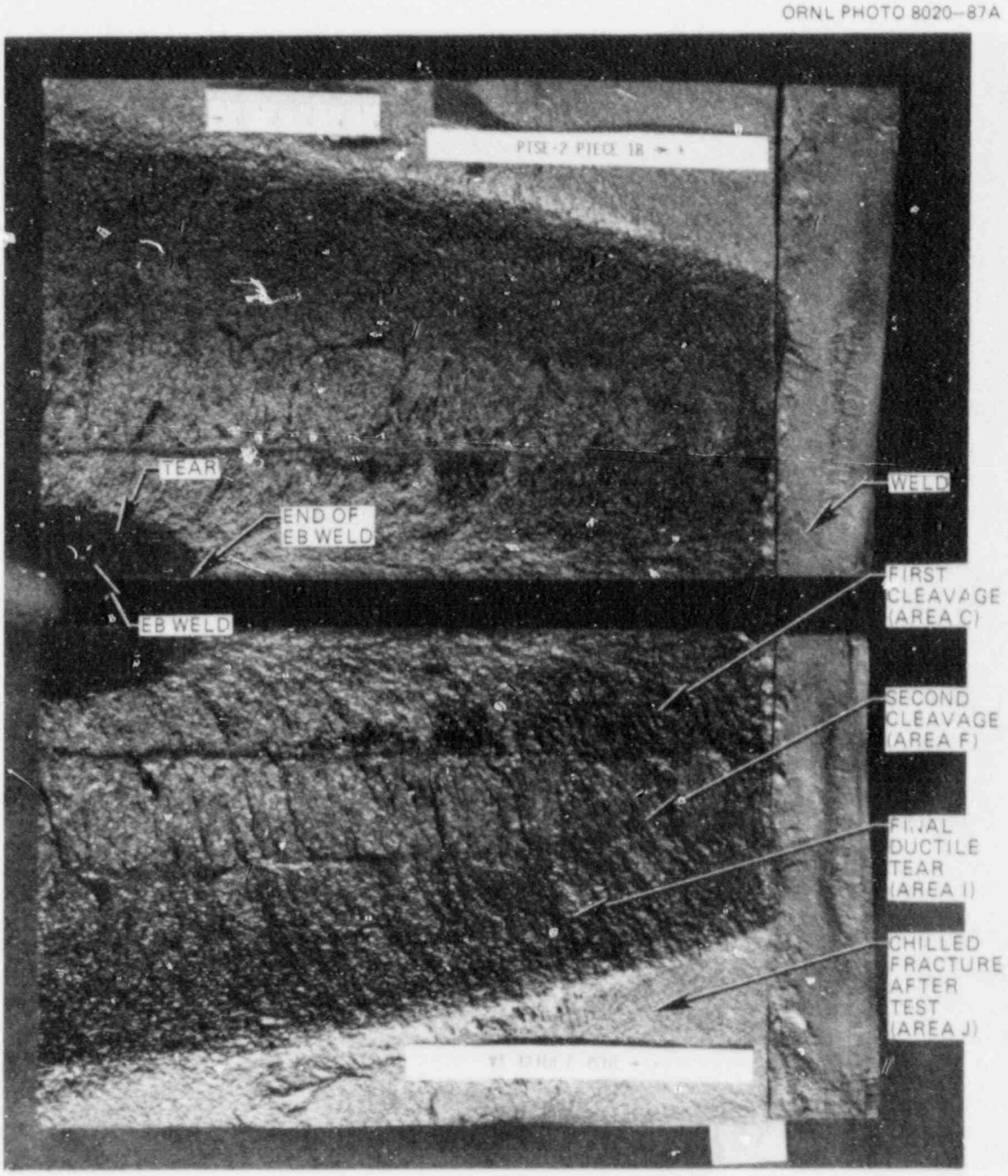

Fig. 9.5. Photograph of an end segment (No. 1) of PTSE-2 fracture surfaces. See Table 9.1 for identification of features.

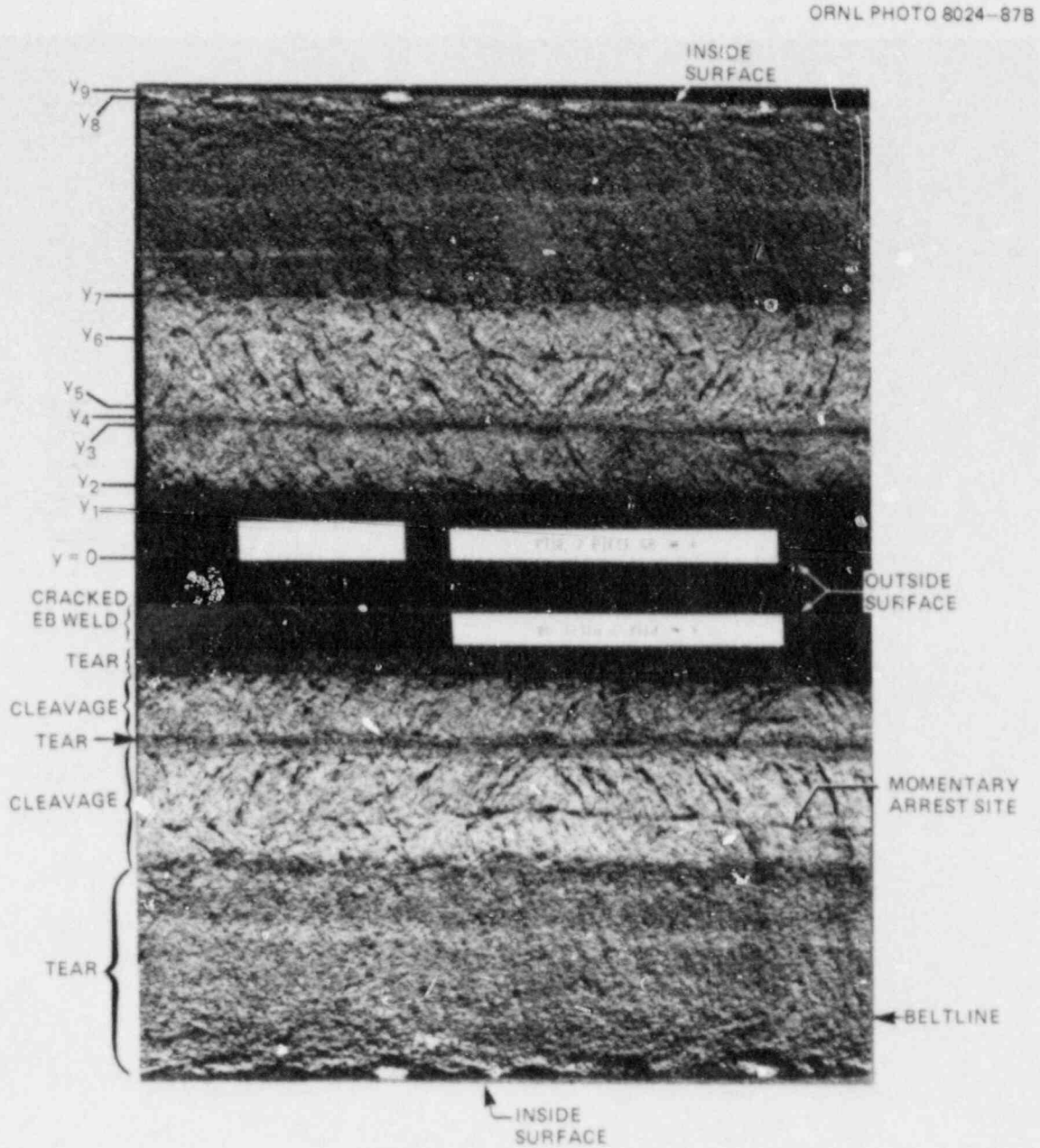

Fig. 9.6. Photograph of a central segment (No. 4) of PTSE-2 fracture surfaces. The depths (y) are described in Table 9.1. See Fig. 9.4 for a definition of the coordinate system.

Table 9.1. Fracture features typical of segments 2 to 5

Area	Deeper boundary	Description
A	y_1	Cracked electron-beam weld, smooth dark gray
B	y_2	Precleavage ductile tear in PTSE-2A, dark gray, rough
C	y_3	Cleavage fracture in PTSE-2A, light gray
D	y_4	Postcleavage ductile tear in PTSE-2A, brown or gray band
E	y_5	Precleavage ductile tear in PTSE-2B, medium gray
F	y_6	Cleavage fracture in PTSE-2B, light gray
G	y_6'	Narrow band of ductile tearing, medium gray
H	y_7	Same as F
I	y_8	Postcleavage ductile tear in PTSE-2B
J	y_9	Light-gray shear lip in ruptured portion; unbroken ligament, very light gray, near both ends of flaw

Table 9.2. Dimensions of fracture features of the PTSE-2 flaw

Feature	Depth[a] (mm)
EB weld crack (y_1)	14.5
Initial ductile tear (y_2)	22.5
First cleavage crack (y_3)	39.3
Intermediate tear	
First phase (y_4)	42.4
Second phase (y_5)	46.1
Second cleavage crack (y_7)	78.8
Momentary arrest site[b] (y_6)	69.2

[a] Average total depth of feature over the central part (~400 mm long) of the flaw.

[b] This linear feature is distinct for ~500 mm in both directions from the beltline. It is generally an area of ductile tearing from 0.5 to 1.5 mm wide.

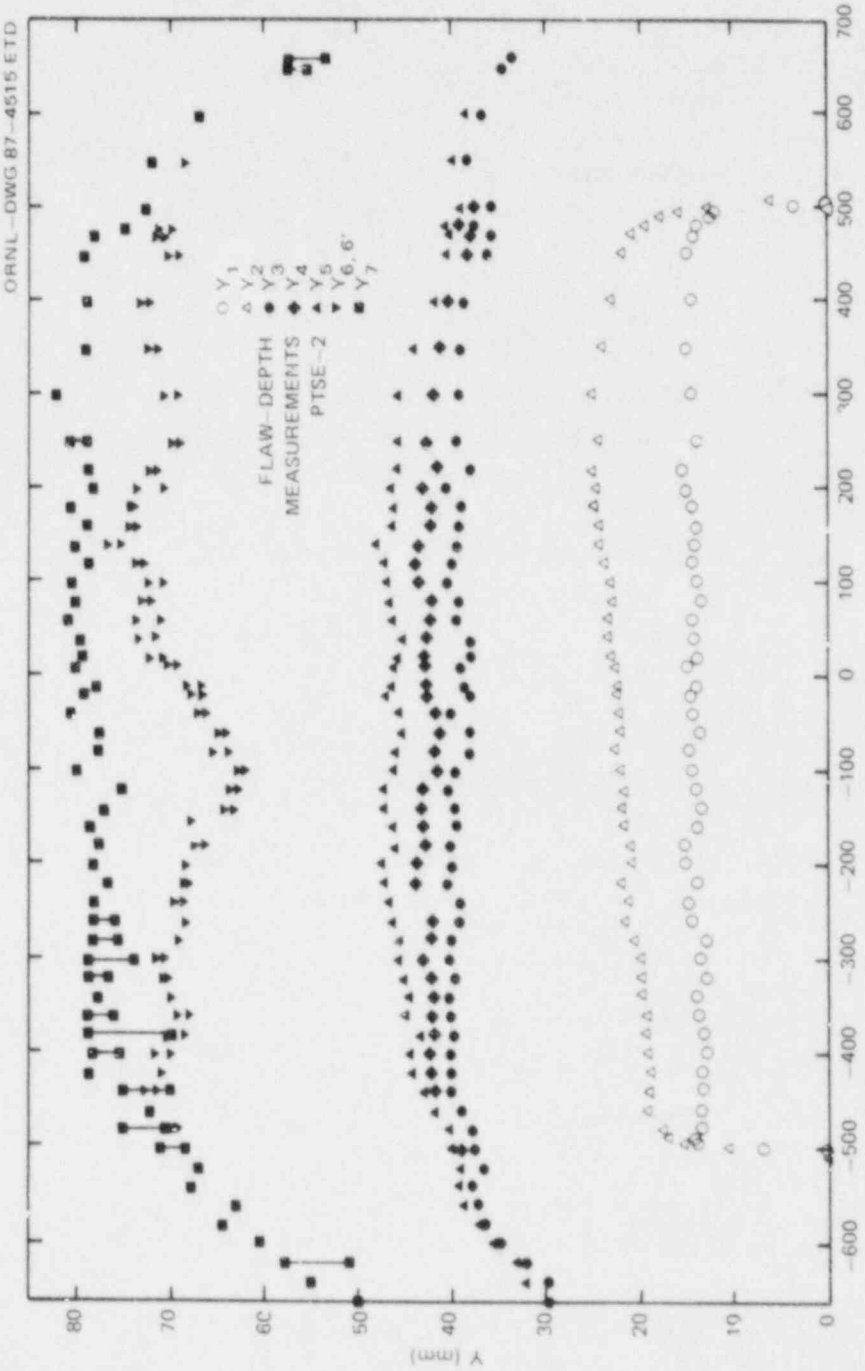

Fig. 9.7. Depths (y) of all phases of fracture in PTSE-2 experiment.

M&C PHOTO YP3644A

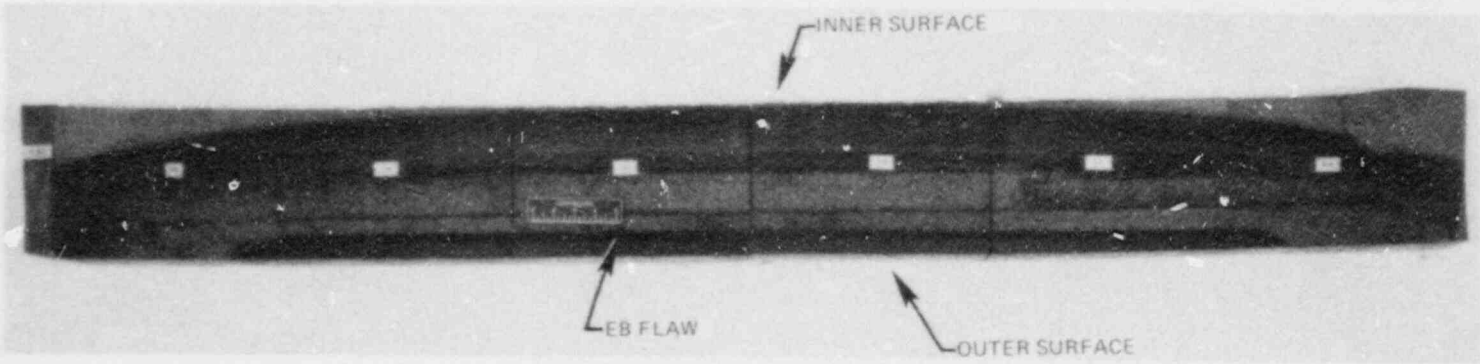

Fig. 9.8. Photograph of fracture surface A from PTSE-2. The fracture surface was reassembled from segments 1A through 6A.

40 mm. In the second transient, ductile tearing preceded cleavage crack propagation with the final cleavage arrest at a depth of about 80 mm. However, it was evident that an intermediate arrest occurred in the neighborhood of 70 mm with subsequent reinitiation by ductile tearing before the final cleavage propagation and arrest. Beyond a depth of 80 mm, the fracture occurred by ductile tearing.

Preparatory to performing the scanning electron fractography, a portion of the fracture surface was removed from segment 4A and cut to the appropriate size for the SEM. This portion, shown in Fig. 9.9, was cut from the end of segment 4A nearest the midplane of the flaw. Punch marks (PM) were made on the fracture surface at or near various features of interest for reference. Figure 9.9 identifies the boundaries (y marks) given in Table 9.1, as well as the punch marks (painted white) and distances between them. The distances from the outer surface to the punch marks will only be similar to those given in Table 9.2 because the punch marks are not necessarily located directly at a particular feature and the features vary in depth, as indicated by Fig. 9.7. Figure 9.10 shows the surface just beyond PM1 near the boundary of the electron-beam weld. The ductile tearing is evident in the fractographs. Figure 9.11 is a series of three fractographs in the region between PM2 and PM3 that show the end of the precleavage ductile tearing in the first transient and the start of the transgranular cleavage propagation (boundary y_2).

Figure 9.12 shows an area beyond PM3 and confirms that the dominant cleavage mode of crack propagation occurred with only a small amount of interspersed tearing in the form of tear ridges between cleavage facets. Figure 9.13 was taken in the region just before PM4 and shows that the fracture mode was still predominantly cleavage at that point, just before arrest. Between PM4 and PM5 is a dark band thought to be ductile tearing associated with the continuation of loading immediately following the crack arrest in the first transient. Figure 9.14 fractographs were taken in that region and show the predominant ductile tearing behavior.

The light band between y_4 and y_5 is ductile tearing that is thought to have occurred during the second transient before mode conversion to cleavage. Figure 9.15 shows the region near PM6 at the boundary y_5 with the change from tearing to cleavage quite evident in Fig. 9.15(*b*). The region from y_5 to y_6 was examined also and was shown to be predominantly cleavage similar to that of the first transient but with slightly more prominent tear ridges.

The boundary y_6 visually appeared to be a possible momentary crack arrest followed by a small region of ductile tearing before cleavage initiation and propagation. This boundary is evident along the entire length of the fracture surface (see Fig. 9.8) although it merges with the final crack-arrest boundary near the ends of the flaw, as shown in Fig. 9.7. Figure 9.16 is a series of fractographs taken in the vicinity of PM7, which is located near the y_6 boundary and shows the narrow band of ductile tearing between the two regions of cleavage. The SEM fractography likewise confirmed the cleavage mode of propagation from y_6' to y_7 and the fact that ductile tearing was the fracture mode beyond y_7 to the inner surface of the vessel.

A sample cut from segment 4A near the location of the fractographic sample was also examined with optical metallography. Figures 9.17 and 9.18 show the general microstructures near the outer surface and at the

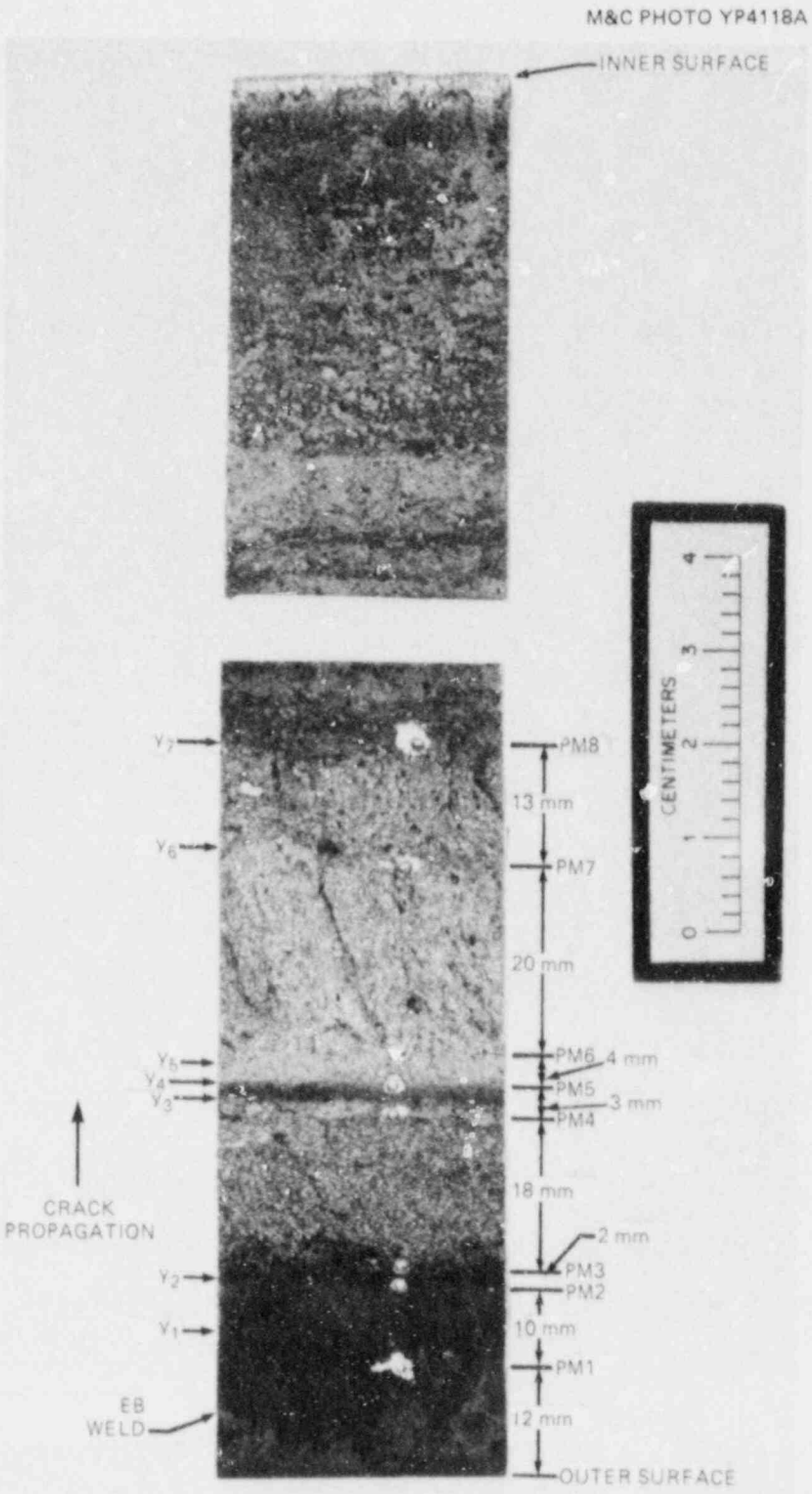

Fig. 9.9. Photograph of part of segment 4A of PTSE-2 fracture surface showing punch marks (PM) used as reference points for scanning electron fractography. The "y" numbers refer to boundary designations defined in Table 9.1.

ORNL PHOTO 7739-87

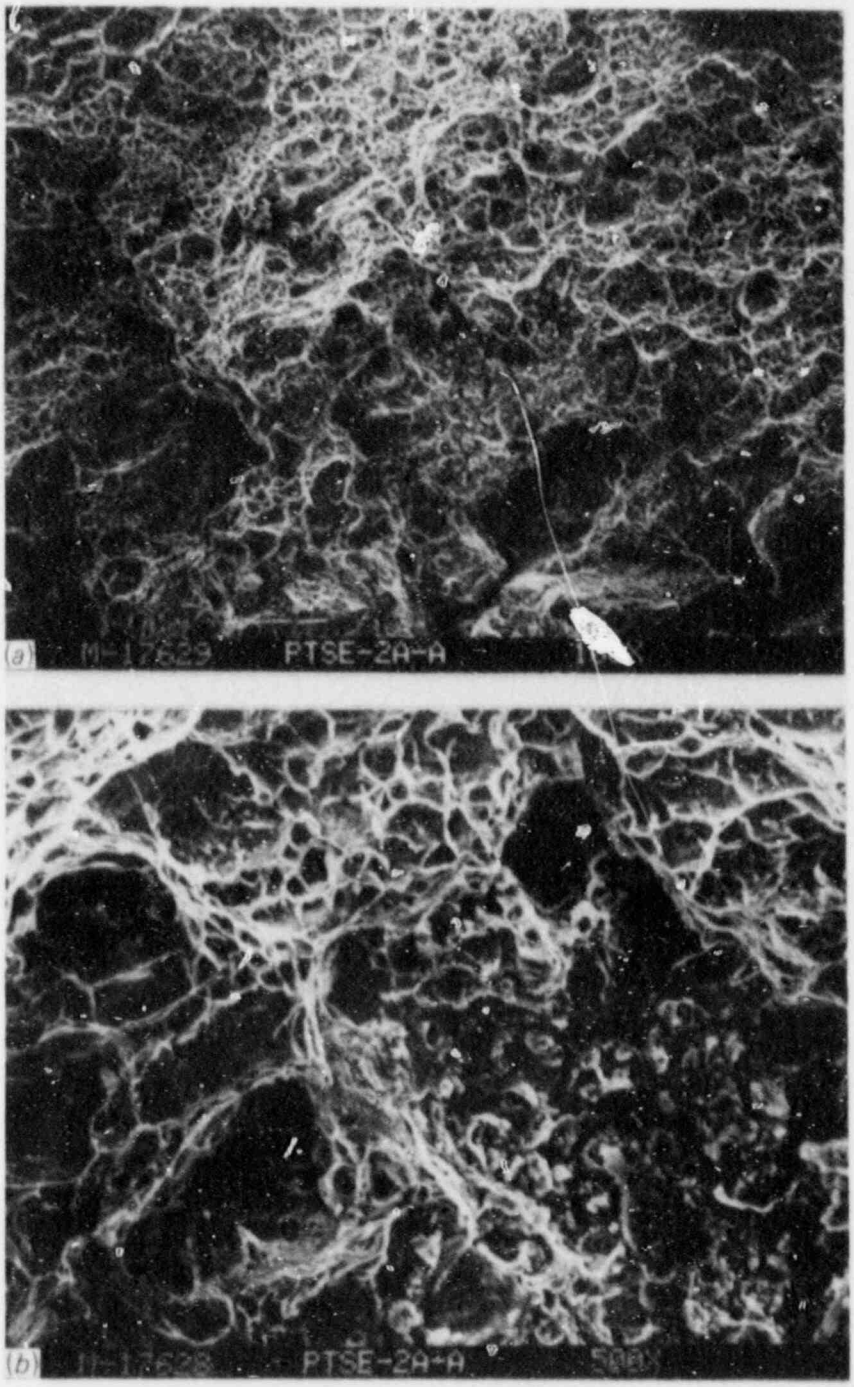

Fig. 9.10. Scanning electron fractographs of PTSE-2 showing ductile tearing region between PM1 and PM2 that preceded cleavage initiation during the first transient. (*a*) 100× and (*b*) 500× in center of part (*a*).

ORNL PHOTO 7740-87

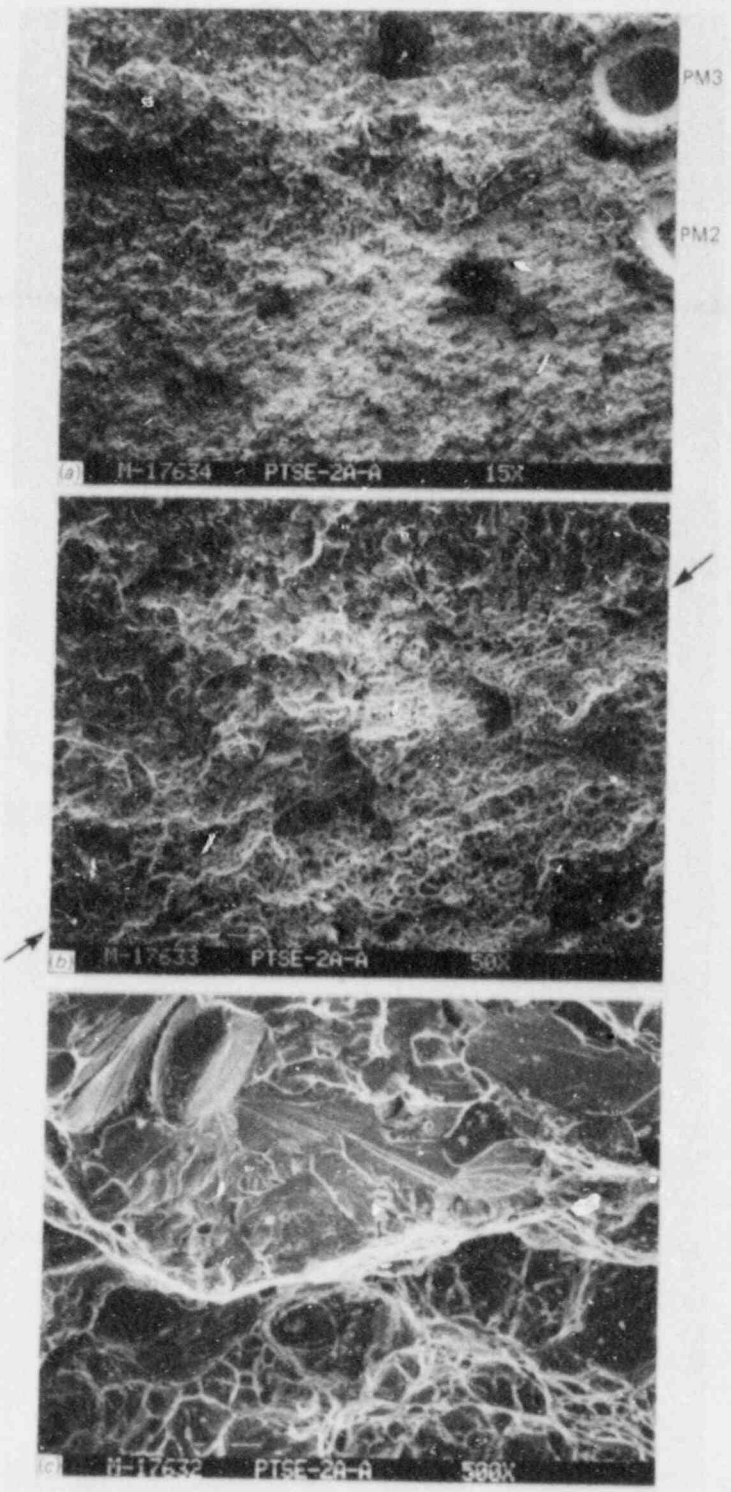

Fig. 9.11. Scanning electron fractographs of PTSE-2 at the boundary between precleavage ductile tearing and cleavage regions in transient PTSE-2A. (*a*) 15× showing PM2 and PM3, (*b*) 50× in center of part (*a*), and (*c*) 500× in center of part (*b*).

ORNL PHOTO 7741-87

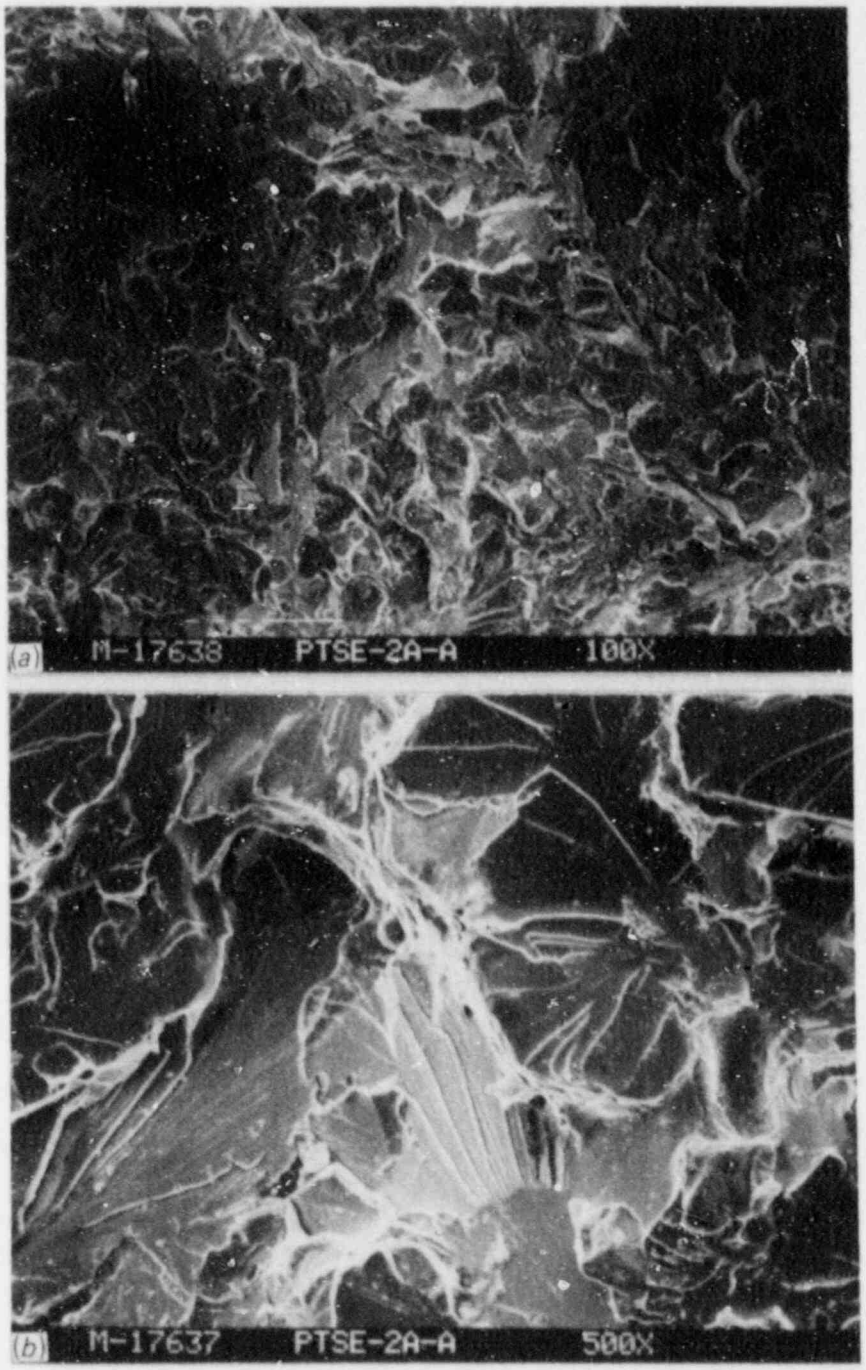

Fig. 9.12. Scanning electron fractographs of PTSE-2 showing transgranular cleavage as fracture mode during crack run event in the first transient. (*a*) 100× just beyond PM3, and (*b*) 500× in center of part (*a*).

ORNL PHOTO 7742-87

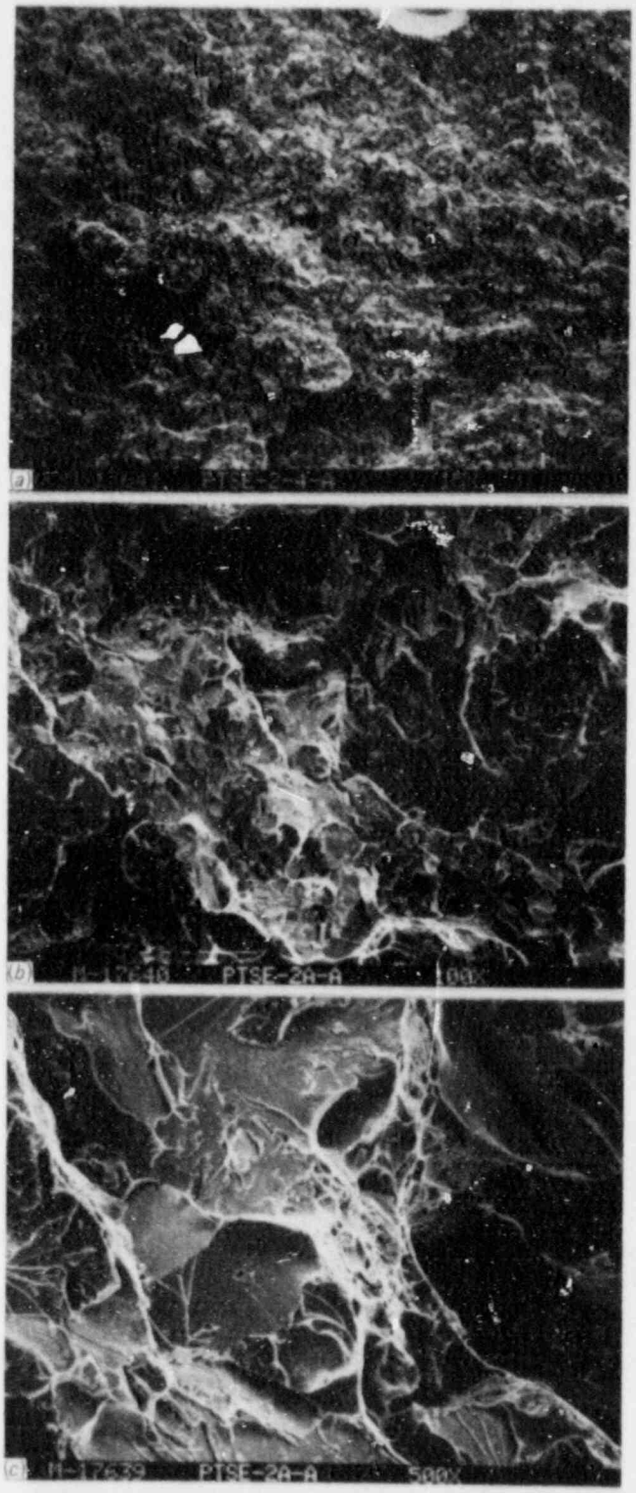

Fig. 9.13. Scanning electron fractographs of PTSE-2 in region just preceding PM4 showing that cleavage was primary mode of fracture with some ductile tearing occurring as tear ridges between cleavage planes. (*a*) 15×, (*b*) 100× in center part of (*a*), and (*c*) 500×, in center of part (*b*).

ORNL PHOTO 7743-87

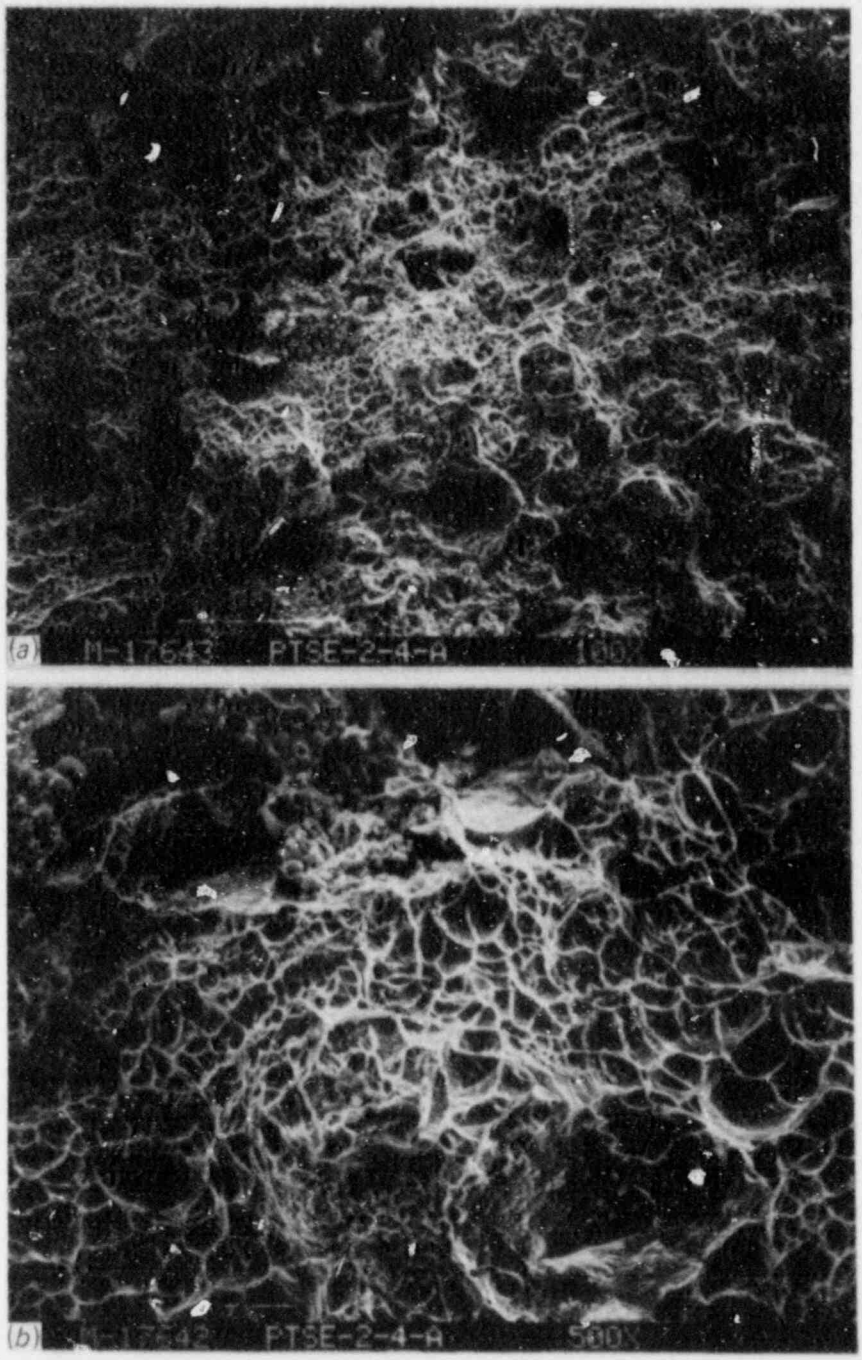

Fig. 9.14. Scanning electron fractographs of PTSE-2 in region of ductile tearing that followed cleavage arrest during the first transient. Region is between PM4 and PM5. (*a*) 100×, and (*b*) 500× in center of part (*a*).

ORNL PHOTO 7744-87

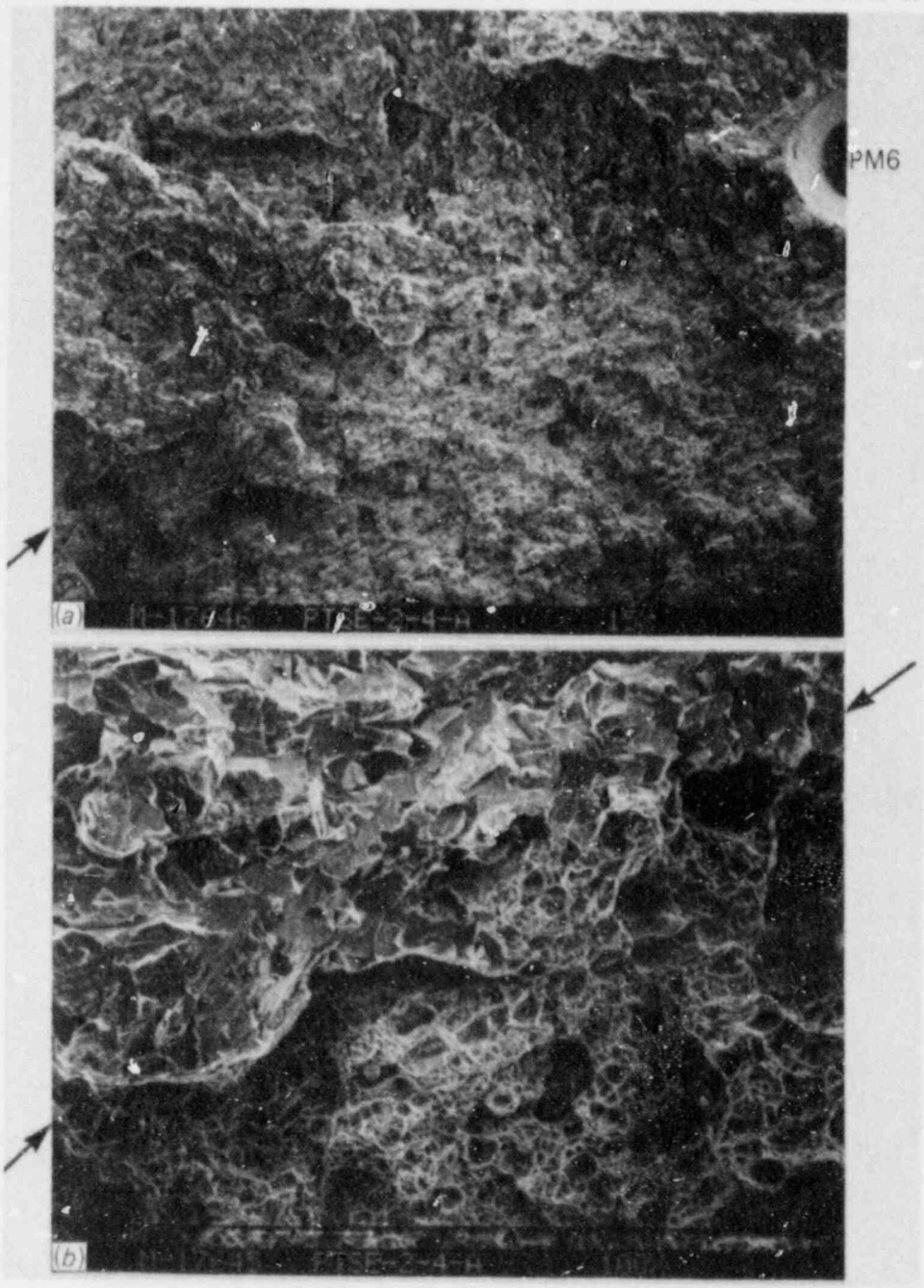

Fig. 9.15. Scanning electron fractographs of PTSE-2 at boundary between ductile tearing and cleavage regions of second transient. (*a*) 15× showing PM6 and (*b*) 100× in center of part (*a*).

ORNL PHOTO 7745-87

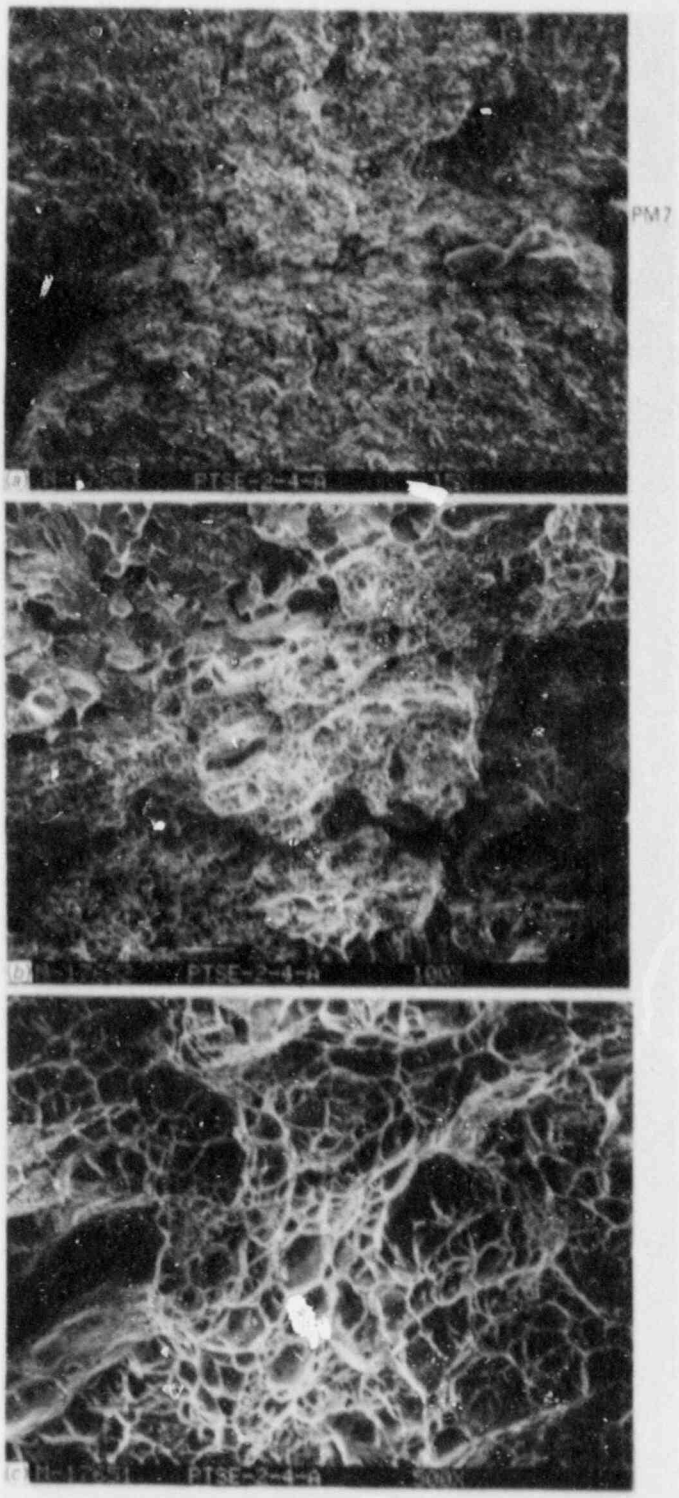

Fig. 9.16. Scanning electron fractographs of PTSE-2 in region of momentary crack arrest during second transient. (*a*) 15× showing PM7, (*b*) 100× in center of part (*a*) showing band of ductile tearing with cleavage before and after tearing band, and (*c*) 500× from center of part (*b*), clearly shows tearing mode.

M&C PHOTO Y209117

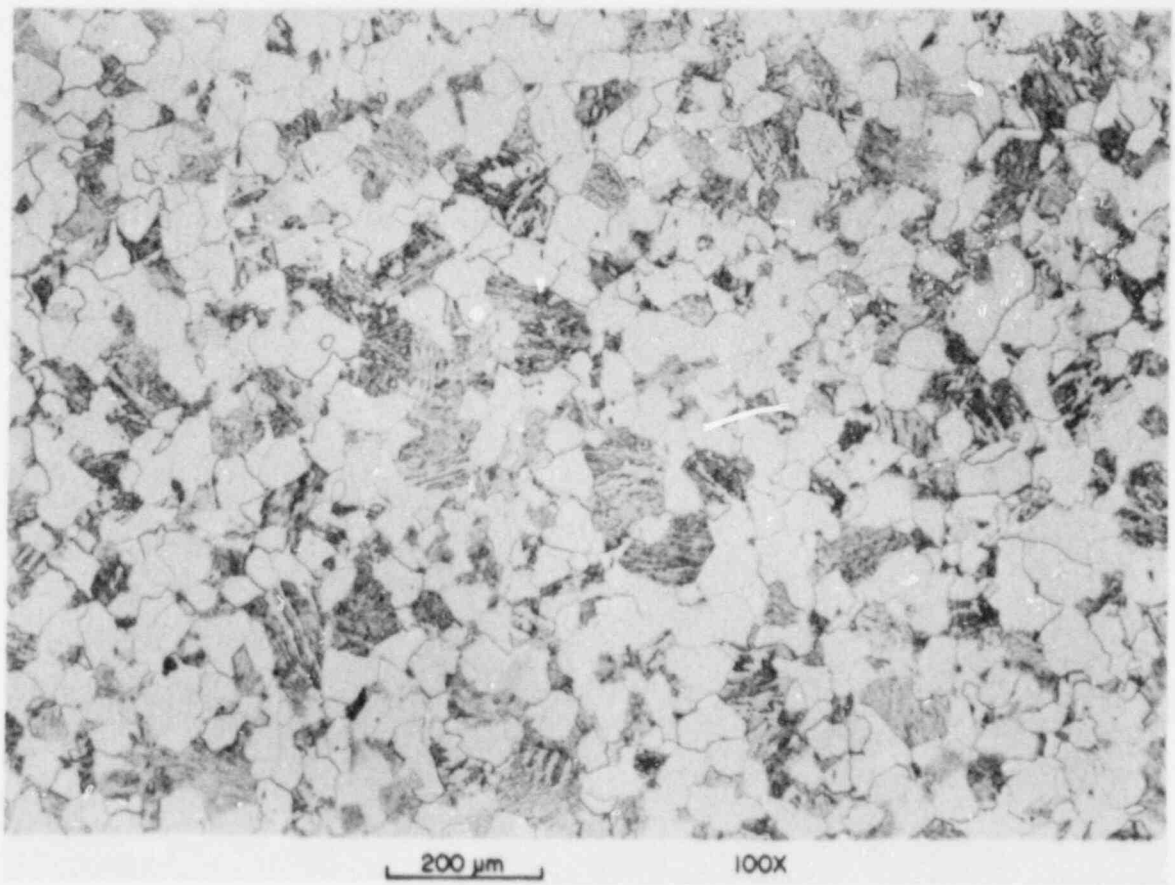

Fig. 9.17. Microstructure of PTSE-2 insert near outer surface of vessel taken on section perpendicular to flaw surface. The microstructure consists of ferrite with about 40% pearlite.

ORNL PHOTO 7746-87

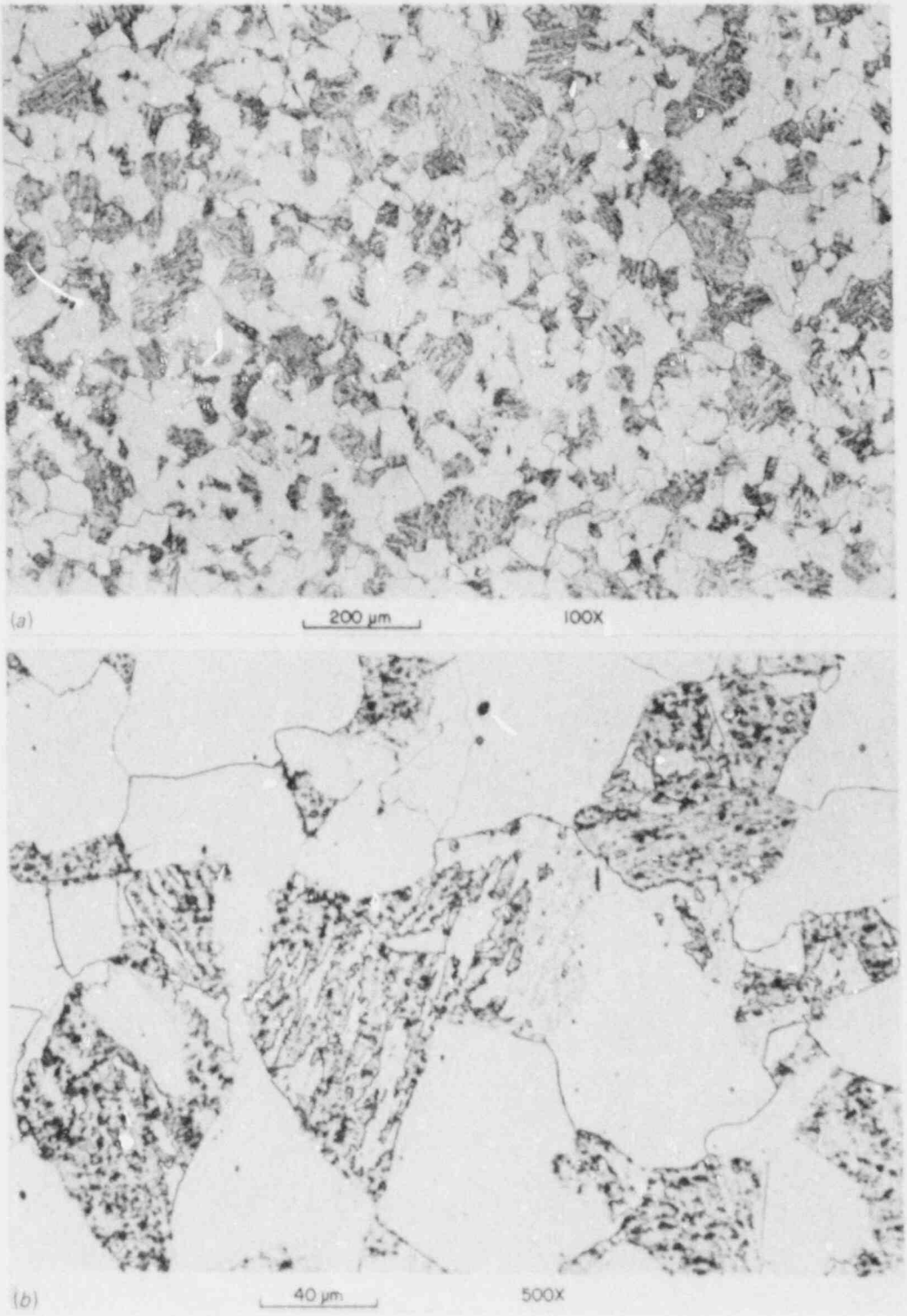

Fig. 9.18. Microstructure of PTSE-2 insert near the quarter-thickness depth taken on section perpendicular to flaw surface. (*a*) 100× shows a microstructure similar to that of Fig. 9.17, and (*b*) 500× shows details of the pearlite patches interspersed with carbides.

quarter-thickness depth, respectively. The microstructures are quite similar, consisting of ferrite and about 40% pearlite. The higher magnification in Fig. 9.18(*b*) shows the pearlite interspersed with carbides.

A microhardness traverse was also performed on a sample cut from segment 4A of the the vessel insert in the region of the fracture surface. Figure 9.19 is a composite photograph showing the fracture path and the microhardness indentations. The left side of the photograph is near the vessel outer surface; the right side is at the inner surface. Because the section had to be cut into three sections for mounting and hardness testing, a few millimeters of material was lost in the cutting operation.

Figure 9.20 is a plot of the measured diamond pyramid hardness (DPH) numbers as a function of depth from the vessel outer surface. Figures 9.19 and 9.20 have been annotated with approximate locations of the various boundary features discussed earlier. As mentioned earlier, the various boundary indications vary in depth with axial position, and distances between features in one axial position may be a few millimeters different from those in another position. Thus, the annotated boundary locations in Fig. 9.20 can be directly compared only with the surface shown in Fig. 9.19.

There are wide variations in DPH, shown in Fig. 9.20, ranging from about 160 to 240 DPH (neglecting the two peaks at ~260 DPH). That range corresponds to HRB 82 to HRB 98. A nominal average then would be about 200 DPH (HRB 91). As discussed in Chap. 2, a hardness of HRB 90 was measured at the quarter-thickness depth of the vessel insert with a larger indenter (Rockwell B). There are also two peak hardnesses at midthickness at about 260 DPH (HRB 101).

The microstructures in the regions of some of the microhardness indentations were examined, and two are shown in Fig. 9.21. Figure 9.21(*a*) was taken about 4 mm from the outer surface, and Fig. 9.21(*b*) was taken at about midthickness. It appears that the percentage of pearlite is greater in the midthickness and that the indenter was located in a fairly large patch of pearlite (harder than ferrite). It has been concluded that most of the variations in DPH are associated with the amount of pearlite sampled by the indenter. However, it is apparent that the average hardnesses are higher at midthickness and near the inner surface than they are near the outer surface.

OVERSIZE DOCUMENT PAGE PULLED

SEE APERTURE CARDS

NUMBER OF OVERSIZE PAGES FILMED ON APERTURE CARDS 1

APERTURE CARD/HARD COPY AVAILABLE FROM RECORD SERVICES BRANCH, TIDC
FTS 492-8989

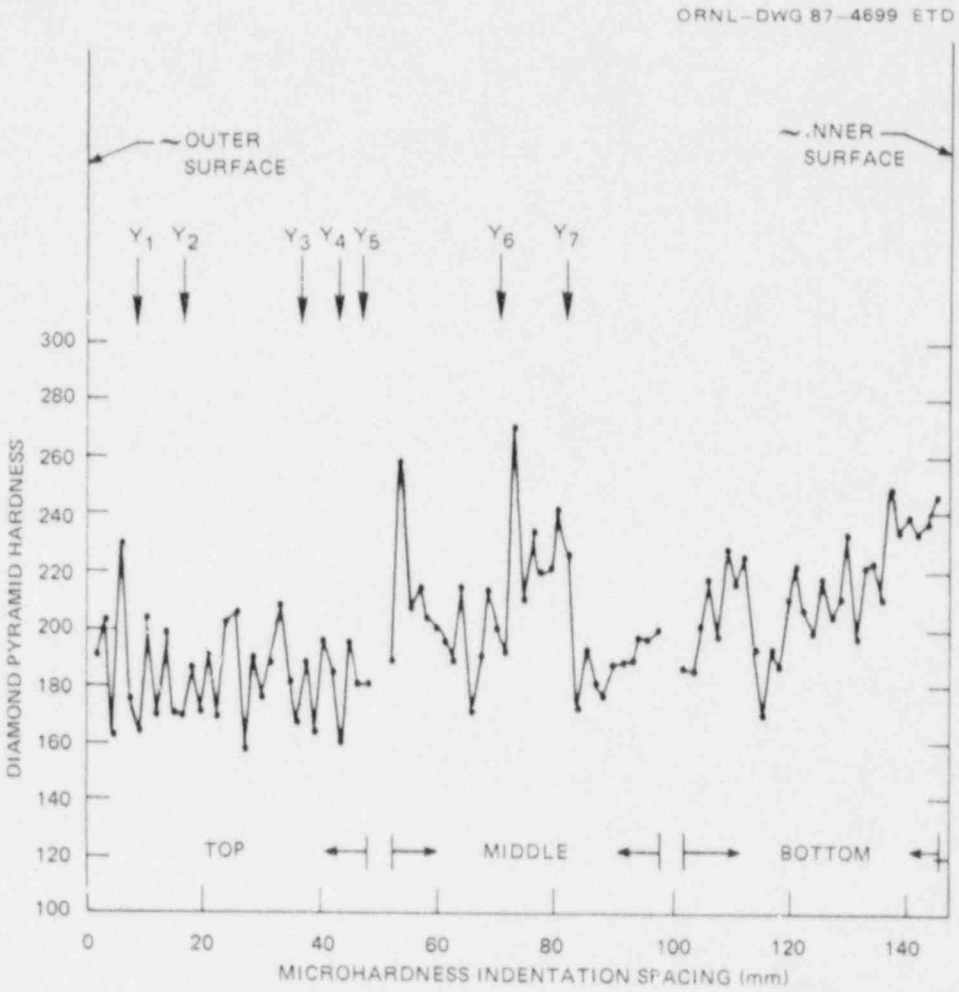

Fig. 9.20. Plot of microhardness (DPH) vs indentation spacing across thickness of the PTSE-2 vessel insert following testing. The "y" numbers refer to boundary designations defined in Table 9.1.

ORNL PHOTO 7748-87

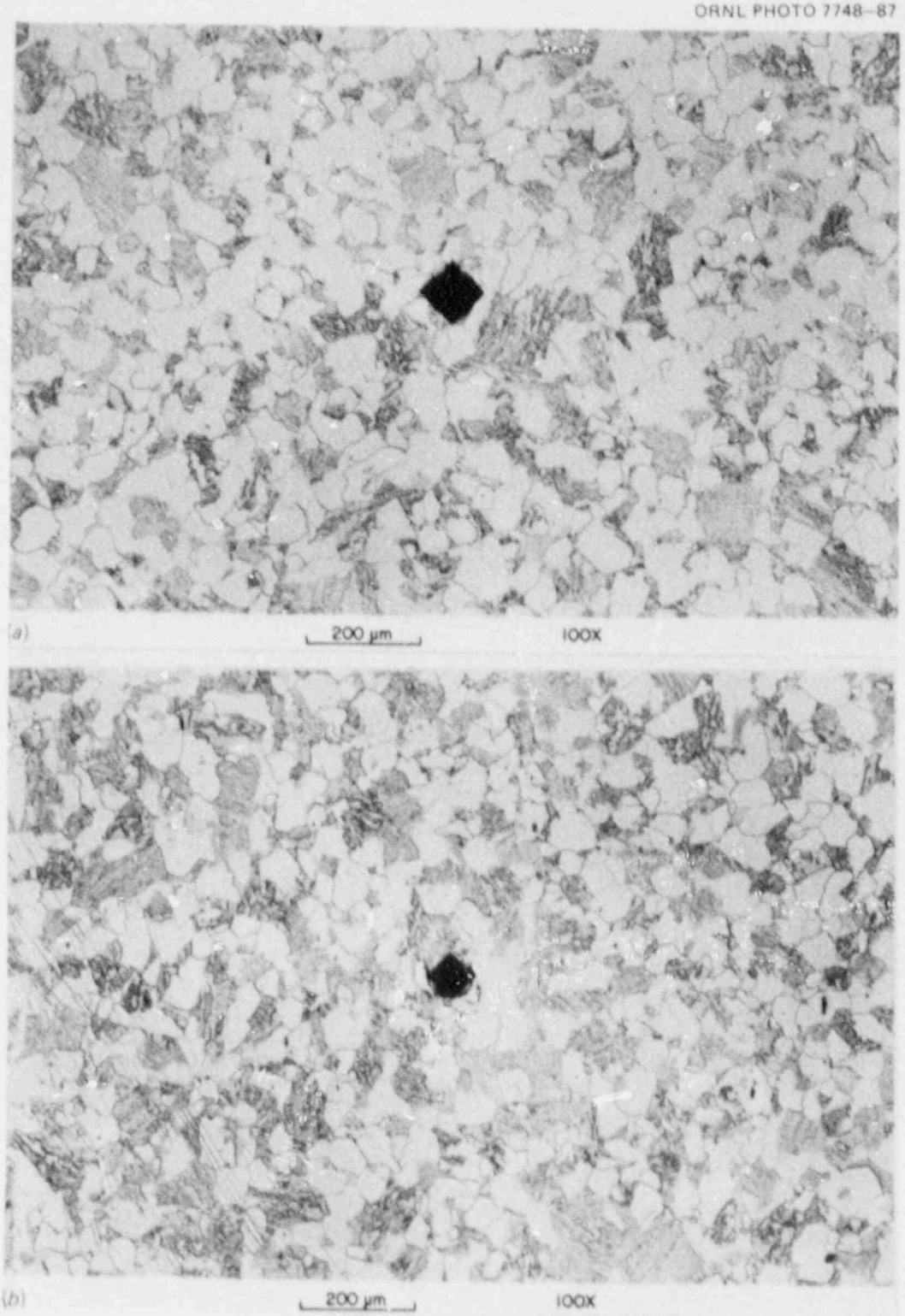

Fig. 9.21. Micrographs of PTSE-2 insert taken near microhardness indentations from (*a*) 162.3 DPH, about 4 mm from the outer surface, and (*b*) 267.9 DPH, near midthickness. The amount of pearlite appears to be somewhat greater at the midthickness.

10. ANALYSIS

10.1 Development of Test Plan

The primary objective of the pressurized-thermal-shock experiments is to provide a basis for evaluating methods of fracture analysis that could be applied to evaluation of pressurized-water-reactor vessels. The principal criteria for planning the experiments are as follows.

1. The tests will be designed to challenge the predictions of analytical methods that are applicable to full-scale reactor pressure vessels under combined loading.
2. The scale of the tests will be large enough to attain effectively full-scale restraint of the flawed region.
3. Material in the flawed region will be characterized by specimen tests before each vessel test.
4. Test conditions and materials will be selected to produce
   (a) realistic reactor pressure-vessel stress fields and gradients around the flaw and
   (b) realistic fracture-toughness conditions in the zone of potential flaw extension.
5. Loading conditions and controls will be used to prevent bursting the vessel (except when desired) to minimize damage to the test facility.
6. The test facility will be capable of producing (with realistic stresses) a variety of fracture possibilities:
   (a) cleavage initiation of small flaws;
   (b) cleavage initiation and arrest below the upper shelf;
   (c) cleavage initiation with arrest on the upper shelf;
   (d) arrest in a high positive K_I gradient;
   (e) warm and antiwarm prestressing states in succession; and
   (f) progressive (upper-shelf) tearing, tearing instability, and restabilization.

An implication of the first four criteria is that the test cylinder must be thick, a prerequisite satisfied by the Heavy-Section Steel Technology intermediate test vessels. Preliminary analyses were performed to evaluate the performance of these test vessels with respect to attaining reactor pressure-vessel-like stress fields. Two important characteristics were evaluated: (1) the small length and radius of the test vessel relative to the dimensions of reactor pressure vessels and (2) the location of the flaw on the outside of the test cylinder rather than the inside, as is assumed in reactor pressure-vessel evaluations. In the thermal-stress analysis of reactor pressure vessels, it is assumed that the vessel is effectively infinitely long. The preliminary studies showed that the nominal stress values near the middle of the vessel were nearly the same as those for an infinitely long cylinder but that the finite lengths of the crack and vessel and the existence of closure heads have to be considered in calculations of K_I for cracks deeper than $a/w = 0.1$ (Refs. 1 and 2). The studies also showed that the outside flaw location was satisfactory because the stress and K_I distributions relative to

the cracked and chilled surface are typical of the distributions in a reactor vessel with the flaw and thermal shock on the inside surface for cracks less than ~80% of the wall thickness.[3]

The PTSE-2 experiment was designed to produce and investigate a cleavage crack propagation and arrest followed by unstable tearing. The PTSE-1 experiment[4] might have approached this condition because J_R-curve analysis indicated that ~10 mm of ductile tearing should have ensued after the final PTSE-1 crack arrest. If the PTSE-1 flaw had been in the low-upper-shelf material used in PTSE-2, the extent of tearing would have exceeded 100 mm, according to a tearing resistance analysis.

The PTSE-2 experiment was also designed to continue the investigation of warm prestressing started in PTSE-1. The first experiment clearly demonstrated the inhibiting effect of warm prestressing for both positive and negative values of $\dot{K}_I$ when K_I was less than a previous relative maximum.[4] Initiation and reinitiation of propagation after periods of warm prestressing were also experienced in PTSE-1, but only after intervening periods of complete unloading. The PTSE-2 experiment was designed to (1) induce simple warm prestressing ($\dot{K}_I < 0$) before the time $K_I = K_{Ic}$, (2) induce simple antiwarm prestressing ($\dot{K}_I > 0$) while $K_I > K_{Ic}$, and (3) during antiwarm prestressing increase K_I to levels substantially above the prior maximum value.

The experiment was planned to be performed in two separate transients, each starting with the vessel at nearly isothermal conditions at about 300°C. In the first transient (PTSE-2A), the warm-prestressing phases of combined loading were pursued with the expectation that the crack would propagate by cleavage and then arrest at a depth suitable for the second transient (PTSE-2B). The second transient was designed to satisfy the primary objective concerning low tearing resistance and to determine also a valid value for K_{Ic}, unperturbed by warm prestressing.

10.2 Methods of Analysis

Extensive computational analyses were performed to determine material parameters and optimum pressure-temperature transients compatible with the proposed test plan and with the capabilities of the pressurized-thermal-shock test facility. Both linear and nonlinear material models, as well as 2- and 3-D finite-element representations of crack geometries, were employed. Computational economy required application of techniques suitable for parametric studies involving a large number of transients. The OCA/USA computer program was developed to perform these parametric studies for the planning of the first test, that is, PTSE-1. OCA/USA combines the previously developed features of OCA-II (Ref. 5), an inelastic ligament instability analysis,[6] and an upper-shelf ductile tearing computer program PTSUSA[7] with a superposition method for calculating K_I for a crack of finite length in a cylindrical vessel with hemispherical heads.[4]

The OCA/USA computer program was used extensively to explore combinations of thermal and pressure transients and material properties. This program performs linear elastic fracture analysis based on superposition of combined loadings with K_I factors determined from both 2- and 3-D

models of the vessel and flaw. In addition, the program determines plastic-zone-size K_I adjustments, giving a pseudo-elastic-plastic K_I, and performs ductile tearing and tensile instability analyses.

Finite-element representations of PTSE-2 were analyzed with the ORMGEN/ADINA/ORVIRT system of computer programs.[8-11] Two-dimensional models were used to investigate elastic-plastic behavior for several loading sequences of importance in planning the PTSE-2 transients. Three-dimensional models were used, first, to calculate influence coefficients for the OCA/USA representation of a finite-length crack in a closed cylinder and, second, to establish the numerical basis for relationships of CMOD-pressure-times vs crack depth for use in rapid interpretation of data while an experiment was under way. Finally, 3-D models were used to analyze all of the crack shapes developed during the PTSE-2 experiment.

10.3 Elastic-Plastic Finite-Element Analysis

10.3.1 Two-dimensional analysis

Two-dimensional plane-strain elastic-plastic finite-element analyses using the ORMGEN/ADINA/ORVIRT fracture analysis system[8-11] were performed to supplement the OCA/USA linear elastic fracture mechanics calculations in both pretest and posttest analyses. Collapsed wedge elements that allow for crack-tip blunting were employed to give the appropriate 1/r singularity at the crack tip for the elastic-plastic computations. Regular eight-noded isoparametric quadrilaterals were used elsewhere in the modeling.

A typical finite-element model for these analyses is shown in Figs. 10.1 and 10.2. This model contains 116 elements and 395 nodes. A 2 by 2 Gauss integration rule was used.

The cylinder was assumed to be a composite of the two materials, A and B, as shown in Fig. 10.1. The dimensions of the model were the same as in the OCA/USA analysis: wall thickness w = 147.6 mm and inside radius = 343.0 mm. The stress-strain properties of material A were from measured tensile properties of material representing the insert of 2 1/4 Cr-1 Mo low-upper-shelf material in the PTSE-2 vessel; the properties of material B represented the balance of the cylinder, which is ASTM A 533 grade B class 1 steel.

Several sets of tensile properties representing the elastic modulus and the stress-strain relationship for material A were used in pretest and posttest analyses. The properties (called set 5) used for the final pretest analysis and for the final posttest analysis of transient PTSE-2A were based on transversely oriented tension specimen tests of the characterization material PTC1. The properties (called set 7) used for the final posttest analysis of transient PTSE-2B were based on similar specimen tests of material cut from the fractured insert. The latter tension tests were performed, first, to help resolve the uncertainty of the pretest properties, which arose from the evident variability of the 2 1/4 Cr-1 Mo steel plate discussed in Chap. 2 and, second, to evaluate the effect of strain hardening that resulted from the PTSE-2 transients themselves.

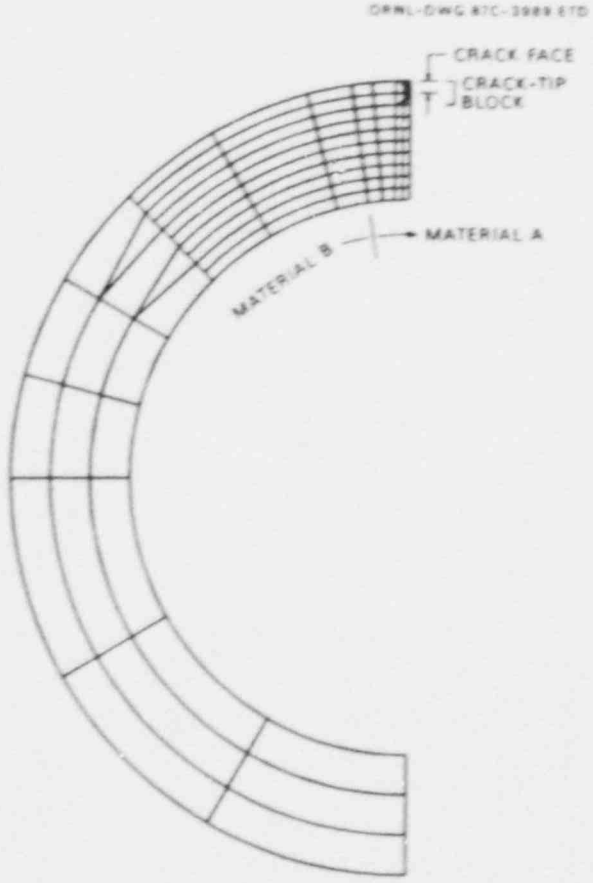

Fig. 10.1. Two-dimensional finite-element mesh for PTSE-2 cylinder with a crack with depth-to-thickness ratio a/w = 0.1.

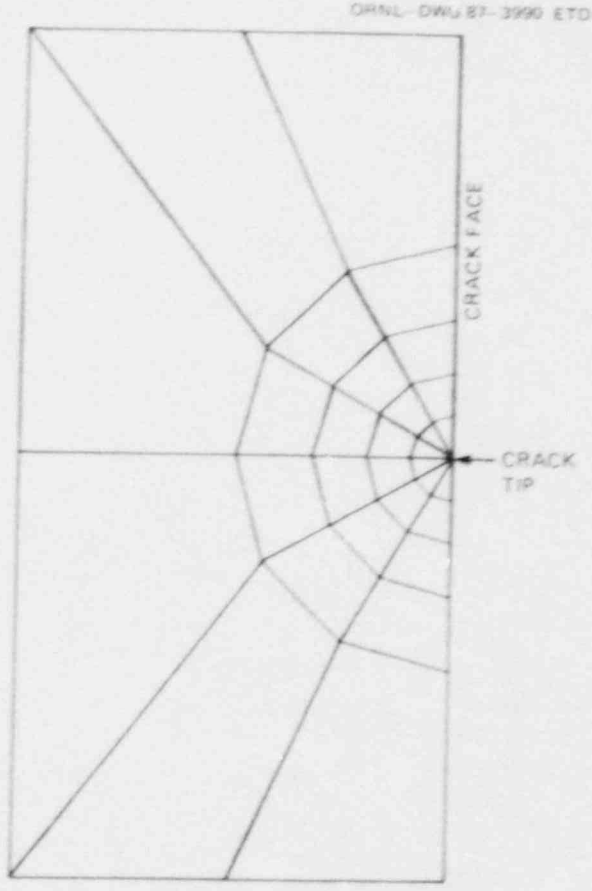

Fig. 10.2. Finite-element mesh of crack-tip block of elements in two-dimensional model of PTSE-2.

The representativeness of PTC1 was not established conclusively. However, studies of all the tensile property data made a plausible basis for representing the vessel insert by property set 5 for the first transient and by property set 7 for the second.

For the finite-element model, the stress-strain properties of the two materials were represented by the temperature-independent piecewise-linear relationships shown in Fig. 10.3. The stress-strain parameters are presented in Table 10.1. Other properties, which are also independent of temperature, are given in Table 10.2.

The ORVIRT program calculates the total strain-energy release rate G, which is converted to K_I by

$$K_I = \sqrt{\frac{E\,G}{1-\nu^2}}\ , \qquad (1)$$

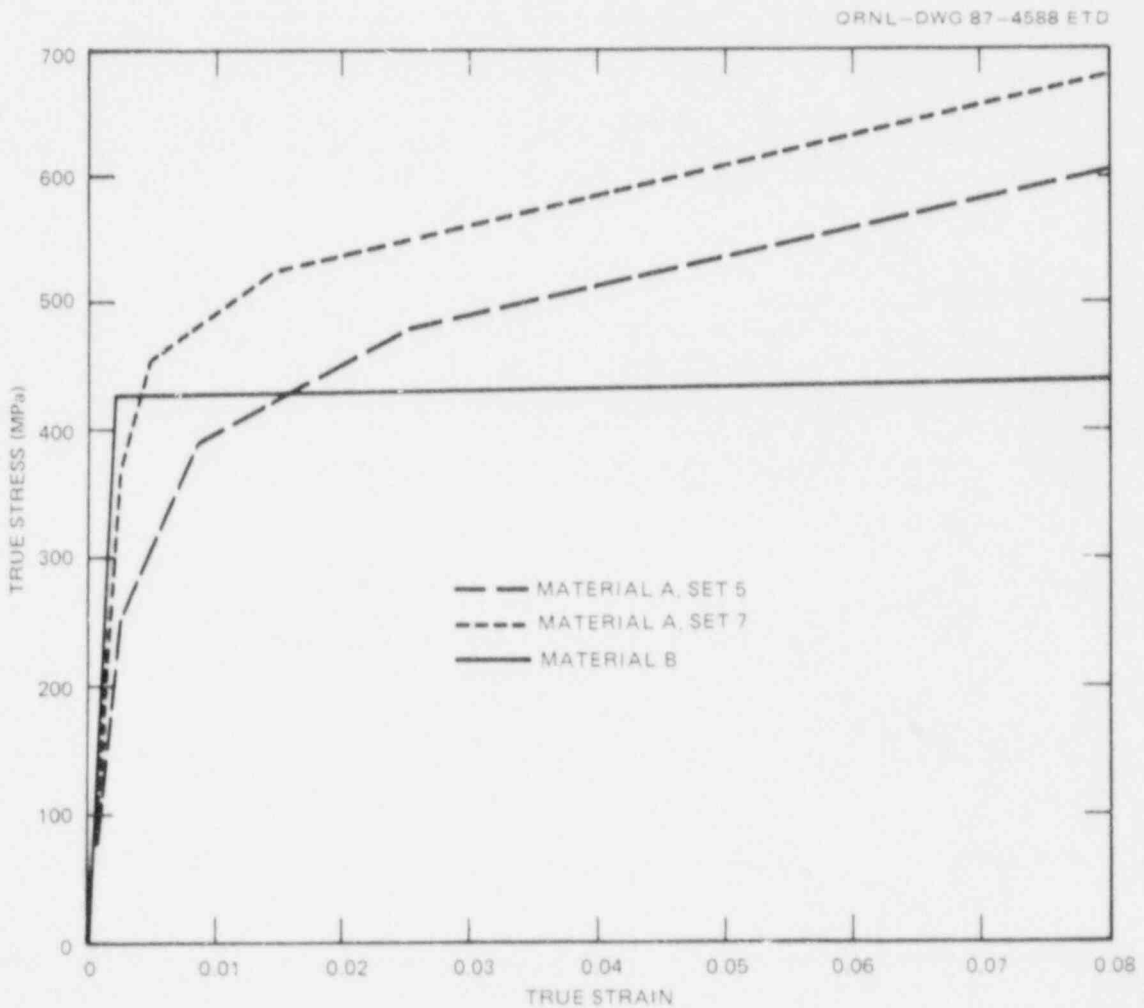

Fig. 10.3. Piecewise linear representations of stress-strain characteristics of low-upper-shelf insert (material A) and base metal (material B). Property set 5 is based on PTC1 data and property set 7 on vessel insert data.

Table 10.1. Stress-strain parameters for elastic-plastic finite-element analysis

(Coordinates of vertices in multilinear representations of material[a])

Material A[b] Set 5[c]		Material A[b] Set 7[d]		Material B	
Strain	Stress (MPa)	Strain	Stress (MPa)	Strain	Stress (MPa)
0	0	0	0	0	0
0.000335	70.731	0.00039	77.220	0.002113	427.47
0.0026	250.	0.00226	360.0	0.05	434.13
0.0088	390.	0.00494	453.2		
0.0250	478.	0.01484	524.2		
0.0600	557.	0.04980	604.7		

[a]For strains greater than the last values tabulated, the modulus for the preceding strain interval applies.

[b]Material A representations are approximations to true stress-true strain data from tension tests described in Chap. 2. The specimen selected for each set exhibited a load-displacement behavior representative of an average for the set.

[c]From specimen PI372, one of six 12.7-mm-diam tension specimens from characterization piece PTC1. The specimens were transversely oriented, which is synonymous with the circumferential orientation in the vessel.

[d]From specimen PE08, 1 of 17 6.4-mm-diam circumferentially oriented specimens from the insert removed from the test vessel. The elastic segment of the representation was adjusted to be consistent with an average measured modulus of elasticity at 100°C.

Table 10.2. Thermoelastic properties used in finite-element models of PTSE-2 for 2- and 3-D elastic-plastic analysis

Property	Material		
	A Set 5	A Set 7	B
Young's modulus, MPa	211,137	198,000	202,300
Elastic limit, MPa	70.731	77.220	427.47
Poisson's ratio, ν	0.3	0.3	0.3
Coefficient of thermal expansion, α (K^{-1})	14.4×10^{-6}	14.4×10^{-6}	14.4×10^{-6}

where E is Young's modulus and ν is Poisson's ratio. Young's modulus for material A is used in this conversion. Heat transfer and thermoelastic properties of material B, which constituted more than 96% of the cylindrical shell, were attributed to the entire shell for calculations of G.

Each set of elastic-plastic analyses was based on a particular pressurized-thermal-shock loading sequence that was also analyzed by the OCA/USA program. In each case, a corresponding set of elastic finite-element calculations was performed for comparison with the results of elastic-plastic and OCA/USA analyses.

Sets of pretest elastic-plastic analyses were made for each planned transient. In each case, calculations were performed for three crack depths: with a/w = 0.1, 0.3, and 0.5. Posttest analyses were made for loadings of pressure and thermal shock represented by experimental pressures p(t) and temperature distributions T(r,t). The measured crack depths appropriate for each phase of the PTSE-2 transients were used in the posttest analyses.

Variations of the finite-element model were analyzed to evaluate effects of mesh refinement and material property models. Figure 10.4 shows the effect of modeling the entire vessel as a homogeneous structure having the properties of the plug, material A. The mesh shown in Figs. 10.1 and 10.2 was used for this set of computations. The difference in K_I for the two linear-elastic cases is not great, partly because the elastic moduli of materials A and B are nearly the same. The elastic-plastic cases demonstrated the necessity of using a nonhomogenous model because differences are 10% or greater for times of importance in the transient.

Two sets of posttest elastic-plastic finite-element calculations were performed to determine the importance of minor variations in the stress-strain relationship near the elastic limit. Values of the computed strain-energy release rate (G) and K_I based on property set 7 (Tables 10.1 and 10.2) were compared with values computed for an identical stress-strain relationship except that the elastic limit was 7.5% lower than the set 7 limit. The values of G differed by <1% and the K_I values by <0.5%. For the substantial differences in the stress-strain relationships of sets 5 and 7 (see Fig. 10.3), values of G generally differed by 2 to 20%, depending on crack depth and loading. Thus, the posttest calculations of K_I depend strongly on which stress-strain behavior is assumed to apply. For reasons discussed in Chap. 2 the posttest calculations of K_I were based on property set 5 (from characterization piece PTC1) for transient PTSE-2A and on property set 7 (from the vessel insert) for transient PTSE-2B.

Two finite-element meshes, one finer and one coarser than that used in the PTSE-2 analyses, were evaluated. The details of these two variants are shown in Fig. 10.5. The elastic-plastic K_I values for the two variants differed from the values for the PTSE-2 mesh by <0.26%. The nonhomogeneous material structure shown in Fig. 10.1 was used in all three cases. Far from the crack, the element structure in the coarse 2-D model is similar to that of the 3-D model.

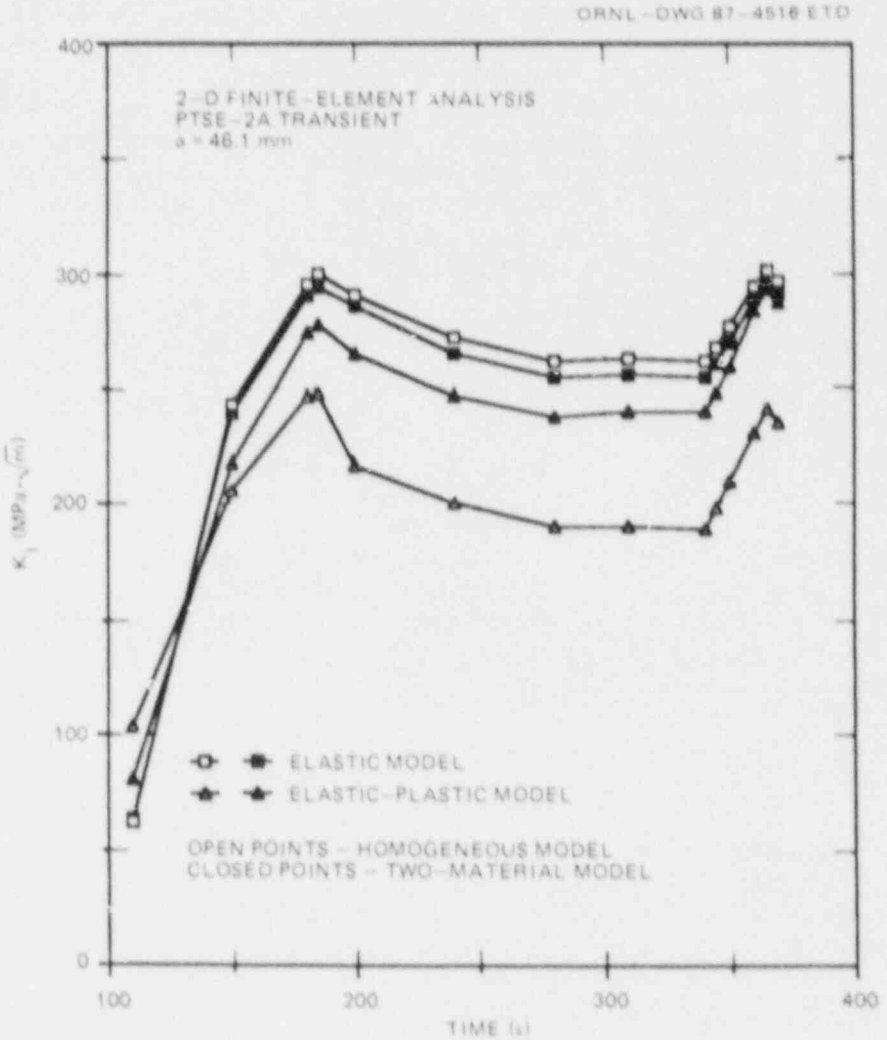

Fig. 10.4. Effect of using a homogeneous two-dimensional finite-element model: comparison of K_I vs t for homogeneous and two-material models for a = 46.1 m.

10.3.2 Three-dimensional analysis

The 3-D finite-element model shown in Fig. 10.6 was used for post-test analysis. The model, which represents one quarter of the test vessel, consists of 20-noded isoparametric brick elements throughout the structure with collapsed wedge elements at the crack tip. Mesh generations and computations were performed with the ORMGEN/ADINA/ ORVIRT system of computer programs. The model for flaws with depths up to 22.5 mm comprises 846 elements with 4239 nodes. The model for deeper flaws has 830 elements with 4143 nodes. There are ten element divisions along the crack tip.

The material properties were represented by the same parameters used in the 2-D elastic-plastic analyses (Tables 10.1 and 10.2 and Fig. 10.3). A comparison of results of 2- and 3-D computations is shown in Fig. 10.7.

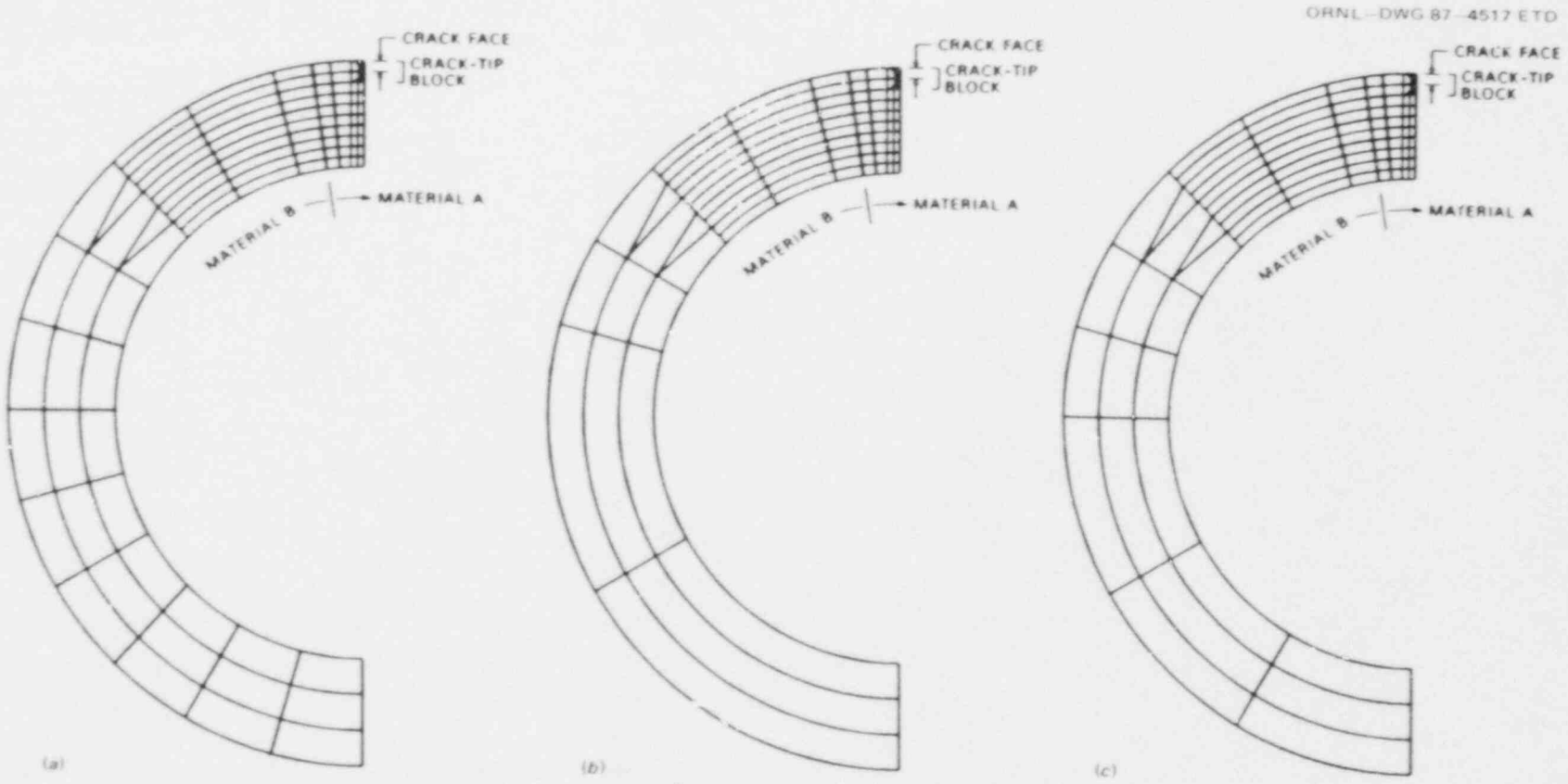

Fig. 10.5. (*a*) Coarser and (*b*) finer two-dimensional finite-element meshes used in refinement study; (*c*) basic PTSE-2 mesh.

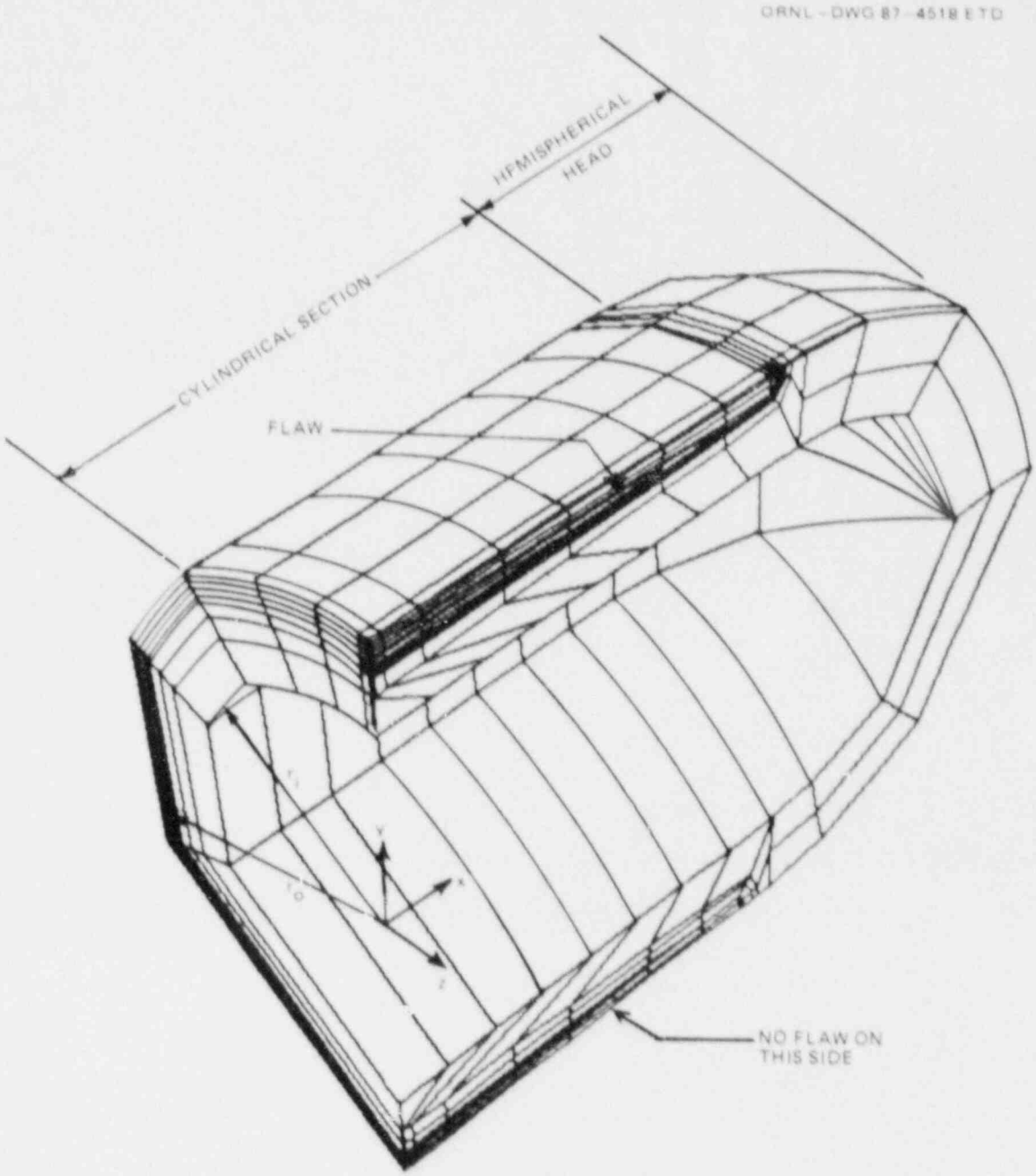

Fig. 10.6. Three-dimensional finite-element model used in PTSE-2 posttest analysis.

Figure 10.7(a) shows the 3-D K_I to be higher than the 2-D result in the latter part of the PTSE-2A transient. This is probably a spurious consequence of the coarseness of the mesh near the crack tip in the 3-D model. Calculations similar to those represented in Fig. 10.7 disclosed that the 3-D results are highly dependent on the size of successive load steps. This suggests that the stress and strain fields in the long, thin crack-tip elements do not well represent a converged solution.

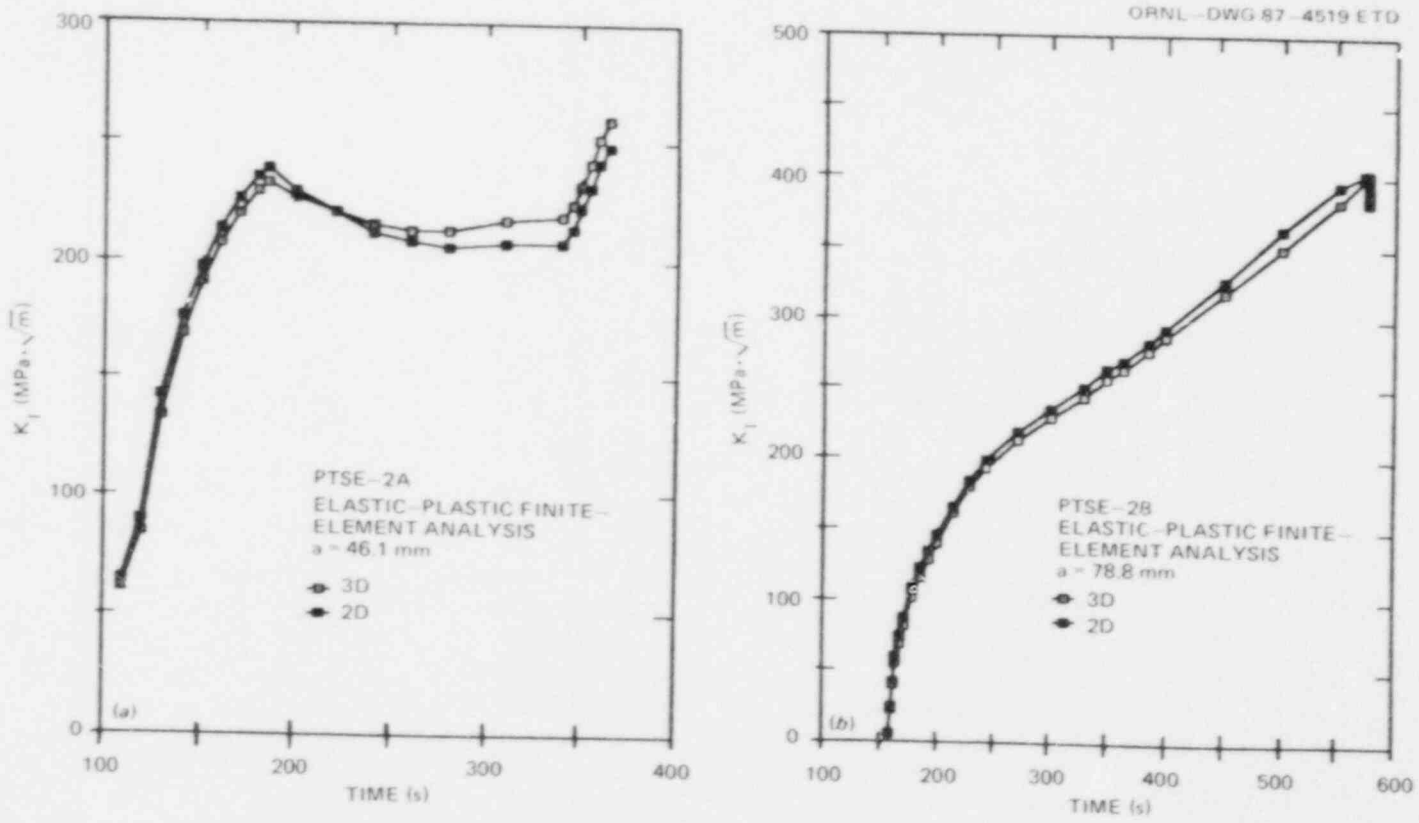

Fig. 10.7. Comparison of results of 2- and 3-D finite-element computations based on measured pressures and temperatures. K_I vs t for (*a*) PTSE-2A transient with a = 46.1 mm and (*b*) PTSE-2B transient with a = 78.8 mm. Values of K_I are for the center of the crack for the 3-D cases.

10.4 Final Pretest Fracture Analysis

10.4.1 Pretest assumptions and data

The principal purpose of pretest analysis was to define thermal and pressure transients that were most likely to produce the conditions and events essential to the objectives of the PTSE-2 experiment. Analyses were also performed to provide the basis for rapid interpretation of data during the experiments so that the test operations could be controlled properly.

Because of the undesirably low yield strength of the PTSE-2 material, it was necessary to perform elastic-plastic finite-element calculations to supplant the plastic-zone-size adjustment routine in the OCA/USA computer program. Two-dimensional ADINA/ORVIRT analyses were performed to model the specific transients being analyzed by the OCA/USA program as candidates for the PTSE-2A and -2B transients.

Early OCA/USA analyses showed that the success of an experiment involving both warm prestressing and anti-warm prestressing depended on properly timing the transient to accommodate uncertainties in the imposed transient and in K_{Ic} and K_{Ia}. Uncertainties in the performance of the test facility were evaluated by performing OCA/USA analyses for ranges of values of the relevant time-dependent parameters: bulk coolant temperature $T_B(t)$, convective heat transfer coefficient $h(t)$, and vessel internal pressure $p(t)$. As significant new toughness data were generated, new K_{Ic} and K_{Ia} vs temperature relationships were adopted as the basis for another iteration of parameter studies. The effects of the choice or assumption of initial vessel temperature, coolant temperature, convective heat transfer, yield strength, flow stress, ductile tearing resistance, and initial crack depth were investigated. Uncertainties in none of these factors had as profound an influence on the selection of the first pressure transient (PTSE-2A) as did the fracture toughnesses K_{Ic} and K_{Ia}. Furthermore, when the transitional temperature range had been defined for PTSE-2 material by Charpy impact tests and when the first K_{Ic} data were obtained, it was evident that the thermal parameters of the PTSE-1C experiment were suitable for PTSE-2A. Consequently, it was decided to try, in the PTSE-2 experiment, to replicate the PTSE-1C heat-transfer conditions. Accordingly, the subsequent OCA/USA analyses were concerned primarily with selecting pressure transients suitable for two successive transients: (1) PTSE-2A for warm prestressing, anti-warm prestressing, initiation of cleavage fracture, and crack arrest at a shallow depth and (2) PTSE-2B for initiation of cleavage and crack arrest under conditions of tearing instability.

Except for the narrow plug of low-upper-shelf material, the PTSE-2 vessel was the same as the PTSE-1 vessel. Therefore, the same geometric and thermo-elastic parameters that were used in the PTSE-1 analysis[4] were used for PTSE-2. The parameter values used in all OCA/USA analyses are given in Table 10.3. The flaw depth before the PTSE-2A transient, 15 mm, was estimated from ultrasonic measurements described in Chap. 3.

Material properties. Properties that were determined early from tests of characterization piece PTC1 were from tensile, Charpy impact, and drop-weight tests. The data from these tests, which are presented in

Table 10.3. Characteristics of the test vessel used in all pretest OCA/USA analyses of PTSE-2

Parameter	Value
Material properties	
E, MPa	202,300
α, K^{-1}	14.4×10^{-6}
Poisson's ratio, ν	0.3
Conductivity K, $W \cdot m^{-1} \cdot K^{-1}$	41.54
Heat capacity c, $J \cdot kg^{-1} \cdot K^{-1}$	502.4
Density ρ, kg/m^3	7833
Geometry of vessel	
Inside radius r_i, mm	343
Wall thickness w, mm	147.6
Flaw length 2b, mm	1000
Initial flaw depth[a]	
a, mm	15
a/w	0.1

[a]Before the PTSE-2A transient.

detail in Chap. 2, are summarized in Table 10.4. Tearing resistance (J_R) data for PTC1 are shown in Fig. 10.8 in comparison with data from irradiated low-upper-shelf welds.[12,13*] Figure 10.8 shows that the PTSE-2 material is a good representation of irradiated low-upper-shelf welds with respect to tearing resistance.

Because yield strength was particularly difficult to evaluate for the characterization material, values of flow stress from 385 to 600 MPa were used as a basis for parametric OCA/USA analysis of tensile instability. For final pretest analyses, limiting values of flow stress of 270 and 428 MPa were chosen from the pretest tensile data (Table 2.5), because they represented a plausible range for data that were considered uncertain.

Evolution of toughness data and transient plans. It was expected that fracture toughness data for the PTSE-2 material would be uncertain, and early OCA/USA parameter studies were designed to reveal the impact of this uncertainty. As K_{Ic}, K_J, and K_{Ia} data were adduced, they became the basis for a succession of $K_{Ic}(T)$ and $K_{Ia}(T)$ relationships used in the OCA/USA analyses by which the PTSE-2 transients were eventually defined. The dependence of toughness on temperature was assumed to have the form

*References 12 and 13 present tearing resistance data in terms of J-deformation and J-Ernst modified, respectively. Tearing resistance in Fig. 10.8 is J-deformation.

Table 10.4. PTSE-2 characterization material (PTC1) properties

Property	Value
Yield strength, MPa	255
Ultimate strength, MPa	518
NDT temperature, °C	49
Onset of Charpy upper shelf (100% shear fracture appearance), °C	150
Charpy upper-shelf energy, J	~50–75[a]
Charpy transition temperature, °C	
At 50% shear fracture app	90
At 0.89-mm lateral expans	98

[a]Range for all depths in ...e. The average at 1/4 depth is ~68 J.

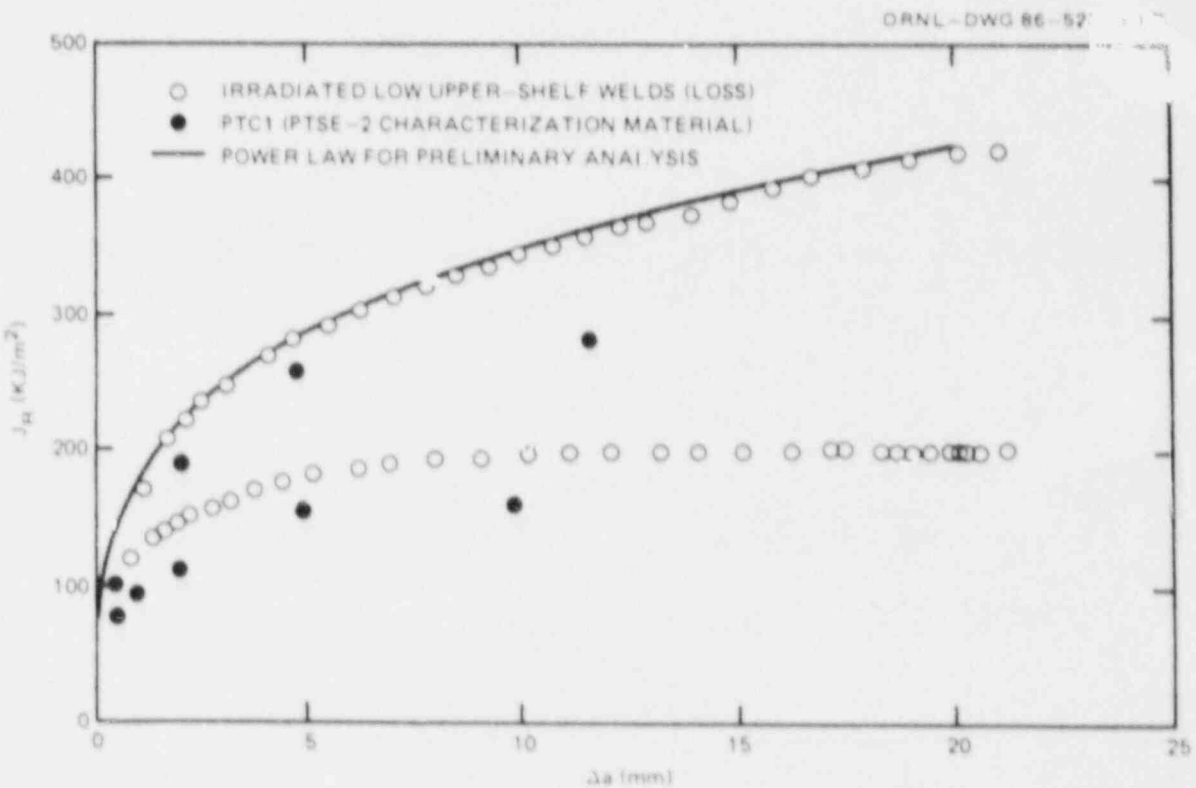

Fig. 10.8. Tearing resistance J_R vs crack extension Δa for PTC1, characterization material for low-upper-shelf plug in the PTSE-2 vessel. PTC1 data are compared with data from tests of irradiated high-copper welds. The points plotted are for the highest and lowest J_R curves for each of the two materials.

$$K_{Ic} \text{ and } K_{Ia} = a + b \exp(cT) , \quad (2)$$

where T is temperature in degrees Celsius and a, b, and c are parameters determined from characterization material test data. Fracture analyses performed to help define useful transients were usually based on both high- and low-toughness assumptions represented in each case by appropriate sets of the parameters a, b, and c.

It was clear that the toughness data from the PTSE-2 characterization material tests (of piece PTC1) were inadequate to define K_{Ic} and K_{Ia} well at temperatures of importance in the PTSE-2 experiment, that is, at temperatures high in the brittle-ductile transition. However, on the basis of PTSE-1 experience,[4] it was presumed that the K_{Ia} data, for which there were many more plausible data than for K_{Ic}, indicated a toughness range appropriate for planning the experiment. Thus, upper and lower K_{Ia} parameters were determined first, and then K_{Ic} expressions that were compatible with these arrest toughnesses were sought.

Before any PTSE-2 characterization data were available, toughness vs temperature relationships for OCA/USA fracture analysis were adopted from Sect. XI of the *ASME Boiler and Pressure Vessel Code*.[14] Because the transition-temperature range was unknown during this phase of analysis (5 to 19 months before the test), transients were analyzed with RT_{NDT} ranging from 40 to 110°C. When K_{Ic} data for PTSE-2 material were first available, it was clear that the adopted asymptotic values of toughness at low temperature should be reduced to be consistent with the valid K_{Ic} data. Consequently, values of the parameter a of 37 and 25 were adopted for $K_{Ic}(T)$ and $K_{Ia}(T)$, respectively, for the next phase of analysis (from 1 to 5 months before the test). Values of the parameters b and c used in PTSE-1 were adopted. The amplitude parameter b was adjusted to account for the apparent RT_{NDT} of PTSE-2 being different from the RT_{NDT} of PTSE-1 (91.3°C). The real RT_{NDT} of PTSE-2 material is ill defined, but values of this parameter from 75 to 90°C were used in OCA/USA analyses to account for uncertainty in toughness.

The first K_{Ia} data for PTSE-2 characterization material were the basis for the next set of K_{Ic} and K_{Ia} parameters used in OCA/USA fracture analysis. The K_{Ia} parameters b and c were determined first (for a = 25) by a least-squares fit of the expression in Eq. (2) to seven K_{Ia} data from 0 to 82°C (see Chap. 2). The parameters for this $K_{Ia}(T)$ were used in OCA/USA analysis as an upper-toughness option (see "Preliminary Curves" in Table 10.5).

The lower-toughness expression for K_{Ia} was based on the expression of Eq. (2) fitted by least squares to β-adjusted K_{Ia} data.[15] In PTSE-1 the K_{Ia} curve based on β-adjusted data agreed best with the pressurized-thermal-shock experiment. The fitted expression was very close to the upper-K_{Ia} expression shifted by 30 K. Therefore, for simplicity in OCA/USA parameter studies, the shifted upper-K_{Ia} expression was used for the lower K_{Ia}.

Upper- and lower-K_{Ic} curves were chosen to fit the low-temperature K_J data from characterization tests at −75 and −25°C, but these data had no bearing on transitional toughness. Consequently, the transitional

Table 10.5. Fracture properties in OCA/USA analyses

Property	Parameter value				
	Tearing[a]		Cleavage[b]		
	c	n	a	b	c
J_R	1.4	0.3			
Preliminary curves					
K_{Ic} upper			37	35.911	0.01769
lower			37	21.122	0.01769
K_{Ia} upper			25	21.619	0.01769
lower			25	12.716	0.01769
Final curves					
K_{Ic} upper[c]			39	19.666	0.02878
lower			39	8.294	0.02878
K_{Ia} upper			34	11.143	0.02413
lower			34	7.96	0.02133

[a] $J_R = c(\Delta a)^n$, where J_R is in megajoules per square meter and Δa is in meters.

[b] K_{Ic} or $K_{Ia} = a + b \exp(cT)$, where K_I is in megapascals times square root meters and T is in degrees Celsius.

[c] These parameters used in Eq. (11) with $T_s = 20.26$ K give a value of K_{Ic} that agrees with the crack initiation observed in PTSE-2B.

portion of the K_{Ic} curves was based, for lack of other reliable hypotheses, on compatibility with the derived K_{Ia} toughness curves. It was noticed that at moderate transitional K_I levels in PTSE-1, the K_{Ic} and K_{Ia} curves were separated by ~30 K, namely,

$$K_{Ic}(T) \approx K_{Ia}(T + 30) , \tag{3}$$

where temperature is in degrees Celsius. The preliminary K_{Ic} parameters in Table 10.5 were obtained by Eq. (3).

The final pretest expressions for K_{Ia} (Table 10.5) were determined by least-squares fits to the complete sets of raw and ß-adjusted data from characterization piece PTC1. The K_{Ia} data are shown in Fig. 10.9 with the upper and lower-K_{Ia} curves.

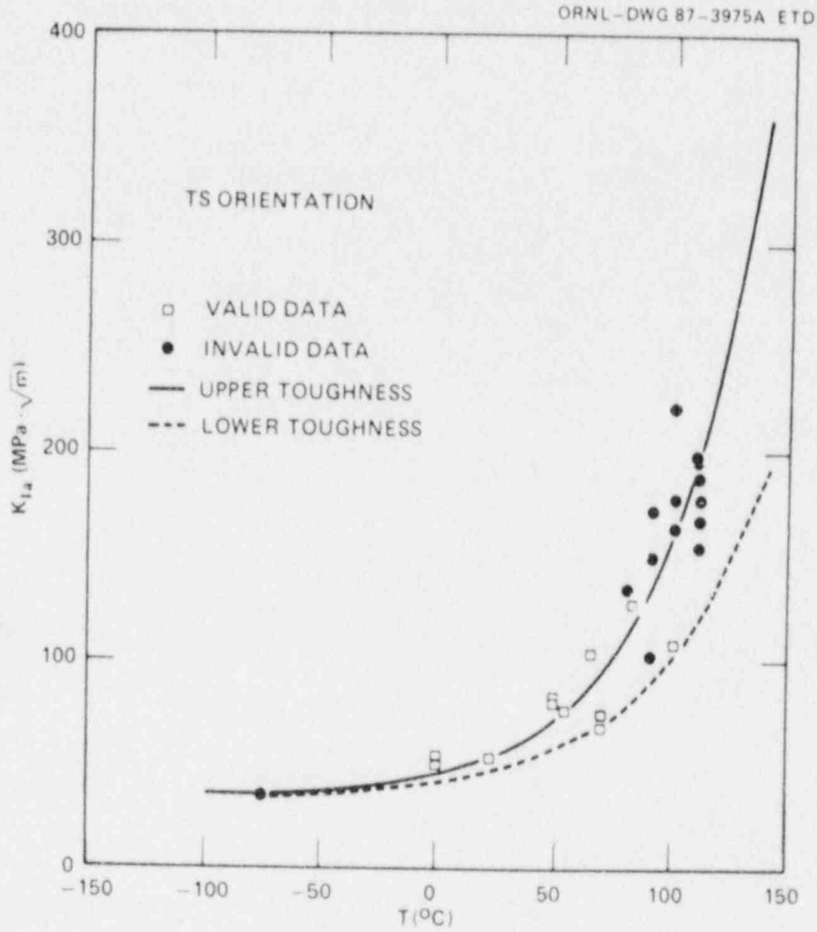

Fig. 10.9. Crack-arrest toughness data for characterization piece PTC1. The upper-toughness curve is a least-squares fit to the data shown. The lower-toughness curve is a similar fit to β-adjusted data (points not shown).

The final upper-K_{Ic} curve was chosen to fit the β-adjusted K_J data at low temperature (−75 and −25°C) and to satisfy Eq. (3) at transitional temperatures. An exploratory least-squares fit was made to 12 points: the set of six β-adjusted data at −75 and −25°C and, at higher temperature, six K_J data adjusted for dependence on both size and strain rate caused by stable crack growth.[4] Because the resulting K_{Ic} expression satisfied Eq. (3), it was used in the final OCA/USA pretest analyses. The lower K_{Ic} expression is essentially the upper K_{Ic} shifted by 30 K. The K_{Ic} and K_J data and the two K_{Ic} curves are shown in Fig. 10.10.

Thermal transient parameters. Sensitivity studies with variations in the time-dependent convective heat-transfer coefficient h(t) and the bulk coolant temperature $T_B(t)$ indicated that the heat-transfer rates experienced in the PTSE-1C transient[4] would be satisfactory for PTSE-2.

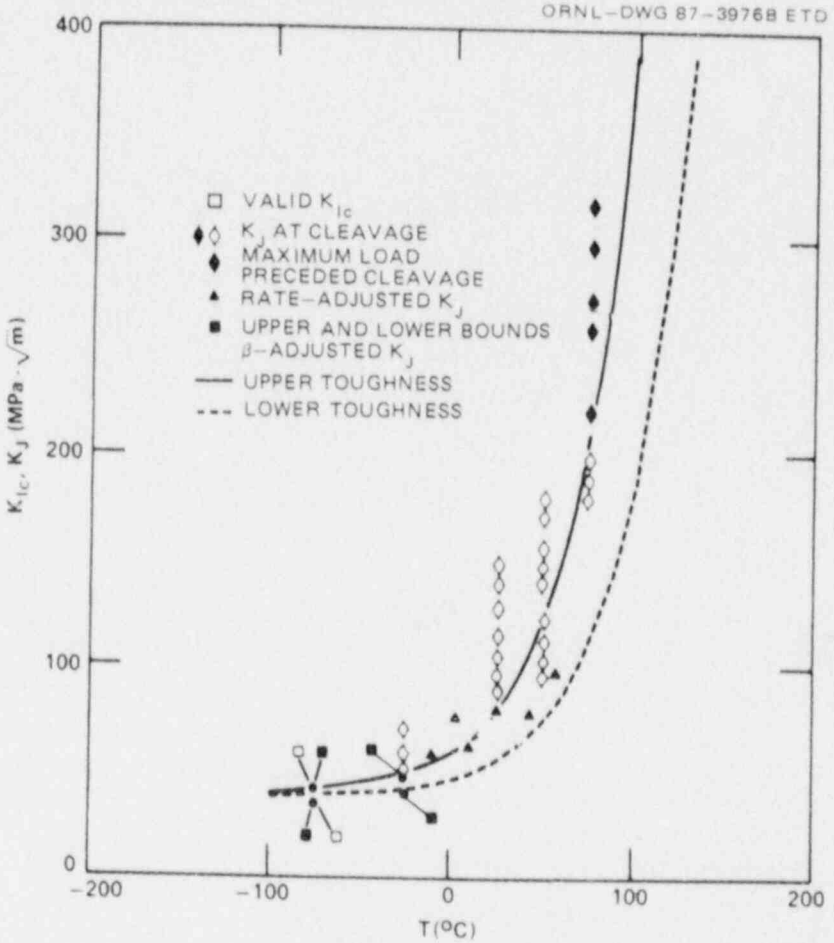

Fig. 10.10. Fracture-toughness data for characterization piece PTC1. The two lowest points are the only valid K_{Ic} data. The upper-toughness curve is a least-squares fit to the lower bound β-adjusted and the rate-adjusted points.

This was important because resources were not available to perform preliminary heat-transfer tests to determine whether a more favorable thermal transient could be generated. The values of h(t) and $T_B(t)$ used for "nominal" OCA/USA transients are given in Fig. 10.11. The pretest flow trials, discussed in Chap. 7, suggested that flow, and, consequently, h(t), might be somewhat unpredictable. Therefore, final pretest OCA/USA analyses included cases for variants of the nominal h(t) 10% above and 10% below the nominal h.

The performance of the PTSE-2A transient experiment confirmed, finally, that the nominal h(t) represented the experiment well. Therefore, final analyses before the PTSE-2B transient were based on the nominal coefficient.

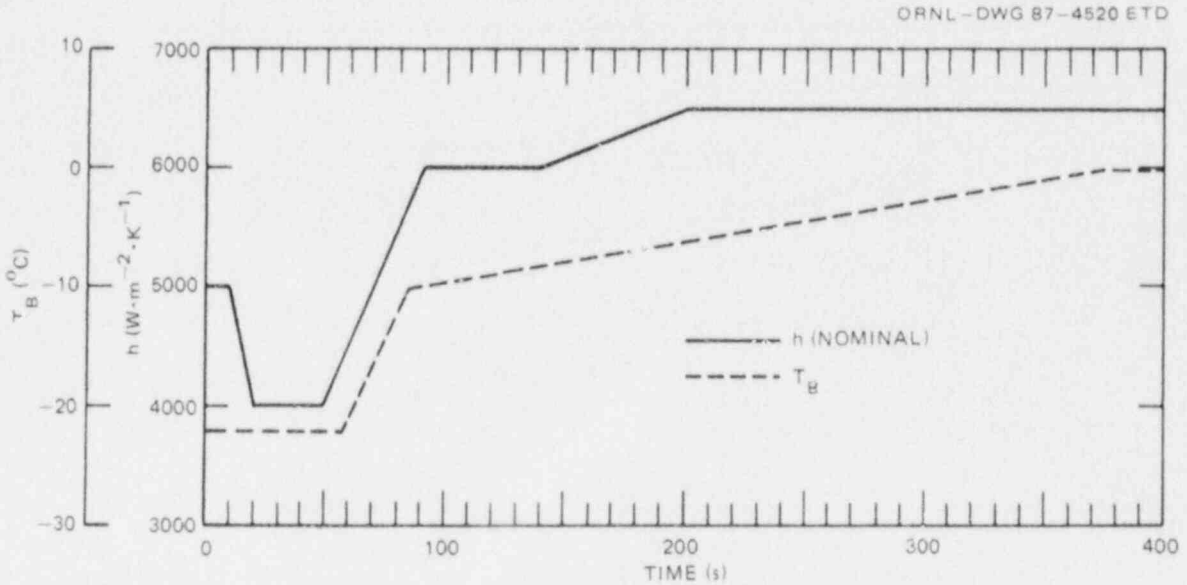

Fig. 10.11. Time-dependent values of h and T_B for nominal case in PTSE-2 OCA/USA analysis. Final pretest analyses included variants of h 10% above and below nominal.

10.4.2 Results of PTSE-2A and -2B analysis

PTSE-2A. A final series of OCA/USA pretest calculations were performed to select a pressure transient for PTSE-2A. In addition to considering variations in the pressure transient, a range of values of the convective heat-transfer coefficient h(t), ranging from 90 to 110% of the nominal h(t) from PTSE-1C, was considered, and both upper and lower toughness cases discussed in Sect. 10.4.1 were analyzed [see Table 10.5 ("Final Curves") and Figs. 10.9 and 10.10]. The pressure transient shown in Fig. 10.12 as curve A1, combined with the nominal h(t), was selected for elastic-plastic analysis. The resulting K_I and K_{Ic} vs time relationships are shown in Fig. 10.13. This transient produced the desired shape in the K_I vs time curve, with the final maximum K_I exceeding the first maximum after a long period of warm prestressing. By extending the low-pressure phase of the transient by 40 s (see curve A2 in Fig. 10.12), the period of simple warm prestressing ($K_I < 0$) would persist almost to the intersection of the K_I and the upper K_{Ic} curves. This extended transient could not be shifted further (later) in time without invoking greater uncertainties in the transient and in flaw behavior. Stable ductile tearing before cleavage would elevate K_I, which would be helpful in one sense, but tearing was not certain. Higher pressures initially and finally in the transient would also elevate K_I, but this might promote too much ductile tearing and a premature tearing instability. Accordingly, the pressure curve A2 (Fig. 10.12) was selected for the PTSE-2A transient.

PTSE-2B. It was expected that the performance of the PTSE-2A transient would remove some uncertainties about the thermal shock performance

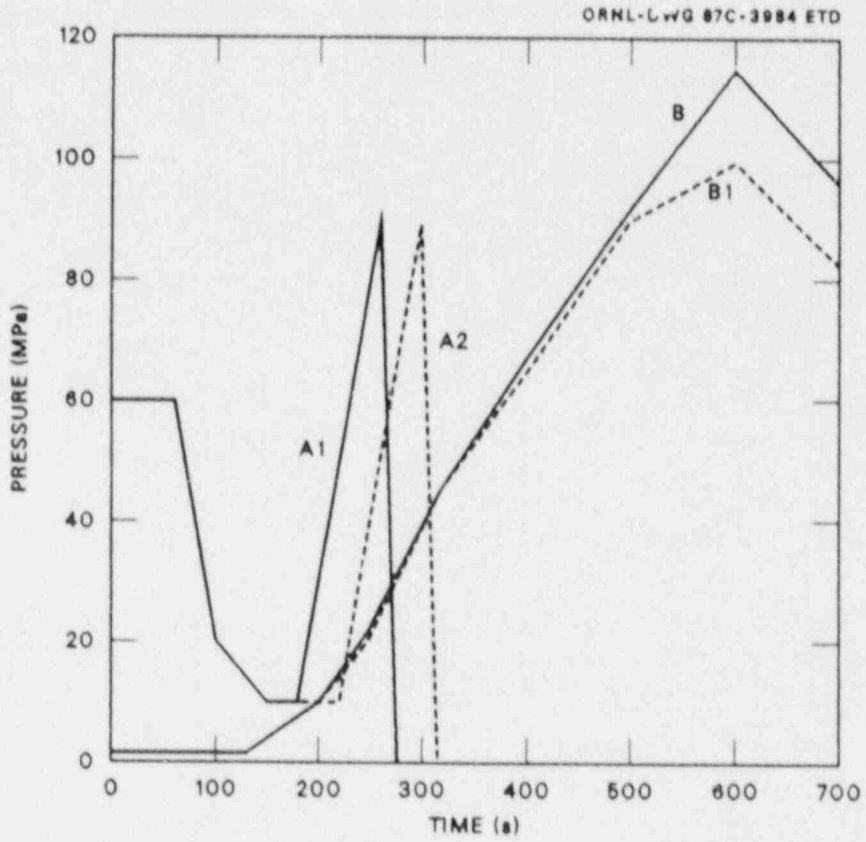

Fig. 10.12. Pressure transients planned for PTSE-2A and -2B experiments. Final PTSE-2A pretest OCA/USA and elastic-plastic analyses were based on curve A1. The planned PTSE-2A transient is curve A2. Curve B is the planned PTSE-2B transient, which was also used for the final pretest OCA/USA analysis. The corresponding elastic-plastic analysis was based on curve B1.

of the test facility and the actual arrest toughness K_{Ia} of the vessel. OCA/USA calculations before PTSE-2A indicated that if toughness were high, the PTSE-2B transient would have to be several minutes long to obtain a crack propagation in cleavage for an initial crack of moderate depth. The principal challenge was to design a pressure transient within the capabilities of the testing facility that would preclude warm prestressing before the time $K_I = K_{Ic}$, even if toughness were high.

Data from PTSE-2A indicated that the crack was ~30 to 45 mm deep, the toughness was high (but probably not as high as the upper-toughness curves), and the thermal transient was approximately as planned. Analyses based on the PTSE-2A data and performed before the B transient considered several thermal and pressure options and uncertainties in K_{Ic}, K_{Ia}, and crack depth. Initial vessel temperatures from 250 to 300°C were considered. The B transient was designed to produce the same thermal parameters as the A transient, except a lower initial vessel temperature (275°C) was chosen. The final OCA/USA pretest analysis was based on the

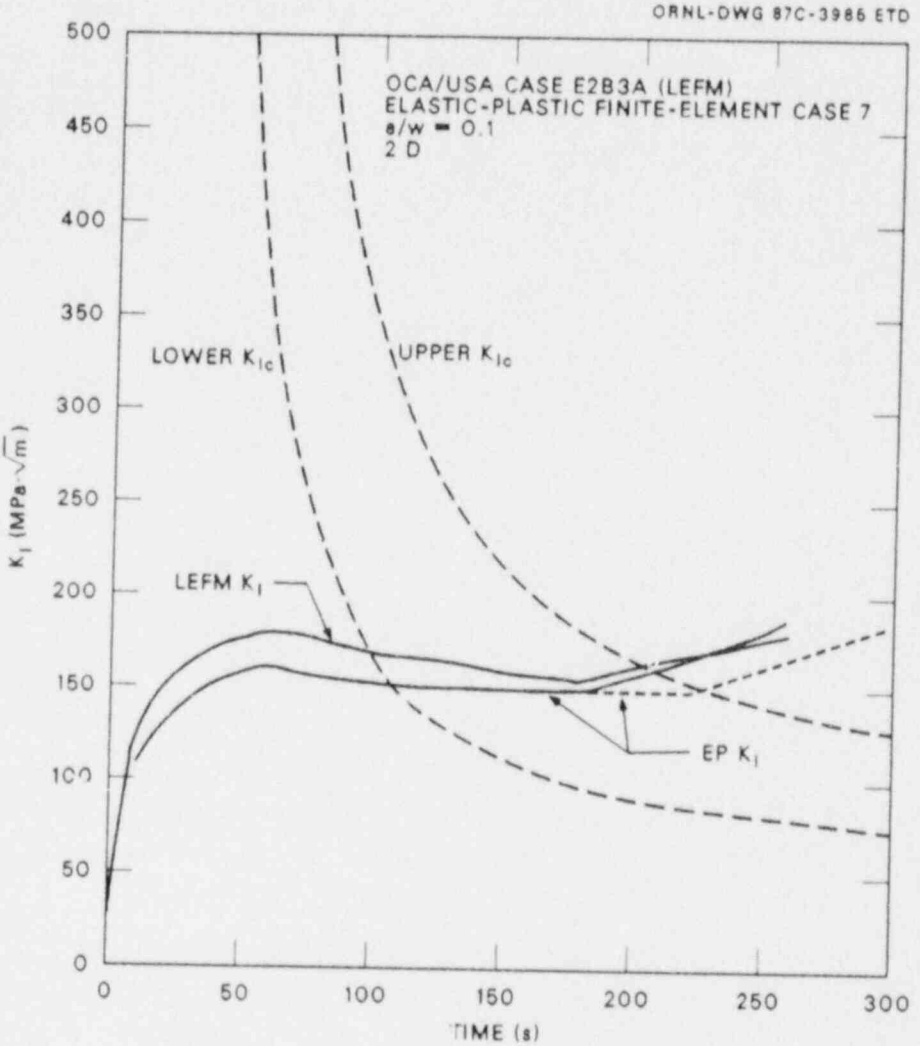

Fig. 10.13. K_I and K_{Ic} vs time from pretest OCA/USA LEFM and elastic-plastic finite-element analyses of planned PTSE-2A transient. The dashed portion of the K_I curve is an extrapolation of the final elastic-plastic analysis, which was based on the p(t) curve A1 of Fig. 10.12.

pressure transient shown by curve B of Fig. 10.12. The corresponding elastic-plastic analysis was based on curve B1. Results of the analysis are shown in Figs. 10.14–10.16. Figure 10.14 shows that a crack 37 mm deep (a/w = 0.25) would propagate after 280 to 460 s, depending on K_{Ic}. Figure 10.15 shows that if low cleavage toughness obtain, cracks for which a/w is initially 0.2 to ~0.3 would arrest and remain stable; a crack with a/w > 0.30, however, would arrest and then tear unstably. If the cleavage toughness were high, the postarrest tearing would tend to be less stable, as shown in Fig. 10.16.

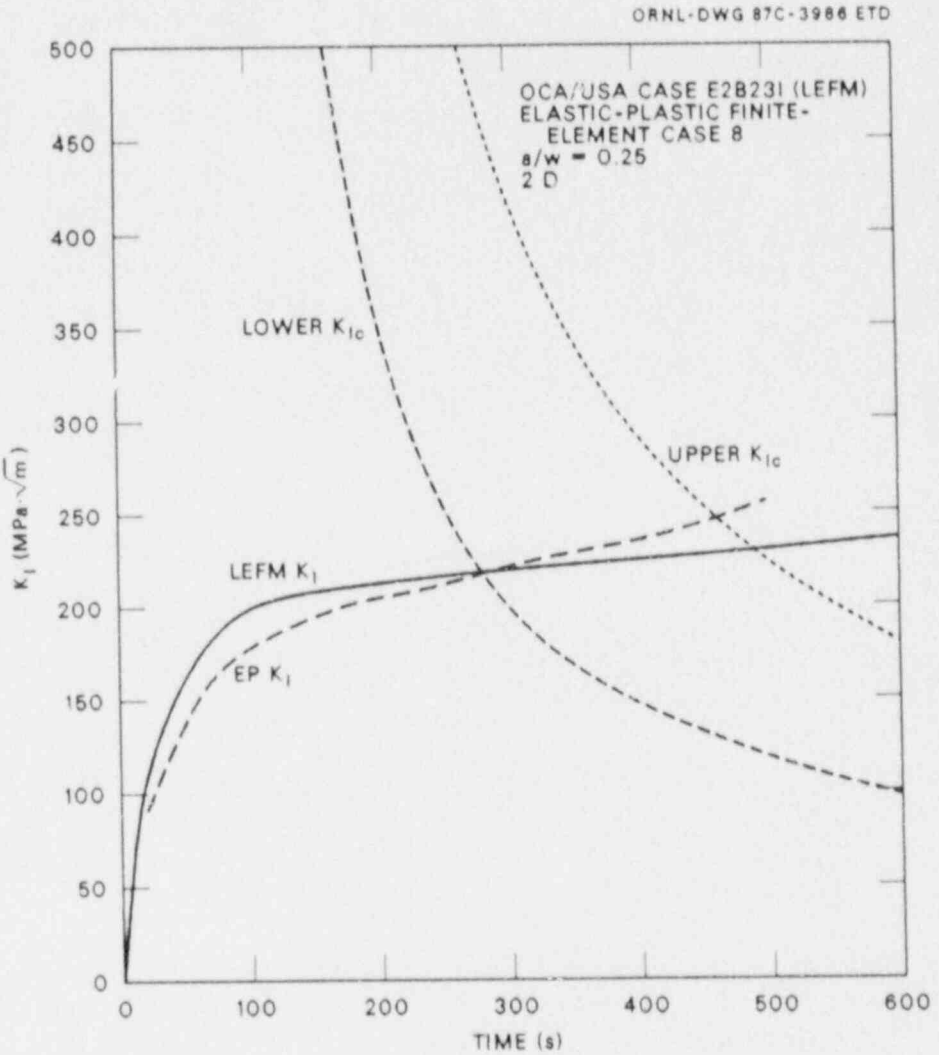

Fig. 10.14. K_I and K_{Ic} vs time from pretest OCA/USA LEFM and elastic-plastic finite-element analyses of the planned PTSE-2B transient. The elastic-plastic analysis was based on the p(t) curve B1 (Fig. 10.12), which differed slightly from the planned transient pressure (curve B).

10.4.3 Crack-depth analysis

It was necessary to estimate the crack depth while the experiment was in progress so that decisions concerning termination of the transients could be made immediately and confidently. This had been accomplished during the PTSE-1 experiment by means of reading rapid changes in CMOD from a strip-chart recording and converting those observations to crack depth by graphs prepared before the test. This procedure allowed the conversion of data in ~10 s after a crack jump.

In PTSE-2 it was important to be able to make this conversion almost instantaneously because it was hoped that when the final cleavage arrest,

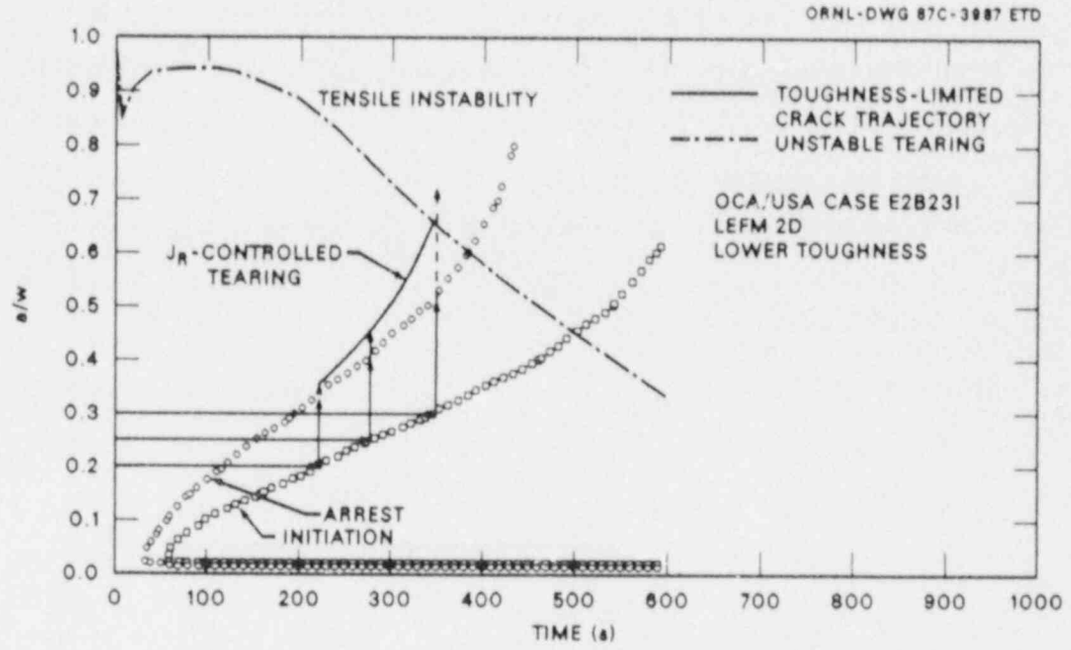

Fig. 10.15. Crack-depth trajectories based on pretest OCA/USA LEFM analysis of PTSE-2B transient with low-toughness option. Cracks with a/w initially $\gtrsim$ 0.295 would eventually be unstable with respect to J_R-controlled tearing.

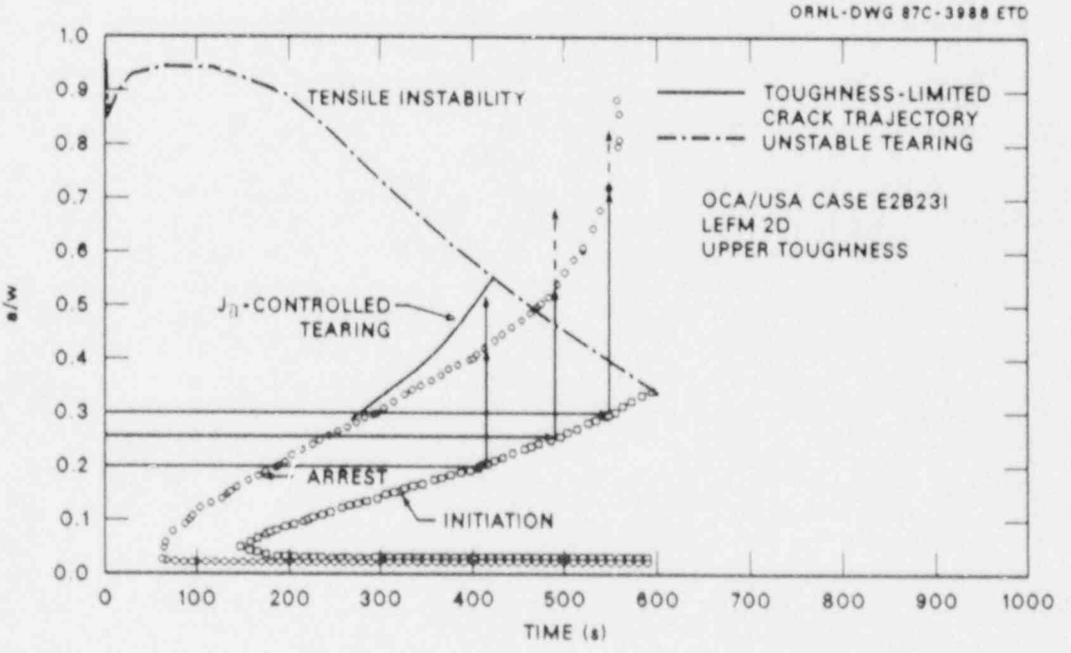

Fig. 10.16. Crack-depth trajectories based on pretest OCA/USA LEFM analysis of PTSE-2B transient with high-toughness option. Cracks with a/w initially $\gtrsim$ 0.23 would eventually be unstable with respect to J_R-controlled tearing.

followed by unstable ductile tearing, occurred, it would be possible to unload the vessel rapidly enough to prevent the complete rupture of the vessel wall. To carry out this task, a microcomputer with inputs from an analog-to-digital conversion interface was programmed to make the necessary computations and plot the results on the computer monitor. Two independent inputs of CMOD and pressure were combined with a time variable to compute crack depth. In pretest trials it was demonstrated that six to ten points per second could be processed and displayed with a delay time no greater than ~0.1 s. In addition to the computer-based scheme, the manual procedure used in PTSE-1 was also used in PTSE-2 for the benefits of redundancy.

Both methods were based on pretest calculations. Three-dimensional quasi-static finite-element analyses of the test vessel were performed with the ORMGEN/ADINA/ORVIRT fracture-mechanics system[8-10] installed on the Oak Ridge CRAY X-MP computer. Results from these analyses were used to correlate incremental changes in crack depth with measured changes in CMOD during a transient. This was accomplished by employing a superposition technique that combines calculated midplane CMOD values for pressure loading with the calculated values for thermal effects over a range of crack-depth ratios and selected times in the transient.

By superposition, the total CMOD (Δ) is the sum of the individual components from the thermal and pressure loadings:

$$\Delta(a/w, t) = \Delta_T(a/w, t) + \Delta_p(a/w, p) , \qquad (4)$$

where Δ_T and Δ_p are the separate thermal and pressure contributions. The thermal CMOD Δ_T for a given thermal transient is an explicit function of a/w and t, but Δ_p does not depend explicitly on t. The graphic-manual procedure used graphs of the total CMOD vs a/w and t. The computer-based method required the solution of Eq. (4) for a/w as a function of Δ, p, and t. To facilitate this solution, algebraic expressions for the functions $\Delta_T(a/w, t)$ and $\Delta_p(a/w, p)$ were derived from the results of 3-D finite-element analysis.

For the PTSE-2A transient, 3-D finite-element analyses were conducted for a series of crack depths in the test vessel subjected only to thermal loading for the planned test transient. Each finite-element model in this series consisted of 3288 nodes and 688 isoparametric elements. Material properties were taken to be Young's modulus $E = 2.00 \times 10^5$ MPa, Poisson's ratio $\nu = 0.3$, and thermal-expansion coefficient $\alpha = 13.0 \times 10^{-6}$ K^{-1}. The temperature distributions for the computations were selected from the output of the OCA/USA case E2B41I, which was nearly identical to the final OCA/USA pretest analysis case. The computations were made for three times, given in Table 10.6. Included in Table 10.6 are the calculated midplane CMOD values as a result of thermal-only loading for the range of crack depths and transient times utilized in the analyses.

For the microcomputer program a cubic expression,

$$\Delta_T = A_T(a/w) + B_T(a/w)^3 , \qquad (5)$$

Table 10.6. Calculated midplane CMOD[a] for selected crack-depth ratios a/w and times for planned PTSE-2A transient (OCA/USA case E2B23I)

(internal pressure p = 0)

a/w	Time (s)		
	30	100	200
0.1	0.274	0.292	0.265
0.2		0.576	
0.3		0.866	
0.4		1.171	
0.5		1.494	
0.6		1.836	

[a]Displacements in millimeters.

was fit by least squares to the CMOD values at 100 s (in Table 10.6). Because Δ_p is proportional to p, the expression

$$\Delta_p = [A_p(a/w) + B_p(a/w)^3]p \tag{6}$$

was assumed, where the coefficients were determined by a least-squares fit to CMOD values calculated for p = 1 by 3-D finite-element analysis (Table 10.7). Values of the coefficients in Eqs. (5) and (6) are given in Table 10.8. The time dependency of Δ_T was ignored because of the weak dependency on time shown in Table 10.6 and in the results of OCA/USA calculations for times of importance.

Combining Eqs. (4)—(6) gives the cubic equation

$$(a/w)^3 + C_1(a/w) + C_2\Delta = 0 \ , \tag{7}$$

where

$$C_1 = \frac{A_T + A_p p}{B_T + B_p p} \quad \text{and} \quad C_2 = -\frac{1}{B_T + B_p p} \ . \tag{8}$$

The classical solution of Eq. (7) for a/w is well known.

The graph used during the PTSE-2A experiment is presented in Fig. 10.17. This is based on the pressure transient shown in Fig. 10.12 as

Table 10.7. Calculated midplane CMOD for selected crack-depth ratios a/w in test vessel for pressure only (p = 1 MPa)

a/w	CMOD (μm)
0.08	0.592
0.10	0.761
0.15	1.213
0.20	1.726
0.30	3.022
0.50	7.308
0.60	10.690

Table 10.8. Coefficients in cubic expressions for CMOD for the PTSE-2A experiment

Coefficient	Value
A_T	2.83852
B_T	0.607226
A_p	0.00714
B_p	0.02965

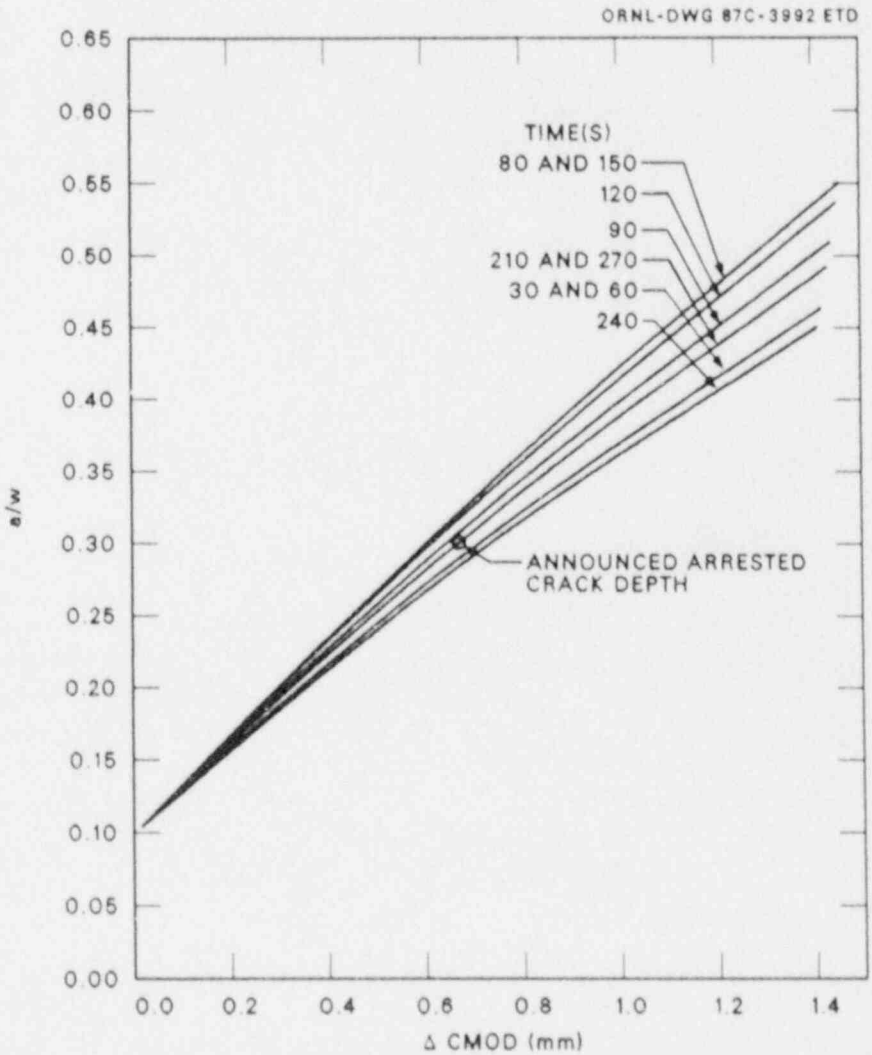

Fig. 10.17. Graphs of a/w vs ΔCMOD for series of times in PTSE-2A transient.

curve A1. During the transient both the graphic-manual procedure and the microcomputer gave reliable indications of the magnitude of the crack jump.

10.5 Posttest Analysis

The experimental purpose of PTSE-2 was to elucidate the mechanisms of fracture by means of an experiment with a structure large enough to provide stress states and toughness states during fracture events particularly representative of those that would exist in a real reactor vessel during a severe overcooling accident. The purpose of the posttest analyses described here is to interpret the raw experimental data, including posttest fractographic, metallographic, and geometric characterizations of the flaw, in terms of fracture mechanisms. Essentially the same computational methods were used before and after the experiment. However, all posttest analyses were based on measured pressures and temperature distributions, thus obviating uncertainties that might have been introduced by heat-transfer calculations. Two- and three-dimensional finite-element analyses were used for calculating K_I and CMODs for the times and crack geometries of interest.

10.5.1 Vessel and flaw characteristics

The material properties used in pretest analyses (Tables 10.1 and 10.2) were assumed for the posttest finite-element analyses. The same vessel geometry was also used (Figs. 10.1 and 10.6). Crack geometries were determined from the measurements of flaw features described in Chap. 9 (Fig. 9.7). Smooth curves, symmetrical about the center of the crack, were fitted to the data, as shown in Fig. 10.18–10.20. The parameters for these crack shapes are given in Table 10.9.

10.5.2 Experimental transient data

The phases of the experiment especially important to the understanding of the fracture behavior are defined by the events identified in Table 10.10. Fourteen separate phases can be distinguished by the physical appearance of the fracture surfaces and the transient data. Experimental pressures and temperatures at time steps relevant to these events were extracted from experimental data sets, as described in Chap. 8. The experimental pressures for the transients are shown in Fig. 10.21. The experimental temperatures at the initial crack depth in each transient are shown in Fig. 10.22. The pressures used as input for finite-element analysis are listed in Table 10.11. The corresponding temperatures are included in Appendix A.

10.5.3 Correlation of crack-depth and CMOD observations

Before initiation of the cleavage fracture in PTSE-2A, the crack increased in depth (from $a = y_1$ to y_2) by 8.0 mm. After the cleavage

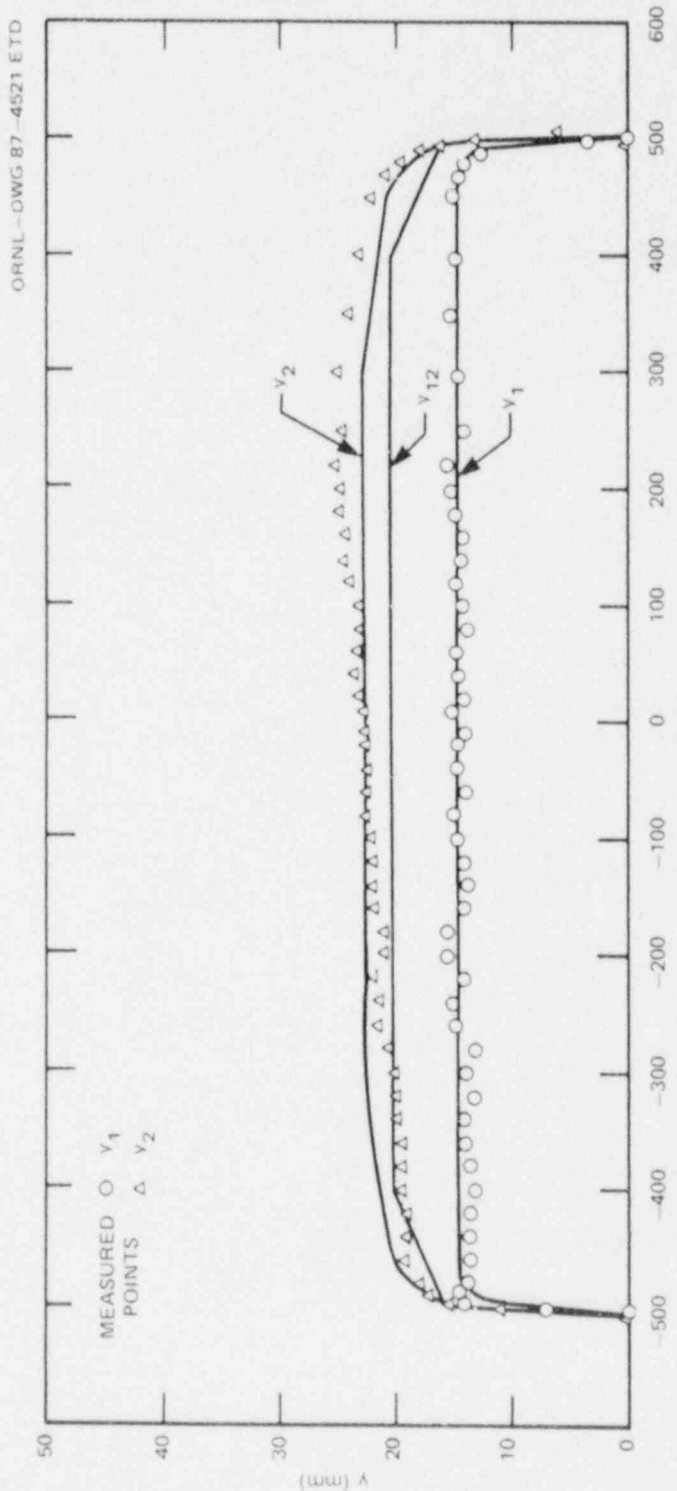

Fig. 10.18. Crack geometries of precleavage cracks in PTSE-2A.

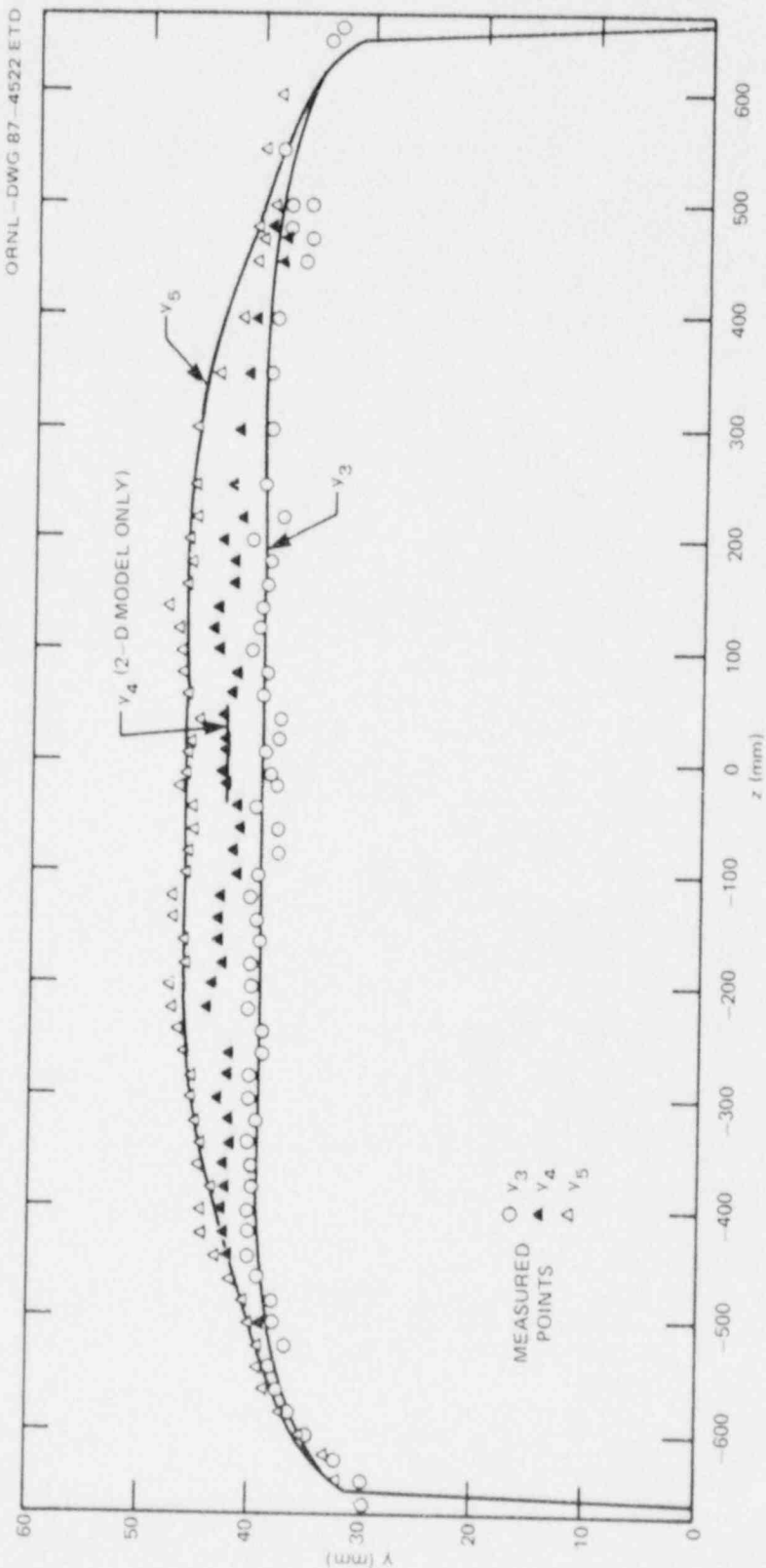

Fig. 10.19. Crack geometries for intermediate depths: crack arrest (y_3) and final tear (y_4) in PTSE-2A and precleavage crack (y_5) in PTSE-2B.

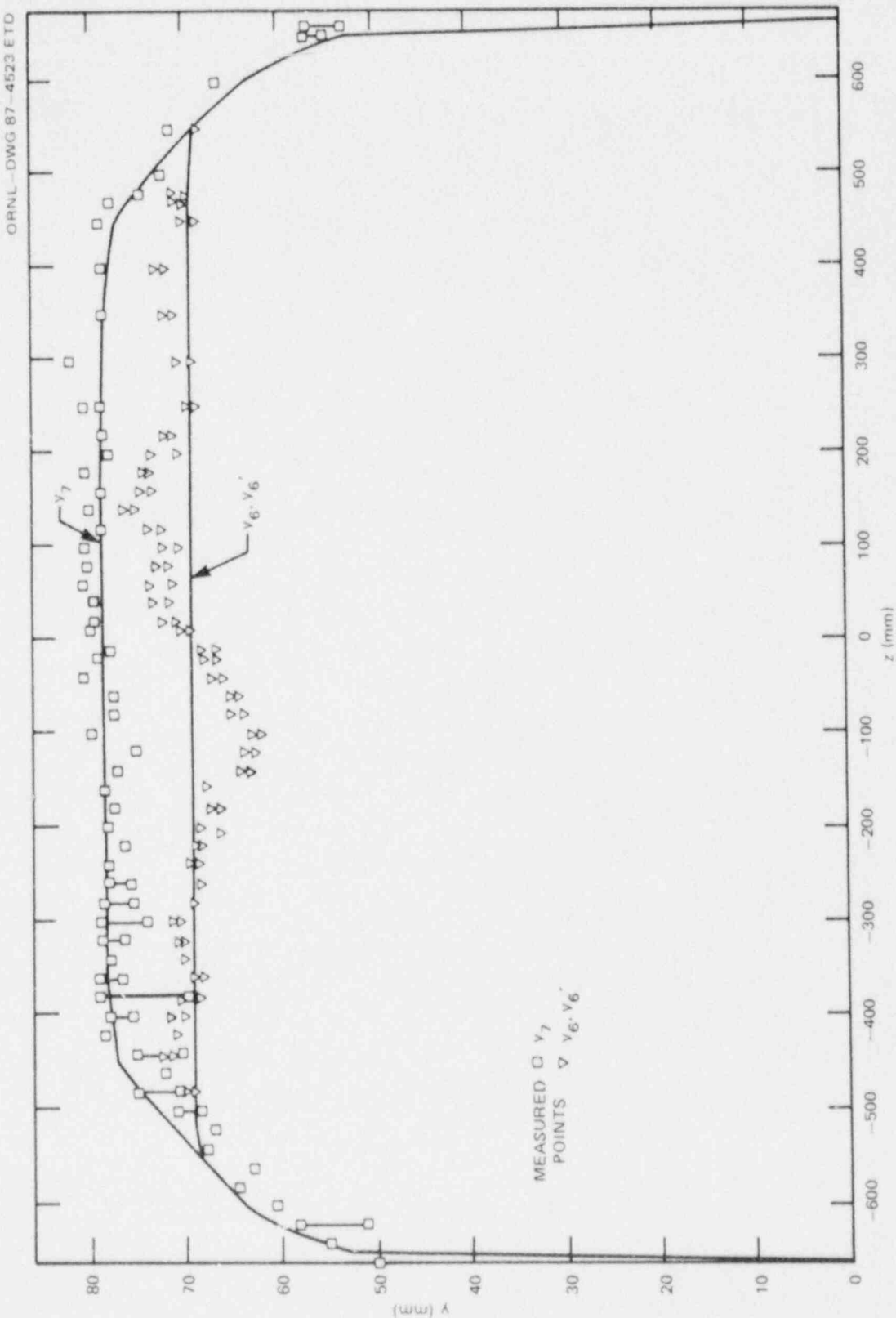

Fig. 10.20. Crack geometries for deep cracks in PTSE-2B: momentary and final arrest depths.

Table 10.9. Coordinates of the PTSE-2 crack tips[a]

±z[b] (mm)	Depth, a or y (mm) at z							
	Crack-stage[c]							
	1	2	3	4	5	6	7	12[d]
0	14.5	22.5	39.3		46.1	69.2	78.8	20.2
100	14.5	22.5	39.3		46.1	69.2	78.8	20.2
200	14.5	22.5	39.3		46.1	69.2	78.8	20.2
300	14.5	22.5	39.3		45.4	69.2	78.6	20.2
350	14.5	22.0	39.3		44.4	69.2	78.4	20.2
400	14.5	21.3	39.3		43.1	69.2	77.9	20.2
450	14.5	20.6	38.9		41.5	69.2	77.2	20.2
470	14.3	19.6						
480	14.0	18.6						
490	13.0	17.4						
495	12.0	15.7						15.7
500	5.0	11.8	38.2		39.9	69.2	73.2	5.0
503	0	0						0
550			37.4		38.3	68.6	68.6	
600			35.6		36.0	63.8	63.8	
620			34.5		34.7	60.2	60.2	
640			32.9		33.4	55.5	55.5	
650			31.2		31.2	52.5	52.5	
660			0		0	0	0	
Depth for 2-D finite-element analysis								
	14.76	22.5	39.3	42.4	46.1	69.2	78.8	20.2

[a]Coordinates of finite-element crack-tip nodes may differ slightly from these coordinates. See Figs. 10.18–10.20 for plots of crack geometries.

[b]Distance from centerline of the flaw.

[c]Fracture features corresponding to each crack stage are described in Table 9.1. Corresponding events are identified in Table 10.10.

[d]The preliminary depth, 20.2 mm, for the finite-element mesh differs slightly from the value (19.6 mm) discussed in the text in Sect. 10.5.3.

Table 10.10. Events in the PTSE-2A and -2B transients

Event	Time[a] (s)	Crack position[b]	Evidence of event	
			Transient data	Fracture surface
	PTSE-2A			
Initiation of thermal shock	~112	y_1	X	
Onset of initial tearing	<184.6	y_1	X	X
First maximum K_I	184.6	y_{12}	X	
Minimum K_I, onset of precleavage tearing	341.8	y_{12}	X	X
Initial cleavage propagation	361.4	y_2	X	X
Crack arrest	361.4[c]	y_3	X	X
Termination of postcleavage tearing (second maximum K_I)	365.6	y_4	X	X
	PTSE-2B			
Initiation of thermal shock	~155	y_4	X	
Onset of precleavage tearing	<575.8	y_4	X	X
Initial cleavage propagation	575.82	y_5	X	X
Interruption of cleavage by ductile tearing	c	y_6		X
Resumption of cleavage propagation	c	y_6		X
Crack arrest	575.82[c]	y_7	X	X
Onset of postcleavage tearing	576.2	y_7	X	X
Rupture of vessel wall	576.7		X	X

[a]Time after start of scanning by the data acquisition system.

[b]Crack depths y_i are identified in Tables 9.1 and 10.9. Depth y_{12} is the depth developed by the initial ductile tearing before warm prestressing in PTSE-2A. The depth was inferred from transient data by finite-element analysis.

[c]Time intervals <10 ms cannot be resolved by the data acquisition system.

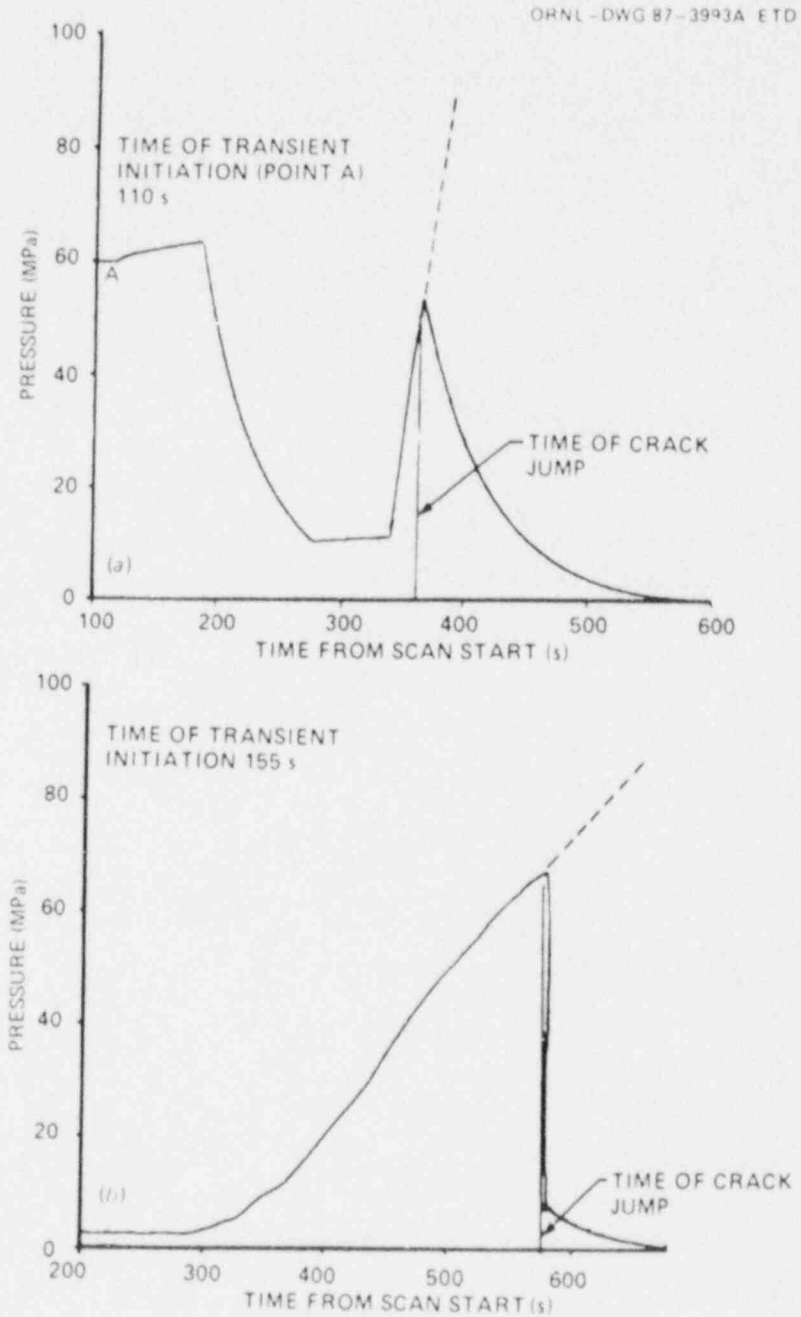

Fig. 10.21. Pressure vs time measured in the PTSE-2 transients. Dashed lines show the planned continuation for pressurization if the crack had not jumped at the times indicated. (*a*) PTSE-2A and (*b*) PTSE-2B.

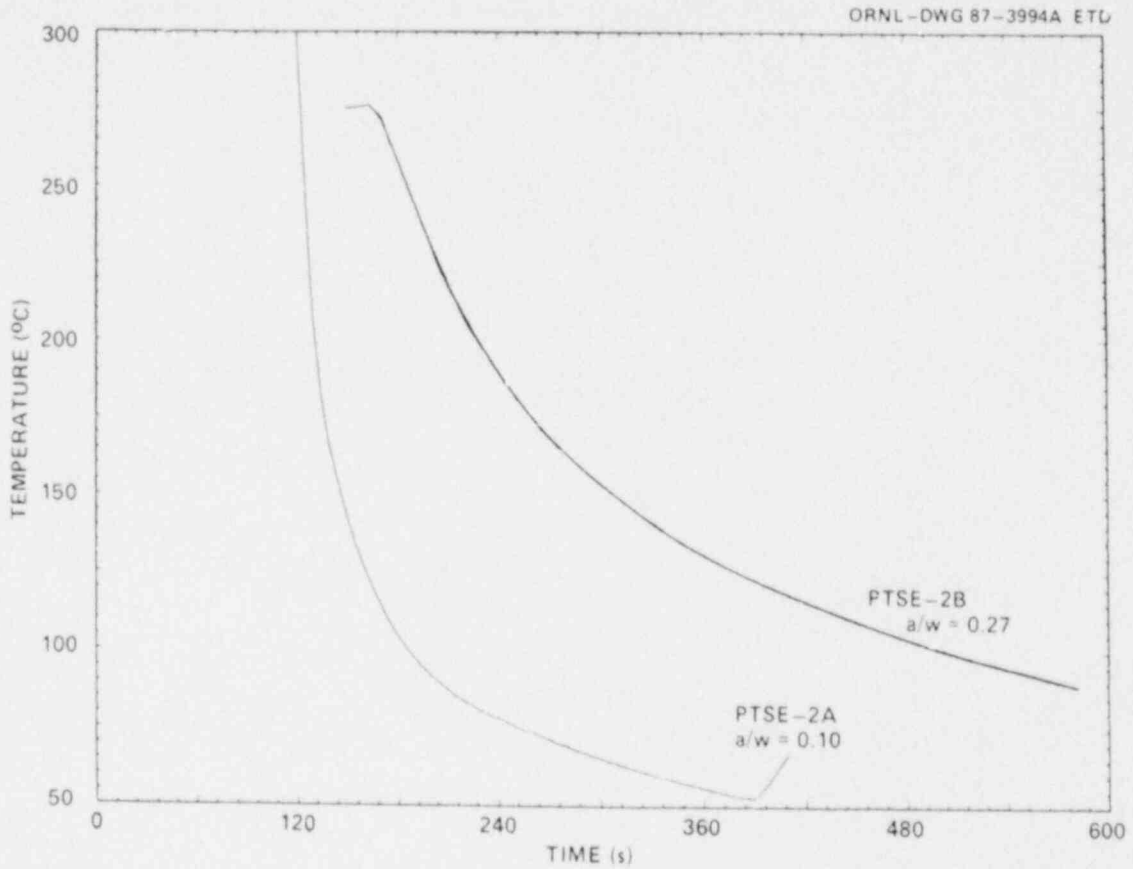

Fig. 10.22. Temperature vs time at radii of initial crack depths in PTSE-2A and -2B transients as measured by thermocouple thimble 5.

Table 10.11. Experimental pressures vs time for PTSE-2A and -2B at time steps analyzed by elastic-plastic finite-element methods

PTSE-2A		PTSE-2B	
Time (s)	Pressure (MPa)	Time (s)	Pressure (MPa)
110	60.0	157.2	2.7
120[a]	60.5	159.6[a]	2.9
130[a]	61.2	161.9[a]	3.0
140[a]	61.8	164.3	3.0
150	62.2	167.9[a]	3.1
160[a]	62.6	171.5[a]	3.1
170[a]	63.0	178.7	3.2
180	63.2	185.8[a]	3.4
185	62.8	193.0[a]	3.2
200	46.5	200.2	2.9
220[a]	31.5	214.5[a]	2.5
240	21.5	228.8[a]	2.5
260[a]	14.8	243.2	2.6
280	10.4	271.8[a]	2.4
310	10.8	300.5	3.1
340	11.1	329.2	5.5
345	16.7	350.7	9.3
350	26.5	365.0	11.2
355[a]	36.5	386.5	16.3
360	45.8	400.8	20.1
365	52.5	451.0	34.9
370	49.4	501.2	50.0
		551.3	62.9
		572.8	66.9
		575.7	67.3
		576.0	65.1
		576.7	62.3

[a]Some 2-D analyses omitted this load step.

arrest further tearing (from a = y_3 to y_4) of 3.1 mm occurred before the A transient was terminated. These observations, based on measurements of the fracture surface, have been correlated with experimentally observed CMOD by means of two-dimensional elastic-plastic finite-element calculations.

Ductile tearing was possible during three periods of the PTSE-2A transient: (1) during increasing thermal and pressure loads before the time of the first maximum K_I (t = 112 to 185 s), (2) during increasing pressure late in the transient but before initiation of cleavage (t = 340 to 361.4 s), and (3) after the cleavage arrest but before unloading (t = 361.5 to 365.6 s). The measured CMOD from a typical gage (YE 83) is shown in Fig. 10.23 for these times.

The measured CMOD is compared with values calculated for the first time period (112 to 185 s) in Fig. 10.24. By nonlinear interpolation of the set of calculated changes in CMOD, the crack depth at the first maximum K_I (t = 185 s) was inferred from the measured CMOD at that time, the result being 19.6 mm.

Calculated and measured changes in CMOD in the second time period (340 to 361.4 s) are compared in Fig. 10.25. The physical evidence of the fracture surface established the crack depth at t = 361.4 s, immediately before initiation of cleavage, to be 22.5 mm.

The calculated and measured CMOD responses to the cleavage crack propagation are shown in Fig. 10.26. The calculated change in CMOD during the cleavage crack jump from a = 22.5 to 39.3 mm is 0.62 mm, which is close to the measured rapid change in CMOD of 0.49 mm.

In the last period during which ductile tearing occurred in the PTSE-2A transient (t = 361.56 to 365.6 s), the crack advanced from a = 39.3 to 42.4 mm. The CMOD variations during this period are shown in Fig. 10.27. The CMOD change calculated for this increment of tearing is 0.17 mm, which agrees with the measured change in CMOD of 0.15 mm. The final crack depth inferred from the measured and calculated CMOD values is 42.1 mm. The differences between calculated and measured CMOD values are within the observed differences in measurements by various CMOD gages.

10.5.4 Results of fracture analysis

PTSE-2A. The behavior of K_I during the transient PTSE-2A is shown in Figs. 10.28 and 10.29 for the crack depths that correspond to the initial depth of the cracked electron-beam weld ($a_1 = y_1$) and the depth of the boundary between the initial ductile tear and the first cleavage initiation ($a_2 = y_2$). Figure 10.28 shows the result of both OCA/USA LEFM and the 2-D elastic-plastic finite-element calculations based on material A property set 5 (Tables 10.1 and 10.2). For the conditions of this transient and the initial crack depth, the results of both methods agree reasonably well.

The K_{Ic} curves shown in Figs. 10.28 and 10.29 are based on the upper-toughness curve of Table 10.5 and Fig. 10.10 shifted upward by 20.26 K to agree with the K_{Ic} inferred from the initiation of cleavage in the PTSE-2B transient. Figure 10.29 shows that K_I for both the intermediate and final precleavage tearing depths (19.6 and 22.5 mm) first exceeded K_{Ic} in the period from B to C, that is, during simple warm prestressing.

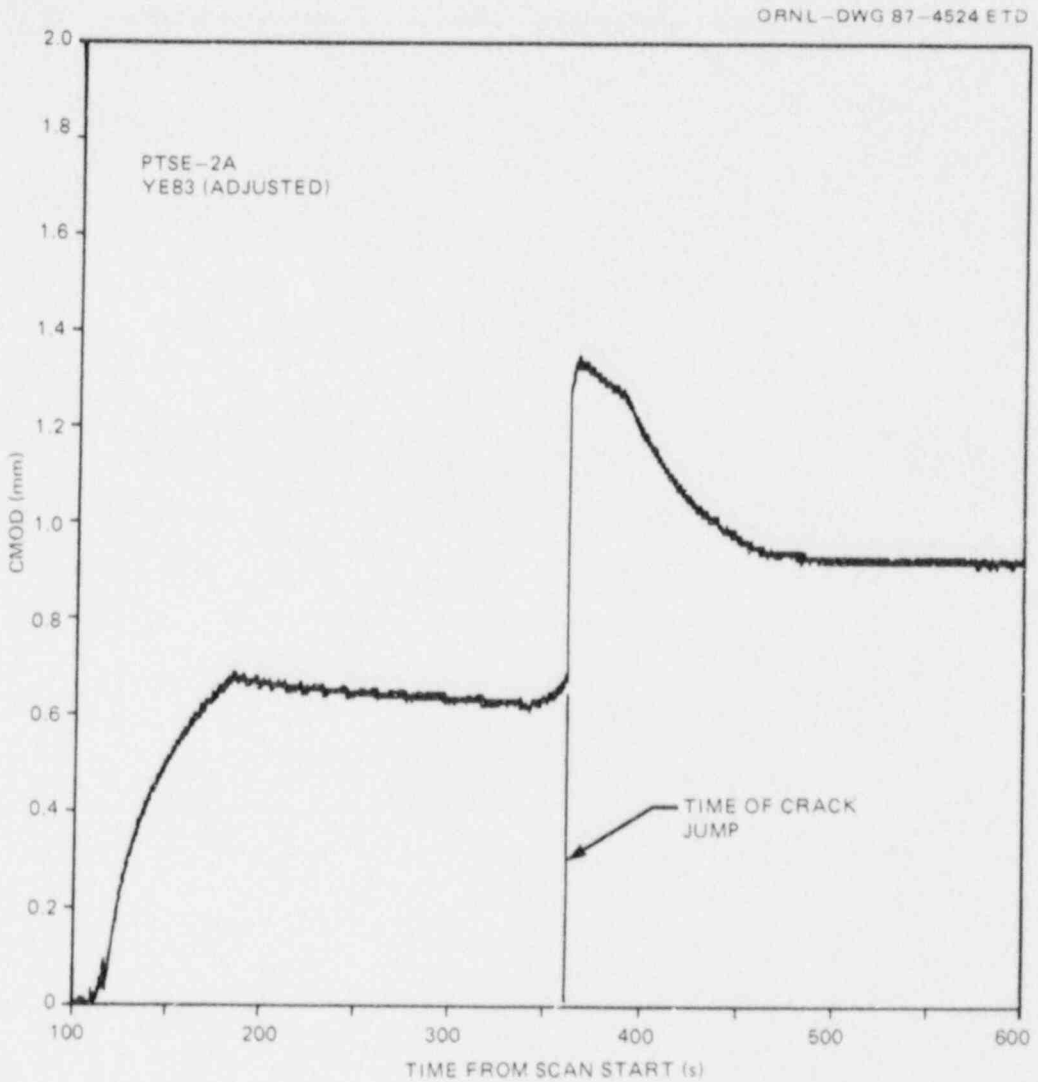

Fig. 10.23. CMOD vs time for PTSE-2A transient.

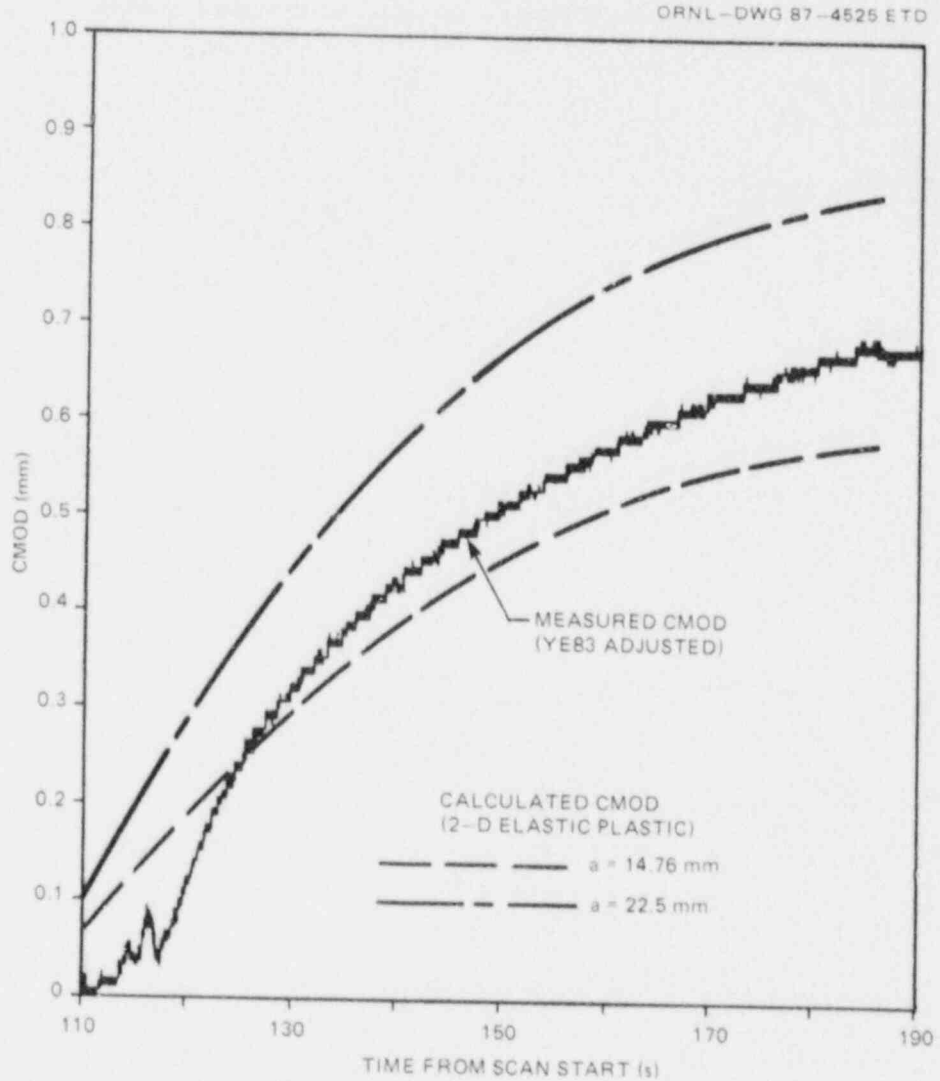

Fig. 10.24. Comparison of measured and calculated CMOD in early phase of PTSE-2A, before onset of warm prestressing.

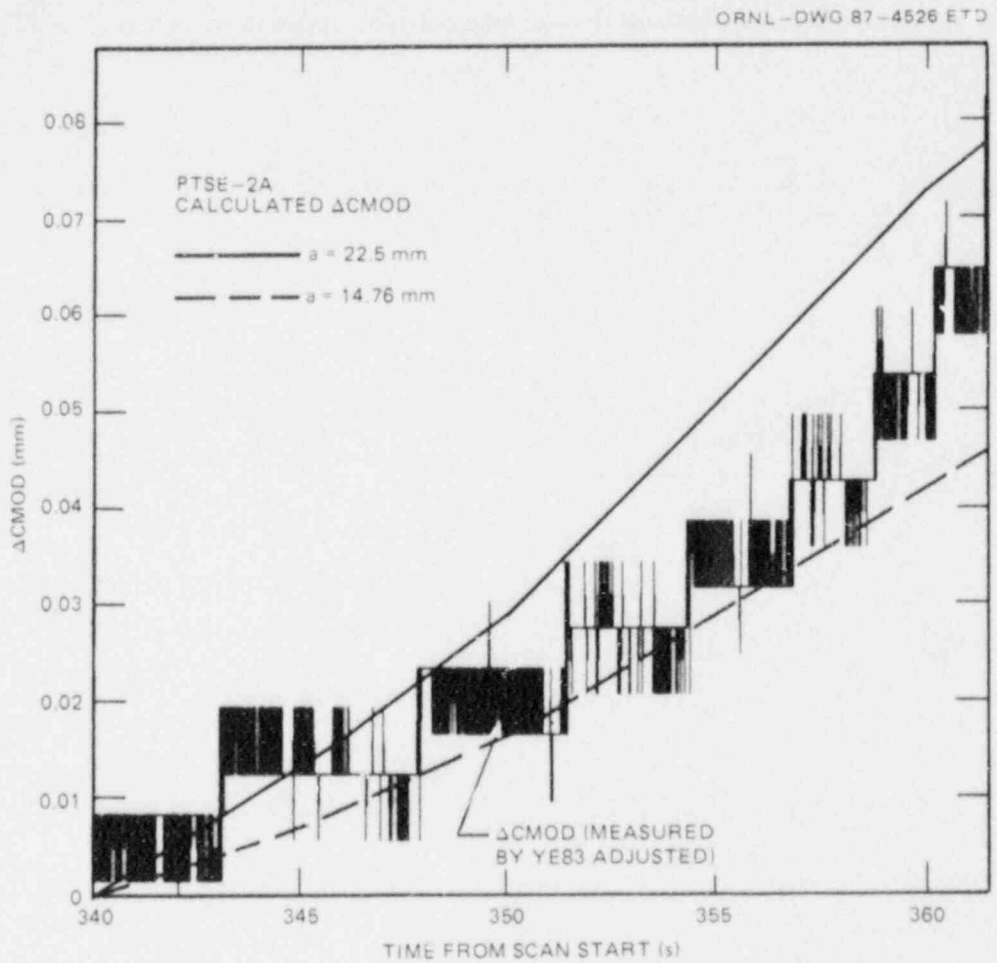

Fig. 10.25. Comparison of measured and calculated changes in CMOD in second period during which ductile tearing was possible in PTSE-2A.

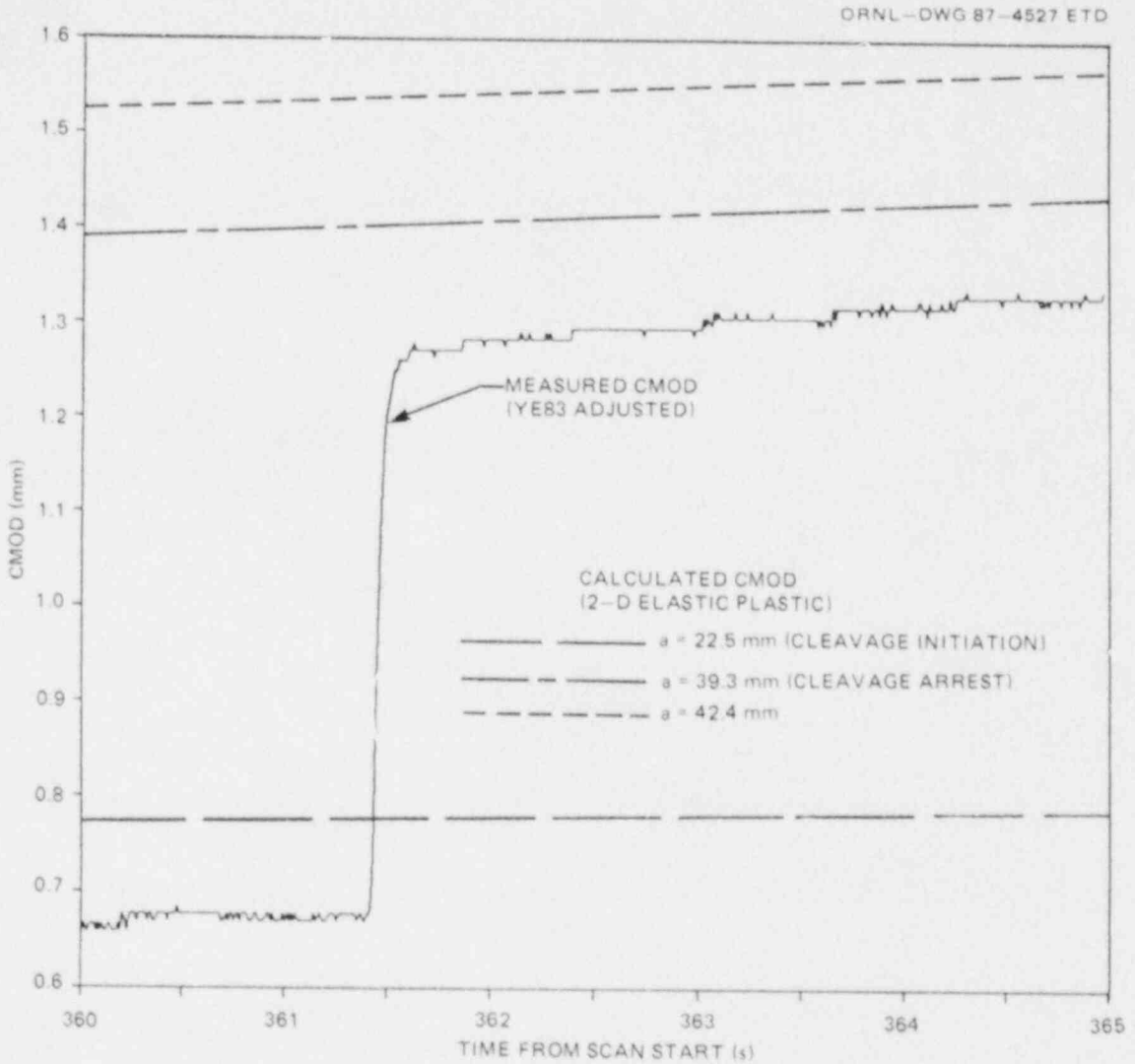

Fig. 10.24. Comparison of measured and calculated changes in CMOD during cleavage crack propagation in PTSE-2A.

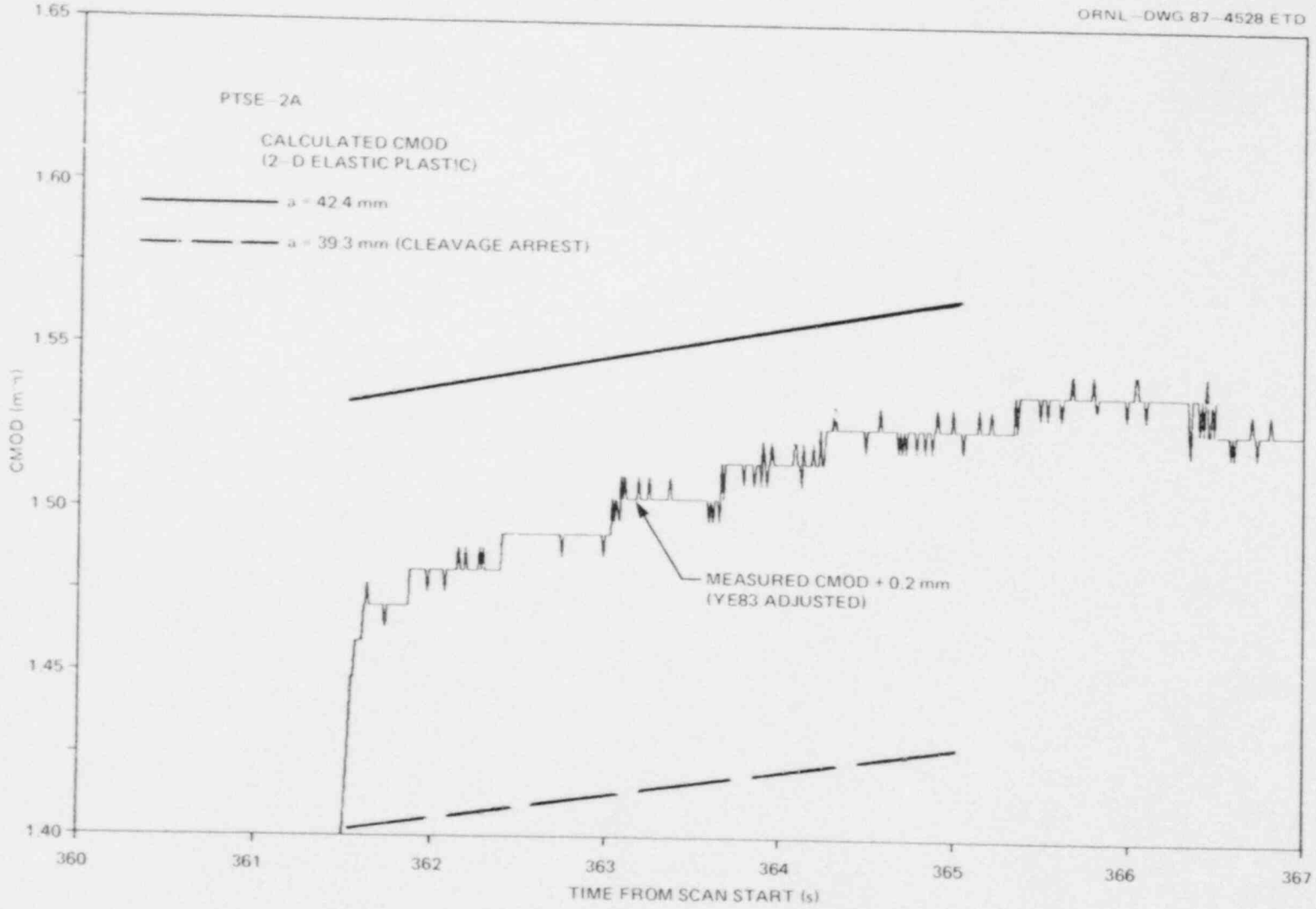

Fig. 10.27. Comparison of measured and calculated changes in CMOD during final period of ductile tearing in PTSE-2A.

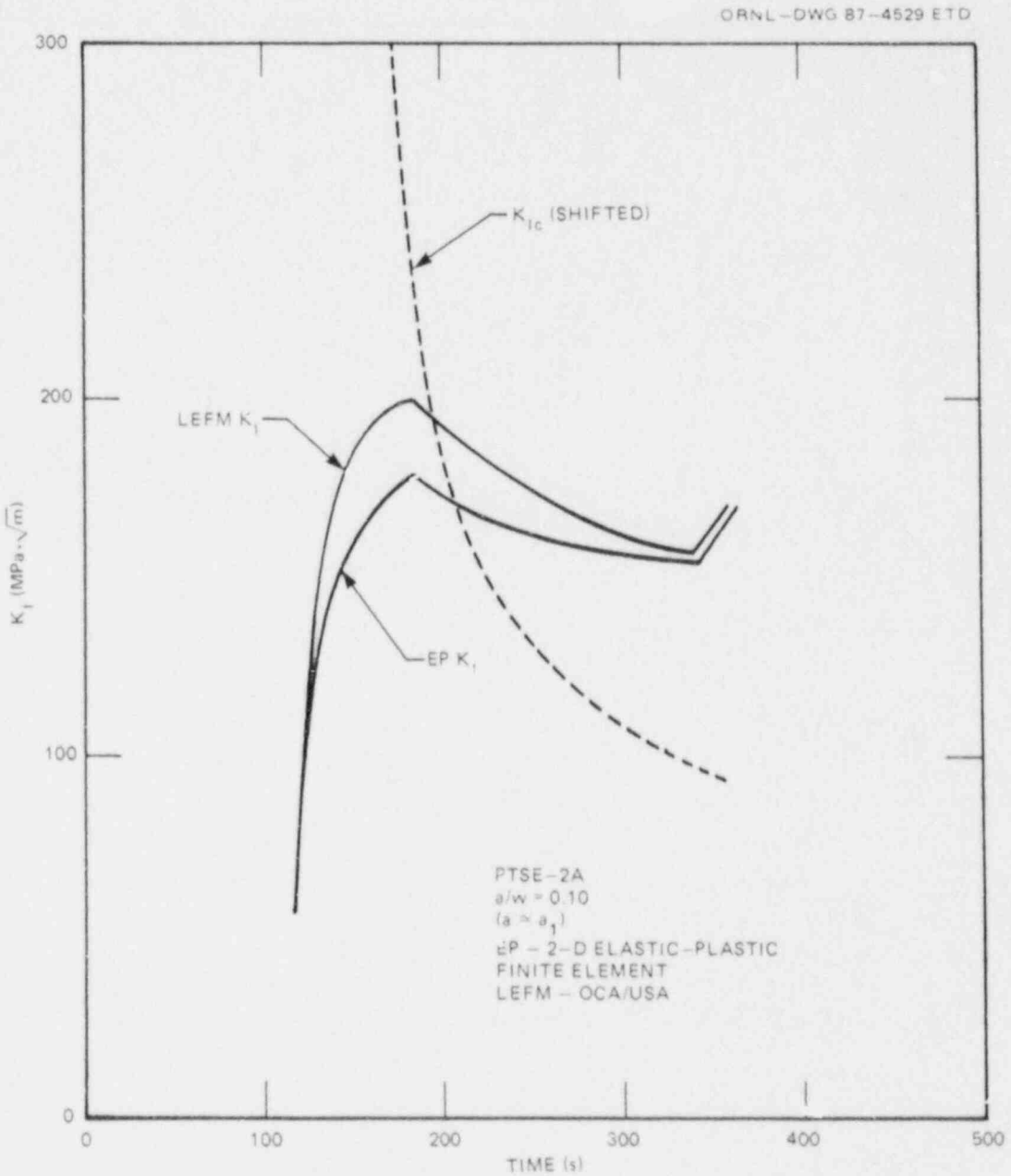

Fig. 10.28. K_I and K_{Ic} vs time from posttest OCA/USA LEFM and elastic-plastic finite-element analyses based on actual pressure and temperatures measured in PTSE-2A for initial flaw depth.

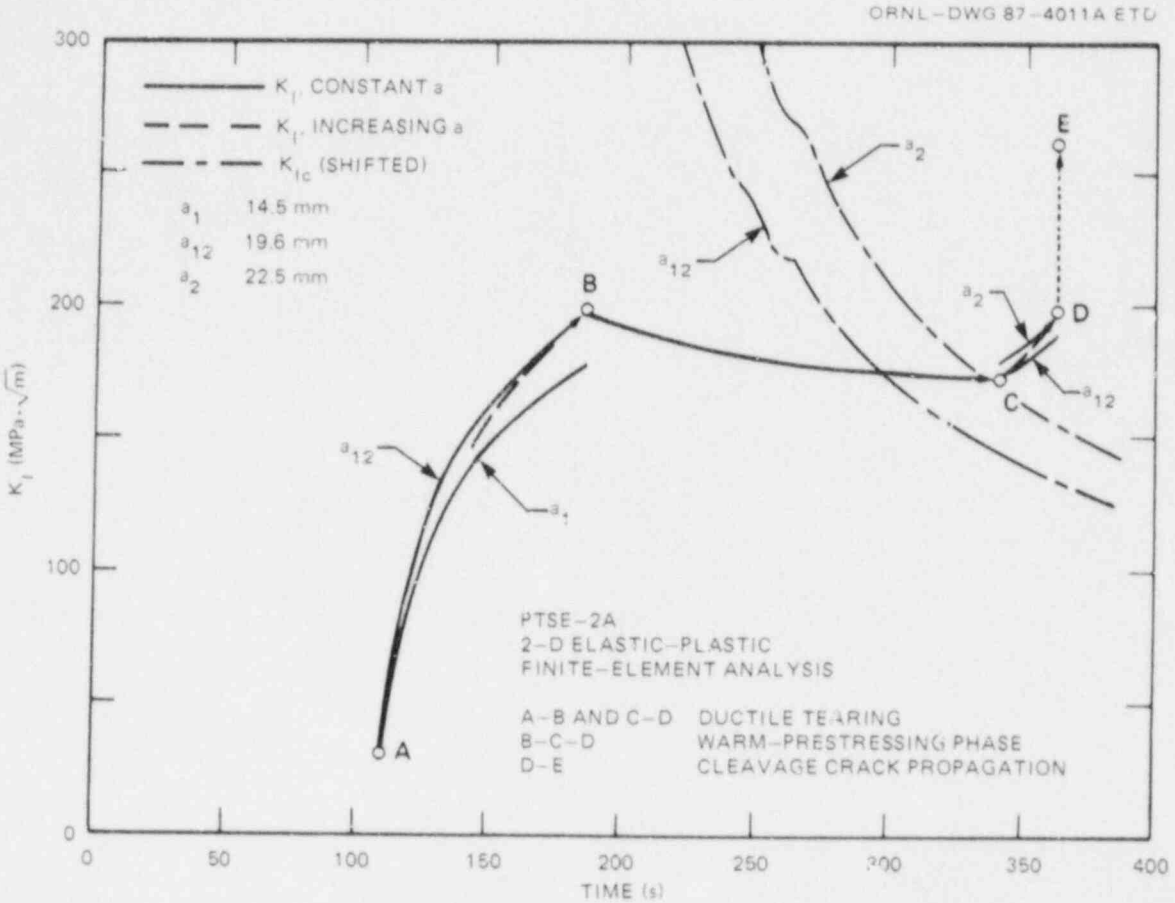

Fig. 10.29. K_I and K_{Ic} vs time from posttest elastic-plastic finite-element analyses based on actual pressure and temperatures measured in PTSE-2A for precleavage crack depths.

This satisfied one of the principal test conditions that had been planned. Figure 10.30 shows the K_I and toughness trajectories for the crack depths a_1, a_{12}, and a_2 for the PTSE-2A transient based on the 2-D elastic-plastic analysis. The K_{Ic} values are from the shifted K_{Ic} curve.

PTSE-2B. The PTSE-2B transient started with a crack of depth a = 42.4 mm as measured on the fracture surfaces. Before the initiation of cleavage, the crack advanced by stable ductile tearing to the depth a = 46.1 mm. Figures 10.31 and 10.32 show K_I and K_{Ic} vs time determined from the 2-D elastic-plastic calculations for these two depths. These figures include the K_{Ic} curve shifted to agree with the actual cleavage initiation point shown on Fig. 10.32. The elastic-plastic calculations for this transient are based on material A property set 7 (Tables 10.1 and 10.2).

The propagating cleavage fracture was interrupted by a small band of tearing at the depth a = 69.2 mm and proceeded to cleave further to the depth a = 78.8 mm. The conditions for these events are displayed in Fig. 10.33, which shows the K_I trajectory for the initial crack depth and the conditions for the cleavage interruption and final arrest. Because

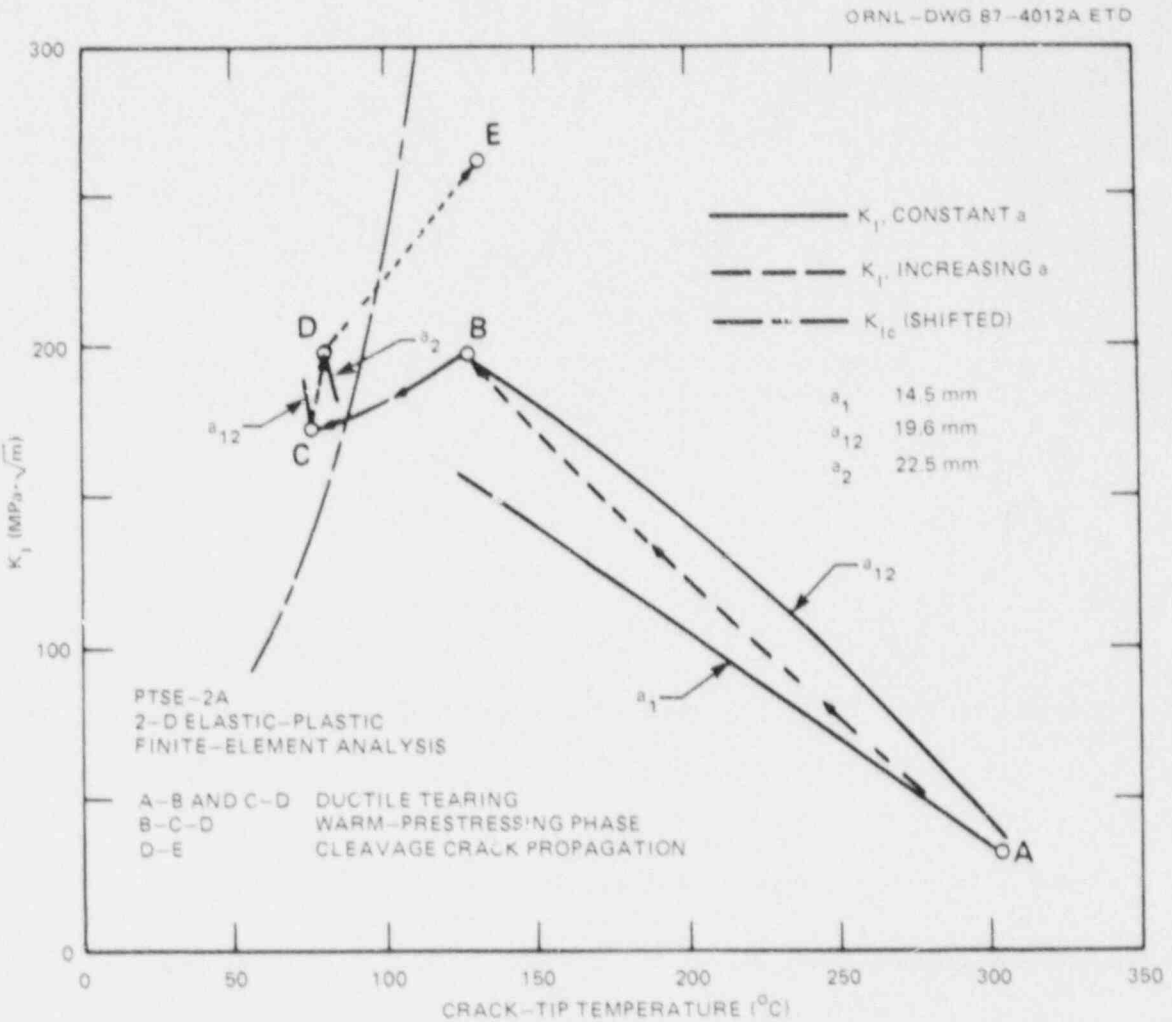

Fig. 10.30. Crack-tip conditions for precleavage crack depths from posttest elastic-plastic finite-element analysis using experimental pressure and temperature data from transient PTSE-2A: K_I and K_{Ic} vs crack-tip temperature.

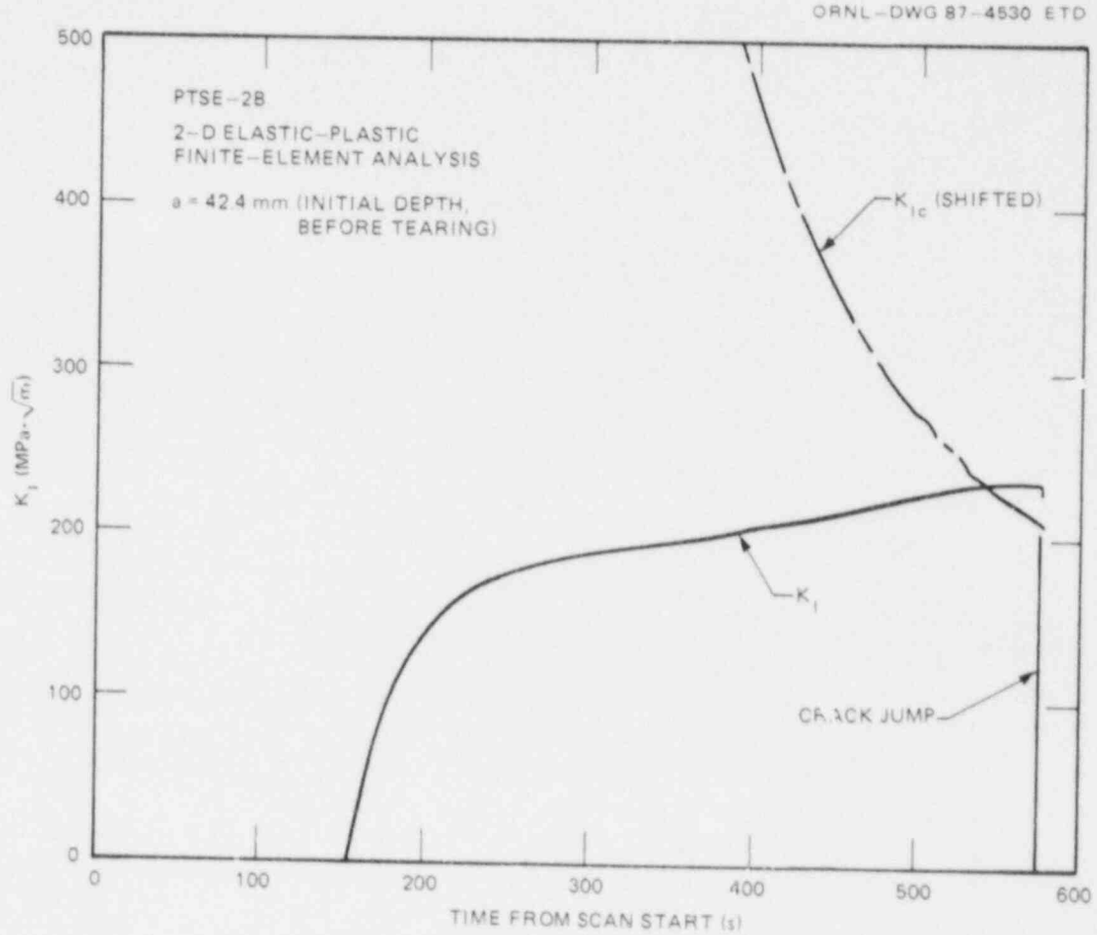

Fig. 10.31. K_I and K_{Ic} vs time for initial crack depth from post-test elastic-plastic finite-element analysis based on actual pressure and temperatures measured in PTSE-2B.

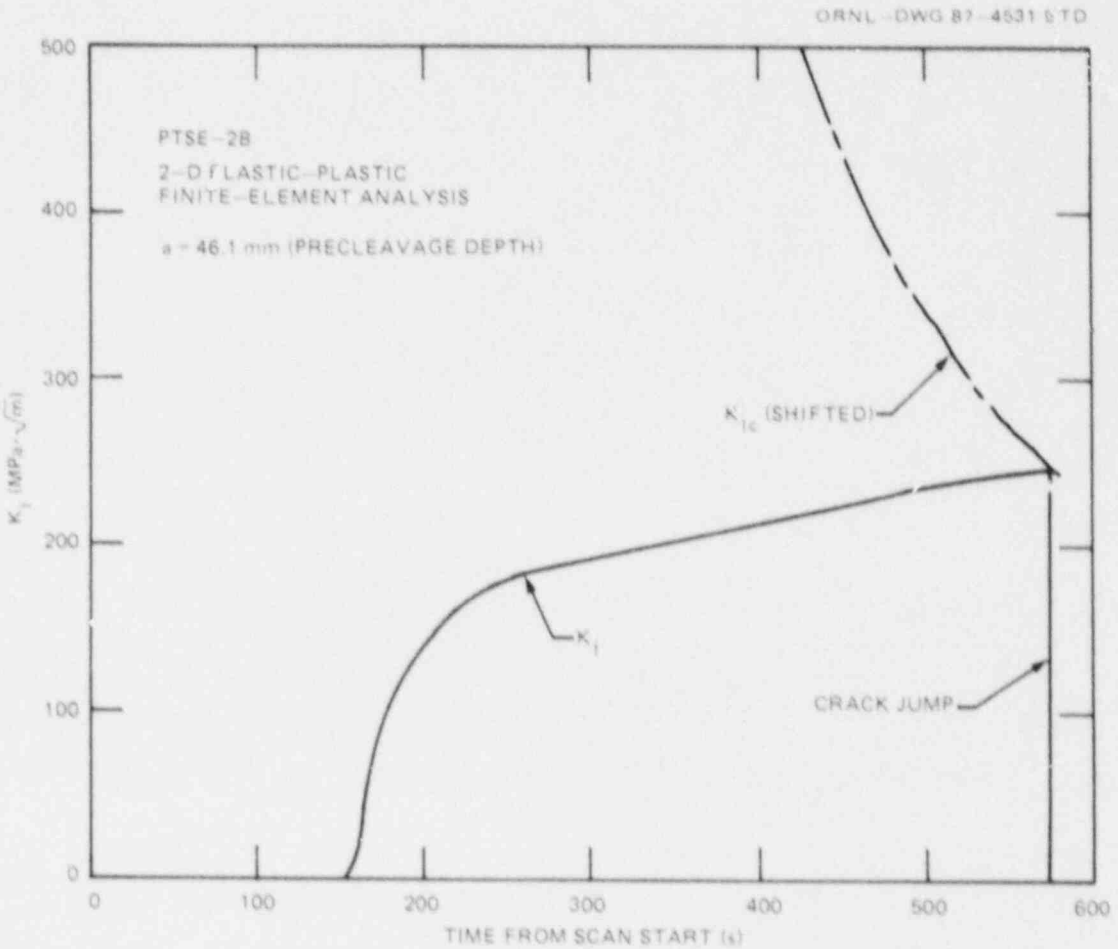

Fig. 10.32. K_I and K_{Ic} vs time for precleavage crack depth from posttest elastic-plastic finite-element analysis based on actual pressure and temperatures measured in PTSE-2B.

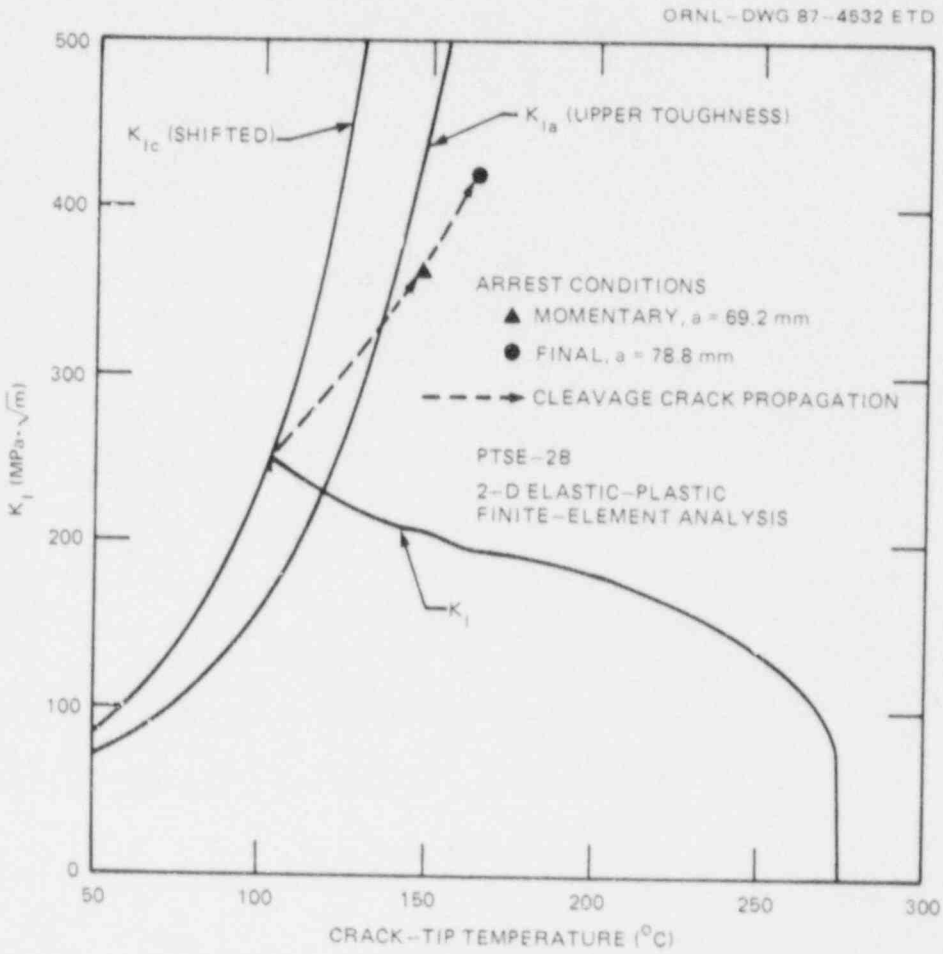

Fig. 10.33. Crack-tip conditions for precleavage crack depth from posttest elastic-plastic finite-element analysis using experimental pressure and temperature data from transient PTSE-2B: K_I, K_{Ic}, and K_{Ia} vs crack-tip temperature.

crack-tip velocities (da/dt) during this event cannot be determined from the experimental data, a conclusive analysis of the dynamics of the cleavage-tear-cleavage episode is not practicable. However, static analysis, on which Fig. 10.33 is based, provides no rationale for the momentary arrest and reinitiation.

The events and conditions during the two PTSE-2 transients are summarized in Table 10.12.

Table 10.12. Events and conditions during the PTSE-2 transients

Event	Time (s)	Crack depth a (mm)	Crack-tip temperature (°C)	K_I[a] (MPa·√m)
	PTSE-2A			
Initiation of thermal shock	~112	14.5	302.8	
First maximum K_I	184.6	19.6	128.0	195.7
Minimum K_I	341.8	19.6	77.0	171.0
Onset of secondary precleavage tearing	341.8	19.6	77.0	171.0
Initiation of cleavage	361.4	22.5	80.7	198.9
Cleavage arrest	361.4	39.3	130.6	261.4
Termination of tearing (by unloading)	365.6	42.4	138.0	278.7
	PTSE-2B			
Initiation of thermal shock	~155	42.4	274.9	
Onset of precleavage tearing	<575.8	42.4	[b]	[b,c]
Initiation of cleavage	575.82	46.1	102.4	248.1[c]
Interruption of cleavage by ductile tearing and reinitiation		69.2	146.8	361.6[c]
Final cleavage arrest	575.82	78.8	162.9	419.3[c]
Onset of ductile tearing	576.2	78.8	162.9	406.5
Vessel rupture (and complete unloading)	576.7	147.6	216.4	

[a] K_I values were calculated from the experimentally observed pressures (Table 10.11) and temperatures (Tables A.1 and A.2) by 2-D elastic-plastic finite-element analysis. The stress-strain parameters (Table 10.1) for material A were set 5 for PTSE-2A and set 7 for PTSE-2B.

[b] At t = 575.82 s, T = 94.8°C and K_I = 233.8 MPa·√m at this depth.

[c] K_I values listed for t = 575.82 s were calculated for the loading condition at 575.7 s.

10.6 Interpretation of Experimental Results

10.6.1 Ductile tearing

The low tearing resistance of the PTSE-2 material promoted ductile tearing before cleavage in both transients. Furthermore, the cleavage propagation in the PTSE-2B transient was interrupted by a small band (~1 mm) of ductile tearing about 10 mm from the final cleavage arrest. The final arrest was followed immediately by ductile tearing that proceeded until the crack penetrated the entire wall of the vessel.

The ductile tearing in the PTSE-2A transient occurred, as discussed in Sect. 10.5.3, while the material at, and immediately ahead of, the crack tip was at temperatures well below the onset of the Charpy upper shelf (150°C). The final ductile tearing (in the PTSE-2B transient) started in material at about 150°C.

The final tearing started with $J_I \approx 0.8$ MJ/m^2. This is much higher than J_{Ic} for normal reactor pressure vessel steels and is high enough to cause a tearing instability in the PTSE-2 transient, irrespective of any other type of instability. If the arrested crack (with a = 78.8 mm) were not deep enough to cause a tensile instability, the J_R-controlled tear would have promoted enough growth to cause a tensile instability.

The applied J_I attained at the end of each phase of tearing was used in calculating the extent of stable tearing that would occur if tearing were controlled by the condition $J_I = J_R$ for a tearing resistance curve

$$J_R = c(\Delta a)^n \quad , \tag{9}$$

where J_R is the tearing resistance, Δa is the increment of crack depth, and c and n are parameters determined by a least-squares fitting of specimen test data to Eq. (9). The highest and lowest tearing resistances from the set of six 25-mm-thick compact specimens of the characterization material PTC1 were used in the calculations to determine the range of uncertainty of Δa estimates. The numerical results are summarized in Table 10.13 based on these parameters.

Tearing resistance parameter	Lowest resistance		Highest resistance	
	Deformation theory	Modified Ernst	Deformation theory	Modified Ernst
c	0.09327	0.09592	0.1178	0.1229
n	0.2722	0.3701	0.4341	0.5372

The specimen data were interpreted in two ways: in terms of (1) J based on deformation theory, as prescribed in the testing standard of Ref. 16, and (2) the J modified by Ernst.[17]

Table 10.13. Tearing calculations based on 2-D elastic-plastic finite-element calculations and tearing resistance J_R-Δa data for characterization piece PTC1[a]

Tearing phase	Time (s)	Initial crack depth a (mm)	Final J_I (MJ/m^2)	Measured Δa (mm)	Calculated Δa[b] (mm)			
					Lowest resistance		Highest resistance	
					Deformation theory	Modified Ernst	Deformation theory	Modified Ernst
			PTSE-2A					
1. Prior to maximum K_I	112–184.6	14.5	0.165	5.1	8.1	4.3	2.3	1.7
2. Secondary precleavage	341.8–361.4	19.6	0.171	2.9	9.2	4.7	2.3	1.9
3. Postcleavage	361.4–365.6	39.3	0.335	3.1	109	29	11	6.5
			PTSE-2B					
4. Precleavage	155–575.82	42.4	0.283	3.7	59	19	7.5	4.7
5. Postcleavage	576.2–576.7	78.8	0.759	Unstable	Unstable	Unstable	Unstable	30

[a]The initial crack depth is the depth at the beginning of the specified phase. The J_I value is for the initial depth plus the measured Δa. J_I values were calculated by the 2-D elastic-plastic finite-element method.

[b]Δa is calculated from $J_I = c(\Delta a)^n$, where c and n are the power-law parameters determined by least-squares fitting the test specimen data. The lowest resistance columns are based on specimen PI235; the highest resistance columns are based on specimen PI230.

Neither the deformation theory J_R nor the modified Ernst J_R gives a consistent estimate of tearing. The lowest resistance deformation J_R data imply tearing in the first two phases of PTSE-2A that is reasonably consistent with the actual tearing. In all other phases, this J_R implies tearing that greatly exceeds the actual tearing. The highest resistance specimen with the modified Ernst interpretation of J_R implies tearing in phases 3 and 4 (Table 10.13) that agrees well with actual tearing, but these J_R data are inconsistent with the actual tearing in all other phases. Furthermore, this J_R case, unlike the other three cases shown in Table 10.13, implies strong tearing stability in phase 5 during the time that the final tearing instability occurred.

10.6.2 Tensile instability

Calculations of ligament stability and instability conditions at various crack depths were made with the OCA/USA program for the PTSE-2B transient. This program models the unbroken ligament beneath the flaw as a perfectly plastic material, as described in Ref. 4. The results of the PTSE-2B analysis, which tends to underestimate the depth at instability, are shown in Fig. 10.34. This indicates that the vessel was practically in a state of tensile instability at the time of the final cleavage arrest. It is likely that a more realistic model of the vessel and the material behavior, including the effects of strain hardening, would indicate that the structure was not unstable. This conclusion is supported

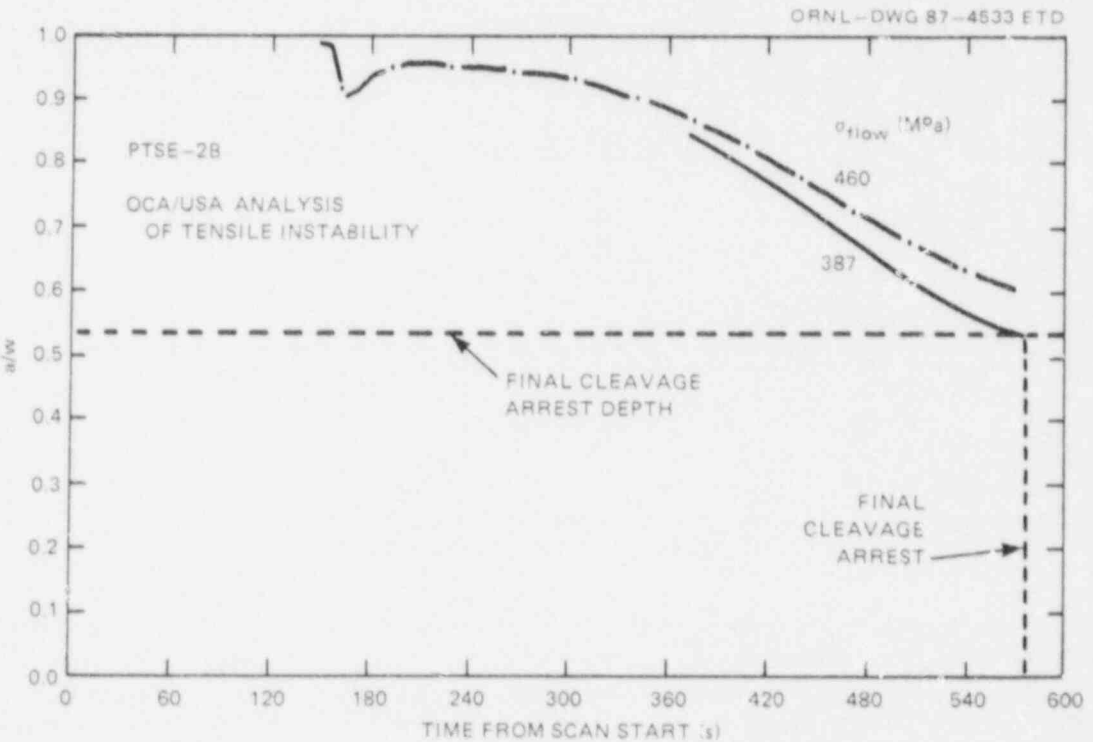

Fig. 10.34. Unstable crack depth vs time for transient PTSE-2B from OCA/USA analysis of perfectly plastic model of unbroken ligament.

by the 2-D elastic-plastic finite-element analyses for the arrested crack depth. The results of those analyses, in terms of CMOD vs time (Fig. 10.35), show no tendency toward structural instability. A more accurate model, including 3-D aspects and large-strain theory, is necessary to determine the tensile state properly for conclusively determining stability.

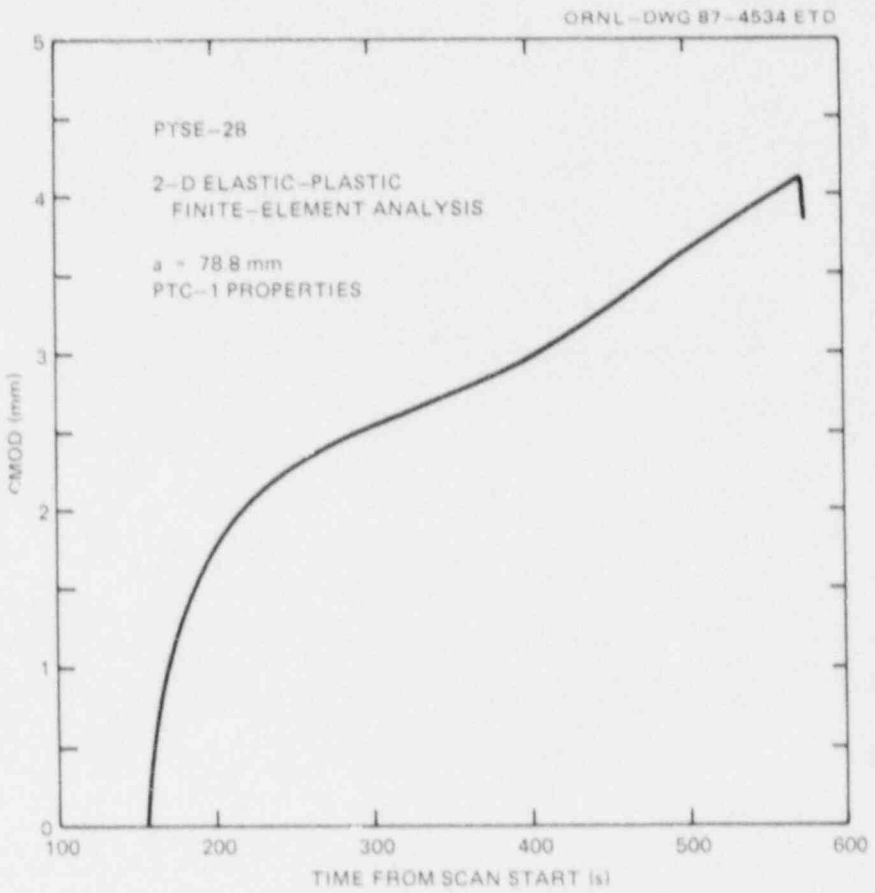

Fig. 10.35. CMOD vs time for arrested crack depth from elastic-plastic finite-element analysis based on actual pressure and temperatures measured in PTSE-2B.

10.6.3 Comparison of PTSE-2 and small-specimen fracture-toughness data

The cleavage initiation and arrest values from PTSE-2 (given in Table 10.12) are shown in Fig. 10.36 with the upper-toughness K_{Ia} curve used in the final pretest analyses and the shifted (by 20.26 K) upper K_{Ic} curve. The PTSE-2 K_{Ia} values were calculated for static crack geometry; consideration of the dynamics of crack propagation would probably result in lower values. The PTSE-2 values are shown in Fig. 10.37 in comparison

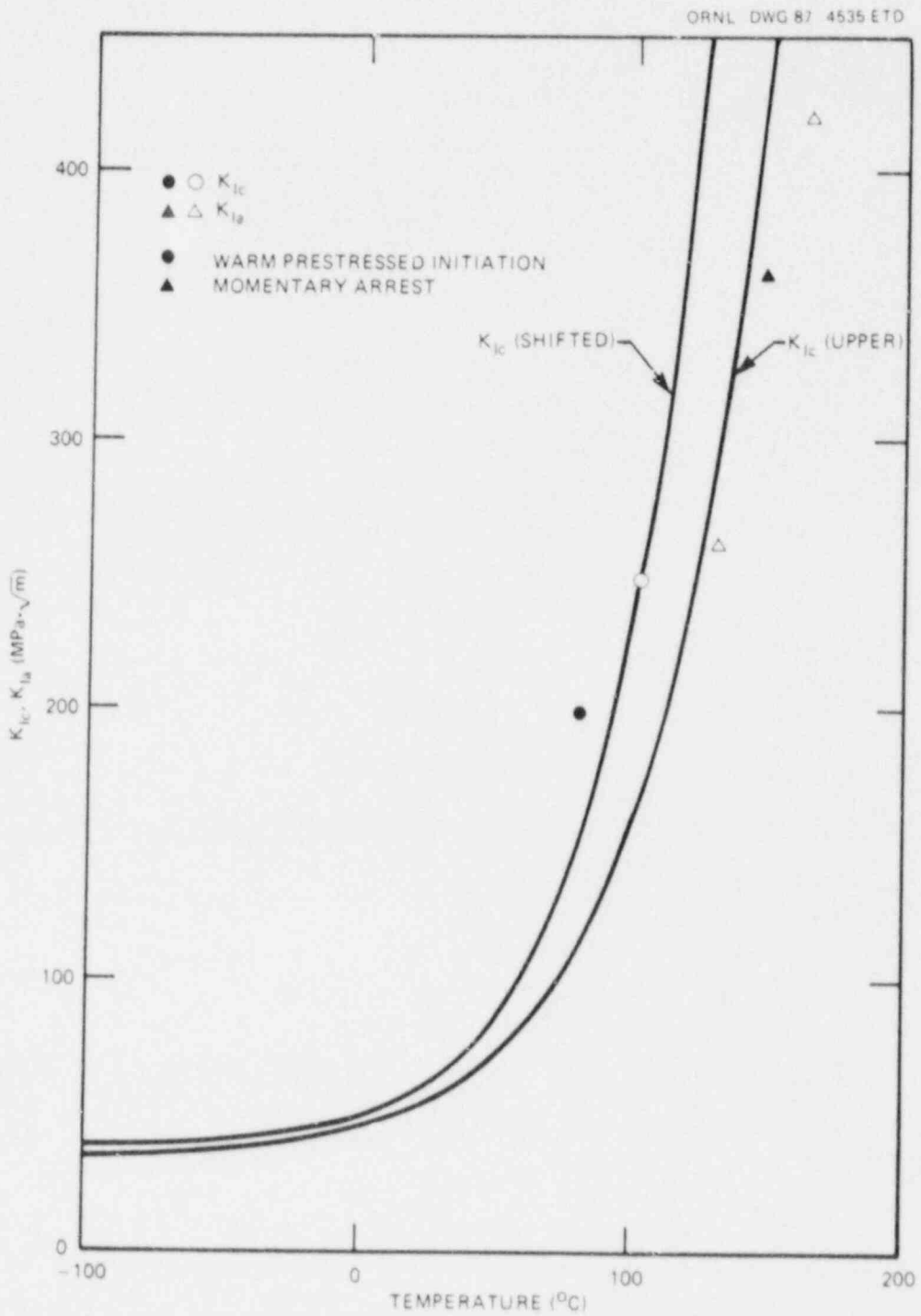

Fig. 10.36. Crack initiation K_{Ic} and arrest K_{Ia} toughness values observed in PTSE-2 compared with shifted pretest K_{Ic} curve and upper toughness K_{Ia} curve.

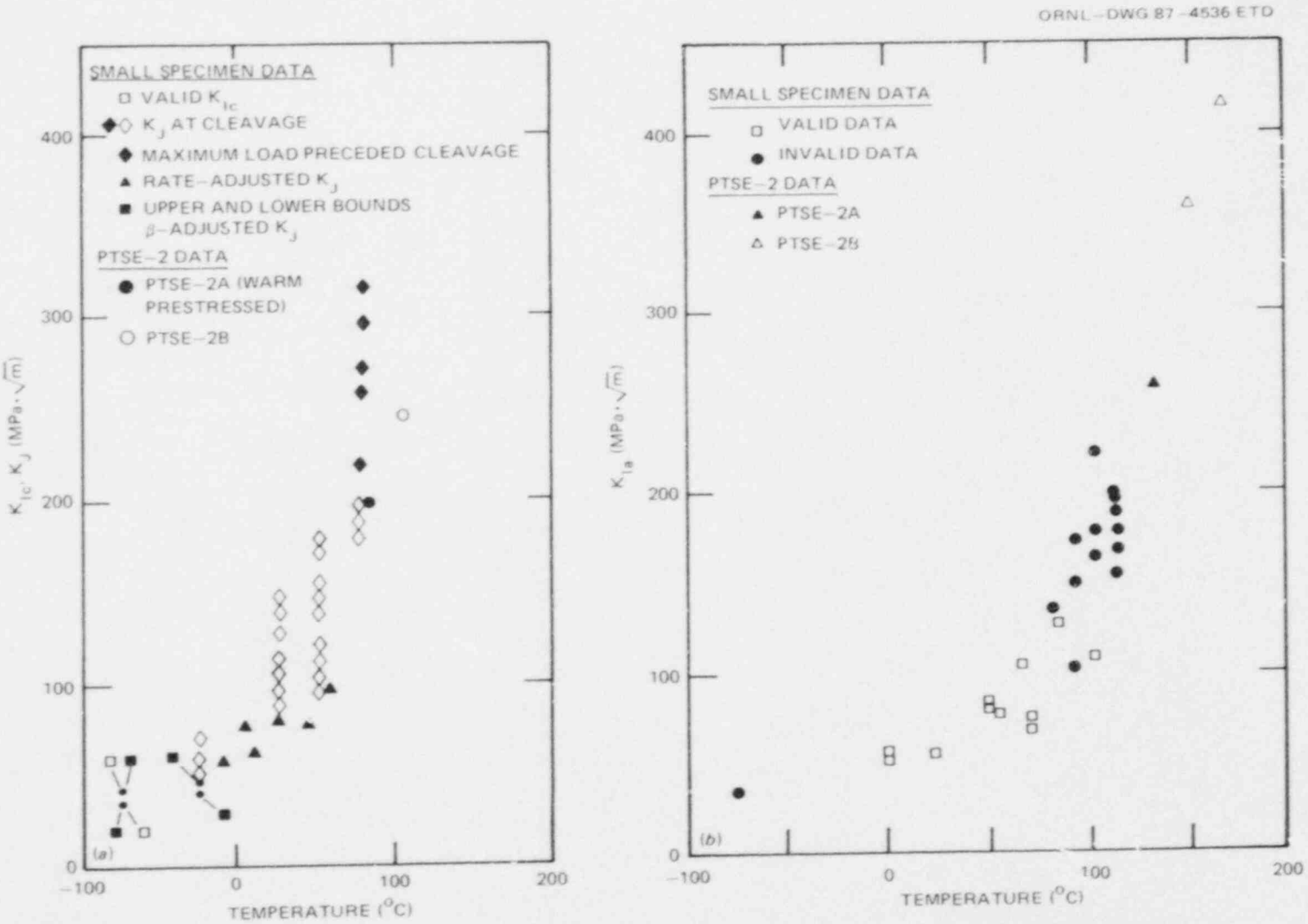

Fig. 10.37. Crack initiation K_{Ic} and arrest K_{Ia} toughness values observed in PTSE-2 compared with (*a*) K_{Ic} and K_J small-specimen data and (*b*) K_{Ia} small-specimen data.

with the raw K_{Ic}, K_J, and K_{Ia} pretest data for characterization piece PTC1. These show that the small specimen data were adequate to permit the definition of experimental conditions that led to successful results in both transients.

10.6.4 Warm-prestressing effects

Analysis of warm prestressing in PTSE-2 was based on a theoretical procedure developed by Chell.[18-20] Chell's procedure is derived from the strip-yield model of a crack with the premise that after warm prestressing, failure occurs when the J-integral reaches a critical value

$$J_{CRIT} = \frac{(1 - \nu^2)}{E} K_{Ic}^2 , \qquad (10)$$

where K_{Ic} is the fracture toughness of pristine material. The J-integral used in Chell's theory is defined on the basis of elastic strains only, even in regions of plasticity.[20] This procedure was applied to the results of the PTSE-1 experiment as discussed in detail in Ref. 4.

In the PTSE-2 experiment, warm prestressing occurred only in transient PTSE-2A. The analysis of PTSE-2A involves the determination of K_I at the times of the first maximum and minimum in $K_I(t)$. These values, together with the flow stresses σ_{flow} at those times, define the plastic zone sizes for the first two states (i.e., the first maximum K_I and the minimum K_I) involved in Chell's theory. The third state, the loading at the time of failure, is defined by the criterion of Eq. (10).

Chell's theory was modified to take account of tearing before cleavage during the loading step that leads from state 2 to state 3. For this modification, it was assumed that this tearing occurred with the material at the state 3 temperature. The modification takes account of the actual change in position of the crack tip relative to the residual plastic zones generated in the state 1 and state 2 loadings. It also introduces virtual crack-face tractions over the incremental surface of the crack. The virtual tractions are equal and opposite in direction to the stresses in the residual plastic zones of states 1 and 2. The modified theory is similar to a modification for subcritical crack growth that Chell described in Ref. 21, which did not come to the attention of the authors of the present report until this work was completed.

Several PTSE-2 warm-prestressing sequences were analyzed to illustrate the effects of various factors. Cases for fracture without the intervention of tearing and for a variety of assumptions regarding flow stress were investigated. In all cases, K_I values for the applied loads were selected from the posttest values given in Table 10.12, and the temperature of the crack tip at the time each loading state was attained was attributed to the entire plastic zone. That is, for the purpose of determining the attributes of plastic zones, they were assumed to be isothermal during the respective loading steps. The temperature of the structure in state 3 was, in each case, the experimental temperature of the actual PTSE-2A crack tip at the instant cleavage propagation commenced.

In the PTSE-2A transient the initial crack (a = 14.5 mm) tore ductilely to a depth of 19.6 mm before the onset of warm prestressing (state 1). After the minimum in K_I (state 2), K_I increased, and for a short time before cleavage occurred, the crack tore ductilely to a depth of 22.5 mm. The loading conditions deduced from the PTSE-2A transient for two of the sequences analyzed are described in Table 10.14. The sequence for a fixed crack depth is important because it represents the course of events that would be predicted if there were no expectation of ductile tearing. The sequence for a variable crack depth represents the actual course as reconstructed from experimental evidence.

The results of the fixed-crack and tearing-crack sequences are shown in Figs. 10.38(*a*) and (*b*), respectively. Figure 10.38 shows the K_I at fracture calculated by the warm-prestressing theory as a function of the K_{Ic} of the material. The experimental points are the actual fracture conditions obtained from the PTSE-2 experimental data. The K_{Ic} values used for plotting the experimental points were derived from the pretest upper-toughness expression shifted to make the K_{Ic} value observed in PTSE-2B fall on the curve. Thus, K_{Ic} was assumed to be

$$K_{Ic} = a + b \exp [c (T - T_s)] , \qquad (11)$$

Table 10.14. Parameters for warm-prestressing analysis of the PTSE-2A transient

Loading state	Time (s)	Crack depth (mm)	Crack-tip temperature (°C)	Flow stress[a] (MPa)	K_I[b] (MPa·$\sqrt{m}$)	K_{Ic}[c] (MPa·$\sqrt{m}$)
Fixed crack depth (19.6 mm)						
1	185	19.6	125.0	392.2	195.7	439.7
2	340	19.6	75.1	409.2	171.0	134.3
3	361.4	19.6	71.4	410.8	187.3	124.7
Variable crack depth (Δa = 2.9 mm)						
1	185	19.6	125.0	392.2	195.7	439.7
2	340	19.6	75.1	409.2	171.0	134.3
3	361.4	22.5	80.9	406.8	198.9	151.6

[a]Flow stresses as a function of temperature were obtained from a polynomial least-squares fit to tensile data for characterization material PTC1. All transversely oriented instrumented specimens were included.

[b]Values interpolated from set of 2-D elastic-plastic finite-element calculations based on PTSE-2A experimental pressure and temperatures.

[c]Values based on the pretest K_{Ic} curve shifted to agree with the PTSE-2B experiment, Eq. (11), at the crack-tip temperature.

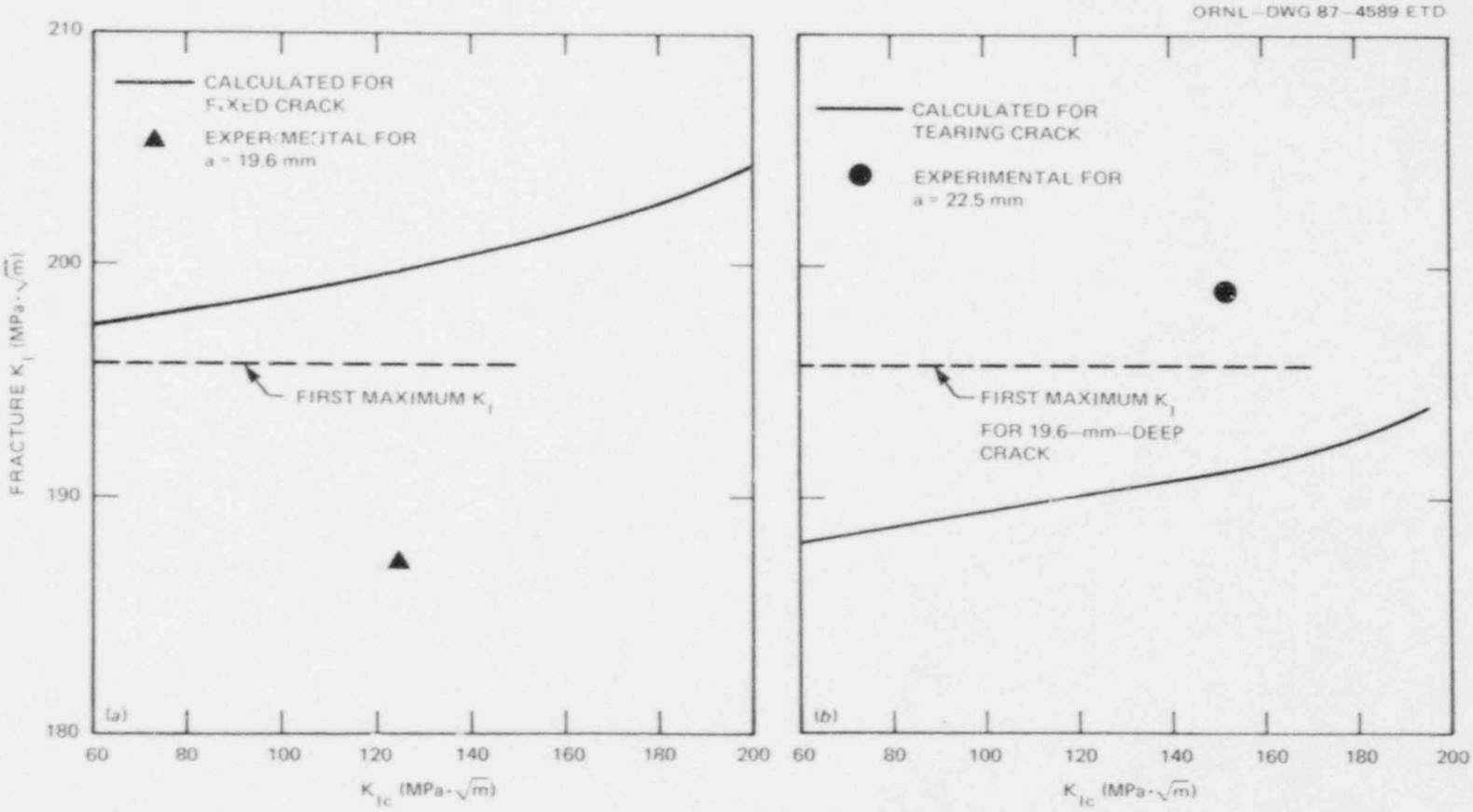

Fig. 10.38. Theoretical prediction of post-warm-prestressing fracture conditions K_I vs K_{Ic} for the PTSE-2A transient compared with actual fracture. Predictions are based on K_I values from posttest elastic-plastic finite-element analysis using measured pressure and temperatures. Plastic zones in the warm-prestressing analysis are based on measured flow stresses for characterization material PTC1. (*a*) Crack without tearing and (*b*) tearing crack.

where the parameters a, b, and c are given in Table 10.5 and the temperature shift determined from PTSE-2B is T_s = 20.26 K.

If the crack, which was 19.6 mm deep, had not torn in the final loading step, the theory predicted that the cleavage initiation would have occurred, as shown in Fig. 10.38(*a*), at K_I = 12 MPa·$\sqrt{m}$ higher than the experimental K_I for a crack of this depth. The experimental point in Fig. 10.38(*a*) would be the perceived crack initiation condition if one did not know that the crack tore. The calculations for the tearing crack predicted that fracture would have occurred at a K_I = 7 MPa·$\sqrt{m}$ lower than the experimental point, as shown in Fig. 10.38(*b*). The important implications of the experimental and analytical results are that (1) warm prestressing combined with the complications of precleavage tearing elevated the fracture point (K_I = 198.9 MPa·$\sqrt{m}$) significantly above the level of the pristine K_{Ic} (151.6 MPa·$\sqrt{m}$) and (2) the modified warm-prestressing theory predicted an elevation of the fracture point about 15% less than the observed elevation.

According to theory, the consequences of warm prestressing are very sensitive to the extent of precleavage tearing and the tensile strength of the material. The effect of the latter factor is illustrated by the result, shown in Fig. 10.39, of a calculation of K_I at fracture based on

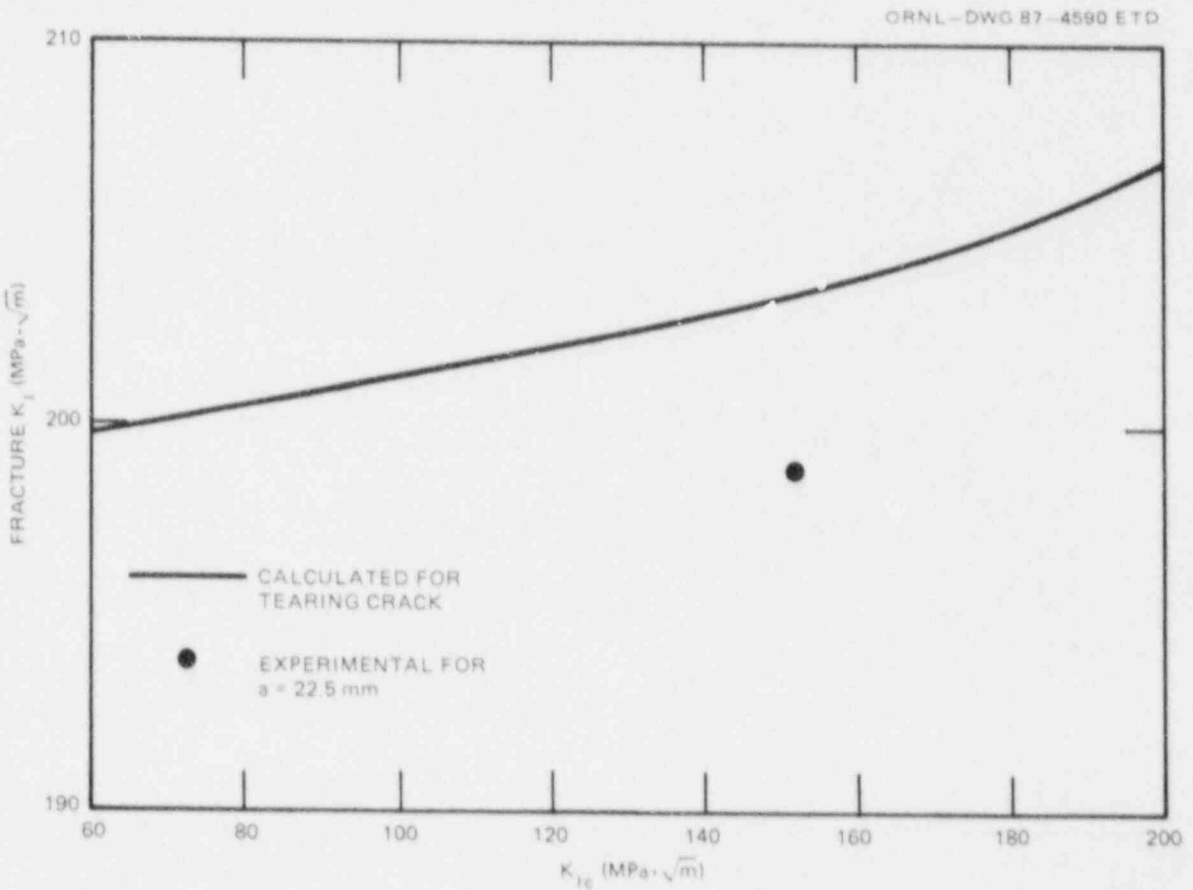

Fig. 10.39. Results of warm-prestressing analysis of tearing crack based on yield stresses for same conditions illustrated in Fig. 10.38(*b*).

the use of yield stress rather than flow stress to characterize the plastic zones. In this case, the yield stresses are about two-thirds of the flow stresses used for the cases illustrated in Fig. 10.38. A comparison of the fracture points in Figs. 10.38(*b*) and 10.39 for the crack-tip toughness at time of actual fracture (K_{Ic} = 151.6 MPa$\cdot\sqrt{m}$) shows that the two predictions differ by ~12 MPa$\cdot\sqrt{m}$. This sensitivity to strength is principally a result of the contributions of virtual crack-face loading, which may in different circumstances increase or decrease the effective stress-intensity factor of the final crack.

References

1. R. H. Bryan et al., "PTS Test Studies," *Heavy-Section Steel Technology Program Quart. Prog. Rep. October–December 1981*, NUREG/CR-2141, Vol. 4 (ORNL/TM-8252), Union Carbide Corp. Nuclear Div., Oak Ridge Natl. Lab.

2. B. R. Bass, R. H. Bryan, and J. W. Bryson, "The OCA/USA Program for Analysis of PTS Experiments," *Heavy-Section Steel Technology Program Quart. Prog. Rep. July–September 1983*, NUREG/CR-3334, Vol. 3 (ORNL/TM-8787/V3), Union Carbide Corp. Nuclear Div., Oak Ridge Natl. Lab.

3. R. H. Bryan and J. W. Bryson, "Pressurized Thermal-Shock Stress and Fracture Analysis," *Heavy-Section Steel Technology Program Quart. Prog. Rep. July–September 1981*, NUREG/CR-2141, Vol. 3 (ORNL/TM-8145), Union Carbide Corp. Nuclear Div., Oak Ridge Natl. Lab.

4. R. H. Bryan et al., *Pressurized-Thermal-Shock Test of 6-in.-Thick Pressure Vessels. PTSE-1: Investigations of Warm Prestressing and Upper-Shelf Arrest*, NUREG/CR-4106 (ORNL-6135), Martin Marietta Energy Systems, Inc., Oak Ridge Natl. Lab., April 1985.

5. D. G. Ball et al., *OCA-II, A Code for Calculating Behavior of 2-D and 3-D Surface Flaws in a Pressure Vessel Subjected to Temperature and Pressure Transients*, NUREG/CR-3491 (ORNL-5934), Union Carbide Corp. Nuclear Div., Oak Ridge Natl. Lab., February 1984.

6. J. G. Merkle, "Elastic-Ideally Plastic Pressurized Thermal-Shock Analysis for a Deep Continuous External Longitudinal Crack in a Cylinder," *Heavy-Section Steel Technology Program Quart. Prog. Rep. January–March 1983*, NUREG/CR-3334, Vol. 1 (ORNL/TM-8787/V1), Union Carbide Corp. Nuclear Div., Oak Ridge Natl. Lab.

7. R. H. Bryan and J. G. Merkle, "Upper-Shelf Arrest Analysis Based on J_R-Controlled Tearing," *Heavy-Section Steel Technology Program Quart. Prog. Rep. January–March 1983*, NUREG/CR-3334, Vol. 1 (ORNL/TM-8787/V1), Union Carbide Corp. Nuclear Div., Oak Ridge Natl. Lab.

8. B. R. Bass and J. W. Bryson, *Applications of Energy Release Rate Techniques to Part-Through Cracks in Plates and Cylinders, Volume 1. ORMGEN-3D: A Finite Element Mesh Generator for 3-Dimensional Crack Geometries*, NUREG/CR-2997, Vol. 1 (ORNL/TM-8527/V1), Union Carbide Corp. Nuclear Div., Oak Ridge Natl. Lab., December 1982.

9. K. J. Bathe, *ADINA — A Finite Element Program for Automatic Dynamic Incremental Nonlinear Analysis*, Report 82448-1, Massachusetts Institute of Technology, Cambridge, September 1975 (revised December 1978).

10. B. R. Bass and J. W. Bryson, *Applications of Energy Release Rate Techniques to Part-Through Cracks in Plates and Cylinders, Volume 2. ORVIRT: A Finite Element Program for Energy Release Rate Calculations for 2-D and 3-D Crack Models*, NUREG/CR-2997, Vol. 2 (ORNL/TM-8527/V2), Union Carbide Corp. Nuclear Div., Oak Ridge Natl. Lab., February 1983.

11. J. W. Bryson and B. R. Bass, *ORMGEN.PC: A Microcomputer Program for Automatic Mesh Generation of 2-D Crack Geometries*, NUREG/CR-4475 (ORNL-6250), Martin Marietta Energy Systems, Inc., Oak Ridge Natl. Lab., March 1986.

12. F. J. Loss, "Toughness and Ductile Shelf Properties of Irradiated Low-Shelf Weld Metals," Nuclear Regulatory Commission 8th Water Reactor Safety Research Information Meeting, Gaithersburg, Maryland, October 27–31, 1980.

13. A. L. Hiser, F. J. Loss, and B. H. Menke, *J-R Curve Characterization of Irradiated Low Upper Shelf Welds*, NUREG/CR-3506 (MEA-2028), Materials Engineering Associates, Inc., Lanham, Md, April 1984.

14. "Rules for In-Service Inspection of Nuclear Power Plant Components," *ASME Boiler and Pressure Vessel Code, Section XI*, American Society of Mechanical Engineers, New York, 1983.

15. J. G. Merkle, *An Examination of the Size Effects and Data Scatter Observed in Small-Specimen Cleavage Fracture Toughness Testing*, ORNL/TM-9088, Union Carbide Corp. Nuclear Div., Oak Ridge Natl. Lab., April 1984.

16. ASTM Standard E813-81, "Standard Test Method for J_{Ic}, A Measure of Fracture Toughness," pp. 762–80 in *1983 Annual Book of ASTM Standards*, American Society for Testing and Materials, Philadelphia, 1983.

17. H. A. Ernst, "Material Resistance and Instability Beyond J-Controlled Crack Growth," pp. 191–213 in *Elastic-Plastic Fracture: Second Symposium*, ASTM STP 803, Vol. I, American Society for Testing and Materials, Philadelphia, 1983.

18. G. G. Chell, J. R. Haigh, and V. Vitek, *A Theory of Warm Prestressing: Experimental Validation and the Implications for Elastic-Plastic Failure Criteria*, RD/L/N63/79, Central Electricity Research Laboratories, Leatherhead, Surrey, England, August 1979.

19. G. G. Chell, *A Theory for Predicting the Failure Loads of Cracked Structures Subjected to Warm Prestressing. 1: Load Changes at Constant Temperature*, RD/L/N78/79, Central Electricity Research Laboratories, Leatherhead, Surrey, England, September 1979.

20. G. G. Chell, "Some Fracture Mechanics Applications of Warm Prestressing to Pressure Vessels," pp. 117–24 in *Proc. 4th Int. Conf. on Pressure Vessel Technology*, Paper C22/80, Institution of Mechanical Engineers, London, 1980.

21. G. G. Chell, "The Effects of Sub-Critical Crack Growth on the Fracture Behavior of Cracked Ferritic Steels After Warm Prestressing," *Fatigue Fract. Eng. Mater. Struct.* 9(4), 259–74 (1986).

11. CONCLUSIONS

The PTSE-2 experiment attained the planned objectives. The two transients proceeded according to pretest plans. Two brittle fractures were initiated and arrested. The first brittle fracture initiated after a period of warm prestressing. After the final crack arrest, the crack immediately tore ductilely until the vessel wall was penetrated. This result had been anticipated because an unstable tear was a major objective.

The arrest events in PTSE-2 were near the points implied by the upper-toughness K_{Ia} curve used for planning the transients. The experimental initiation and arrest points all lay within the range used for planning. The K_{Ic} value obtained from the PTSE-2B transient implied an upward, temperature-wise shift of 20.26 K in the pretest upper-toughness curve, based on characterization testing. This is consistent with the difference found in the Charpy transition temperature of the characterization piece PTC1 and the vessel insert for which the Charpy transition temperatures were separated by 20 K. The data from the experiment and the supporting characterization specimen tests are potentially a useful source of information for relating fracture toughness to transition temperatures for materials with upper-shelf energies too low for determination of RT_{NDT}.

The final cleavage arrest was a particularly remarkable event. It indicates that this material with very low tearing resistance exhibited high arrest toughness even though the K_I gradient was positive and the crack was unstable with respect to other modes of fracture. This empirical result, observed with a well-constrained crack, suggests that in vessel integrity evaluations one can safely assume that low ductile toughness does not itself imply low cleavage toughness.

The unresolved ambiguity in the tensile properties of the vessel insert before the experiment leaves a significant uncertainty in the values of the strain energy release rate G and K_I attributed to arrests and other events. For example, if the final arrest is analyzed on the basis of pretest properties of the characterization material, the final K_{Ia} is 456 MPa$\cdot\sqrt{m}$, a value 9% higher than the result stated in Chap. 10.

Ductile tearing was evident in every phase of the PTSE-2 experiment. This behavior had been predicted qualitatively by analysis based on J_R-Δa tearing resistance data. Posttest analysis of the four distinct phases of stable ductile tearing in PTSE-2 failed to demonstrate quantitative agreement between J_R-Δa data and tearing in the experiment. J_R curves that fit the early phases of the experiment were poor fits for the later phases and vice versa.

Precleavage ductile tearing was observed in the first pressurized-thermal-shock experiment,[1] PTSE-1, although the extent was small and was confined to the irregular areas of the tip of the initial flaw in that experiment, which involved normally high toughness material. A small amount of tearing was predicted in the early phases of PTSE-1 although the amount was not sufficient to have significantly affected the eventual cleavage crack propagation. However, it is clear from the PTSE-2 experiment that tearing can promote cleavage propagation to greater depths than would occur without tearing. The tearing analyses of both experiments

indicate that the quantitative effect cannot be predicted well from J_R-Δa data. This experience and the imprecision of similar tearing predictions for the isothermal hydrostatic test of intermediate test vessel V-8A[2] suggest that it would be useful to investigate the applicability of other theoretical procedures based on tensile properties.

Unstable tearing after the final cleavage arrest was conspicuous. Analysis suggests that it was not a consequence of a structural tensile instability, which implies, rather, that the cause was low tearing resistance or high local tensile strains or some combination of the two. Instability analyses based on the J_R-Δa data generally predicted instability except for the steepest J_R-Δa curves derived from the modified Ernst definition of J_R. The apparent agreement with the J_R-Δa analysis may be fortuitous because logically the possibility of an instability depends on the magnitude of the strain-energy release rate irrespective of Δa. Therefore, as in the matter of stable tearing, other theoretical techniques should be investigated.

Beneficial effects of warm prestressing were clearly demonstrated in PTSE-2A. The interpretation of the experiment in a theoretical framework was complicated by the unfortunate use of a material that was susceptible to precleavage tearing and that also had somewhat uncertain tensile properties. Furthermore, the experiment itself had to determine the K_{Ic} property unperturbed by superfluous loadings. An interpretation has been made that consists of quantitative conclusions and indications of the effects of uncertainties.

With regard to the importance of uncertainty in K_{Ic} values, the theoretical analysis demonstrates that the K_I at fracture after warm prestressing is a slowly varying function of K_{Ic} for the range of interest in this experiment. Therefore, some imprecision in the inference of K_{Ic} from the PTSE-2B transient can be tolerated.

The analysis was performed by a procedure described by Chell[3] that is very easy to apply because computations can be performed by simple expressions. Consequently, the significance of variations or uncertainty in flow stress was identified, and the importance of tearing in calculating the effect of warm prestressing was demonstrated. For conditions similar to those experienced in PTSE-2, tearing diminishes the benefits of warm prestressing relative to those that could be realized without tearing. A physically more reasonable application of Chell's postulates would require extensive numerical analysis using incremental plasticity procedures. The results of the simpler analysis agree well with the experimental results.

References

1. R. H. Bryan et al., *Pressurized-Thermal-Shock Test of 6-in.-Thick Pressure Vessels. PTSE-1: Investigations of Warm Prestressing and Upper-Shelf Arrest*, NUREG/CR-4106 (ORNL-6135), Martin Marietta Energy Systems, Inc., Oak Ridge Natl. Lab., April 1985.

2. R. H. Bryan et al., *Test of 6-in.-Thick Pressure Vessels. Series 3: Intermediate Test Vessel V-8A — Tearing Behavior of Low Upper-Shelf Material*, NUREG/CR-4760 (ORNL-6187), Martin Marietta Energy Systems, Inc., Oak Ridge Natl. Lab., May 1987.

3. G. G. Chell, "Some Fracture Mechanics Applications of Warm Prestressing to Pressure Vessels," pp. 117–24 in *Proc. 4th Int. Conf. on Pressure Vessel Technology*, Paper C22/80, Institution of Mechanical Engineers, London, 1980.

ACKNOWLEDGMENTS

The authors gratefully acknowledge the essential contributions of H. A. Domian and coworkers of the Babcock & Wilcox Company Alliance Research Center for work on vessel fabrication; A. R. Rosenfield and coworkers of Battelle Columbus Division for crack-arrest toughness measurements; S. K. Iskander and J. Strizak for tensile testing and specimen fabrication; R. S. Crouse for scanning electron fractography; T. M. Cate and F. R. Gibson for work on instrumentation, controls, and data acquisition systems; D. A. Steinert for development and application of data processing computer programs; J. K. Walker for assistance with finite-element computations; C. E. Pugh for management, advice, and support; G. D. Whitman for guidance and advice; and M. Vagins of the U.S. Nuclear Regulatory Commission for support, encouragement, and guidance. The authors also appreciate the contributions of R. H. Baldwin; H. D. Curtis; E. H. Guinn; T. G. Hill; W. F. Jackson; T. N. Jones; E. T. Manneschmidt; T. D. Owings, Jr.; and R. L. Swain for their work on material testing, vessel preparation, and test facility operation.

Appendix A

TEMPERATURE PROFILES FROM THERMOCOUPLE THIMBLE 5

The sets of temperature profiles T(r,t) determined experimentally and used in posttest finite-element analysis are given in Tables A.1 and A.2 for PTSE-2A and -2B, respectively. The profiles are based on corrected thermocouple locations. The pressures for the same time steps are listed in Table 10.11.

Computer-generated plots of temperature profiles at several times in transients PTSE-2A and -2B are presented in Figs. A.1 and A.2. The first profile in each set is for a time immediately before the vessel started to cool, at ~112 and 155 s in the A and B transients, respectively.

Table A.1. Experimental temperature profile set used for posttest elastic-plastic finite-element analysis of PTSE-2A[a]

RADIAL COORDINATE r (mm)	TIME (s)					
	0.11000D+03	0.12000D+03	0.13000D+03	0.14000D+03	0.15000D+03	0.16000D+03
0.49060D+03	0.30283D+03	0.19330D+03	0.96881D+02	0.65838D+02	0.50558D+02	0.39666D+02
0.48946D+03	0.30282D+03	0.20323D+03	0.10553D+03	0.73787D+02	0.57937D+02	0.46640D+02
0.48830D+03	0.30281D+03	0.21321D+03	0.11425D+03	0.81790D+02	0.65369D+02	0.53663D+02
0.48683D+03	0.30280D+03	0.22587D+03	0.12534D+03	0.91966D+02	0.74819D+02	0.62593D+02
0.48537D+03	0.30279D+03	0.23844D+03	0.13642D+03	0.10212D+03	0.84255D+02	0.71511D+02
0.48349D+03	0.30277D+03	0.25433D+03	0.15058D+03	0.11509D+03	0.96301D+02	0.82895D+02
0.48162D+03	0.30276D+03	0.26963D+03	0.16475D+03	0.12800D+03	0.10830D+03	0.94232D+02
0.47923D+03	0.30273D+03	0.28556D+03	0.18289D+03	0.14426D+03	0.12339D+03	0.10843D+03
0.47684D+03	0.30271D+03	0.29613D+03	0.20098D+03	0.16008D+03	0.13792D+03	0.12196D+03
0.47378D+03	0.30267D+03	0.30299D+03	0.22335D+03	0.17944D+03	0.15556D+03	0.13822D+03
0.47073D+03	0.30263D+03	0.30471D+03	0.24392D+03	0.19771D+03	0.17234D+03	0.15372D+03
0.46683D+03	0.30256D+03	0.30331D+03	0.26597D+03	0.21925D+03	0.19281D+03	0.17306D+03
0.46293D+03	0.30248D+03	0.30201D+03	0.28168D+03	0.23850D+03	0.21248D+03	0.19251D+03
0.45795D+03	0.30236D+03	0.30198D+03	0.29340D+03	0.25933D+03	0.23574D+03	0.21672D+03
0.45297D+03	0.30221D+03	0.30254D+03	0.29874D+03	0.27552D+03	0.25558D+03	0.23843D+03
0.44661D+03	0.30197D+03	0.30230D+03	0.30087D+03	0.28894D+03	0.27406D+03	0.25985D+03
0.44025D+03	0.30168D+03	0.30127D+03	0.30115D+03	0.29592D+03	0.28550D+03	0.27428D+03
0.43214D+03	0.30124D+03	0.30060D+03	0.30096D+03	0.29960D+03	0.29343D+03	0.28569D+03
0.42402D+03	0.30073D+03	0.30025D+03	0.30051D+03	0.30024D+03	0.29689D+03	0.29192D+03
0.41365D+03	0.29998D+03	0.29962D+03	0.29986D+03	0.29989D+03	0.29855D+03	0.29584D+03
0.40328D+03	0.29916D+03	0.29900D+03	0.29928D+03	0.29936D+03	0.29895D+03	0.29752D+03
0.39004D+03	0.29811D+03	0.29852D+03	0.29869D+03	0.29870D+03	0.29881D+03	0.29828D+03
0.37681D+03	0.29717D+03	0.29769D+03	0.29780D+03	0.29783D+03	0.29800D+03	0.29785D+03
0.35990D+03	0.29637D+03	0.29668D+03	0.29682D+03	0.29691D+03	0.29698D+03	0.29699D+03
0.34300D+03	0.29623D+03	0.29650D+03	0.29665D+03	0.29675D+03	0.29680D+03	0.29683D+03

[a]Temperatures are in degrees Celsius. The temperature profile at 572.83 s was used for the three subsequent time steps listed in Table 10.11.

Table A.1 (continued)

RADIAL COORDINATE r (mm)	TIME (s)					
	0.17000D+03	0.18000D+03	0.18500D+03	0.20000D+03	0.22000D+03	0.24000D+03
0.49060D+03	0.31145D+02	0.25704D+02	0.23775D+02	0.18849D+02	0.15765D+02	0.13408D+02
0.48946D+03	0.37782D+02	0.31912D+02	0.29793D+02	0.24537D+02	0.21049D+02	0.18425D+02
0.48830D+03	0.44464D+02	0.38163D+02	0.35853D+02	0.30266D+02	0.26370D+02	0.23478D+02
0.48683D+03	0.52962D+02	0.46113D+02	0.43560D+02	0.37552D+02	0.33139D+02	0.29905D+02
0.48527D+03	0.61446D+02	0.54051D+02	0.51256D+02	0.44830D+02	0.39899D+02	0.36326D+02
0.48349D+03	0.72277D+02	0.64186D+02	0.61085D+02	0.54126D+02	0.48534D+02	0.44530D+02
0.48162D+03	0.83063D+02	0.74289D+02	0.70890D+02	0.63405D+02	0.57154D+02	0.52726D+02
0.47923D+03	0.96603D+02	0.87070D+02	0.83342D+02	0.75220D+02	0.68135D+02	0.63191D+02
0.47684D+03	0.10959D+03	0.99594D+02	0.95660D+02	0.86964D+02	0.79074D+02	0.73662D+02
0.47378D+03	0.12536D+03	0.11517D+03	0.11114D+03	0.10178D+03	0.92921D+02	0.86973D+02
0.47073D+03	0.14052D+03	0.13037D+03	0.12631D+03	0.11633D+03	0.10657D+03	0.10013D+03
0.46683D+03	0.15950D+03	0.14936D+03	0.14525D+03	0.13439D+03	0.12361D+03	0.11654D+03
0.46293D+03	0.17855D+03	0.16798D+03	0.16362D+03	0.15174D+03	0.14008D+03	0.13236D+03
0.45795D+03	0.20234D+03	0.19078D+03	0.18592D+03	0.17268D+03	0.16009D+03	0.15149D+03
0.45297D+03	0.22405D+03	0.21169D+03	0.20634D+03	0.19208D+03	0.17874D+03	0.16927D+03
0.44661D+03	0.24661D+03	0.23442D+03	0.22887D+03	0.21435D+03	0.20024D+03	0.18980D+03
0.44025D+03	0.26309D+03	0.25222D+03	0.24700D+03	0.23327D+03	0.21888D+03	0.20788D+03
0.43214D+03	0.27726D+03	0.26855D+03	0.26419D+03	0.25221D+03	0.23851D+03	0.22760D+03
0.42402D+03	0.28598D+03	0.27945D+03	0.27612D+03	0.26627D+03	0.25400D+03	0.24388D+03
0.41365D+03	0.29231D+03	0.28807D+03	0.28592D+03	0.27876D+03	0.26874D+03	0.26025D+03
0.40328D+03	0.29556D+03	0.29294D+03	0.29160D+03	0.28575D+03	0.27902D+03	0.27246D+03
0.39004D+03	0.29744D+03	0.29606D+03	0.29523D+03	0.29251D+03	0.28742D+03	0.28326D+03
0.37681D+03	0.29752D+03	0.29691D+03	0.29647D+03	0.29502D+03	0.29228D+03	0.29000D+03
0.35990D+03	0.29694D+03	0.29689D+03	0.29682D+03	0.29624D+03	0.29549D+03	0.29466D+03
0.34300D+03	0.29683D+03	0.29687D+03	0.29686D+03	0.29641D+03	0.29599D+03	0.29540D+03

Table A.1 (continued)

RADIAL COORDINATE r (mm)	TIME (s)					
	0.26000D+03	0.28000D+03	0.31000D+03	0.34000D+03	0.34500D+03	0.35000D+03
0.49060D+03	0.12068D+02	0.11322D+02	0.99936D+01	0.90189D+01	0.88509D+01	0.85812D+01
0.48946D+03	0.16841D+02	0.15804D+02	0.14120D+02	0.12858D+02	0.12650D+02	0.12347D+02
0.48830D+03	0.21647D+02	0.20319D+02	0.18277D+02	0.16725D+02	0.16476D+02	0.16140D+02
0.48683D+03	0.27762D+02	0.26062D+02	0.23565D+02	0.21644D+02	0.21344D+02	0.20966D+02
0.48537D+03	0.33872D+02	0.31801D+02	0.28850D+02	0.26561D+02	0.26210D+02	0.25789D+02
0.48349D+03	0.41680D+02	0.39138D+02	0.35608D+02	0.32847D+02	0.32432D+02	0.31955D+02
0.48162D+03	0.49484D+02	0.46473D+02	0.42368D+02	0.39135D+02	0.38655D+02	0.38122D+02
0.47923D+03	0.59470D+02	0.55865D+02	0.51036D+02	0.47189D+02	0.46629D+02	0.460..D+02
0.47684D+03	0.69494D+02	0.65300D+02	0.59760D+02	0.55288D+02	0.54652D+02	0.53955D+02
0.47378D+03	0.82271D+02	0.77339D+02	0.70920D+02	0.65648D+02	0.64922D+02	0.64107D+02
0.47073D+03	0.94900D+02	0.89265D+02	0.82006D+02	0.75959D+02	0.75144D+02	0.74211D+02
0.46683D+03	0.11061D+03	0.10415D+03	0.95898D+02	0.88931D+02	0.88004D+02	0.86926D+02
0.46293D+03	0.12563D+03	0.11846D+03	0.10932D+03	0.10155D+03	0.10051D+03	0.99302D+02
0.45795D+03	0.14369D+03	0.13578D+03	0.12567D+03	0.11707D+03	0.11588D+03	0.11453D+03
0.45297D+03	0.16049D+03	0.15201D+03	0.14113D+03	0.13191D+03	0.13058D+03	0.12912D+03
0.44661D+03	0.18011D+03	0.17116D+03	0.15956D+03	0.14982D+03	0.14837D+03	0.14677D+03
0.44025D+03	0.19777D+03	0.18861D+03	0.17664D+03	0.16660D+03	0.16508D+03	0.16334D+03
0.43214D+03	0.21761D+03	0.20856D+03	0.19660D+03	0.18639D+03	0.18486D+03	0.18295D+03
0.42402D+03	0..3455D+03	0.22598D+03	0.21448D+03	0.20438D+03	0.20289D+03	0.20082D+03
0.41365D+03	0.25230D+03	0.24471D+03	0.23432D+03	0.22476D+03	0.22338D+03	0.22111D+03
0.40328D+03	0.26617D+03	0.25980D+03	0.25087D+03	0.24215D+03	0.24092D+03	0.23846D+03
0.39004D+03	0.27908D+03	0.27431D+03	0.26736D+03	0.25984D+03	0.25886D+03	0.25615D+03
0.37681D+03	0.28739D+03	0.28399D+03	0.27871D+03	0.27230D+03	0.27152D+03	0.26870D+03
0.35990D+03	0.29322D+03	0.29094D+03	0.28702D+03	0.28157D+03	0.28095D+03	0.27808D+03
0.34300D+03	0.29415D+03	0.29206D+03	0.28836D+03	0.28307D+03	0.28248D+03	0.27960D+03

Table A.1 (continued)

RADIAL COORDINATE r (mm)	TIME (s)			
	0.35500D+03	0.36000D+03	0.36500D+03	0.37000D+03
0.49060D+03	0.85024D+01	0.81536D+01	0.79810D+01	0.76770D+01
0.48946D+03	0.12215D+02	0.11848D+02	0.11623D+02	0.11294D+02
0.48830D+03	0.15954D+02	0.15570D+02	0.15291D+02	0.14937D+02
0.48683D+03	0.20711D+02	0.20305D+02	0.19958D+02	0.19573D+02
0.48537D+03	0.25465D+02	0.25037D+02	0.24623D+02	0.24206D+02
0.48349D+03	0.31544D+02	0.31087D+02	0.30587D+02	0.30129D+02
0.48162D+03	0.37623D+02	0.37138D+02	0.36553D+02	0.36054D+02
0.47923D+03	0.45412D+02	0.44888D+02	0.44197D+02	0.43645D+02
0.47684D+03	0.53250D+02	0.52682D+02	0.51888D+02	0.51280D+02
0.47378D+03	0.63287D+02	0.62653D+02	0.61734D+02	0.61053D+02
0.47073D+03	0.73287D+02	0.72573D+02	0.71544D+02	0.70788D+02
0.46683D+03	0.85880D+02	0.85048D+02	0.83905D+02	0.83056D+02
0.46293D+03	0.98145D+02	0.97174D+02	0.95957D+02	0.95022D+02
0.45795D+03	0.11324D+03	0.11208D+03	0.11082D+03	0.10978D+03
0.45297D+03	0.12769D+03	0.12636D+03	0.12507D+03	0.12394D+03
0.44661D+03	0.14517D+03	0.14369D+03	0.14234D+03	0.14110D+03
0.44025D+03	0.16157D+03	0.16000D+03	0.15855D+03	0.15722D+03
0.43214D+03	0.18097D+03	0.17929D+03	0.17768D+03	0.17631D+03
0.42402D+03	0.19868D+03	0.19691D+03	0.19518D+03	0.19380D+03
0.41365D+03	0.21884D+03	0.21697D+03	0.21520D+03	0.21383D+03
0.40328D+03	0.23610D+03	0.23415D+03	0.23240D+03	0.23107D+03
0.39004D+03	0.25366D+03	0.25161D+03	0.24986D+03	0.24867D+03
0.37681D+03	0.26604D+03	0.26386D+03	0.26212D+03	0.26100D+03
0.35990D+03	0.27525D+03	0.27295D+03	0.27124D+03	0.27012D+03
0.34300D+03	0.27675D+03	0.27443D+03	0.27271D+03	0.27160D+03

Table A.2. Experimental temperature profile set used for posttest elastic-plastic finite-element analysis of PTSE-2B[a]

RADIAL COORDINATE r (mm)	TIME (s)					
	0.15717D+03	0.15956D+03	0.16194D+03	0.16433D+03	0.16792D+03	0.17150D+03
0.49060D+03	0.27129D+03	0.21930D+03	0.16732D+03	0.11533D+03	0.10339D+03	0.91450D+02
0.48946D+03	0.27167D+03	0.22285D+03	0.17404D+03	0.12522D+03	0.11211D+03	0.98992D+02
0.48830D+03	0.27205D+03	0.22642D+03	0.18080D+03	0.13517D+03	0.12088D+03	0.10659D+03
0.48683D+03	0.27254D+03	0.23096D+03	0.18939D+03	0.14781D+03	0.13204D+03	0.11626D+03
0.48537D+03	0.27302D+03	0.23548D+03	0.19795D+03	0.16041D+03	0.14317D+03	0.12593D+03
0.48349D+03	0.27363D+03	0.24124D+03	0.20886D+03	0.17647D+03	0.15739D+03	0.13831D+03
0.48162D+03	0.27421D+03	0.24691D+03	0.21962D+03	0.19232D+03	0.17152D+03	0.15072D+03
0.47923D+03	0.27485D+03	0.25367D+03	0.23250D+03	0.21131D+03	0.18902D+03	0.16672D+03
0.47684D+03	0.27531D+03	0.25941D+03	0.24350D+03	0.22760D+03	0.20519D+03	0.18278D+03
0.47378D+03	0.27565D+03	0.26514D+03	0.25472D+03	0.24411D+03	0.22340D+03	0.20269D+03
0.47073D+03	0.27580D+03	0.26933D+03	0.26286D+03	0.25639D+03	0.23874D+03	0.22108D+03
0.46683D+03	0.27583D+03	0.27288D+03	0.26993D+03	0.26698D+03	0.25395D+03	0.24091D+03
0.46293D+03	0.27582D+03	0.27491D+03	0.27399D+03	0.27308D+03	0.26415D+03	0.25521D+03
0.45795D+03	0.27578D+03	0.27595D+03	0.27611D+03	0.27628D+03	0.27122D+03	0.26616D+03
0.45297D+03	0.27568D+03	0.27594D+03	0.27621D+03	0.27647D+03	0.27395D+03	0.27143D+03
0.44661D+03	0.27539D+03	0.27546D+03	0.27553D+03	0.27560D+03	0.27474D+03	0.27387D+03
0.44025D+03	0.27505D+03	0.27506D+03	0.27506D+03	0.27507D+03	0.27480D+03	0.27453D+03
0.43214D+03	0.27479D+03	0.27482D+03	0.27484D+03	0.27487D+03	0.27486D+03	0.27484D+03
0.42402D+03	0.27471D+03	0.27477D+03	0.27482D+03	0.27488D+03	0.27491D+03	0.27493D+03
0.41365D+03	0.27477D+03	0.27481D+03	0.27486D+03	0.27490D+03	0.27494D+03	0.27497D+03
0.40328D+03	0.27493D+03	0.27495D+03	0.27498D+03	0.27500D+03	0.27505D+03	0.27510D+03
0.39004D+03	0.27511D+03	0.27518D+03	0.27525D+03	0.27532D+03	0.27535D+03	0.27538D+03
0.37681D+03	0.27512D+03	0.27521D+03	0.27529D+03	0.27538D+03	0.27540D+03	0.27542D+03
0.35990D+03	0.27504D+03	0.27511D+03	0.27518D+03	0.27525D+03	0.27528D+03	0.27530D+03
0.34300D+03	0.27503D+03	0.27509D+03	0.27516D+03	0.27522D+03	0.27525D+03	0.27527D+03

[a]Temperatures are in degrees Celsius.

Table A.2 (continued)

RADIAL COORDINATE r (mm)	TIME (s)					
	0.17867D+03	0.18583D+03	0.19300D+03	0.20017D+03	0.21450D+03	0.22883D+03
0.49060D+03	0.75590D+02	0.64738D+02	0.57366D+02	0.51331D+02	0.37128D+02	0.26768D+02
0.48946D+03	0.82591D+02	0.71530D+02	0.63889D+02	0.57556D+02	0.43066D+02	0.32407D+02
0.48830D+03	0.89641D+02	0.78371D+02	0.70457D+02	0.63825D+02	0.49045D+02	0.38087D+02
0.48683D+03	0.98611D+02	0.87071D+02	0.78812D+02	0.71798D+02	0.56650D+02	0.45310D+02
0.48537D+03	0.10757D+03	0.95764D+02	0.87157D+02	0.79763D+02	0.64246D+02	0.52525D+02
0.48349D+03	0.11903D+03	0.10687D+03	0.97818D+02	0.89937D+02	0.73947D+02	0.61739D+02
0.48162D+03	0.13049D+03	0.11797D+03	0.10846D+03	0.10009D+03	0.83628D+02	0.70935D+02
0.47923D+03	0.14522D+03	0.13217D+03	0.12202D+03	0.11303D+03	0.95933D+02	0.82630D+02
0.47684D+03	0.16011D+03	0.14642D+03	0.13549D+03	0.12588D+03	0.10812D+03	0.94229D+02
0.47378D+03	0.17893D+03	0.16439D+03	0.15234D+03	0.14198D+03	0.12337D+03	0.10880D+03
0.47073D+03	0.19687D+03	0.18160D+03	0.16850D+03	0.15750D+03	0.13817D+03	0.12302D+03
0.46683D+03	0.21735D+03	0.20166D+03	0.18765D+03	0.17613D+03	0.15620D+03	0.14048D+03
0.46293D+03	0.23394D+03	0.21869D+03	0.20461D+03	0.19301D+03	0.17302D+03	0.15699D+03
0.45795D+03	0.24950D+03	0.23593D+03	0.22287D+03	0.21178D+03	0.19245D+03	0.17642D+03
0.45297D+03	0.25993D+03	0.24877D+03	0.23748D+03	0.22738D+03	0.20934D+03	0.19373D+03
0.44661D+03	0.26773D+03	0.25982D+03	0.25118D+03	0.24276D+03	0.22689D+03	0.21242D+03
0.44025D+03	0.27168D+03	0.26654D+03	0.26031D+03	0.25367D+03	0.24024D+03	0.22737D+03
0.43214D+03	0.27398D+03	0.27127D+03	0.26742D+03	0.26275D+03	0.25242D+03	0.24182D+03
0.42402D+03	0.27471D+03	0.27344D+03	0.27121D+03	0.26810D+03	0.26055D+03	0.25220D+03
0.41365D+03	0.27497D+03	0.27459D+03	0.27359D+03	0.27183D+03	0.26705D+03	0.26115D+03
0.40328D+03	0.27516D+03	0.27509D+03	0.27464D+03	0.27368D+03	0.27082D+03	0.26686D+03
0.39004D+03	0.27548D+03	0.27550D+03	0.27525D+03	0.27482D+03	0.27345D+03	0.27127D+03
0.37681D+03	0.27552D+03	0.27557D+03	0.27543D+03	0.27527D+03	0.27473D+03	0.27373D+03
0.35990D+03	0.27540D+03	0.27547D+03	0.27544D+03	0.27544D+03	0.27545D+03	0.27532D+03
0.34300D+03	0.27538D+03	0.27545D+03	0.27544D+03	0.27546D+03	0.27556D+03	0.27556D+03

Table A.2 (continued)

RADIAL COORDINATE r (mm)	TIME (s)					
	0.24317D+03	0.27183D+03	0.30050D+03	0.32916D+03	0.35066D+03	0.36500D+03
0.49060D+03	0.21091D+02	0.14813D+02	0.11320D+02	0.90769D+01	0.78018D+01	0.72545D+01
0.48946D+03	0.26485D+02	0.19653D+02	0.15730D+02	0.13131D+02	0.11656D+02	0.10963D+02
0.48830D+03	0.31917D+02	0.24527D+02	0.20172D+02	0.17215D+02	0.15537D+02	0.14698D+02
0.48683D+03	0.38825D+02	0.30727D+02	0.25822D+02	0.22410D+02	0.20476D+02	0.19450D+02
0.48537D+03	0.45726D+02	0.36921D+02	0.31467D+02	0.27601D+02	0.25411D+02	0.24199D+02
0.48349D+03	0.54541D+02	0.44833D+02	0.38681D+02	0.34236D+02	0.31719D+02	0.30270D+02
0.48162D+03	0.63339D+02	0.52735D+02	0.45888D+02	0.40868D+02	0.38027D+02	0.36341D+02
0.47923D+03	0.74542D+02	0.62808D+02	0.55089D+02	0.49345D+02	0.46094D+02	0.44107D+02
0.47684D+03	0.85679D+02	0.72851D+02	0.64281D+02	0.57837D+02	0.54180D+02	0.51898D+02
0.47378D+03	0.99709D+02	0.85556D+02	0.75940D+02	0.68643D+02	0.64478D+02	0.61833D+02
0.47073D+03	0.11342D+03	0.98038D+02	0.87433D+02	0.79332D+02	0.74670D+02	0.71683D+02
0.46683D+03	0.13026D+03	0.11351D+03	0.10173D+03	0.92678D+02	0.87401D+02	0.84017D+02
0.46293D+03	0.14618D+03	0.12829D+03	0.11546D+03	0.10554D+03	0.99677D+02	0.95949D+02
0.45795D+03	0.16493D+03	0.14599D+03	0.13204D+03	0.12117D+03	0.11463D+03	0.11054D+03
0.45297D+03	0.18181D+03	0.16228D+03	0.14751D+03	0.13591D+03	0.12880D+03	0.12443D+03
0.44661D+03	0.20046D+03	0.18088D+03	0.16554D+03	0.15338D+03	0.14579D+03	0.14118D+03
0.44025D+03	0.21598D+03	0.19705D+03	0.18174D+03	0.16941D+03	0.16160D+03	0.15685D+03
0.43214D+03	0.23183D+03	0.21451D+03	0.19996D+03	0.18791D+03	0.18011D+03	0.17533D+03
0.42402D+03	0.24394D+03	0.22878D+03	0.21559D+03	0.20427D+03	0.19677D+03	0.19207D+03
0.41365D+03	0.25508D+03	0.24306D+03	0.23207D+03	0.22216D+03	0.21539D+03	0.21093D+03
0.40328D+03	0.26267D+03	0.25377D+03	0.24514D+03	0.23690D+03	0.23107D+03	0.22696D+03
0.39004D+03	0.26891D+03	0.26346D+03	0.25766D+03	0.25150D+03	0.24688D+03	0.24332D+03
0.37681D+03	0.27265D+03	0.26977D+03	0.26614D+03	0.26171D+03	0.25805D+03	0.25498D+03
0.35990D+03	0.27521D+03	0.27430D+03	0.27236D+03	0.26931D+03	0.26640D+03	0.26376D+03
0.34300D+03	0.27561D+03	0.27503D+03	0.27336D+03	0.27055D+03	0.26776D+03	0.26519D+03

Table A.2 (continued)

RADIAL COORDINATE r (mm)	TIME (s)					
	0.38650D+03	0.40083D+03	0.45100D+03	0.50116D+03	0.55133D+03	0.57283D+03
0.49060D+03	0.65668D+01	0.60037D+01	0.49145D+01	0.40236D+01	0.37404D+01	0.36474D+01
0.48946D+03	0.10080D+02	0.94230D+01	0.79788D+01	0.68255D+01	0.63155D+01	0.61301D+01
0.48830D+03	0.13618D+02	0.12867D+02	0.11065D+02	0.96475D+01	0.89092D+01	0.86307D+01
0.48683D+03	0.18120D+02	0.17249D+02	0.14992D+02	0.13238D+02	0.12209D+02	0.11813D+02
0.48537D+03	0.22619D+02	0.21629D+02	0.18918D+02	0.16827D+02	0.15508D+02	0.14993D+02
0.48349D+03	0.28372D+02	0.27230D+02	0.23938D+02	0.21417D+02	0.19727D+02	0.19061D+02
0.48162D+03	0.34125D+02	0.32833D+02	0.28959D+02	0.26007D+02	0.23945D+02	0.23130D+02
0.47923D+03	0.41488D+02	0.40008D+02	0.35385D+02	0.31876D+02	0.29337D+02	0.28334D+02
0.47684D+03	0.48876D+02	0.47213D+02	0.41833D+02	0.37764D+02	0.34743D+02	0.33556D+02
0.47378D+03	0.58307D+02	0.56412D+02	0.50075D+02	0.45295D+02	0.41655D+02	0.40241D+02
0.47073D+03	0.67675D+02	0.65546D+02	0.58292D+02	0.52822D+02	0.48566D+02	0.46929D+02
0.46683D+03	0.79446D+02	0.77012D+02	0.68689D+02	0.62391D+02	0.57367D+02	0.55447D+02
0.46293D+03	0.90897D+02	0.88140D+02	0.78915D+02	0.71874D+02	0.66114D+02	0.63910D+02
0.45795D+03	0.10500D+03	0.10183D+03	0.91687D+02	0.83812D+02	0.77179D+02	0.74616D+02
0.45297D+03	0.11852D+03	0.11500D+03	0.10414D+03	0.95531D+02	0.88107D+02	0.85206D+02
0.44661D+03	0.13498D+03	0.13115D+03	0.11956D+03	0.11011D+03	0.10181D+03	0.98535D+02
0.44025D+03	0.15048D+03	0.14648D+03	0.13437D+03	0.12419D+03	0.11518D+03	0.11157D+03
0.43214D+03	0.16883D+03	0.16473D+03	0.15220D+03	0.14132D+03	0.13159D+03	0.12759D+03
0.42402D+03	0.18560D+03	0.18153D+03	0.16879D+03	0.15739D+03	0.14706D+03	0.14271D+03
0.41365D+03	0.20476D+03	0.20085D+03	0.18809D+03	0.17616D+03	0.16512D+03	0.16039D+03
0.40328D+03	0.22128D+03	0.21761D+03	0.20504D+03	0.19274D+03	0.18107D+03	0.17600D+03
0.39004D+03	0.23831D+03	0.23498D+03	0.22287D+03	0.21033D+03	0.19805D+03	0.19258D+03
0.37681D+03	0.25061D+03	0.24755D+03	0.23605D+03	0.22355D+03	0.21095D+03	0.20507D+03
0.35990D+03	0.25993D+03	0.25710D+03	0.24620D+03	0.23384D+03	0.22107D+03	0.21482D+03
0.34300D+03	0.26145D+03	0.25866D+03	0.24786D+03	0.23553D+03	0.22273D+03	0.21642D+03

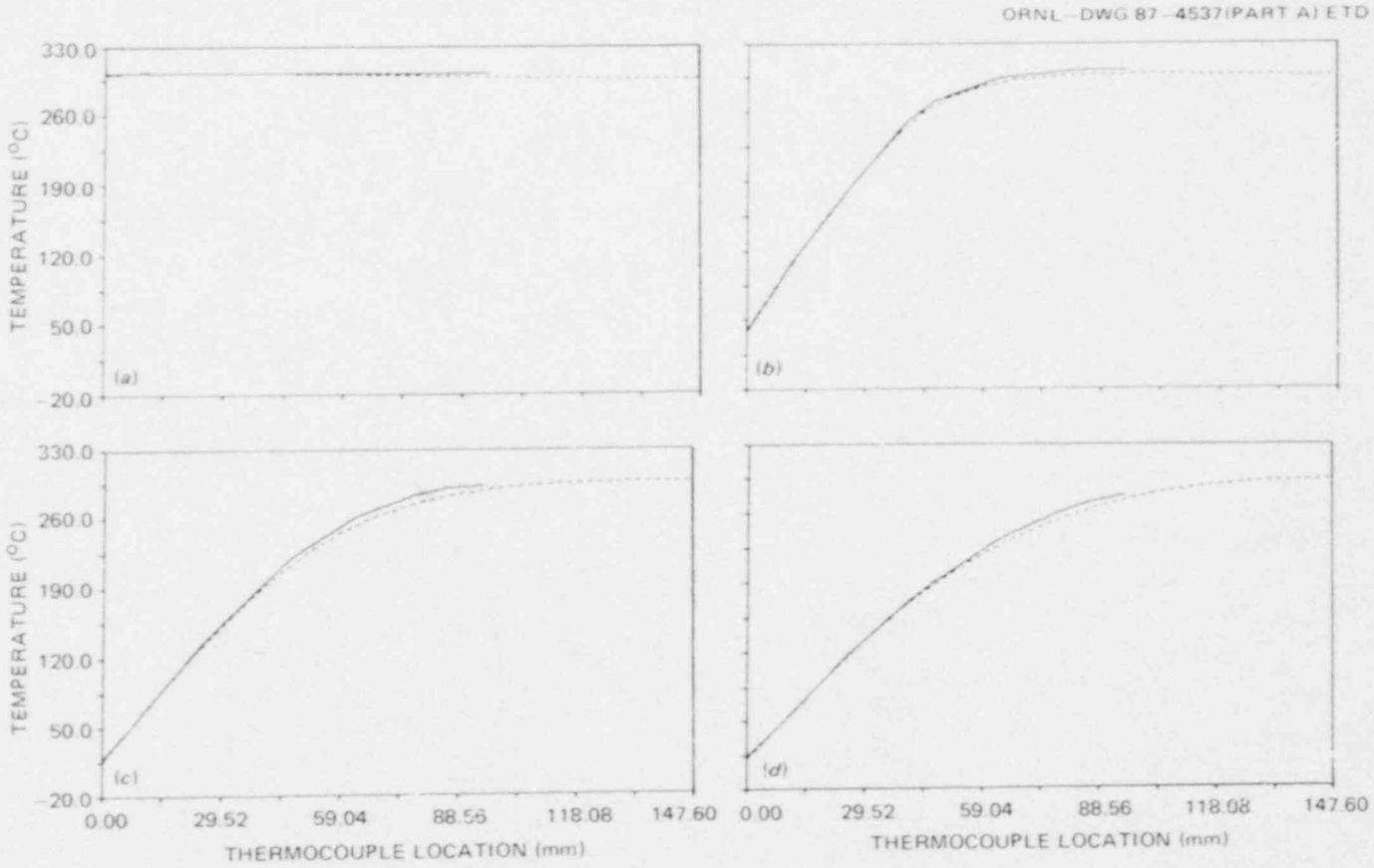

Fig. A.1. Temperature profiles at seven times in transient PTSE-2A. The solid curves represent temperatures at actual thimble thermocouple positions. The dashed curves are the mapped temperature-location points (see Chap. 8). (*a*) 110 s, (*b*) 160 s, (*c*) 210 s, (*d*) 260 s, (*e*) 310 s, (*f*) 360 s, and (*g*) 410 s.

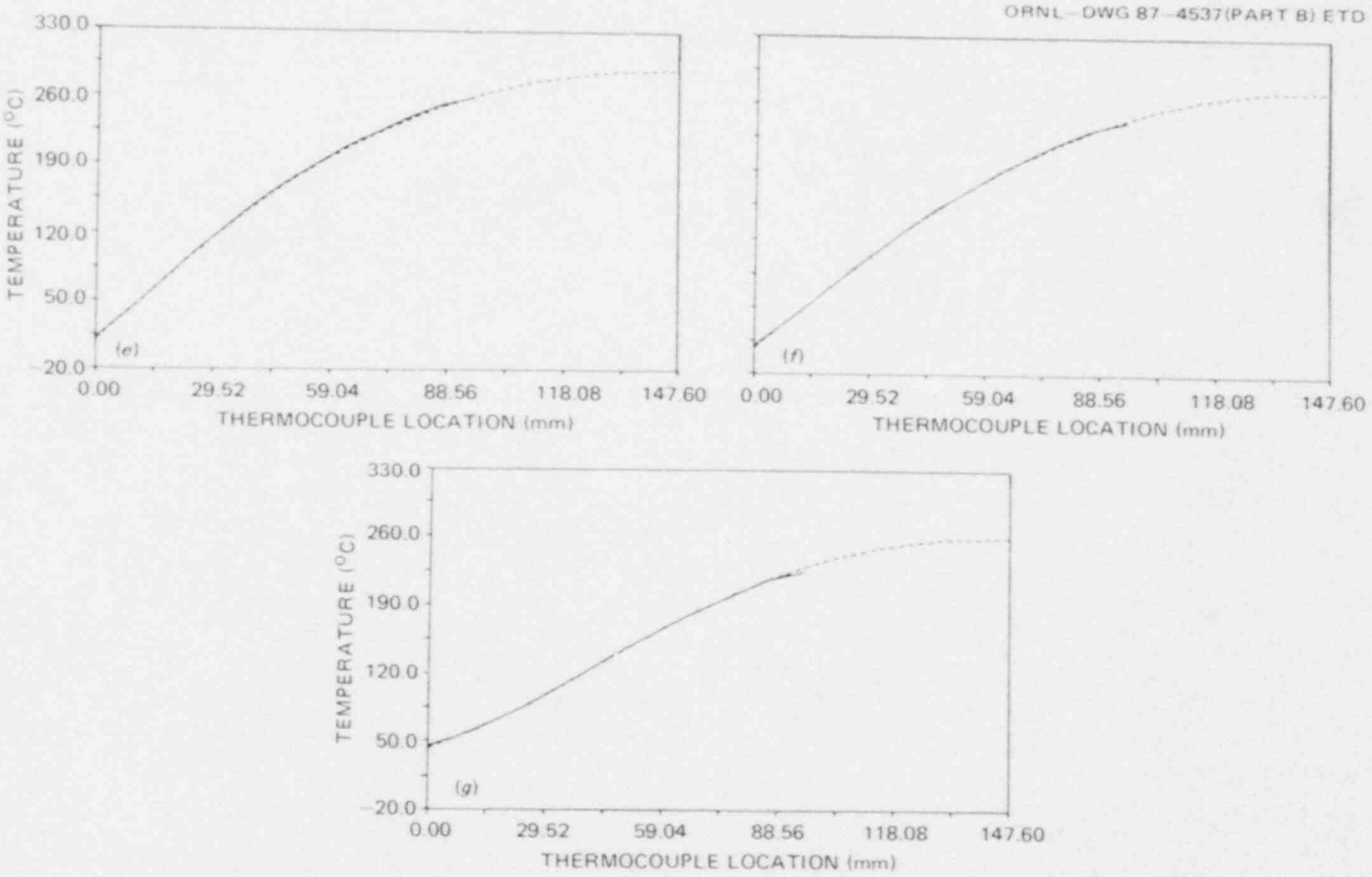

Fig. A.1 (continued)

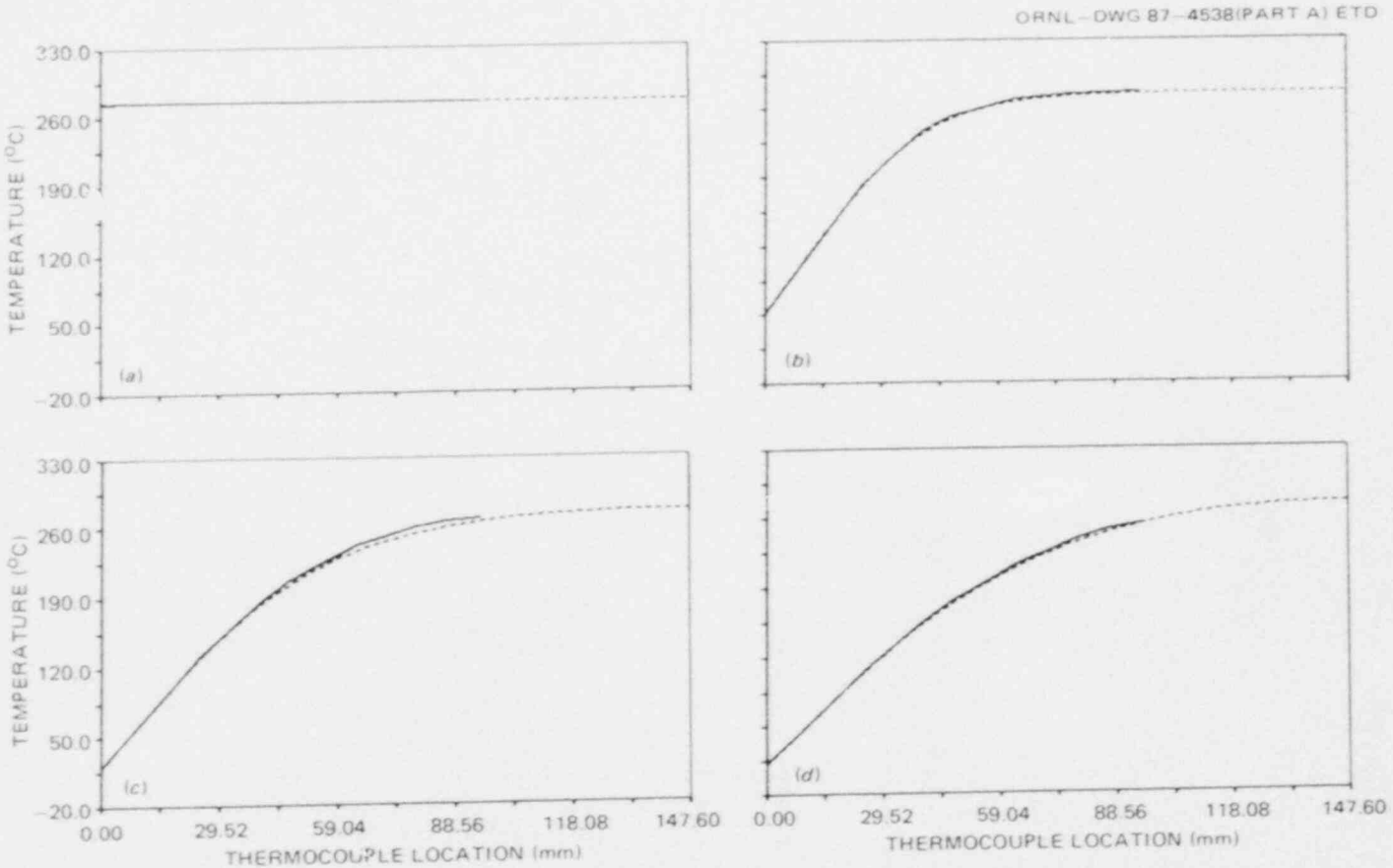

Fig. A.2. Temperature profiles at ten times in transient PTSE-2B. The solid and dashed curves are defined in Fig. A.1. (*a*) 150 s, (*b*) 200 s, (*c*) 250 s, (*d*) 300 s, (*e*) 350 s, (*f*) 400 s, (*g*) 450 s (*h*) 500 s, (*i*) 550 s, and (*j*) 600 s.

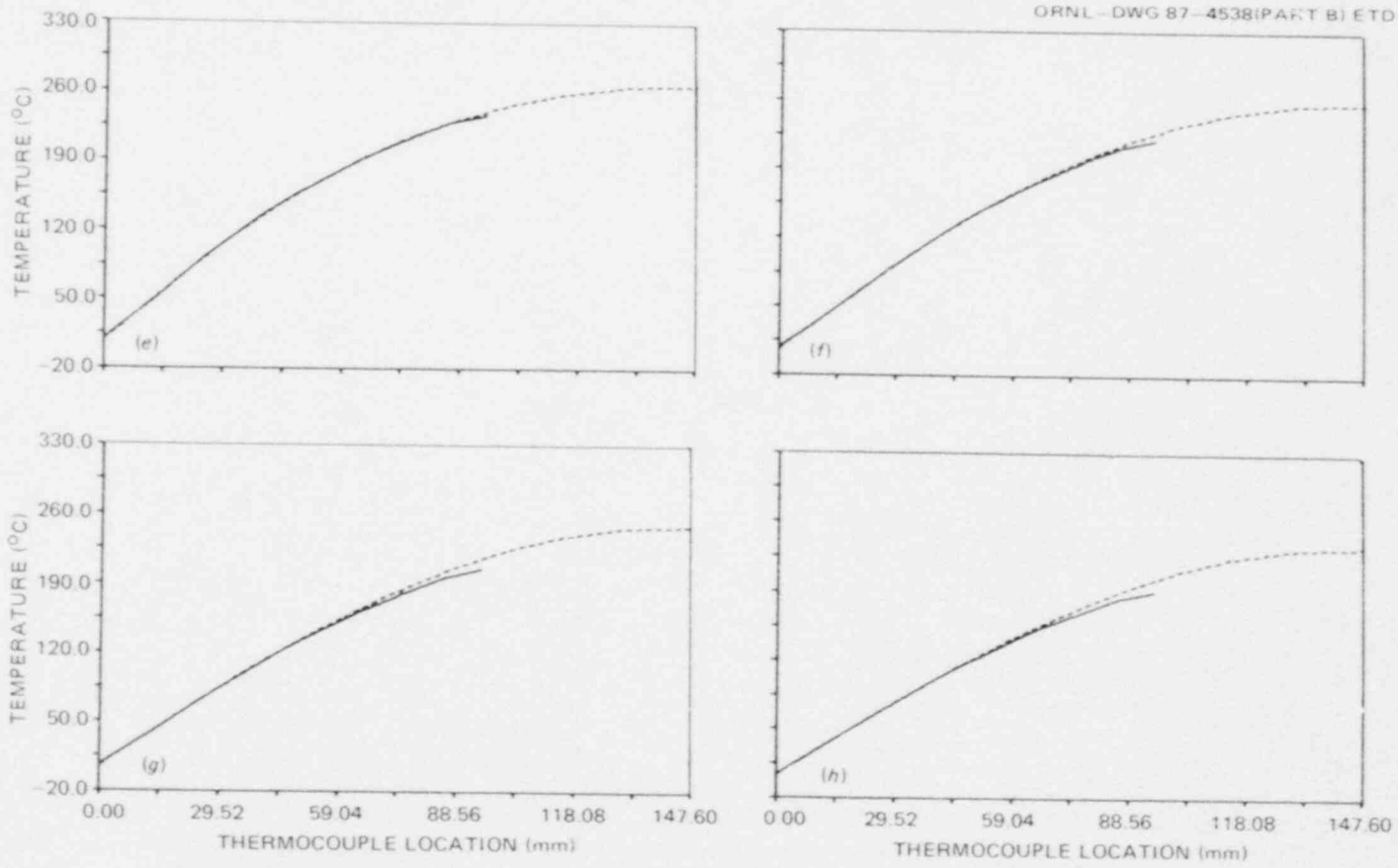

Fig. A.2 (continued)

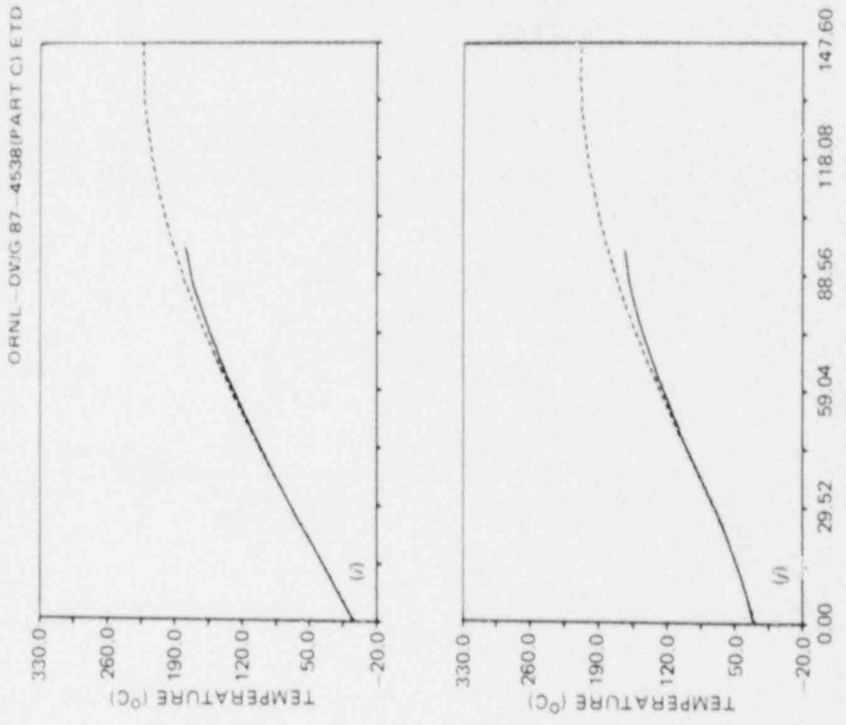

Fig. A.2 (continued)

APPENDIX B

TEMPERATURE, PRESSURE, CMOD, AND STRAIN DATA FOR PTSE-2

Computer-generated plots of data vs time for the two transients, PTSE-2A and -2B, are presented in this appendix. Temperature values are the raw data recorded by the primary data acquisition system. See Chap. 8 for discussion of adjustments.

For each transient the following data are presented in the order listed:

Temperature

TE5-1 and TE18

Pressure

PE97 and PE98

CMOD

YE51, YE54, and YE79 to YE88

Dummy CMOD

YE50 and YE56

Strain

XE48, XE52, XE53, and XE55

Each plot identifies the transient, the data tape, and the sensor and gives a brief description of the sensor. Gages XE53 and XE55 were not operative during the PTSE-2B transient. A discussion of instrumentation is in Chap. 6. Locations of thermocouples are given in Table 6.2 and Figs. 6.1 and 6.2. Locations of CMOD and strain gages are shown in Fig. 6.3.

Sensors are generally identified by a symbol consisting of a two-letter prefix and a numeral. The first letter identifies the type of measurement, the second identifies a circuit component, and the numeral uniquely identifies the sensor.

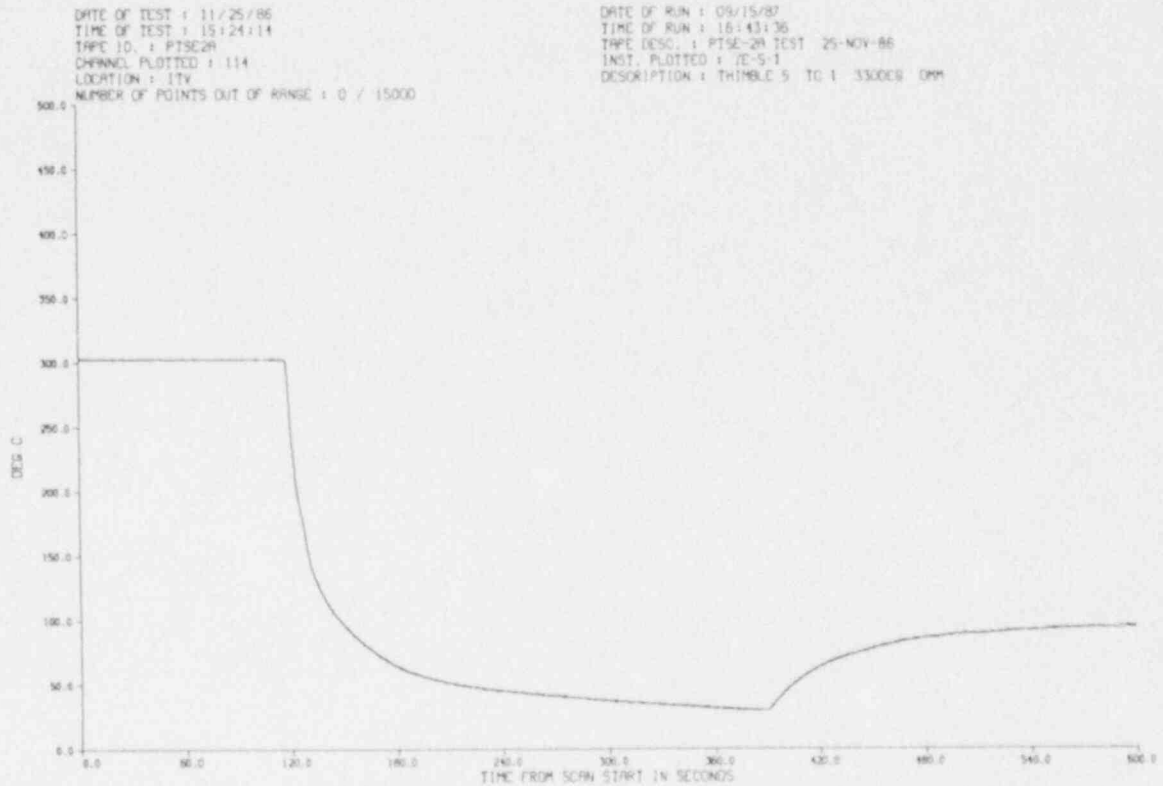
DATE OF TEST : 11/25/86
TIME OF TEST : 15:24:14
TAPE ID. : PTSE2A
CHANNEL PLOTTED : 114
LOCATION : ITV
NUMBER OF POINTS OUT OF RANGE : 0 / 15000
DATE OF RUN : 09/15/87
TIME OF RUN : 16:43:36
TAPE DESC. : PTSE-2A TEST 25-NOV-86
INST. PLOTTED : /E-5-1
DESCRIPTION : THIMBLE 5 TC 1 3300CB DMM
DEG C
TIME FROM SCAN START IN SECONDS


DATE OF TEST : 11/25/86
TIME OF TEST : 15:24:14
TAPE ID. : PTSE2A
CHANNEL PLOTTED : 147
LOCATION : ITV
NUMBER OF POINTS OUT OF RANGE : 0 / 15000
DATE OF RUN : 09/17/87
TIME OF RUN : 9:42:59
TAPE DESC. : PTSE-2A TEST 25-NOV-86
INST. PLOTTED : TE-18
DESCRIPTION : ITV INSIDE TEMP 90DEG 300MM
DEG C
TIME FROM SCAN START IN SECONDS

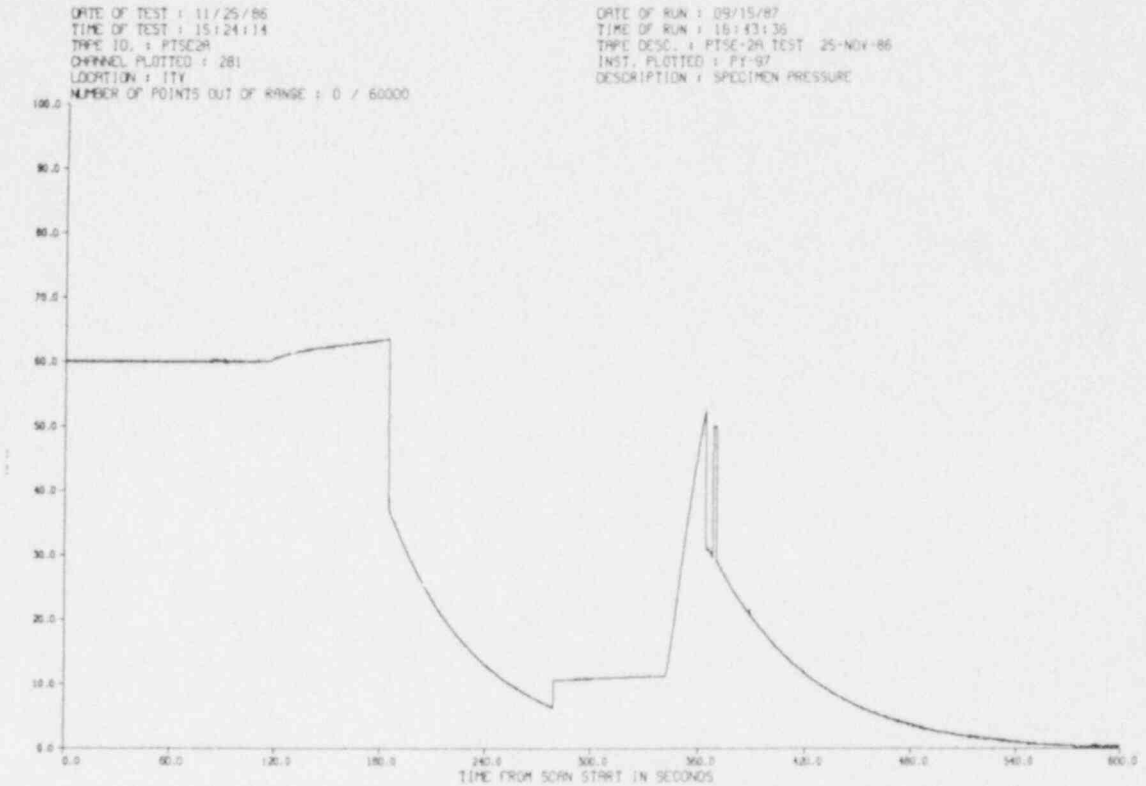
DATE OF TEST : 11/25/86
TIME OF TEST : 15:24:14
TAPE ID. : PTSE2A
CHANNEL PLOTTED : 281
LOCATION : ITV
NUMBER OF POINTS OUT OF RANGE : 0 / 60000
DATE OF RUN : 09/15/87
TIME OF RUN : 16:43:36
TAPE DESC. : PTSE-2A TEST 25-NOV-86
INST. PLOTTED : Py-97
DESCRIPTION : SPECIMEN PRESSURE
100.0
90.0
80.0
70.0
60.0
50.0
40.0
30.0
20.0
10.0
0.0
0.0
60.0
120.0
180.0
240.0
300.0
360.0
420.0
480.0
540.0
600.0
TIME FROM SCAN START IN SECONDS

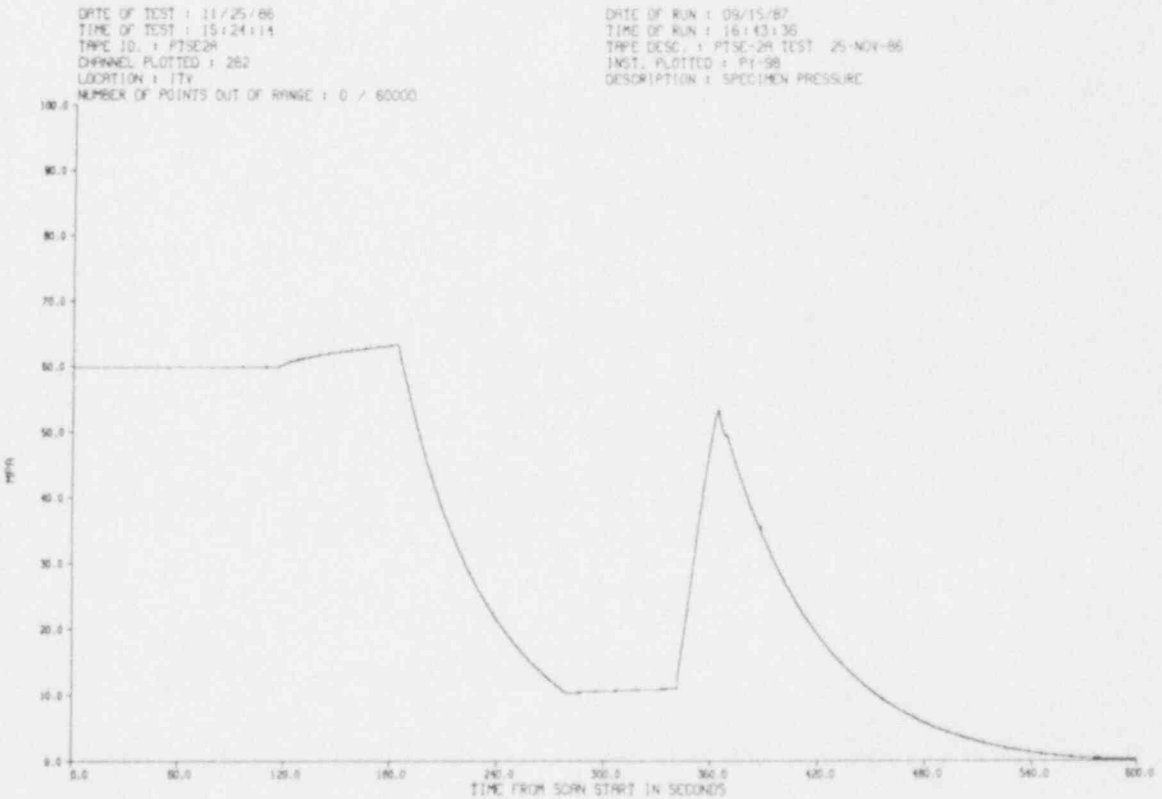
DATE OF TEST : 11/25/86
TIME OF TEST : 15:24:14
TAPE ID. : PTSE2A
CHANNEL PLOTTED : 282
LOCATION : ITV
NUMBER OF POINTS OUT OF RANGE : 0 / 60000
DATE OF RUN : 09/15/87
TIME OF RUN : 16:43:36
TAPE DESC. : PTSE-2A TEST 25-NOV-86
INST. PLOTTED : Py-98
DESCRIPTION : SPECIMEN PRESSURE
MPA
100.0
90.0
80.0
70.0
60.0
50.0
40.0
30.0
20.0
10.0
0.0
0.0
60.0
120.0
180.0
240.0
300.0
360.0
420.0
480.0
540.0
600.0
TIME FROM SCAN START IN SECONDS

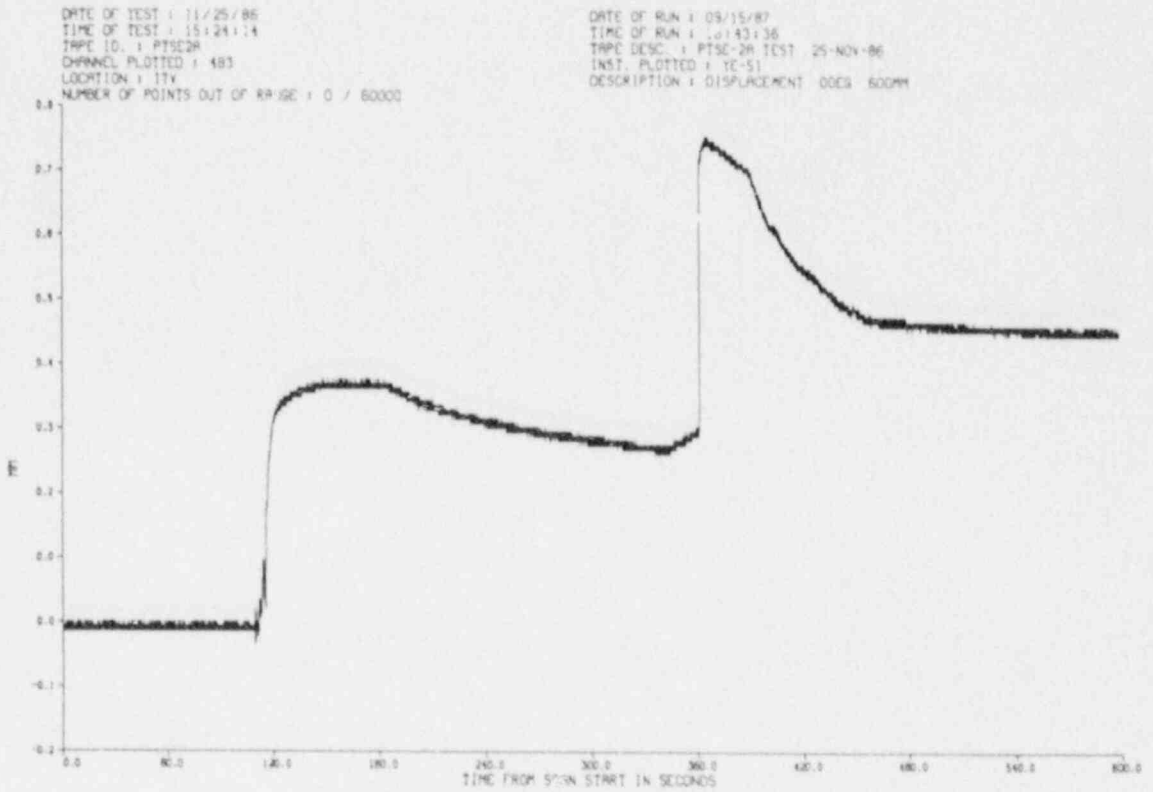
DATE OF TEST : 11/25/86
TIME OF TEST : 15:24:14
TAPE ID. : PTSC2A
CHANNEL PLOTTED : 483
LOCATION : ITV
NUMBER OF POINTS OUT OF RANGE : 0 / 60000
DATE OF RUN : 09/15/87
TIME OF RUN : 16:43:36
TAPE DESC. : PTSC-2A TEST 25-NOV-86
INST. PLOTTED : YE-51
DESCRIPTION : DISPLACEMENT 000S 600MM
E
TIME FROM SCAN START IN SECONDS

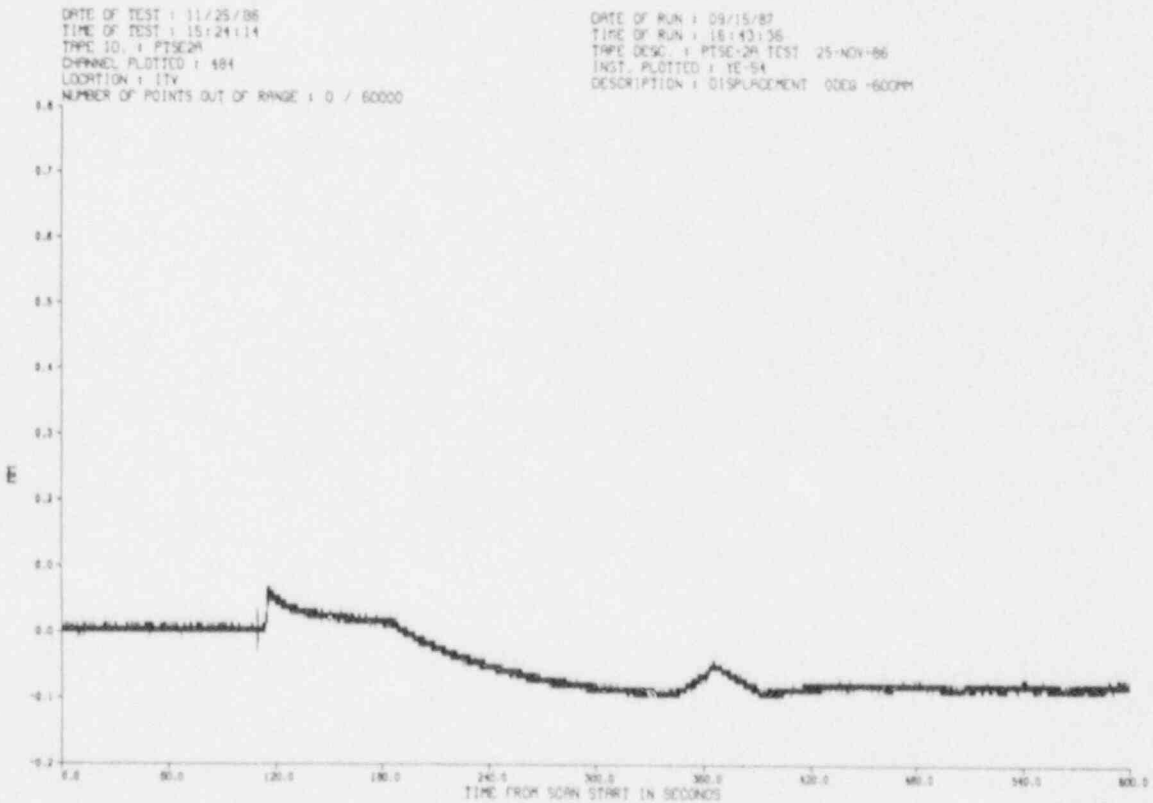
DATE OF TEST : 11/25/86
TIME OF TEST : 15:24:14
TAPE ID. : PTSC2A
CHANNEL PLOTTED : 484
LOCATION : ITV
NUMBER OF POINTS OUT OF RANGE : 0 / 60000
DATE OF RUN : 09/15/87
TIME OF RUN : 16:43:36
TAPE DESC. : PTSC-2A TEST 25-NOV-86
INST. PLOTTED : YE-54
DESCRIPTION : DISPLACEMENT 000S -600MM
E
TIME FROM SCAN START IN SECONDS

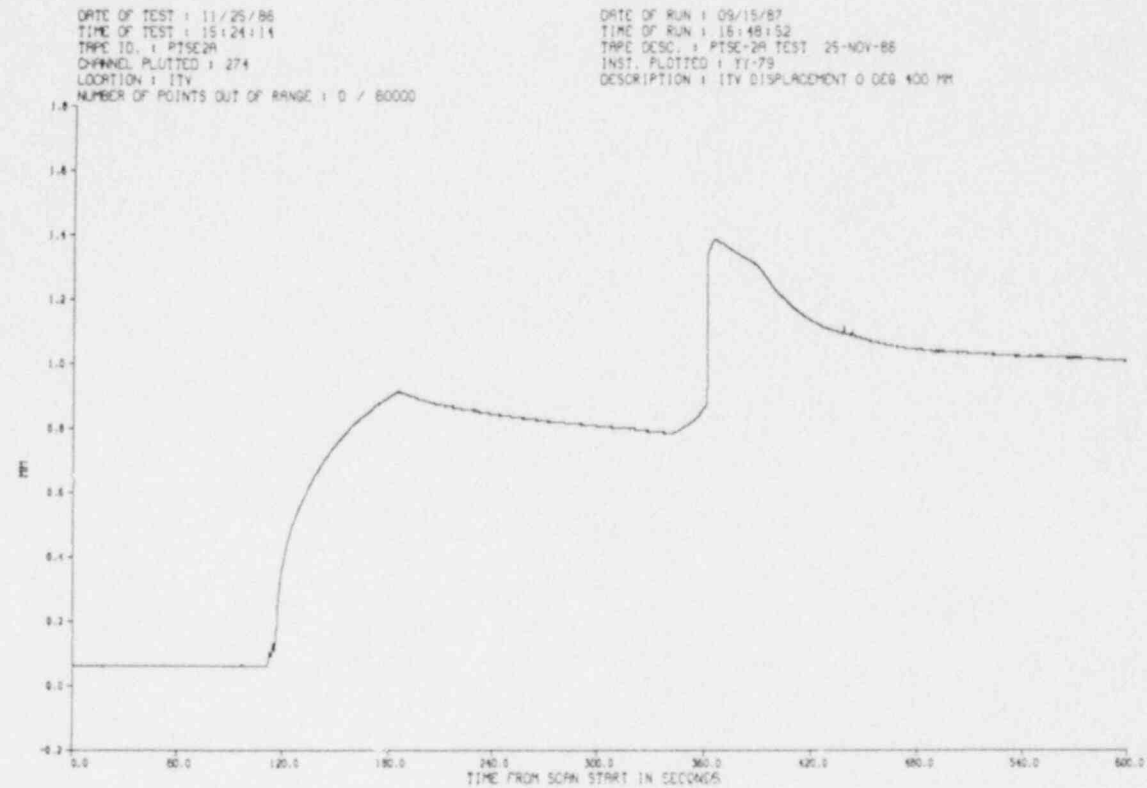
DATE OF TEST : 11/25/86
TIME OF TEST : 15:24:14
TAPE ID. : PTSE2A
CHANNEL PLOTTED : 274
LOCATION : ITV
NUMBER OF POINTS OUT OF RANGE : 0 / 60000
DATE OF RUN : 09/15/87
TIME OF RUN : 16:48:52
TAPE DESC. : PTSE-2A TEST 25-NOV-86
INST. PLOTTED : YY-79
DESCRIPTION : ITV DISPLACEMENT 0 DEG 400 MM
E
1.8
1.6
1.4
1.2
1.0
0.8
0.6
0.4
0.2
0.0
-0.2
0.0
60.0
120.0
180.0
240.0
300.0
360.0
420.0
480.0
540.0
600.0
TIME FROM SCAN START IN SECONDS

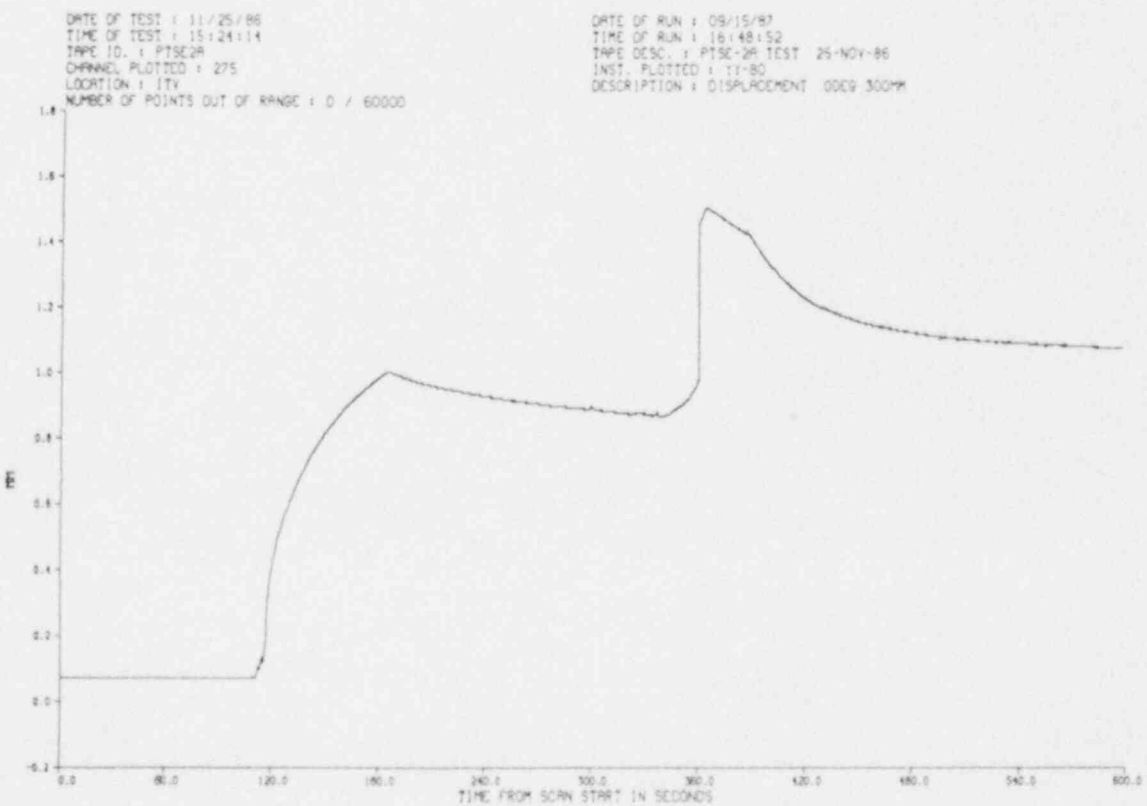
DATE OF TEST : 11/25/86
TIME OF TEST : 15:24:14
TAPE ID. : PTSE2A
CHANNEL PLOTTED : 275
LOCATION : ITV
NUMBER OF POINTS OUT OF RANGE : 0 / 60000
DATE OF RUN : 09/15/87
TIME OF RUN : 16:48:52
TAPE DESC. : PTSE-2A TEST 25-NOV-86
INST. PLOTTED : YY-80
DESCRIPTION : DISPLACEMENT 00EG 300MM
E
1.8
1.6
1.4
1.2
1.0
0.8
0.6
0.4
0.2
0.0
-0.2
0.0
60.0
120.0
180.0
240.0
300.0
360.0
420.0
480.0
540.0
600.0
TIME FROM SCAN START IN SECONDS

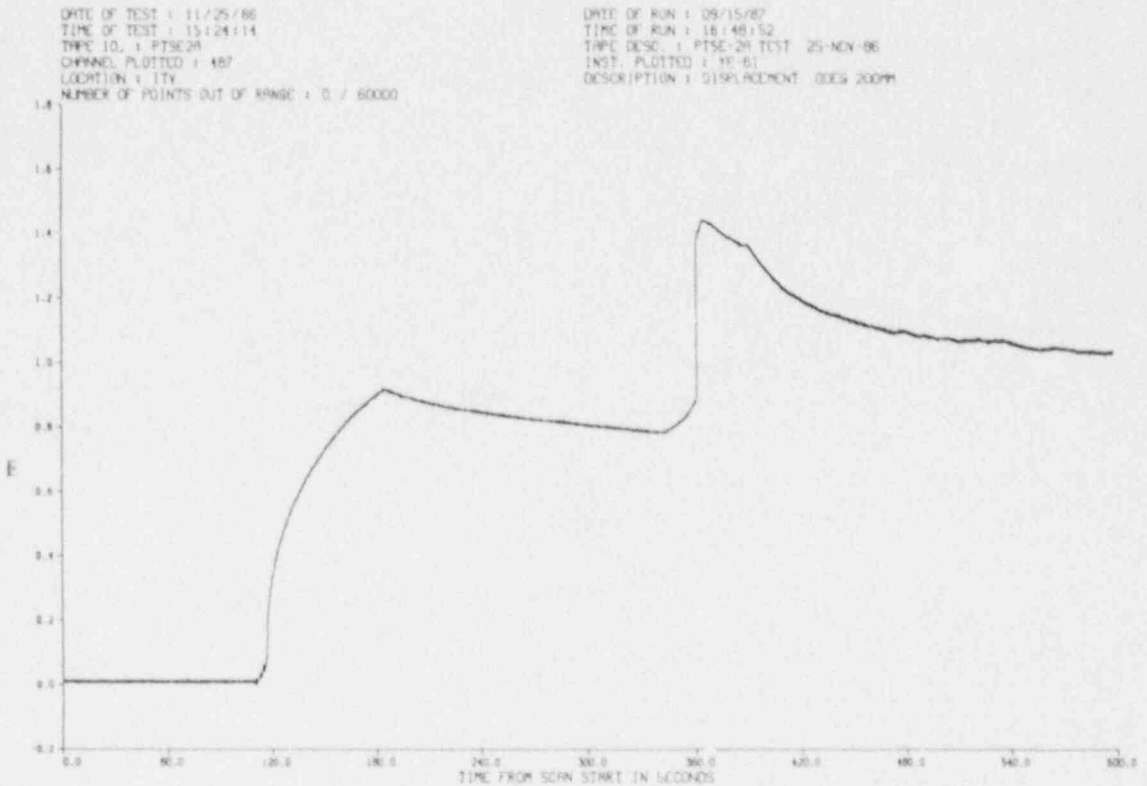
DATE OF TEST : 11/25/86
TIME OF TEST : 15:24:14
TAPE ID. : PTSC2A
CHANNEL PLOTTED : 487
LOCATION : ITV
NUMBER OF POINTS OUT OF RANGE : 0 / 60000
DATE OF RUN : 09/15/87
TIME OF RUN : 16:48:52
TAPE DESC. : PTSE-2A TEST 25-NOV-86
INST. PLOTTED : YY-61
DESCRIPTION : DISPLACEMENT .00EG 200MM
E
TIME FROM SCAN START IN SECONDS

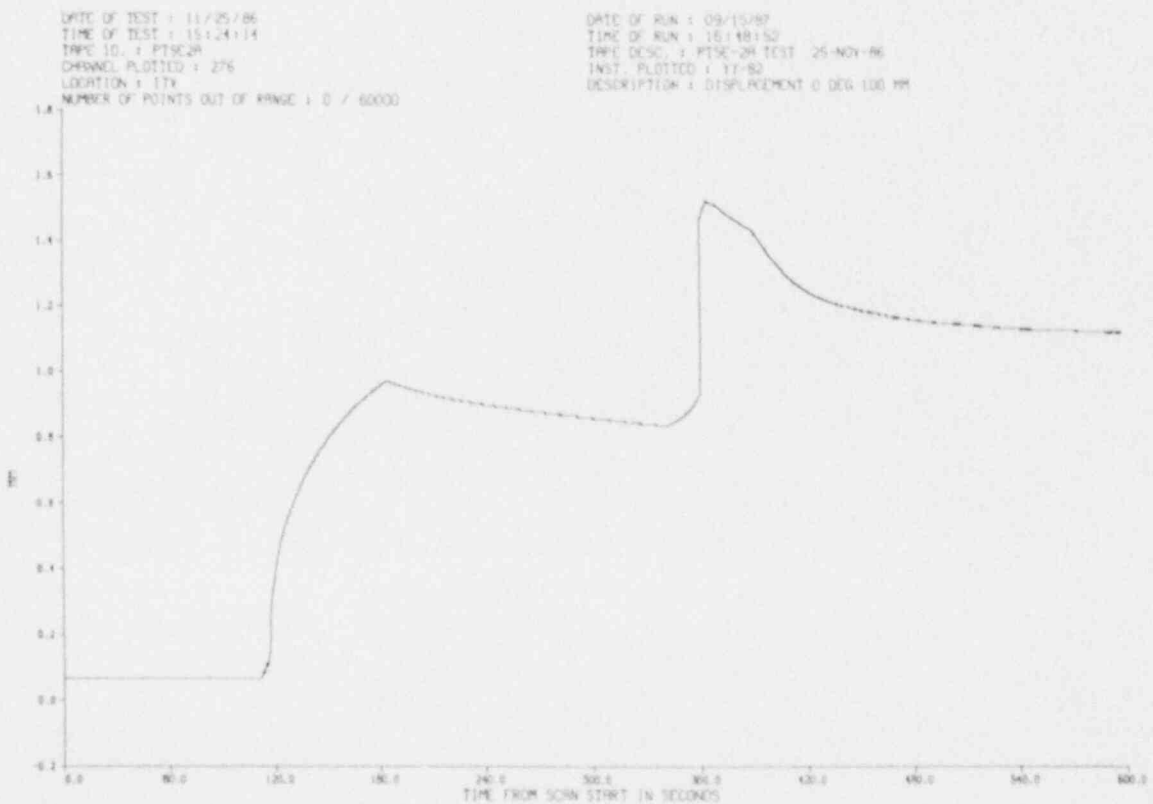
DATE OF TEST : 11/25/86
TIME OF TEST : 15:24:14
TAPE ID. : PTSC2A
CHANNEL PLOTTED : 276
LOCATION : ITV
NUMBER OF POINTS OUT OF RANGE : 0 / 60000
DATE OF RUN : 09/15/87
TIME OF RUN : 16:48:52
TAPE DESC. : PTSE-2A TEST 25-NOV-86
INST. PLOTTED : YY-82
DESCRIPTION : DISPLACEMENT 0 DEG 100 MM
E
TIME FROM SCAN START IN SECONDS

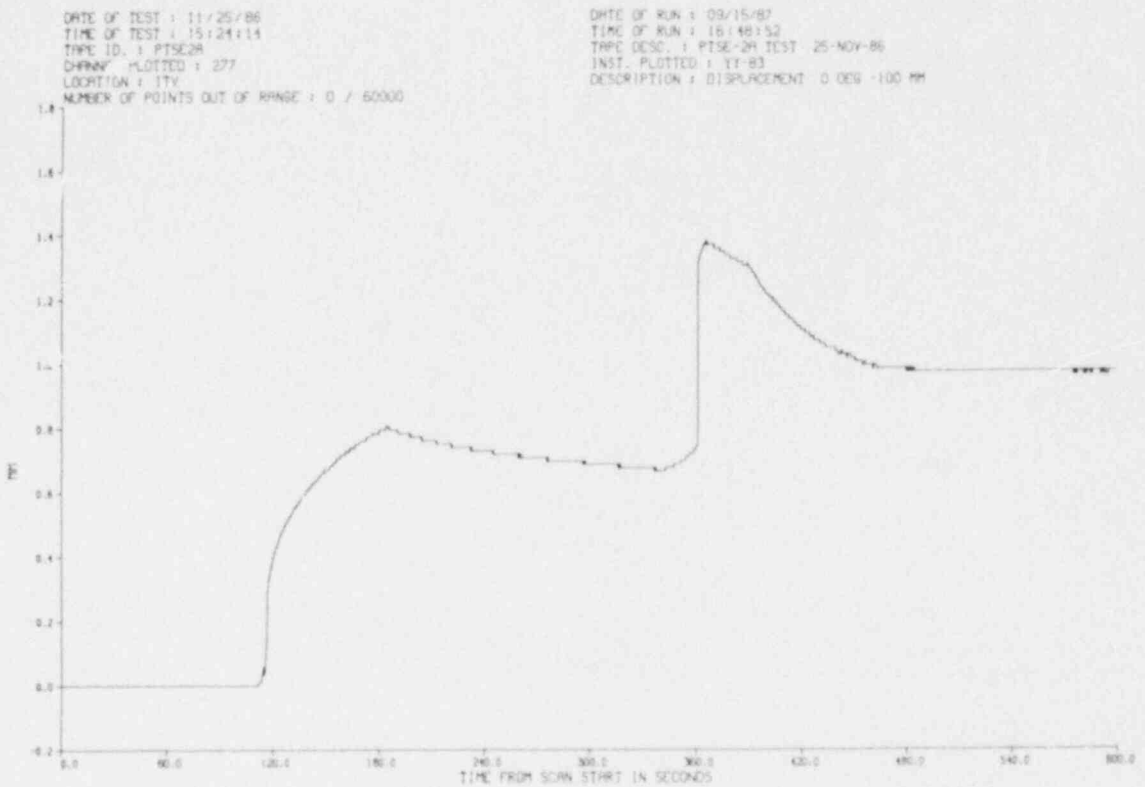
DATE OF TEST : 11/25/86
TIME OF TEST : 15:24:14
TAPE ID. : PTSE2A
CHANNEL PLOTTED : 277
LOCATION : ITV
NUMBER OF POINTS OUT OF RANGE : 0 / 60000
DATE OF RUN : 09/15/87
TIME OF RUN : 16:48:52
TAPE DESC. : PTSE-2A TEST 25-NOV-86
INST. PLOTTED : YY-83
DESCRIPTION : DISPLACEMENT 0 DEG -100 MM
IN
TIME FROM SCAN START IN SECONDS

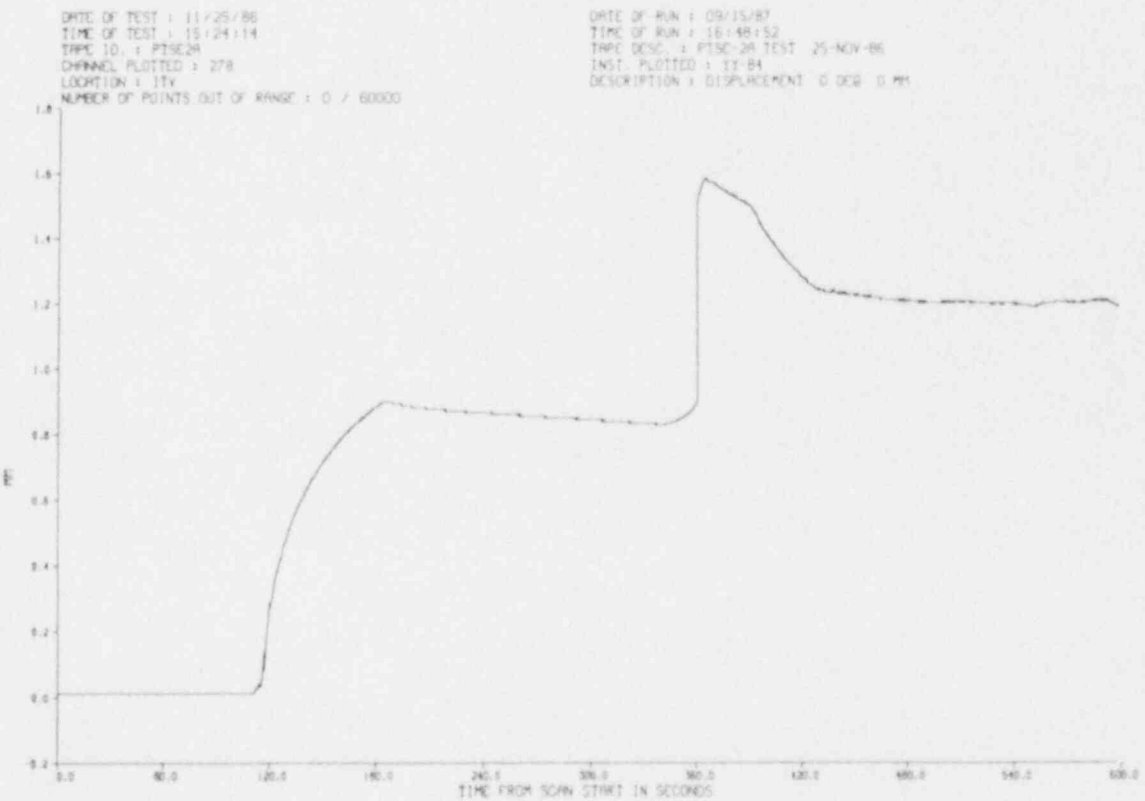
DATE OF TEST : 11/25/86
TIME OF TEST : 15:24:14
TAPE ID. : PTSE2A
CHANNEL PLOTTED : 278
LOCATION : ITV
NUMBER OF POINTS OUT OF RANGE : 0 / 60000
DATE OF RUN : 09/15/87
TIME OF RUN : 16:48:52
TAPE DESC. : PTSE-2A TEST 25-NOV-86
INST. PLOTTED : YY-84
DESCRIPTION : DISPLACEMENT 0 DEG 0 MM
IN
TIME FROM SCAN START IN SECONDS

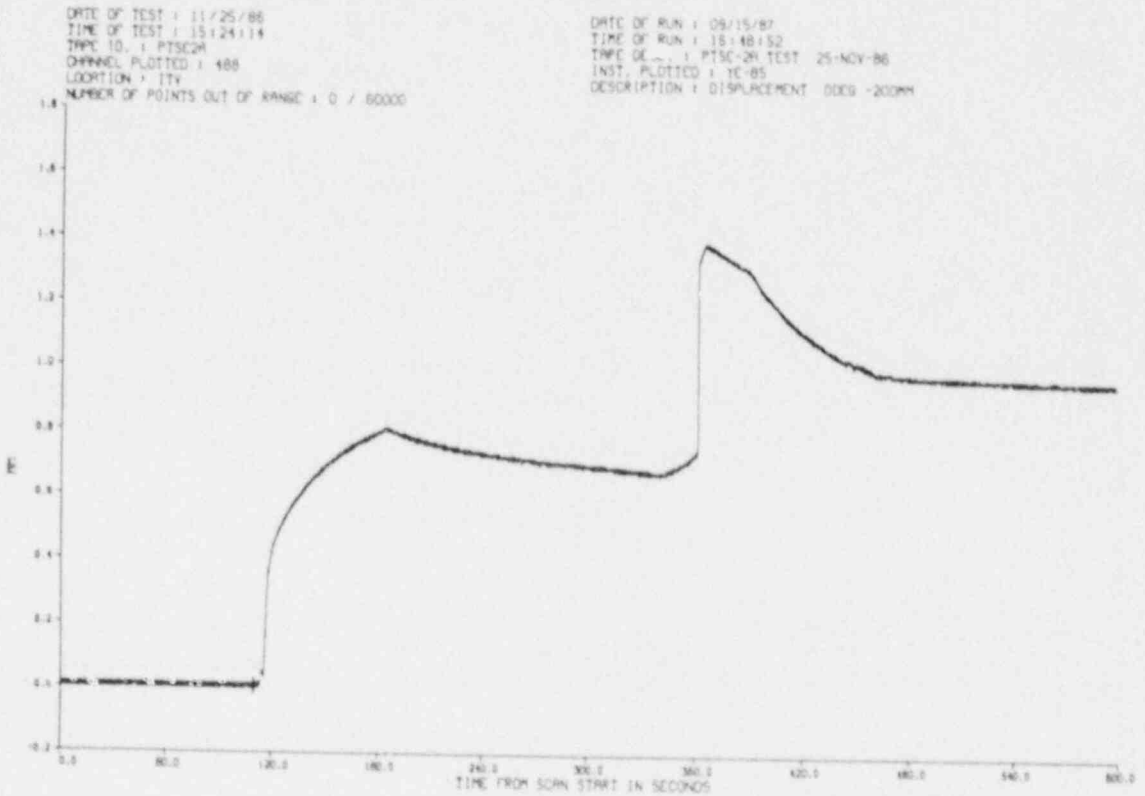
DATE OF TEST : 11/25/86
TIME OF TEST : 15:24:14
TAPE ID. : PTSC2A
CHANNEL PLOTTED : 488
LOCATION : ITV
NUMBER OF POINTS OUT OF RANGE : 0 / 60000
DATE OF RUN : 09/15/87
TIME OF RUN : 15:48:52
TAPE DESC. : PTSC-2A TEST 25-NOV-86
INST. PLOTTED : TC-85
DESCRIPTION : DISPLACEMENT 000 -200MM
E
TIME FROM SCAN START IN SECONDS

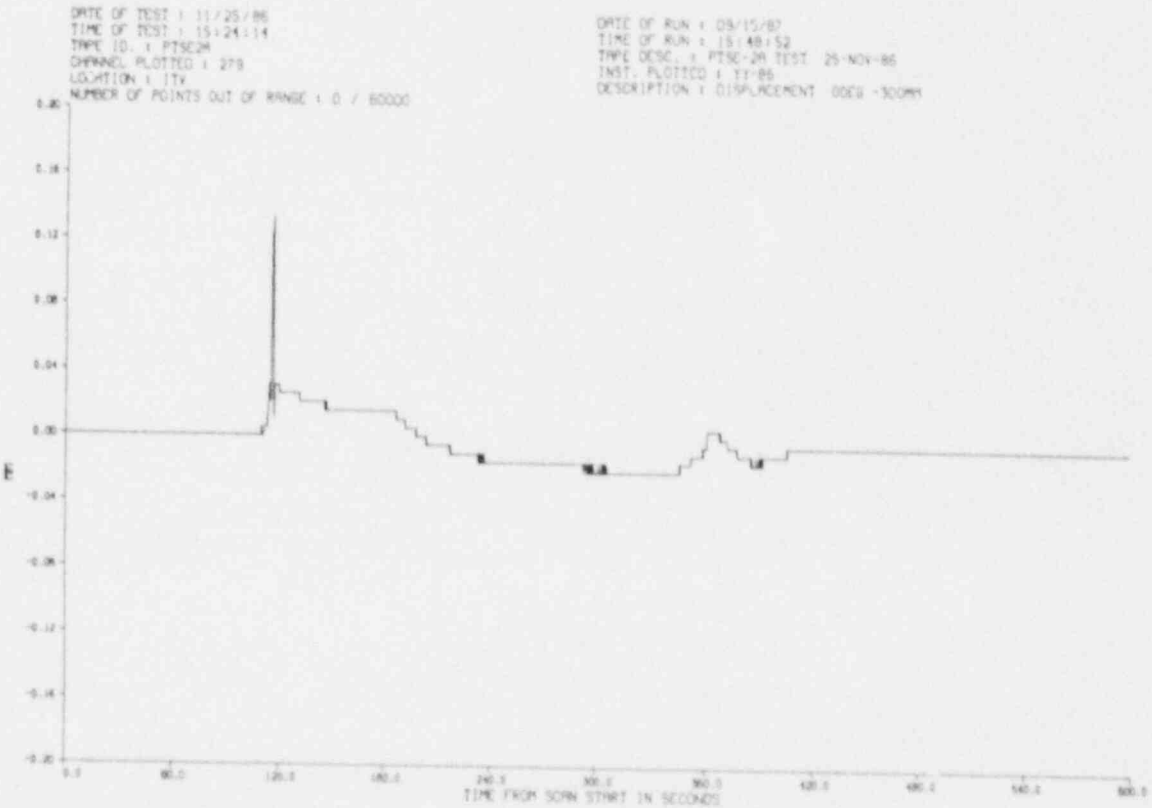
DATE OF TEST : 11/25/86
TIME OF TEST : 15:24:14
TAPE ID. : PTSC2A
CHANNEL PLOTTED : 279
LOCATION : ITV
NUMBER OF POINTS OUT OF RANGE : 0 / 60000
DATE OF RUN : 09/15/87
TIME OF RUN : 15:48:52
TAPE DESC. : PTSC-2A TEST 25-NOV-86
INST. PLOTTED : TT-86
DESCRIPTION : DISPLACEMENT 000 -300MM
E
TIME FROM SCAN START IN SECONDS

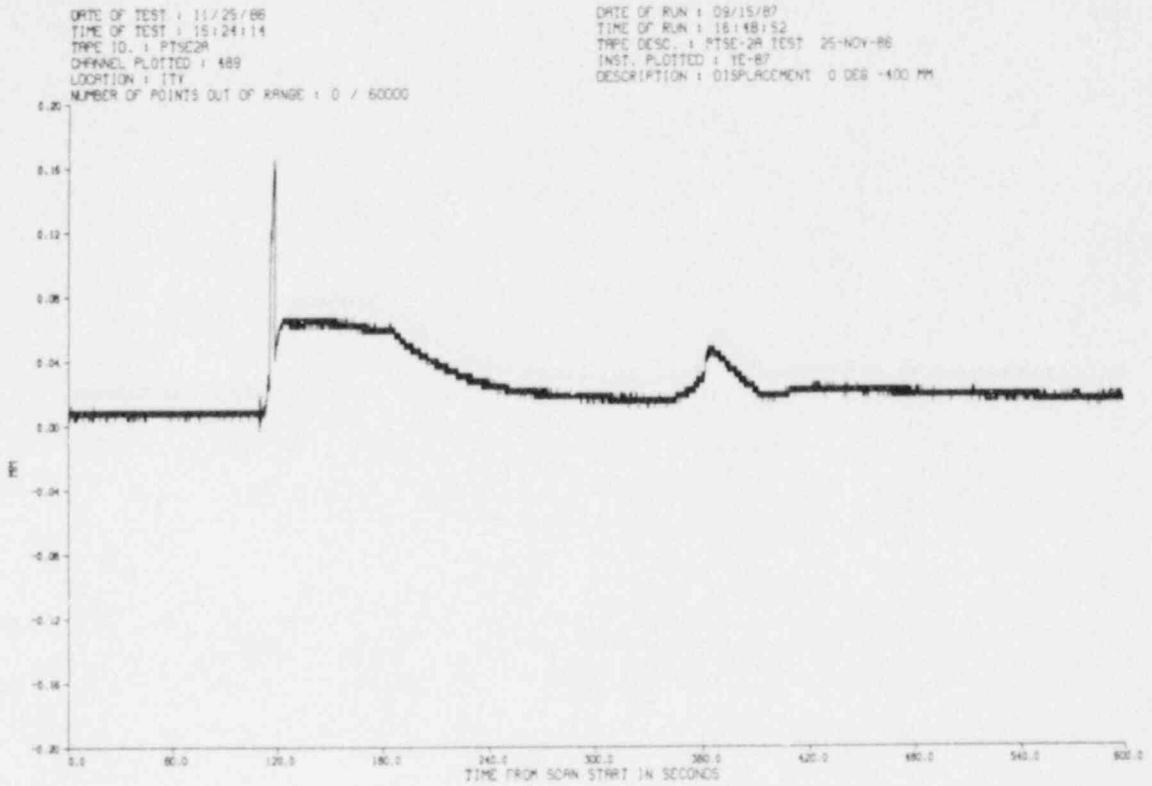
DATE OF TEST : 11/25/86
TIME OF TEST : 15:24:14
TAPE ID. : PTSC2A
CHANNEL PLOTTED : 489
LOCATION : ITV
NUMBER OF POINTS OUT OF RANGE : 0 / 60000
DATE OF RUN : 09/15/87
TIME OF RUN : 16:48:52
TAPE DESC. : PTSE-2A TEST 25-NOV-86
INST. PLOTTED : TE-87
DESCRIPTION : DISPLACEMENT 0 DEG -400 MM
0.20
0.16
0.12
0.08
0.04
0.00
-0.04
-0.08
-0.12
-0.16
-0.20
0.0
60.0
120.0
180.0
240.0
300.0
360.0
420.0
480.0
540.0
600.0
TIME FROM SCAN START IN SECONDS

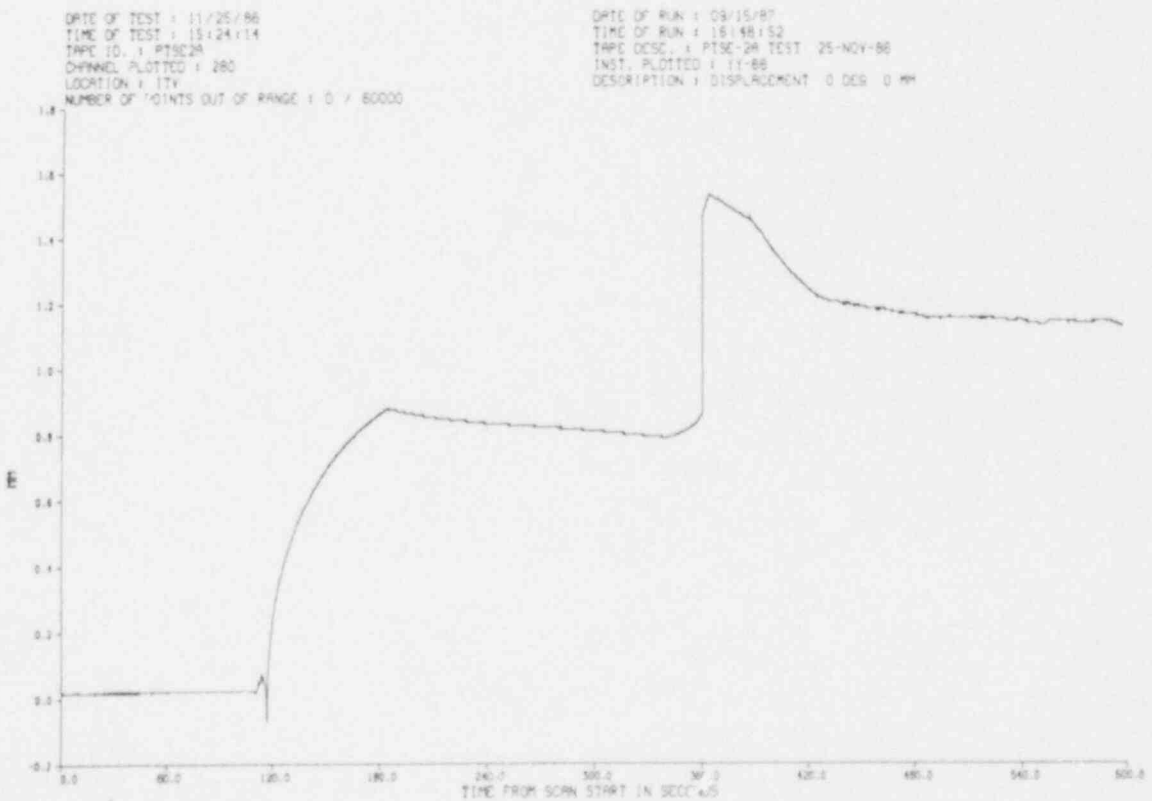
DATE OF TEST : 11/25/86
TIME OF TEST : 15:24:14
TAPE ID. : PTSC2A
CHANNEL PLOTTED : 280
LOCATION : ITV
NUMBER OF POINTS OUT OF RANGE : 0 / 60000
DATE OF RUN : 09/15/87
TIME OF RUN : 16:48:52
TAPE DESC. : PTSE-2A TEST 25-NOV-86
INST. PLOTTED : TE-88
DESCRIPTION : DISPLACEMENT 0 DEG 0 MM
1.8
1.6
1.4
1.2
1.0
0.8
0.6
0.4
0.2
0.0
-0.2
0.0
60.0
120.0
180.0
240.0
300.0
360.0
420.0
480.0
540.0
600.0
TIME FROM SCAN START IN SECONDS

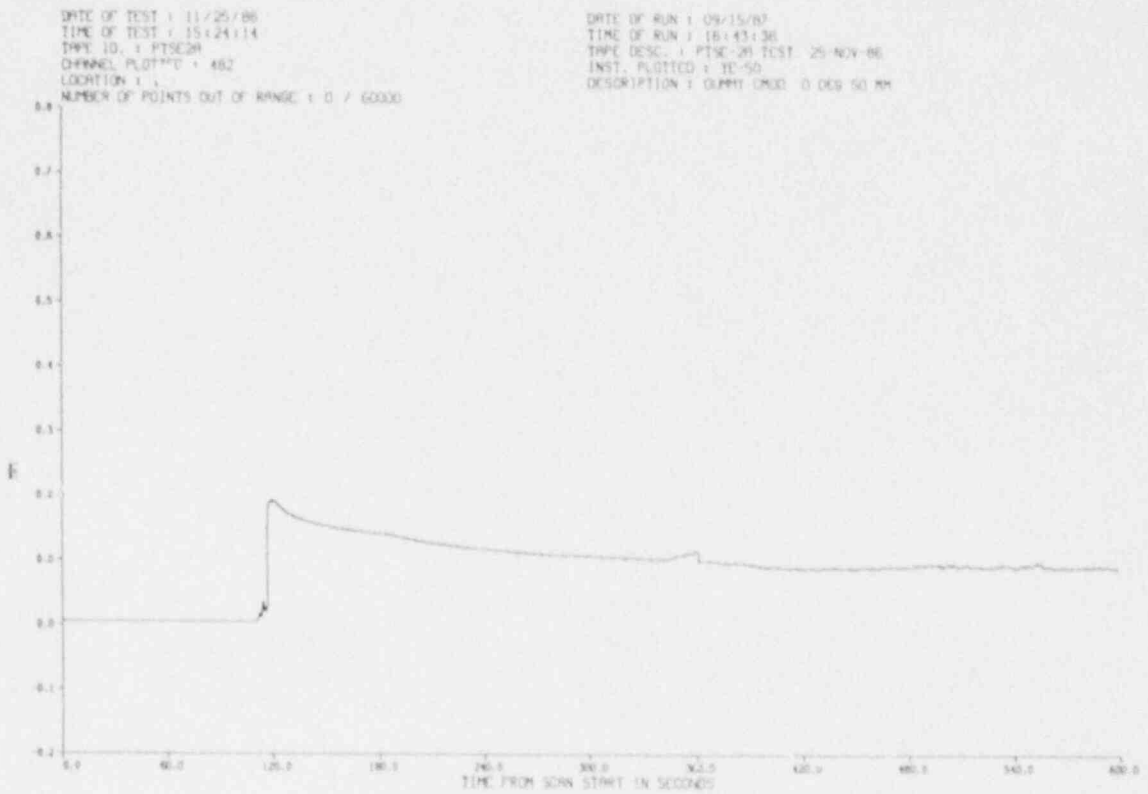
DATE OF TEST : 11/25/86
TIME OF TEST : 15:24:14
TAPE ID. : PTSC2R
CHANNEL PLOTTED : 482
LOCATION : ,
NUMBER OF POINTS OUT OF RANGE : 0 / 60000
DATE OF RUN : 09/15/87
TIME OF RUN : 16:43:36
TAPE DESC. : PTSC-2R TEST 25-NOV-86
INST. PLOTTED : TE-50
DESCRIPTION : DUMMY CMOD 0.006 50 RR
F
TIME FROM SCAN START IN SECONDS

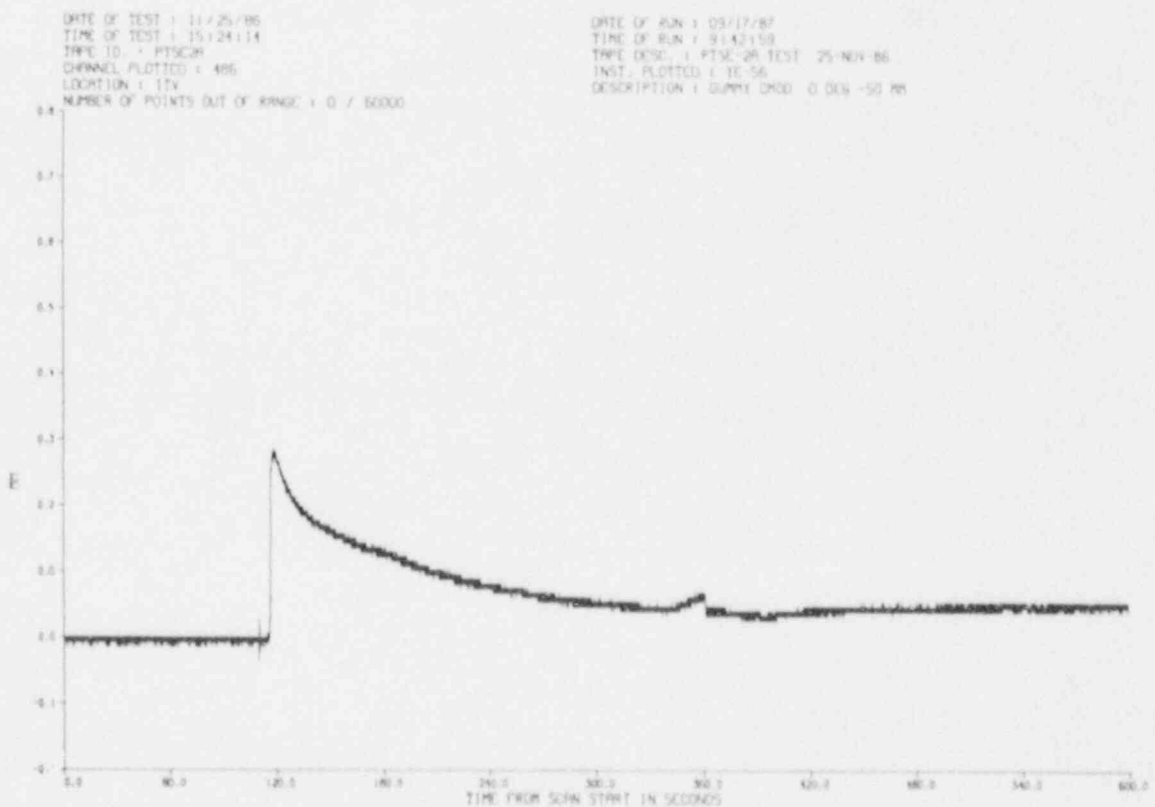
DATE OF TEST : 11/25/86
TIME OF TEST : 15:24:14
TAPE ID. : PTSC2R
CHANNEL PLOTTED : 486
LOCATION : ITv
NUMBER OF POINTS OUT OF RANGE : 0 / 60000
DATE OF RUN : 09/17/87
TIME OF RUN : 9:42:59
TAPE DESC. : PTSC-2R TEST 25-NOV-86
INST. PLOTTED : TE-56
DESCRIPTION : DUMMY CMOD 0.006 -50 RR
F
TIME FROM SCAN START IN SECONDS

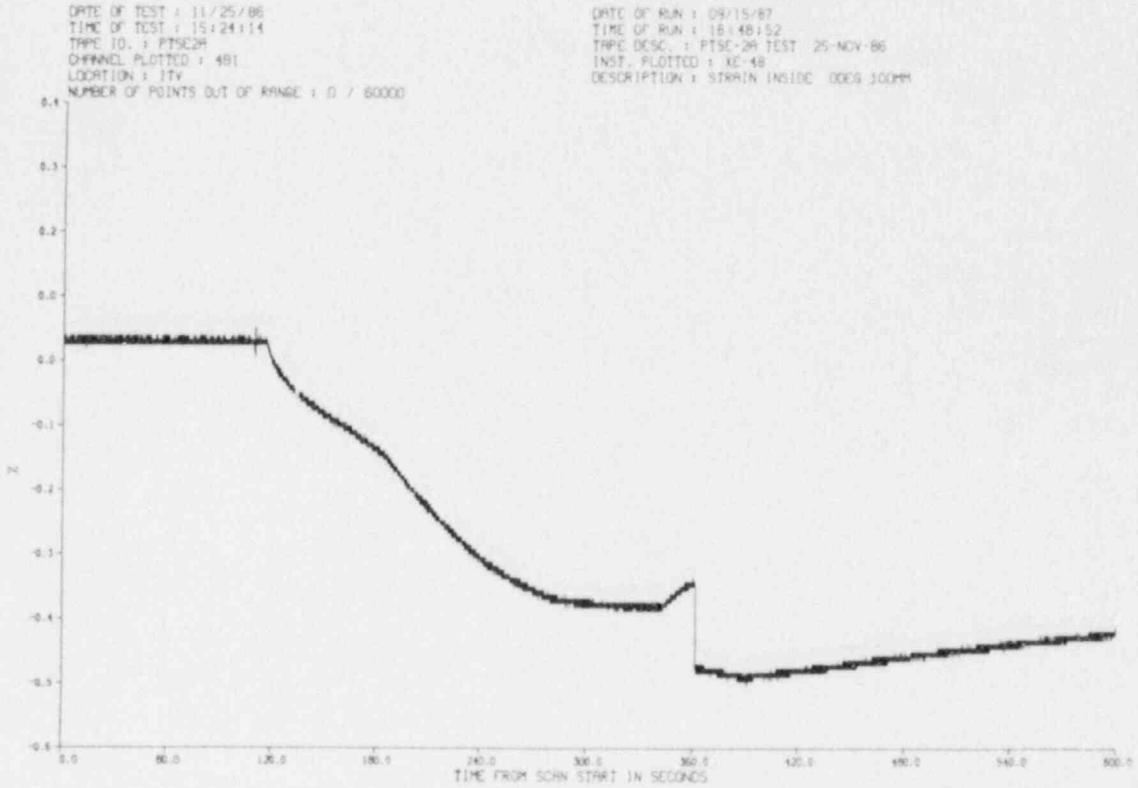
DATE OF TEST : 11/25/86
TIME OF TEST : 15:24:14
TAPE ID. : PTSC2A
CHANNEL PLOTTED : 481
LOCATION : ITV
NUMBER OF POINTS OUT OF RANGE : 0 / 60000
DATE OF RUN : 09/15/87
TIME OF RUN : 16:48:52
TAPE DESC. : PTSC-2A TEST 25-NOV-86
INST. PLOTTED : XE-48
DESCRIPTION : STRAIN INSIDE 0DEG 100MM
Z
TIME FROM SCAN START IN SECONDS

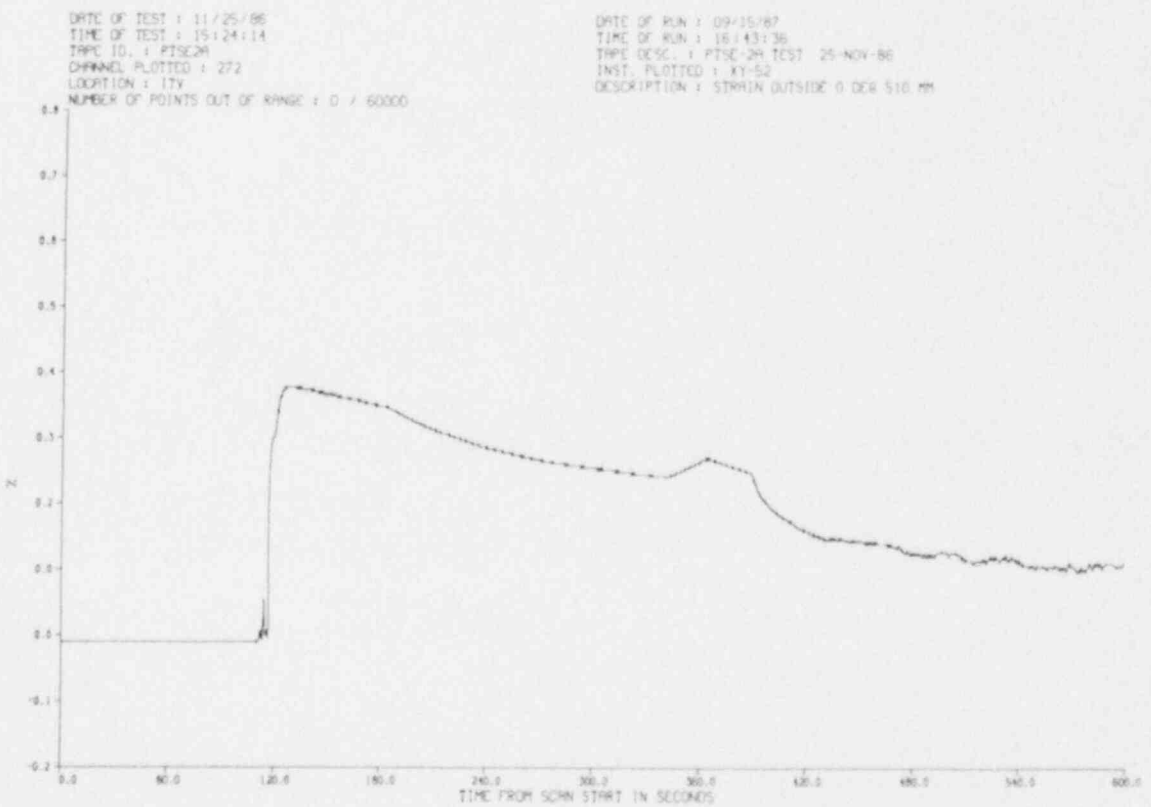
DATE OF TEST : 11/25/86
TIME OF TEST : 15:24:14
TAPE ID. : PTSC2A
CHANNEL PLOTTED : 272
LOCATION : ITV
NUMBER OF POINTS OUT OF RANGE : 0 / 60000
DATE OF RUN : 09/15/87
TIME OF RUN : 16:43:36
TAPE DESC. : PTSC-2A TEST 25-NOV-86
INST. PLOTTED : KY-52
DESCRIPTION : STRAIN OUTSIDE 0 DEG 510 MM
Z
TIME FROM SCAN START IN SECONDS

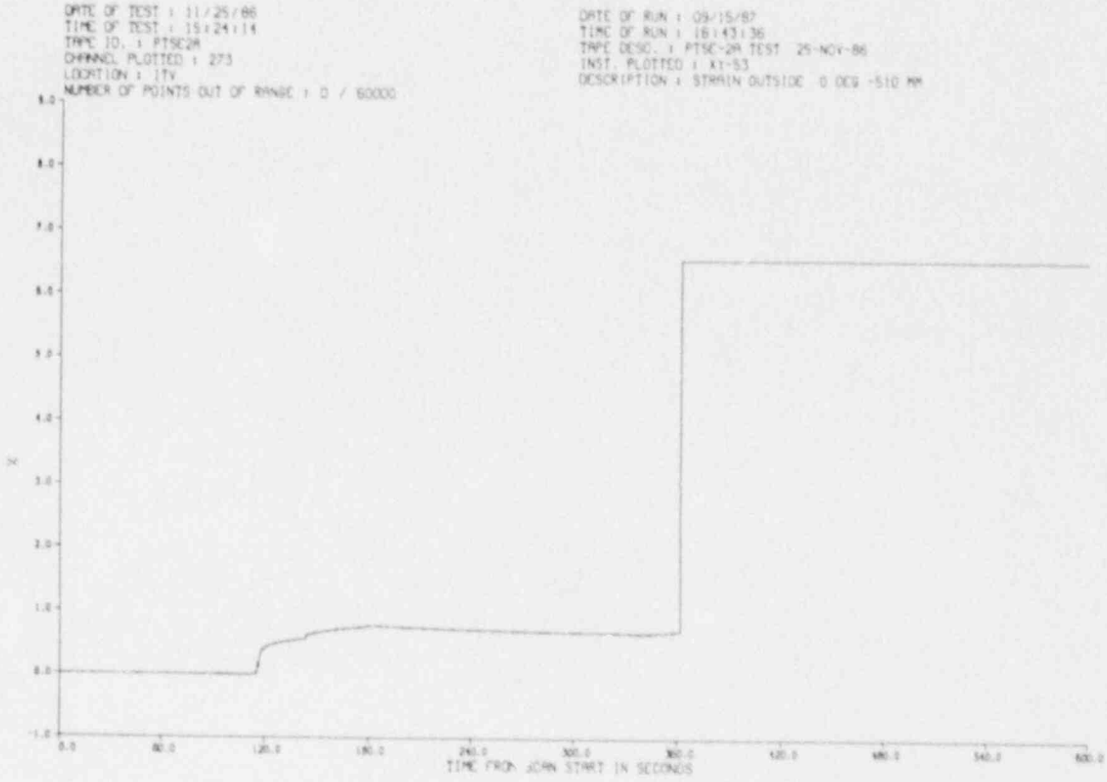
DATE OF TEST : 11/25/86
TIME OF TEST : 15:24:14
TAPE ID. : PTSC2A
CHANNEL PLOTTED : 273
LOCATION : ITV
NUMBER OF POINTS OUT OF RANGE : 0 / 60000
DATE OF RUN : 09/15/87
TIME OF RUN : 16:43:36
TAPE DESC. : PTSC-2A TEST 25-NOV-86
INST. PLOTTED : X1-53
DESCRIPTION : STRAIN OUTSIDE 0.0C9 -510 MM
X
TIME FROM SCAN START IN SECONDS

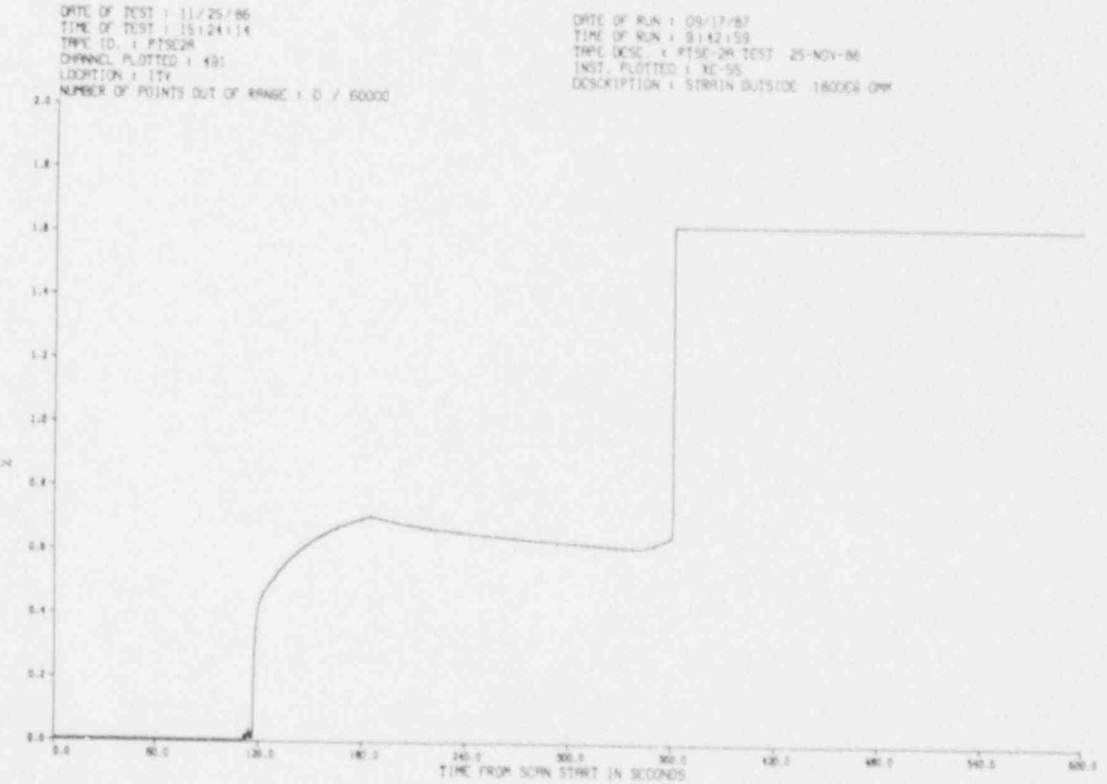
DATE OF TEST : 11/25/86
TIME OF TEST : 15:24:14
TAPE ID. : PTSC2A
CHANNEL PLOTTED : 491
LOCATION : ITV
NUMBER OF POINTS OUT OF RANGE : 0 / 60000
DATE OF RUN : 09/17/87
TIME OF RUN : 9:42:59
TAPE DESC. : PTSC-2A TEST 25-NOV-86
INST. PLOTTED : XC-55
DESCRIPTION : STRAIN OUTSIDE 180DEG OPP
X
TIME FROM SCAN START IN SECONDS

DATE OF TEST : 12/10/86
TIME OF TEST : 15:24:57
TAPE ID. : PT5C2B
CHANNEL PLOTTED : 114
LOCATION : 17V
NUMBER OF POINTS OUT OF RANGE : 0 / 22500

DATE OF RUN : 09/15/87
TIME OF RUN : 16:59:56
TAPE DESC. : PT5C-2B TEST 10-DEC-86 (COPY 1)
INST. PLOTTED : TE-5-1
DESCRIPTION : THIMBLE 5 TC : 3300Ea OMM

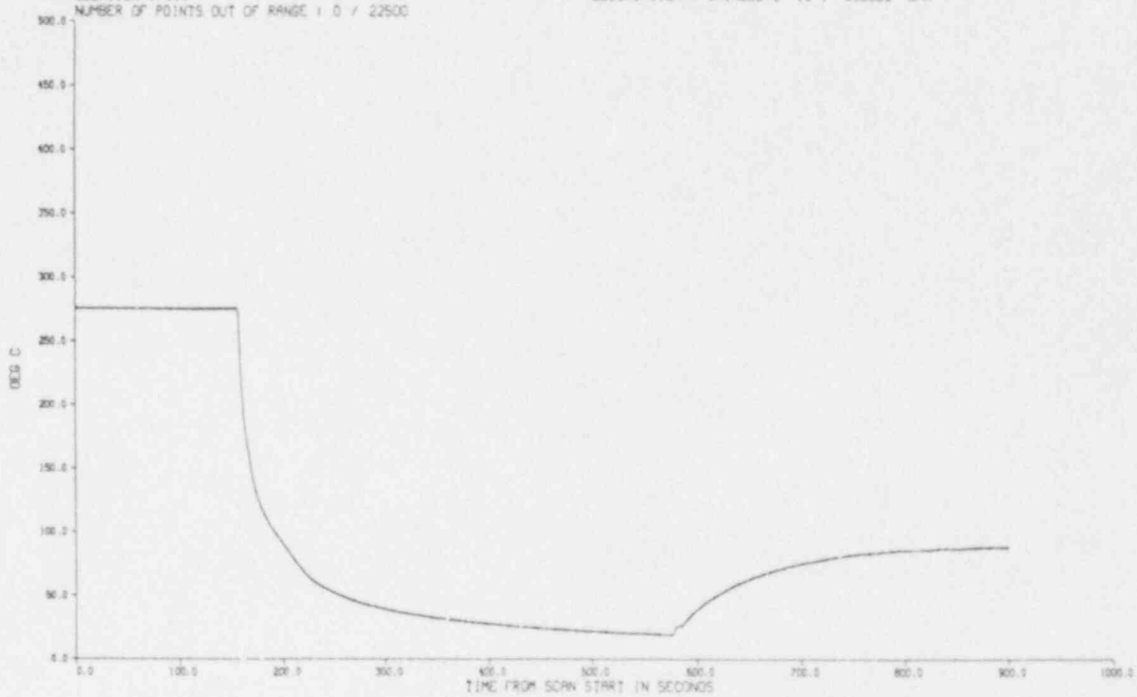

DATE OF TEST : 12/10/86
TIME OF TEST : 15:24:57
TAPE ID. : PT5C2B
CHANNEL PLOTTED : 147
LOCATION : 17V
NUMBER OF POINTS OUT OF RANGE : 0 / 22500

DATE OF RUN : 09/15/87
TIME OF RUN : 16:59:56
TAPE DESC. : PT5C-2B TEST 10-DEC-86 (COPY 1)
INST. PLOTTED : TE-18
DESCRIPTION : 17V INSIDE TEMP 900CB 300MM

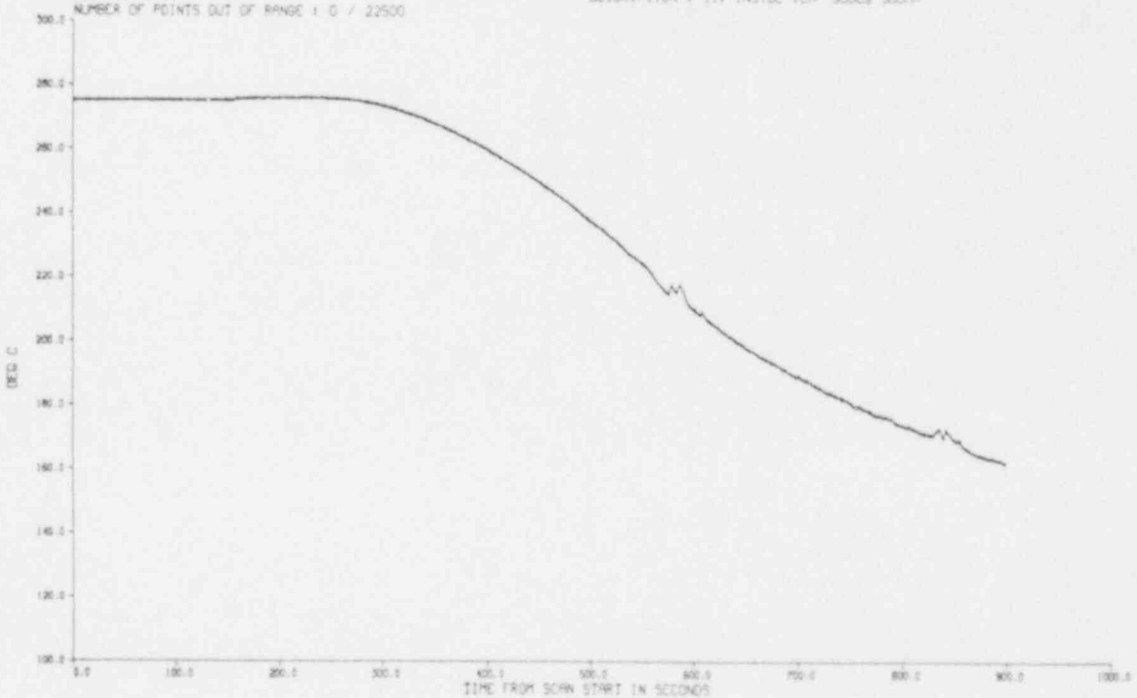

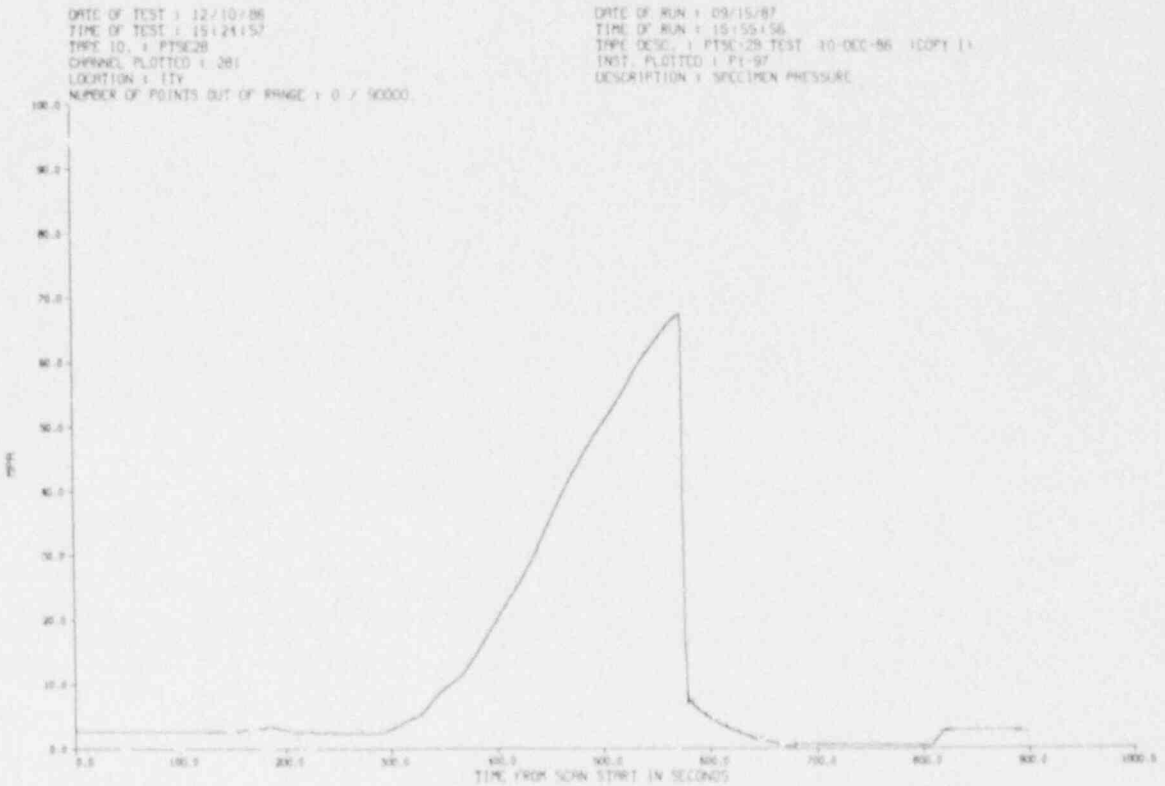
DATE OF TEST : 12/10/86
TIME OF TEST : 15:24:57
TAPE ID. : PTSC28
CHANNEL PLOTTED : 281
LOCATION : ITV
NUMBER OF POINTS OUT OF RANGE : 0 / 90000.
DATE OF RUN : 09/15/87
TIME OF RUN : 15:55:56
TAPE DESC. : PTSC-28 TEST 10-DEC-86 (COPY 1)
INST. PLOTTED : P1-97
DESCRIPTION : SPECIMEN PRESSURE
PSIA
TIME FROM SCAN START IN SECONDS

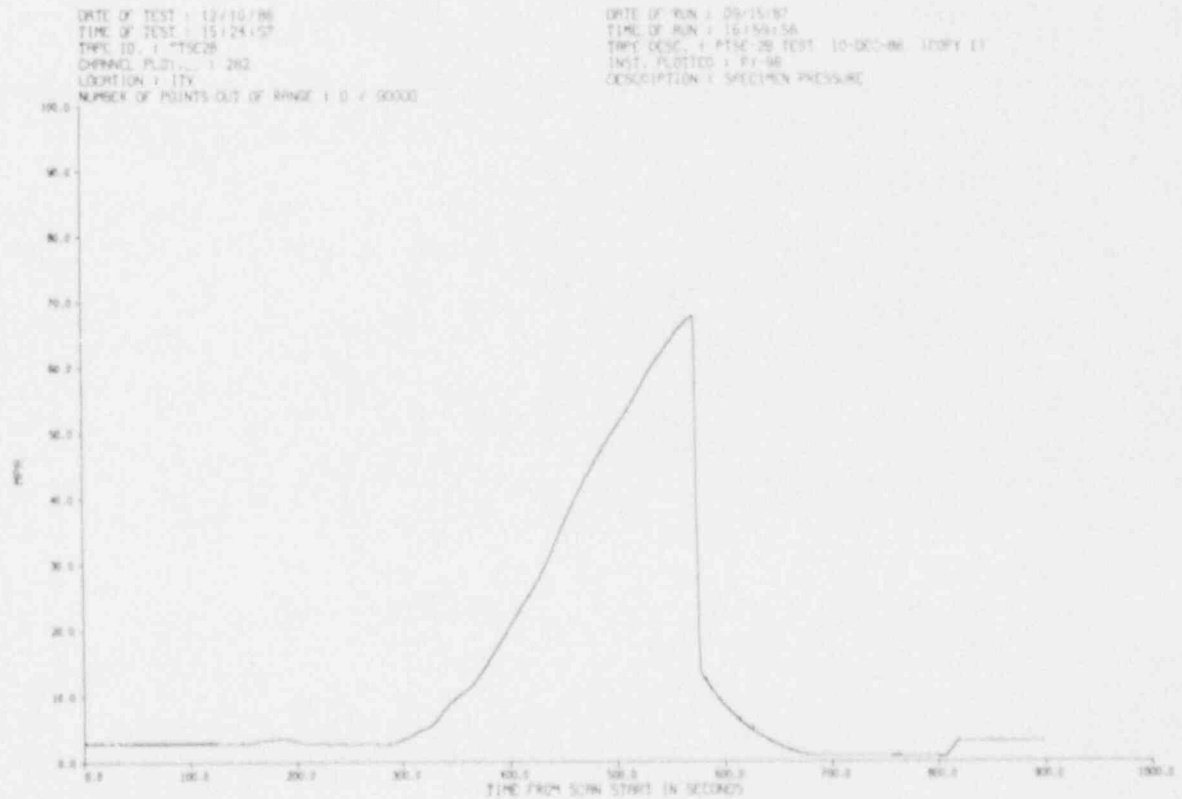
DATE OF TEST : 12/10/86
TIME OF TEST : 15:24:57
TAPE ID. : PTSC28
CHANNEL PLOTTED : 282
LOCATION : ITV
NUMBER OF POINTS OUT OF RANGE : 0 / 90000
DATE OF RUN : 09/15/87
TIME OF RUN : 16:59:56
TAPE DESC. : PTSC-28 TEST 10-DEC-86 (COPY 1)
INST. PLOTTED : P4-98
DESCRIPTION : SPECIMEN PRESSURE
PSIA
TIME FROM SCAN START IN SECONDS

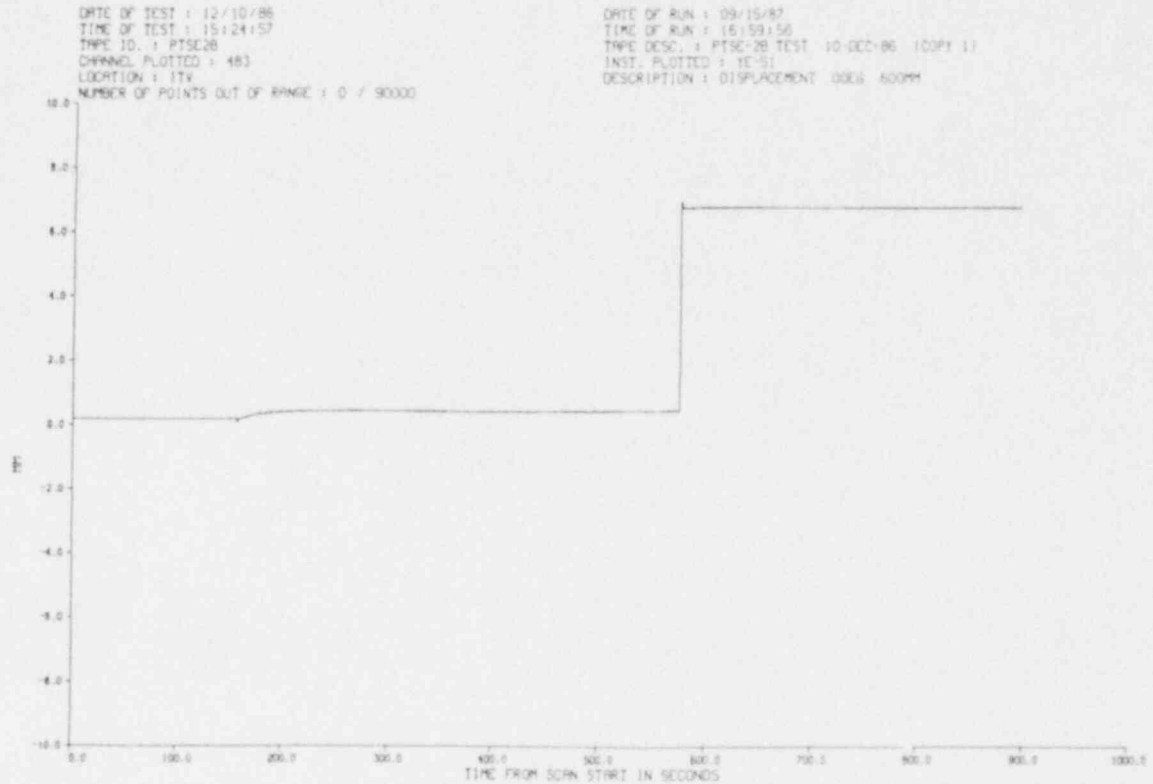
DATE OF TEST : 12/10/86
TIME OF TEST : 15:24:57
TAPE ID. : PTSC2B
CHANNEL PLOTTED : 483
LOCATION : ITV
NUMBER OF POINTS OUT OF RANGE : 0 / 90000
DATE OF RUN : 09/15/87
TIME OF RUN : 16:59:56
TAPE DESC. : PTSC-2B TEST 10-DEC-86 (COPY 1)
INST. PLOTTED : YE-51
DESCRIPTION : DISPLACEMENT 0DEG 600MM
MM
TIME FROM SCAN START IN SECONDS

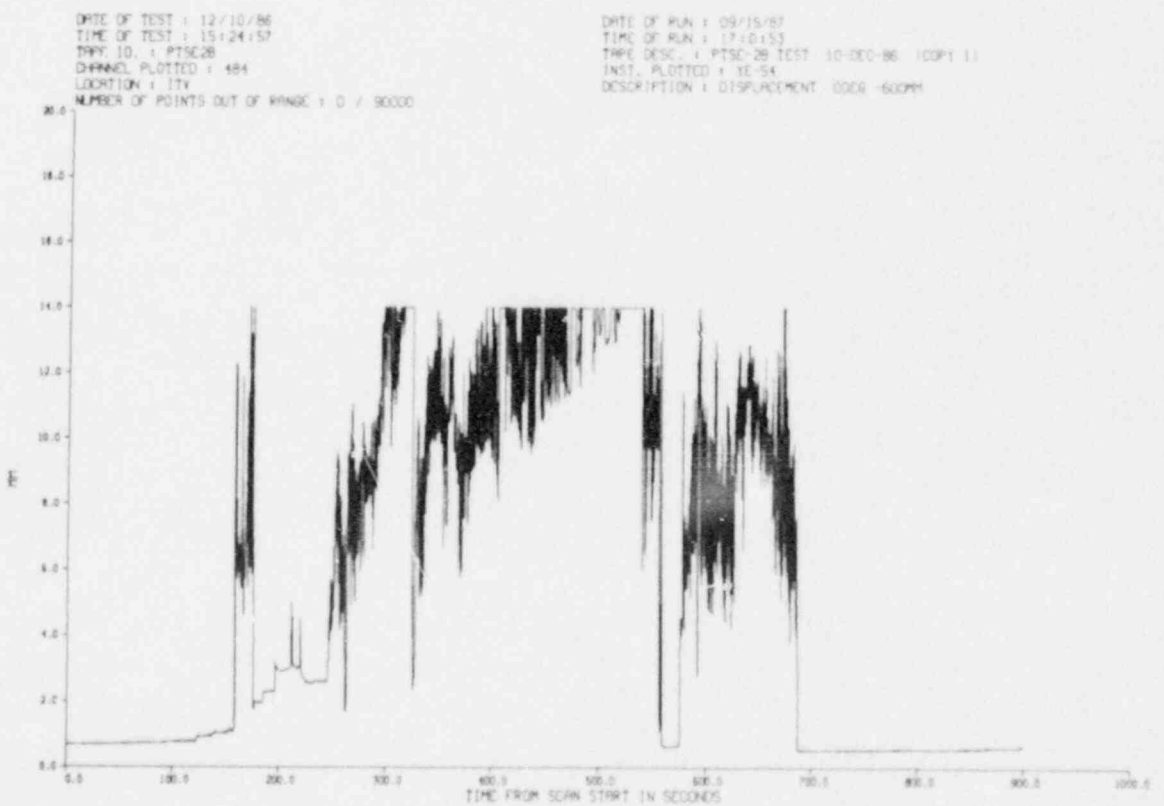
DATE OF TEST : 12/10/86
TIME OF TEST : 15:24:57
TAPE ID. : PTSC2B
CHANNEL PLOTTED : 484
LOCATION : ITV
NUMBER OF POINTS OUT OF RANGE : 0 / 90000
DATE OF RUN : 09/15/87
TIME OF RUN : 17:03:53
TAPE DESC. : PTSC-2B TEST 10-DEC-86 (COPY 1)
INST. PLOTTED : YE-54
DESCRIPTION : DISPLACEMENT 0DEG -60MM
MM
TIME FROM SCAN START IN SECONDS

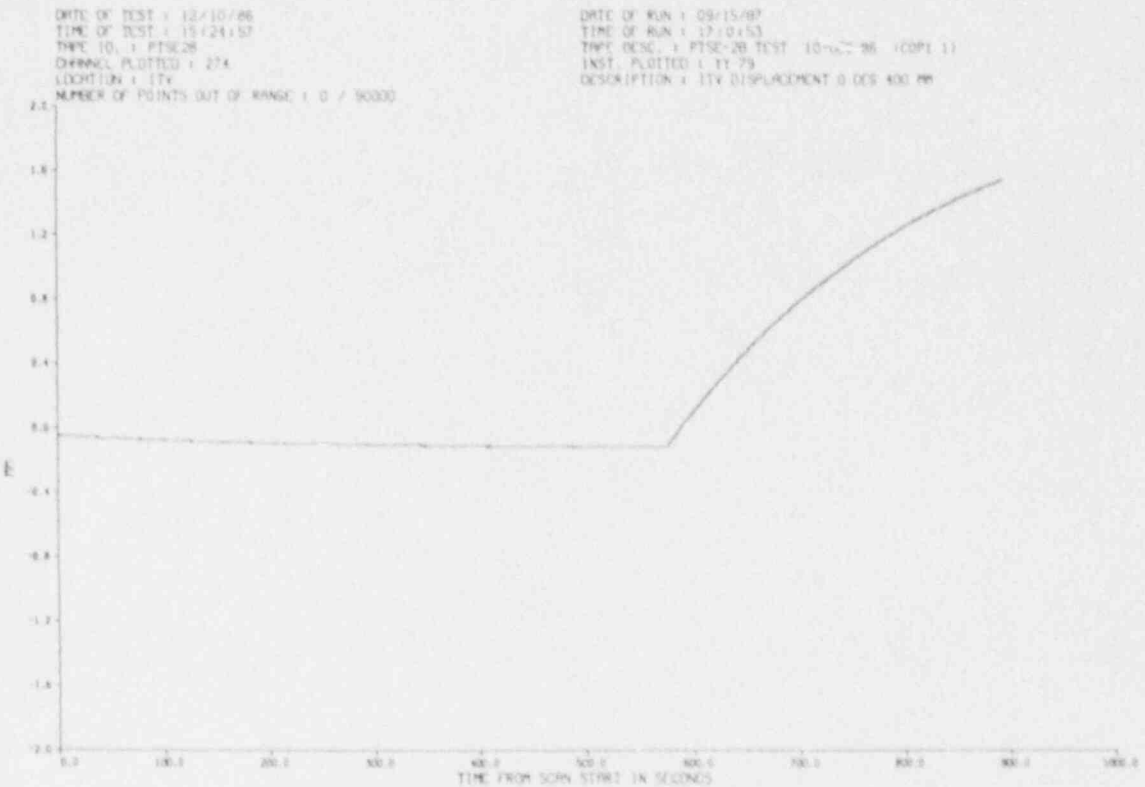
DATE OF TEST : 12/10/86
TIME OF TEST : 15:24:57
TYPE ID. : PTSE28
CHANNEL PLOTTED : 274
LOCATION : 1TV
NUMBER OF POINTS OUT OF RANGE : 0 / 90000
DATE OF RUN : 09/15/87
TIME OF RUN : 17:01:53
TYPE DESC. : PTSE-28 TEST 10-DEC-86 (COPY 1)
INST. PLOTTED : TY-79
DESCRIPTION : 1TV DISPLACEMENT 0 DCS 400 MM
TIME FROM SCAN START IN SECONDS

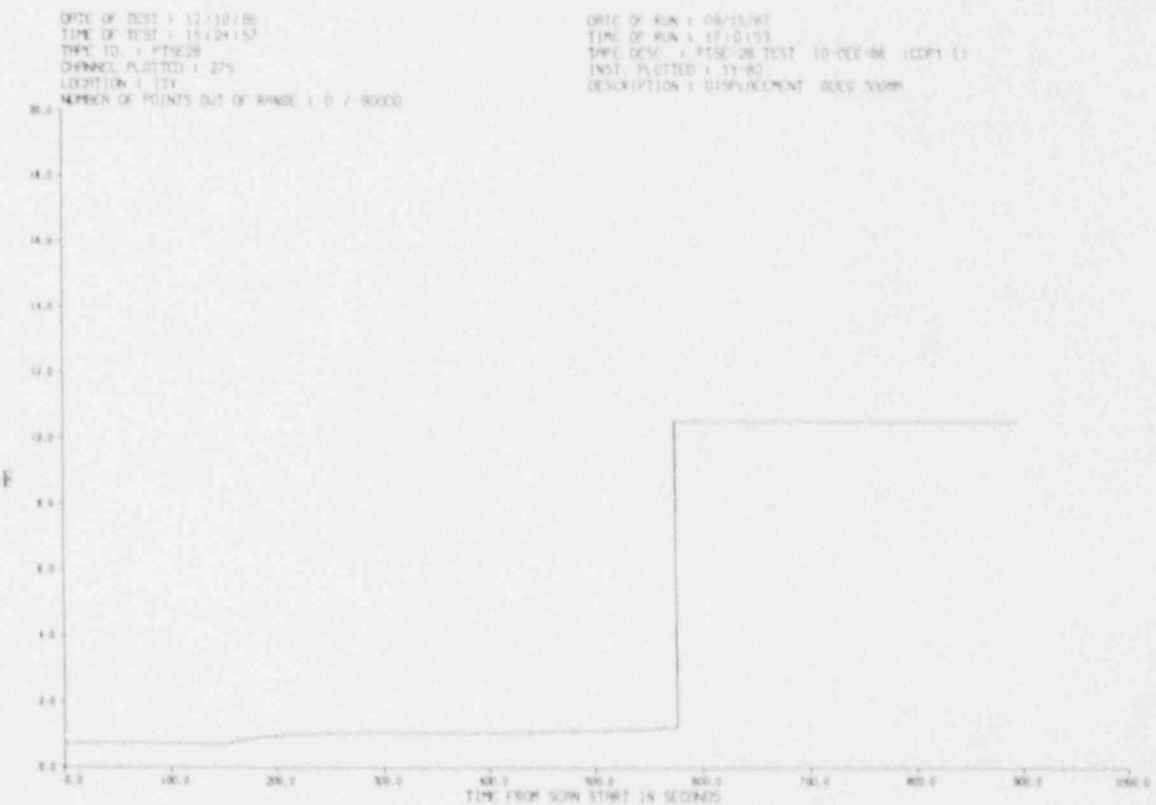
DATE OF TEST : 12/10/86
TIME OF TEST : 15:24:57
TYPE ID. : PTSE28
CHANNEL PLOTTED : 275
LOCATION : 1TV
NUMBER OF POINTS OUT OF RANGE : 0 / 90000
DATE OF RUN : 09/15/87
TIME OF RUN : 17:01:53
TYPE DESC. : PTSE-28 TEST 10-DEC-86 (COPY 1)
INST. PLOTTED : TY-80
DESCRIPTION : DISPLACEMENT 0DCS 500MM
TIME FROM SCAN START IN SECONDS

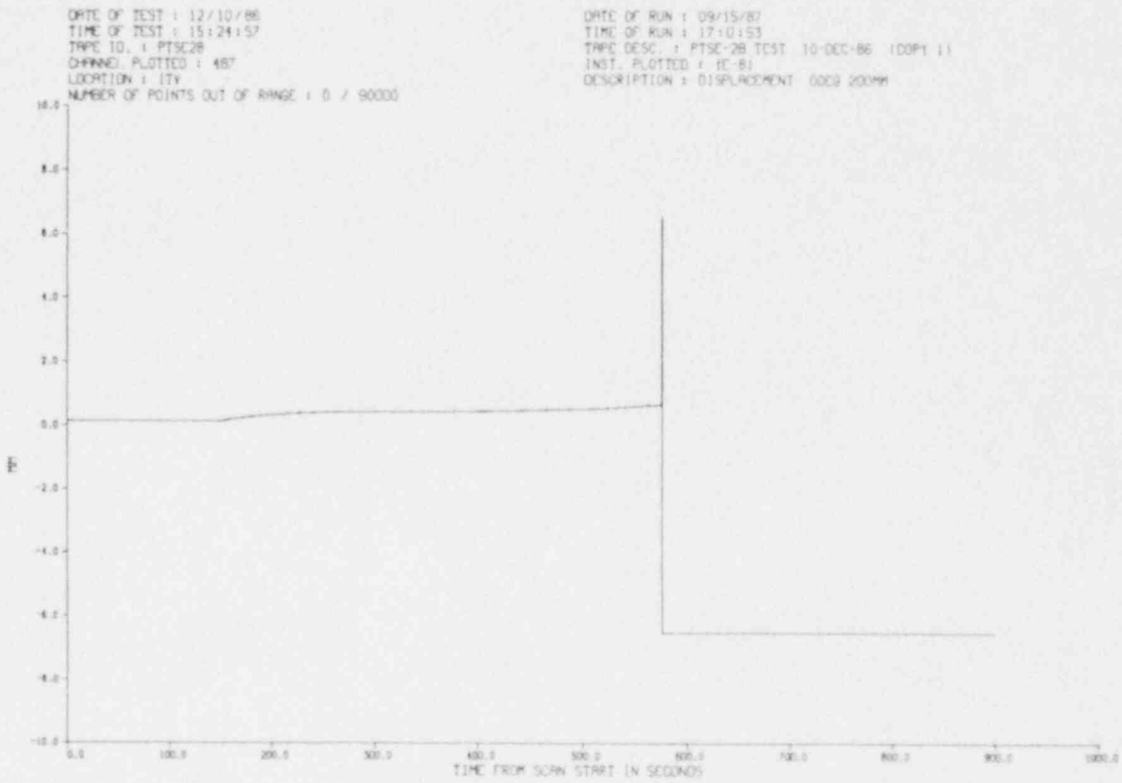
DATE OF TEST : 12/10/86
TIME OF TEST : 15:24:57
TAPE ID. : PTSC28
CHANNEL PLOTTED : 487
LOCATION : ITV
NUMBER OF POINTS OUT OF RANGE : 0 / 90000
DATE OF RUN : 09/15/87
TIME OF RUN : 17:0:53
TAPE DESC. : PTSE-28 TEST 10-DEC-86 (COPY 1)
INST. PLOTTED : EC-81
DESCRIPTION : DISPLACEMENT .00C9 200MM
10.0
8.0
6.0
4.0
2.0
0.0
-2.0
-4.0
-6.0
-8.0
-10.0
0.0
100.0
200.0
300.0
400.0
500.0
600.0
700.0
800.0
900.0
1000.0
TIME FROM SCAN START IN SECONDS

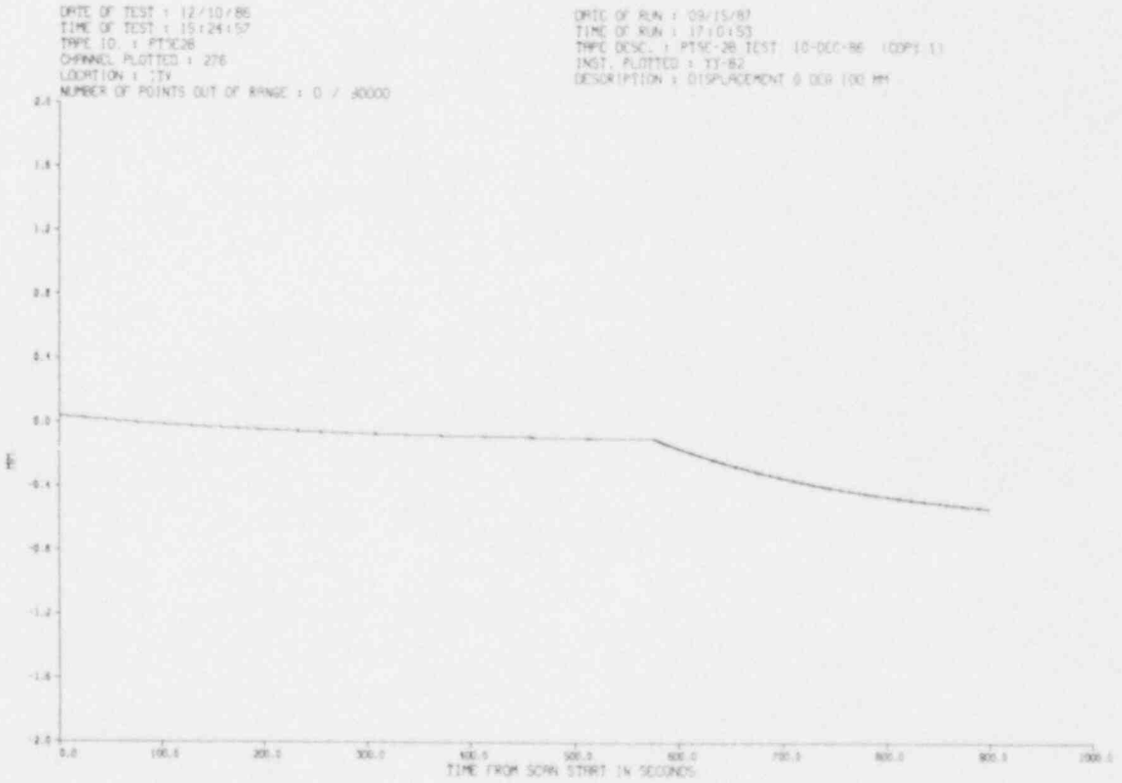
DATE OF TEST : 12/10/86
TIME OF TEST : 15:24:57
TAPE ID. : PTSC28
CHANNEL PLOTTED : 276
LOCATION : ITV
NUMBER OF POINTS OUT OF RANGE : 0 / 90000
DATE OF RUN : 09/15/87
TIME OF RUN : 17:0:53
TAPE DESC. : PTSE-28 TEST 10-DEC-86 (COPY 1)
INST. PLOTTED : TT-82
DESCRIPTION : DISPLACEMENT 0 DEG (00 MM
2.0
1.6
1.2
0.8
0.4
0.0
-0.4
-0.8
-1.2
-1.6
-2.0
0.0
100.0
200.0
300.0
400.0
500.0
600.0
700.0
800.0
900.0
1000.0
TIME FROM SCAN START IN SECONDS

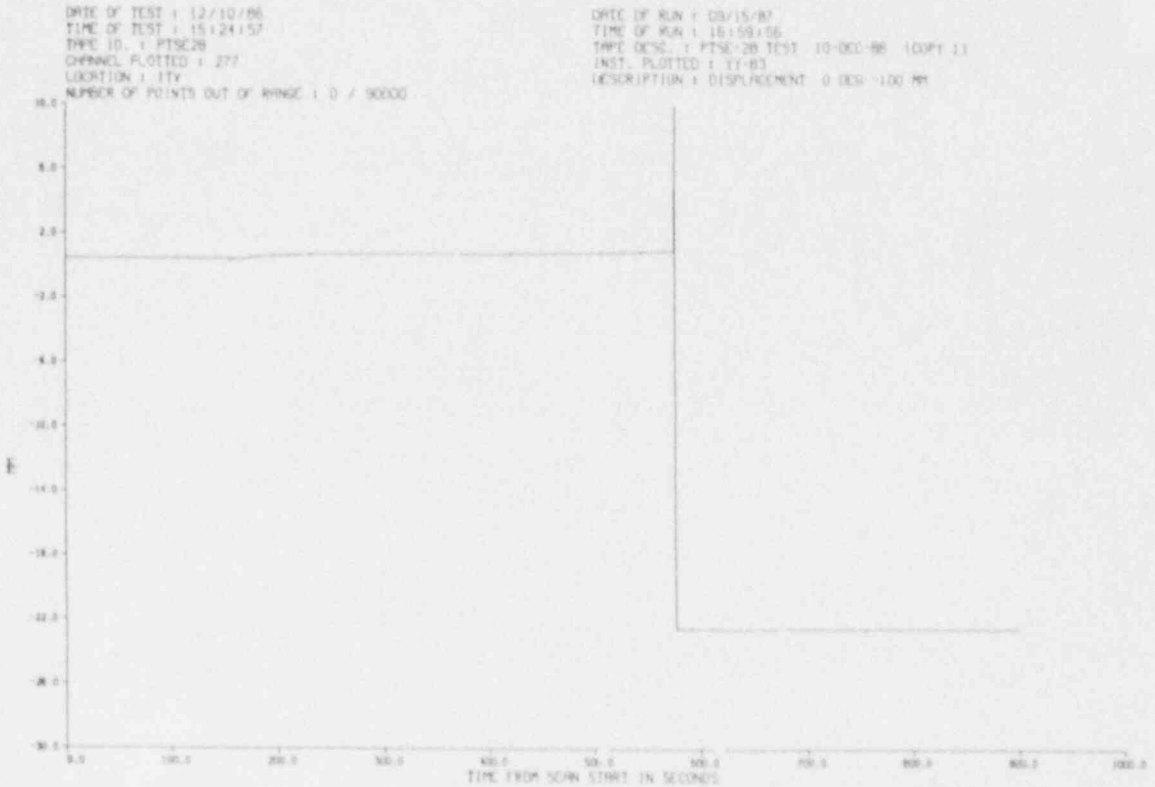
DATE OF TEST : 12/10/86
TIME OF TEST : 15:24:57
TAPE ID. : PTSC28
CHANNEL PLOTTED : 277
LOCATION : ITv
NUMBER OF POINTS OUT OF RANGE : 0 / 90000
DATE OF RUN : 09/15/87
TIME OF RUN : 16:59:56
TAPE DESC. : PTSE-28 TEST 10-DEC-86 (COPY 1)
INST. PLOTTED : YY-83
DESCRIPTION : DISPLACEMENT 0 DEG -100 MM
E
TIME FROM SCAN START IN SECONDS

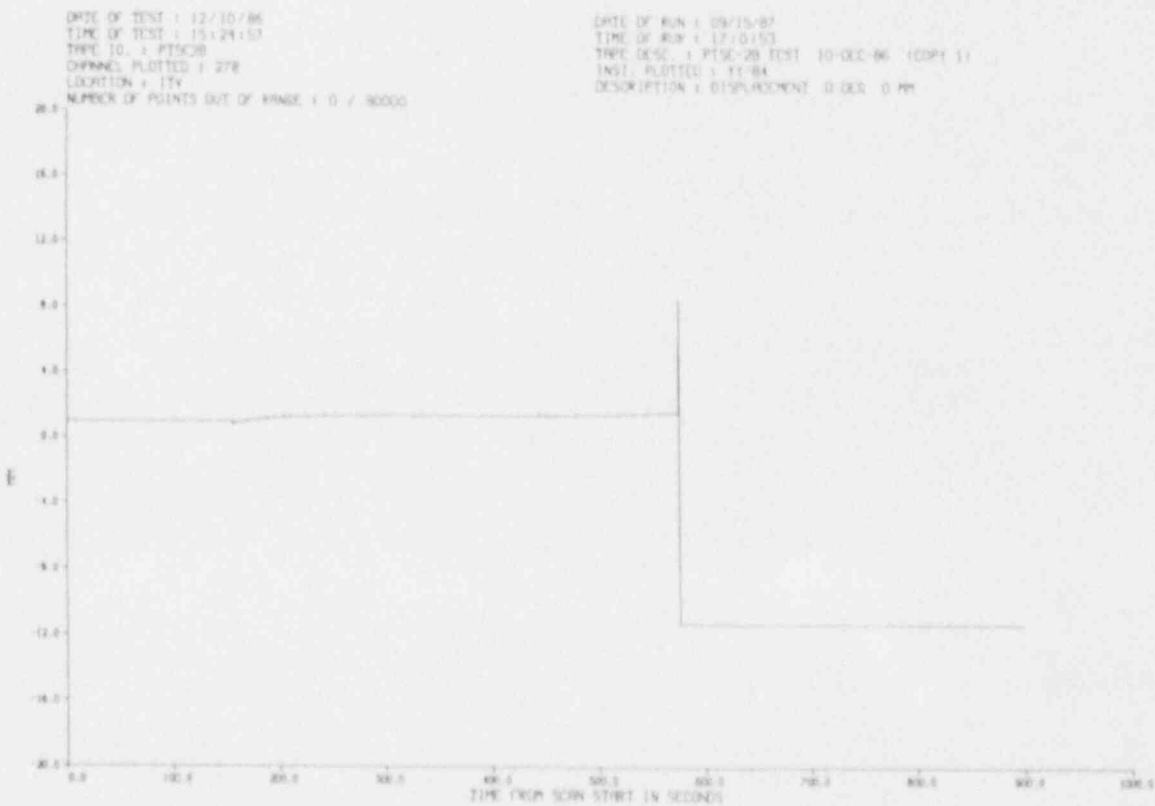
DATE OF TEST : 12/10/86
TIME OF TEST : 15:24:57
TAPE ID. : PTSC28
CHANNEL PLOTTED : 278
LOCATION : ITv
NUMBER OF POINTS OUT OF RANGE : 0 / 90000
DATE OF RUN : 09/15/87
TIME OF RUN : 17:01:53
TAPE DESC. : PTSC-28 TEST 10-DEC-86 (COPY 1)
INST. PLOTTED : YY-84
DESCRIPTION : DISPLACEMENT 0 DEG 0 MM
E
TIME FROM SCAN START IN SECONDS

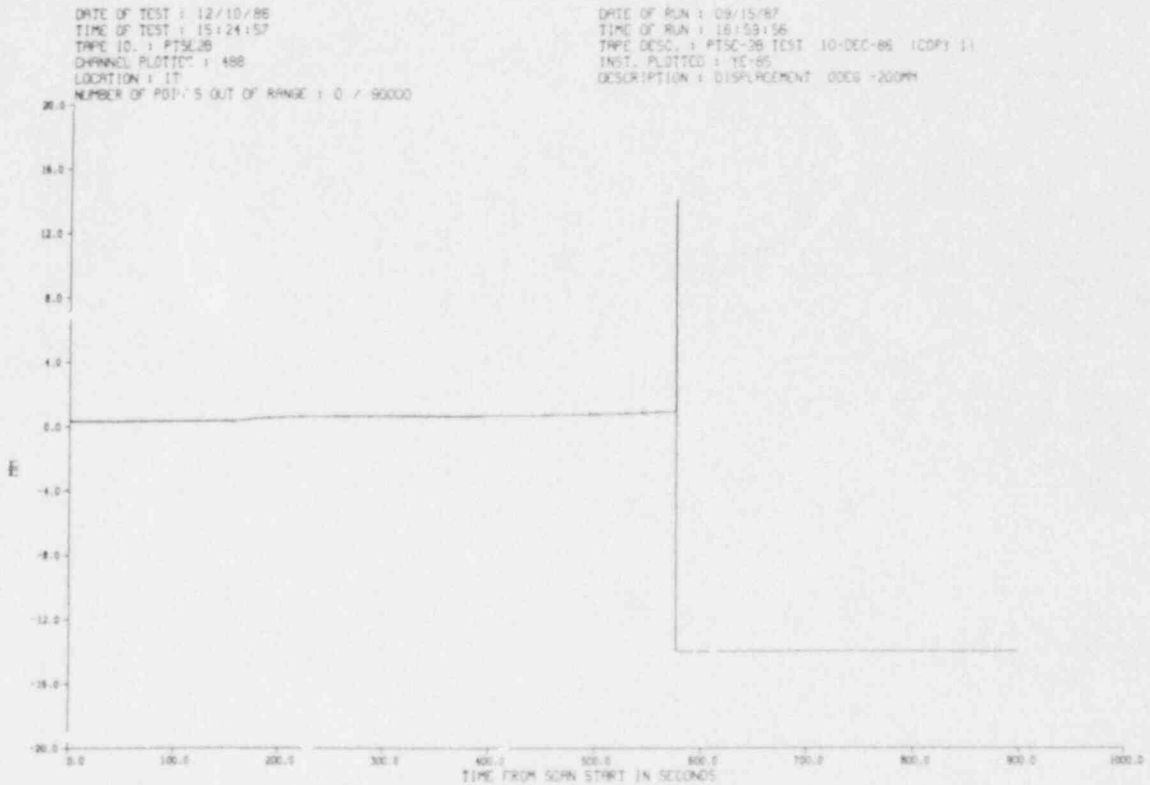
DATE OF TEST : 12/10/86
TIME OF TEST : 15:24:57
TAPE ID. : PTSC28
CHANNEL PLOTTED : 488
LOCATION : IT
NUMBER OF POINTS OUT OF RANGE : 0 / 90000
DATE OF RUN : 09/15/87
TIME OF RUN : 16:59:56
TAPE DESC. : PTSC-28 TEST 10-DEC-86 (COPY 1)
INST. PLOTTED : TC-65
DESCRIPTION : DISPLACEMENT (DCG -200MM
20.0
16.0
12.0
8.0
4.0
0.0
-4.0
-8.0
-12.0
-16.0
-20.0
0.0
100.0
200.0
300.0
400.0
500.0
600.0
700.0
800.0
900.0
1000.0
TIME FROM SCAN START IN SECONDS

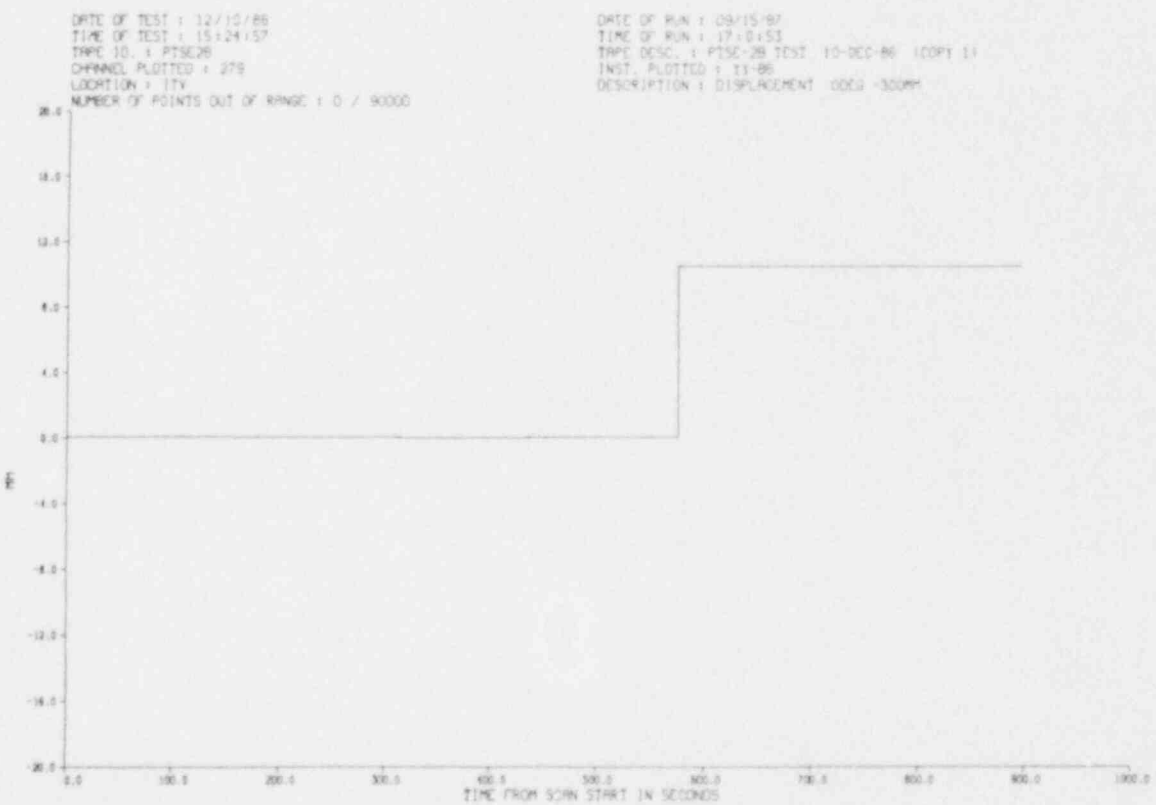
DATE OF TEST : 12/10/86
TIME OF TEST : 15:24:57
TAPE ID. : PTSC28
CHANNEL PLOTTED : 279
LOCATION : ITV
NUMBER OF POINTS OUT OF RANGE : 0 / 90000
DATE OF RUN : 09/15/87
TIME OF RUN : 17:0:53
TAPE DESC. : PTSC-28 TEST 10-DEC-86 (COPY 1)
INST. PLOTTED : I3-86
DESCRIPTION : DISPLACEMENT (DCG -300MM
20.0
16.0
12.0
8.0
4.0
0.0
-4.0
-8.0
-12.0
-16.0
-20.0
0.0
100.0
200.0
300.0
400.0
500.0
600.0
700.0
800.0
900.0
1000.0
TIME FROM SCAN START IN SECONDS

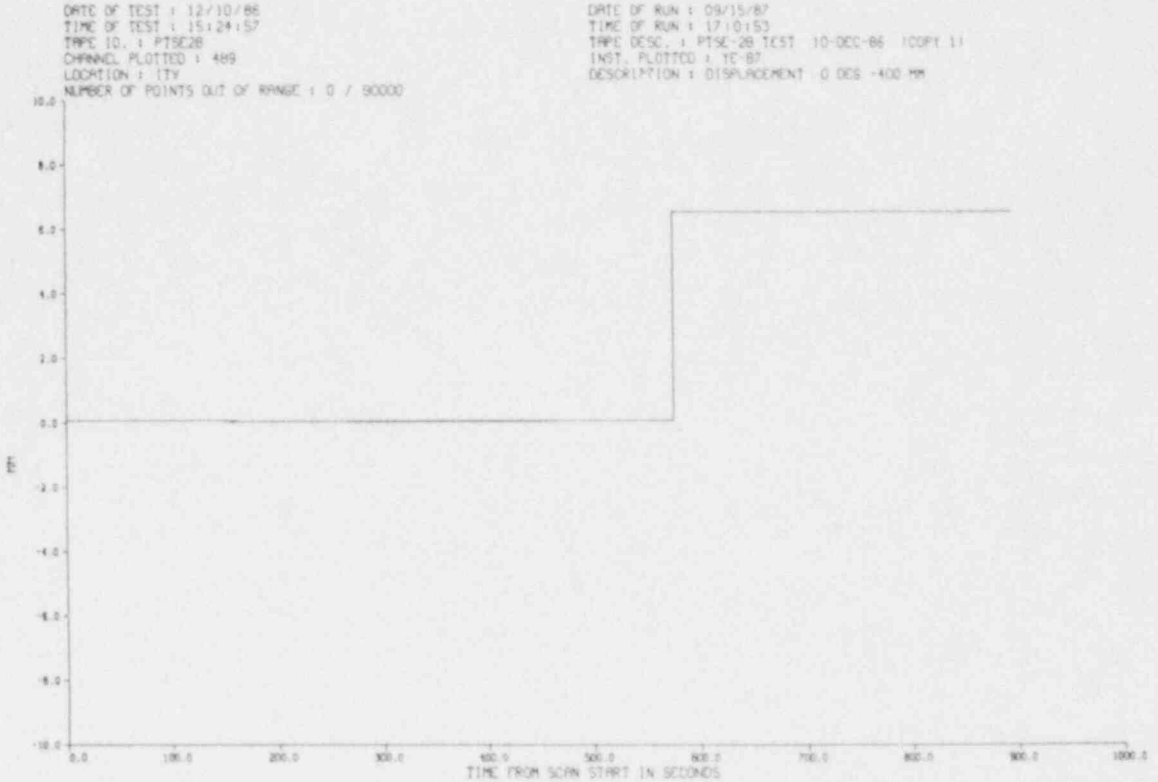
DATE OF TEST : 12/10/86
TIME OF TEST : 15:24:57
TAPE ID. : PTSE2B
CHANNEL PLOTTED : 489
LOCATION : ITV
NUMBER OF POINTS OUT OF RANGE : 0 / 90000
DATE OF RUN : 09/15/87
TIME OF RUN : 17:10:53
TAPE DESC. : PTSE-2B TEST 10-DEC-86 (COPY 1)
INST. PLOTTED : YE-87
DESCRIPTION : DISPLACEMENT 0 DEG -400 MM
10.0
8.0
6.0
4.0
2.0
0.0
-2.0
-4.0
-6.0
-8.0
-10.0
0.0
100.0
200.0
300.0
400.0
500.0
600.0
700.0
800.0
900.0
1000.0
TIME FROM SCAN START IN SECONDS

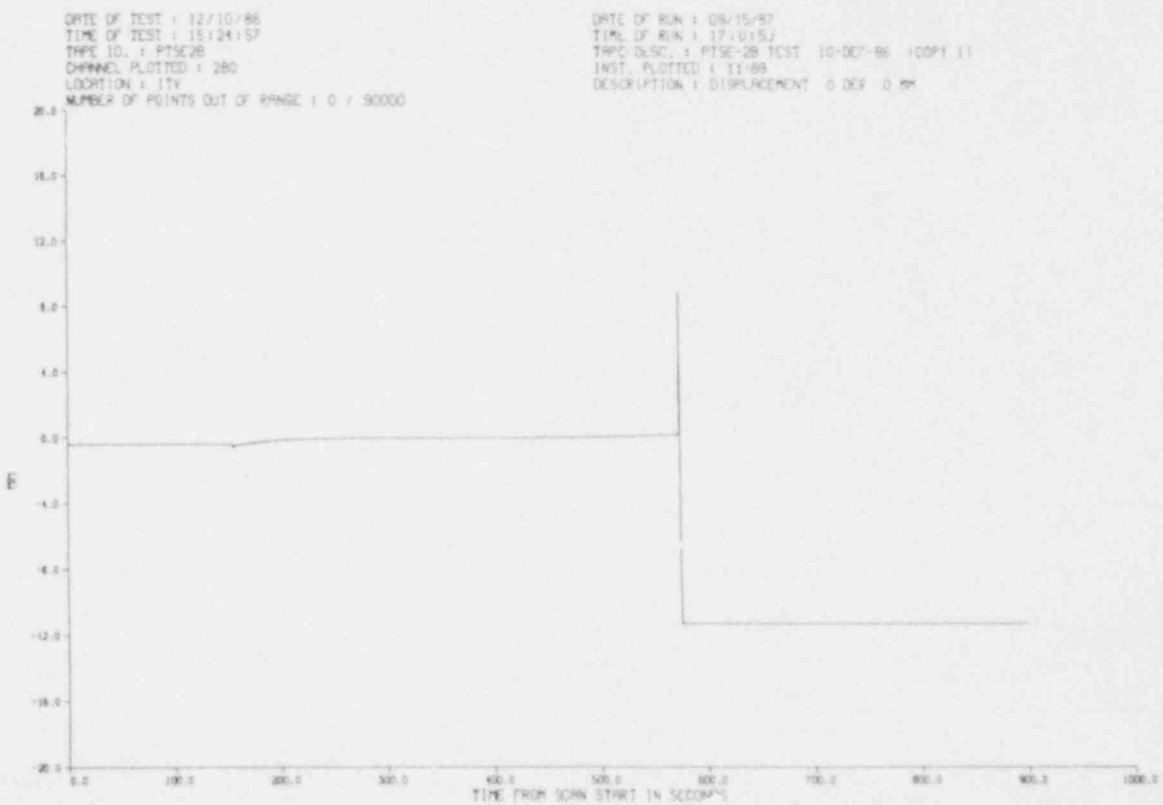
DATE OF TEST : 12/10/86
TIME OF TEST : 15:24:57
TAPE ID. : PTSE2B
CHANNEL PLOTTED : 280
LOCATION : ITV
NUMBER OF POINTS OUT OF RANGE : 0 / 90000
DATE OF RUN : 09/15/87
TIME OF RUN : 17:10:53
TAPE DESC. : PTSE-2B TEST 10-DEC-86 (COPY 1)
INST. PLOTTED : II-89
DESCRIPTION : DISPLACEMENT 0 DEG 0 MM
20.0
16.0
12.0
8.0
4.0
0.0
-4.0
-8.0
-12.0
-16.0
-20.0
0.0
100.0
200.0
300.0
400.0
500.0
600.0
700.0
800.0
900.0
1000.0
TIME FROM SCAN START IN SECONDS

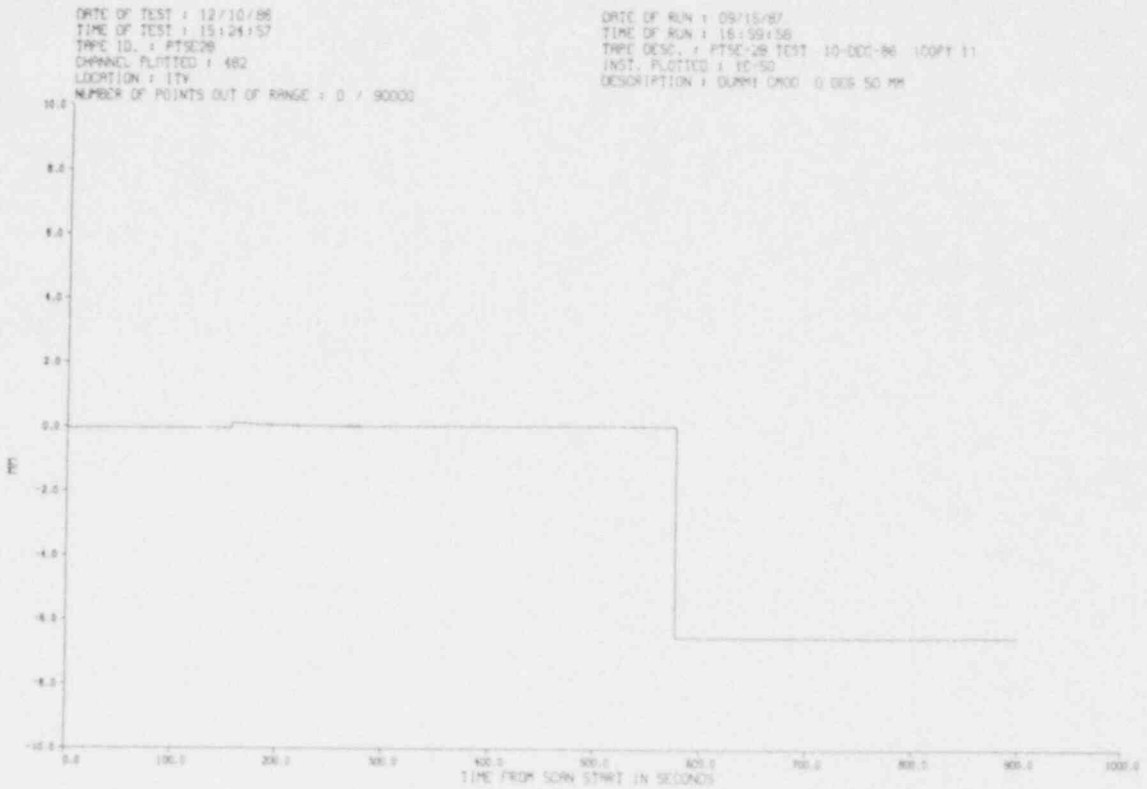
DATE OF TEST : 12/10/86
TIME OF TEST : 15:24:57
TAPE ID. : PTSE2B
CHANNEL PLOTTED : 482
LOCATION : ITV
NUMBER OF POINTS OUT OF RANGE : 0 / 90000
DATE OF RUN : 09/15/87
TIME OF RUN : 16:59:56
TAPE DESC. : PTSE-2B TEST 10-DEC-86 (COPY 1)
INST. PLOTTED : FE-50
DESCRIPTION : DUMMY CMOD 0.005 50 MM
E
TIME FROM SCAN START IN SECONDS

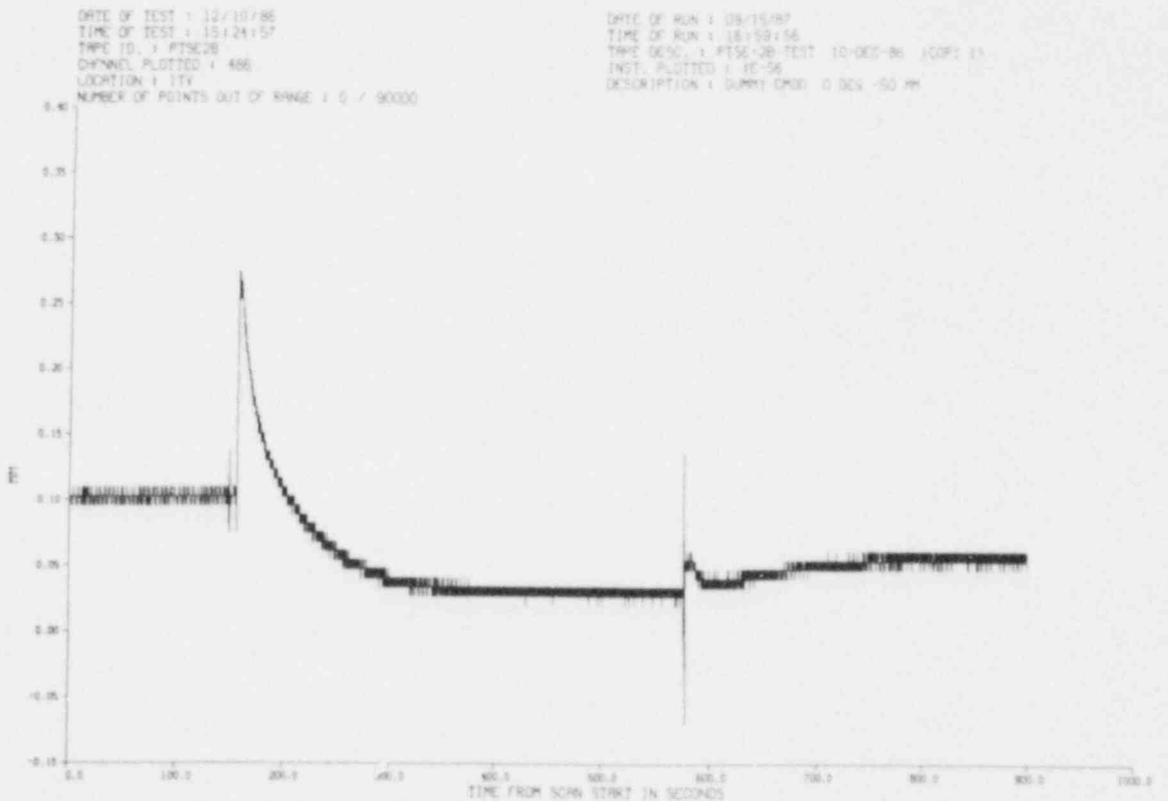
DATE OF TEST : 12/10/86
TIME OF TEST : 15:24:57
TAPE ID. : PTSE2B
CHANNEL PLOTTED : 486
LOCATION : ITV
NUMBER OF POINTS OUT OF RANGE : 0 / 90000
DATE OF RUN : 09/15/87
TIME OF RUN : 16:59:56
TAPE DESC. : PTSE-2B TEST 10-DEC-86 (COPY 1)
INST. PLOTTED : FE-56
DESCRIPTION : DUMMY CMOD 0.005 -50 MM
E
TIME FROM SCAN START IN SECONDS

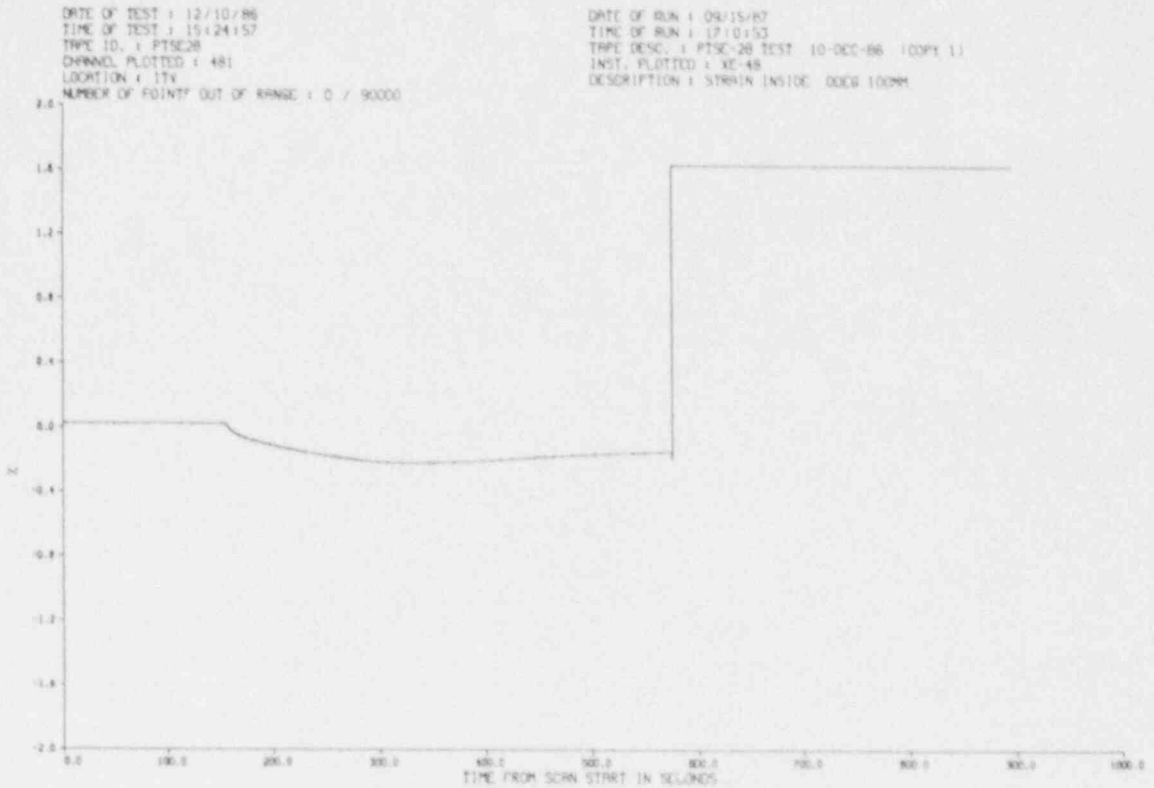
DATE OF TEST : 12/10/86
TIME OF TEST : 15:24:57
TAPE ID. : PTSE28
CHANNEL PLOTTED : 481
LOCATION : ITV
NUMBER OF POINTS OUT OF RANGE : 0 / 90000
DATE OF RUN : 09/15/87
TIME OF RUN : 17:10:53
TAPE DESC. : PTSC-28 TEST 10-DEC-86 (COPY 1)
INST. PLOTTED : XE-48
DESCRIPTION : STRAIN INSIDE 000 100MM
2.0
1.6
1.2
0.8
0.4
0.0
-0.4
-0.8
-1.2
-1.6
-2.0
X
0.0
100.0
200.0
300.0
400.0
500.0
600.0
700.0
800.0
900.0
1000.0
TIME FROM SCAN START IN SECONDS

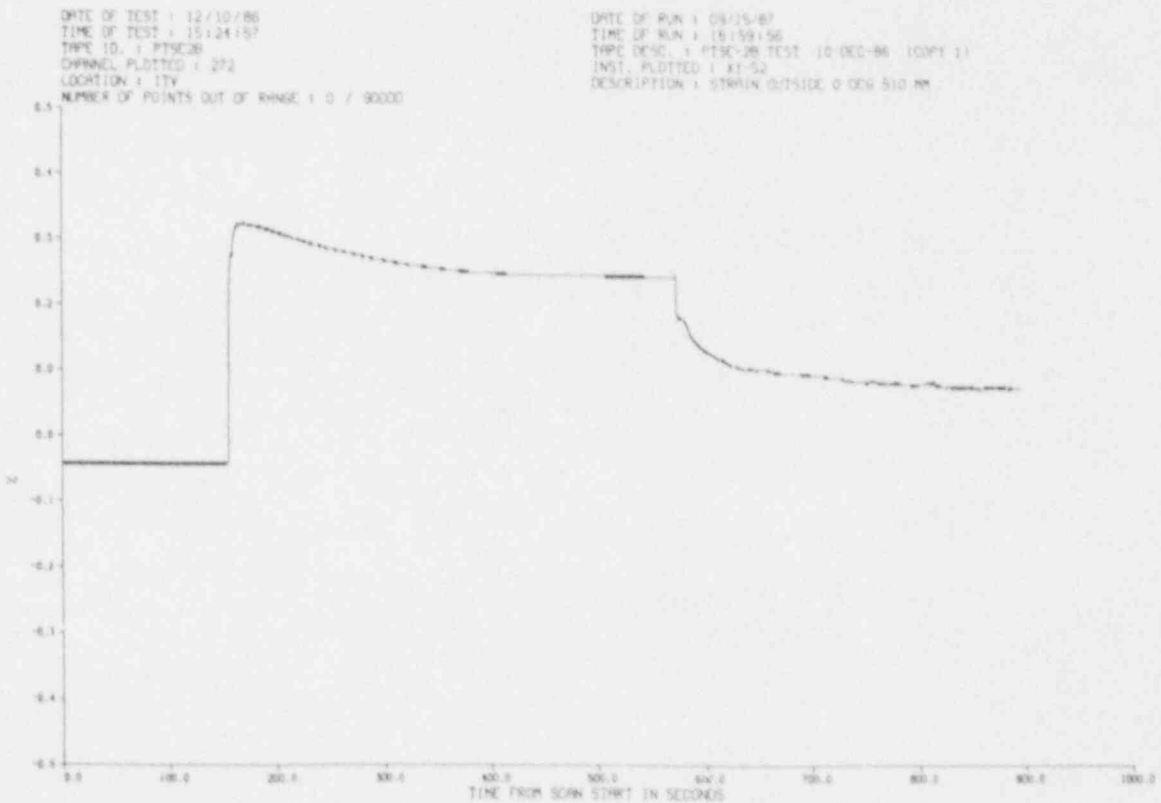
DATE OF TEST : 12/10/86
TIME OF TEST : 15:24:57
TAPE ID. : PTSE28
CHANNEL PLOTTED : 272
LOCATION : ITV
NUMBER OF POINTS OUT OF RANGE : 0 / 90000
DATE OF RUN : 09/15/87
TIME OF RUN : 15:59:56
TAPE DESC. : PTSC-28 TEST 10-DEC-86 (COPY 1)
INST. PLOTTED : AT-52
DESCRIPTION : STRAIN OUTSIDE 0 000 510 MM
0.5
0.4
0.3
0.2
0.1
0.0
-0.1
-0.2
-0.3
-0.4
-0.5
X
0.0
100.0
200.0
300.0
400.0
500.0
600.0
700.0
800.0
900.0
1000.0
TIME FROM SCAN START IN SECONDS

Appendix C

PHOTOGRAPHS OF PTSE-2 FRACTURE SURFACES

The flaw was removed from the PTSE-2 test vessel by flame-cutting along a rectangle 1372 mm long by 178 mm wide, as shown in Fig. C.1. The block was sawed transversely to the crack to divide it into six segments, each about 240 mm long. The end segments, 1 and 6, were trimmed on the unbroken ends, chilled in liquid nitrogen, and broken along the plane of the flaw.

The mating fracture surfaces of the entire flaw are shown in the photographs in Figs. C.2—C.4. Locations of segments are described in Fig. C.1. Features of the fracture surfaces are discussed in Chap. 9.

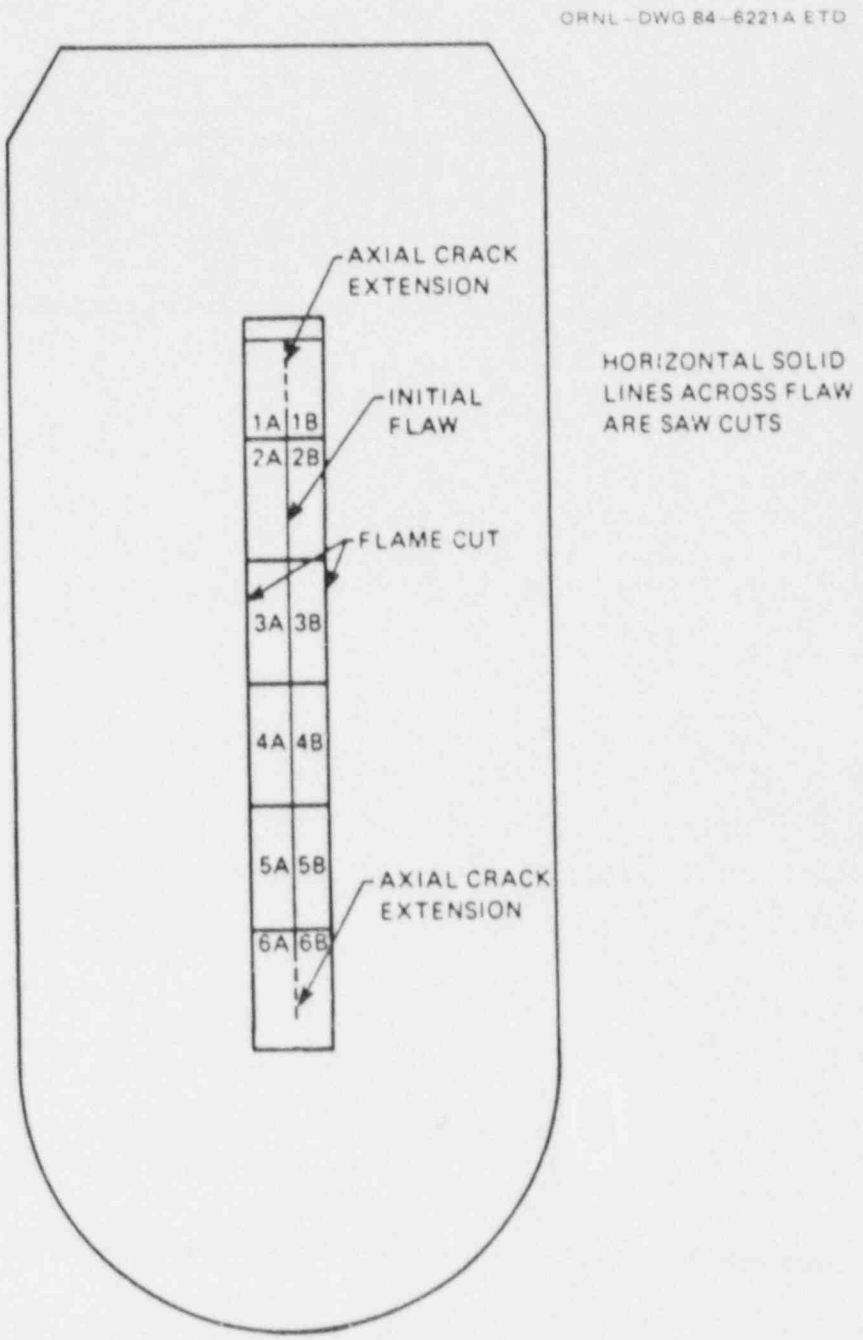

Fig. C.1. Scheme for cutting and labeling PTSE-2 fracture surfaces. Surfaces labeled A are viewed toward left and B, toward right.

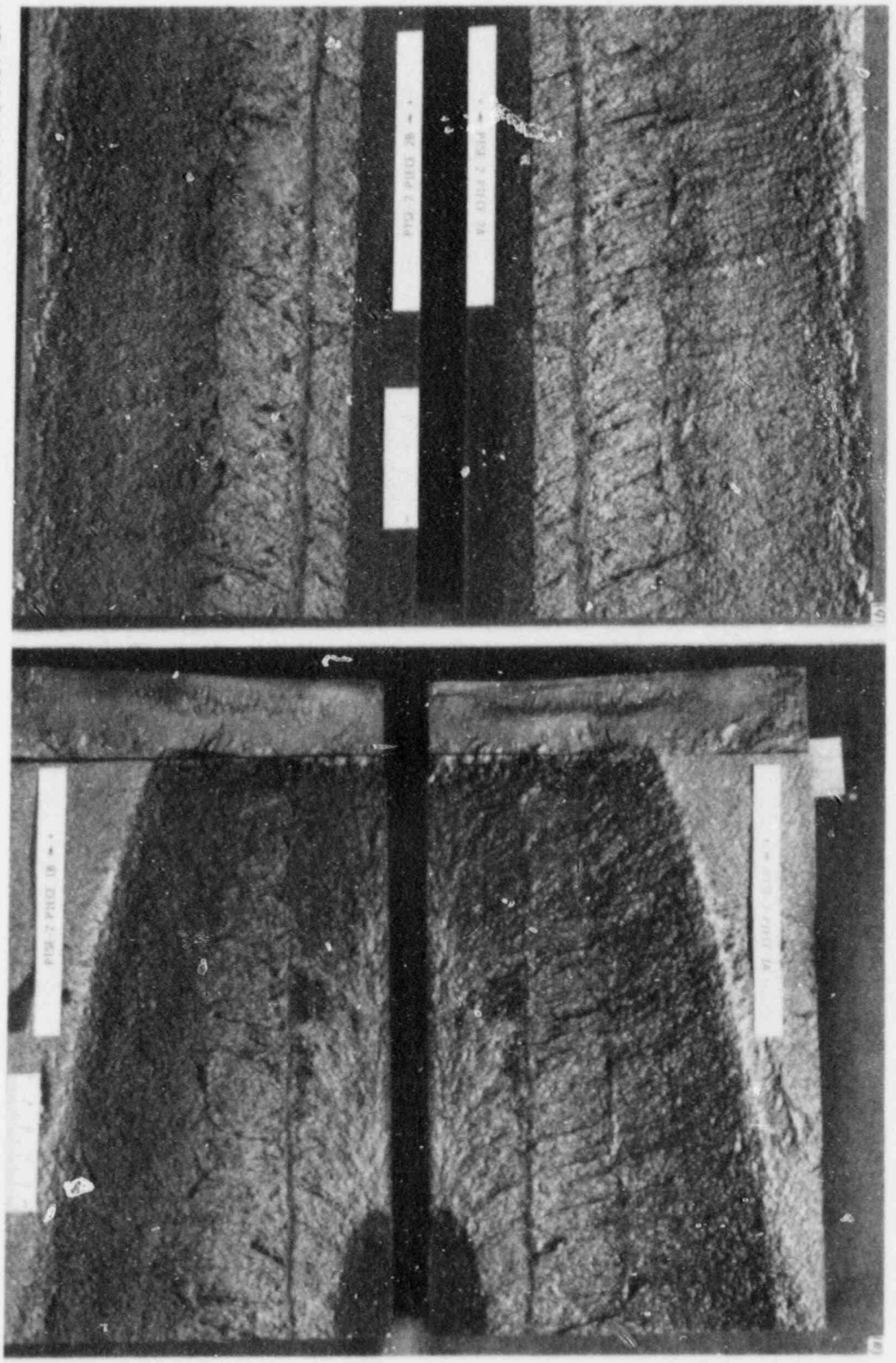

Fig. C.2. Photographs of mating fracture surfaces in (*a*) segment 1 and (*b*) segment 2.

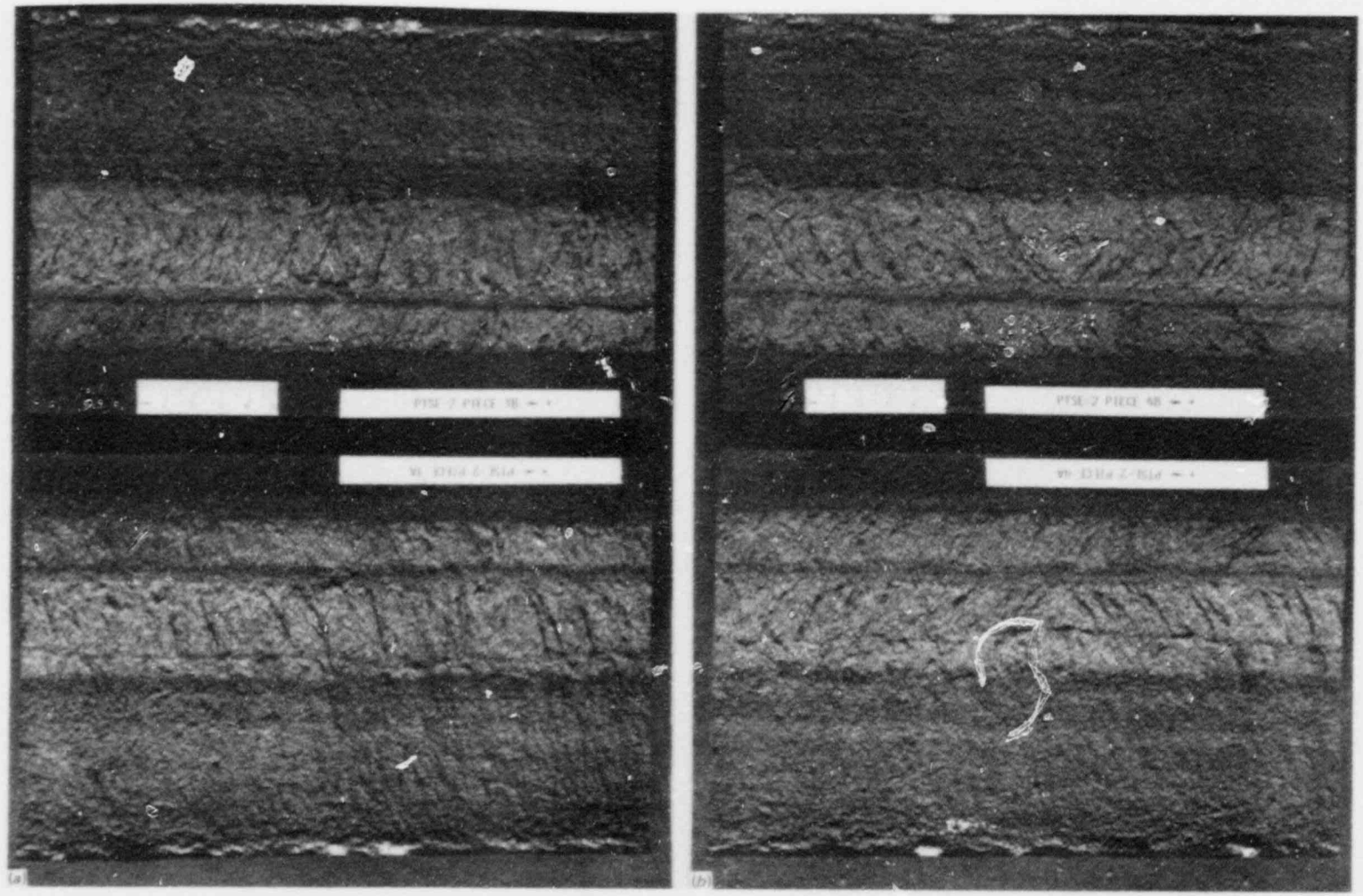

Fig. C.3. Photographs of mating fracture surfaces in (*a*) segment 3 and (*b*) segment 4.

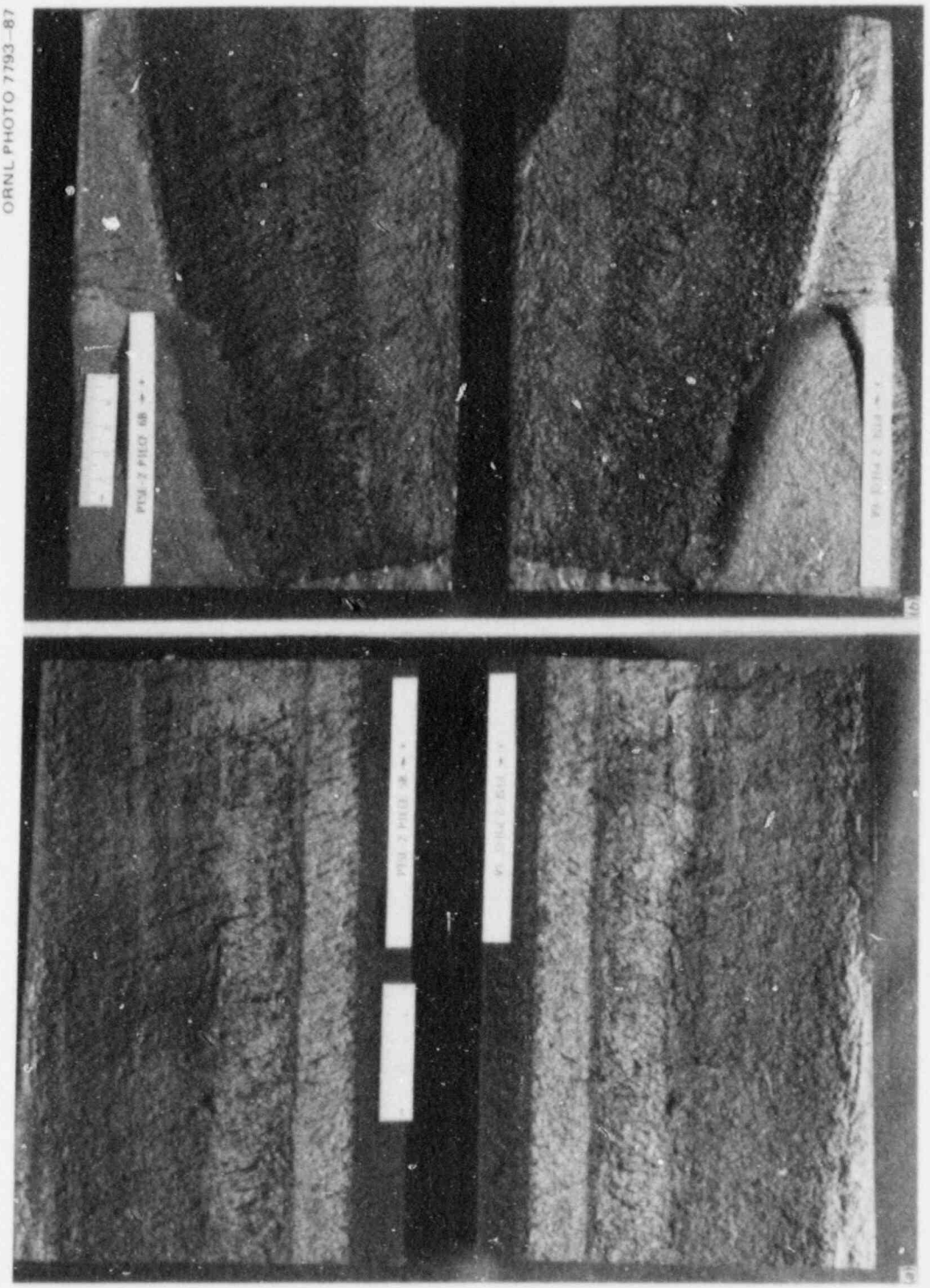

Fig. C.4. Photographs of mating fracture surfaces in (*a*) segment 5 and (*b*) segment 6.

CONVERSION FACTORS[a]

SI unit	English unit	Factor
mm	in.	0.0393701
cm	in.	0.393701
m	ft	3.28084
m/s	ft/s	3.28084
m^3	gallon (U.S. liquid)	264.172
m^3/s	gpm	15,850.3
kN	lb_f	224.809
Pa	torr	7.50064×10^{-3}
kPa	psi	0.145038
MPa	ksi	0.145038
$MPa \cdot \sqrt{m}$	$ksi \cdot \sqrt{in.}$	0.910048
J	ft·lb	0.737562
kW	ton (refrigeration)	0.284349
K	°F or °R	1.8
kJ/m^2	$in.\text{-}lb/in.^2$	5.71015
W/m^2	$Btu/(ft^2 \cdot h)$	0.317210
$W \cdot m^{-2} \cdot K^{-1}$	$Btu/h \cdot ft^2 \cdot °F$	0.176110
$W \cdot m^{-1} \cdot K^{-1}$	$Btu \cdot in./(s \cdot ft^2 \cdot °F)$	0.00192596
$J \cdot kg^{-1} \cdot K^{-1}$	Btu/(lb·°F)	2.38846×10^{-4}
kg	lb	2.20462
kg/m^3	$lb/in.^3$	3.61273×10^{-5}
mm/N	$in./lb_f$	0.175127
$T(°F) = 1.8\ T(°C) + 32$		

[a]Multiply SI quantity by given factor to obtain English quantity.

NUREG/CR-4888
ORNL-6377
Dist. Category RF

Internal Distribution

1.	D. J. Alexander	27-28.	R. K. Nanstad
2.	B. R. Bass	29.	D. J. Naus
3.	S. E. Bolt	30.	N. Perrone
4-7.	R. H. Bryan	31-35.	C. E. Pugh
8.	J. W. Bryson	36.	G. C. Robinson
9.	T. M. Cate	37.	G. M. Slaughter
10.	R. D. Cheverton	38.	J. E. Smith
11.	J. M. Corum	39.	D. A. Steinert
12-16.	W. R. Corwin	40.	H. E. Trammell
17.	J. A. Getsi	41.	ORNL Patent Office
18.	R. C. Gwaltney	42.	Central Research Library
19.	F. M. Haggag	43.	Document Reference Section
20.	S. K. Iskander	44-45.	Laboratory Records Department
21-26.	J. G. Merkle	46.	Laboratory Records (RC)

External Distribution

47. C. Z. Serpan, Division of Engineering Technology, Nuclear Regulatory Commission, Washington, DC 20555
48. M. E. Mayfield, Division of Engineering Technology, Nuclear Regulatory Commission, Washington, DC 20555
49. M. Vagins, Division of Engineering Technology, Nuclear Regulatory Commission, Washington, DC 20555
50. Office of Assistant Manager for Energy Research and Development, Department of Energy, Oak Ridge Operations Office, Oak Ridge, TN 37831
51-52. Technical Information Center, DOE, Oak Ridge, TN 37831
53-302. Given distribution as shown in category RF (NTIS-10)

NRC FORM 335 (2-84) NRCM 1102, 3201, 3202

U.S. NUCLEAR REGULATORY COMMISSION

BIBLIOGRAPHIC DATA SHEET

SEE INSTRUCTIONS ON THE REVERSE

1 REPORT NUMBER (Assigned by TIDC, add Vol. No., if any)
NUREG/CR-4888
ORNL-6377

2 TITLE AND SUBTITLE
Pressurized-Thermal-Shock Test of 6-in.-Thick Pressure Vessels. PTSE-2: Investigation of Low Tearing Resistance and Warm Prestressing

3 LEAVE BLANK

4 DATE REPORT COMPLETED
MONTH: November YEAR: 1987

5 AUTHOR(S)
R. H. Bryan, B. R. Bass, S. E. Bolt, J. W. Bryson, W. R. Corwin, J. G. Merkle, R. K. Nanstad, G. C. Robinson

6 DATE REPORT ISSUED
MONTH: December YEAR: 1987

7 PERFORMING ORGANIZATION NAME AND MAILING ADDRESS (Include Zip Code)
Oak Ridge National Laboratory
P.O. Box X
Oak Ridge, Tennessee 37831

8 PROJECT/TASK/WORK UNIT NUMBER

9 FIN OR GRANT NUMBER
B0119

10 SPONSORING ORGANIZATION NAME AND MAILING ADDRESS (Include Zip Code)
Division of Engineering Technology
Office of Nuclear Regulatory Research
U.S. Nuclear Regulatory Commission
Washington, DC 20555

11a TYPE OF REPORT
ORNL topical

b PERIOD COVERED (Inclusive dates)

12 SUPPLEMENTARY NOTES

13 ABSTRACT (200 words or less)

The second pressurized-thermal-shock test of a 148-mm-thick steel pressure vessel with a 1-m-long flaw was performed to investigate fracture behavior of a vessel under conditions relevant to a flawed nuclear reactor pressure vessel during an overcooling accident. The objectives were to observe transitional crack behavior in a steel with low tearing resistance and the effects of warm prestressing on crack initiation. Two combinations of pressure and thermal transient conditions were imposed on the vessel with initial vessel temperatures of ~300 and 275°C. The first transient, designed for studying warm prestressing, required a depressurization from ~63 MPa and repressurization to ~52 MPa. The crack propagated after being warm prestressed while $K_I > K_{Ic}$. Warm prestressing elevated the load at fracture significantly above K_{Ic}. The second transient produced a cleavage crack propagation and arrest followed immediately by unstable tearing. Stable ductile tearing preceded both brittle fractures and also followed the first crack arrest. The final cleavage propagation arrested at high K_I levels (~420 MPa$\cdot\sqrt{m}$) in spite of the low ductile tearing resistance.

14 DOCUMENT ANALYSIS - a. KEYWORDS/DESCRIPTORS
Experiment
Fracture mechanics
Pressurized thermal shock
Pressure vessel
Cleavage
Crack arrest
Ductile tearing
Fracture toughness
Warm prestressing

b IDENTIFIERS/OPEN-ENDED TERMS

15 AVAILABILITY STATEMENT
Unlimited

16 SECURITY CLASSIFICATION
(This page) Unclassified
(This report) Unclassified

17 NUMBER OF PAGES

18 PRICE

U.S. GOVERNMENT PRINTING OFFICE: 1988—549-484